ISINN-15 Neutron Spectroscopy Nuclear Structure, Related Topics 9 10 6 15 16 Dubna 2008

экз.чит.зала

Joint Institute for Nuclear Research

N-50

NEUTRON SPECTROSCOPY, NUCLEAR STRUCTURE, RELATED TOPICS

XV International Seminar on Interaction of Neutrons with Nuclei

Dubna, May 16-19, 2007

Proceedings of the Seminar

Объединенный институт ядерных исследований БИБЛИОТЕКА Dubna 2008 УДК 539.125.5(042) ББК 22.383.2я431+22.383.5я431+22.383.25я431 N48

Organizing Committee

W. I. Furman (co-chairman), V. N. Shvetsov (co-chairman),
T. S. Donskova (seminar coordinator), M. V. Frontasyeva,
Yu. N. Kopatch, S. V. Kozenkov, Zh. V. Mezentseva, P. V. Sedyshev,
A. M. Sukhovoj

Secretariat: O. E. Karpova, N. A. Malysheva, V. S. Rumyantseva, S. F. Yarovikov

The contributions are reproduced directly from the originals presented by the Organizing Committee.

Neutron Spectroscopy, Nuclear Structure, Related Topics: Proceedings N48 of the XV International Seminar on Interaction of Neutrons with Nuclei (Dubna, May 16–19, 2007). — Dubna: JINR, 2008. — 338 p.

ISBN 5-9530-0169-X

This collection of papers reflects the present state of neutron-aided investigations of the properties of the nucleus, including fundamental symmetries, properties of the neutron itself, neutron-excited reactions and the parameters of the nucleus that determine the reaction cross section, as well as the latest theoretical development of all these problems. The works on experimental investigations in the physics of fission by neutrons of various energies are presented in great detail. The present state of experiments on the physics of ultracold neutrons and facilities to obtain them is described at length. The status achieved by now of the newest (from the viewpoint of technique) experiments and environment studies is covered as well.

Нейтронная спектроскопия, структура ядра и связанные вопросы: Труды XV Международного семинара по взаимодействию нейтронов с ядрами (Дубна, 16–19 мая 2007 г.). — Дубна: ОИЯИ, 2008. — 338 с.

ISBN 5-9530-0169-X

В сборнике представлено современное состояние исследований свойств ядра с помощью нейтронов: фундаментальных симметрий и свойств самого нейтрона, возбуждаемых им реакций и параметров ядра, определяющих их сечения, а также последние теоретические разработки всех этих вопросов. Очень детально представлены работы по всем аспектам, связанным с экспериментальными исследованиями физики деления ядра нейтронами различных энергий. Достаточно полно описано современное состояние экспериментов по физике ультрахолодных нейтронов и установок для их получения, а также достигнутый к настоящему времени статус методически новейших экспериментов и результатов экологических исследований.

УДК 539.125.5(042) ББК 22.383.2я431+22.383.5я431+22.383.25я431

> © Joint Institute for Nuclear Research, 2008

CONTENTS

UCN physics, fundamental properties of the neutron Neutron gamma irradiation method to measure neutron inelastic scattering cross section using very cold neutrons Arzumanov A., Bondarenko L., Chernyavsky S., Geltenbort P., Morozov V:, Panin Yu
The neutron EDM project at PSI Ban G., Lefort T., Naviliat-Cuncic O., Bodek K., Kistryn S., Kuźniak M., Zejma J., Khomutov N., Sabirov B.M., Knowles P., Rebetez M., Weis A., Plonka C., Rogel G., Quéméner G., Rebreyend D., Roccia S., Tur M., Daum M., Henneck R., Heule S., Kasprzak M., Kirch K., Knecht A., Mtchedlishvili A., Pichlmaier A., Zsigmond G14
Project for precise neutron lifetime measurement by the method of ultra- cold neutron (UCN) storage with registration of inelastic scattered neutrons Geltenbort P., Nesvizhevsky V., Arzumanov S., Bondarenko L., Morozov V., Panin Yu., Strepetov A
The Berry phase in neutron physics Ignatovich V.K
Sign of the singlet length of neutron scattering on the proton, neutron radiative capture by the proton and problem of the virtual level of the (np)-system Lyuboshitz V.L., Lyuboshitz V.V
On neutron electromagnetic constants derived from neutron scattering by ²⁰⁸ Pb Mitsyna L.V., Nikolenko V.G., Popov A.B., Samosvat G.S
GRANIT project: a trap for gravitational quantum states of UCN Nesvizhevsky V.V., Petukhov A.K., Börner H.G., Soldner T., Schmidt-Wellenburg P., Kreuz M., Pignol G., Protasov K.V., Rebreyend D., Vezzu F., Forest D., Ganau P., Mackowski J.M., Michel C., Montorio J.L., Morgado N., Pinard L., Remillieux A., Gagarski A.M., Petrov G.A., Kusmina A.M., Strelkov A.V., Abele H., Baeßler S., Voronin A.Yu
New experimental method to determine the averaged squared radius of the nuclei in the process of the direct and isomer fission Panteleev Ts., Oprea C.D., Oprea A.I
Comments to the problem of experimental determination of the neutron- electron scattering length and its theoretical interpretation Popov A.B., Tretvakova T.Yu

A source of ultra-cold neutrons for the gravitational spectrometer "GRANIT" Schmidt-Wellenburg P., Geltenbort P., Nesvizhevsky V.V., Plonka C., Soldner T., Vezzu F., Zimmer O
Nuclear structure 95Mo neutron resonances measured with the DANCE array Krtička M., Agvaanluvsan U., Becker J.A., Bečvár F., Bredeweg T.A., Haight R.C., Jandel M., Mitchell G.E., O'Donnell J.M., Parker W., Reifarth R., Rundberg R.S., Sharapov E.I., Sheets S.A., Ullmann J.L., Vieira D.J., Wilhelmy J.B., Wouters J.M., Wu C.Y
Approximation of sums of experimental radiative strength functions of dipole gamma-transitions in the region $E_{\gamma} \approx B_n$ for the atomic masses $40 \le A \le 200$ Sukhovoj A.M., Furman W.I., Khitrov V.A.
Problems of the experimental determination of parameters of nucleus and applicability of the Bohr-Mottelson hypothesis Sukhovoj A.M., Khitrov V.A
Gamma decay of the compound state and change of structure of the ¹²⁴ Te excited levels Sukhovoj A.M., Khitrov V.A
Calculation of the total gamma-spectra of the fast neutrons capture in the isotopes ^{117,119} Sn for the different parameters of cascade gamma-decay Sukhovoj A.M., Khitrov V.A
Reanalysis of the process of the cascade gamma decay of ¹⁹⁸ Au compound state Sukhovoj A.M., Khitrov V.A., Crawford B.E., Stephenson S.L
Reactions with charged particles. Nuclear data Differential and angle-integrated cross section measurement for the 64 Zn $(n,\alpha)^{61}$ Ni reaction at 2.54, 4.00 and 5.50 MeV Gledenov Yu.M., Sedysheva M.V., Khuukhenkhuu G., Szalanski P. J., Zhang Jiaguo, Cao Rongtai, Guo Li-an, Chen Jinxiang, Wang Jianyong, Zhang Guohui
Investigation of the resonance structure of neutron cross sections of Mo, Ho, Ta, W at the 50 m flight path of the MMF (INR, Troitsk) Grigoriev Yu. V., Pavlova O.N., Zhuravlev B. V., Alekseev A.A., Berlev A.I., Koptelov E.A., Mezentseva Zh. V
文章 (Manager) Angeles (Manager) - Manager (Manager) - Manager (Manager) - Manager (Manager) - Manager (Manager) - Manager (Manager) - Manager
Statistical model analysis for (n, α) reaction cross sections Khuukhenkhuu G., Gledenov Yu.M., Sedysheva M.V., Odsuren M., Badamsambuu J.
등 기계

Complete files of neutron- and proton-induced nuclear data up to 1 GeV for ⁰⁸ Pb, ²⁰⁹ Bi, ²³⁵ U and ²³⁸ U targets Martirosyan J.M., Grudzevich O.T., Yavshits S.G
- and <i>n</i> -induced fission of ²³² Th and ²³⁸ U up to 200 MeV Maslov V.M
Cotal and partial cross-sections of Nb in the energy region from 10 eV to 100 keV Mezentseva Zh.V., Grigoriev Yu.V., Sinitsa V.V., Faikov-Stanczyk H
Nuclear Analytical Methods in the Life Science Application of an electron linac of the IREN facility for multielemental photon activation analysis and production of radionuclides Saljinnyam N., Belov A.G., Ganbold G., Gangrskii Yu.P., Gerbish Sh., Maslov O.D., Theorem V.N
Current status and future needs of nuclear analytical techniques and their applications: A review of IAEA consultants' meeting Crontasyeva M.V
Bremsstrahlung emission from a thick target Khai N.T., Thiep T.D., An T.T., Vinh N.T., Belov A.G., Maslov O.D
Air pollution studies in Opole region, Poland, using the moss biomonitoring technique and neutron activation analysis **Corzekwa S., Pankratova Yu.S., Frontasyeva M.V
Cemporal variations of elemental content in atmospheric aerosol in Bratislava, Slovakia Meresova J., Florek M., Frontasyeva M.V., Pavlov S.S., Holy K., Sykora I
Potential of the Tamarindus Indica leaves as biomonitors or atmospheric contamination in Vietnam Frinh T.T. My, Frontasyeva M.V., Nguyen Hong Nhung
Experimental setup and data processing in studying of the reaction ²³⁵ U(n _{th} , f) t the IBR-2 beam Mexandrov A.A., Alexandrova I.A., Borzakov S.B., Voronov Yu.N., Denisov S.V., Efimov G.L., Kamanin D.V., Kopatch Yu.N., Kuznetsova E.A., Lavrova Yu.E., Mitrofanov S.V., Panteleev Ts., Pyatkov Yu.V., Salamatin V.S., Tsurin I.P., Pyukavkin A.N., Zhuchko V.E
The theory of the T-odd correlations in ternary fission Bunakov V.E., Kadmensky S.G

The estimation of scission neutron parameters from n-n angular Guseva I.S., Gagarski A.M., Petrov G.A., Sokolov V.E., Val'ski G.V. Study of the multi-cluster decays in the neutron induced fission of ²³⁵IJ Kamanin D.V., Kopach Yu.N., Pyatkov Yu.V., Alexandrov A.A., Borzakov S.B., Collinear multicluster decays of Pu* isotopes Printkov Vv. V for HENDES and FOBOS collaborations. 281 Investigations of the angular dependence of neutron-neutron coincidences from ²³⁵U fission induced by thermal neutrons and spontaneous fission of 252Cf Sokolov V.E., Petrov G.A., Gagarski A.M., Krinitsin D.O., Nikolaev D.V., Violations of fundamental symmetries Multilevel approach in the evaluation of the asymmetry effects on (n, p) reaction for ³⁵Cl and ¹⁴N nuclei Search for PT-noninvariant effect in neutron induced gamma transitions Nikolenko V.G., Okunev I.S., Parzhitski S.S., Popov Yu.P., Sinyakov A.V., Tchuvil'sky Yu.M. Reports received after deadline Factor analysis of neutron data Experiment for the measurement of the neutron-electron scattering length in liquid Pb at the TS-3000K thermostat from IBR-2 reactor Oprea C., Oprea A.I., Samosvat G.S., Nikolenko V.G., Savostin V.V., Morozov V.M., Kozlov Zh.A. 328 "Zero" experiment and final result of the measurements of the p-odd asymmetry in the 6 Li $(n,\alpha)^{3}$ H reaction Vesna V.A., Gledenov Yu.M., Nesvizhevsky V.V., Petukhov A.K.,

ISINN-15 Preface

The 15th International Seminar on Interaction of Neutrons with Nuclei: "Fundamental Interactions & Neutrons, Nuclear Structure, Ultracold Neutrons, Related Topics" (ISINN-15), was organized by the Frank Laboratory of Neutron Physics of the Joint Institute for Nuclear Research (Dubna, Russia). The Seminar continues the tradition of the FLNP annual workshops and seminars in the field. ISINN-15 was held in Dubna, Russia from May 16 to 19, 2007. 107 participants attended ISINN-15 representing leading scientific centers of Czech Republic, France, Germany, Republic of Korea, Romania, Russia, Slovak Republic, Switzerland, and other countries. More than 70 oral and poster reports were presented at the Seminar.

The seminar has traditionally attracted many scientists from all over the world, working in the field of neutron nuclear physics. It became traditional to discuss within Seminar the problems of Life Sciences also. ISINN-15 program was not exclusion – two sessions dedicated to the Nuclear Analytical Methods in the Life Sciences were held.

ISINN-15 gave the possibility to know about recent development in construction of the new UCN sources promising outstanding parameters for providing experiments on neutron life time, EDM search and other. First five sessions of the Seminar were dedicated to these problems.

Traditional topics were presented during sessions on reactions with charged particles; nuclear data; violations of fundamental symmetries; nuclear structure and fission induced by slow neutrons.

As usual many informal discussions took place in free time between and after sessions as well as during the Welcome Party and Conference Dinner. Favorable conditions for the Seminar were provided by JINR Directorate. We would like also to acknowledge the traditional support of the Seminar by the Russian Foundation for Basic Research (grant # 07-02-06035-r). This allowed many scientists from Russia to take part in the Seminar and made it possible to publish the Seminar Proceedings.

We wish to thank all the members of the Advisory Committee for their fruitful propositions concerning the scientific program of the Seminar, the Organizing Committee and the Secretariat for their efforts in preparation and holding of the Seminar.

ISINN-15 Co-chairmen

W.I. Furman V.N. Shvetsov

NEUTRON GAMMA IRRADIATION METHOD TO MEASURE NEUTRON INELASTIC SCATTERING CROSS SECTION USING VERY COLD NEUTRONS

Arzumanov¹ A., <u>Bondarenko¹ L.</u>, Chernyavsky¹ S., Geltenbort² P., Morozov¹ V., Panin¹ Yu.

1. RRC KI, Moscow, Russia
2. ILL, Grenoble, France

Abstract

The method utilizes measurement with the help of a (HP)-Ge γ -ray detector by concurrent counting events of neutron capture and neutron up-scattering in the sample that is irradiated by a flux of VCN. The capture event is accompanied by prompt characteristic γ -rays with the well known energies of γ -quanta that correspond to isotopes composed the sample. The up-scattering event transfers VCN into thermal neutron that flies away the sample and then being captured by a special 10 B-converter generates γ -ray with energy 477 keV. Both kinds of events are proportional to corresponding (capture and inelastic scattering) cross sections. Thus the ratio of registered counts of both kinds events does not depend on neither parameters of VCN flux nor sample geometry. Finally the required neutron inelastic scattering cross section is deduced from this ratio basing on known capture cross section for main isotopes of the sample.

Introduction. The total neutron cross section for neutron energy lower than "Bregg's threshold" is equal to $\sigma_{tot} = \sigma_{ie} + \sigma_c + \sigma_{incoh}$ where $\sigma_{ie} \approx 1/\nu$ is cross section for the inelastic scattering, $\sigma_c \approx 1/\nu$ - same for capture, σ_{incoh} - same for elastic coherent scattering and ν is the neutron velocity in the matter. The value $\sigma_{incoh} \le 1$ b and it does not dependent on ν . An additional elastic scattering for very cold neutrons (VCN) with velocity $\nu \le 10$ m/s becomes noticeable if the matter density has a spatial heterogeneity. Corresponding cross section depends on both the neutron velocity and the structure of matter heterogeneity. Existence of the elastic scattering causes indefiniteness of the neutron way in the matter that, in its turn, makes difficult to measure values of σ_{ie} and σ_c by the method of neutron transmission through the sample with definite thickness, see [1,2]. While the neutron capture cross sections are well known, the inelastic ones which depend on both temperature and phonon spectra were poorly investigated. At the same time, the precise knowledge of these cross section values is necessary for:

- 1. determination of the reduced UCN loss coefficient at the wall reflection $\eta = k(\sigma_{ie} + \sigma_c)/(4\pi b)$ (where k is the neutron wave number and b is the coherent scattering length). It is required for the fundamental neutron investigations by storage method (neutron lifetime, anomaly UCN losses etc.);
- 2. calculation the neutron lifetime in the matter $\tau = [nv(\sigma_{ie} + \sigma_c)]^{-1}$ where n is the nuclei density. These values are required for working up the new kind of UCN sources [3] and for cold neutron storage [4];
- 3. solid state physics where σ_{ie} is calculated using different theoretical models of the lattice dynamics. The experimental data for σ_{ie} was obtained for a poor material rank with a bad precision.

12821 F.S.

Experimental installation. UCN with energy E of 50-200 neV come from TGV source of the ILL High Flux reactor to the spectrum shaper which wall is coated by Fomblin oil with limited energy 106 neV, see fig.1.

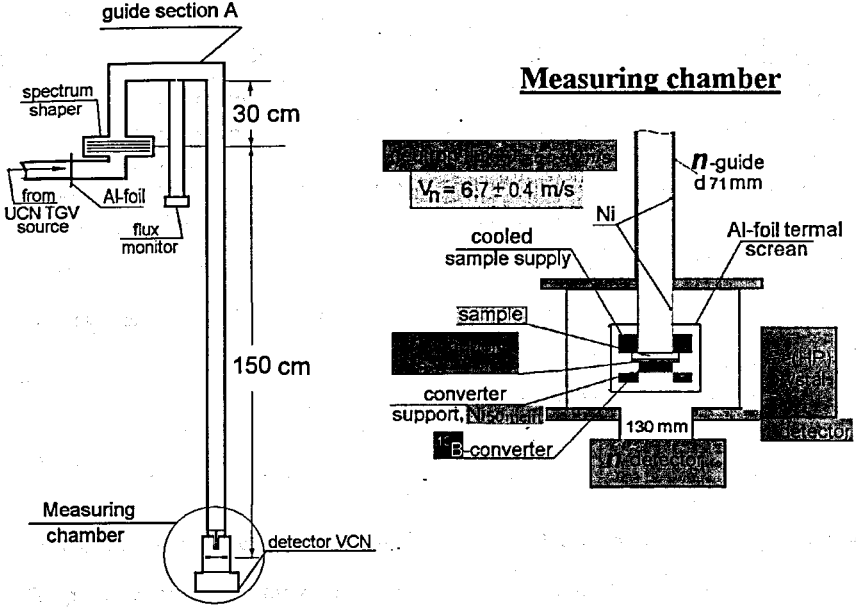


Fig.1. Experimental installation scheme.

Leaving the shaper with $E \approx 50\text{-}106$ neV and accelerating in the vertical neutron guide 150 or 200 cm long and made of Ni, neutrons with $E \approx 200\text{-}255$ or 250-305 neV hit the plane sample of total absorption placed in the chamber. The neutron flux and its absorption are controlled by the ³He filled neutron detector. The chamber has a ¹⁰B-converter and supplied with Ge(HP)- γ -ray detector. The capture event is accompanied by prompt characteristic γ -rays with the known energies of γ -quanta that correspond to isotopes composed the sample. The up-scattering event transfers VCN into thermal neutron that flies away the sample and then being captured by the ¹⁰B-converter generates γ -ray with energy 477 keV at the reaction $^{10}B + n \rightarrow ^{7}Li + \alpha + \gamma(477keV)$. Both kinds of events are proportional to corresponding (capture and inelastic scattering) cross sections. The ratio of registered counts of both kind events does not depend neither on parameters of VCN flux nor sample geometry. The required neutron inelastic scattering cross section is deduced from this ratio basing on known capture cross section for basic isotopes of the sample.

Set-up calibration. Main calibration aim was to define the energy dependence of the ratio $\varepsilon_{ie}/\varepsilon_c(E_i)$ where $\varepsilon_c(E_i)$ is the efficiency to register γ -quanta from the sample with energy E_i and ε_{ie} is the registration efficiency of inelastic scattered neutrons using the count rate at the total absorption peak with energy 477 keV. The 1st step of the calibration procedure was made with the Al-sample 2 mm

thick. Isotope ²⁷Al has a rich characteristic γ -ray spectrum with well defined yield $\gamma^{Al}(E_i)$. The count rate of the γ -detector for γ -ray with energy E_i at the total absorption peak is equal to

 $J_c^{Al}(E_i) = I_0 \frac{\sigma_c^{Al}}{\sigma_c^{Al} + \sigma_{ie}^{Al}} \varepsilon_c(E_i) \gamma^{Al}(E_i) \text{ where } I_0 \text{ is the incident neutron flux, } \sigma_c^{Al}, \sigma_{ie}^{Al} \text{ are neutron}$

capture and inelastic scattering cross sections at room temperature per one atom of the sample correspondingly. Fig.2. presents data of $\varepsilon_c(E_i)$ deduced from the set of experimental values $J_c^{Al}(E_i)$ (dots) and its interpolation curve (full line), the value of $\varepsilon_c(E)$ is shown in related units as the flux I_0 was measured by the UCN detector with unknown absolute value of registration efficiency. Then the energy dependence of the ratio $\varepsilon_{ie}/\varepsilon_c(E)$ was measured using samples with known values of cross sections σ_c^S , σ_{ie}^S (per atom) and chemical content (polyethylene: $(CH_2)_n$, fluorine substituted oil YL VAC 18/8: $(F_3CCF_2OCF_2CF_5)_n$). Count rate at the total absorption peak with energy 477 keV is

equal to $J_{ie}^{S}(477) = I_0 \frac{\sigma_{ie}^{S}}{\sigma_c^{S} + \sigma_{ie}^{S}} \varepsilon_{ie} \gamma_{ie} (477)$ where $\gamma_{ie}(477) = 0.96$ is the yield of γ -quanta with

energy 477 keV from the reaction ${}^{10}B + n \rightarrow {}^{7}Li + \alpha + \gamma (477 keV)$. The corresponding count rate at the peak of neutron capture with energy E_i for definite isotope K is equal to

$$J_c^K(E_i) = I_0 P^K \frac{\sigma_c^S}{\sigma_c^S + \sigma_{ie}^S} \varepsilon_c(E_i) \gamma^K(E_i) \text{ where } P^K = \frac{N_K \sigma_c^K}{\frac{M}{\sum} N_m \sigma_c^M}, N_K, N_m \text{ are the atom quantities of } \sum_{m=1}^{K} N_m \sigma_c^m$$

the basic isotope K and all isotopes m=1,2,...,M that compose the sample, σ_c^K , σ_c^m are their capture cross section (per atom), $\sigma_c^S = \sum_{m=1}^M N_m \sigma_c^m / \sum_{m=1}^M N_m$ and $\gamma^K(E_i)$ is the yield of γ -quanta with energy E_i for isotope K.

So the ratio of $\varepsilon_{ie}/\varepsilon_c(E_i)$ is equal to $\frac{\varepsilon_{ie}}{\varepsilon_c(E_i)} = \frac{J_{ie}^S(477)\gamma^K(E_i)}{J_c^K(E_i)\cdot\gamma_{ie}(477)} \times P^K\left(\frac{\sigma_c^S}{\sigma_{ie}^S}\right).$

For the polyethylene calibrating sample it was measured the γ -peak with energy 2223 keV from the reaction (npd γ) with yield γ^p (2223)=1. Under room temperature for polyethylene the following data

have place: $\left(\frac{\sigma_{ie}^{S}}{\sigma_{c}^{S}}\right) = 16.4$ and $\frac{\varepsilon_{ie}}{\varepsilon_{c}(2223)} = 0.27$.

Measurements. For a sample made of material X that contains a basic isotope B the value of σ_{ie}^{X} is equal to $\sigma_{ie}^{X} = \sigma_{c}^{B} P^{B} \frac{J_{ie}^{X}(477)}{J_{c}^{B}(E_{i})} \times \frac{\gamma^{B}(E_{i})}{\gamma_{ie}(477)} \times \frac{\varepsilon_{c}(E_{i})}{\varepsilon_{ie}}$ where $P^{B} = \frac{N_{B}\sigma_{c}^{B}}{\frac{L}{c}N_{I}\sigma_{c}^{J}}$, N_{B} , N_{I} are the atom quantities of the basic isotope B and all isotopes l=1,2,...,L that compose the investigated sample,

 σ_c^B , σ_c^I are their capture cross section (per atom), J_{ie}^X (477) is the count rate of γ -quanta with energy 477 keV from ¹⁰B-convertor, $J_c^B(E_i)$ is the corresponding count rate at the total absorption peak of basic isotope B with energy E_i and $\gamma^B(E_i)$ is the yield of γ -quanta with energy E_i for isotope B.

The cooling supply allows change the sample temperature in the range 100-300K. So, the measurement enables the value of $\sigma_{ie}^N(T)$ as a function of the sample temperature. This method is applicable for any complex material (alloys, polymers, hydrides etc) with definite content of basic element with known capture cross section and investigated γ -spectra.

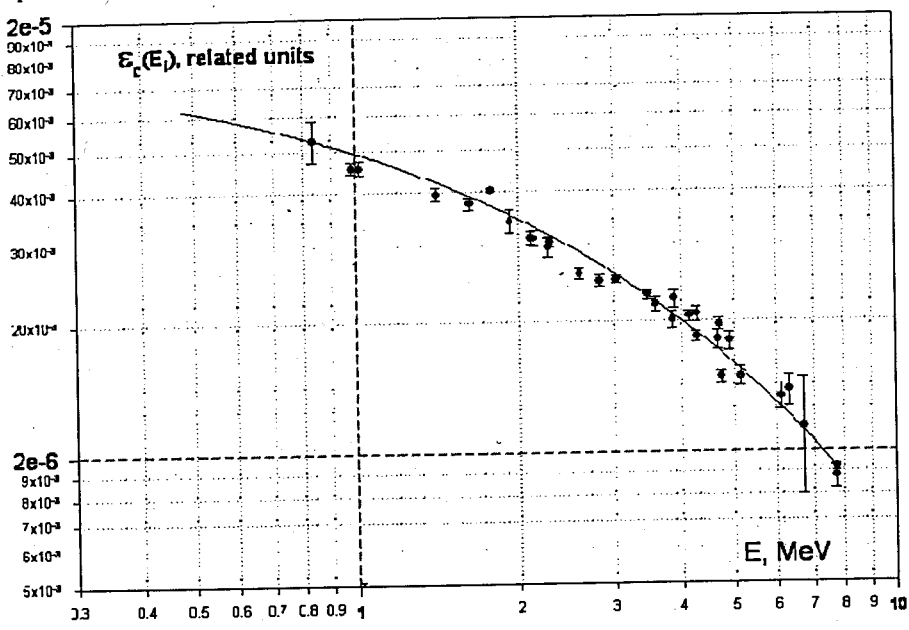


Fig.2. Calibration of the energy dependence of the γ -ray registration efficiency of γ -detector. Dots correspond to $\varepsilon_c(E_i)$ that were measured for row of energy E_i , the curve presents its interpolation.

<u>Results.</u> Below on fig. 3 the temperature dependence presented for samples: solid polymers Polyethylene and Teflon, metals Be, Al, Ni, Graphite for reactors and three types of liquid fluorine polymers.

This investigation was made under the support of RFBR grant 06-02-16417-a and Grant of Russian Research Center "Kurchatov Institute".

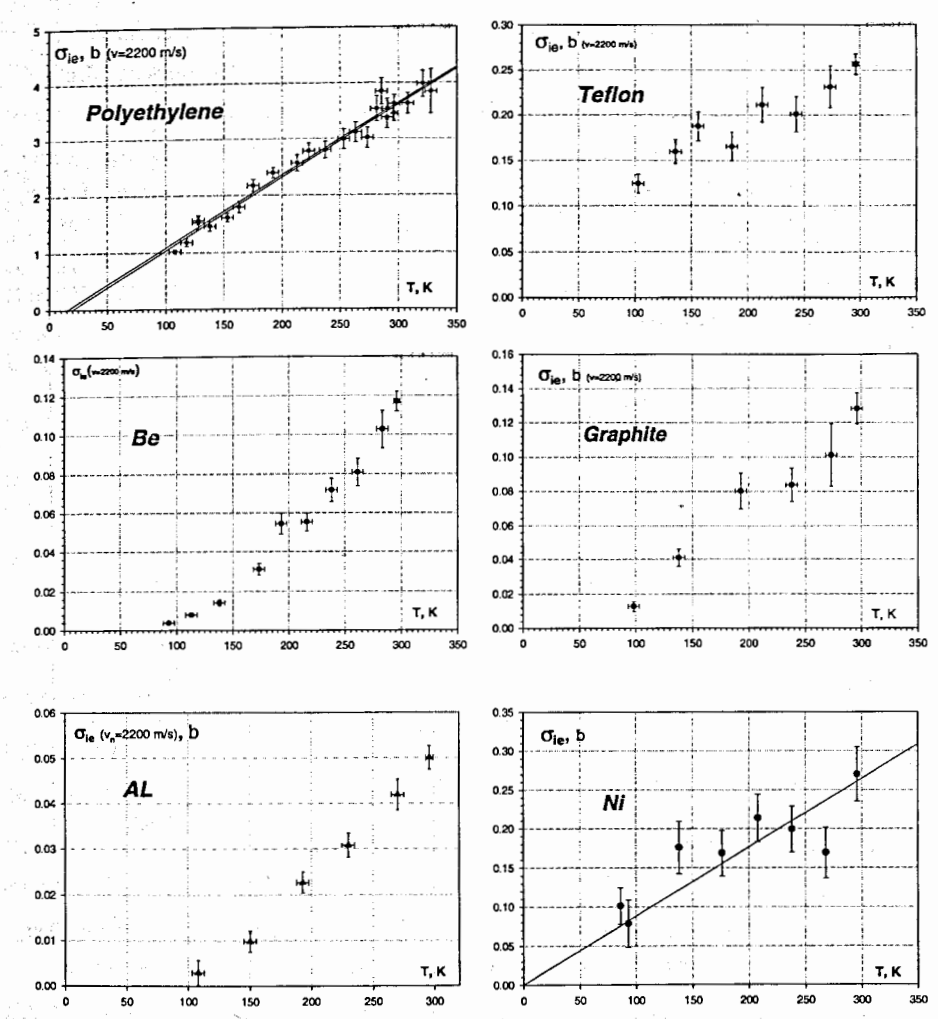
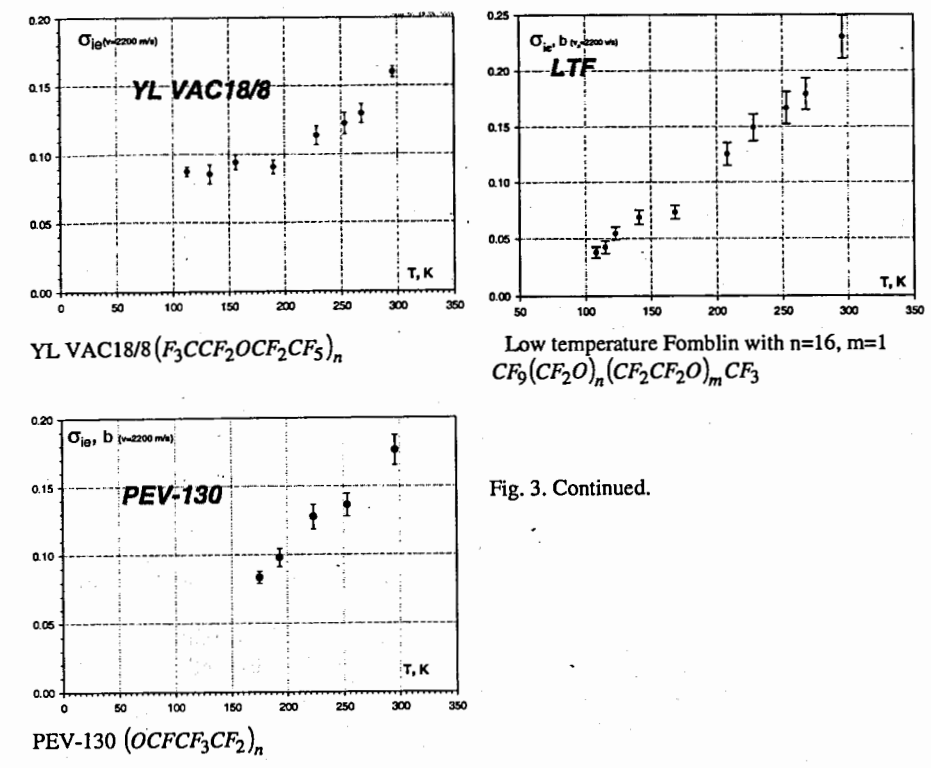


Fig. 3. The inelastic scattering cross section σ_{ie} for different samples as function of temperature T



Authors are in a debt of gratitude to S.T.Belyaev and Yu.M. Kagan for their interest and support of these studies.

References.

- Measurement of total cross sections for interaction of very cold neutrons (VCN) with a rank of materials at temperature range of 80-300K V.Morozov, S.Arzumanov, Yu.Panin, P.Geltenbort(1), L.Bondarenko. ISINN-10, p.376-381, Dubna, 2003.
- Investigation of the radiative capture of UCN at the matter surface S.Arzumanov, L.Bondarenko, P.Geltenbort, E.Korobkina, V.Morozov, Yu.Panin, A.Fomin³, S.Chemjavsky Nuclear Instruments and Methods in Physics Research A 440 (2000) 690-694
- V.V.Nesvizhevsky et al., ILL Annual report 1997, 62-64; EPJ AP 6, 151-154, 1999; Nuclear Physics 62(5), 832-834, 1999
- 4. V.Morozov et al., ILL Experimental Report 3-14-84, 1999

THE NEUTRON EDM PROJECT AT PSI

G. Ban, T. Lefort, O. Naviliat-Cuncic LPC: Laboratoire de Physique Corpusculaire, Caen, France

K. Bodek, S. Kistryn, M. Kuźniak¹, J. Zejma JUC: Jagellonian University, Cracow, Poland

N. Khomutov, B.M. Sabirov JINR: Joint Institute for Nuclear Research, Dubna, Russia

P. Knowles, M. Rebetez, A. Weis FRAP: University of Fribourg, Switzerland

C. Plonka, G. Rogel²
ILL: Institut Laue Langevin, Grenoble, France

G. Quéméner, D. Rebreyend, S. Roccia, M. Tur LPSC: Laboratoire de Physique Subatomique et de Cosmologie, Grenoble, France

> M. Daum, R. Henneck, S. Heule³, M. Kasprzak⁴, K. Kirch, A. Knecht, A. Mtchedlishvili, A. Pichlmaier, G. Zsigmond PSI: Paul Scherrer Institut, Villigen, Switzerland

Abstract

We propose to perform a new high precision measurement of the neutron Electric Dipole Moment (nEDM). Our goal is to reach an accuracy of 5×10^{-28} e.cm or better, i.e an improvement of nearly two orders of magnitude over the present best measurement. Our experiment will use the new spallation UCN source under construction at the Paul Scherrer Institute and will optimize the in vacuum Ramsey resonance technique at room temperature.

1 Motivations

Electric dipole moments (EDM) of particles are direct signatures of T violation and, by virtue of the CPT theorem, also of CP violation. Due to a unique CP violation phase, the Standard Model (SM) predicts extremely small EDM values, far too small for the present experimental sensitivity but also for the next generation of experiments. On the other hand, most of its extensions like SUSY incorporate new CP violation mechanisms and predict much larger EDMs. Actually, the present limit on the neutron EDM, $d_n \leq$

 2.9×10^{-26} e.cm [1], obtained by the RAL-Sussex collaboration at ILL in Grenoble, brings already stringent constraints on the parameters of these models. Improving the accuracy over the present limit provides therefore a valuable opportunity to observe new physics.

2 Experimental technique and planning

Our experiment will optimize the in vacuum Ramsey resonance technique at room temperature and use the new spallation source under construction at the Paul Scherrer Institute [2]. It is expected to become operational towards the end of 2008 and to deliver UCN densities of more than 1000 cm⁻³, i.e. almost two orders of magnitude more than presently available at ILL.

The basic features of our experiment will include (i) an increased sensitivity due to much larger UCN densities at the PSI source, larger storage volume, better polarization product and possibly larger electric field strength, (ii) a better control of systematics thanks to a double-chamber system, (iii) an improved monitoring and stabilization of the magnetic field with an array of laser pumped Cs magnetometers, (iv) an improved co-magnetometer system.

The final goal of 5×10^{-28} e.cm will be reached in three steps: (i) operating and improving the existing room temperature apparatus of the former RAL/Sussex/ILL collaboration until 2008 at ILL, while designing in parallel of a new spectrometer, (ii) gaining a factor 5 in sensitivity to reach $\sim 5\times 10^{-27}$ e.cm with this upgraded apparatus at PSI in 2009-2010, (iii) running with a new apparatus at PSI in 2011-2015 in order to reach an other order of magnitude improvement.

Phase I: While the PSI UCN source is under construction we operate and improve the apparatus of the former RAL/Sussex/ILL collaboration at ILL Grenoble. In order to better control the systematic issues, the magnetic field and its gradients will be monitored and stabilized using an array of laser optically pumped Cs-magnetometers [3, 4]. An order of magnitude improvement compared to the existing field fluctuations within the typical measurement times of 100 s appears certainly feasible. It is also necessary to improve the sensitivity of the Hg co-magnetometer. Other improvements of the system concern new materials, UCN polarization and detection as well as upgrading the data acquisition system. The hardware efforts are accompanied by a full simulation of the system.

Phase II: We intend to move the apparatus from ILL to PSI towards the end of 2008 in order to be ready for data taking for about two years, 2009 and 2010. In addition to the improvements of phase I, an external magnetic field stabilization system and a temperature stabilization are envisaged. Furthermore, work on developing a second co-magnetometer using a hyperpolarized (nuclear paramagnetism) noble gas species is ongoing and might further improve the systematics control. In case of a successful development, also the replacement of the Hg system together with an increase of the electric field strength may become possible. In any case, we anticipate a five-fold sensitivity increase due to the higher UCN intensity, corresponding to a new limit of about 5×10^{-27} e.cm. In parallel to the described activities, the design of a new experimental apparatus has been started

¹also at PSI

²also at LPC

³also at University of Zürich

⁴also at SMI Vienna

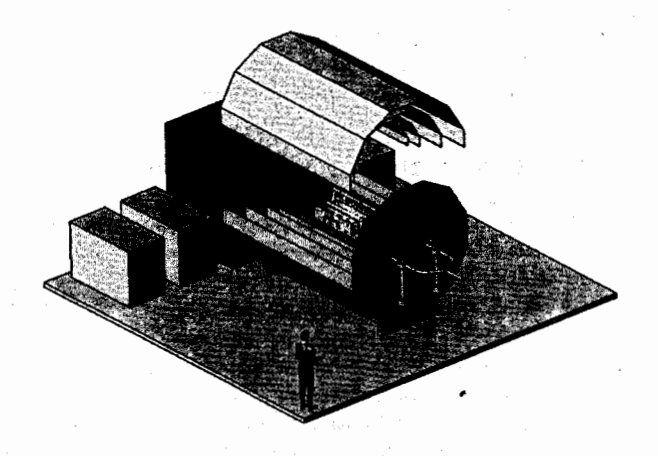


Figure 1: Preliminary concept of the future nEDM spectrometer.

and will be intensified in 2007. After a major design effort in 2008, construction of the new apparatus will start in 2009.

Phase III: The new experiment will be an optimized version of the room-temperature in-vacuum approach, featuring a double neutron chamber system, improved magnetic field control and stabilization with multiple laser optically pumped Cs-magnetometers, and an improved co-magnetometry system. Another order of magnitude gain in sensitivity will be obtained by a considerable increase of the statistics due to a larger experimental volume $(\times\sqrt{5})$, a better adaption to the UCN source $(\times\sqrt{2})$, longer experimental running times $(\times\sqrt{3})$ and by an electric field strength increase $(\times2)$. Completion of the new experimental apparatus is anticipated by the end of 2010, with data taking to occur over 2011–2015.

A preliminary sketch of the future spectrometer is shown on fig.1.

References

- [1] C.A. Baker et al., Phys. Rev. Lett. 97, 131801 (2006).
- [2] http://ucn.web.psi.ch
- [3] S. Groeger, J.-L. Schenker, R. Wynands, and A. Weis, Eur. Phys. J. D 38, 239 (2006).
- [4] S. Groeger, A. S. Pazgalev, and A. Weis, Appl. Phys. B 80, 645 (2005).

PROJECT FOR PRECISE NEUTRON LIFETIME MEASUREMENT BY THE METHOD OF ULTRACOLD NEUTRON (UCN) STORAGE WITH REGISTRATION OF INELASTIC SCATTERED NEUTRONS

ILL: Geltenbort P., Nesvizhevsky V.
RRC KI: Arzumanov S., <u>Bondarenko L.</u>, Morozov V., Panin Yu., Strepetov A.
mor@foton.polyn.kiae.su

Abstract

The method and installation to measure neutron lifetime with precision better than one second are described. The measurements will utilize the method of ultracold neutron (UCN) storage with concurrent registration of neutrons that escape from the storage vessels due to inelastic scattering. The analysis of statistical and methodical errors and the estimate of achievable precision are presented.

Introduction. The precise neutron lifetime value is of a great interest for tests of the Standard Model (SM) at physics of elementary particles. At SM the quarks mixing is described by the unitary matrix by Cabibbo-Kobayashi-Maskava. In particular, the 1st line of the matrix is responsible for mixing of u, d, s, b quarks and its matrix elements have to satisfy the unitary equation: $|V_{ud}|^2 + |V_{us}|^2 + |V_{ub}|^2 = 1$. The V_{ud} -

value from neutron β -decay is equal to $|V_{ud}|^2 = \frac{4908 \pm 4}{\tau_n (1 + 3\lambda^2)} s$ where τ_n is the neutron

lifetime and λ -value can be deduced from the correlation coefficient $\lambda(\lambda+1)$

$$A_0 = -2\frac{\lambda(\lambda+1)}{1+3\lambda^2}$$
 at free neutron β-decay. The recent data of (A₀ = -0.1189(7) [1])

and world mean value (τ_n =885.7(7)s, [2]) lead to $|V_{ud}|$ =0.9717(13). The last result [3] on $|V_{us}|$ = 0.2254±0.0021 from K-decay with a small $|V_{ub}|$ value presents $|V_{ud}|^2 + |V_{us}|^2 + |V_{ub}|^2 = 1 - \Delta = 0.9997(40)$, where $\Delta = 0.0003(40)$. At the same time, the best result [4] on neutron lifetime, that differs from the world mean value on 6.5 standard deviations, 878.5±0.7_{stst}±0.3_{syst}s, gives the value $|V_{ud}|^2 + |V_{us}|^2 + |V_{ub}|^2 = 1 + \Delta = 1.0075(40)$ which is more than unit on about of 2σ [5].

Thus it is of a keen interest to measure the neutron lifetime with a precision better than one second. Project presented below allows to rich the precision level at the range of 0.5-0.9 s with measurement at High Flux Reactor beam PF2 at ILL.

UCN storage process. In the case of mono energy of UCN its amount N(t) changes with time t as $N(t) = N(0) \exp(-\lambda_{\beta}t - \lambda_{l}t)$ where $\lambda_{\beta} = 1/\tau_{\beta}$ is the neutron β-decay probability per time unit while the loss probability λ_{l} presents two aspects of UCN interaction with vessel wall: the UCN capture λ_{c} and its inelastic scattering λ_{ie} . The last process enlarges the neutron energy into almost thermal range. If the vessel dimensions are comparable with the height of the UCN rise in Gravity the time dependence of N(t) remains exponential while the UCN velocity V and density n(z) of UCN gas depend on the level z relatively to vessel bottom: (i) $V = \sqrt{(v_0^2 - 2gz)}$ where V_0 is the UCN velocity at the bottom level and g is gravity acceleration constant:

(ii)
$$n(z) = \sqrt{1 - \left(\frac{2gz}{V_0^2}\right)}$$
 when $z \le \frac{V_0^2}{2g}$.

Объединенный институт ядерных исследований 17 БИБЛИОТЕКА The balance equation is equal to $\frac{d}{dt} \left[\int_{\Omega} n(z) d\Omega \right] = -\frac{1}{4} \int_{S} \mu(V) \cdot n(z) V dS - \lambda \beta \int_{\Omega} n(z) d\Omega$, where $\overline{\mu} = \frac{2\eta}{y^2} \left[\arcsin(y) - y\sqrt{1-y^2} \right]$ is the mean value of the loss coefficient (per one collision), $y = V/V_{\text{lim}}$, V_{lim} is the limiting velocity of the wall material, parameter $\eta = k(\sigma_c + \sigma_{ie})/4\pi b_{cog}$ with the coherent length b_{cog} , σ_c and σ_{ie} are the capture and inelastic scattering cross sections correspondingly, k is the neutron wave number. The loss probability defined as $\lambda_l = \int_{S} \mu(V) \cdot n(z) \cdot V dS / (4 \int_{\Omega} n(z) d\Omega)$. Presenting this value by two factors: $\lambda_l = \eta \times \gamma(V_0)$ where $\gamma(V_0)$, usually called as "geometry factor", depends on velocity and the vessels geometry and is equal to:

$$\gamma(V_0) = \frac{\int_{(s)}^{s} V_{\text{lim}}^2 \left[\arcsin \frac{V}{V_{\text{lim}}} - \frac{V}{V_{\text{lim}}} \sqrt{1 - \left(\frac{V}{V_{\text{lim}}}\right)^2 dS} \right]}{2 \int_{(\Omega)}^{s} V d\Omega}.$$

In the case when stored UCN has a spread velocity spectrum $F(v_0)$ the time dependency of UCN amount is equal to $N(t) = \int_0^{V_{\text{max}}} F(v_0) \exp((-\eta \gamma(v_0) - \lambda_\beta) \cdot t) dv_0$ that leads to the state equation $\frac{dN}{dt} = -\lambda_l(t)N - \lambda_\beta N$ where the loss probability is

expressed by
$$\lambda_{t}(t) = \eta - \frac{\int_{V_{\text{max}}}^{V_{\text{max}}} F(V_{0}) \gamma(V_{0}) \exp(-\eta \gamma(V_{0}) \cdot t) dV_{0}}{\int_{0}^{V_{\text{max}}} F(V_{0}) \exp(-\eta \gamma(V_{0}) \cdot t) dV_{0}} = \eta \cdot \gamma(t).$$

The instantaneous values $\lambda_l(t)$ and $\gamma(t)$ for a rank of UCN spectrum can be presented as $\lambda_l(t) = \eta \gamma(0)(1-kt)$ where $\gamma(0)$ is the initial value of the geometry factor and k is the relative speed of its reduction.

Main states of measurement by UCN storage method. Mean value of the total loss probability is equal to $\mathcal{X} = \lambda_{\beta} + \eta \gamma(0) \left[1 - \frac{kt}{2} \right] = \frac{1}{t} \ln \frac{N(0)}{N(t)}$ where N(0), N(t) are initial (accumulated) and final (remained after store time interval t) amounts of UCN in the vessel. It means that in one experiment it is possible to define only the sum $\mathcal{X}_1 = \lambda_{\beta} + \eta \gamma_1(0) \left[1 - \frac{k_1 t_1}{2} \right] = \lambda_{\beta} + \mathcal{X}_{l1}$. Carrying out the second experiment with higher frequency of UCN collisions on vessel walls one measures the second sum: $\mathcal{X}_2 = \lambda_{\beta} + \eta \gamma_2(0) \left[1 - \frac{k_2 t_2}{2} \right] = \lambda_{\beta} + \mathcal{X}_{l2}$. So, if the ratio $\xi = \frac{\mathcal{X}_{l2}}{\mathcal{X}_{l1}}$ is defined with an error $\delta \xi$ then the value of λ_{β} deduced from $\lambda_{\beta} = \frac{\mathcal{X}_1 \xi - \mathcal{X}_2}{\xi - 1}$ is defined with the error

as $\frac{\delta \lambda_{\beta}}{\lambda_{\beta}} = \sqrt{\left(\frac{\xi}{\xi-1}\right)^2 \left(\frac{\delta \overline{\lambda}_1}{\lambda_{\beta}}\right)^2 + \left(\frac{1}{\xi-1}\right)^2 \left(\frac{\delta \overline{\lambda}_2}{\lambda_{\beta}}\right)^2 + \left(\frac{\overline{\lambda}_{11}}{\lambda_{\beta}}\right)^2 \left(\frac{\delta \xi}{\xi-1}\right)^2}$ where $\delta \overline{\lambda}_1$ and $\delta \overline{\lambda}_2$ are

statistic errors of experimental measurements of corresponding loss probabilities. At all analogue experiments on neutron lifetime measurement, except of [6,7], the calculations has been made to define the ξ -value basing on the assumption that the parameter η is the same for both vessels. Moreover, the ξ -value is defined as $\xi^{\otimes} = \frac{\gamma_2(0)}{\gamma_1(0)}$. Practically the η -value for the same wall material became slightly different $\Delta \eta = \eta_2 - \eta_1$ depending on many technical factors (surface roughness, any contamination and so on). It leads to systematic error $\delta \xi = \xi - \xi^{\otimes} = \frac{\Delta \eta}{\eta_1} \frac{\gamma_2(0)}{\gamma_1(0)}$ and

then methodical error that equal to $\frac{\delta \lambda_{\beta}}{\lambda_{\beta}} = \frac{\chi_{I1}}{\lambda_{\beta}} \frac{\delta \xi}{\xi - 1} = \frac{\chi_{I1}}{\lambda_{\beta}} \frac{\xi}{\xi - 1} \frac{\Delta \eta}{\eta_{1}}$

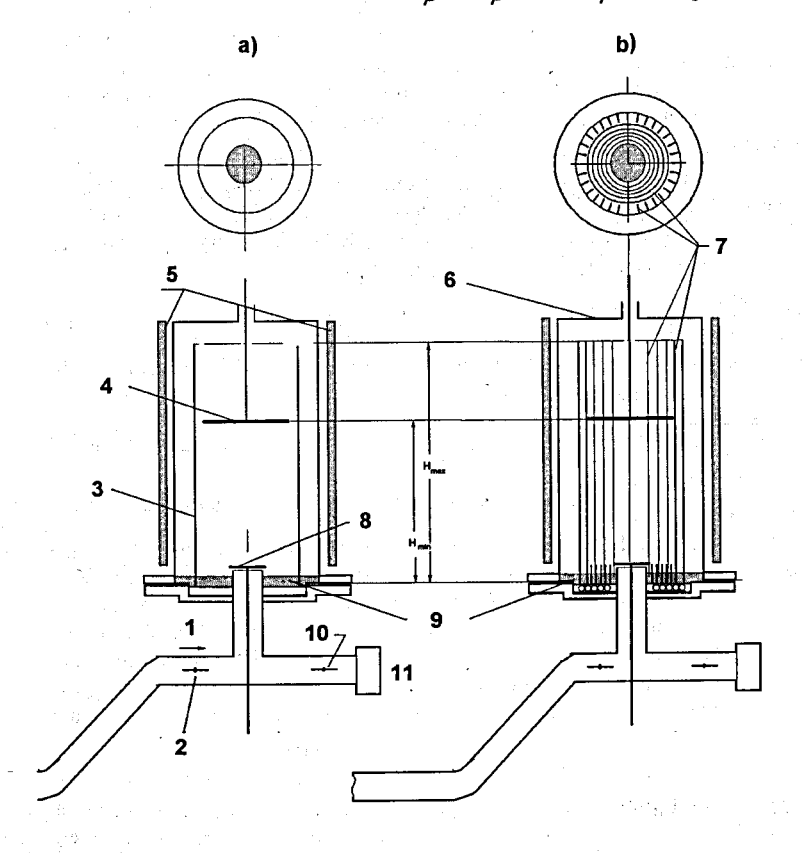


Fig.1. Scheme of complex experiment: a)- experiment no.1, b)- experiment no.2 with additional surface. *I*- neutrons from the UCN source, 2- input UCN shutter, 3-19

cylindrical storage vessel, 4- movable disk-absorber made of polyethylene, 5-counters of the thermal neutron detector, 6- vacuum housing, 7- additional surface, 8-inlet UCN shutter of storage vessel, 9- liquid fluorine polymer, 10- the UCN detector shutter, 11- the UCN detector.

Main states of the method with concurrent registration of inelastic scattered **neutrons.** Firstly the experimental way to define ξ -value was realized in works [6,7]. Interaction of stored UCN with the vessel wall in the case when $\sigma_{ie} >> \sigma_{c}$ leads to the fact that the main part of neutrons escapes from the vessel due to inelastic scattering. At this act neutrons enlarge their energy into thermal range kT (T is the wall temperature). So this neutron flux can be detected with the help of outer neutron counters. Fig.1 (a, b) shows the scheme of a complex experiment. The vacuum housing of the storage installation is surrounded with a vertical set of thermal neutron counters. The storage vessel consists of a vertical cylinder and the bottom of housing. The inner surface of the cylinder is coated by a layer of liquid fluorine polymer while the bottom is covered by the same polymer. During filling interval $t_{\rm fill}$ UCN come from the source into the vessel through the bottom inlet shutter while the shutter of the UCN detector is closed. The upper limit of the UCN energy spectrum $E_{
m up}$ is defined by the level H_{min} of a movable polyethylene disc-absorber. In the end of filling both shutters do close while the UCN detector shutter opens. During the next time interval $t_{\rm cl}$ the UCN spectrum cleans from neutrons with energy that supersedes $E_{\rm un}$. This time interval ends by rising of disc-absorber into the level H_{max} . Then inlet shutter does open and all survival UCN flows into detector to register figure $N_1(0)$. These procedures (filling and cleaning) repeat once more and after the disc-absorber rises up the UCN continue dwelling during store time interval t_1 . In the end of that survival UCN registers as $N_1(t_1)$ and the $\bar{\lambda}_1$ - value is deduced. During interval t_1 outer detector registers the count rate $j_1(\tau)$ of up-scattered UCN:

 $j_1(\tau) = \frac{\varepsilon_{th}}{\varepsilon_{ucn}} \frac{\sigma_{ie} N_1(\tau)}{(\sigma_{ie} + \sigma_c)} \eta_1 \gamma_1(0) (1 - k_1 \tau) = \frac{\varepsilon_{th}}{\varepsilon_{ucn}} \frac{\sigma_{ie} N_1(\tau)}{(\sigma_{te} + \sigma_c)} \lambda_{t1}(\tau)$ where τ is a current time, ε_{th} and ε_{ucn} are the register efficiency of up-scattered neutrons and UCN accordingly. The total amount of up-scattered neutrons is equal to

$$J_{1} = \int_{0}^{t_{1}} \frac{\varepsilon_{th}}{\varepsilon_{tecn}} \frac{\sigma_{te} N_{1}(\tau)}{\left(\sigma_{te} + \sigma_{c}\right)} \lambda_{t1}(\tau) d\tau = \frac{\varepsilon_{th}}{\varepsilon_{tecn}} \frac{\sigma_{te}}{\left(\sigma_{te} + \sigma_{c}\right)} \frac{\left(N_{1}(0) - N_{1}(t_{1})\right)}{\overline{\lambda}_{1}} \overline{\lambda}_{1}. \text{ Then loss probability is equal}$$

to $\overline{\lambda}_{I1} = \frac{\varepsilon_{ucn}}{\varepsilon_{th}} \frac{(\sigma_{te} + \sigma_c)}{\sigma_{te}} \frac{J_1 \overline{\lambda}_1}{(N_1(0) - N_1(t_1))}$. At the second experiment an additional surface

coated by the same liquid fluorine polymer is involved into the vessel. Additional surface consists of thin and narrow strips that hang along the vertical cylinder wall so that the inner limiting cross dimension is very close to cylinder diameter. Analogous thin cylinders of a small height situate coaxially on the bottom in such a way that bottom area increases in the same rate as cylinder one. If the UCN absorption into additional surface is small then the ε_{th} -values for both experiments differ negligibly. As a result of measurement at the second storing experiment one has the value

$$\overline{\lambda}_{12} = \frac{\varepsilon_{ucn}}{\varepsilon_{th}} \frac{(\sigma_{ie} + \sigma_c)}{\sigma_{ie}} \frac{J_2 \overline{\lambda}_2}{(N_2(0) - N_2(t_2))} \text{ and } \xi = \frac{J_2 \overline{\lambda}_2}{J_1 \overline{\lambda}_1} \frac{(N_1(0) - N_1(t_1))}{(N_2(0) - N_2(t_2))}$$

Experimental installation. The double vacuum housing (see fig.2) is made of stainless steel (SS) and consists of two coaxial vertical cylinders, one inside the other, placed on the double bottom flange. Both cylinders, outer 46 cm diameter, inner -42 cm, are sealed to bottom flanges. In the slot (2 cm) between cylinders on the inner

one, the spiral of copper tubes is mounted to transport a coolant fluid from cooling machine to cool the storage vessel. The analogous copper tube spiral is mounted on the inner plane surface of the upper bottom flange. The slit space as well as the room between two flanges is supplied with a turbo pump to evacuate them to the pressure 10⁻⁵ mbar. The bottom of the storage vessel, which is the upper horizontal plane surface of the upper flange, is deepened on 5 cm compared to the outer flange plane. The inner side of the storage vessel is a cylinder made of copper (1 mm thick, 40.5) mm in diameter) coated by a polymer. Cylinder is deepened on 2 cm into fluorine polymer on the bottom. In the vessel bottom a cylinder of 12 cm in diameter is mounted coaxially as a continuation of the inlet neutron guide to fill in it by UCN. The upper cut of this cylinder has a plane edge, on which the inlet UCN shutter seals the vessel when shutter is close. The disk-absorber (36 cm in diameter) is mounted on a rod that moves disk through a vacuum guide connected to a turbomolecular pump that supplies the vacuum at storage vessel on the level of 10⁻⁶ mbar. The 1st experiment is carried out when UCN are stored in copper cylinder. For the 2^d one the additional surface is mounted inside this vessel. The 40 strips and 23 additional cylinders are made of copper foil 100 µm thick. Strips are 1.5 cm broad while additional cylinders are 1.5 cm high. For the storage vessel cooling the cooling machine is used. In the beginning working liquid coolant, coming through copper spiral from cooling machine, cools the inner surface of the housing down to ~ -40°C. Then into the vessel a portion of ⁴He gas fills in while vacuum valve to the pump and inlet UCN shutter are close. During a short time the surface temperature of the storage vessel becomes homogeneous and very close to -40°C. After the He gas is pumped out of the vessel the thermal irradiation supports the surface temperature in a range of $(\pm 3^{\circ}C)$. The UCN detector is a ³He filled proportional counter with an inlet window made of Alfoil (100 µm thick and 15 cm in diameter). The thermal neutron detector is a set of 24 counters of SNM-57 type. Each counter has a cylinder form of 1 m long and 3 cm in diameter and filled with a mixture of 'He (5 atm) and Ar (4 atm). The whole detector is mounted vertically outside of the housing and has two shields: the inner one is a rectangular jacket made of Cd 1 mm thick, the 2^d one is made of the B-contained polyethylene.

The main properties of liquid fluorine polymer YL VAC18/8 and supposed gaskinetics parameters of storage vessel. YL VAC18/8 is a viscous fluid $(F_3CCF_2OCF_2CF_5)$, with molecular weight 2650. As a coating it makes on surface a viscous layer with $E_{lim} = 106.5$ neV, $V_{lim} = 4.55$ m/s. Its inelastic scattering and capture cross sections are correspondingly equal to σ_{ie} =47.5 b and σ_{c} =2.16 b at room temperature for neutrons with velocity 7.76 m/s. The measurement will be carried out at the vessel temperature T_{vess} =-40°C that allows suppress both, the inelastic scattering and quasi elastic reflection with a small energy transfer. The evaluated parameter η is correspondingly equal to 8×10^{-5} at $T_{\text{vess}}=+25^{\circ}\text{C}$, (5-6)×10⁻⁶ at -40°C. These values are the theoretical limits for the loss coefficient due to capture and inelastic scattering into a thermal energy range [8]. However, it is known that results of storage experiments in vessels coated by fluorine polymers does not correspond to evaluated value of the parameter η . Two causes exist to explain it. It was shown [9,10] that in the beginning of cooling down to -40°C theη-value decreases from 2.5-3.5×10⁻⁵ to 5-8×10⁻⁶ that is practically the limited value for this temperature. It takes place due to suppressing of a weak heating [11]. Under continue of cooling (to -50°C) the fluorine polymer layer losses the liquid properties and cracks with production of surface roughness and effective value of the parameter η arises to $2\text{-}2.5\times10^{-5}$. So, the temperature -40°C is optimal for the experiment as the polymer layer remains entire, parameter η is about $5\text{-}8\times10^{-6}$ and weak heating is lower than 2×10^{-6} per one collision. The last value depends not only on the temperature but on the upper energy limit of the UCN spectrum. As it was shown in [11], the estimate of the energy jump of neutron at the weak heating process with liquid fluorine polymer

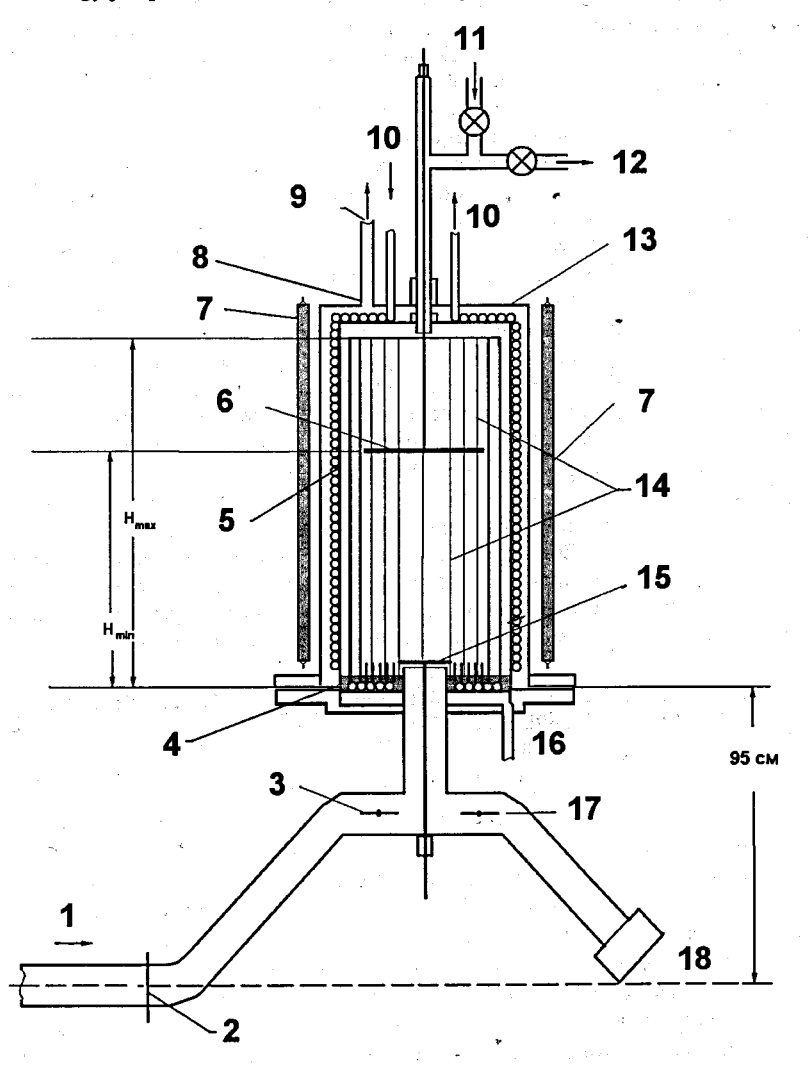


Fig.2. The experimental installation. 1- neutrons from the UCN source, 2- Al foil 100 μ m thick, 3- input UCN shutter, 4- liquid fluorine polymer, 5- inner cylinder of the vacuum housing, 6- movable disk-absorber made of polyethylene, 7- counters of SNM-57 type of the thermal neutron detector, 8- the cooled vacuum housing, 9- is

vacuum guide to pump out the slot between outer and inner cylinders of the vacuum housing, 10- liquid coolant form cooling machine, 11- He-gas source, 12- to storage vessel turbomolecular pump, 13- outer cylinder of the vacuum housing, 14- additional surface, 15- inlet UCN shutter of storage vessel, 16- vacuum guide of the bottom slit in lower flange, 17- the UCN detector shutter, 18- the UCN detector.

is limited by the E_{\max} -value of the main UCN spectrum. Basing on these reasons, the UCN with the maximal arise height of 47 cm will be store at the vessel 95 cm high without a noticeable growth of the UCN losses due to weak heating. Let us suppose that in the end of the cleaning interval (t_{cl}) the energy spectrum of stored UCN is maxwellian: $F(V_0) \propto V_0^2$ where $V_0 < \sqrt{2g H_{\min}} = 3.0$ m/s. So, at the Exp. no.1 the value of $\gamma_1(0) = 4.9718$ s⁻¹. During the store interval $t_1 = 1000$ s, considering that parameter $\eta = 5.10^{-6}$ and the spectrum change due to weak heating is negligible, the γ -factor will be equal to $\gamma_1(t_1) = \gamma_1(0)(1 - k_1 t_1) = 4.9676$ s⁻¹. Hence $k_1 = 1.68.10^{-6}$ s⁻¹, $\overline{\lambda}_1 = 2.4838 \times 10^{-5}$ s⁻¹ and storing time $\tau_1 = (\overline{\lambda}_{II} + \lambda \beta)^{-1} = 867$ s. At the Exp. no.2 the involved additional surface increases the wall area into 3 times, so $\gamma_2(0) = 14.9154$ s⁻¹, and $k_2 = 5.03 \times 10^{-6}$. The storage time interval t_2 has to be changed in order to have the same evolution of the UCN spectrum, i.e. $t_2 = \frac{t_1}{\xi} = \frac{1000s}{3} = 330s$. The analogue figures for Exp. no.2 are as following: $\gamma_2(t_2) = \gamma_2(0)(1 - k_2 t_2) = 14.903$, $\overline{\lambda}_2 = 7.451 \times 10^{-5} \text{s}^{-1}$ and storing time $\tau_2 = (\overline{\lambda}_{IJ} + \lambda_B)^{-1} = 831$ s.

Estimates of statistical and methodical precision of measurement.

The amount of accumulated UCN in the vessel at the PF2 source of ILL will be of 10^5 scale. Considering that $\varepsilon_{th} \approx 0.3$, $\varepsilon_{ucn} \approx 0.7$, $N_1(0) \approx N_2(0) \approx 7.10^4$, the estimate of statistical error $\frac{\delta \overline{\lambda}_1}{\lambda_{\beta}} = \frac{1}{\lambda_{\beta t_1}} \sqrt{\frac{1}{N_1(0)} + \frac{1}{N_1(t_1)}}$ per one measurement cycle will be equal to 0.7% for the experiment no.1 and 1.6% for the 2^d one. Taking into account that the measurement cycle $(t_{ms1,2})$ consists of procedures filling $(t_{ms1}=50 \text{ s})$, spectrum cleaning $(t_{cl}=50 \text{ s})$, storing $(t_{st}=t_1 \text{ or } t_2)$, emptying UCN into detector $(t_c=50 \text{ s})$ and background measurement $(t_{bgr}=330 \text{ s})$, it is possible to manage about 44 cycles per day for Exp.no.1 or 67 – for Exp.no.2. So, during 10 days the achieved statistical error $\frac{\delta \overline{\lambda}_1}{\lambda_{\beta}}$ will be 0.033% and similarly $\frac{\delta \overline{\lambda}_2}{\lambda_{\beta}} = 0.061\%$. Analogously, the statistical error to

define the ξ -value using J_1 and J_2 is equal to: $\delta \xi = \frac{N_2(0) - N_2(t_2)}{N_1(0) - N(t_1)} \frac{J_1}{J_2} \sqrt{\frac{(\delta J_2)^2}{J_1^2} + \frac{(\delta J_1)^2}{J_1^2}}$. Forthcoming values are: for background about 1 s^{-1} and for $J_1 = 410$ and $J_2 = 600$ per a cycle that leads to similar errors $\frac{\delta J_1}{J_1} \approx 0.16$ and $\frac{\delta J_2}{J_2} \approx 0.06$ per measuring cycle or 0.0076 and 0.0023 correspondingly during 10 days run. Resulting statistical error per a 20 day run for $\frac{\delta \lambda_{\beta}}{\lambda_{\alpha}} = 0.059 \times 10^{-2}$ or $\delta \tau_{\beta} = 0.52$ s.

<u>Methodical errors</u>. The 1st source of methodical error is the difference between the registration efficiencies ε_{th1} and ε_{th2} for the 1st and 2^d experiments that appears due to slight difference in geometry of scattering surfaces relatively to the thermal neutron

detector. A small additional inclusion into this difference becomes due to different absorption and scattering of detected neutrons at both experiments. Preliminary evaluation of these efficiencies under the propositions concerning the initial UCN spectrum like $F(v_0) \approx v_0^2$ and mean velocity value of scattered neutrons as 1100 m/s

gives
$$\left|\frac{\varepsilon_{ih1} - \varepsilon_{ih2}}{\varepsilon_{ih1}}\right| < 0.01$$
 from that the error $\left(\frac{\delta \lambda \beta}{\lambda \beta}\right)_{m1} = \frac{\overline{\lambda}_{11}}{\lambda_{\beta}} \frac{\delta \xi}{\xi - 1} = 3.7 \times 10^{-4}$ or

 $(\delta \tau_{\beta})_{m1}$ =0.33 s. Detailed evaluation will be made after measurement of real spectrum of accumulated UCN by the method of plunge disk-absorber.

The 2^d origin of a methodical error is the possible temperature difference between the vessel wall and additional surface. Considering that for the polymer the value of

$$\frac{d\sigma_{ie}}{dT} \approx 0.16$$
 b/grad and $\frac{\sigma_{ie}}{\sigma_c + \sigma_{ie}} \approx 0.9328$ at T=-40°C and basing on the measurement

result of the temperature distribution along all the vessel surfaces, it is possible to expect the mean value of the temperature divergence as ±3°C. Under the proposition that the temperature difference between vessel wall and additional surface is 3°C the

corresponding error
$$\left(\frac{\delta \lambda \beta}{\lambda \beta}\right)_{m2} = \frac{\overline{\lambda}_{11}}{\lambda_{\beta}} \frac{\delta_{5}^{E}}{\xi - 1} = 3.7 \times 10^{-5} \text{ or } (\delta \tau_{\beta})_{m2} = 0.03 \text{ s.}$$

The 3^d kind of methodical error comes from a difference between the UCN registration efficiencies ε_{ucn1} and ε_{ucn2} at both experiments. The specific emptying time, during which UCN flow from storage vessel to detector, is about $t_{emp} \approx 15$ s. So

$$\frac{\varepsilon_{\nu cn1}}{\varepsilon_{\nu cn2}} = \frac{(\overline{\lambda}_2 + \lambda_{emp}) \left[1 - \exp(-(\overline{\lambda}_1 + \lambda_{emp})t_c)\right]}{(\overline{\lambda}_1 + \lambda_{emp}) \left[1 - \exp(-(\overline{\lambda}_2 + \lambda_{emp})t_c)\right]} = 0.999839 \text{ and it leads to } \left(\frac{\delta \lambda \beta}{\lambda \beta}\right)_{m3} \approx 6.4 \times 10^{-6} \text{ or }$$

 $(\delta \tau_{\beta})_{m3}$ =0.006 s.

The estimate of the total resulting error is equal to $(\delta \tau_{\beta}) = [\delta \tau_{\beta}]_{\pi} + [\delta \tau_{\beta}]_{\pi} = (0.52 + 0.33 + 0.03 + 0.006) \text{ s} \approx 0.9 \text{ s}.$

Acknowledges.

Authors should like to express their gratitude to V.L. Aksenov and A.A. Vasil'ev for the help into organizing the experimental study of the physical properties of fluorine polymers. Authors also are thankful to S.M. Chernyavsky, I.M. Morozov, M.V. Lomonosov and A.Korobeinikov for the help in creation of the outer detector of neutrons and other details of the installation.

This work was made under the support of RFBR grant 06-02-16417-a.

References

- 1. Abele H et al. Phys. Rev. Lett. 88 211801 (2002)
- 2. Particle Data Group, Eidelman S et al. Phys. Lett. B 592 1 (2004)
- 3. N. Severijns, M. Beck, O. Naviliat-Cuncic, Rev. Mod. Phys. 78, 991 (2006).
- 4. Serebrov A, Varlamov V, Kharitonov A et al. Phys. Lett. B 605 72 (2005)
- 5.Yu.V. Gaponov, V.V. Khruschov, S.V. Semenov.arXiv:hep-ph/0612283.
- 6. Mampe W, Bondarenko L., at al. JETF Lett. 57 (2) 77 (1993)
- 7. Arzumanov S, Bondarenko L, Chermyavsky S. et al. Phys. Lett. B 483 15 (2000)
- 8. V.Morozov, P.Geltenbort, L.Bondarenko et al. ISINN-10, Dubna, p.376, 2002.
- 9.S.S.Arzumanov et al. Physics of Atomic Nucle, Vol.66, No.10, 2003, p. 1820-1830.
- 10. Evolution of precise measurement of the neutron lifetime. Exp.Rep.ILL. 3-14-216.
- 11. Nesvizhtvsky V.V. et. al. Preprint JINR. Dubna, 1998, P3-98-79.

The Berry phase in neutron physics

V.K.Ignatovich

October 29, 2007

Abstract

The Berry phase in neutron physics is shown to be a linear approximation in adiabaticity parameter of the exact phase, which can be derived analytically. The role of the Berry phase in the experimental search for an electric dipole moment (EDM) of the neutron with ultracold neutrons (UCN) is discussed.

1 Introduction

The Berry phase, θ_B , can be defined as follows. Let's consider the precession of the neutron spin inside a magnetic field B that slowly rotates around z-axis with the angular speed ω (fig. 1). Suppose the neutron spin state is initially $|\xi(0)\rangle$, and after one full revolution of the field, $t \equiv T = 2\pi/\omega$, the spin state becomes $|\xi(T)\rangle = \exp(i\varphi)|\xi(0)\rangle$. The phase φ is usually represented in the form $\varphi = 2\mu BT/\hbar + \theta_B$. The first term is called dynamical phase, and the second term is called Berry phase. The dynamical phase describes the precession of the spin (with the magnetic moment μ) around the field B, as if it was not rotating. The Berry phase is the additional phase, which appears because of the field rotation. It is equal to the half of the solid angle subtended by the field B during its rotation. This angle is equal to b^2/B^2 , where $b = \sqrt{B^2 - B_z^2}$, and B_z is the z-component of the B. So, it looks as if the Berry phase is not related to dynamical interaction of the spin with magnetic field, but only to geometry of the magnetic field variation.

Usually even in the case of a simplest system consisting of just one 1/2 spin particle, the Berry phase is derived using sophisticated mathematics. In [1] the derivation is accompanied by the discussion of the vector potential and magnetic monopoles. In [2] the Berry phase is considered in terms of the level crossing. In [3] the phase is formulated with the second quantization technique and is analyzed by the path-integral formalism.

The complex mathematics may be unavoidable in the general case of an arbitrary spin and an arbitrary hamiltonian with the periodic time dependence. However, to get feeling what the Berry phase is, it is sufficient to get an analytical solution for a simplest system. Such a simplest system is represented by the neutron spin in the field of rf spin flipper. In such a flipper we have a dc permanent field B_z along z axis, and rf field B_{rf} rotating with frequency ω in the (x,y)-plane. The elementary considerations show that the Berry phase is not a fundamental or a "mystical" entity, but rather the result of a linear approximation of the effective spin precession phase $\varphi = \chi(B_z, B_{rf}, \omega)t$, which depends on all parameters

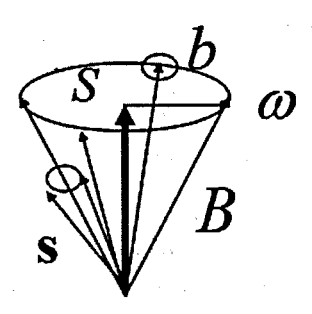


Figure 1: To the definition of the Berry phase. Neutron spin s precesses with the Larmor frequency $\omega_L = 2\mu B/\hbar$ around magnetic field B, which slowly rotates around z axis. After period $T = 2\pi/\omega$ the magnetic field returns to its initial direction. The neutron spin state, which initially was $|\xi(0)\rangle$, acquires the phase factor $\exp(i\varphi)$. The phase φ can be represented by a sum of two terms, $\varphi = \varphi_d + \theta_B = \gamma BT + S/2B^2$. The first term, γBT , is the dynamical phase, which is related to the spin precession around field B. The second term, $\theta_B = S/2B^2$, is the Berry phase. The ratio S/B^2 , where $S = \pi b^2$, and $b = \sqrt{B^2 - B_z^2}$ is the solid angle subtended by the field B during one revolution.

of the system, i.e. on the magnetic fields and ω . The expansion over ω in the adiabatic case, $\varepsilon = \omega/\gamma B_z \ll 1$, is $\chi(B_z, B_{rf}, \omega) = \chi_0(B_z, B_{rf}) + \chi'_\omega \omega$, where $\gamma = 2|\mu|/\hbar$, μ is the magnetic moment of the particle, and

$$\chi'_{\omega} = \frac{d\chi(B_z, B_{rf}, \omega)}{d\omega}\bigg|_{\omega=0}.$$

The Berry phase θ_B is just $\chi'_{\omega}\omega T$. The Berry phase is said to be the geometrical phase $\varphi_g = \chi'_{\omega}\omega t$ after one period of the field rotation, $t = T = 2\pi/\omega$, and the geometric phase φ_g is a linear correction to the dynamical phase $\varphi_d = \gamma B_z t$.

The expression for $\chi(B_z, B_{rf}, \omega)$ is exact for all values of the parameters. Using this expression we can find not only the adiabatic approximation, but also the contradiabatic one, when $\gamma B_z/\omega \ll 1$, $\chi(B_z, B_{rf}, \omega) = \chi_0(B_{rf}, \omega) + \chi_B'B_z$, where

$$\chi_B' = \frac{d\chi(B_z, B_{rf}, \omega)}{dB_z}\bigg|_{B_z=0}.$$

In the following sections, we first find the exact analytical solution to Schrödinger equation for a neutron moving in the two fields. From this solution we can extract the exact expression for the evolution phase $\varphi = \chi t$ of two orthogonal spinor states $|\Phi_{\pm\Omega(t)}\rangle$ polarized along and opposite some pre-defined vector $\Omega(t)$ that rotates synchronously with $B_{rf}(t)$. If the states are $|\Phi_{\pm\Omega(0)}\rangle$ at t=0, then they become $\exp(\mp i\chi t)|\Phi_{\pm\Omega(t)}\rangle$ at time t. Here we will call χt the "effective" phase. For small ω (adiabatic case) it can be expanded in powers of ω , and for large ω (contr-adiabatic case) it can be expanded in powers of $1/\omega$.

Evolution of the state $|\Phi(t)\rangle$ with an arbitrary initial polarization $|\Phi(0)\rangle$ can be represented by the superposition of two orthogonal states $|\Phi_{\pm\Omega(t)}\rangle$. We can find a classical vector that corresponds to $|\Phi(t)\rangle$. We will call this vector a "spin arrow" s(t). It is defined as $s = \langle \Phi(t)|\sigma|\Phi(t)\rangle$, where $\sigma = (\sigma_x, \sigma_y, \sigma_z)$, and σ_i (i = x, y, z) are the Pauli matrices. The motion of the spin arrow tip over the surface of a unit sphere $s^2(t) = 1$ is a good representation of the spin dynamics. We can easily follow it and analytically calculate full phase of its rotation.

In Section 4 we consider the role of the Berry phase in UCN experiments on search of the neutron EDM, and show how the phase is excluded.

2 Formulation of the problem

Let's consider the evolution of the neutron spin in a superposition of two spatially uniform fields, $B_0 = (0, 0, B_z)$ and $B_{rf}(t) = B_{rf}(\cos(\omega t), \sin(\omega t), 0)$. The Schrödinger equation for the neutron wave function $|\psi(r, t)\rangle$ is

$$i\hbar d|\psi(\mathbf{r},t)\rangle/dt = \left(-\frac{\hbar^2 \Delta}{2m} - \mu[\sigma \mathbf{B}_z + \sigma \mathbf{B}_{rf}(t)]\right)|\psi(\mathbf{r},t)\rangle,$$
 (1)

where m and μ are the neutron mass and the magnetic moment respectively. The solution of this equation can be written as

$$|\psi(rr,t)\rangle = \exp(i\mathbf{k}\mathbf{r} - it\hbar^2k^2/2m)|\Psi(t)\rangle.$$
 (2)

Substitution of (2) into (1) gives

$$id|\Psi(t)\rangle/dt = \frac{\gamma_n}{2}[\sigma B_z + \sigma B_{rf}(t)]|\Psi(t)\rangle,$$
 (3)

where γ_n denotes $2|\mu_n|/\hbar$ (neutron's μ_n is negative). To find the solution we need to define the initial condition $|\Psi(\mathbf{r},0)\rangle = |\xi_0\rangle$, i.e. choose the initial neutron polarization.

To solve (3), we use the well known and easily checked relation

$$\sigma B_{rf}(t) = B_{rf}[\sigma_x \cos(\omega t) + \sigma_y \sin(\omega t)] = B_{rf}e^{-i\omega\sigma_x t/2}\sigma_x e^{i\omega\sigma_x t/2}.$$
 (4)

We then represent the solution of (3) in the form

$$|\Psi(t)\rangle = e^{-i\omega\sigma_z t/2} |\phi(t)\rangle. \tag{5}$$

Substitution of (4) and (5) into (3) gives

$$id|\phi(t)\rangle/dt = \frac{(\sigma\Omega)}{2}|\phi(t)\rangle,$$
 (6)

where $\Omega \equiv \Omega(0) = (\gamma_n B_{rf}, 0, \gamma_n B_z - \omega)$ is an effective field for which the Larmor precession frequency is $\Omega = |\Omega|$. It does not depend on time, therefore the solution to (6) is

$$|\phi(t)\rangle = \exp(-i\sigma\Omega(0)t/2)|\phi(0)\rangle.$$
 (7)

The initial condition $|\Psi(0)\rangle = |\xi_0\rangle$ is equivalent to $|\phi(0)\rangle = |\xi_0\rangle$. Substituting the latter into (5) gives

$$|\Psi(t)\rangle = \exp(-i\omega\sigma_z t/2) \exp(-i\sigma\Omega(0)t/2)|\xi_0\rangle = \exp(-i\sigma\Omega(t)t/2) \exp(-i\omega\sigma_z t/2)|\xi_0\rangle,$$
(8)

where

$$\sigma\Omega(t) = e^{-i\omega\sigma_z t/2}\sigma\Omega(0)e^{i\omega\sigma_z t/2} = \sigma_x \gamma_n B_{rf}\cos(\omega t) + \sigma_y \gamma_n B_{rf}\sin(\omega t) + \sigma_z (\gamma_n B_z - \omega). \tag{9}$$

It is important to note that in the argument of the exponent in (8) we have $\Omega(t)t$ instead of $\int_0^t \Omega(t')dt'$ (see [1] Eq. (7)).

Assume that initially the spin is oriented along $\Omega(0)$, therefore

$$|\boldsymbol{\xi}_0\rangle = |\Phi_{\Omega(0)}\rangle = \frac{I + \boldsymbol{\sigma}\boldsymbol{\sigma}(0)}{\sqrt{2(1+o_z)}} |\boldsymbol{\xi}_u'\rangle \equiv |\boldsymbol{\xi}_{\boldsymbol{O}(0)}\rangle,$$
 (10)

where $|\xi_u\rangle$ is the eigen spinor of the matrix σ_z , i.e. $\sigma_z|\xi_u\rangle = |\xi_u\rangle$, and $o(0) = \Omega(0)/\Omega$, i.e. o(0) is the unit vector along the effective field Ω . It is also seen that $|\xi_{O(0)}\rangle$ is an eigen spinor of the matrix $\sigma o(0)$: $\sigma o(0)|\xi_{O(0)}\rangle = |\xi_{O(0)}\rangle$.

The solution to (8) can then be represented as

$$|\Psi(t)\rangle = e^{-i\omega t/2} \exp(-i\sigma\Omega(t)t/2) \frac{I + \sigma o(t)}{\sqrt{2(1+o_z)}} |\xi_u\rangle = e^{-i(\omega+\Omega)t/2} \frac{I + \sigma o(t)}{\sqrt{2(1+o_z)}} |\xi_u\rangle, \quad (11)$$

where $\Omega = |\Omega| = \sqrt{\gamma_n^2 B_{rf}^2 + (\gamma_n B_z - \omega)^2}$, and where we used the fact that for an arbitrary function $f(\sigma o)$ the eigen spinors are $|\xi_{\pm o}\rangle$ and the eigen values are $f(\pm 1)$. We see that the neutron polarization follows exactly direction of the effective field $\Omega(t)$ and only phase of the spinor state changes with time.

The exact expression for the phase is

$$\chi t = \frac{\omega + \Omega}{2}t,\tag{12}$$

which is valid for arbitrary parameters. Now we can approximate the phase in adiabatic $\omega \ll \gamma B_z$ and contradiabatic $\omega \gg \gamma B_z$ cases.

In the adiabatic case we can expand Ω in (12) in powers of ω . In the linear approximation we get

$$\omega + \Omega \approx \gamma_n B + \frac{\omega}{B} (B - B_z) \approx \gamma_n B + \frac{B_{rf}^2}{2B^2} \omega,$$
 (13)

where in the last term we assumed $B_{rf}^2/B^2 \ll 1$, and we made a linear expansion $B_z = \sqrt{B^2 - B_{rf}^2} \approx B - B_{rf}^2/2B$, where $B = \sqrt{B_z^2 + B_{rf}^2}$. Therefore

$$\chi t \equiv (\omega + \Omega) \frac{t}{2} \approx \gamma_n B_z \frac{t}{2} + \frac{1}{4} \frac{B_{rf}^2}{B_z^2} (\gamma_n B_z + \omega) t = \varphi_d(t) + \varphi_g(t). \tag{14}$$

The second term $\varphi_g(t) = B_{rf}^2 \omega t/4B^2$ is called geometric phase. After the time of one cycle, $t = T = 2\pi/\omega$, the geometric phase becomes the Berry phase,

$$\theta_B = \varphi_g(T) = \frac{1}{2} \frac{\pi B_{rf}^2}{B^2}.$$
 (15)

It is equal to the solid angle subtended by the magnetic field during one cycle and multiplied by the magnetic quantum number 1/2.

In the contr-adiabatic case we can expand Ω in (12) in powers of γB_z . In the linear approximation over $1/\omega$ we get

$$\chi t = \frac{\omega + \Omega}{2} t \approx \omega t - \frac{\gamma B_z}{2} t + \frac{\gamma^2 B_{rf}^2}{4\omega} t. \tag{16}$$

Note that the precession frequency $\gamma B_z/2$ around the magnetic field becomes negative, which is equivalent to the change of sign of the magnetic moment.

3 The state with an arbitrary polarization

In real experiments, some of which are discussed in the following, the initial neutron polarization is not necessarily collinear with the direction of the effective field $\Omega(0)$, so we have to consider an initial neutron state $|\Phi(0)\rangle$ with an arbitrary polarization.

Lets consider the initial state to be polarized along the arbitrary vector \mathbf{a} :

$$|\Phi(0)\rangle = |\xi_{\mathbf{a}}\rangle = \frac{1+\sigma \mathbf{a}}{\sqrt{2(1+a_z)}}|\xi_{\mathbf{u}}\rangle.$$
 (17)

This state can be represented as a superposition of the basis states $|\Phi_{\pm\Omega(0)}\rangle$

$$|\xi_{\boldsymbol{a}}\rangle = |\Phi_{\boldsymbol{\Omega}(0)}\rangle\langle\Phi_{\boldsymbol{\Omega}(0)}||\xi_{\boldsymbol{a}(0)}\rangle + |\Phi_{-\boldsymbol{\Omega}(0)}\rangle\langle\Phi_{-\boldsymbol{\Omega}(0)}||\xi_{\boldsymbol{a}(0)}\rangle, \tag{18}$$

where $a(0) \equiv a$. According to Eqs. (8) and (11) the variation of the state (18) can be described by

$$|\Phi(t)\rangle = e^{-i\omega\sigma_x t/2} e^{-i\boldsymbol{\sigma}\Omega t/2} |\xi_{\boldsymbol{a}(0)}\rangle \equiv |\xi_{\boldsymbol{a}(t)}\rangle =$$
 (19)

$$= e^{-i\chi t} |\Phi_{\Omega(t)}\rangle \langle \Phi_{\Omega(0)}||\xi_{\mathbf{a}(0)}\rangle + e^{i\chi t} |\Phi_{-\Omega(t)}\rangle \langle \Phi_{-\Omega(0)}||\xi_{\mathbf{a}(0)}\rangle, \tag{20}$$

where a(t) is defined by the last equality in Eq. (19). The direction of a(t) is the direction of the neutron polarization, or, in other words, the direction of a classical spin arrow $s(t) \equiv a(t)$, defined as $s(t) = \langle \Phi(t) | \sigma | \Phi(t) \rangle$. Lets prove that $a(t)\Omega(t) = a(0)\Omega(0)$; that is, the angle between the neutron spin a(t) and the effective field $\Omega(t)$ does not depend on time. To do so we need to find expectation value of the matrix $\sigma\Omega(t)$ in the state in Eq. (20): $\langle \sigma\Omega(t) \rangle = \langle \Phi(t) | \sigma\Omega(t) | \Phi(t) \rangle$. The substitution of Eq. (20) into this relation gives

$$\langle \sigma \Omega(t) \rangle = \left[e^{i\chi t} \langle \xi_{\boldsymbol{\alpha}(0)} || \Phi_{\Omega(0)} \rangle \langle \Phi_{\Omega(t)} || + e^{-i\chi t} \langle \xi_{\boldsymbol{\alpha}(0)} || \Phi_{-\Omega(0)} \rangle \langle \Phi_{-\Omega(t)} || \right] \langle \sigma \Omega(t) \rangle$$

$$\times \left[e^{-i\chi t} |\Phi_{\Omega(t)} \rangle \langle \Phi_{\Omega(0)} || \xi_{\boldsymbol{\alpha}(0)} \rangle + e^{i\chi t} |\Phi_{-\Omega(t)} \rangle \langle \Phi_{-\Omega(0)} || \xi_{\boldsymbol{\alpha}(0)} \rangle \right] \tag{21}$$

$$= \Omega \left[\langle \xi_{\boldsymbol{a}(0)} || \Phi_{\Omega(0)} \rangle \langle \Phi_{\Omega(0)} || \xi_{\boldsymbol{a}(0)} \rangle - \langle \xi_{\boldsymbol{a}(0)} || \Phi_{-\Omega(0)} \rangle \langle \Phi_{-\Omega(0)} || \xi_{\boldsymbol{a}(0)} \rangle \right], \tag{22}$$

where in Eq. (22) we used the relation $(\sigma\Omega(t))|\Phi_{\pm\Omega(t)}\rangle = \pm\Omega|\Phi_{\pm\Omega(t)}\rangle$. Equation (22) is equivalent to

 $\langle \xi_{\boldsymbol{a}(0)} | (\boldsymbol{\sigma} \Omega(0)) | \xi_{\boldsymbol{a}(0)} \rangle = \boldsymbol{a}(0) \Omega(0) \equiv \Omega a_{\Omega}, \tag{23}$

and this result shows that the projection of the neutron polarization a(t) onto the effective field $\Omega(t)$ is constant; that is, the vector a(t) only rotates around the direction $\Omega(t)$. By taking the constancy of a_{Ω} into account we can represent the initial state Eq. (17) in the more convenient form

 $|\xi_a\rangle = \frac{1+\sigma a}{\sqrt{2(1+a_{\Omega})}} |\Phi_{\Omega(0)}\rangle. \tag{24}$

The state $|\Phi(t)|$ is represented as

$$|\Phi(t)\rangle = e^{-i\omega\sigma_z t/2} e^{-i\sigma\Omega t/2} |\xi_a\rangle = e^{-i\varphi(t)} \frac{1 + \sigma a(t)}{\sqrt{2(1 + a_\Omega)}} |\Phi_{\Omega(t)}\rangle, \tag{25}$$

where

$$\sigma \mathbf{a}(t) = \exp(-i\sigma \mathbf{\Omega}(t)t/2) \exp(-i\omega \sigma_z t/2)(\sigma \mathbf{a}(0)) \exp(i\omega \sigma_z t/2) \exp(i\sigma \mathbf{\Omega}(t)t/2). \tag{26}$$

The part

$$\sigma \mathbf{a}(\omega t) = \exp(-i\omega\sigma_z t/2)(\sigma \mathbf{a}(0)) \exp(i\omega\sigma_z t/2) \tag{27}$$

describes the rotation with angular speed ω of the polarization vector around the z-axis: $\mathbf{a}(\omega t) = (a_{\perp} \cos(\omega t), a_{\perp} \sin(\omega t), a_z)$, where $a_{\perp} = \sqrt{1 - a_z^2}$. Two external operators rotate the neutron polarization around the effective field $\Omega(t)$. Hence, the motion of the neutron spin is a superposition of two rotations: around the z axis with angular speed ω and around the direction $\Omega(t)$ with angular speed Ω .

After a period $t = T = 2\pi/\omega$ we have $a(T) = a(0) \equiv a$ and $\Omega(T) = \Omega(0) \equiv \Omega$. Therefore, according to Eq. (26), we have

$$\sigma \cdot a(T) = e^{-i\sigma\Omega T/2}(\sigma a)e^{i\sigma\Omega T/2} = \sigma \left\{ \frac{\Omega}{\Omega} a_{\Omega} + \frac{[\Omega a]}{\Omega} \sin(\Omega T) + \frac{[\Omega[a\Omega]]}{\Omega^2} \cos(\Omega T) \right\},$$
(28)

and

$$a(T) = \frac{\Omega}{\Omega} a_{\Omega} + \frac{[\Omega a]}{\Omega} \sin(\Omega T) + \frac{[\Omega [a\Omega]]}{\Omega^2} \cos(\Omega T).$$
 (29)

Thee unit vectors

$$e_1 = \frac{\Omega}{\Omega}, \qquad e_2 = \frac{[\Omega[a\Omega]]}{\Omega^2}, \qquad e_3 = \frac{[\Omega a]}{\Omega}$$

constitute orthogonal basis for right clock coordinate system, therefore vector a(T) is obtained by rotation of the vector a(0) around the vector $\Omega(T)$ by the angle ΩT .

This angle is dynamical precession angle of the classical spin arrow around the effective field without any additional terms. However to find the total angle of the spin arrow rotation we need to add to ΩT the angle 2π of rotation around the z-axis. If we expand the

angular speed Ω in ω to the first order and approximate $B_z = \sqrt{B^2 - B_{\rm rf}^2}$ by $B - B_{\rm rf}^2/2B$, we obtain

$$\phi = \Omega T + 2\pi \approx \gamma_n B T - \frac{B_z}{B} \omega T + 2\pi \approx 2 \left(\frac{1}{2} \gamma_n B T + \frac{\pi B_{\rm rf}^2}{2B^2} \right). \tag{30}$$

We see that $\phi(T) = 2\varphi(T)$, that is, the rotation angle of the spin is equal to twice the precession phase (14) at t = T. The factor of two is a typical difference between quantum and classical phases, which is illustrated in Eqs. (4) and (5). Magnetic field $B_{\rm rf}$ rotates with frequency ω (Eq. (4)), while phase of the quantum state $|\Psi(t)\rangle$ changes with frequency $\omega/2$ (Eq. (5))

In the following we shall approximate B in Eq. (30) by B_z , which is acceptable when $B_{\rm rf} \ll B_z$.

4 The Berry phase in neutron EDM experiments

The Berry phase was found to be important, for instance, in experiments [4] with ultracold neutrons (UCN) searching for neutron electric dipole moment (EDM). Before we show how it appears in these experiments, lets first refresh the idea of these experiments and point out the commonly met difficulties.

4.1 The idea of the UCN storage experiment

In the EDM experiments UCN are stored in a cylindrical bottle [4] oriented vertically along the axis z. There is a uniform magnetic field, $\mathbf{B} = (0, 0, B_z)$, and an electrical field, $\mathbf{E} = (0, 0, \pm E)$ inside the bottle. Both fields are oriented parallel to the cylinder. The goal of the experiment is to measure the precession frequency, ω_n , of the neutron spin,

$$\hbar\omega_n = 2|\mu_n|(B_z + d_n E),\tag{31}$$

and its linear dependence on the electric field E. Here, contrary to typical notations, d_n is dimensionless, $d_n = eD_n/|\mu_n|$, where $|\mu_n| = e \times 1.91\hbar/2m_nc = e \times 2 \cdot 10^{-14}$ cm is the absolute value of the neutron magnetic moment, e is the elementary charge, and D_n has units of length and is currently found to be less than $2.9 \cdot 10^{-26}$ cm [4]. Thus, $d_n \leq 1.45 \cdot 10^{-12}$. Fields B_z and E in (31) should have the same units. So, if B_z is measured in Gauss, E must be in CGS units, i.e. its value is (10/3)E when E is in kV/cm.

To reliably measure the linear dependence on E we must be sure that the field B_z does not change during the measurements. In reality B_z fluctuates due to changes in environment. The fluctuations can be compensated by measuring the magnetic field B_z with the help of polarized mercury atoms ¹⁹⁹Hg stored in the bottle along with the UCN. The precession frequency for ¹⁹⁹Hg atoms is given by the similar equation,

$$\hbar\omega_{Ha} = 2\mu_{Ha}(B_z + d_{Ha}E),\tag{32}$$

where $\mu_{Hg} = |\mu_n|/3.842$, and d_{Hg} is measured to be less than $8 \cdot 10^{-14}$ in units of μ_{Hg} .

The ratio of Equations (32) and (32) is

$$\frac{\omega_n}{\omega_{Hg}} = \frac{\mu_n}{\mu_{Hg}} \frac{B_z + d_n E}{B_z + d_{Hg} E} \approx \frac{\mu_n}{\mu_{Hg}} \left(1 + (d_n - d_{Hg}) \frac{E}{B_z} \right). \tag{33}$$

Alternatively, the ratio can be represented with the help of R_a , defined as

$$R_a(\uparrow,\uparrow) \equiv \frac{\mu_{Hg}}{\mu_n} \frac{\omega_n}{\omega_{Hg}} = 1 + (d_n - d_{Hg}) \frac{E}{B_z}, \tag{34}$$

where the first arrow shows the direction of the magnetic field B_z , and the second arrow shows the direction of the electric field. Thus, in absence of the electric field, the ratio R_a should be equal to unity. Later we shall see that it is not so simple!

4.2 A false effect

The main problem in EDM experiments is to understand whether there are no false effects that can mimic the EDM. The most dangerous false effect is related to the relativistic correction to magnetic field,

$$\boldsymbol{B}_{nv} = [\boldsymbol{v}_n \times \boldsymbol{E}]/c, \tag{35}$$

which gives false EDM $d_f = v/c = \approx 10^{-8}$ for UCN moving with the speed¹ $v_n = 5$ m/s. The value of d_f is four orders of magnitude larger than the searched EDM, but it seems to be not dangerous because UCN have the isotropic distribution of v_n and thus the field B_{nv} averages to zero. However, B_{nv} is orthogonal to z-axis. Neutrons that move around z-axis² with the speed

 $\omega_{nv} \sim \frac{v_n}{R},$ (36)

where R is the cylinder's radius, see the rotating field, and this field creates additional geometric phase. Nevertheless, this phase is not dangerous because it is quadratic in electric field and has the opposite sign for neutrons rotating around z-axis in the opposite directions.

4.3 An interference neutron Berry phase

The geometric phase becomes dangerous when the magnetic field B is not completely homogeneous. If B_z slightly changes along z-axis as shown in Fig. 2 [5], this change, $B'_z = dB_z/dz$, inevitably creates magnetic field B_r perpendicular to z-axis

$$B_{r} = -\frac{B_{z}^{\prime}}{2} r_{\perp}, \tag{37}$$

where $r_{\perp}=(x,y,0)$. The total field perpendicular to z-axis and rotating in the reference frame of the neutron becomes $b_n=B_{nv}+B_r$. The geometric phase $(b_n^2/4B_z^2)\omega_{nv}t$ now contains the interference term $\varphi_{ni}=(B_r\cdot B_{nv}/2B_z^2)\omega_{nv}t$, which is linear in E and has

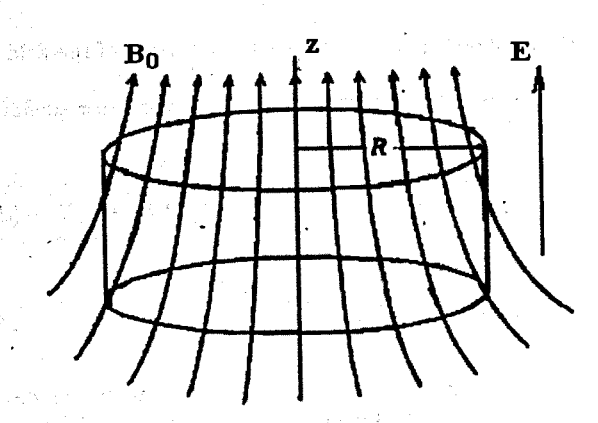


Figure 2: Inhomogeneous magnetic field [5] containing components perpendicular to z-axis.

the same sign for neutrons rotating in both directions. Therefore, it does not average to zero and raises the correction to the precession frequency,

$$\omega_{ni} = \frac{B_r \cdot B_{nv}}{B_z^2} \omega_{nv} = B_z' Q_n E, \tag{38}$$

where constant Q_n accounts for averaging over the spectrum, trajectories and the angular distribution of neutrons. This constant can be calculated as shown in [5]. We do not reproduce these calculations because experimenters usually try to exclude the term (38) from their results. In the following Section we show how this term is excluded. The most important feature of (38) is its linear proportionality to B_2' and E.

4.4—Exclusion of the Berry phase

By taking into account the false effect, equation (34) can be modified as follows

$$R_a(\uparrow,\uparrow) = 1 + (d_n - d_{Hg})\frac{E}{B_z} + B_z'(Q_n + Q_{Hg})\frac{E}{B_z}.$$
 (39)

We see that the term which is linear in E contains the false effect due to the geometric phase. The geometric phase is also linear in B'_z . So, if we can change the sign of B'_z and take an average of measurements with two opposite signs of B'_z , we can exclude the geometric phase. To change sign of B'_z we need to change direction of B_z and direction z-axis since it is always considered to be along B_z . Because of these reversions the gradient B'_z changes its sign. At the same time direction of E if B_z and E are to be parallel also must be reversed. The average

$$\overline{R}_a(E) \equiv \frac{1}{2} [R_a(\uparrow,\uparrow) + R_a(\downarrow,\downarrow)] = 1 + (d_n - d_{Hg}) \frac{E}{B_z}$$
(40)

¹UCN move with speeds up to a limiting speed v_l , corresponding to the reflecting optical potential of the bottle walls. We take $v = v_l = 5$ m/s, which is sufficient to obtain good estimates.

²The neutrons move on the straight, however every rectilinear motion perpendicular to z-axis can be decomposed into radial and azimuthal directions. The rotation, we speak about, is the azimuthal motion.

does not contain the geometric phase. However the reversion of the field brings two new effects into play.

First of all, since B_z is not a homogenous field, we need to re-define the precession frequencies (31) and (32),

$$\hbar\omega_{n} = 2|\mu_{n}| \left(\int_{0}^{H} \rho_{n}(z)dz B_{z}(z) + (d_{n} + B'_{z}Q_{n})E \right) = 2|\mu_{n}|[B_{z} + \overline{z}_{n}B'_{z} + (d_{n} + B'_{z}Q_{n})E],$$
(41)

$$\hbar\omega_{Hg} = 2\mu_{Hg} \left(\int_{0}^{H} \rho_{Hg}(z) dz B_{z}(z) + (d_{Hg} - B'_{z}Q_{Hg}) E \right) = 2\mu_{Hg} [B_{z} + \overline{z}_{Hg} B'_{z} + (d_{Hg} - B'_{z}Q_{Hg}) E],$$
(41)

where $\rho_n(z)$ is the distribution of neutrons, $\rho_{Hg}(z)$ is the distribution of Hg atoms along the height $0 \le z \le H$, z_n is the center of gravity of neutrons, and z_{Hg} is the center of gravity of Hg atoms. We also used the approximation

$$\int_{0}^{H} \rho(z)dz B_{z}(z) = B_{z} + \overline{z}B'_{z}. \tag{43}$$

Second, we need to take into account the action of the earth rotation! [6] In the non-inertial reference frame tied to the earth surface, the precession frequency of the neutron spin is $\omega_{\oplus} = 7.2 \cdot 10^{-5}$ rad/s. If we attribute this precession to neutron's EDM in the field of 10 kV/cm, it is equivalent to $d \approx 10^{-10}$ which is two orders of magnitude larger then the EDM found in [4]. Therefore, (41) and (42) can be rewritten as

$$\hbar\omega_n = 2|\mu_n|[B_z + \overline{z}_n B_z' + (d_n + B_z' Q_n)E] - \hbar\omega_{\oplus} \cos\theta_L, \tag{44}$$

$$\hbar\omega_{Hg} = 2\mu_{Hg}[B_z + \overline{z}_{Hg}B_z' + (d_{Hg} - B_z'Q_{Hg})E] + \hbar\omega_{\oplus}\cos\theta_L, \tag{45}$$

where θ_L is the latitude of the laboratory, where the experiment is conducted. The ratio (34) should now be replaced by

$$R_a(\uparrow,\uparrow) = 1 - \Delta h \frac{B_z'}{B_z} + [d_n - d_{Hg} + B_z'(Q_n + Q_{Hg})] \frac{E}{B_z} - \frac{\omega_{\oplus} \cos \theta_L}{\gamma B_z}, \tag{46}$$

where

$$\frac{1}{\gamma} = \frac{1}{\gamma_n} + \frac{1}{\gamma_{H_0}},\tag{47}$$

and

$$\Delta h = \overline{z}_{Hg} - \overline{z}_n > 0, \tag{48}$$

because the center of gravity of UCN (their effective temperature is ≈ 3 mK) is somewhat lower than that of much warmer (room temperature) Hg atoms.

Denote

$$T(\uparrow,\uparrow) = R_a(\uparrow,\uparrow) - 1 + \frac{\omega_{\oplus} \cos \theta_L}{\gamma B_z}, \qquad T(\downarrow,\downarrow) = R_a(\downarrow,\downarrow) - 1 - \frac{\omega_{\oplus} \cos \theta_L}{\gamma B_z}. \tag{49}$$

With these notations we have

$$T(\uparrow,\uparrow) = -\Delta h \frac{B_z'}{B_z} + [d_n - d_{Hg} + B_z'(Q_n + Q_{Hg})] \frac{E}{B_z}, \tag{50}$$

$$T(\downarrow,\downarrow) = +\Delta h \frac{B_z'}{B_z} + [d_n - d_{Hg} - B_z'(Q_n + Q_{Hg})] \frac{E}{B_z}.$$
 (51)

In the first approximation we can define

$$T = \frac{1}{2} (T(\uparrow, \uparrow) + T(\uparrow, \downarrow)) \approx T(\uparrow, \uparrow) \approx -\Delta h \frac{B_z'}{B_z}.$$
 (52)

The gradient B'z can be varied by changing currents in trimming coils placed around the UCN bottle. The variation of these currents results in changes in measured T. From (50) it follows that the difference

$$\frac{1}{2}\left(T(\uparrow,\uparrow)-T(\uparrow,\downarrow)\right) = \left[d_n - d_{Hg} - \frac{T}{|\Delta h|}B_z(Q_n + Q_{Hg})\right]\frac{E}{B_z},\tag{53}$$

changes linearly with T, and the exclusion of the Berry phase corresponds to T=0. Similar difference for the reversed fields is

$$\frac{1}{2}(T(\uparrow,\uparrow) - T(\uparrow,\downarrow)) = \left[d_n - d_{Hg} + \frac{T}{|\Delta h|} B_z(Q_n + Q_{Hg})\right] \frac{E}{B_z},\tag{54}$$

and again the exclusion of the Berry phase corresponds to T = 0. This point is at the crossing of two lines (53) and (54), and the crossing point corresponds to $d_n < 1.45$.

The procedure of excluding the Berry phase, and some corrections (which we did not not mention here), are explained in [4, 5, 7].

5 Conclusion

We showed how to calculate the Berry phase in the simplest case of a neutral particle with spin 1/2 moving in a superposition of two magnetic fields: the constant field parallel to z-axis, and the rotating RF field perpendicular to z-axis. Such calculation gives the understanding of what the Berry phase is. We also showed how the Berry phase causes the false effect in the experiments with UCN searching for neutron EDM. We did not calculate the Berry phase in these experiments because it is not measured there, but excluded. However, the Berry phase can be measured and can be calculated with high precision (see, for example, [5]).

Acknowledgement

The author is very much grateful to Filipp Ignatovich for his help, to Peter Geltenbort and Mike Pendelbury for their consultations.

References

- [1] B.R.Holstein, Am. J. Phys. 57 (1989) 1079.
- [2] K.Fujikawa, Mod. Phys. Lett. A 20 (2005) 335.
- [3] S.Deguchi and K.Fujikawa, Phys. Rev. A 72 (2005) 012111.
- [4] C. A. Baker et al., Phys. Rev. Lett. 97 (2006) 131801.
- [5] J. Pendlebury et al., Phys. Rev. A 70 (2004) 032102.
- [6] S.K. Lamoreaux and R. Golub, Phys. Rev. Lett. 98 (2007) 149101.
- [7] C. A. Baker et al., Phys. Rev. Lett. 98 (2006) 149102.

SIGN OF THE SINGLET LENGTH OF NEUTRON SCATTERING ON THE PROTON, NEUTRON RADIATIVE CAPTURE BY THE PROTON AND PROBLEM OF THE VIRTUAL LEVEL OF THE (np)-SYSTEM

V.L.Lyuboshitz, V.V.Lyuboshitz[†]

Joint Institute for Nuclear Research, 141980 Dubna, Moscow Region, Russia
† E-mail: Valery.Lyuboshitz@jinr.ru

Abstract

The low-energy neutron scattering on the proton is analyzed. As it follows from the experimental data, the length of singlet np-scattering is negative (the singlet scattering amplitude at zero energy is positive: $f_s(0) = -a_s > 0$). According to the optical theorem, the process of neutron radiative capture by the proton at zero energy leads to the fact that the singlet scattering length becomes a complex quantity and acquires a negative imaginary additional term: $\operatorname{Im} a_s = -\operatorname{Im} f_s(0) < 0$. It is shown, that, taking into account the signs of the real and imaginary parts of the length of singlet np-scattering, the singlet scattering amplitude has a pole on the second sheet of the Riemann surface at a complex energy E_s , the real part of which is negative and the imaginary part is positive. Since the imaginary part of the energy of a true quasistationary level should always be negative ($\operatorname{Im} E = -\Gamma/2$, where Γ is the level width), the inequalities $\operatorname{Re} E_s < 0$, $\operatorname{Im} E_s > 0$ mean that a singlet state of the (np)-system, which would decay into the deuteron in the ground state and the γ -quantum ("singlet deuteron") does not exist, and the pole E_s corresponds to the virtual but not true quasistationary level.

1 General structure of the neutron-proton elastic scattering amplitude at low energies

The amplitude of the s-wave elastic scattering of a slow neutron on a proton has the following form:

$$\hat{f}(k) = f_t(k)\hat{Q}_t + f_s(k)\hat{Q}_s,$$

$$\hat{Q}_{t} = \frac{3\hat{I} + \hat{\sigma}^{(n)}\hat{\sigma}^{(p)}}{4}, \qquad \hat{Q}_{s} = \frac{\hat{I} - \hat{\sigma}^{(n)}\hat{\sigma}^{(p)}}{4}. \tag{1}$$

Here $f_t(k)$ is the amplitude of triplet scattering, corresponding to the total spin of the (np)-system S=1; $f_s(k)$ is the amplitude of singlet scattering, corresponding to the total spin of the (np)-system S=0; \hat{I} is the 4-row unit matrix; $\hat{\sigma}^{(n)}$ and $\hat{\sigma}^{(p)}$ are the vector Pauli operators acting between spin states of the neutron and proton, respectively; $\hbar k = \sqrt{mE}$ is the neutron momentum in the center-of-mass frame of the (np)- system (in so doing, E is the total energy of the neutron and proton in this frame, m is the nucleon mass); \hat{Q}_t and \hat{Q}_s are the mutually orthogonal matrices of projection onto the triplet and singlet states of the (np)-system, respectively:

$$\hat{Q}_{t}^{2} = \hat{Q}_{t}, \qquad \hat{Q}_{s}^{2} = \hat{Q}_{s}, \qquad \hat{Q}_{t}\hat{Q}_{s} = 0.$$
 (2)

Taking into account Eqs.(1) and (2), the total cross-section of elastic scattering of a polarized neutron on a polarized proton can be presented in the following form:

$$\sigma = 4\pi \left[|f_i(k)|^2 \frac{3 + \mathbf{P}_n \mathbf{P}_p}{4} + |f_s(k)|^2 \frac{1 - \mathbf{P}_n \mathbf{P}_p}{4} \right], \tag{3}$$

where P_n and P_p are the polarization vectors of the neutron and proton, respectively. The relation (3) is valid at neutron laboratory energies below several MeV, when the s-wave scattering takes place.

Formula (1) may be rewritten also in the form:

$$\hat{f}(k) = c(k)\hat{I} + d(k)(\hat{\boldsymbol{\sigma}}^{(n)}\hat{\boldsymbol{\sigma}}^{(p)}),$$

where

$$c(k) = \frac{3f_t(k) + f_s(k)}{4}, \qquad d(k) = \frac{f_t(k) - f_s(k)}{4}. \tag{4}$$

It should be stressed that the magnitude $c(k) = \langle \hat{f}(k) \rangle$ has the meaning of the "coherent" amplitude of (np)-scattering (averaged over all spin states of the neutron and proton).

2 Scattering length and effective radius

In the framework of the effective radius theory [1,2], the amplitudes of the low-energy triplet and singlet (np)-scattering are parametrized as follows:

$$\frac{1}{f_{t(s)}(k)} = -\frac{1}{a_{t(s)}} - ik + \frac{1}{2}r_{0t(s)}k^2.$$
 (5)

Here $a_{t(s)}$ is the triplet (singlet) scattering length:

$$a_{t(s)} \equiv -f_{t(s)}(0); \tag{6}$$

 $r_{0i(s)}>0$ is the effective radius of triplet (singlet) scattering ($r_{0i(s)}^2\ll a_{i(s)}^2$) .

It is essential that the lengths of the triplet and singlet scattering of the neutron on the proton have the strongly different absolute values and mutually opposite signs: $a_t = +5.38$ fm, $a_s = -23.6$ fm.

The positive sign of the length of the triplet (np)-scattering follows directly from the elementary theory of deuteron [1]. At the same time, the experimental data on scattering of very slow neutrons on the parahydrogen (total spin of two protons S=0) and orthohydrogen (total spin of two protons S=1) testify to the fact that the signs of the lengths of singlet and triplet (np)-scattering are opposite $(a_sa_t<0)$ [3,4]. Actually, the experimental ratio $\sigma_{ortho}/\sigma_{para}\approx 31$. Meantime, if a_t and a_s had the same sign, then this ratio would be equal to 1.4 [2]. The conclusion about the opposite signs of the amplitudes a_t and a_s is confirmed also by the experimental data on the cross-section of the deuteron photodisintegration [5].

The numerical values of the lengths of triplet and singlet scattering a_t and a_s , together with their signs, follow definitely from the combined data on the cross-section of the low-energy (np)-scattering and on the coherent scattering (diffraction) of slow neutrons in

crystals containing the atoms of hydrogen (see [2] for more details). The difference of scattering lengths $\Delta a = a_t - a_s$ can be determined independently at the experimental investigation of another coherent effect: the precession of neutron spin in the polarized hydrogen target [6].

Both the triplet and singlet effective radii are positive, just as it should be from the viewpoint of the effective radius theory [1,2]: $r_{0t} = 1.7$ fm, $r_{0s} = 2.7$ fm. The coefficients c(k) and d(k) at zero energy, determined according to Eq.(4), are c(0) = 1.865 fm, d(0) = -7.275 fm.

Scattering lengths and poles of the triplet and singlet scattering amplitudes

The amplitudes $f_t(k)$ and $f_s(k)$ have the poles at negative energies being close to zero. The pole values of momenta \widetilde{k}_t , \widetilde{k}_t and energies \widetilde{E}_t , \widetilde{E}_s are determined by the equation:

$$-\frac{1}{a_{t(s)}} - i \widetilde{k}_{t(s)} + \frac{1}{2} r_{0(ts)} \widetilde{k}_{t(s)}^2 = 0, \tag{7}$$

from which it follows that:

$$\widetilde{k}_{t(s)} = \frac{i}{r_{Ot(s)}} \left(1 - \sqrt{1 - \frac{2r_{Ot(s)}}{a_{t(s)}}} \right) \approx \frac{i}{a_{t(s)}}, \tag{8}$$

$$\widetilde{E}_{t(s)} = -\frac{\hbar^2}{mr_{0t(s)}^2} \left(1 - \sqrt{1 - \frac{2r_{0t(s)}}{a_{t(s)}}} \right)^2 \approx -\frac{\hbar^2}{ma_{t(s)}^2}.$$
 (9)

It follows from Eq. (8) that in the case of triplet scattering, when the scattering length is positive (the scattering amplitude at zero energy is negative), the imaginary part of the pole momentum is positive: $\text{Im } \tilde{k}_t > 0$. This means that the amplitude of triplet (np)-scattering has the pole on the physical sheet, where $\text{Im } \sqrt{E} > 0$ [1]. The pole energy

$$\widetilde{E}_{t} = -\frac{\hbar^{2}}{ma_{t}^{2}} \left(1 + \frac{r_{0t}}{a_{t}} + \frac{5}{4} \frac{r_{0t}^{2}}{a_{t}^{2}} - \dots \right)$$
(10)

(the result of expansion of the formula (9)) is the energy of bound state of the neutron and proton with the total spin of two nucleons S = 1, i.e. the energy of the ground state of the deuteron. Obviously, the deuteron binding energy is $\epsilon_d = |E_t|$.

On the other hand, it follows from Eq. (8) that in the case of singlet scattering, when the scattering length is negative (the scattering amplitude at zero energy is positive), the imaginary part of the pole momentum is negative: $\text{Im } \tilde{k}_s < 0$. This means that the amplitude of singlet (np)-scattering has the pole on the second, unphysical sheet of the Riemann surface of complex energies, where $\text{Im } \sqrt{E} < 0$ [1]. In so doing, the negative pole energy

$$\widetilde{E}_{s} = -\frac{\hbar^{2}}{ma_{s}^{2}} \left(1 + \frac{r_{0s}}{a_{s}} + \frac{5}{4} \frac{r_{0s}^{2}}{a_{s}^{2}} - \dots \right)$$
(11)

corresponds not to the true but to the virtual level of the (np)-system.

Let us introduce the "radii" of the ground state and virtual state of the neutron and proton:

 $\rho_t = \frac{1}{|\widetilde{k}_t|} = \frac{\hbar}{\sqrt{m |\widetilde{E}_t|}}, \qquad \rho_s = \frac{1}{|\widetilde{k}_s|} = \frac{\hbar}{\sqrt{m |\widetilde{E}_s|}}.$ (12)

The experimental values of the pole energies are $|\widetilde{E}_t| = 2.23$ MeV, $|\widetilde{E}_s| = 0.067$ MeV. In accordance with this, $\rho_t = 4.32$ fm, $\rho_s = 24.39$ fm. Let us note that ρ_t is the radius characterizing the coordinate dependence of the wave function of the deuteron.

Taking into account Eqs. (7) and (12), we obtain simple relations between the scattering lengths a_t , a_s and "radii" ρ_t , ρ_s :

$$-\frac{1}{a_t} = -\frac{1}{\rho_t} + \frac{r_{0t}}{2\rho_t^2}, \qquad a_t = \frac{\rho_t}{1 - (r_{0t}/2\rho_t)}, \tag{13}$$

$$-\frac{1}{a_s} = \frac{1}{\rho_s} + \frac{r_{0s}}{2\rho_s^2}, \qquad a_s = -\frac{r}{1 + (r_{0s}/2\rho_s)}, \tag{14}$$

Since the effective radius r_0 is always positive, the following inequalities are valid:

$$a_t > \rho_t, \qquad |a_s| < \rho_s. \tag{15}$$

In the case of singlet scattering $r_{0s}/2a_s \approx 0.055 \ll 1$, and with the precision of < 1 %

$$a_s = -\rho_s + \frac{1}{2} r_{0s}. {16}$$

4 Process of radiative capture $n + p \rightarrow d + \gamma$ and the imaginary part of the singlet scattering length

Let us consider now how the length of the singlet np-scattering changes if the neutron radiative capture by the proton with the production of the deuteron $n+p \to d+\gamma$ is taken into account. It is known that in the limit of very low energies this process is conditioned by the M1-transition from the singlet state of the (np)-system [5,7]. In accordance with the general behaviour of cross-sections of inelastic processes at the energies being close to zero (see, for example, [1]), the radiative capture cross-section, averaged over the neutron and proton polarizations, has the following structure:

$$\sigma_{np\to d\gamma} = \frac{A}{k},\tag{17}$$

where A is a positive constant with the dimensionality of length, $\hbar k = \sqrt{mE}$ is the neutron momentum in the center-of-mass frame.

For unpolarized nucleons the relative fraction of the singlet state is equal to 1/4. On account of this, the radiative capture cross-section, corresponding to the purely singlet state, is

$$\sigma_{np\to d\gamma}^{(s)} = 4\sigma_{np\to d\gamma} = \frac{4A}{k}.$$
 (18)

According to the optical theorem [1], due to the radiative capture $n+p \to d+\gamma$ the singlet length of the scattering of the neutron on the proton becomes complex, acquiring a small additional imaginary term:

$$\widetilde{a}_s = a_s + ib_s, \qquad b_s = -\frac{\lim_{k \to 0} \sigma_{np \to d\gamma}^{(s)}}{4\pi} = -\frac{A}{\pi} < 0. \tag{19}$$

Using the explicit expression for the cross-section of the radiative capture of the neutron by the proton at zero energy [5], we obtain:

$$b_{s} = -\text{Im} f_{s}(0) = -\frac{e^{2}}{\hbar c} \left(\frac{\hbar}{mc}\right)^{2} (g_{p} - g_{n})^{2} \frac{|\widetilde{E}_{t}|^{3/2} [\sqrt{|\widetilde{E}_{t}|} - (\hbar/\sqrt{m}a_{s})]^{2}}{(\hbar^{2}/ma_{s})\sqrt{mc^{2}} \hbar c} \frac{1}{1 - (\sqrt{m|\widetilde{E}_{t}|}/\hbar) r_{0t}}$$

Here $e^2/\hbar c$ is the fine structure constant, m is the nucleon mass, $g_p = 2.78$ and $g_n = -1.91$ are magnetic moments of the proton and neutron in nuclear magnetons. In so doing,

$$\left| \frac{\hbar}{\sqrt{m}a_s} \right| pprox \sqrt{|\widetilde{E}_s|}, \qquad \sqrt{|\widetilde{E}_t|} - \frac{\hbar}{\sqrt{m}a_s} pprox \sqrt{|\widetilde{E}_t|} + \sqrt{|\widetilde{E}_s|},$$

where E_t and E_s are the above-considered pole energies for the triplet and singlet states of the (np)-system.

Finally calculations give:

$$|b_s| pprox 2.69 \cdot 10^{-4} \text{ fm}, \qquad \left| \frac{b_s}{a_s} \right| \sim 10^{-5} \gg 1.$$

5 Imaginary part of the pole energy for the singlet scattering amplitude

Since Im $a_s \neq 0$, it is obvious that the pole energy \widetilde{E}_s will also acquire an additional imaginary part.

Taking into account that $|b_s|/|a_s| \ll 1$, the following formula is valid:

$$\operatorname{Im} \widetilde{E}_s = \frac{d\widetilde{E}_s(a_s)}{d\,a_s}\,b_s,\tag{21}$$

where, according to Eq. (9),

$$\frac{d\widetilde{E}_s}{da_s} = -\frac{2\hbar^2}{mr_{0s}} \left(1 - \frac{1}{\sqrt{1 - (2r_{0s}/a_s)}} \right) \approx \frac{2\hbar^2}{ma_s^3}. \tag{22}$$

It is clear that, since the singlet scattering length $a_s < 0$ and $b_s < 0$, we obtain for the singlet state of np-system:

$$\frac{d\widetilde{E}_s}{da_s} < 0, \qquad \operatorname{Im} \widetilde{E}_s > 0.$$

Meantime, it is known that for a true quasistationary state the imaginary part of its energy is always negative: the magnitude $\Gamma = -2 \, \mathrm{Im} \, E$ has the meaning of the decay width [1]. Thus, the inequality $\mathrm{Im} \, \widetilde{E}_s > 0$ implies that the singlet quasistationary state of the (np)-system with the negative energy (with the mass being smaller than the sum of neutron and proton masses), decaying into the deuteron in the ground state and γ -quantum, does not exist. In accordance with this, we think that the resonance (Breit-Wigner) scattering of the photon on the deuteron at the subthreshold energy $E_{\gamma} = |\widetilde{E}_t| - |\widetilde{E}_s| \approx 2.163 \, \mathrm{MeV}$, corresponding to the deuteron virtual level, should be absent, in contrast to the point of view presented in some works [8,9]. As it was shown in the paper [10], the influence of the virtual singlet state of the (np)-system upon the energy dependence of the elastic γd -scattering near the threshold of the deuteron photodisintegration manifests itself only as a threshold anomalous cusp.

The existence of a singlet unstable level of the deuteron would be possible only in the case if the scattering length a_s were positive (i.e. if the value $f_s(0)$ were negative).

6 Summary

- 1. The properties of the amplitudes of the s-wave neutron elastic scattering on the proton are analyzed, taking into account the process of radiative capture $n + p \rightarrow d + \gamma$.
- 2. Due to the fact that the real and imaginary parts of length of the singlet (np)-scattering are negative, the amplitude of singlet (np)-scattering has the pole at the complex energy, the real part of which is negative but the imaginary part is positive. This excludes the existence of a singlet quasistationary state of the deuteron, which would decay into the γ -quantum and the deuteron in the ground state.

We are grateful to S.B.Borzakov, who has drawn our attention to the problem of the singlet level of the deuteron.

References

- L.D. Landau and E.M. Lifshitz. Quantum Mechanics. Nonrelativistic Theory. Moscow, Nauka, 1989, §§133, 134, 142, 143.
- 2. H.A. Bete and F. Morrison. *Elementary Nuclear Theory*, New York. John Wiley & Sons, Inc., 1956, §11 [Russ. transl.: Moscow, 1958].
- 3. J. Schwinger and E. Teller. Phys. Rev., v. 52, p. 286 (1937).
- 4. R. Satton et al., Phys. Rev., v. 72, p. 1147 (1947).
- 5. A.S. Davydov. Theory of Atomic Nucleus, Moscow, Fizmatgiz, 1958, §79.
- 6. V.G. Baryshevsky, M.I. Podgoretsky. JETP, v. 47, p. 1050 (1964).
- V.B. Berestetsky, E.M. Lifshitz and L.P. Pitaevsky. Quantum Electrodynamics, Moscow, Nauka, 1989, §58.

- 8. S.B. Borzakov. Yadernaya Fizika, v. 57, p. 517 (1994); Proceedings of the XIII International Seminar on Interaction of Neutrons with Nuclei (ISINN-13), Dubna, 2006, p. 170.
- 9. W. Hackenburg. BNL Report BNL-77482-2007-IR
- 10. L.I. Lapidus, Chou Kuang Chao. JETP, v. 39, p. 112 (1960).

On Neutron Electromagnetic Constants Derived from Neutron Scattering by ²⁰⁸Pb

L.V.Mitsyna, V.G.Nikolenko, A.B.Popov, G.S.Samosvat

Joint Institute for Nuclear Research, 141980, Dubna, Russia

1. The results of the present paper supplement the data of the investigations with the enriched ²⁰⁸Pb target, which were carried out by the collaboration Dubna-Garching-Kiev-Riga and described in [1-3]. The total cross sections σ_i were measured for the purpose of extracting the neutron electric polarizability coefficient α_n and the neutron-electron scattering length b_{ne} . Measured in Garching [1] four points of σ_i at the neutron energies 1.26, 18.6,128 and 1970 eV allowed to get the polarizability coefficient

$$\alpha_n = \begin{cases} (0.4 \pm 1.5) \cdot 10^{-3} \text{ fm}^3 \text{ at } b_{ne} = -1.32 \cdot 10^{-3} \text{ fm}, \\ (-1.1 \pm 1.5) \cdot 10^{-3} \text{ fm}^3 \text{ at } b_{ne} = -1.59 \cdot 10^{-3} \text{ fm}. \end{cases}$$
(1)

Thirteen values of the total cross sections at more wide energy range up to 24 keV measured in Dubna [2] gave both discussed values:

$$\alpha_n = (2.5 \pm 3.4) \cdot 10^{-3} \text{ fm}^3,$$
 (2)

$$b_{ne} = (-1.63 \pm 0.20) \cdot 10^{-3} \text{ fm}.$$
 (3)

At last the most precise point of σ_i at the energy 24 keV was obtained in Garching in 2000 [3].

Now we complete all available total cross sections by the data of last work cycle of the booster IBR-30 in 2001.

2.The measurements were carried out with the cylinder-shaped lead sample containing 97.5% of ²⁰⁸Pb, 232.46 grams weight, 50 mm across diameter and 10.43 mm thick. It was placed at the distance ~70 m from the source in the beam and out of its range every 20 min by turns. The sectional neutron detector consisted of 16 ³He-counters was installed at the 242.3 m time-of-flight path. Whole system was divided into 16 independent detecting-counting subsystems.

Fig.1 presents the experimental spectra with and without target in the beam. Each of them was accumulated within 36.7 hours of running time. The channel widths were 1 mcs (lower part of figure), 2 mcs (middle part) and 16 mcs (the upper section). Various minima on the spectra are caused by filters of Al, Mn and Au, which were located in the beam permanently. The backgrounds demonstrated in Fig.1 were constructed on the basis of broad "black" resonances of Mn (2.37 keV and 336 eV) and Au (4.906 eV) and were calculated by a/(t-d)+b+ct-law, where t is the time-of-flight and a, b, c, d are the fitted coefficients. As at the channels numbers < 350 we didn't know the background course for sure, so in high-energy region we applied for taking it into account a new method described in [4].

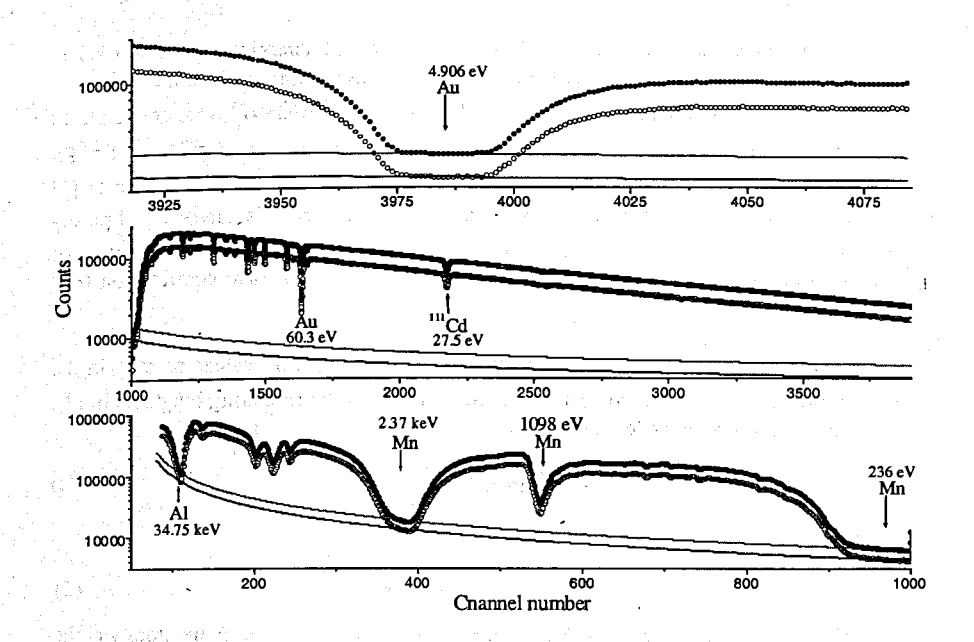


Fig.1.The experimental spectra of counts with the ²⁰⁸Pb in the neutron beam (open points) and without the target in the beam (black points). Lines are the fitted backgrounds.

Table 1

			5 Tale 4 For 19 Tale 1	I able I
Channel interval	$\langle E_n \rangle$, eV	σ_i , b	σ_{s}^{208} , b	σ_{pot}^{208} , b
4010 – 4050	4.14	11.414(40)	11.425(40)	12.461(40)
3920 – 3960	5.97	11.477(24)	11.484(24)	12.520(24)
3201 – 3900	8.3	11.420(12)	11.428(12)	12.464(12)
2601 – 3000	14.6	11.462(10)	11.469(10)	12.505(10)
1901 – 2400	28.5	11.442(07)	11.447(07)	12.483(07)
1501 – 1900	54.1	11.438(06)	11.442(06)	12.478(06)
1201 – 1500	108	11.458(07)	11.461(07)	12.497(07)
1001 – 1200	219	11.444(10)	11.448(10)	12.484(10)
801 – 900	461	11.442(20)	11.446(20)	12.481(20)
601 – 800	691	11.449(09)	11.455(09)	12.490(09)
411 – 600	1352	11.418(10)	11.426(10)	12.460(10)
310 – 460	2516	11.390(22)	11.388(22)	12.420(22)
251 – 300	4830	11.403(19)	11.410(19)	12.440(19)
191 – 223	9104	11.318(65)	11.326(65)	12.350(65)

All the obtained results are listed in Table 1 for 14 energies of neutrons. The intervals of the σ_i averaging and averaged energies corresponding to them are presented in the first and second columns. The measured total cross sections σ_i were converted to the scattering cross sections σ_i^{208} by subtracting the contributions of σ_i^{206} Pb and σ_i^{207} Pb isotopes, of different chemical admixtures and of Schwinger and solid-state effects [5] (the capture contribution is less then 1 mb). The cross section σ_{poi}^{208} is a measure of purely potential s-wave scattering and has been obtained by subtracting negative contribution of σ_i^{208} Pb s-resonances (mostly of one at 507 keV) and of a small p-wave contribution (< 8 mb).

3. Thus, together with the data from reports [1-3] we have 32 values of σ_{pot}^{208} in the energy range from ~ 1 eV up to 25 keV for analyzing the total scattering length as in [3]. The experimental scattering length

$$a = \frac{1}{k} \arcsin \left(k \sqrt{\frac{\sigma_{pot}^{208}}{4\pi}} \right) \tag{4}$$

was written as

$$a = R + \frac{A}{A+1}b_{ne}ZF + hE - a_{p}Q,\tag{5}$$

where E is the neutron energy, k is the neutron wave number, A, Z and F are atom weight, charge number of ²⁰⁸Pb and integrated electron form factor [5]. The energy-dependent α_n contribution is presented by the last term in (5), the nuclear part of the total scattering length R (first term) includes also the energy-independent value $a_p = -3.916 \cdot 10^{-2} \alpha_n$ fm (if α_n is in 10^{-3} fm³), the second and the third terms in (5) define quantities of the contributions of b_{ne} -scattering and of the distant and unknown resonances. The polarizability form factor Q is determined by the charge ball radius $R_N = 7.13$ fm for ²⁰⁸Pb

$$Q = \frac{5\pi}{18} kR_N - \frac{5}{21} (kR_N)^2 + \frac{2}{243} (kR_N)^4.$$
 (6)

Thus, by the method of minimization of χ^2 functional we fitted the expression (5) to all experimental total scattering lengths calculated by (4) with purpose to get four parameters R, b_{ne} , h and α_n , which are presented by the first line of Table 2, and the Fig.2 demonstrates the quality of fitting.

Table 2

N	<i>R</i> , fm	$10^3 \cdot b_{ne}$, fm	$10^7 \cdot h$, fm · eV ⁻¹	$10^3 \cdot \alpha_n$, fm ³	χ^2/n^*
	9.9755±0.0016		-2.2±5.6	-1.9±1.9	1.40
	9.5685±0.0006		-20.4±0.3	1.68±0.19	1.23
3	9.9733±0.0012	-1.57±0.15	-13.8	1.94±0.26	1.61

^{*)} n is the number of experimental points

A similar task was being solved in our paper [6] with the considerably more precise data for ²⁰⁸Pb [7] in the neutron energy interval from ~ 50 eV up to 40 keV. The fitting with those data led to the parameters shown in line 2 of Table 2.

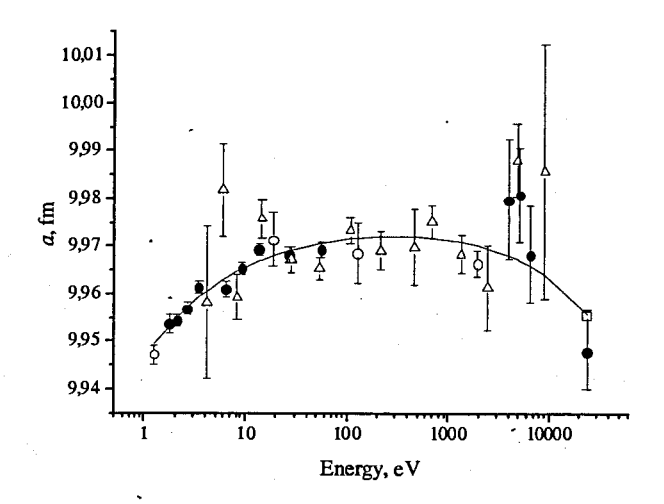


Fig.2.The experimental a values obtained from [1] (open circles), from [2] (black circles), from [3] (one open square) and from the present work (triangles).

As far as the correlations between h and α_n is very strong we decided to use much more precise h obtained from the data of [7] by our method in paper [6] in order to get more definite α_n from our data. The value of R in line 2 is essentially less than R in line 1 because the negative contribution of the s-wave resonance 507 keV to σ , was not removed in [7]. Since this resonance gives $h = -6.6 \cdot 10^{-7}$ fm/eV thereby we took it into account and fixed $h = (-20.4 + 6.6) \cdot 10^{-7}$ fm/eV in our fitting (see line 3 in Table 2).

From the series of fittings with different fixed h we obtained the correlation $\Delta \alpha_n / \Delta h = 0.335$. Taking into consideration this relation we attributed a certain error to h and obtained with $h = (-13.8 \pm 0.6) \cdot 10^{-7}$ fm/eV

$$\alpha_n = (1.94 \pm 0.33) \cdot 10^{-3} \,\text{fm}^3$$
 (7)

as the combined result with our σ_{pot}^{208} and h from the data of [7]. Thus, we have a right to state that this result does not contradict to one of the best results $\alpha_n = (1.20 \pm 0.15 \pm 0.20) \cdot 10^{-3}$ fm³ obtained in [7].

4. The low-energy region of Garching and Dubna data were also analyzed by the method of $\sigma_{s}(E)$ extrapolation to neutron energy $E_{n} = 0$ [8]. Here the b_{ne} values were

evaluated from the old σ_r data for ²⁰⁸Pb without making use of the coherent scattering length. At low energies the contribution of α_r is neglected.

The scattering cross sections were described as

$$\sigma_{s} = \frac{\pi}{k^{2}} (1 + \mu^{2} - 2\mu \cos 2\delta_{0}), \tag{8}$$

where

$$\mu = \exp\left[-\frac{1}{2} \sum \frac{\Gamma_{nl} \Gamma_{l}}{(E - E_{c.})^{2} + \Gamma^{2} / 4}\right], \tag{9}$$

$$\delta_0 = -k[R + \frac{1}{2k} \sum \frac{\Gamma_{ni}(E - E_{0i})}{(E - E_{0i})^2 + \Gamma_i^2/4} + R_c(E - E_c) + b_{ne}F].$$
 (10)

Here E_c is the middle energy of the analyzed interval. The near resonances are taken into account in (9) and (10) directly through their parameters. The third term in (10) corresponds to the contribution of distant resonances, and it is equivalent to hE in (5).

In analysis of σ , for E < 130 eV there were only two fitted parameters at $R_c = 0$: R and b_{ne} . At the higher energies R_c was fitted as a parameter too. Calculations showed that the extracted b_{ne} value was not changed if we took the strong resonance at 507 keV into account directly or not, because the σ , data did not exceed the energy more then 2 keV.

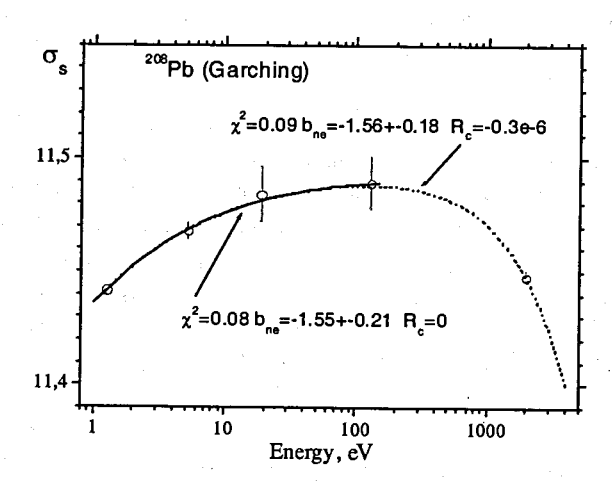


Fig.3. The results of fitting obtained with the data [9].

The results of fitting are presented in Fig.3 and Fig.4, and our estimations of b_{**} are

$$b_{ne} = (-1.56 \pm 0.18) \cdot 10^{-3} \text{ fm}$$
 (11)

for the data of [9], and for data of [2]

$$b_{ne} = (-1.70 \pm 0.15) \cdot 10^{-3} \text{ fm.}$$
 (12)

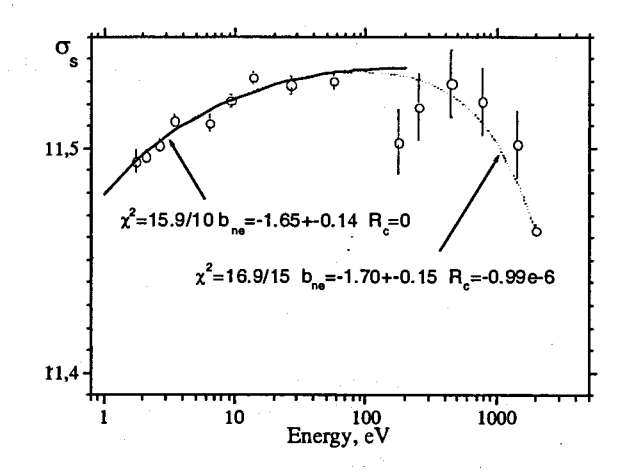


Fig.4. The results of fitting obtained with the data [2].

When these results were included in global analysis of all existent experimental b_{ne} values [10] the neutron mean-square charge radius evaluation obtained from the other data was not changed. It is explained by significant errors of b_{ne} , which we extracted from the data for 208 Pb.

References

- Yu.A.Alexandrov, L.Koester, G.S.Samosvat, W.Washkowski. JINR Rapid Communications, Ne6/45, 48-50, Dubna (1990).
- T.L.Enik, L.V.Mitsyna, V.G.Nikolenko, A.B.Popov, G.S.Samosvat, P.Prokofjevs, A.V.Murzin, W.Washkowski. Proceedings ISINN-3, JINR E3-95-307, 238-242, Dubna (1995).
- O.O.Gritzay, V.A.Libman, A.V.Murzin, V.G.Nikolenko, A.B.Popov, G.S.Samosvat, W.Washkowski. Proceedings ISINN-8, JINR E3-2000-192, 165-170, Dubna (2000).
- T.L.Enik, V.A.Ermakov, R.V.Kharjusov, L.V.Mitsyna, V.G.Nikolenko, S.S.Parzhitski, A.B.Popov, G.S.Samosvat, V.A.Vtjurin. Yadernaja Physica 66, №1(2003)59.
- 5. V.F.Sears. Phys. Rep. 141, №5 (1986)281.
- T.L.Enik, L.V.Mitsyna, V.G.Nikolenko, A.B.Popov, G.S.Samosvat. Yadernaja Physica 60, №4(1997)648.
- 7. J.Schmiedmayer, P.Riehs, J.A.Harvey, N.W.Hill. Phys. Rev. Let, 66, No.8(1991)1015.
- 8. V.G.Nikolenko, A.B.Popov. JINR3-92-254, Dubna, 1992; Proc. of 8th Int. Symp. Capture Gamma-ray Spectroscopy, Fribourg, 20-24 Sept. 1993, p.815.
- L.Koester, W.Washkowski, L.V.Mitsyna, G.S.Samosvat, P.Prokofjevs, J.Tambergs. Phys.Rev. C 51, №6(1995)3363.
- 10. A.B.Popov, T.Yu.Tret'yakova. Report on the present Seminar.

GRANIT project: a trap for gravitational quantum states of UCN

V. V. Nesvizhevsky, A. K. Petukhov, H. G. Börner, T. Soldner, P. Schmidt- Wellenburg, M. Kreuz Institut Laue-Langevin, Grenoble, France

G. Pignol, K. V. Protasov, D. Rebreyend, F. Vezzu LPSC, UJF/CNRS-IN2P3/INPG, Grenoble, France

D. Forest, P. Ganau, J. M. Mackowski, C. Michel, J. L. Montorio, N. Morgado, L. Pinard, A. Remillieux Laboratoire des Matériaux Avancés, Villeurbanne, France

A. M. Gagarski, G. A. Petrov Petersburg Nuclear Physics Institute, Gatchina, Russia

> A. M. Kusmina Khlopin Institute, St.Petersburg, Russia

A. V. Strelkov Joint Institute of Nuclear Research, Dubna, Russia

> H. Abele University of Heidelberg, Germany

S. Baeßler University of Mainz, Germany

A. Yu. Voronin Lebedev Physical Institute, Moscow, Russia

Abstract

Previous studies of gravitationally bound states of ultracold neutrons showed the quantization of energy levels, and confirmed quantum mechanical predictions for the average size of the two lowest energy states wave functions. Improvements in position-like measurements can increase the accuracy by an order of magnitude only. We therefore develop another approach, consisting in accurate measurements of the energy levels. The GRANIT experiment is devoted to the study of resonant transitions between quantum states induced by an oscillating perturbation.

According to Heisenberg's uncertainty relations, the accuracy of measurement of the energy levels is limited by the time available to perform the transitions. Thus, trapping quantum states will be necessary, and each source of losses has to be controlled in order to maximize the lifetime of the states. We discuss the general principles of transitions between quantum states, and consider the main systematical losses of neutrons in a trap.

1 Introduction

As predicted by quantum mechanics, a neutron bouncing above a mirror has discrete energy states. Due to the extreme weakness of gravity, these quantum states exhibit outstanding properties.

First, the mean height of the n^{th} state is much larger than atomic size,

$$z_n \approx (n - 1/4)^{2/3} \times 11 \ \mu \text{m},$$
 (1)

which has been used to prove the quantization of energy at the ILL high flux reactor in Grenoble [1, 2]. A neutron flux has been measured through a narrow slit between a horizontal mirror and a scatterer above. We observed the discrete behaviour of this flux as a function of the height of the slit. In particular, the flux is zero if the height is less than $10 \,\mu\text{m}$, since no quantum state can penetrate throught the slit. The classical turning points of the two first states have then been determined to be [3],

$$z_1^{\text{exp}} = 12.2 \pm 1.8_{\text{sys}} \pm 0.7_{\text{stat}} \, \mu\text{m},$$
 (2)
 $z_1^{\text{th}} = \frac{3}{2} (1|\hat{z}|1) = 13.7 \, \mu\text{m},$

$$z_2^{\text{exp}} = 21.6 \pm 2.2_{\text{sys}} \pm 0.7_{\text{stat}} \, \mu\text{m},$$
 (3)
 $z_2^{\text{th}} = \frac{3}{2} \langle 2 | \hat{z} | 2 \rangle = 24.0 \, \mu\text{m}.$

Higher states are more difficult to resolve. We expect to be able to improve the precision of position-like observables by one order of magnitude at most.

One second important property of the quantum states is the extreme smallness of the energies. Indeed, the energy of the $n^{\rm th}$ state is, within the Bohr-Sommerfeld approximation,

$$E_n \approx (n - 1/4)^{2/3} \times 1.7 \text{ peV}.$$
 (4)

Then, the corresponding frequencies $f_n = \frac{E_n}{h}$ are small as well. They are in the kilohertz range, which makes it possible to probe the quantum states with an oscillating perturbation at these easily accessible frequencies. In the next section, we will discuss the principle of the GRANIT experiment, which aims to induce resonant transitions between quantum states. The accuracy of the transition frequencies is limited by the lifetime in the quantum levels. To increase the duration of the perturbation, a trap has to be built, and the third section is devoted to the estimation of lifetimes of quantum states in this trap.

2 Resonant transitions in the GRANIT experiment

Let us assume that a given neutron bouncing above a horizontal mirror stands in a pure initial state $|N\rangle$ concerning its vertical motion. We apply a periodic perturbation,

 $\hat{V}(t) = Re\left(V(z)e^{i\omega t}\right),\tag{5}$

induced by an oscillating magnetic gradient, oscillations of the horizontal mirror itself, or by the motion of neighbouring mass. If the angular frequency ω is close to $\frac{E_n-E_N}{\hbar}$, which corresponds to the transition to an excited state $|n\rangle$, then a Rabi resonance is expected. The probability to observe this transition is well known,

$$P_{N\to n}(t) = \frac{1}{1 + \left(\frac{\omega - \omega_{Nn}}{\Omega_{Nn}}\right)^2} \sin^2\left(\sqrt{(\omega - \omega_{Nn})^2 + \Omega_{Nn}^2} \frac{t}{2}\right),\tag{6}$$

where $\Omega_{Nn}=\frac{2}{\hbar}\langle n|V(z)|N\rangle$ is the Rabi frequency, defining the perturbation strength for the $N\to n$ transition. The maximum of the transition probability,

$$P_{N \to n}^{\text{max}} = \frac{1}{1 + \left(\frac{\omega - \omega_{N_n}}{\Omega_{N_n}}\right)^2} \tag{7}$$

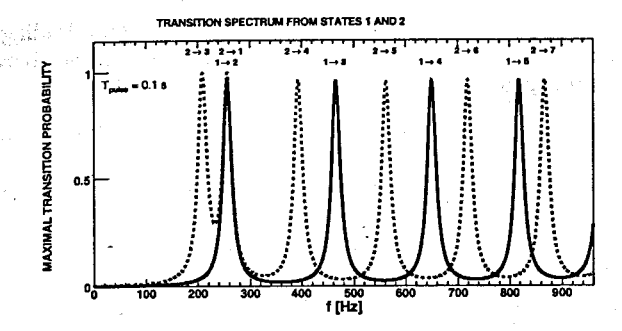


Figure 1: Maximum transition probability for neutrons prepared in the first quantum state (straight line) and for neutrons prepared in the second quantum state (dotted line), as a function of the perturbation frequency. The Rabi angular frequency Ω satisfies $\frac{\pi}{\Omega}=0.1$ s.

has a Lorentzian shape, and is reached if the perturbation is applied for the so-called *pulse time*,

$$T_{\text{pulse}} = \frac{\pi}{\sqrt{(\omega - \omega_{Nn})^2 + \Omega_{Nn}^2}}.$$
 (8)

Fig. 1 shows the maximum transition probability of the first two quantum states for frequencies below 1 kHz.

Obviously, the pulse time must be smaller than the storage time of neutrons in a given quantum state. Thus, we can deduce from the previous discussion the two fundamental reasons to increase the storage time. First, the resonance formula (6) contains the Heisenberg's uncertainty relation, $\Delta E \cdot T > h/2$, where T is the storage time ($T > T_{\rm pulse}$) and ΔE the width of the resonance curve. As a work hypothesis we consider that the accuracy of GRANIT to measure energy transitions equals this resonance width, which is then inversely proportional to the storage time. In expression (8) we can see the second reason to increase the storage time, since the perturbation strength needed for a 100% probability at the resonance is inversely proportional to the pulse time as well. In the remaining of this section we will explicit this relation connecting strength of perturbation and storage time in the case of magnetically induced transitions, and in the next section, we will estimate the lifetime of the quantum states in the GRANIT trap, which is of primary importance.

For now, let us list the characteristic timescales of the problem:

- 1. The pulse time needed to resolve the states is about 10 ms, leading to a resonance curve with a width of half the separation frequency between neighbouring states.
- 2. The flow through mode time is about 75 ms, which is the time a neutron of horizontal velocity 4 m/s takes to pass above a 30 cm long horizontal mirror. Of course this time could be increased with slower neutrons or a longer mirror, but we need to trap neutrons to gain orders of magnitude. Let us notice, however, that it is possible to resolve the states in flow through mode.
- 3. The ultimate storage time is given by the β decay lifetime of the neutron, i.e. 886 s. If neutrons can be trapped in a given quantum level that long, energy levels could be measured with a relative accuracy of about 10^{-6} .
- 4. We may consider the possibility of radiative decays of the quantum states by spontaneous graviton emissions. Nonetheless the corresponding time has been found to exceed the age of the universe by several orders of magnitude [4], and can be completely neglected. Therefore, contrary to quantum levels in atomic or nuclear physics, the gravitational quantum levels are absolutely stable, except for external perturbation or the decay of the neutron itself.

2.1 Transitions induced by magnetic field

Let us examine how strong this perturbation has to be in the case of magnetically induced transitions. Since an uniform magnetic field does not couple different quantum states, we apply the magnetic gradient¹

$$\mathbf{B} = (\beta_z \mathbf{e}_z + \beta_x \mathbf{e}_x) z \cos(\omega t), \tag{9}$$

whose variation with time induces two different transitions. The first one does not change the spin-state and is induced by the gradient of the vertical component,

$$\hat{V}(t) = -\hat{\mu}_z \beta_z \ \hat{z} \ \cos(\omega t), \tag{10}$$

where μ is the magnetic moment of the neutron. Contrary, the second transition is induced by the gradient of the horizontal component and changes the spin-state of the neutron,

$$\hat{V}_{\text{flip}}(t) = -\hat{\mu}_x \beta_x \ \hat{z} \ \cos(\omega t). \tag{11}$$

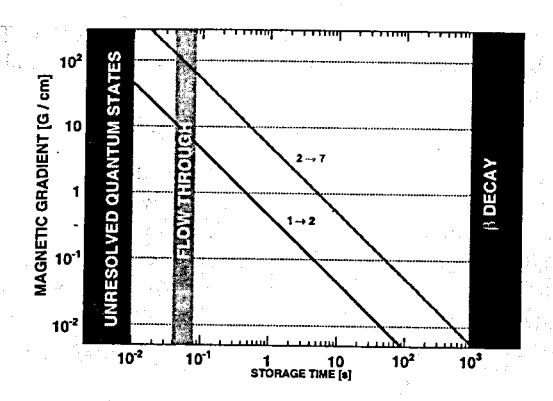


Figure 2: Magnetic field gradient needed for a 100% transition probability at resonance as a function of the time during which the transition is performed, for the $1 \to 2$ and the $2 \to 7$ transition. Also shown is the minimum time needed to resolve the quantum states, the ultimate β decay time, and the typical time in flow through mode.

This property of spin-flipping is important since it can be used to detect that a transition has occured. In any case, the Rabi angular frequency is given by

$$\Omega_{N \to n}^{\text{magnetic}} = \frac{2}{\hbar} \mu \beta \langle n | \hat{z} | N \rangle.$$
 (12)

Fig. 2 shows the magnetic gradient needed for a 100% transition probability at the resonance as a function of the pulse time. If a storage time of 10 s is achieved, then we can use a magnetic gradient as low as 0.01 T/m to induce the $2 \rightarrow 7$ transition. In flow through mode, a 100be induced by a magnetic gradient of 0.1 T/m. By using the spin-flip, the sensitivity to detect the transition can be increased significantly permitting to observe transitions even with smaller gradients.

2.2 Effects of the Earth' rotation

Besides the β decay lifetime of the neutron, there is another (almost) unavoidable effect limiting the precision of the transitions energies. Indeed, the rotation of the Earth induces non-inertial effects, described by the potential $-\Omega_{\rm Earth} \cdot \hat{\bf L}$, where $\Omega_{\rm Earth}$ is the rotation vector of the Earth, and $\hat{\bf L}$ is the

¹This field actually violates Maxwell's equations. We may add the gradient term $(\beta_x \mathbf{e}_z - \beta_z \mathbf{e}_x) x \cos(\omega t)$, but this term does not couple different quantum states.

angular momentum of the neutron relatively to the Earth' center. The main effect induced by this potential is the coupling between horizontal velocity and vertical motion,

$$V_{\text{Earth rotation}} = -\Omega_{\text{Earth}} \cos \theta \ m v_{NS} \ \hat{z} \tag{13}$$

where v_{NS} is the neutron velocity in North-South direction and θ is the latitude (in Grenoble $\cos\theta=0.7$). Thus, the effective vertical acceleration of the neutrons is shifted, depending on its horizontal velocity. For the first energy state, we can estimate the shift between neutrons travelling in North-South direction and neutrons travelling in East-West direction, for an absolute velocity of 5 m/s,

$$\left(\frac{\Delta E}{E_1}\right)_{\text{Earth rotation}} \approx 10^{-6}.$$
 (14)

Figure 6 shows the corresponding frequency shifts as a function of the state number. This effect is close to the ultimate sensitivity for energy levels measurements for the ground state, and is even higher for excited states. Let us notice that Earth rotation also induces a Zeeman shift between spin-up and spin-down states, but this effect is much smaller than the ultimate sensitivity,

$$(\Delta E)_{\text{Earth Zeeman}} = \hbar \Omega_{\text{Earth}} \approx 6 \times 10^{-8} \text{ peV}.$$
 (15)

3 Lifetimes of quantum states in the trap

The trap of quantum states in the GRANIT setup will look like in fig. 3. It is a 30 cm square bottom horizontal mirror surrounded by vertical side walls. The horizontal velocity of neutrons in the trap will be about 5 m/s, this velocity is limited by the Fermi potential of the side walls. In this section, we estimate the loss rate of neutrons due to geometrical imperfections of the trap as shown in fig. 3, that is, the waviness of the bottom mirror, the deviation from verticality of the side walls, and the corner defects. Other sources of losses, such as the seismic noise, a possible remaining inhomogeneous static magnetic field, interaction with magnetic impurities under the surface, interaction with dust or a hydrogen layer on the surface, interaction with low-energy phonons in the mirror and diffuse scattering, will not be considered here.

3.1 Losses due to waviness of the bottom mirror

Let us assume that the bottom mirror has a wavy profile $\xi(x)$, so that a neutron with horizontal velocity v sees in its rest frame a time-dependent

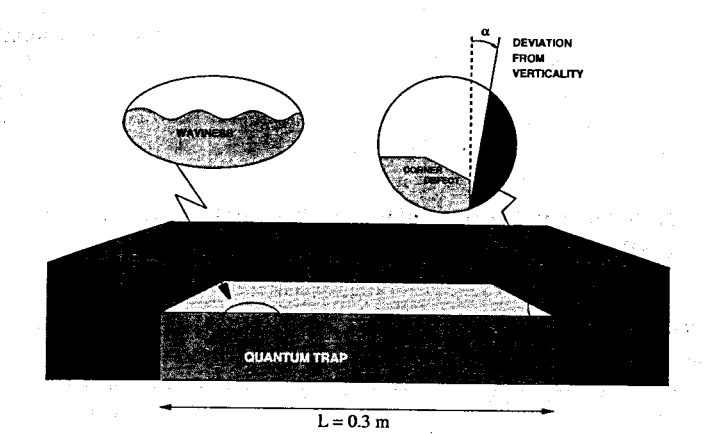


Figure 3: Scheme of the GRANIT trap for gravitational quantum levels of UCN. It shows the main geometrical sources for losses of neutrons: the waviness of the bottom mirror, the deviation from verticality of the side wall, and the corner defect.

boundary $\xi(vt)$. We aim to calculate the loss rate due to the transfer of horizontal velocity to vertical motion. This problem has already been solved in the case of seismic noise [5], and will be developed in more details in a forthcoming publication. Following this perturbation approach, it can be shown that the rate for the $N \to n$ loss channel reads

$$\Gamma_{N \to n}^{\text{wavy}} = \left(\frac{mg}{\hbar}\right)^2 \frac{1}{v} PSD\left(\frac{f_{Nn}}{v}\right) \tag{16}$$

where f_{Nn} is the frequency of the $N \to n$ transition and PSD(K) is the power spectral density of spectral noise,

$$PSD(K) = \lim_{L \to +\infty} \frac{1}{L} \left| \int_0^L \xi(x) e^{2i\pi Kx} dx \right|^2.$$
 (17)

The GRANIT bottom mirror has not been nuilt yet, but the power spectral density of a high-quality 300 mm Si substrate has been measured with several characterisation methods [6],

$$PSD(K) = \left(\frac{K}{1 \text{ mm}^{-1}}\right)^{-2.9} 2 \times 10^{-4} \text{ nm}^2 \text{ mm}.$$
 (18)

It is thus possible to estimate the loss rate of a given quantum level, summing all final states in eq. (16). The result is shown in fig. 6, as a function of initial state quantum number, and for a horizontal velocity of 5 m/s. For the first 30 quantum states of interest, the rate of losses due to the waviness of the bottom mirror is much smaller than the β decay rate.

3.2 Losses due to deviation from verticality of the side wall

A vertical side wall is obviously a necessary feature of the GRANIT trap. Here we estimate how precisely vertical this wall has to be. The probability of transition to different states due to deviation from verticality of the side walls can be calculated in the framework of the "sudden kick" approximation. Indeed, the collision with a wall can be treated as a sudden kick, during which the neutron gets the vertical momentum $k \sin(2\alpha)$, where α is an angle between the wall and the vertical direction, $k = mv/\hbar$ is the wave number of horizontal motion. Following the solution given by A.B. Migdal (see e.g. [7]), we immediately get the probability to leave a given state $|N\rangle$ during a collision,

$$P_N^{\text{wall}} = 1 - |\langle N | \exp(ik\sin(2\alpha)z) | N \rangle|^2$$
(19)

The result is shown in fig. 4, for neutrons with horizontal velocity of 5 m/s, and for different values of α . Notice that this probability is a quadratic function of v α (for small α). As shown in fig. 6, the corresponding loss rate $\Gamma_N^{\rm wall} = \frac{v}{L} P_N^{\rm wall}$ (for $\alpha = 10^{-5}$ rad and v = 5 m/s) is comparable to the β decay rate for the very first quantum states, and is more than ten times larger for state number bigger than 10. We conclude that specific efforts have to be undertaken to set the verticality at an accuracy better than 10^{-5} . This will be challenging, because the height of the side mirror is as low as ≈ 1 mm, but such a precision seems possible.

3.3 Losses due to defects in the edges

The bottom mirror edges cannot be perfectly flat, we will consider the realistic case where a 50 μm brink, considered here as a hole, is present for the whole boundary. Neutrons can either be lost in this hole, or be reflected by the hole in a different quantum state. To estimate the probability of leaving the initial state $|N\rangle$ during the collision at the corner, we assume a free fall evolution (without bottom mirror) during the classical time:

$$t_{\text{free fall}} = \frac{2 \times 50 \ \mu\text{m}}{5 \ \text{m/s}} = 20 \ \mu\text{s},$$
 (20)

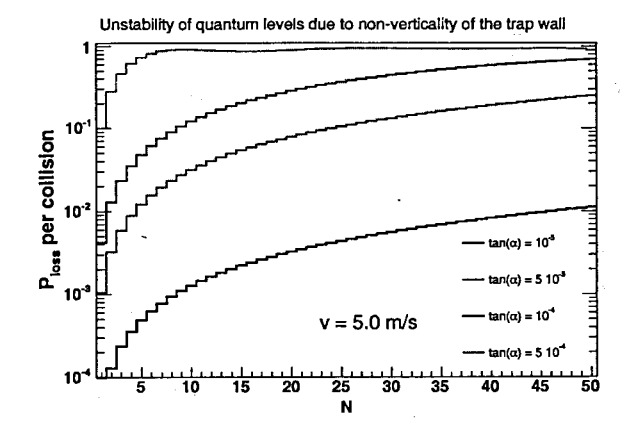


Figure 4: Escape probability from quantum states while colliding at the side wall as a function of the quantum state number, for different values of the angle α between side wall and vertical axis.

the effective size of the hole is twice the geometrical size due to reflection on the vertical mirror. Since the propagator of free fall evolution is well known, the wave function at time $t_{\text{free fall}}$ reads:

$$\psi(z, t_{\text{free fall}}) = \left(\frac{m}{2i\pi\hbar t}\right)^{1/2} \int e^{i\frac{m}{2\hbar}\left(\frac{(z-z')^2}{t} - (z+z')gt\right)} \psi(z', 0)dz'. \tag{21}$$

The amplitude for the neutron to be reflected in the same quantum state $|N\rangle$ is thus given by the overlap of this evolved wave function with the wave function corresponding to $|N\rangle$:

$$A_N(t) = \int \psi_N(z)\psi(z, t_{\text{free fall}})dz$$
 (22)

The loss probability, $1-|A_N|^2$, is shown in fig. 5 as a function of the falling time, for the first quantum states. This figure shows clearly that the quantum states are completely lost after an elapsed time corresponding to $10~\mu m$ free fall $\sqrt{2\cdot 10~\mu m/g}=1$ ms. It also shows that for smaller times, all quantum states have the same probability to be lost, that is, $P^{\rm corner}\approx 10^{-3}$ for $t_{\rm free~fall}$. As shown in fig. 6, the related loss rate $\Gamma_N^{\rm corner}=\frac{v}{L}P^{\rm corner}$ is ten times larger than the β decay rate. To reach the ultimate sensitivity, specific efforts have to be undertaken to minimize the corner defects. However, even in

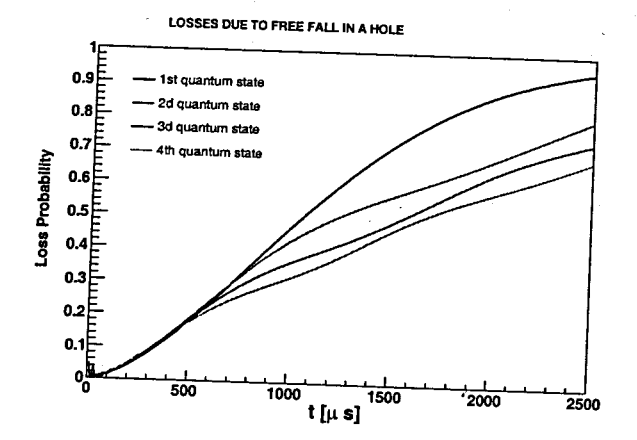


Figure 5: Probability for losing quantum states due to free fall as a function of free fall time, for the first quantum states.

the pessimistic situation presented above, corner defects do not forbid $10~\mathrm{s}$ storage time for trapped quantum levels.

4 Conclusion

The GRANIT experiment will measure the transition energies of gravitationally bound quantum states of neutrons below the kilohertz range, by inducing resonant transitions. The commissionning phase of GRANIT will start in April, 2008, and the first measurements are expected in 2009. We argued that increasing the storage time of trapped neutrons is an essential feature of the GRANIT experiment, since the width of the resonance curve is inversely proportional to the pulse time. We showed that magnetically induced transitions are doable even in flow through mode, and it will be possible to resolve the first resonances in the very first stage of the GRANIT experiment. The accuracy of the transition energies is limited by the β decay lifetime, and by the shift in energies due to noninertial effects induced by Earth rotation. This last subtle effect can in principle be avoided using only neutrons travelling in the East-West direction, but this will not be necessary since this effect will be dangerous only if we approach the ultimate sensitivity. Then the lifetime of trapped quantum levels due to imperfections of the

trap were estimated, and compared to the ultimate β decay storage time. We showed that the waviness of the bottom mirror is by no means a problem. The main source of losses comes from the side walls of the trap: both the deviation from verticality and the corner defects have to be minimized. Even in the most pessimistic case, a storage time of 10 s in the trap can be reached, corresponding to the relative accuracy 10^{-4} of transition energies.

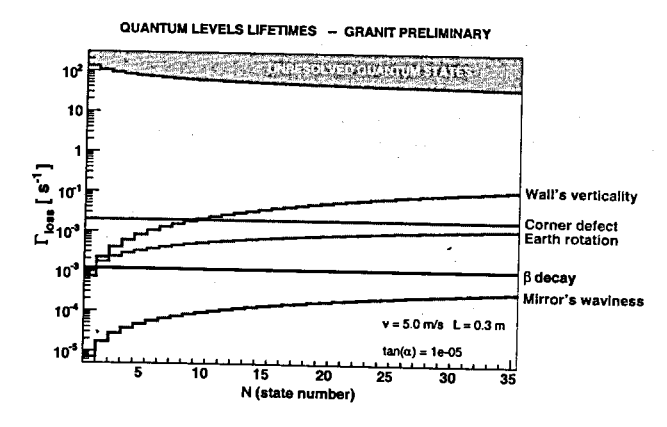


Figure 6: Loss rate of trapped quantum states as a function of the level number, due to effects analysed in the text: β decay, waviness of the bottom mirror, free fall in the corner defect, deviation from verticality of the side walls. Also shown the minimum loss rate needed to resolve the state, and minimum loss rate needed to be sensitive to Earth rotation bluring of the energy levels.

Acknowledgements

We are grateful to the French Agence Nationale de la Recherche (ANR) for supporting this project.

References

- [1] V. V. Nesvizhevsky et al., Nature 415, 297 (2002).
- [2] V. V. Nesvizhevsky et al., Phys. Rev. D 67, 102002 (2003).
- [3] V. V. Nesvizhevsky et al., Eur. Phys. J. C 40 (2005) 479.
- [4] G. Pignol, K. V. Protasov, V. V. Nesvizhevsky, Class. Quantum Grav. 24 2439-2441 (2007).
- [5] V. V. Nesvizhevsky et al., Proceedings ISINN-14, JINR, Dubna, Russia, (2006).
- [6] L. Assoufid *et al.*, Advances in Metrology for X-Ray and EUV Optics. Proceedings of the SPIE, **5921**, 129 (2005).
- [7] L. Landau, E. Lifchitz, Mécanique quantique (Éditions Mir Moscou 1988)p. 176.

New experimental method to determine the averaged squared radius of the nuclei in the process of the direct and isomer fission

Ts. Panteleev, C.D. Oprea, A.I. Oprea 141980 Dubna, FLNP-JINR

Abstract. It is proposed a method for the measurement of the mean squared radius of the ^{236}U nucleus during the fission process from the first and second potential barriers. This approach consists on precision determination of the energetic isomer shift of the X-ray quanta of the ^{236}U nucleus or difference in the intensity of the K_{α} and K_{β} lines measured in coincidence with processes of isomer and $(n,\gamma f)$ fission.

1. Isomer displacement of the X lines

Electric charge of the nucleus (monopol) interacts with the electrons from the atom shells, the finite dimensions of the nucleus and the non zero value of the electron wave function changes the energy of the atomic nuclei. Approximately we can write [1]:

$$\Delta E = \frac{2}{3}\pi e^2 Z |\Psi(0)|^2 \langle R^2 \rangle \tag{1}$$

 $\langle R^2 \rangle$ = averaged squared radius of the electric charge distribution of the nucleus

 $\Psi(0)$ = the electron wave function in the range of nucleus (supposed to be constant)

To evaluate the isomer displacement of X lines it is necessary to know the density of the K-electrons in the range of atomic nucleus. In the case of the nerelativistic case of hydrogen type atoms we have:

$$\Psi(r) = \frac{1}{\sqrt{\pi}} \left(\frac{2Z}{a_0}\right)^{\frac{3}{2}} \exp\left(-\frac{2Zr}{a_0}\right) \text{ (eV)}$$

$$\Delta E = 87.07Z^4 \left(\frac{R_{nucl}}{a_0} \right) \tag{3}$$

For $^{238}_{42}U$ $\Delta E = 123 \text{ eV}$

- in the relativistic case

- For $^{238}_{42}U$ $\Delta E = 2240 \text{ eV}$

These evaluations are only a higher limits of displacement as the screening effect due to the presence of electrons in atom is neglected

Necessary condition to observe and measure in experiments the isomer displacements

$$\tau_{nucl} > \tau_{el} \tag{4}$$

The time of life of excited nucleus must be more higher than the time of life of excited electron in atomic shell. If this condition is not respected the nucleus de-excites faster than the electronic shell and the information about excited nucleus will be loosed. So $\tau_{nucl} \ge 10^{-7}$ s.

2. Isomer displacement of neutron resonances [2-6].

The isomer displacement of the neutron resonances is the result of hyperfine interaction of the nucleus charge with the electronic shells of the atom. With approximation we can write:

$$\Delta E^{IS} = \frac{1}{6\varepsilon_0} e^2 Z \Delta \rho_{\epsilon}(0) \Delta \langle R_p^2 \rangle \tag{5}$$

 $\rho_{\epsilon}(0)$ = different electron density in the nucleus in the chemical liaisons

 ΔR_p^2 = the modification of the squared averaged charged radius of the nucleus after the capture of the neutron

In the papers [2-6] the problematic is very well described experimentally taking into account the oscillation of the crystal, different chemical liaisons, corrections of the isomer displacement. In [6] there are a very good theoretical description of the isomer displacement taking into account temperature corrections, recoil energy corrections and other. From [6] the isomer displacement of neutron resonance is very small and is of the order of 26 10-6 eV.

3. The new method of the determination of the averaged squared radius.

When the nucleus capture a neutron the radius of the nucleus is increasing and also the radius of the nucleus charge also is modifying. In the case of spherical nucleus the perturbation induced by the radius modification is very small (the Rydberg correction [7-8]). In this case the influence to the wave functions of the electrons is very small and the difference in the X lines intensity are also very small.

The situation is different when is the case of heavy deformed nuclei participating in the fission reaction. In this case it is expected that due to the deformation of the nucleus to have a modification that cannot be neglected in the wave function of the electron.

The nucleus captures a neutron and the time of life of suppose that the compound nucleus respect condition (4), $\tau_{nucl} > \tau_{el}$.

The neutron capture acts like a sudden perturbation and the atom can be ionized and electrons from K or L shells can be captured by the nucleus. In this condition it is possible to observe difference between the ratio of K_{α} and K_{β} lines. This ratio contains information of the averaged squared radius and a modification of this ratio gives us information about the averaged squared radius.

To evaluate the ratio of K lines we must evaluate the modification of the electron wave function due to the sudden perturbation realized by neutron capture in condition of well deformed compound nucleus. Problems of sudden perturbation are treated in [7-9]

As starting point is the evaluation of the amplitude of an electron be in an state i in one atom (not deformed) for example and a state f in perturbed atom, f [9].

$$a_{ij} \sim \int \Psi_f^* \Psi_i d^3 r \tag{6}$$

A difficult represents the evaluation of the wave function in the final state f in deformed nuclei. Using (6) it is possible to evaluate the transition in different final states f including one free state, for example an electron due to a sudden perturbation to become free. The intensity of an X line due to the transition of an electron to inner shells is proportional to the sum of square conjugate of coefficients (6).

4. Discussion. In the present now the authors are working to the theoretical evaluation of the difference in the intensities and to the setup of the experiment. Also a clear theoretical approach for the evaluation of the intensities of the X-rays lines there is not. One difficult of the choosing of the theoretical is connected with the existent experimental data on the ratios intensities of the X-ray transitions. We have decided to analyze the intensities when the nucleus is not excited by the capture of a neutron and in the case when the nucleus is excited by capture of a neutron. A heavy nucleus by capturing a slow neutron forms a compound nucleus with a high density of states. It is expected also after the capture of the

neutron the compound nucleus will be deformed. By deformation the compound nucleus will change his radius and for high excitation the compound nucleus can change also his shape and As is expected the deformation of the compound nucleus will influence the distribution of electrons shell. The interaction of the target nucleus with the neutron leads to the modification of the form, radius of the nucleus and distribution of the charge in the nucleus and as results the compound nucleus will emit gamma quanta. This gamma quanta by traversing the electron shell will strike out an electron from the inner levels and an electron from outer level will occupy the lower level by emission of an X gamma quanta. In this way the difference in intensities when the nucleus interact with a neutron and when the nucleus is not interacting with the neutron can give us an information about the averaged squared radius of the nucleus.

References.

- [1] V.K. Ignatovich, Yu. Ostanevich, Ts. Panteleev, Preprint Dubna, P4 7696, 1974
- [2] G. G. Akopian, V.A. Vagov, K. Zeydel, A. Meyster, D. Lubst, L. B. Pikelner, S. Szalai, Preprint Dubna, P3 11740, 1978
- [3] K. Zeydel, A. Meyster, D. Lubst, L. B. Pikelner, Preprint Dubna, P3 11741, 1978
- [4] K. Zeydel, A. Meyster, D. Lubst, Preprint Dubna, P3 11742, 1978
- [5] K. Zeydel, A. Meyster, D. Lubst, L. B. Pikelner, Preprint Dubna, P3-80-135, 1980
- [6] V.K. Ignatovich, Preprint Dubna, P4-2001-256, 2001
- [7] A.B. Migdal, B.P. Krainov, Priblizhenye Metody Kvantovoy Mekhaniki, Izdatelstvo Nauka, Glav. Red. Fiz-Mat. Lit, Moskva, 1966
- [8] G. Breit, Phys. Rev., Vol.42, p.348, 1 November 1932
- [9] J. S. Levinger, Phys. Rev., Vol. 90, №1, 1 April, 1953

Comments to the problem of experimental determination of the neutronelectron scattering length and its theoretical interpretation

A.B. Popov, T.Yu. Tretyakova Joint Institute for Nuclear Research, 141980 Dubna, Russia

Abstract

We discuss the experimental data on the n,e-scattering length b_{ne} and the values of mean square charge radius of the neutron $\langle r_e^2 \rangle_n$ obtained from them. It is shown that the accumulated during the last 50 years most significant experimental estimates of the b_{ne} are not contradictory and lead to the average value

$$\langle r_e^2 \rangle = -0.1178 \pm 0.0037 \text{ fm}^2$$
.

Assuming that all the authors have underestimated the errors of their measurements by a factor of 1.7, the combined fit of all available experimental data would lead to $\chi^2 \sim 1$ per degree of freedom. Different modern theoretical predictions of $\langle r_e^2 \rangle_n$ are considered. They are found to be in a good agreement with the obtained experimental value $\langle r_e^2 \rangle_n$. However the existing theoretical description of the structure of neutron does not provide a value of $\langle r_e^2 \rangle_n$ with a sufficient accuracy.

Introduction

Since first work of E. Fermi [1] for more than 50 years the question about n,e-interaction attracts attention of both experimentalists and theorists. During these years many experiments with different methods for determination of n,e-scattering length b_{ne} were carried out and theoretical ideas about connection of b_{ne} with mean square charge radius of a neutron $\langle r_e^2 \rangle_n$ were developed. The view of nucleon internal structure has changed significantly and now it is based on Standard Model principles. Unfortunately, the existing experimental estimates of b_{ne} are widely different, which allows to divide these values in two groups which differ by more than three standard deviations [2, 3, 4, 5]. Moreover, in the beginning of 50th Foldy has showed that n,e-scattering length b_{ne} could be devided in two parts, the second one depended on anomalous magnetic moment of neutron and named as "Foldy length" $b_{ne} = \frac{\mu e^2}{2M_n c^2} = -1.468 \cdot 10^{-3} \text{ fm}$ [6]. Taking into account this Foldy length one can obtain so-

called "intrinsic" charge radius of neutron $\langle r_1^2 \rangle$, which will have different sign for the two groups of experimental results. The physical meaning of $\langle r_1^2 \rangle$, at least its sign, was the subject of a long-term discussion. The positive value was admitted by some authors as unphysical [3], that put under doubt results of the most numerous group of experiments, which gave values of n,e-scattering length $b_{ne} = -(1.32 \pm 0.03) \cdot 10^{-3} \text{ fm}$.

In work [7] the Foldy's description of n,e-scattering length was revised on the basis of the Dirac's equation and it was emphasized that b_{ne} is related to the complete coefficient in front of $div\overline{E}$ - term in the equation, so that the charge distribution is connected with the total

value of b_{ne} only. Consequently the mean square charge radius of a neutron is related only to this value, i.e.

$$\langle r_e^2 \rangle_n = \frac{3\hbar^2}{M_e e^2} b_{ne}. \tag{1}$$

Since papers [8] and [9] it is accepted to estimate the value of $\langle r_e^2 \rangle_n$ using this equation.

The coefficient before b_{ne} can be expressed through the other constants: $\frac{3m_e}{M_n}a_0$ (where

$$a_0 = \frac{\hbar^2}{m_e e^2}$$
 is the Bohr radius) or $\frac{3\hbar c}{\alpha M_n c^2}$ ($\alpha = \frac{e^2}{\hbar c}$).

In the compilation of the Particle Data Group [10] the ten experimental results are shown and the recommended value is obtained by averaging only five of them:

$$\langle r_{\rm s}^2 \rangle_n = -0.1161 \pm 0.0022 \ fm^2$$
 (2)

In this compilation the authors use the result of [11], obtained in 1986 from the neutron total cross section of Bi, which was subjected to serious criticism in [12]. On the other hand the largest absolute value of $b_{ne} = -1.60 \pm 0.05 \, mfm$ from neutron diffraction on a single crystal of ¹⁸⁶W [13] was ignored.

Analysis of existing measurements

In present work we consider a more complete set of b_{ne} experimental data and corresponding values of $\langle r_e^2 \rangle_n$, adding estimates of b_{ne} from works [13] (for a single crystal of ¹⁸⁶W), [14], [15], [16] (corrected for Schwinger's scattering in [2]) and recent result [17], obtained from the structural factors for liquid Kr by method proposed in [5].

All collected data are summarized in Table 1 and fig. 1. The calculations of the average $\langle r_n^2 \rangle$ value are performed using the MINUIT program [23] for several approaches. The corresponding results are shown in Table 2. We use different sets of experimental results: first 14 experiments from Table 1, the same set but without the value for ^{186}W , the set with two additional points from new estimations of b_{ne} from neutron scattering total cross section on ^{208}Pb , obtained from the analysis of Garching group data [8] and the result of FLNP experiment [22]. In the last set we also use the original result [11] instead of reestimated value of $\langle r_n^2 \rangle$ for Bi from [20].

Thus, we can conclude from Table 2 that the existing estimates of b_{ne} give an average value of $\langle r_n^2 \rangle$:

$$\langle r_{\star}^2 \rangle_{\star} = -0.1178 \pm 0.0037 \text{ fm}^2$$
. (3)

In the fig. 1 we show the fitting results of average $\langle r_e^2 \rangle_n$ value using the original experimental data. It can be seen that all experimental points differ from the average value by not more than three standard deviations except the result for ¹⁸⁶W [13]. Rejection of this point does not change the result significantly and leads to the average value:

$$\langle r_s^2 \rangle_n = -0.1153 \pm 0.0024 \text{ fm}^2$$
. (4)

Both results correspond to 95% confidential interval and are in a good agreement within errors with the value recommended by Particle Data Group.

It is possible to draw a conclusion, that all available experimental estimates of b_{ne} ($\langle r_e^2 \rangle_n$) are not in contradiction with each other under assumption that the authors have underestimated errors of their experiments by less than a factor of two. This assumption is quite realistic taking into account the presence of strong corrections of a different origin in each experiment, which accuracy is really limited and requires a serious reassessment.

Table 1. n,e-scattering length b_{ne} and mean square charge radius of neutron $\langle r_n^2 \rangle$.

Bold font in column "Year" marks the value used in later averaging.

Experiment	Year	$b_{ne} \cdot 10^{-3}$, fm	$< r_n^2 > , fm^2$
W. Havens, liquid Bi σ_i [14]	1951	-1.89 ± 0.36	-0.163 ± 0.31
Huhges, mirror Bi/O ₂ [15]	1953	-1.39 ± 0.13	-0.120 ± 0.011
Melkonian, Bi cryst spectr σ_i [16]	1959	-1.56 ± 0.05	-0.135 ± 0.004
Re-estimation, Koester	1976	-1.49 ± 0.05	-0.127±0.004
Re-estimation, Kopecky [2]	1997	$-1.44 \pm 0.03 \pm 0.06$	$-0.124 \pm 0.003 \pm 0.008$
Krohn, angle distribution on gases	1966	-1.34 ± 0.03	-0.116 ± 0.003
Re-estimation, Krohn [18]	1973	-1.33 ± 0.03	-0.115 ± 0.003 *
Alexandrov, ¹⁸⁶ W [13]	1975	-1.60 ± 0.05	-0.138 ± 0.004
Koester, filters - b_{coh} Pb [19]	1976	-1.364 ± 0.025	-0.118±0.002**
Re-estimation, Nikolenko [20]	1990	-1.32 ± 0.03	-0.114 ± 0.003
Koester, filters - b_{coh} Bi [19]	1976	-1.393 ± 0.025	-0.120±0.002**
Re-estimation, Nikolenko [20]	1990	-1.33 ± 0.03	-0.115±0.003
Alexandrov, TOF σ_i - b_{coh} Bi [11]	1986	-1.55 ± 0.11	-0.134 ± 0.009 *
Re-estimation, Nikolenko [20]	1990	-1.40 ± 0.04	-0.121±0.004
Koester, filters - b _{coh} Pb, Bi [21]	1986	-1.32 ± 0.04	$-0.114 \pm 0.003^{**}$
Kopecky, liquid ^{208}Pb TOF σ_{i} [9]	1995	$-1.31\pm0.03\pm0.4$	$-0.113 \pm 0.002 \pm 0.003$
Koester, ²⁰⁸ Pb, Bi TOF [8]	1995	-1.32 ± 0.03	-0.114 ± 0.003 *
Kopecky, liquid ^{208}Pb TOF σ_i [2]	1997	$-1.33 \pm 0.03 \pm 0.03$	$-0.115 \pm 0.003 \pm 0.003^*$
Kopecky, liquid Bi TOF σ_i [2]	1997	$-1.44 \pm 0.03 \pm 0.04$	$-0.124 \pm 0.003 \pm 0.005^*$
Magli, diffraction on liquid Kr [17]	2006	-1.40 ± 0.10	-0.121±0.009
WaschLNP, ²⁰⁸ Pb	2006	-1.56 ± 0.18	-0135 ± 0.016
LNP, ^{208}Pb TOF σ_{t} -old [22]	2006	-1.70 ± 0.15	-0.147 ± 0.013
Estimation of Particle Data Group	2006		-0.1161±0.0022
[10]			

Data used for estimation of average $\langle r_{\perp}^2 \rangle$ by Particle Data Group

Theoretical aspects

Let us consider the modern theoretical view on neutron charge structure. First of all it should be noted that the definition of mean square charge radius $\langle r_e^2 \rangle_n$ works in coordinate space in non-relativistic assumption. But in most of modern theoretical

Table 2. Average values of $\langle r_{\epsilon}^2 \rangle_n$.

Number of points	χ ²	$\langle r_e^2 \rangle_n$, fm^2	Confidence interval
14 points	39.4	$-0.1172 \pm 0.0012 (0.0021^{\circ})$	67%
14 points	39.4	$-0.1172 \pm 0.0023 (0.0040^*)$	95%
Without 186W	9.87	-0.1153 ± 0.0012	67%
- "-	9.87	-0.1153 ± 0.0024	95%
With two last points for ²⁰⁸ Pb and Bi from [11], 17 points	46.5	-0.1178±0.0022 (0.0037*)	95%
17 points, errors are increased by $\times \sqrt{\frac{\chi^2}{n-1}}$	16.1	-0.1178 ± 0.0037	95%

*Error corrected by factor $\times \sqrt{\frac{\chi^2}{n-1}}$

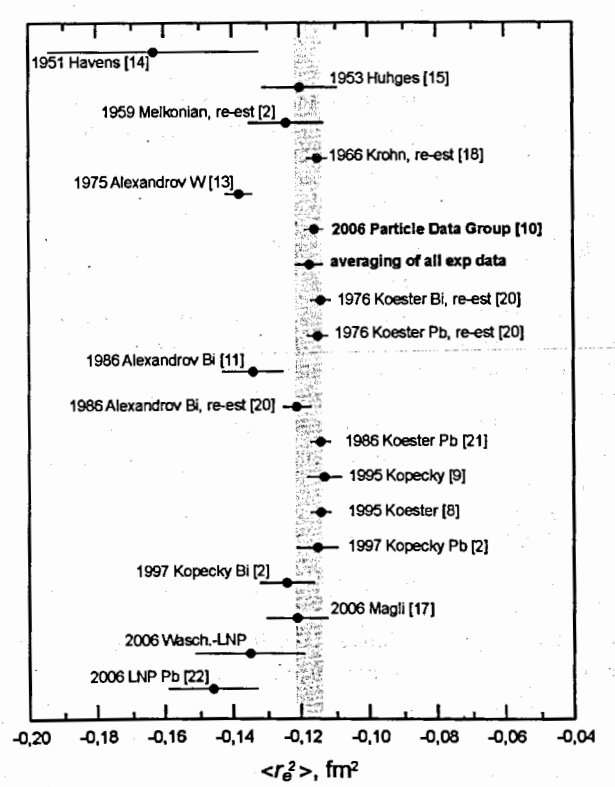


Fig. 1. Neutron mean square charge radius $\langle r_e^2 \rangle_n$ from different experiments and the average value. The shaded area shows the 95 % confidential interval.

^{**} Data included in Table of Particle Data Group but not used for estimation of $\langle r_n^2 \rangle$

approaches hadron charge structure is considered in impulse space and its distinctive characteristic is the dependence of nucleon electromagnetic form factors on momentum transfer. At small values of momentum transfer form factors reflect such nucleon features as its charge and magnetic moment, radii of charge and magnetic moment distributions, whereas at large ones they constitute the information on quark structure of nucleon corresponding to quantum chromodynamics.

Electromagnetic structure of nucleon is determined by matrix element of current operator j, which can be expressed via two form factors:

$$\langle \mathbf{p}' | j_{\mu} | \mathbf{p} \rangle = \overline{u}(\mathbf{p}') [F_1(q^2) \gamma_{\mu} + F_2(q^2) i \sigma_{\mu\nu} q^{\nu} / 2M] u(\mathbf{p}),$$

where M is the nucleon mass, q^2 is the square of momentum transfer. $F_1(q^2)$ is Dirac form factor carried information on charge and normal magnetic moment of nucleon, $F_2(q^2)$ is the Pauli form factor corresponded to particle anomalous magnetic moment. Form factors $F_1(q^2)$ and $F_2(q^2)$ for proton and neutron are normalized at $q^2=0$ on their charge and magnetic moment values:

$$F_1^{p}(0) = 1, F_1^{n}(0) = 0, F_2^{p}(0) = 1,79, F_2^{n}(0) = -1,91$$

For description of the nucleon total magnetic moment and charge radius in [24] charge and magnetic form factors were introduced

$$G_E(q^2) = F_1(q^2) - \frac{q^2}{4M^2} F_2(q^2)$$
 and (5)

$$G_{M}(q^{2}) = F_{1}(q^{2}) + F_{2}(q^{2}). \tag{6}$$

Such expressions are optimal from the experimental analysis point of view because they do not interfere in well known Roesenbluth formulae for differential cross section of electron scattering on space target with spin ½:

$$\frac{d\sigma}{d\Omega} = \left(\frac{d\sigma}{d\Omega}\right)_{Most} \left\{ \frac{G_{E}^{2} - \frac{q^{2}}{4M^{2}}G_{M}^{2}}{1 - \frac{q^{2}}{4M^{2}}} - \frac{q^{2}}{2M^{2}}G_{M}^{2}tg^{2}\left(\frac{\Theta}{2}\right) \right\}$$

Sacks showed [25] that in Breit system just form factors of such form corresponded to Fourier transforms of the charge and magnetization distributions, that is why they were named as electric and magnetic ones. Formally all other form factors (Dirac, Pauli, their isovector or isoscalar combinations) also can be presented as Fourier transforms of some space distributions too, but most likely it would be formal presentations without any physical sense. Respectively for every form factor at $q^2 \rightarrow 0$ the mean square radius of associated space distribution can be defined:

$$\langle r_i^2 \rangle = -6 \frac{dF_i(q^2)}{dq^2} \Big|_{q^2=0}$$
.

In the case of charge form factor G_E this quantity corresponds to nucleon mean square charge radius obtained from experiment.

As soon as G_E is expressed through combination of Dirac and Pauli form factors, the neutron charge radius $\langle r_e^2 \rangle_n$ can be presented as a sum:

$$\langle r_e^2 \rangle_n = r_1^2 + r_{Foldy}^2 , \qquad (7)$$

where $r_1^2 = -6 \frac{dF_1^n(q^2)}{dq^2}\Big|_{q^2=0}$ and $r_{Foldy}^2 = \frac{3\mu_n}{M^2}$ $(\mu_n = F_2^n(0))$ the neutron anomalous

magnetic moment). The second part, Foldy term [6], appears due to the generation of the electric field by the anomalous neutron magnetic moment because of its "zitterbewegung". With the neutron magnetic moment $\mu_n = -1.91$ the value of this term is $r_{Foldy}^2 = -0.126 \text{ fm}^2$ and it is very close to experimental estimations of $\langle r_e^2 \rangle_n$.

This fact attracts the attention of theoreticians and during last years several works have evolved which consider the radius r_1^2 , connected with Dirac form factor [26, 27, 28, 29, 30] and attempt to find the physical meaning of this quantity. It was shown that in non-relativistic approximation, with the SU(6) symmetric wave function, the neutron charge form factor is identically zero $G_E^n(q^2) \equiv 0$. Attempts to incorporate the relativistic effects result in $r_1^2 = -r_{Foldy}^2$, so in this approximation the value of neutron charge radius is still zero $\langle r_e^2 \rangle_n = 0$ [27, 28].

In [26] the higher order in expansion on $1/m^n$ (where m is the quark mass) was used and the dependence of nucleon characteristics on quark anomalous magnetic moments was considered. The fit of the nucleon static properties results in the reasonable values for nucleon magnetic moments $\mu_n = -1.92$ and $\mu_p = 3.09$, and neutron charge radius $\langle r_e^2 \rangle_n = -0.125 \ fm^2$ ($r_i^2 = 0.002 \ fm^2$, $r_{coldy}^2 = -0.127 \ fm^2$)

The other authors [29] believe that the agreement between $\langle r_e^2 \rangle_n^{\text{exp}}$ and r_{Foldy}^2 is accidental and underline that the rest frame charge distribution of the neutron should be associated with the form factor G_E^n and not with F_1^n . In this work it was shown that in non-relativistic regime the cancellation between r_1^2 and r_{Foldy}^2 happens indeed for large nucleon sizes and it is independent of the detailed form of quark spin coupling scheme and wave functions, while at the physical nucleon scale the value of r_1^2 is strongly dependent on the choice of quark spin coupling scheme.

In [28] the connection of neutron charge radius with Dirac equation is discussed more closely. Authors consider the Dirac equation for a finite-size neutron in an external electric field and incorporate Dirac-Pauli form factors in it explicitly. After a non-relativistic reduction, the Darwin-Foldy term is cancelled by a contribution from the Dirac form factor,

so that the only coefficient of the external field charge density is $\frac{e}{6} < r_e^2 >_n$, i. e. the mean square radius associated with the electric Sachs form factor G_E^n . This result is similar to a result of [27], however it is independent from any definite neutron quark substructure. The

neutron just has to have a form factor. Furthermore, the analysis is in keeping with the philosophy that the basic equations for the neutron should be expressed in terms of a Dirac Hamiltonian, while the physical picture emerges from a non-relativistic reduction, which only contains $\langle r_e^2 \rangle_n$. In [28] it is noted that G_E^n contains the buried term, which depends on neutron anomalous magnetic moment and contributes the most to the neutron charge radius. The analysis and conclusion are in good agreement with the analysis of [31] for low-energy Compton scattering from nucleon.

The results of these calculations and nucleon features obtained in other models are given in table 3.

It should be noted that we are interested in region of low momentum transfer, which is beyond the limits of perturbative quantum chromodynamics, so for nucleon static characteristics description some models should be used. The one exception is the lattice calculations share basic principles of QCD. During the past few years this field has progressed substantially and now the results for nucleon properties agree satisfactorily with the experimental data [36, 37]. However these calculations have not given an understanding the physical picture, the different model approaches as quark model, for example, retain their importance. A reliable calculation of the nucleon static characteristics should incorporate many contributions, such as relativistic effects in the nucleon wave function, its nontrivial spin structure, exchange currents within nucleon, pionic

Table 3. Theoretical estimations of nucleon magnetic moments and mean square charge radii.

	Reference	μ_p	μ_n	$\langle r_e^2 \rangle_p$, fm ²	$\langle r_e^2 \rangle_n$, fm ²	$\langle r_1^2 \rangle$, fm ²
Experiment			-1.91		-0.118	
PDG	[10]	2.79	-1.91	0.757(14)	-0.1161(22)	
Model						
RQM	[30]				4	005 ÷ 0.009
	[32]	2.88	-1.58	0.62	-0.185	-0.084
	[26]	3.09	-1.92		-0.125	0.002
QM	[33]	3.05	-1.55	0.58	-0.256	
PQCD	[34]			0.689	-0.119	
LFCBM	[35]	2.95	-1.79		-0.110	
LC	[36]				-0.113 (17)	
	[37]	2.72 (26)	-1.82(34)	0.685 (47)	-0.158 (29)	

fluctuations of constituent quarks [30], anomalous quark magnetic moments, etc [26]. Calculations of these corrections are a difficult enough problem so it is difficult to treat the accuracy of one model or another and to wait for precise description of experimental data. At present state the experimental results are more accurate than theoretical calculations. They can be used as a criteria in deciding between different theoretical models [30].

Thus it can be stated that in recent publications (except [3]) the authors do not mention the separation of Foldy term from experimental value of b_{ne} . Obtained from b_{ne} experimental estimate of $\langle r_e^2 \rangle_n$ is considered as a total mean square charge radius of neutron. The statement [3] about division of experimental data in two groups and that part of these data are in contradiction to modern physical theories has no meaning evidently (see table 1 and figure). Considering theoretical approaches mentioned above one can notice that $\langle r_e^2 \rangle_n$ can be divided into two components, related to Dirac and Pauli form factors, but in different models the relation between these two components is different and so-called "intrinsic" charge radius of neutron $\langle r_i^2 \rangle$ connected with the Dirac form factor may have either positive or negative sign. Moreover in some papers it was shown that consideration of Dirac equation for neutron at non-relativistic limit leads to vanishing the Foldy term, while the term, expressed through $\langle r_e^2 \rangle_n$, is still present. It is responsible for interaction of neutron with external electric field. This means that in Born approximation the n,e-scattering length b_{ne} depends only on the total charge radius of neutron $\langle r_e^2 \rangle_n$, as stated previously in [7].

Conclusions

The problem of b_{ne} and neutron charge radius estimation appears to be less pressing. It is unlikely that existing set of experimental data should be considered as self-contradictory. The average value from all experiments

$$\langle r_e^2 \rangle_n = -0.1178 \pm 0.0037 \ fm^2$$

within limits of its accuracy of 4% corresponds to confidence interval of 95% even including the result for ^{186}W , which differ from the average value by more than 5 standard deviations. If this measurement is excluded, the average value becomes

$$\langle r_e^2 \rangle_n = -0.1153 \pm 0.0024 \text{ fm}^2$$

with accuracy $\langle r_e^2 \rangle_n - 2.5\%$ for confidence interval of 95%.

Of course, extraction of $b_{ne}^{\rm exp}$ from different experiments required important corrections to be made. That is why new experimental proposals using new approaches are very interesting, however it is naive to expect that they could lead to abrupt changes in the problem considered. It is very important to perform an experiments with accuracy better than 2.5%. Proposals of precise measurements using interferometers are worth to mention [4, 38, 39]. The experiments to measure the structure factors of noble gases [5, 17] may be useful also. However more precise experimental determination of $\langle r_e^2 \rangle_n$ cannot improve its physical interpretation due to ambiguity of theoretical descriptions of nucleon structure nowadays. But this precise experimental value of $\langle r_e^2 \rangle_n$ would be very helpful in future development of nucleon characteristics.

References

- 1. E. Fermi, L. Marshal, Phys. Rev. 72, 1139 (1947).
- 2. S. Kopecky et al., Phys. Rev., C56, 2229 (1997).
- 3. Yu.A. Alexandrov, Phys. Part. And Nuclei, 30, 72 (1999).
- 4. J.M. Sparenberg, H. Leeb, arXiv:quant-ph/0201059 v1 15 Jan 2002.
- 5. L.V. Mitsyna et al., Eur. Phys. J., C40, 473 (2005).
- 6. L. Foldy, Rev. Mod. Phys. 30 (1958) 471.
- 7. G.G. Bunatian et al., Z. Phys., A359, 337 (1997).
- 8. L. Koester et al., Phys. Rev., C51, 3363 (1995)
- 9. S. Kopecky et al., Phys. Rev. Lett., 74, 2427 (1995).
- 10. V.M. Yao et al., J. Phys., G33,1 (2006).
- 11. Ya.A. Alexandrov et al., Yad. Fizika, 44, 1384 (1986).
- 12. V.G. Nikolenko, A.B. Popov, Z. Phys., A341, 365 (1992).
- 13. Yu.A. Alexandrov et al., Sov. J. Nucl. Phys., 60, 623 (1975).
- 14. W. Havens, I. Rabi, L. Reinwater, Phys. Rev., 82, 345 (1951).
- 15. D.J. Hughes et al., Phys. Rev., 90, 497 (1953).
- 16. E. Melkonian, B.M. Rustad, W. Havens, Phys. Rev., 114,1571 (1959).
- 17. R. Magli, L.V. Mitsyna et al., Proc. ISINN-14, Dubna, May, 2006, in print.
- 18. V. Krohn, J. Ringo, Phys. Rev., D8, 1305 (1973)
- 19. L. Koester, N. Nistler, W. Waschkowski, Phys. Rev. Lett., 36, 1021 (1976).
- V.G. Nikolenko, A.B. Popov, Proc. of 8th Int. Symp. Capture Gamma-ray Spectroscopy, Fribourg, 20-24 Sept, 1993, p.815.
- 21. L. Koester, W. Waschkowski, A.Kluver, Physica, 137B, 282 (1986).

22. L. Mitsyna et al., Proc. ISINN-15, Dubna May, 2007, in print.

23. CERN Program Library Long Writeup D506. James. F. MINUIT. CERN, Geneva, Switzerland.

24. F.J. Ernst, R.G. Sachs, K.C. Wali, Phys. Rev 119 (1960) 1105

25. R.G. Sachs, Phys. Rev 126 (1962) 2256

26. V.A. Karmanov, arXiv:hep-ph/0106349 v1 29 Jun 2001.

27. N. Isgur, arXiv:hep-ph/9812243 v1 3 Dec 1998.

28. M. Bawin, S.A. Coon, arXiv:nucl-th/9906014 v1 5 Jun 1999.

29. W. de Araujo et al., arXiv:hep-ph/0305120 v1 12 May 2003.

30. L.Ya. Glozman and D.O. Riska, arXiv:hep-ph/9812224 v2 14 Mar 1999

31. A.I.L'vov, Int. J. Mod. Phys., A8, 5267 (19930.

32. J.C.R. Bloch et al. Phys. Rev.C60, 062201 (1999).

33. R.Alkofer et al, arXiv:nucl-th/0412046 v1 13 Dec 2004

34. M.A. Belushkin, H.W. Hummer, U.G. Meissner, arXiv:hep-ph/0608337 v1 31 Aug 2006

35. G.A. Miller, arXiv:nucl-th/0301041 v1 12 Jan 2003

36. A. Tang, W. Wilcox, R. Lewis, arXiv:hep-lat/0307006 v2 30 Sept 2003

37. D.B. Leinweber et al, arXiv:hep-lat/0601025 v2 18 Jul 2006

38. A. Ioffe, M. Vrana, Applied Physics, A74, S314 (2002).

39. P. Wietfeld et al., arXiv:nucl-ex/0509018 v1 14 Sep 2005.

A source of ultra-cold neutrons for the gravitational spectrometer "GRANIT"

P. Schmidt-Wellenburg*1,2, P. Geltenbort¹, V.V. Nesvizhevsky¹, C. Plonka¹, T. Soldner¹, F. Vezzu³, O. Zimmer^{1,2}

1) Institut Laue Langevin,

6, rue Jules Horowitz, BP-156, 38042 Grenoble Cedex 9, France

2) Physik-Department E18,

Technische Universität München, 85748 Garching, Germany

3) Laboratoire de Physique Subatomique et de Cosmologie, IN2P3/4JF, 53 Avenue des Martyrs, 38026 Grenoble Cedex, France

September 11, 2007

Abstract

We present the status of the development of a dedicated high density ultra-cold neutron (UCN) source dedicated to the gravitational spectrometer GRANIT. The source employs superthermal conversion of cold neutrons to UCN in superfluid helium. Tests have shown that UCN produced inside the liquid can be extracted into vacuum. Furthermore a dedicated neutron selection channel was tested to maintain high initial density and extract only neutrons with a vertical velocity component $v_{\perp} \leq 20$ cm/s for the spectrometer. This new source would have a phase-space density of $\Gamma_{\rm UCN} \approx 0.18~{\rm cm}^{-3} ({\rm m/s})^{-3}$ for the spectrometer.

Introduction

The solutions for Schrödinger's equation for a neutron bouncing on a reflecting horizontal surface in the earth gravitational field are given by Airy functions [1]. This textbook example of bound energy states in a linear potential has been demonstrated experimentally at the high flux reactor of the Institut Laue Langevin [2, 3]. A new gravitational spectrometer, GRANIT [5], is being built to investigate these quantum states further, and to induce resonant transitions between gravitationally bound quantum states. Applications are a refined measurement of the electrical charge of the neutron, the search for the axion [4], and other additional forces beyond the

^{*}Corresponding author: Tel.: +33 4 76 20 70 27; fax: +33 4 76 20 77 77. E-mail address: schmidtw@ill.fr

standard model. Experiments at the present UCN source are limited by counting statistics and systematic effects¹. In these conference proceedings the advances of a dedicated UCN source, based on superthermal conversion of cold neutrons in superfluid helium are described.

General aspects of Helium-4 based superthermal converters

The dominant process in the conversion is the excitation of a single phonon inside the superfluid helium. Cold neutrons with a wavelength around 8.9 Å $(k=2\pi/\lambda^*=0.7~\text{Å}^{-1})$, i.e. 1.0 meV kinetic energy, can be scattered down to the ultra-cold energy range by emission of one single phonon [6]. Multiphonon processes may also occur, depending on the incoming neutron spectrum [7, 8]. The resulting saturated UCN density,

 $\rho_{\text{UCN}} = P \cdot \tau, \qquad \bullet \tag{1}$

is determined by production rate density P and neutron storage time τ inside the converter volume. The rate

$$1/\tau = \frac{1}{\tau_{\beta}} + \frac{1}{\tau_{\text{wall}}} + \frac{1}{\tau_{\text{up}}} + \frac{1}{\tau_{\text{abs}}}, \qquad (2)$$

includes contributions from all existing loss channels (neutron beta decay, losses due to wall collisions, up-scattering due to phonons, nuclear absorption by ³He-impurities in the helium). As the absorption cross section of ⁴He is zero there is no absorption inside a pure converter.

The equation of detailed balance,

$$\sigma\left(E_{\text{UCN}} \longrightarrow E^{*}\right) = \frac{E^{*}}{E_{\text{UCN}}} \exp\left(-\frac{E^{*} - E_{\text{UCN}}}{k_{\text{B}}T}\right) \cdot \sigma\left(E^{*} \longrightarrow E_{\text{UCN}}\right),\tag{3}$$

relates the cross sections of a two level system, as our one-phonon excitation process, dependent on temperature. For $T \longrightarrow 0$ K the up-scattering cross section will be arbitrarily small. In pure ⁴He only two contributions to the total storage time remain; the neutron beta decay and losses due to wall collisions. The UCN production rate density is defined as the conversion rate of neutrons to energies below the Fermi potential of the walls of the converter volume and is thus dependent on the wall material. The production rate density expected for the 1-phonon process in a beryllium ($V_F = 252$ neV) coated converter volume ($V_F = 252$ neV) is $P_F = (4.55 \pm 0.25) \cdot 10^{-8} d\Phi/d\lambda/\lambda^* s^{-1} cm^{-3}$, with the differential flux at $\lambda^* = 8.9$ Å given in cm⁻²s⁻¹Å⁻¹[9].

Source concept

GRANIT and its source will be positioned on the neutron beam H172 on level C of the high flux reactor at the ILL (see fig. 1). A crystal monochromator, positioned

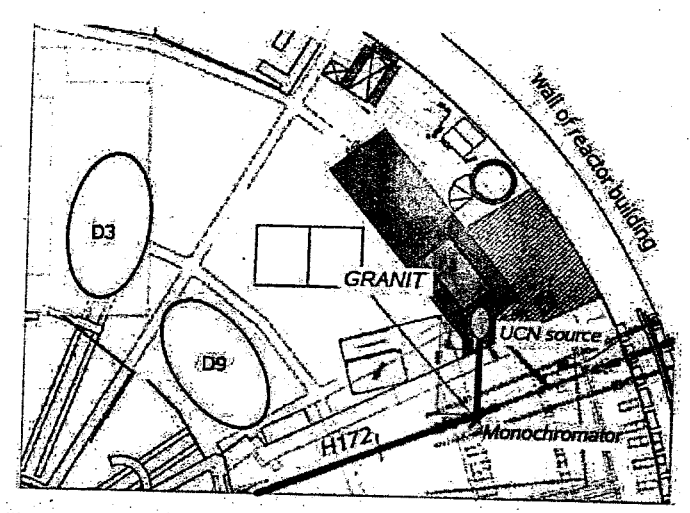


Figure 1: Setting of the monochromator, the source, and GRANIT inside level C of the ILL. (For more details see: www.ill.fr/pages/science/imgs/PlanInstILL.gif)

12 m downstream from the cold source, will reflect 8.9 Å neutrons under a take-off angle of $\theta=61.2^{\circ}$. Between monochromator and converter volume a 3 m long neutron guide with m=2 supermirror coating will be installed. The reduction in background will outweight by far the decrease in conversion rate due to the imperfect monochromator and the omission of multi-phonon processes. A nitrogen cooled beryllium filter will be installed further upstream of the monochromator to reduce high energy neutrons at the monochromator position. As source we will employ an existing apparatus [10] modified for our new requirements; a continuous flux of UCN within a narrow phase space element.

A sketch of the converter volume with heat screens and extraction is shown in figure 2. The UCN will diffuse from the converter volume through a highly specular guide into an intermediate volume. This second volume at room temperature allows a vertical tube extraction from the converter. Thus avoiding cryogenic difficulties of a direct horizontal extraction with foils which has posed problems in the past [11] and reduces background from directly scattered cold neutrons. Furthermore it evenly distributes all neutrons to the semidiffuse channel [12]. Which is used to select neutrons with small vertical energy E < mgh < 20 peV for the spectrometer whereas all other neutrons are reflected back or are lost on wall collisions. This method will increase the storage time inside the intermediate volume and the converter volume, as more than 85% of the neutrons incident on the channel entrance will be reflected back. Thus the UCN density is increased which in turn increases the flux of extracted neutrons.

¹For a discussion of systematic effects concerning these measurements see G. Pignol (these proceedings).

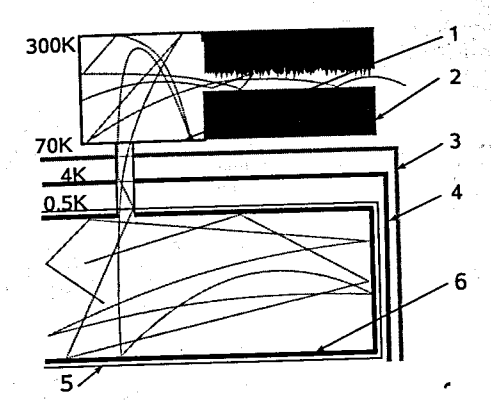


Figure 2: Schematic sketch of the source with extraction. 1) Intermediate storage volume, 2) semidiffuse extraction channel, 3) 70 K heat screen, 4) 4 K heat screen, 5) vessel for superfluid helium, 6) converter volume. Neutrons entering the channel with $E_{\perp} \geq mgh$ (--) are reflected back, the energy components are redistributed due to the rough surfaces of the intermediate volume thus it may pass the channel in the next attempt. A neutron with $E_{\perp} \leq mgh$ (--) can pass the channel immediately.

Neutron monochromator

Only a narrow range of wavelengths around 8.9 Å of incident neutrons is suitable for the dominant 1-phonon downscattering in superfluid helium. This allows to benefit from a crystal monochromator which reflects apt neutrons and diminishes background at the experiment.

Crystal monochromators reflect neutrons of the desired wavelengths away from the primary beam under the d-spacing dependent Bragg angle:

$$\theta_{\rm B} = \arcsin\left(\frac{n\lambda}{2d}\right). \tag{4}$$

The d-spacing of a monochromator for $\lambda=8.9$ Å has to be $d>\lambda/2=4.45$ Å. In a perfect single crystal the line width for Bragg reflected neutrons is extremely small, $\Delta k/k=10^{-4}$ [13] leading to a very narrow acceptance angle of incident neutrons:

$$\frac{\Delta k}{k} = \cot \theta \Delta \theta. \tag{5}$$

The incident beam has a divergence of typically $\pm 2^{\circ}$ at 8.9 Å due to the m=2 supermirrors used in the guide. Therefore a "mosaic crystal" [13] will be used. Such a crystal can be regarded as a collection of microscopic small perfect crystals with differing angles ϵ with respect to the overall crystal orientation. Although the angular distribution is in general arbitrary, it resembles a cylindrically symmetric Gaussian distribution:

$$W(\epsilon) = \frac{1}{\sqrt{2\pi\eta}} \exp\left(-\epsilon^2/2\eta^2\right),\tag{6}$$

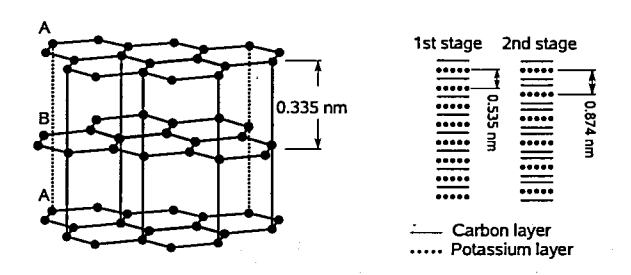


Figure 3: Crystal structure of graphite and staging of GiC. The intercalant diffuses into the graphite and thus increases the lattice spacing. Different stages of GiC can be produced. The stage number refers to the number of unperturbed graphite layer between two layers of intercalant atoms.

where η , called the mosaicity, is the width. To obtain a high acceptance the mosaicity should be in the range of the divergence of the incident beam [14]. A high integral reflectivity of the crystal is demanded to ensure an acceptable 8.9 Å flux for the converter. This requires a small absorption cross-section.

There are two materials which match these requirements, mica and graphite intercalated compounds (GiC) with alkali metals. Due to the small mosaicity $\approx 0.3^{\circ}$ of mica we are employing a potassium intercalated graphite monochromator of the type previously developed at the NIST [15]. The d-spacing for highly oriented pyrolytic graphie is d=3.35 Å with a typical mosaicity of $1^{\circ}-2^{\circ}$. It is increased by placing guest species in between graphite layers (see fig. 3), this process is called intercalation.

The monochromator for GRANIT will be made of stage-2 (C_{24} K) potassium intercalated graphite providing a lattice spacing of d=8.74 Å giving a take-off angle of $2\theta=61.2^{\circ}$. The typical mosaic spread of the produced crystals is $\eta=1.5^{\circ}-2.2^{\circ}$ which matches fine with the incident divergence of beam H172. An integral reflectivity of $r\geq80$ % can be achieved [15]. Furthermore the absorption cross section of graphite (0.0035 barn) and potassium (2.1 barn) are rather small. The d-spacing of Rubidium and Caesium intercalated compounds are of the same magnitude. Rubidium would be an interesting alternative due to its small cross section of 0.38 barn, whereas Cesium (29 barn) is less interesting. For these two alkali metals the production method is not yet sufficiently refined.

Alkali intercalated graphite compounds are conveniently produced using the "two-bulb" technique, where the graphite is maintained at a temperature $T_{\rm c}$ which is higher than $T_{\rm a}$ of the alkali metal [16]. The stage which is formed depends on the temperature difference $\Delta T = T_{\rm c} - T_{\rm a}$ and the quantity of potassium available. For stage-1, stage-2 we are employing 5 g, 1 g ampoules of potassium at $T_{\rm a} = 255 \pm 3$ °C and $\Delta T_{\rm 1} = 10 \pm 3$ °C, $\Delta T_{\rm 2} = 102 \pm 3$ °C, respectively. A photograph of such a two-bulb cell is shown in figure 4.

A second monochromator with a take-off angle of $2\theta = 112.5^{\circ}$ will include a set of stage-1 (C₈K) crystals (d = 5.35 Å) placed close to the first on a rotary table. The two different monochromators can be interchanged (see fig. 5) making two separate

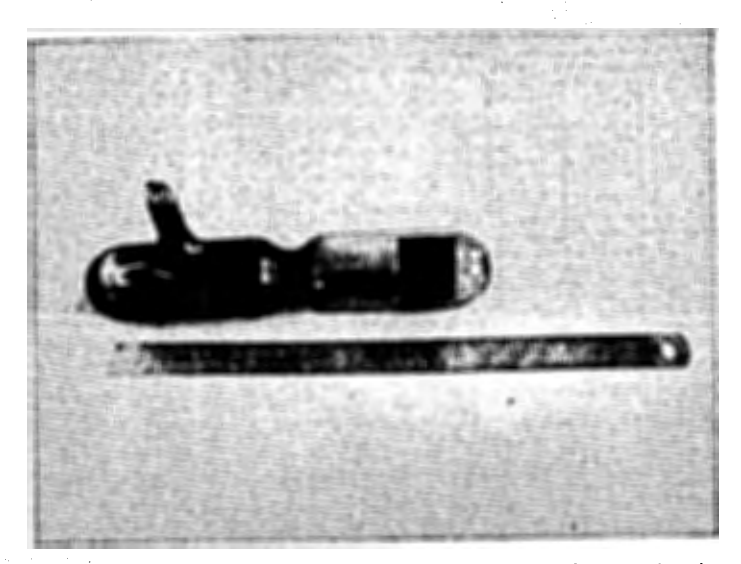


Figure 4: Typical cell made from Pyrex used for intercalation. The potassium is on the left and causes at $T \ge 250$ °C the brown colouring of the glass. On the right: a stage-2 intercalated graphite.

8.9 Å beam ports at H172 available. The second beam will feed a position with neutrons for further tests and developments on liquid helium based UCN-sources, and later the cryo-EDM experiment [9].

Converter and cryostat

As the incident neutron beam has a divergence of $\alpha\approx 2^\circ$, the differential flux will be a function of position inside the volume. In order to guide divergent cold neutrons incident on the walls it is convenient to use polished wall materials with a high critical angle. For the storage of UCN we need a high Fermi potential, rough surfaces for an isotrop momentum distribution, and a small loss per bounce coefficient μ to minimise wall losses. Obviously it is impossible to have polished and rough surfaces at the same place, therefore the source will have rough surfaces only on the entrance and exit window of the converter volume, whereas the rest is polished. Beryllium, beryllium-oxide, and diamond like carbon (DLC) all have Fermi potentials $V_F \geq 250$ neV, and $\mu \leq 1 \cdot 10^{-4}$.

Calculations for a divergent beam, a Fermi potential $V_{\rm F}=252$ neV, a mirror like wall (m=1), and varying loss coefficients are shown in figure 6. The incident beam flux on the monochromator with a reflectivity of r=85 %, was taken to be ${\rm d}\phi/{\rm d}\lambda|_{\lambda^*}=6\cdot 10^8{\rm s}^{-1}{\rm cm}^{-3}$. This value was calculated from known cold source data and a transmission simulation for the existing guide. The m=2 neutron guide between monochromator and source converges from a $80\times 80{\rm mm}^2$ to the cross section indicated in the figure over a length of 3 m. Both guide parts have

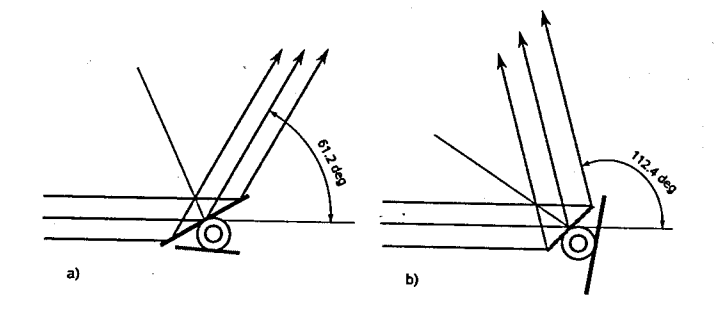


Figure 5: Monochromator setup on rotary table. a) stage-2 potassium intercalated graphite monochromator in position, b) stage-1 (potassium) monochromator. This setup allows relatively short switching time.

been simulated with a Monte Carlo algorithm.

The combination of simulated transmissions and divergence for the beam and analytic calculations for a converter volume of length 600 mm, a cross section of $70\times70~\mathrm{mm}^2$, and an average $\mu=1\cdot10^{-4}$ give a density of $\rho_{calc}\geq1250~\mathrm{cm}^3$.

The behaviour of the coatings during cooldown still has to be investigated. Thermal tension could create cracks and degrade the surface quality significantly. A cooling test with several coatings and substrates will be performed to find the best choice. For filling and cooling the converter volume with liquid helium we employ a cryostat previously developed at Munich [10, 17]. Primary cooling power is provided by a Gifford McMahon cryocooler with 1.5 W at 4.2 K. It liquefies helium and provides the cooling power for the 50 K and 4 K heat screens. The liquefaction is described in detail in ref. [17]. A ⁴He evaporation stage cools the liquid helium below the λ -transition point $T_{\lambda}=2.177$ K, which then allows us to use a superleak to remove ³He. The cooling of the converter volume is achieved with a ³He closed cycle evaporation stage. Using a roots blower pump with 500 m³/h nominal pumping speed backed by a 40 m³/h multiroots pump we were so far able to cool the filled converter to 0.7 K. Further improvements, including a new heat exchanger between ³He and ⁴He will allow us to reach temperatures below 0.5 K. More details about the cryostat will be published elsewhere.

UCN selection with semidiffuse channel

The converter volume will be connected to the intermediate volume by a highly polished, beryllium, nickel, or DLC coated guide. This additional volume will be made of DLC coated aluminium plates. Having rough surfaces it distributes the UCN evenly on the entrance window of the semidiffuse channel and avoids cryogenic complications which would arise form a direct attachement of the channel to the converter volume. The optimum cross section was determined by simulations with Geant4UCN [18] to be 40×40 mm², the length 300 mm is given by the dimensions

of the spectrometer. A challenging task is to minimise heat input without reflecting UCN back into the converter volume before they have reached the intermediate volume. Using thin aluminium or mylar foils as heat screens seems to be an option, although losses due to multiple passages will increase due to multiple passages. The UCN will be extracted via a 0.2 mm high horizontal semidiffuse extraction channel (see fig. 2). Measurements [12] have shown that such a channel increases the storage time and selects only the desired fraction of the phase space. The extraction channel is made of DLC coated quartz plates [19], the lower surfaces are polished, the upper rough. The channel dimensions are $h=200~\mu\mathrm{m},\ l=100~\mathrm{mm},\ w=300~\mathrm{mm},\ \mathrm{which}$ will provide a reflectivity $r\geq85~\%$ for neutrons with a vertical energy component $E_{\perp}\geq mgh=20~\mathrm{peV}.$

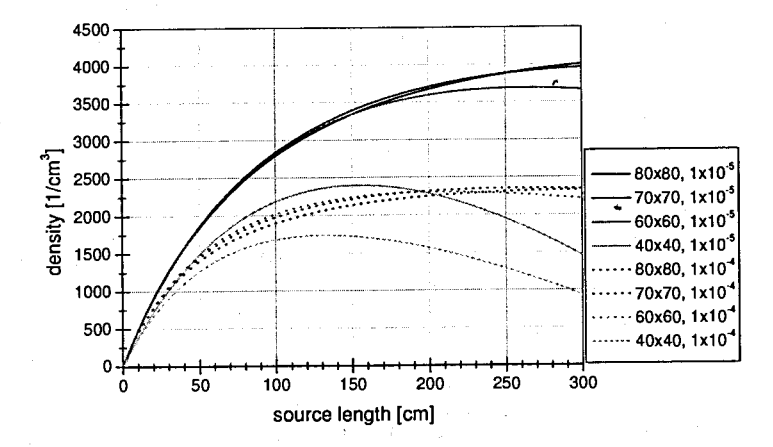


Figure 6: Simulation of UCN-density as a function of converter volume length, various rectangular cross sections, and two wall loss coefficients. The incident beam is taken to have a Gaussian divergence $\alpha \geq 1.8^{\circ}$ dependent on the converging guide and differential flux $\mathrm{d}\phi/\mathrm{d}\lambda|_{\lambda^*}=3\cdot 10^8~\mathrm{cm}^{-2}\mathrm{s}^{-1}~\mathrm{Å}^{-1}$ at the entrance of the volume. These values result from the simulations described in the text. The extraction opening is a hole of $\emptyset=10~\mathrm{mm}$. UCN once passed through the hole are taken to be lost from the volume, in reality there is a certain reflection probability.

Conclusion

The crystals of the monochromator, the converter, and the semidiffuse channel have all been tested separately. Their integration remains a challenging task. Present calculation with an incident differential flux $\mathrm{d}\phi/\mathrm{d}\lambda|_{\lambda^*}=6\cdot 10^8~\mathrm{s^{-1}cm^{-3}}$ on the monochromator give a UCN density of $\rho_{\mathrm{UCN}}\approx 1250~\mathrm{cm^{-3}}$ in the converter, $\rho_{\mathrm{int}}=800~\mathrm{cm^{-3}}$ in the intermediate volume. This yields for a critical velocity of 7 m/s for the materials used an available phase-space density of $\Gamma_{\mathrm{He}}\approx 0.18~\mathrm{cm^{-3}}(\mathrm{m/s})^{-3}.$ Compared to the phase-space density $\Gamma_{\mathrm{Turbine}}\approx 0.013~\mathrm{cm^{-3}}(\mathrm{m/s})^{-3}$ of the UCN turbine at the ILL this is more than a factor ten of improvement. This calculation assumes perfect conditions and in all parts optimal transmissions, experience with other simulations have shown that the actual value might be lower.

Acknowledgement

We are greatful to all our colleagues from the GRANIT collaboration, the monochromator collaboration with NIST, and the DPT of the ILL for fruitful discussions and support. This work is partly supported by the French Agence de la Recherche (ANR)

References

- [1] V.I. Luschikov and A.I. Frank, JETP Lett. 28 (1978), 559.
- [2] V.V. Nesvizhevsky et al., Nature 67 (2002), 297.
- [3] V.V. Nesvizhevsky et al., Phys. Rev. D 67 (2003), 102002.
- [4] S. Baeßler, V.V. Nesvizhevsky, K.V. Protosov and A.V. Voronin, Phys. Rev. D 75 (2007), 1.
- [5] V.V. Nesvizhevsky and K.V. Protasov, Quantum states of neutrons in the earth's gravitational field: state of the art, application, perspective, in: D.C. Moore, Trends in quantum gravity search, Nova Science Publishers, New York.
- [6] R. Golub and J.M. Pendlebury, Phys. Lett. 53A (1975), 133.
- [7] E. Korobkina, R. Golub, B.W. Wehring and A.R. Young, Phys. Lett. A 301 (2002), 462.
- [8] W. Schott et al., Eur. Phys. J. A 16 (2003), 599.
- [9] C.A. Baker et al., Phys. Lett. A 308 (2003), 67.
- [10] O. Zimmer et al., accepted for Phys. Rev. Lett. (2007), (arXiv:0.705.3960).
- [11] A.I. Kilvington, R. Golub, W. Mampe and P. Ageron, Phys. Lett. A 125 (1987), 416.
- [12] P. Schmidt-Wellenburg et al., NIM A 577 (2007), 623.
- [13] M.L. Goldberger and F. Seitz, Phys. Rev. 71, 294.
- [14] K.-D. Liss and A. Magerl, NIM A 338 (1994), 90.
- [15] C.E.H. Mattoni et al., Physica B 244 (2004), 343.
- [16] A. Hérold, Bull. Soc. Chim. 9 (1955), 999.
- [17] P. Schmidt-Wellenburg and O. Zimmer, Cryogenics 46 (2006), 799.
- [18] F. Atchison et al., NIM A 552 (2005), 513.
- [19] V.V. Nesvizhevsky et al., NIM A 578 (2007), 435.

%Mo NEUTRON RESONANCES MEASURED WITH THE DANCE ARRAY

M. Krtička, ¹ U. Agvaanluvsan, ² J.A. Becker, ² F. Bečvář, ¹ T.A. Bredeweg, ³ R.C. Haight, ³ M. Jandel, ³ G.E. Mitchell, ⁴ J.M. O'Donnell, ³ W. Parker, ² R. Reifarth, ³ R.S. Rundberg, ³ E.I. Sharapov, ⁵ S.A. Sheets, ⁴ J.L. Ullmann, ³ D.J. Vieira, ³ J.B. Wilhelmy, ³ J.M. Wouters, ³ C.Y. Wu ²

Charles University in Prague, V Holešovičkách 2, CZ-180 00 Prague 8, Czech Republic
 Lawrence Livermore National Laboratory, 7000 East Avenue, Livermore, CA 94551
 Los Alamos National Laboratory, Los Alamos, New Mexico 87545
 North Carolina State University, Raleigh, NC 27695
 and Triangle Universities Nuclear Laboratory, Durham, NC 27708
 Joint Institute for Nuclear Research, 141980 Dubna, Russia

Abstract

The γ rays following the 95 Mo(n, γ) 96 Mo reactions have been studied by the time-of-flight method with the DANCE (Detector for Advanced Neutron Capture Experiments) array of 160 BaF₂ scintillation detectors at the Los Alamos Neutron Science Center. The γ -ray multiplicities and energy spectra for different multiplicities were measured in s- and p-wave resonances up to $E_n=2$ keV. Preliminary analysis assigned definite spins and parities in 96 Mo for about 60% of the resonances, while tentative spins and parities were assigned for almost all other observed resonances.

1 Introduction

A classic problem in neutron resonance spectroscopy is the assignment of the total angular momentum for resonances formed on targets with non-zero spin. The γ -ray multiplicity method is an approach to determining the spins of neutron resonances that uses the spin dependence of (n,γ) spectra. The method was initiated in the 1960s by Coceva et al. [1] at the electron linac of the Institute for Reference Materials and Measurements at Geel, Belgium, and later was developed into multiplicity spectrometry by Muradyan et al. [2] at the Kurchatov Atomic Energy Institute in Moscow. The advent of BaF₂ detector arrays for studies of radioactive and/or very small samples at the LANSCE spallation neutron source at Los Alamos and at the n_TOF facility at CERN opened new possibilities for the determination of spins and parities of neutron resonances. The DANCE facility at Los Alamos National Laboratory is a 160 crystal array [3], while the n_TOF array [4] has 40 crystals. Here we report on the measurement at DANCE of γ -ray multiplicities and energy spectra for the resonant reaction 95 Mo(n, γ) 96 Mo up to $E_n = 2$ keV.

Data for the molybdenum isotopes are important for nuclear reactor design since molybdenum is used in some uranium fuel elements. Molybdenum isotopes are also fission products; their capture cross sections are required for fuel cycle calculations. These isotopes are also of considerable nuclear physics interest, since they belong to the mass region where strong "nonstatistical" electric dipole transitions from p-wave capturing states to low-lying positive parity states have been observed and interpreted in the framework of the valence-neutron model (see Ref. [5] and references therein). The neutron capture

cross sections for molybdenum isotopes for energies $3 < E_n < 90$ keV have been measured at the Oak Ridge Electron Linear Accelerator [6], and total cross sections were measured in several investigations – see the Atlas of Neutron Resonances by Mughabghab [7].

Relatively strong p-wave resonances are known to be abundant in the atomic mass region A=90-100; the p-wave neutron strength function in this region is about 10 times stronger than the s-wave neutron strength function. Therefore a significant number of negative parity resonances are expected. Parity evaluations for the Mo isotopes are reported in [7]. This evaluation (of the orbital angular momentum and therefore the parity of the resonance) is based on the separation of the statistical distributions of the reduced neutron widths of s- and p-wave resonances [8] with the use of Bayes' theorem on conditional probability. An independent experimental measurement of neutron resonance parities is important to supplement this Bayesian probabilistic argument.

The multiplicity method is described in section 2.1, while modeling of the statistical γ ray cascade is described in section 2.2. The experimental method and the data processing
are described in sections 3 and 4. The experimental results and analysis are presented in
section 5, followed by a brief summary.

2 Gamma-Ray Multiplicity Method

2.1 Method

The γ -ray multiplicity method consists of the measurement of the cascade gamma spectra after the de-excitation of the compound nucleus formed by neutron capture. The method is based on the systematics of probabilities for transitions of various multipolarities. Systematics of the photon strength functions (see e.g. Ref. [9]) indicate that except for transitions between low-lying levels, partial radiation widths of dipole (E1, M1) transitions are on average much larger than those of quadrupole (E2, M2) transitions and that the E1 transitions in heavy nuclei are usually almost an order of magnitude stronger than M1 transitions at γ ray energies above about 5 MeV. Because of the dipole multipolarity, after each transition the difference between the spins of the initial and final states in a given transition is 0 or 1.

For s-wave neutron resonances the spin J has the values $J_{+} = I + 1/2$ and $J_{-} = I - 1/2$; the target spin of 95 Mo is $I^{\pi} = 5/2^{+}$. The average multiplicity is expected to be different for J_{-} than for J_{+} . The J_{-} -spin effect on multiplicity, although not large for 96 Mo, results in the separation of $\langle M_{J} \rangle$ values of s-wave resonances into two different groups, corresponding to the two possible spin values $J_{+} = 3$ and $J_{-} = 2$ - relative difference in $\langle M_{J} \rangle$ is about $\sim 7\%$. For p-wave resonances in 96 Mo the possible spins are 1, 2, 3, and 4, and the situation is more complicated. This is discussed in section 2.2.

Naturally, the spin of the neutron resonance should affect not only the multiplicity distributions, i.e. $\langle M_J \rangle$, but also the gross structure of the γ -energy spectra for individual multiplicities. In some cases the γ -ray energy spectra from neutron resonances should depend significantly also on the parity of the resonances. For the 96 Mo compound nucleus all low-lying excited states up to $E_x \simeq 2.5$ MeV have only positive parities. Therefore, the prevalence of E1 primary high energy transitions to these low-lying states should be a signature of p-wave resonances. This fingerprint feature of the shape of primary gamma

spectra should also hold for the shape of the coincidence gamma spectra for individual observed multiplicities (especially for multiplicity M=2). Therefore the shape of γ spectra can probably be used for parity assignments of neutron resonances in 96 Mo.

2.2 Modeling molybdenum photon cascades

In order to support the general arguments of section 2.1, simulations for the 95 Mo target were performed using the DICEBOX code [10]. In these simulations, the input consists of the experimental level energies, their spins and decay modes for the discrete part of the nuclear excitation spectrum below $E_{\rm crit}=2.8$ MeV, and nuclear models for the level density $\rho(E_a,J_a^{\pi_a})$ and the photon strength function (PSF), f_{XL} , of a given multipolarity L and electromagnetic type X used in the quasi-continuum above $E_{\rm crit}$. Various models can can be used. For description of some of them see e.g. [10].

The complete level scheme and decay mode of all levels is assumed in both the quasi-continuum and discrete regions in the DICEBOX code. The levels in quasi-continuum, i.e. above $E_{\rm crit}$, are generated by a random discretization of the chosen level density formula. The statistical cascade gamma-decay in this region is then simulated by the Monte Carlo technique. The partial radiation widths for transitions between levels a and b are obtained with the formula

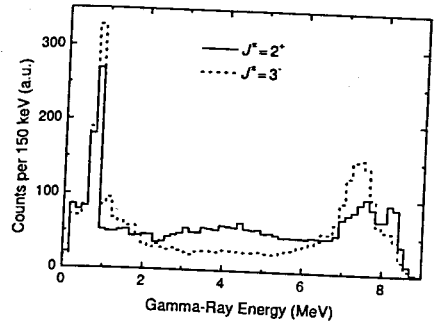
$$\Gamma_{ab} = \sum_{X,L} y_{XL}^2 (E_a - E_b)^{2L+1} \frac{f_{XL}(E_a - E_b)}{\rho(E_a, J_a^{\pi_a})},\tag{1}$$

where y_{XL} is a randomly generated number from a normal distribution with zero mean and unit variance. This provides a simulation of the Porter-Thomas distribution of partial gamma widths. The combination of the levels generated and the transition probabilities between these levels is defined as one *nuclear realization*. Within each nuclear realization the code generated 100,000 cascade events statistically populating levels below the energy of the capture state. Usually about 20 realizations are required in order to provide a statistically significant approximation for the cascade characteristics and to provide estimates of their fluctuations.

Examples of simulated average multiplicities for all initial spins and parities are listed in Table I. They were obtained with the use of a constant temperature level density, the KMF model for the (E1) PSF, and single particle estimates for the PSF of other multipolarities. Calculated total radiative widths $\Gamma_{\gamma}^{9} = 154 \pm 8$ meV and $\Gamma_{\gamma}^{p} = 185 \pm 20$ meV agree well with experimental values reported in [7]. Only events with multiplicity higher than one were considered, in order to ease comparison with experimental results, see Sec. 4.2. More important than the absolute values of $\langle M_J \rangle$, which depend slightly on the model adopted, is an absolute difference of about 0.3 between (M_J) for resonances with the same parity and spin differing by one. This difference is also reproduced when other models of level density and photon strength functions are used. All simulations also predict similar average multiplicities for 3- and 2+ resonances as well as for 4and 3^+ . Table 1 also provides information on the size of expected fluctuations in $\langle M_J \rangle$ due to the statistical nature of the γ -decay. Generally, p-wave resonances have larger fluctuations in their average multiplicity than s-wave resonances. With the use of only average multiplicity values it is possible to identify $J^{\pi} = 1^-$ and 2^- resonances but it is not possible to determine the spin for the parity mixed groups of spins (2+,3-) and $(3^+, 4^-)$ from the $\langle M_J \rangle$ value alone.

Table 1: Average multiplicity $\langle M_J \rangle$ calculated for s- and p-wave resonances in 96 Mo.

Quantity		<u> </u>	1.\	-wave reso
J	1	2	3	1
s-waves		3.90(5)	4.23(7)	
<i>p</i> -waves	3.30(15)	3.68(20)	/	4.30(25)



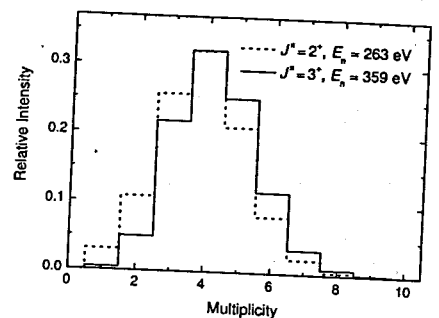


Figure 1: Calculated two-step cascade γ -ray energy spectra for s-wave resonances $(J^{\pi}=2^{+})$ (full red line) and p-wave resonances $(J^{\pi}=3^{-})$ (dotted blue line) in the $^{95}\text{Mo}(n,\gamma)^{96}\text{Mo}$ reaction. The size of the energy bins in the histograms is 150 keV.

Figure 2: Multiplicity spectra for s-wave resonances at 263 eV $(J^{\pi} = 2^{+})$ and 359 eV $(J^{\pi} = 3^{+})$.

We calculated, using DICEBOX with the same model parameters as above, the γ -ray energy spectra from the two-step cascades ending on the ground and first excited state of 96 Mo for the initial J^{π} combinations $(2^+,3^-)$ and $(3^+,4^-)$. Fig. 1 presents an example of spectra for the $(J^{\pi}=2^+,J^{\pi}=3^-)$ case. The shape of these two spectra is quite different especially the pronounced bump in the middle part of the $J^{\pi}=2^+$ spectrum and the strong peaks at the spectrum wings for the $J^{\pi}=3^-$ case. The calculated spectra for $J^{\pi}=3^+$ and $J^{\pi}=4^-$ resonances have similar but much weaker differences.

More elaborate modeling of n-step cascades and sum energy gamma-spectra for different theoretical models of PSF and inclusion of the γ -ray energy response of the DANCE detector system was also performed using the GEANT3 package. The details will be published elsewhere but it should be stressed that simulations of detector response do not change either $\langle M_J \rangle$ or the shapes of spectra significantly. In the present paper we consider only the multiplicity two spectra, since they contain the most information on the spin and parity values of the neutron resonances.

3 Experimental setup and measurements

The experiments were performed at the spallation neutron source of the Los Alamos Neutron Science Center (LANSCE) [11]. The 800-MeV H⁻ beam of about 625 μ s duration

from the LANSCE linac is converted to protons by thin foil stripping and injected into the proton storage ring. The injected beam is stacked on itself until protons from the entire linac macropulse are stored. This reduces the proton pulse width to about 125 ns full width at half maximum. This pulsed beam is extracted with a repetition rate of 20 Hz and transported to a tungsten spallation target, where fast neutrons are created. After passing through a water moderator, the moderated neutrons with a white energy spectrum enter evacuated flight paths. The DANCE detector array is installed on the 20-m neutron flight path 14 at the Manuel Lujan Jr. Neutron Scattering Center.

The DANCE spectrometer [3] is a $\simeq 4\pi$ BaF₂ crystal array designed for studying neutron capture cross sections on small quantities of radioactive material or isotopic samples. The DANCE array consists of 160 BaF₂ scintillation crystals, which detect γ -rays following neutron capture. The array is highly segmented to reduce the high instantaneous count rate per detector. Neutrons scattered into the detector can be captured on the barium isotopes and produce an undesirable background. To reduce this background, a ⁶LiH shell about 4-cm thick is placed between the sample and the BaF₂ crystals. The remaining background is subtracted in the off-line analysis.

4 Data analysis

4.1 On-line data processing

The DANCE acquisition system [12] is based on waveform digitization of signals from all 160 barium fluoride detectors. The waveforms provide information on timing, particle type, and absorbed energy for each physical event in the crystals. Crystals are connected to Acqiris DC265 digitizers through two channels able to handle both high and low amplitudes with a resolution of 8 bits at a sampling rate of 500 MHz. Each digitizer has 128 kbytes of fast memory per channel. The digitizers are arranged into 14 compact PCI crates with six digitizers per crate, one crate per 12 BaF2 crystals. Each crate contains an embedded Intel based 1.8-GHz single board computer running the Linux operating system, and a front-end acquisition program written using the MIDAS (Maximum Integrated Data Acquisition System) framework [13]. Written without any selection, the DANCE typical raw data rate would be of the order of 1 Terabyte per hour, which is not practical. The problem with the disk space is bypassed by on-line partial processing of waveforms from digitizers using MIDAS. In this step information on the fast and slow parts of the signal is integrated and the integrals are stored instead of the whole waveforms; this led to a compression factor of 20. Once processed, the data are sent over a dedicated 100-Mbit/sec network to a dual 2.5-GHz Intel based computer with a 5-Terabyte disk space. All data from a given proton pulse are collected into one 'Midas event' on a disk.

4.2 Off-line data processing

The background, which comes almost exclusively from capture of scattered neutrons on Ba, was subtracted using spectra measured with a carbon target. Carbon has very high cross section for neutron scattering and at the same time a very low cross section for neutron capture. The influence of the background for many resonances is quite negligible for multiplicities greater than one, but it often dominates spectra for multiplicity one.

The extraction of the γ -ray multiplicity, the so-called "cluster multiplicity", from the instrumental "crystal multiplicity" is performed based on the timing and location characteristics of an event. The photons often do not deposit their full energy in one crystal. Therefore all contiguous crystals, that have fired during an event, are combined into one single cluster event. As a result the cluster multiplicity is much closer to the true multiplicity of the gamma cascade than is the crystal multiplicity, which simply counts the total number of crystals that fire. The capture events in the off-line analysis were sorted by gates on the cluster multiplicity for each multiplicity value and for each neutron resonance. The average value $\langle M \rangle$ was calculated as:

$$\langle M \rangle = \frac{\sum_{i=2}^{7} M_i C_i}{\sum_{i=2}^{7} C_i},\tag{2}$$

where M_i and C_i are the cluster multiplicities and counts for the corresponding multiplicity after subtracting background contributions. We cannot ensure reliable background subtraction in the M=1 spectra, and there are almost no events for M>7.

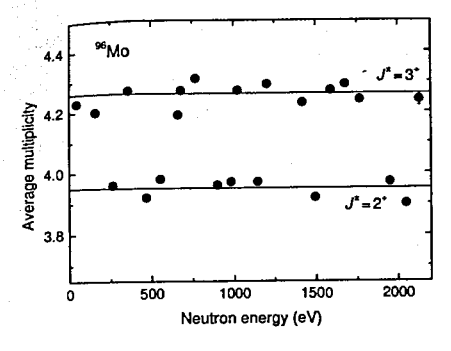
Because of its nearly 4π geometry and high photon detection efficiency, the DANCE array is able to measure the total reaction energy released in the neutron capture event, which is $E_{\text{total}} = B_n + E_n$ where B_n is the neutron binding energy in the compound nucleus and E_n is the center-of-mass kinetic energy of the neutron. In the off-line analysis, only those γ -ray events, for which the detected sum energy was within the interval 7.6-9.2 MeV ($B_n = 9.15 \text{ MeV}$) were considered while calculating average multiplicity as well as spectra for two-step cascades.

5 Experimental results

A target with the thickness of 25 mg/cm² enriched to 96.47% in 95 Mo was used in the measurement. As an example of the measured multiplicity distributions for s-wave resonances with different spins, in Fig. 2 multiplicity spectra are shown for the 554-eV (J=2) and 44.5-eV (J=3) resonances. The average value is higher for the resonance with the higher J value. The average multiplicity values for all s-wave neutron resonances measured in the 95 Mo(n, γ) 96 Mo reaction are shown in Fig. 3.

The $\langle M \rangle$ values are distributed into two distinct groups corresponding to spins J=2 (lower line with $(M_J)=3.95$) and J=3 (upper line with $(M_J)=4.26$). In obtaining this plot, it was crucial to separate s-wave resonances from p-wave resonances. This was achieved by the inspection of shapes of γ -ray energy spectra for multiplicity M=2, as explained in Section 2.2. A representative example of a two-step cascade spectra from a pair of resonances from the mixed group $(2^+, 3^-)$ is shown in Fig. 4. As predicted by the modeling, the $J=2^+$ spectrum is characterized by a bump near $E_{\gamma}=4$ MeV. Spectra from $(3^+, 4^-)$ group of resonances can be examined in a similar fashion, although the difference are not as pronounced.

Since the target 95 Mo spin is $I^{\pi}=5/2^{+}$, p-wave capture leads to resonances with spins and parities of 1^{-} , 2^{-} , 3^{-} , and 4^{-} . As shown in simulations (see section 2.2 and Tab. 1), the average multiplicity values of p-wave neutron resonances in 95 Mo should also



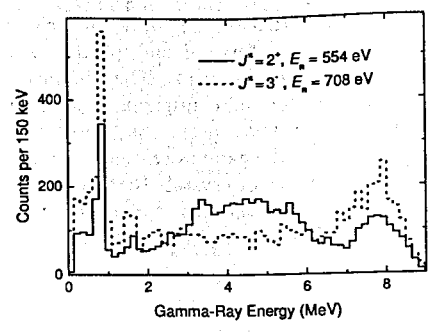


Figure 3: Multiplicities of s-wave neutron resonances from the 95 Mo(n, γ) 96 Mo reaction in the neutron energy range from 40 to 2100 eV. Values along the lower line correspond to spin J=2 and along the upper line to spin J=3.

Figure 4: Measured γ -ray energy spectra for an s-wave resonance at 554 eV ($J^{\pi} = 2^{+}$) and a p-wave resonance at 708 eV ($J^{\pi} = 3^{-}$). These spectra correspond to two-step cascades with detected γ -ray sum energy between 7.6 and 9.2 MeV.

depend on the resonance spin value. However, as expected from simulations, the measured individual $\langle M_J \rangle$ -values fluctuate considerably. These fluctuations do not allow to make a firm J^π assignment in all cases. Resonances, for which the $\langle M_J \rangle$ fall between groups, were assigned a restricted range of spins. Due to the lack of space here, the final results of the J^π assignments of neutron resonances will be published elsewhere [14].

6 Summary and conclusion

Measurements of the γ -ray energy and multiplicity spectra following neutron resonance capture in isotopic 95 Mo target were performed with the DANCE detector array at LANSCE by the time-of-flight method.

From the average multiplicity and spectral shape, spin and parity assignments were made for resonances in the $^{95}\text{Mo}(n,\gamma)^{96}\text{Mo}$ reaction below about 2 keV. The previously known indirect parity assignments were confirmed, and several new assignments were made. For s-wave resonances, the separation between the two $\langle M_J \rangle$ -value groups and the agreement of our results with those of other authors demonstrate the successful application of the multiplicity method with the DANCE detector array. For p-wave resonances, where the separation of the different spin groups was not perfect the definite assignment of 15 spins was made. Most of the results for the spins of the p-wave resonances are new.

Acknowledgments

This work was supported in part by the U. S. Department of Energy Grants No. DE-FG52-06NA26194, No. DE-FG02-97-ER41042 and No. DE-AC52-06NA25396, and was performed under the auspices of the U. S. Department of Energy by the University of

California, Lawrence Livermore National Laboratory and Los Alamos National Laboratory under contract Nos. W-7405-ENG-48 and W-7405-ENG-36, respectively. This work has benefited from the use of the LANSCE accelerator facility, supported under DOE contract No. W-7405-ENG-36. It was also partly supported by the research plan MSM 0021620859 of the Ministry of Education of the Czech Republic.

References

- [1] C. Coceva, F. Corvi, P. Giacobbe and G. Carraro, Nucl. Phys. A 117, 586 (1968).
- [2] G. V. Muradyan, Yu. V. Adamchuk, Yu. G. Shchepkin, and M. A. Voskanyan, Nucl. Sci. Eng. 90, 60 (1985). F. Bečvář and M. Krtička, Nucl. Instrum. Meth. Phys. Res. A 513, 585 (2003).
- [3] M. Heil, R. Reifarth, M.M. Fowler, R.C. Haight, F. K'appeler, R.S. Rundberg, E.H. Seabury, J.L. Ullmann, and K. Wisshak, Nucl. Instrum. Meth. Phys. Res. A 459, 229 (2001).
- [4] n_TOF Collaboration, Report INTC-2003-036, CERN, Switzerland, 2003.
- [5] R. E. Chrien, G. W. Cole, G. G. Slaughter and J. A. Harvey, Phys. Rev. C 13, 578 (1976).
- [6] A. R. de L. Musgrove, B. J. Allen, J. W. Boldeman, and R. L. Macklin, Nucl. Phys. A270, 108 (1976).
- [7] S. F. Mughabghab, Atlas of neutron resonances (Elsevier, Amsterdam, 2006).
- [8] L. M. Bollinger and G. E. Thomas, Phys. Rev. 171, 1293 (1968).
- [9] C. M. McCullagh, M. L. Stelts, and R. E. Chrien, Phys. Rev. C 23, 1394 (1981).
- [10] F. Bečvář, Nucl. Instrum. Meth. Phys. Res. A 417, 434 (1998).
- [11] P. W. Lisowski, C. D. Bowman, G. J. Russell, and S. A. Wender, Nucl. Sci. Eng., 106, 208 (1990).
- [12] Jan M. Wouters, Ana Alpizar Vicente, Todd A. Bredeweg, Ernst Esch, Robert C. Haight, Robert Hatarik, J. M. O'Donnell, Rene Reifarth, Robert S. Rundberg, Jon M. Schwantes, Steven A. Sheets, John L. Ullmann, David J. Vieira, and Jerry B. Wilhelmy, IEEE Transactions on Nuclear Science, 53, 880 (2006).
- [13] S. Ritt and P. -A. Amaudruz, MIDAS Maximum Integrated Data Acquisition System, http://midas.psi.ch.
- [14] G.E. Mitchell et al., contribution to the Workshop on Photon Strength Functions and Related Topics (PSF07), Prague, June 17-20, 2007, available at http://pos.sissa.it/

APPROXIMATION OF SUMS OF EXPERIMENTAL RADIATIVE STRENGTH FUNCTIONS OF DIPOLE GAMMA-TRANSITIONS IN THE REGION $E_{\gamma} \approx B_{\eta}$ FOR THE ATOMIC MASSES $40 \le A \le 200$

A.M. Sukhovoj, W.I. Furman, V.A. Khitrov

Frank Laboratory of Neutron Physics, Joint Institute for Nuclear Research, 141980, Dubna, Russia

The sums k(E1) + k(M1) of radiative strength functions of dipole primary gammatransitions were approximated with high precision in the energy region of $0.5 < E_1 < B_n - 0.5$ MeV for $0.5 < E_1 < B_n - 0.5$ MeV for nuclei: 40 K, 60 Co, 71,74 Ge, 80 Br, 114 Cd, 118 Sn, 124,125 Te, 128 I, 137,138,139 Ba, 140 La, 150 Sm, 156,158 Gd, 160 Tb, 163,164,165 Dy, 166 Ho, 168 Er, 170 Tm, 174 Yb, 176,177 Lu, 181 Hf, 182 Ta, 183,184,185,187 W, 188,190,191,193 Os, 192 Ir, 196 Pt, 198 Au, 200 Hg by sum of two independent functions. It has been shown that this parameter of gamma-decay are determined by the structure of the decaying and excited levels, at least, up to the neutron binding energy.

1 Introduction

At present there are no doubts that the qualitatively differing types of nuclear excitations co-exist, interact and have defining influence on the structure and parameters of any nucleus. Namely, they are quasiparticle and vibrational ones. This is the main conclusion of such fundamental nuclear models as QPNM [1] and different variants of IBM [2].

Unfortunately, the majority of experiments carried out by now gives direct and quite reliable information on the structure of a nucleus only for too small energies of its excitation. Practically, for example, in [3] even-odd heavy nucleus this region is up to now limited by the excitation energy interval of ≈ 2 MeV order. Up to the present radiative strength functions of $k = f/A^{2/3} = \Gamma_{\lambda f}/(E_{\gamma}^3 \times A^{2/3} \times D_{\lambda})$ gamma-transitions in the whole range of their energies E_{γ} , appearing at decay of any levels with the excitation energies $E_i < B_n$, have been experimentally studied to the least degree.

Main problems of the experiment, which occur at the determination of ρ and k consist in the necessity to:

- (a) really estimate the most serious systematical errors and to minimize their values as much as possible;
- (b) maximally exclude any model representations, which are unavoidable at extracting the parameters of the process from the registered spectra in an indirect experiment.

First of all, the latter refers to the basic hypothesis [4] on the independence of the cross section of any reverse reaction from the excitation energy of final nucleus used for the analysis of all the experiments conducted up to the present.

According to particular calculations [5] of the probabilities of gamma-transitions below $E_i \sim 3$ MeV and experimental data [6] on the level cascade populating ability of

different types of nuclei below $0.5B_n$, for example, it is expected that the hypothesis [4] is completely inapplicable in even-even deformed nuclei.

2 The current state of experiment

Between the decaying of compound states λ and a group of the low lying levels f of the studied nucleus [7] both tasks of the experiment are solved to the most possible degree by the registration of two-step cascade intensities $I_{\gamma\gamma}$ with the summed energy 5-10 MeV.

It is just the analysis of two-step cascade intensities of thermal neutrons radiative capture in the fixed by [8] ΔE energy intervals of their intermediate levels $E_i = B_n - E_1$:

$$I_{\gamma\gamma}(E_1) = \sum_{\lambda,f} \sum_{i} \frac{\Gamma_{\lambda i}}{\Gamma_{\lambda}} \frac{\Gamma_{if}}{\Gamma_{i}}$$
 (1)

that first revealed the possibility of the model-free simultaneous determination of ρ and k with their guarantee reliability.

In the initial variant [9] it was performed at assuming the independence of partial radiative widths Γ_{lm} of the gamma-transitions of given energy and multipolarity from energies of any primary l and final m levels (that is, using hypothesis [4]). In contemporary version [6] it is accomplished without its use in the region of the low lying levels $(E_i < 0.5B_n)$.

In order to practically calculate the cascade intensities and compare them with the experiment it is necessary to take into account the real specific character of the studied process. In certain energy interval $\Delta E_j >> FWHM$ of the excited levels there is only the value of $\Delta \Gamma_j$ sum of partial radiative widths available for comparison with the calculation. For any interval of number j excitation energy this sum may be always mathematically presented as a multiplication of a certain average of partial width $<\Gamma_j>$ at $n_j=\rho\Delta E_j$ number of excited levels. Equation (1) is transformed into

$$I_{\gamma\gamma}(E_j) = \sum_{\lambda, f} \frac{\langle \Gamma_j \rangle}{\sum_k \langle \Gamma_k \rangle n_k} n_j \frac{\langle \Gamma_l \rangle}{\sum_m (\langle \Gamma_m \rangle n_m)}.$$
 (2)

for any interval number j.

Since this sum includes partial widths of gamma-transitions between levels of different structure (see, for example, [5]), the average width of primary $\langle \Gamma_l \rangle$ and secondary $\langle \Gamma_m \rangle$ gamma-transitions is an averagely weighted value for any j and i intervals in the indicated representation. It is determined by a particular ratio of quasiparticle and phonon components of wave functions of the studied nucleus levels, belonging to the ΔE_j interval. It is necessary to take into account this circumstance when comparing experimental k values with theoretical representations.

System (2) includes N of nonlinear equations and 2N of unknown parameters. (In case, when the retio of radiative strength functions of primary and secondary gamma-transitions is given on the basis of an additional information [6].) It describes a certain closed surface in the space of 2N sought parameters. Naturally, it is impossible to determine ρ and

k unambiguous values from (2) even when all available information on the considered nucleus is used. However, in principle, it is always possible to determine approximately or precisely the interval of variation of ρ and k values, setting given values of $I_{\gamma\gamma}$, $<\Gamma_l>$ and other parameters of a particular nucleus. Corresponding experiments have been carried out at the thermal neutron capture for 51 and analyzed without using hypothesis [4] for 22 nuclei.

3 Main problems of determination and theoretical description of parameters of cascade gamma-decay

In [6, 9] techniques the maximum values of errors $\delta\rho$ and δk of determined parameters are very strongly limited by the type of spectra measured in the experiment. Therefore, they always have quite acceptable value [10] for practically obtainable systematical errors $\delta I_{\gamma\gamma}$ of measured distributions of cascade intensities.

It is just the obtained degree of accuracy of ρ and k values determined by [6, 9] that defines both the reliability of conclusion about factors determining the indicated nuclear parameters and possibilities to extract new information on properties of particular nuclei and, probably, on structure of initial cascade levels fixed by conditions of the experiment.

For the most efficient extraction of data on the influence of nuclear structure on k(E1)+k(M1) and ρ values from the experiment, it is also necessary to use all the information accumulated by theory on these parameters of nucleus. Specifically, it is possible to separate two asymptotic variants of behavior of the congruent radiative strength functions. They appear when in an amplitude of gamma-transition dominate:

- a) quasiparticle components of wave function of initial and final states or
- b) their one- or two-phonon components.

Such possibility follows from the successful description [11, 12] of the experimental data for ρ from [6, 9] by the superposition of partial level densities, determined by n-quasiparticle excitations with enhancement of the quasiparticle level densities of $K_{vibr} >> 1$ times at the phonon type excitations expense of the ofdomination.

Based on the main principles of fragmentation of nucleus compound-states [13], it is impossible to eliminate the probability of dominating of either one or another component in the neutron resonance structure. It is also impossible not to take into account the specific character of excitations of various types.

Quasiparticle excitations (although with different number of quasiparticles) are present at any excitation energy of nucleus. Phonon ones, as it follows from the theoretical analysis of A.V. Ignatyuk [14], most probably become excited at energies close to those of quadrupole (octopole) phonon and phonons of greater multipolarity. In other words the excitations of phonon type may provide a significant increase in radiative strength functions in the limited intervals of nucleus excitation energy. Therefore, the excitations of quasiparticle type may rather well determine the basic part of radiative strength functions when gamma-transition energy is changing (first of all – primary), whereas monophonon

(multiphonon) one – determine a position of local region and the degree of increasing of strength functions in it.

Both variants [6, 9] of techniques use k(E1) and k(M1) unknown independent random functions to extract ρ and k from $I_{\gamma\gamma}$ experimental values, as parameters of equation (2). But near $E_{\gamma}=B_n$ (or smaller energy) they necessarily fix k(M1)/k(E1) ratio on the basis of the experimental data. The same refers to the level densities of positive and negative parity. Unfortunately, variations of the obtained random functions are rather large. However, due to the strong anticorrelation of pairs of the listed parameters, their sums fluctuate noticeably weak and, therefore, are quite informative. Namely, these are well described by $\rho=\psi(E_{ex})$ and $k=\phi(E_1)$ functions, the parameters of which differ sufficiently weak at changing of masses of the studied nuclei or when their changing does not contradict the unconditionally set theoretical notions about nucleus.

4 Model for the semiphenomenological description of k(E1) + k(M1)

All practically applicable [15] models of radiative strength functions consider nucleus as a monocomponent object. Owing to the historically prevalent representations, it is viewed as a system of Fermi-particles. Moreover, though model [16] considers nucleus only as Fermi-liquid, it reproduces a series of parameters of the cascade gamma-decay process with better accuracy than is made possible by the simplest extrapolation [17] of cross section of reverse reaction into the region of nucleus excitation below B_n . By this reason, it is appropriate to use the representations [16] as basic in the performed analysis, because they are based on the most realistic notion about nucleus produced by theorists by now.

A fraction of levels with purely dominating vibration components of wave functions (at least lower than $\sim 0.5 B_n$) is very significant [11, 12]. However, the existing and practically used [15] models of the radiative strength functions do not completely take into account this fact. Therefore, at this stage of the analysis it is necessary to postulate the contribution of the vibrational nucleus excitations into k(E1) + k(M1) values in a purely phenomenological way.

Below it is accepted that for a spherical nucleus fraction of partial radiative width of dipole primary gamma-transitions with energy E_{γ} , specified by the quasiparticle excitations, is described by model [16]:

$$k(E1, E_{\gamma}) + k(M1, E_{\gamma}) = w \frac{1}{3\pi^{2}\hbar^{2}c^{2}A^{2/3}} \frac{0.7\sigma_{G}\Gamma_{G}^{2}(E_{\gamma}^{2} + \kappa 4\pi^{2}T^{2})}{E_{G}(E_{\gamma}^{2} - E_{G}^{2})^{2}},$$
 (3)

with two free parameters: κ and w. For the deformed one – by sum of two Lorenz curves, respectively. Fraction k(E1)+k(M1), supposedly connected with the vibrational nucleus excitations, is approximated by peak, shape of which is preset by two exponential functions: $Pexp(\alpha(E-E_p))$, $Pexp(\beta(E_p-E))$ for its low and high energy parts. A resolved single peak (doublet or multiplet of peaks) is observed, at least, in 30 out of 40 nuclei in the energy range of primary transitions $E_p \sim 3-6$ MeV. In these k(E1)+k(M1) and ρ values are simultaneously determined from cascade intensities with a moderate

systematical error. Exponential dependence of form of its peaks successfully describes all the data obtained by the present.

Parameter κ in (3) takes into account a possible change of nucleus thermodynamic temperature in form $T = \sqrt{\kappa U/a}$, whereas parameter w – net effect of changing in retio of levels fraction of quasiparticle and vibration types, both in the region of neutron resonances, and intermediate $(E_i < B_n)$ levels of nucleus. Or it considers the fact of changing in ratio of quasiparticle and vibration components in the normalization of wave functions of decaying and excited levels, respectively. Such conclusion follows from the strong anticorrelation of amplitudes of local peaks in the experimental data on k(E1) + k(M1) and their uninterrupted distribution (approximated by function (3)).

First of all the approximation of the experimental values of k(E1) + k(M1) sums from [6] is used in the analysis. When they are absent, those from [9] are used. The results are presented in Fig.1-4 for the main part of the studied by the present nuclei. Particular values of the parameters by the approximating curve for all nuclei [11, 12] are given in the Table.

Upon taking into account the type of compound state established by theory of components of wave function and laws of nuclear states fragmentation determining their value, the value of w parameter is to a greater or lesser extent determined by the structure of the wave function of neutron resonance. This implies that w parameter may change from resonance to resonance and, probably, correlate with values of their reduced neutron widths.

5 Results of k(E1) + k(M1) approximation

Proposed for all studied nuclei the simplest form of functional dependence of the sum of radiative strength functions provides rather accurate reproduction of the experimental data [6] or [9] in the energy interval of primary gamma-transitions $0.5 < E_1 < B_n - 0.5$ MeV. For many of them it is sufficient to postulate the existence of the single peak. However, when the experimental data for nuclei close to magic ones is taken into account, most probably there are no less than two local peaks in the radiative strength functions. Positions of peaks well correspond to the region of step structure in levels density (Fig.5). This circumstance in an ensemble with a wide variety of values of the adjusted parameter alpha in different nuclei is the basis for interpretation of increasing of the strength function in regard to model predicted value [16] for those of $E_1 > 1 - 3$ MeV.

The excitation energy, corresponding to the positions of local peaks in the radiative strength functions of the considered nuclei (for $E_1>1$ MeV) is compared with the threshold energy of appearing four (five)-quasiparticle levels in Fig.5. Taking into account unavoidable errors and ambiguity of the analysis [11], their complete compliance with the position of one of the peaks is observed. In the first approximation in the scale of B_n-E_1 the position of another one coincides with the energy of quadrupole phonons (for example, about 1 MeV for the deformed even-even nuclei) or the region of mainly one- or two-particle levels in even-odd and odd-odd nuclei, respectively.

Amplitudes of peaks, supposedly caused by phonon excitations, for the most of analyzed nuclei are in a quite limited interval of values (Fig.6). Their noticeable increase is observed for 40 K, 60 Co, 184 W, 188,190 Os, 192 Ir 200 Hg. That is for nuclei close to the double magic ones with nucleon number N(Z)=20, 28 and for those in the region about Z=82 and N=126.

The best values of parameters κ and w, as it may be seen from Fig.6, obviously indicate smaller temperature of nucleus than the thermodynamic ones even near B_n and significant decrease of a component k(E1) + k(M1) by the approximating function (3).

Unfortunately, κ and w parameters very strongly correlate both with one another and with α parameters in the region of the smallest energies of primary gamma-transitions. There are also no theoretical grounds to regard the form of local peaks as the only possible in strength functions. By this reason it is also impossible to exclude a possibility of an additional systematical error of κ and w parameters.

In the proposed interpretation of the approximation data of radiative strength functions appearing of the local peaks is postulated by the presence of the amplified gammatransitions on levels with the large phonon components of wave functions. If that is true, α parameter may be determined by change rate of the nucleon correlation function in a heated nucleus. In Fig.7 frequency distribution of this parameter is presented in nuclei of different nucleon parity. Additionally, frequency distribution of Δ_0^{-1} value is given for even-even compound nuclei. (By positioning of maximum and width, it is close to an analogous distribution Δ_0 for nuclei with A-2).

The spread in α values is maximal for even-odd nuclei and intermediate for odd-odd ones. Assuming that $\alpha \propto \Delta_0^{-1}$, it is possible to determine that two unpaired nucleons of the single type decrease Δ_0 value by 25-50% at increasing of correlation function from one to three MeV. A pair of neutron and proton quasiparticles decreases Δ_0 somewhat more intensely. Its most decrease is observed for even-odd nuclei. In other words, in the region below the neutron binding energy the radiative strength function depends on the type and number of nucleons causing the appearance of excitations of quasiparticle type.

6 Conclusion

By the present the most reliable systematical experimental data on sums of the radiative strength functions of dipole cascade gamma-transitions of the thermal neutrons capture may be approximated in the frames of the experiment unsertain in the $0.5 < E_1 < B_n - 0.5$ MeV region by a superposition of two components having rather different form of the dependence on energy of gamma-transition. At the present they may be interpreted only as a contribution of fermion and boson nucleus excitations into the partial radiative width, respectively.

Noticeable variation of the obtained parameters of $k(E1)+k(M1)=F(E_1)$ dependence in nuclei of different masses may be caused by strong influence of the structure of cascade initial level on the correlation of contributions of nuclear common and superfluid states into the probability of gamma-quanta emission. This effect appears as an addition to the observed in [6] strong influence of the intermediate level structure on this value.

Correspondingly, the radiative strength functions of primary gamma-transitions of the decay of compound states may be determined by the structure of levels connected by them at least up to the energy of neutron binding.

Table 1. Parameters of approximation.

Mass	κ	w	E_1 , MeV	$P, 10^{-9}, \text{ MeV}^{-3}$	α , MeV ⁻¹	β , MeV ⁻¹
71	-0.01(37)	0.004(1)	5.49(7)	1.07(9)	0.86(10)	2.07(46)
			6.52(5)	1.24(7)	2.06(43)	0.22(18)
			0.77(11)	0.46(11)	0(17)	3.2(15)
125	0.42(8)	0.35(4)	4.79(9)	0.83(10)	0.52(10)	2.4(8)
	` ′		6.02(9)	0.89(20)	2.56(84)	-0.2(51)
137	0.26(2)	3.6(1)	1.84(6)	3.98(27)	0.74(10)	1.85(27)
		, ,	4.72(1)	42.7(9)	29(2)	9.28(26)
139	1.0(3)	0.5(1)	3.94(9)	1.99(29)	2.81(85)	0.10(42)
			0.50(39)	0.8(6)	1.8(18)	2.0(21)
163	0.002(9)	0.04(56)	3.9(4)	1.1(16)	1(25)	0.7(11)
1	` ,	` '	2.9(7)	0.8(11)	1.5(13)	0.7(30)
			5.4(20)	1.0(77)	0.9(78)	-1.4(44)
165	-0.00(10)	0.05(78)	3.56(6)	7.6(8)	2.04(31)	0.68(27)
181	$0.06(\hat{5})$	0.62(9)	3.8(1)	0.99(20)	1.07(31)	3.2(12)
	` ` `	` .	2.95(27)	0.39(15)	1.38(95)	1.04(69)
183	0.17(13)	0.04(1)	2.9(1)	0.72(7)	0.77(13)	1.00(22)
	` ′		5.37(1)	8.83(18)	3.49(12)	0.66(37)
185	0.29(5)	0.45(3)	3.23(3)	2.27(7)	1.55(10)	0.80(4)
	` '	` `	4.74(1)	2.09(7)	3.58(35)	1.43(32)
187	0.23(4)	1.03(5)	3.15(7)	1.08(9)	1.19(20)	1.16(16)
	, ,	\ \ \	5.14(9)	1.05(46)	5.1(15)	1(86)
191	0(77)	-0.0(30)	4.3(2)	2.2(14)	2(15)	1(11)
	` ′	` ′	3.8(2)	2.3(11)	2.2(83)	1(12)
193	-0.1(10)	0.00(1)	3.3(2)	2.0(46)	2.2(45)	0.4(48)
	` ´		3.9(3)	1.9(78)	1.7(84)	0.7(71)
177	0.30(7)	0.43(8)	6.0(1)	3.71(28)	0.56(7)	0.44(30)
1	1 3 6 5		4.0(2)	2.59(19)	0.63(10)	0.00(5)
40	-0.01(11)	0.07(2)	5.33(1)	21.2(3)	1.48(4)	0.84(12)
	` ′	, ,	4.22(3)	7.24(33)	1.65(9)	1.23(11)
60	-0.02(3)	0.8(5)	6.01(6)	12.8(6)	0.41(2)	1.63(37)
			6.80(2)	17.9(20)	6.0(13)	1.6(10)
80	0.43(3)	0.75(6)	5.17(6)	3.84(34)	1.11(17)	2.(4)
			7.42(2)	10.38(63)	3.76(30)	0.10(24)
	1		0.52(8)	4.3(15)	1(90)	4.2(14)

128	Mass	κ	w ·	E_1 , MeV	P, 10 ⁻⁹ , MeV ⁻³	α , MeV ⁻¹	β , MeV ⁻¹
140							
140	120	0.00(2)	0.00(0)				
160	140	0.07(15)	-0.02(4)				
$ \begin{array}{c ccccccccccccccccccccccccccccccccccc$	140	0.01(20)	0.02(1)				
$ \begin{array}{c ccccccccccccccccccccccccccccccccccc$	160	0.29(2)	1.20(7)				
$ \begin{array}{c ccccccccccccccccccccccccccccccccccc$	100	0.20(2)	1.20(1)				
$ \begin{array}{c ccccccccccccccccccccccccccccccccccc$	166	0.15(6)	0.60(16)				
$ \begin{array}{c ccccccccccccccccccccccccccccccccccc$	100	0.10(0)	0.00(20)				
$ \begin{array}{ c c c c c c c c c c c c c c c c c c c$	170	0.19(6)	0.78(11)				
$ \begin{array}{c ccccccccccccccccccccccccccccccccccc$	1.0	0.10(0)	0.10(22)				
$\begin{array}{c ccccccccccccccccccccccccccccccccccc$	176	0.0(55)	0.5(19)				
$\begin{array}{c ccccccccccccccccccccccccccccccccccc$	1.0	0.0(00)	0.0(10)				
$\begin{array}{c ccccccccccccccccccccccccccccccccccc$	182	0.14(9)	0.14(7)				
$\begin{array}{c ccccccccccccccccccccccccccccccccccc$	102	0.11(0)	0.11(1)				
$\begin{array}{c ccccccccccccccccccccccccccccccccccc$	192	0.11(1)	2 92(13)				
$ \begin{array}{c ccccccccccccccccccccccccccccccccccc$							
74 0.14(6) 0.25(4) 5.37(6) 3.03(12) 0.59(35) 0.58(4) 114 0.18(9) 0.10(4) 5.68(6) 4.06(25) 0.89(6) 1.11(20) 118 0.04(25) 0.01(4) 5.04(7) 3.36(24) 0.90(8) 0.95(16) 118 0.04(25) 0.01(4) 5.04(7) 3.36(24) 0.90(8) 0.95(16) 124 0.18(3) 0.56(6) 7.3(1) 2.87(32) 0.80(9) 0.98(8) 138 0.12(6) 0.42(13) 6.1(5) 0.85(59) 1.28(85) 2(20) 150 0.09(5) 0.22(4) 4.81(8) 2.45(17) 0.80(8) 0.89(13) 150 0.09(5) 0.22(4) 4.81(8) 2.45(17) 0.80(8) 0.89(13) 150 0.09(5) 0.22(4) 4.81(8) 2.45(17) 0.80(8) 0.89(13) 150 0.09(5) 0.22(4) 4.81(8) 2.45(17) 0.80(8) 0.89(13) 150 0.28(14) 0.19(3) 5.56(5) 3.33(9) </td <td>150</td> <td>0.00(2)</td> <td>2.02(11)</td> <td></td> <td></td> <td></td> <td></td>	150	0.00(2)	2.02(11)				
$\begin{array}{c ccccccccccccccccccccccccccccccccccc$	74	0.14(6)	0.25(4)				
$ \begin{array}{c ccccccccccccccccccccccccccccccccccc$	1.1	0.14(0)	0.20(1)				
$\begin{array}{c ccccccccccccccccccccccccccccccccccc$	114	0.18(9)	0.10(4)				
$ \begin{array}{ c c c c c c c c c c c c c c c c c c c$	***	0.10(0)	0.10(1)				
$\begin{array}{c ccccccccccccccccccccccccccccccccccc$	118	0.04(25)	0.01(4)				
$ \begin{array}{c ccccccccccccccccccccccccccccccccccc$	110	0.01(20)	0.01(1)				
$\begin{array}{c ccccccccccccccccccccccccccccccccccc$	124	0.18(3)	0.56(6)				
$ \begin{array}{c ccccccccccccccccccccccccccccccccccc$							
$\begin{array}{c ccccccccccccccccccccccccccccccccccc$							
$ \begin{array}{c ccccccccccccccccccccccccccccccccccc$	100	0.00(0)	5.22(1)				
$\begin{array}{c ccccccccccccccccccccccccccccccccccc$	156	0.28(14)	0.19(3)				
$\begin{array}{c ccccccccccccccccccccccccccccccccccc$	100	0.20(22)	0.10(0)				
$ \begin{array}{ c c c c c c c c c c c c c c c c c c c$	158	0.20(7)	0.41(8)				
$ \begin{array}{ c c c c c c c c c } \hline 168 & 0.002(3) & 0.27(36) & 0.2(17) & 0.40(30) & 1(50) & 0.43(42) \\ \hline 164 & 0.02(8) & 0.29(18) & 5.3(1) & 5.8(7) & 0.98(15) & 0.98(23) \\ \hline 174 & 0.08(9) & 0.16(9) & 5.0(3) & 1.4(2) & 0.58(15) & 0.32(22) \\ \hline 184 & 0.1(48) & -0.01(23) & 5.11(3) & 29.7(7) & 0.93(2) & 0.97(7) \\ \hline 188 & -0.001(3) & -0.06(9) & 5.55(2) & 24.8(7) & 1.45(6) & 1.24(8) \\ \hline 190 & 0.09(3) & 0.53(10) & 5.18(6) & 14.8(8) & 0.75(6) & 0.57(6) \\ \hline 196 & 0.02(7) & 0.04(5) & 5.34(6) & 4.2(3) & 1.09(12) & 0.89(13) \\ \hline 200 & -0.02(8) & 0.04(2) & 4.95(1) & 11.7(1) & 1.39(2) & 1.08(2) \\ \hline \end{array} $	-55	0.20(.)	0.11(0)				
$ \begin{array}{ c c c c c c c c c c c c c c c c c c c$]						
$ \begin{array}{ c c c c c c c c c c c c c c c c c c c$	168	0.002(3)	0.27(36)				
$ \begin{array}{ c c c c c c c c c c c c c c c c c c c$		(-,					
$ \begin{array}{ c c c c c c c c c c c c c c c c c c c$	164	0.02(8)	0.29(18)				
$ \begin{array}{ c c c c c c c c c c c c c c c c c c c$		` ′	, ,				
$ \begin{array}{ c c c c c c c c c c c c c c c c c c c$	174	0.08(9)	0.16(9)		1.4(2)	0.58(15)	0.32(22)
$ \begin{array}{ c c c c c c c c c c c c c c c c c c c$. ` ′	ì í				-0.12(26)
$ \begin{array}{ c c c c c c c c c c c c c c c c c c c$	184	0.1(48)	-0.01(23)			0.93(2)	0.97(7)
$ \begin{array}{ c c c c c c c c c c c c c c c c c c c$		i ` ´				53(76)	0.06(24)
$ \begin{array}{ c c c c c c c c c c c c c c c c c c c$	188	-0.001(3)	-0.06(9)				1.24(8)
196 0.02(7) 0.04(5) 6.47(4) 20.3(7) 1.22(13) 0.47(5) 5.34(6) 4.2(3) 1.09(12) 0.89(13) 6.57(2) 6.0(38) 16.4(79) 44(42) 1.39(2) 1.08(2)	190				14.8(8)	0.75(6)	0.57(6)
196 0.02(7) 0.04(5) 5.34(6) 4.2(3) 1.09(12) 0.89(13) 200 -0.02(8) 0.04(2) 4.95(1) 11.7(1) 1.39(2) 1.08(2)		, ,	, ,			1.22(13)	0.47(5)
200 -0.02(8) 0.04(2) 6.57(2) 6.0(38) 16.4(79) 44(42) 1.39(2) 1.08(2)	196	0.02(7)	0.04(5)			1.09(12)	0.89(13)
200 -0.02(8) 0.04(2) 4.95(1) 11.7(1) 1.39(2) 1.08(2)		, ,			6.0(38)		
	200	-0.02(8)	0.04(2)	4.95(1)	11.7(1)		
					9.0(2)	1.56(5)	7.0(3)

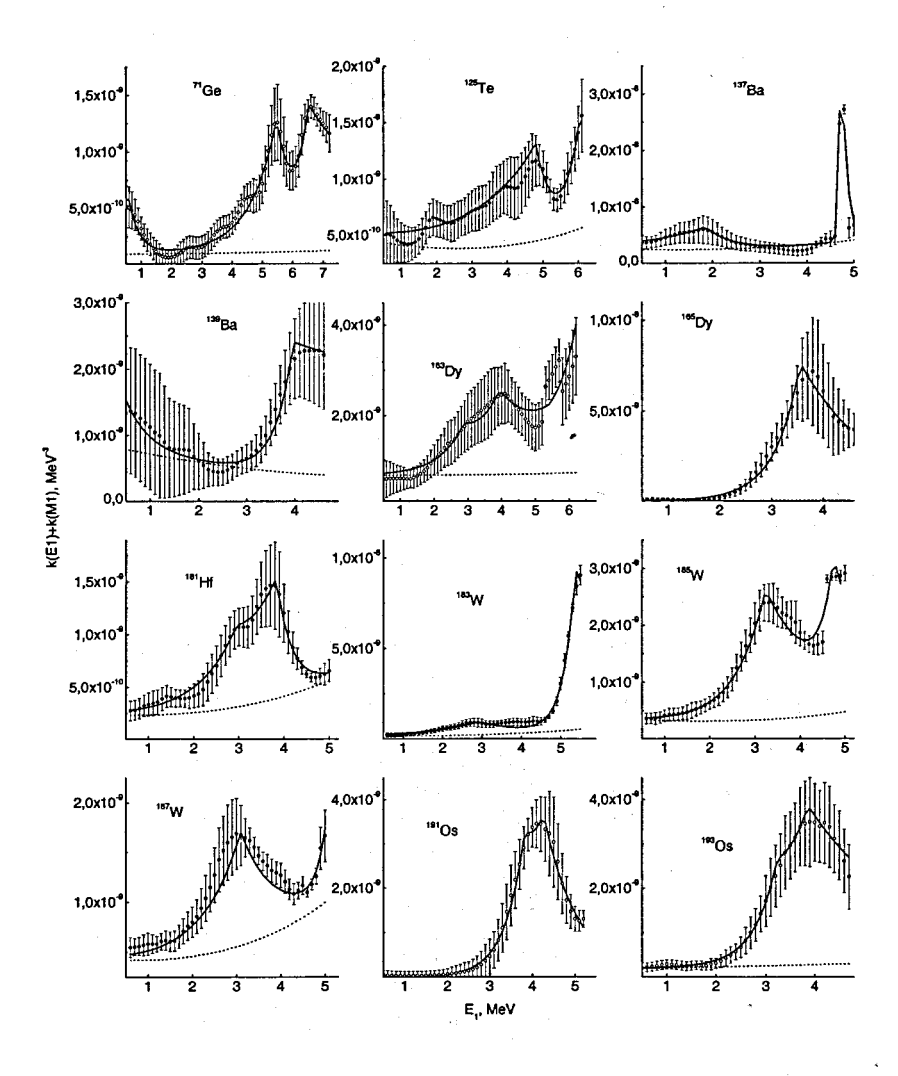


Fig. 1. Points with errors –the most probable values of sums of radiative strength functions and interval of their values, corresponding to minimum values χ^2 for even-odd compound nuclei. Open points – data from [9], full ones – from [6]. Line – the best fitting. Dots - component corresponding to equation (3).

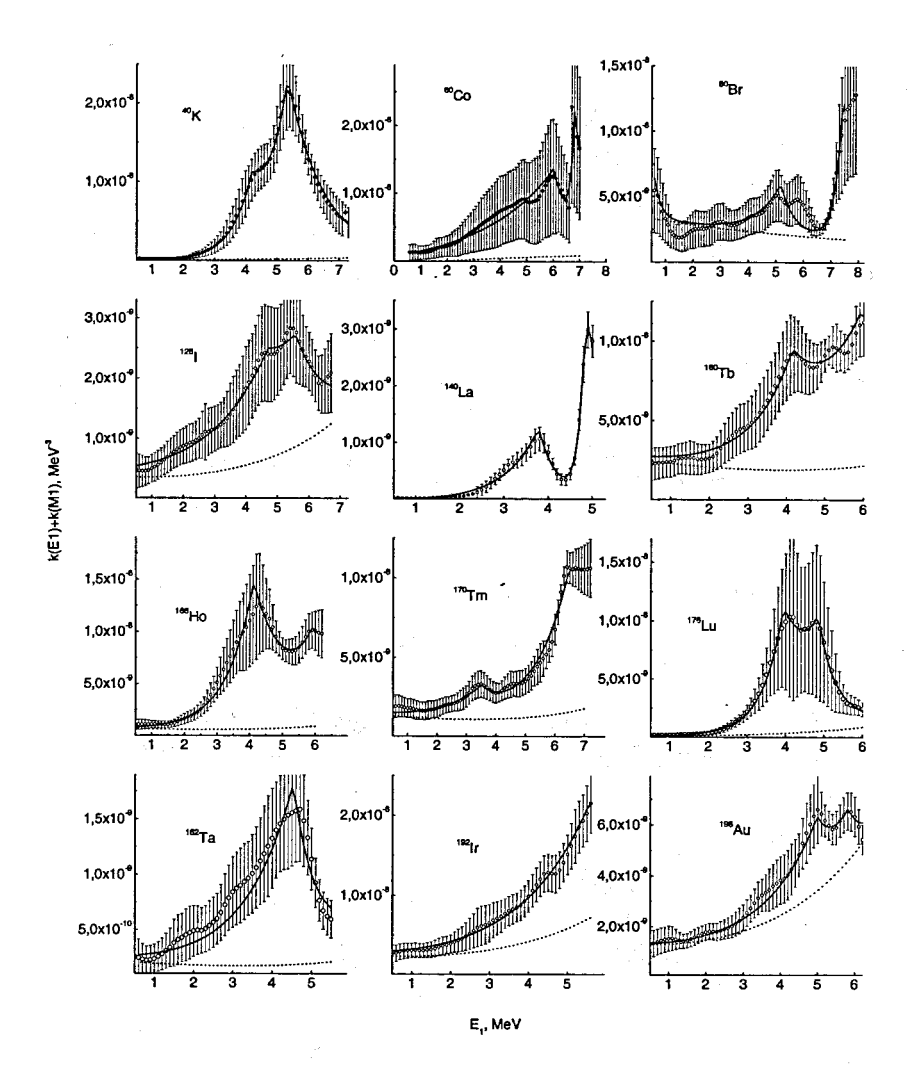


Fig. 2. The same as in Fig.1 for odd-odd nuclei.

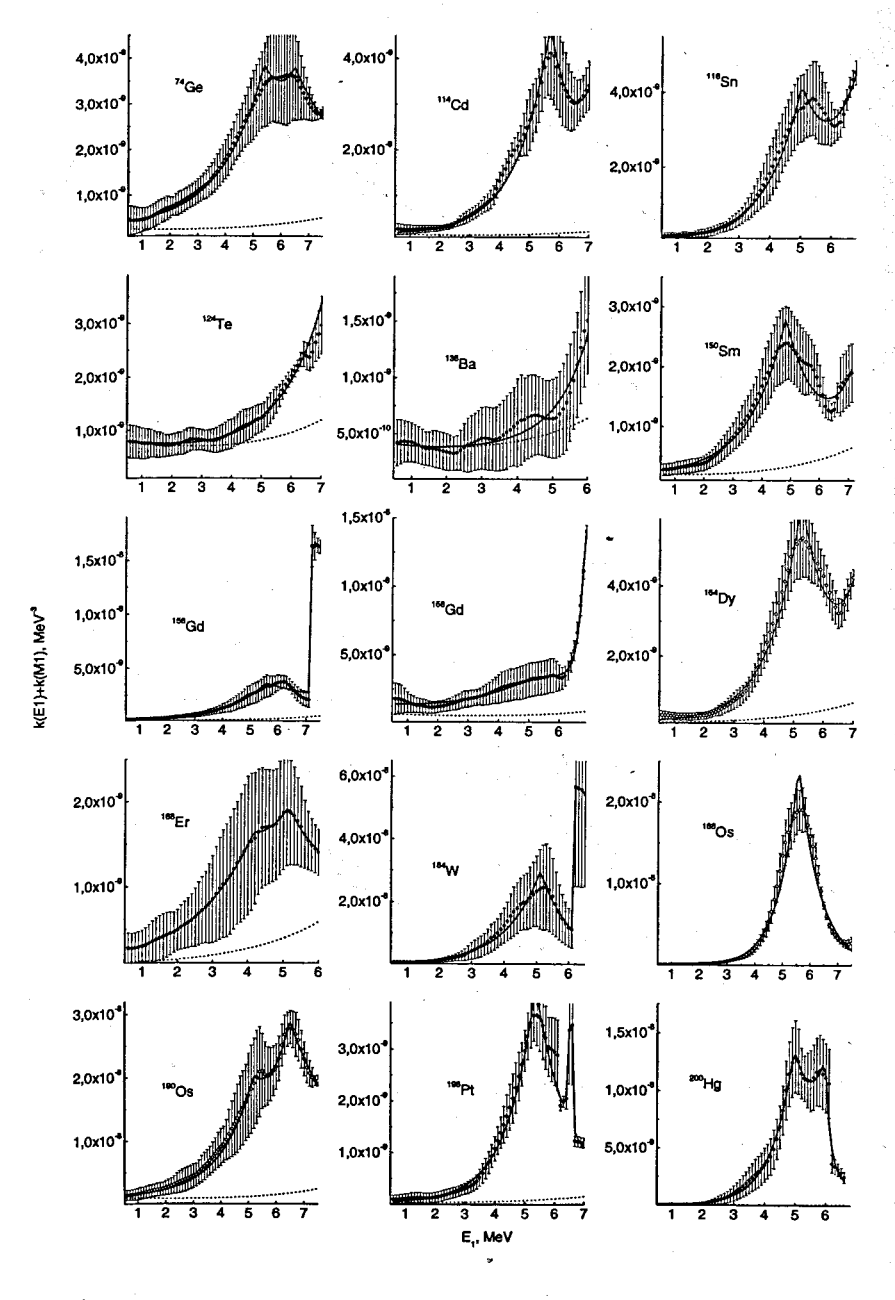


Fig. 3. The same as in Fig.1 for even-even nuclei.

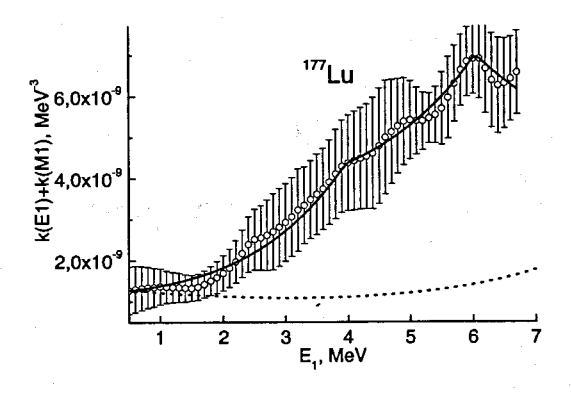


Fig. 4. The same as in Fig.1 for 177 Lu odd-even nucleus.

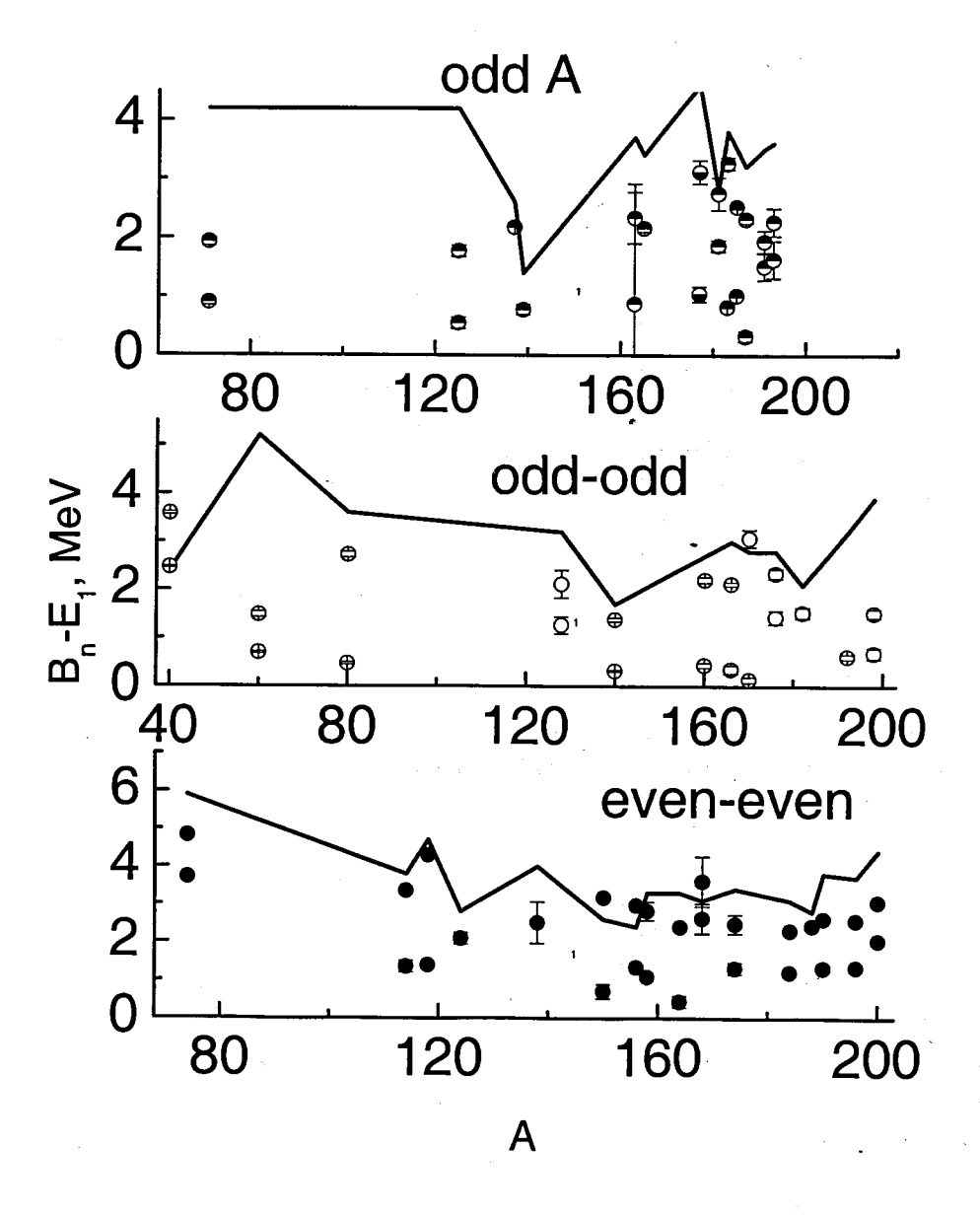


Fig. 5. Excitation energy of studied nuclei corresponding to positions of local fluctuations (maxima) k(E1) + k(M1) – points. Broken line – threshold of the excitation of four- and five quasiparticles in A-even and A-odd nuclei, respectively, for variant of approximation from [11]. Data for ¹⁷⁷Lu are registered with those for even-odd nuclei.

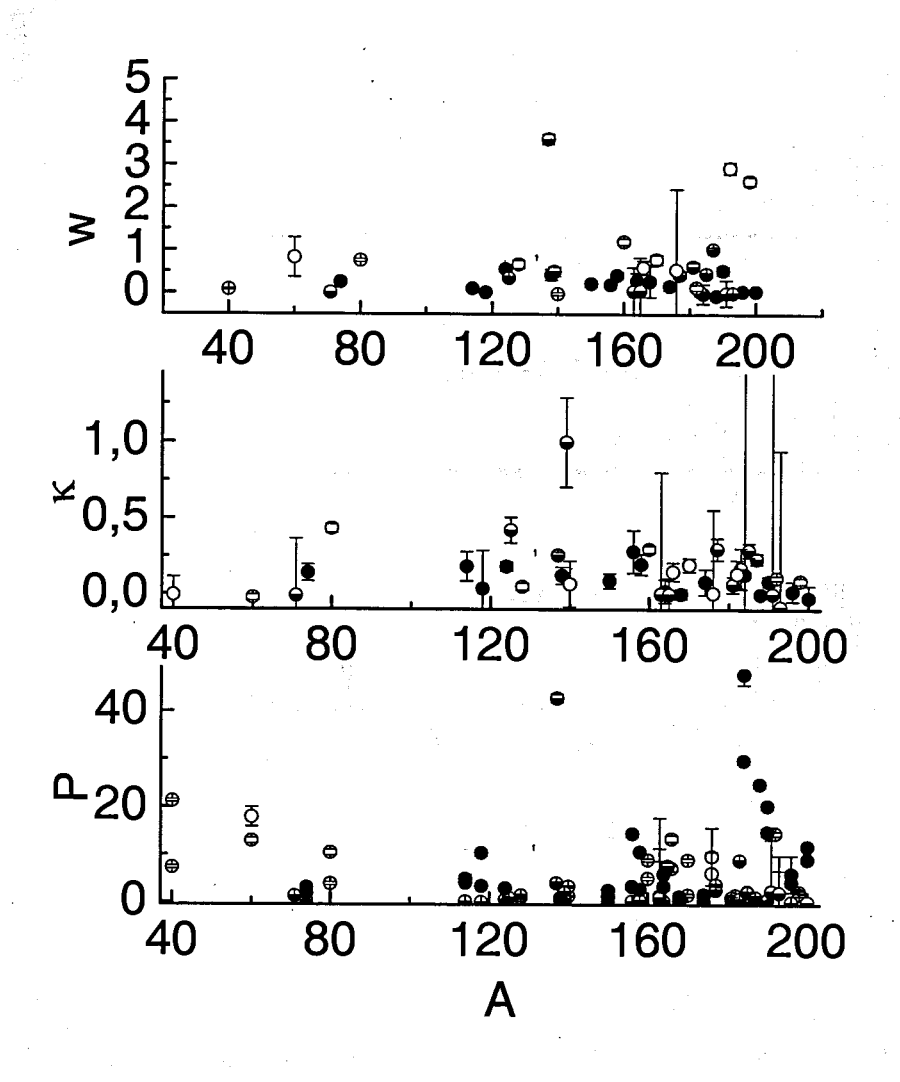


Fig. 6. Amplitudes P of local peaks (multiplied by 10^9). Values of κ and w parameters for function (3). Labels of nucleon number parity are analogous to those in Fig.5.

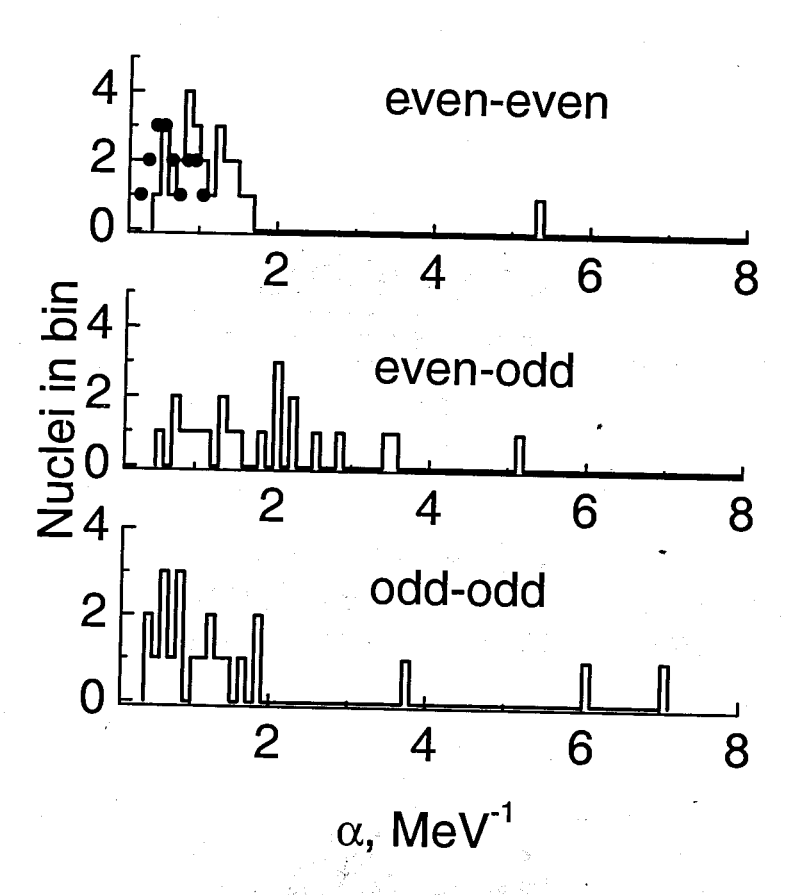


Fig. 7. Histogram – frequency distribution of α parameter in nuclei with different nucleon number parity. Points – the same for Δ_0^{-1} .

References

- [1] V.G. Soloviev, Theory of atomic Nuclei: Quasiparticles and Phonons, Institute of Physics Publishing, Bristol and Philadelphia, 1992.
- [2] Iachello F. and Arima A., The Interacting Boson Model, Cambridge University Press, Cambridge, 1987.
- [3] V. Bondarenko et all, Nucl. Phys. A762 (2005) 167.
- [4] A. Bohr, B.R. Mottelson, Nuclear structure, Vol. 1, W.A. Benjamin, Inc. New York, Amsterdam, (1969).
- [5] Solov'ev V.G., Sushkov A.V., Shirikova N.Yu., Part. and Nuc., 27(6) (1996) 1661 (in Russian).
- [6] A.M. Sukhovoj, V.A. Khitrov, Phys. Particl. and Nuclei, 36(4) (2005) 359. http://www1.jinr.ru/Pepan/Pepan-index.html (in Russian)
- [7] S.T. Boneva et al., Sov. J. Part. Nucl., 22(2) (1991) 232.
 S.T. Boneva et al., Sov. J. Part. Nucl., 22(6) (1991) 698.
- [8] S.T. Boneva, V.A. Khitrov, A.M. Sukhovoj, Nucl. Phys. A589 (1995) 293.
- [9] E.V. Vasilieva, A.M. Sukhovoj, V.A. Khitrov, Phys. At. Nucl. 64(2) (2001) 153, nucl-ex/0110017
- [10] Khitrov V.A., Li Chol, Sukhovoj A.M., In: XI International Seminar on Interaction of Neutrons with Nuclei, Dubna, May 2003, E3-2004-9, Dubna, 2004, p. 98. nucl-ex/0404028.
- [11] A.M. Sukhovoj, V.A. Khitrov, Phys. Particl. and Nuclei, 37(6) (2006) 899.
- [12] A.M. Sukhovoj, V.A. Khitrov, JINR preprint E3-2005-196 http://www1.jinr.ru/Preprints/Preprints-index.html
- [13] Malov L.A., Solov'ev V.G., Yad. Phys., 26(4) (1977) 729.
- [14] A.V. Ignatyuk, Report INDC-233(L) (IAEA Vienna 1985).
- [15] Reference Input Parameter Library RIPL-2. Handbook for calculations of nuclear reaction data. IAEA-TECDOC, 2002, http://www-nds.iaea.or.at/ripl2/
- [16] S.G. Kadmenskij, V.P. Markushev, V.I. Furman, Sov. J. Nucl. Phys. 37 (1983) 165.
- [17] P. Axel, Phys. Rev. 1962, 126(2), (1962) 671.

PROBLEMS OF EXPERIMENTAL DETERMINATION OF PARAMETERS OF NUCLEUS AND APPLICABILITY OF THE BOHR-MOTTELSON HYPOTHESIS

A.M. Sukhovoj, V.A. Khitrov

Frank Laboratory of Neutron Physics, Joint Institute for Nuclear Research, 141980, Dubna, Russia

Population of a number of excited levels of 51 V and 57 Fe has been determined from the data of the ENDSF file up to the excitation energy of about 7 and 5.2 MeV, respectively. It cannot be reproduced in the region of their maximal energies in the framework of assumption on the independence of partial radiative widths on the structure of decaying level and excited one, at least, lower than $0.5B_n$. Therefore, it is impossible to estimate the actual degree of reliability of data on the level density and radiative widths of cascade gamma-transitions in light spherical nuclei obtained from the spectrum analysis of nuclear reactions, which do not take into account this circumstance.

1 Introduction

Large level density at the excitation energy higher than 0.5Bn does not allow one to obtain experimental data on the level density and partial widths of gamma transitions by means of the classical nuclear spectroscopy. These parameters may only be found here from the solution of inverse problem of the mathematical analysis - the determination of parameters x, y, z... of the function S from its values at the relation prescribed a priori S=f(x,y,z...). In general case the function f(x,y,z...) is determined with some uncertainty, for example, using an erroneous hypothesis instead of the lacking experimental information. In such case the presence and value of the error in the function f(x,y,z...) may only be determined from experiment, for example, using a hypothesis on the independence of values of partial radiative widths of Γ gamma-transitions of the assigned type and energy on the nucleus excitation energy. In the general form this hypothesis has been formulated by Bohr and Mottelson [1] as an assumption on the independence of the interaction cross section of the nuclear reaction product on the nucleus excitation energy U. In other words, it does not depend on the structure of nucleus at the energy U, and up to now [2] it is used at the determination of level density from spectra of evaporative nucleons without any verification. The same hypothesis in the form of "the Axel-Brink hypothesis" serves as a basis for the technique of joint extraction of ρ and Γ from gamma spectra of the reaction (${}^{3}\text{He}, \alpha$) in technique [3].

The necessity of introducing any "zero" hypothesis (of the type [1]) is determined by the lack of necessary experimental data. Therefore, the main task of experimenters is conducting of new experiments giving unambiguous conclusion on the domain of applicability and on the domains of studied phenomena, which require its significant specification.

Calculations of probabilities of the emission of gamma-quanta in the framework of the quasi-particle-phonon model of a nucleus and their comparison with the experiment show that the value of Γ is determined by the relation of components of the quasi-particle and phonon type in the structure of wave functions of the decaying and excited level. In other words, the hypothesis on the independence of probability of interaction of a gamma quantum with an excited nucleus cannot be described [4] by some universal function, at least, lower than 3 MeV in even-even deformed nuclei.

Similar argument but purely experimental one follows from the comparison of the level density of various nuclei extracted [5] from intensities of two-step cascades, on the one hand, and spectra of evaporative nucleons and primary gamma-quanta, on the other hand. In the first case, this parameter of nucleus demonstrates evident and abrupt change of entropy of the nucleus at two, at the minimum, energies of its excitation. In the second case – its smooth increase at the increase of the nucleus excitation energy. Practically, this distinction may only be related to a very small degree of influence of the hypothesis on the independence of probability of the emission of gamma-quanta of the given multipolarity and energy (of an evaporative nucleon) on the structure of nucleus in the first case, and a very strong one – in the second case.

In other words, at present there are some data prejudicing hypothesis [1]. In this case, an experimental check of the hypothesis is obligatory with revealing of conditions, at which its application provides for the acceptable accuracy of experimental data.

2 Experimental check of the Bohr-Mottelson hypothesis

Direct extraction of the cross section $\sigma(E,U)$ in the classical experiment (target+beam) for ordinary nuclei is practically impossible. Nevertheless, a possibility to obtain some experimental information on the relation $\sigma(E,U)/\sigma(E,U=0)$ for an arbitrary nucleus exists, at least, in the $(n,2\gamma)$ reaction. The relation

$$P = i_{\gamma\gamma}/i_1 i_2 \tag{1}$$

may be determined for any level of the nucleus under study on condition that out of two independent experiments absolute intensities $i_{\gamma\gamma}$ of any two-step cascade and intensities of its primary gamma transition i_1 and the secondary one i_2 have been determined.

This value (total level population) may be presented for two arbitrary levels l and m as a sum of the product of high-lying levels l on the partial cross sections of gammatransitions $l \to m$: $P_m = \sum P_l \times \sigma_{lm}$. It has been determined in the form of only the cascade population $P_m - i_1$ and has been compared with different model calculations on the basis of experimental information accumulated by now in many nuclei from the mass region of $40 \le A \le 200$ for a hundred of levels almost in each of them. The data level for P may be increased abruptly in possible experiments with more effective HPGe-detectors.

Although it is impossible to determine the value of σ_{lm} directly from equation (1), these experimental data due to their high sensitivity made it possible to evaluate [5] the sign and value of the relation $\sigma_{lm}(U < B_n)/\sigma_{ij}(U = B_n)$.

Similar analysis may be carried out for some nuclei, in which the intensity of two-step

cascades has not been measured so far. To do this, the data [6] on the estimated schemes of gamma decay from the existing files are sufficient. Unfortunately, a small value of the excitation energy overlapped by these schemes restricts the number of nuclei, in which the observation of violation of hypothesis [1] is possible for gamma-decay.

Such analysis has been performed [7] for 124 Te. Useful information may also be obtained for compound nuclei 51 V and 57 Fe. During the analysis one must take into account that the accuracy of $P_m - i_1$ determination from the estimated decay schemes may not exceed the accuracy of its determination from expression (1), and the number of levels, for which it is possible to determine this value on the basis of the data of type [6] is much smaller, respectively.

Comparison of the experimental data with the calculations using various level densities and radiative strength functions is presented in Figs. 1 and 2. At small excitation energies of levels good concurrence of the experiment and any variants of the calculation is attained almost in any case due to a very small sensitivity of the cascade population of the most low-lying levels to variations of the calculated level densities and radiative strength functions. The presence of considerable discrepancy for a few levels most likely testifies either to an erroneous determination of the level spin in the estimated decay scheme, or to a very strong influence of the structure of its wave function on the partial cross sections of gamma-transitions exciting it.

3 Conclusion

The region of excited levels of an arbitrary nucleus with high level density (the spacing D is smaller than the resolution FWHM of the used spectrometer) remains so far either unexplored, or scantily explored. Reliability of the main part of the data obtained earlier from experiment on the level density and radiative strength functions of gamma-transitions in it raises grave doubts, first of all, due to the absence of absolute experimental proofs of the validity of basic hypothesis [1] of the analysis carried out here.

Currently, there is no alternative for the explanation obtained in [5] of the physical nature for a considerable discrepancy of the experimental data and calculations reproducing them presented here and in [2,3]. Therefore, on the basis of the whole experimental data on intensities of two-step cascades, with a high probability, one must not exclude a strong influence of the nucleus structure on the level density and probabilities of the emission of nuclear reaction products up to the neutron binding energy or even higher energy.

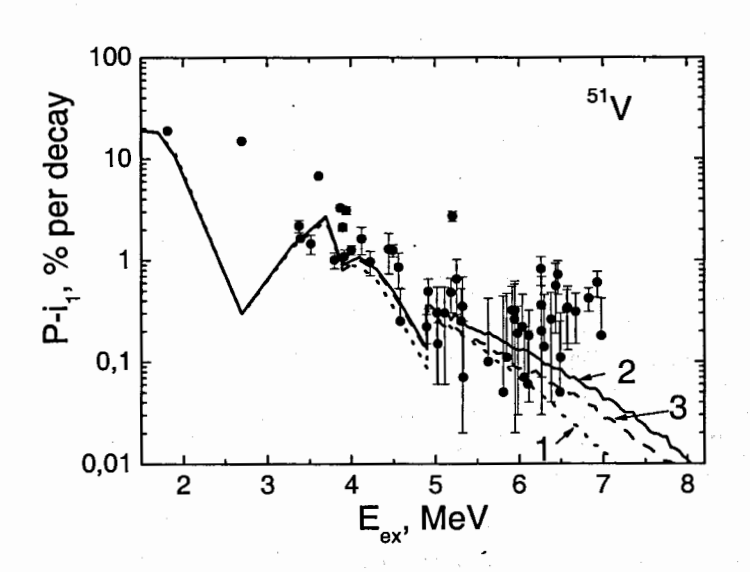


Fig. 1. Points with errors - experimental data from [6]. Line 1 – calculation using models [8,9]. Line 2, 3 - data from [10] with an increase of strength functions of the low-energy E1- or M1-transitions, only.

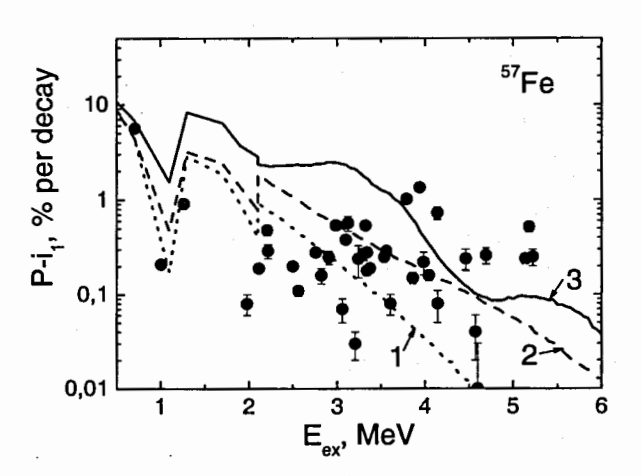


Fig. 2. The same as in Fig. 1. Line 2 - data from [11] (they do not reproduce the main part of intensities of two-step cascades). Line 3 - one of the variants of the level density and radiative strength functions reproducing [12] the cascade intensity in all the 27 intervals, is used.

References

- O. Bohr, B.R. Mottelson, Nuclear Structure, Vol. 1 (Benjamin, NY, Amsterdam, 1969).
- H. Vonach, Proc. IAEA Advisory Group Meeting on Basic and Applied Problems of Nuclear Level Densities (New York, 1983), INDC(USA)-092/L, (1983) P.247
 B.V. Zhuravlev, Bull. Rus. Acad. Sci. Phys. 63 (1999) 123.
- [3] A. Schiller et al., Nucl. Instrum. Methods Phys. Res. A447 (2000) 498.
- [4] V.G. Soloviev et al., Part. Nucl. 27(6) (1997) 1643.
- [5] Sukhovoj A.M., Khitrov V.A., Physics of Paricl. and Nuclei, 36(4) (2005) 359. http://www1.jinr.ru/Pepan/Pepan-index.html (in Russian)
- [6] http://www.nndc.bnl.gov/nndc/ensdf.
- [7] Sukhovoj A.M., Khitrov V.A., JINR Communication E3-2007-22, Dubna, 2007.
- [8] W. Dilg, W. Schantl, H. Vonach, M. Uhl, Nucl. Phys. A217 (1973) 269.
- [9] S.G. Kadmenskij, V.P. Markushev, V.I. Furman, Sov. J. Nucl. Phys. 37 (1983) 165.
- [10] A. C. Larsen et al., Phys. Rev. C 73, 064301 (2006)
- [11] Voinov A. et all, Phys. Rev. Let., 2004, 93(14) 142504-1.
- [12] Sukhovoj A.M. et al., In: XIII International Seminar on Interaction of Neutrons with Nuclei, Dubna, May 2006, E3-2006-7, Dubna, 2006, pp. 72.

GAMMA DECAY OF THE COMPOUND STATE AND CHANGE OF STRUCTURE OF THE 124Te EXCITED LEVELS

A.M. Sukhovoj, V.A. Khitrov

Frank Laboratory of Neutron Physics, Joint Institute for Nuclear Research, 141980, Dubna, Russia

Abstract.

Independent analysis of a large amount of data on the spectrum of gamma-rays of the radiative capture of thermal neutrons in 123 Te $(\sum (i_{7}E_{7})/B_{n}=0.49)$ obtained in Řež made it possible to obtain new and reliable information on the dependence of sums of radiative strength functions of dipole gamma-transitions on the energy of levels excited by them. These data, as does the level density in 124 Te, demonstrate a strong change of structure of the nucleus practically for the whole region of the levels excited by a captured neutron.

As in the earlier studied nuclei (using data on the intensities of two-step cascades), it is possible to reproduce the stated parameters of the gamma-decay process to the accuracy of experiment only by the models directly taking into account the coexistence and interaction of the usual and superfluid component of the nuclear matter.

1 Introduction

Properties of the nucleus at its low energies are determined by the coexistence and interaction of quasi-particles and phonons. Here, only the excitation region E_{ex} , lying lower than the neutron binding energy B_n is implied.

This most general physical result has been obtained both by the authors of the quasiparticle-phonon model [1], and those of the model of interacting bosons and fermions [2]. The main details of this process may be generalized and interpreted by theorists without serious errors only on the basis of reliable data from experiments, which are maximally sensitive to the structure of excited levels of the studied nuclei. In the first place this statement refers to the region of level energies of any nuclei, which cannot be resolved by the spectrometers used in experiment.

This is the most complicated object of investigation of the low-energy nuclear physics. Any experiment in this excitation region produces spectra S (including the interaction cross sections), the value of which is always determined by an unknown level density ρ and strength functions, for example, of gamma-quanta $k = \Gamma_{\lambda f}/(E_{\gamma}^3 \times A^{2/3} \times D_{\lambda})$ of the cascades connecting the compound state λ and the low-lying level f. An inevitable error of determining the measured intensity usually varies from several percent to several tens of percent. Since the S amplitude in ordinary spectra is determined by the product of ρ and k, the accuracy of solving the inverse problem diminishes very much.

Experimental spectra for any nucleus may be used in two ways, either:

- a) for testing of some model representations on ρ and k, or as the initial data
- b) at solving the inverse problem of mathematical analysis the determination of values of the function parameters by its quantity.

Reliability of the obtained conclusions may be partially or utterly lost both in the first and in the second case.

2 Main problems of analysis of experimental data

1. Any model of ρ and/or k under test is obtained in the framework of some hypotheses and a priory may describe the predictable value only with certain usually unknown error. Moreover, potentially, models of the same values having a different theoretical basis are possible, but they can provide even more precise reproduction of experimental spectra. At the same time, the degree of discrepancy between various models may reach utter incompatibility of their basic theoretical representations. In addition, the error transfer coefficients $\delta\rho$ and δk to the errors δS are usually very small. As a consequence, the same spectra (cross sections) within the limits of total errors δS may be described by fundamentally differing models. One may see this from compilations [3] of practically used models of ρ and k. This circumstance is not taken into account, for example, in the analysis [4]. Therefore, the use of the criterion χ^2 in the first method of comparison of models and experiment provides for the correct and error-free conclusion on the model under test only at its unconditional falseness. Due to this, it cannot be used in conclusion on the correctness of certain model representations and particularly – for the unstudied region of nuclei and their excitation energies.

The reason for this circumstance is obvious: information on the studied phenomenon may only be obtained from the experiment adequate to the studied object. Mathematics and mathematical statistics may not generate new physical information in principle. Actually, the result of analysis obtained on the basis of χ^2 smallness may utterly distort the picture of the studied process.

2. Solution of the inverse problem of mathematical analysis may not be unique practically in any experiment to determine ρ and/or k. And transfer coefficients of inevitable errors of the δS spectrum to the errors of parameters $\delta \rho$ and δk may reach module 10-100 and more.

The situation with function $S = f(\rho, k)$ relating unknown parameters with the measured spectrum may also be ambiguous. For example, up to now the extraction of data on ρ and k from gamma-spectra has been carried out for the most part in the framework of assumption on the k independence on the excitation energy of nucleus. The corresponding hypothesis on the independence of cross section of nuclear interaction on the excitation energy of target nucleus has been formulated in general form in [5] and is used without verification to present day in analysis of any experiments to determine the level density. In addition, in nuclear reactions with charged particles, for example, spin window of the determined level density usually may not be recorded precisely. As a consequence, tran-

sition to the total level density inevitably introduces an additional error. It is impossible to obtain its estimation from experiment.

Therefore, a direct determination of the level density and partial widths Γ of the emission of products of the studied reaction is preferable. And solution of this problem from the spectra measured in the experiment should be performed using experimental techniques providing the minimum total error of the measured spectrum, minimum error transport factors and the maximum use of all available information for the given nucleus.

3 Possibilities of the present-day experiment to determine ρ and k

An experiment to measure intensities of two-step cascades with the total energy $E_1 + E_2 = B_n - E_f$ satisfies the above-mentioned conditions as much as possible. A possibility of its realization with Ge-detectors has been demonstrated for the first time in Dubna [6, 7]. The technique to determine ρ and k and results obtained for many nuclei in the variants, which use and do not use the hypothesis [5] is described in [8, 9], respectively.

Approximation [10, 11] of the level density obtained in such way by the V.M. Strutinsky model [12] adequate to the experiment for various assumptions on the shape of correlation function of a nucleon pair in a heated nucleus and the energy dependence of density of single-particle states g near the Fermi surface was performed for all nuclei, in which two-step cascades were measured. Except for those, in which small statistics of useful events did not allow one to determine [13] the shape of energy dependence

$$I_{\gamma\gamma}(E_1) = \sum_{\lambda,f} \sum_i \frac{\Gamma_{\lambda i}}{\Gamma_{\lambda}} \frac{\Gamma_{if}}{\Gamma_i} \tag{1}$$

with an acceptable systematic error for all possible cascades connecting 3 levels: $\lambda \to i \to f$.

The estimation [14] of influence of the error $\delta I_{\gamma\gamma}$ on the desired parameters shows that its variation from -25 to +25% changes the obtained values of ρ and k no more than by a factor of 2-3. Simultaneously, both the deviation value and its sign change depending on the excitation energy of nucleus. However, the specific shape of the energy dependence of ρ and k remains entirely. In order to reach the same level of $\delta\rho$ and δk , an alternative technique of simultaneous determination of these parameters because of very large error transport factors [15] requires a measurement of total gamma-spectra for arbitrary excitation energy with an error considerably less than 1%. Therefore, maximum reliable representations on the properties of a nucleus manifesting themselves in the process of gamma decay may at present be obtained only from intensities of two-step cascades and from methodically similar two-step reactions.

4 Experimental level density and strength functions of cascade gamma-transitions in ¹²⁴Te

The intensities of two-step cascades necessary for analysis for the ground and first excited states of ¹²⁴Te were measured for the first time [16] in Dubna at the coincidence spectrometer with Ge-detectors of low effeciency and poor resolution. Nevertheless, small level density of this nucleus below $\sim 0.5 B_n$ made it possible to obtain the dependence required for the analysis [8, 9] with a satisfactory systematic error. Contemporary data on the i spectrum of gamma-rays of the thermal neutron capture [17] allowed one to obtain values of the total population $P = i_1 i_2 / i_{rr}$ for 29 levels of this nucleus up to their maximum energy 4.37 MeV. Use of these data to normalize $I_{\gamma\gamma}$ somewhat increased the value of two-step cascade intensities. The obtained values of ρ and k have been published in [18]. Comparison of the shape of energy dependence of ρ and k for all the nuclei studied in Dubna, Riga and Řež for both variants of their determination allows one to suppose that the level density of this nucleus obtained both in [8] and in [18] has been overestimated at the energy of $E_i > 3$ MeV, and the radiative strength functions – have been underestimated, respectively. In the first place, this is due to a small width of the energy region of levels, for which their total population has been determined by primary gamma-transitions and cascades of arbitrary multiplicity of gamma-quanta in them.

A very large amount of spectroscopic information presented in [4] makes it possible to obtain significantly more accurate data for ρ and k comparing to the ones published in [18].

4.1 Main problems of analysis of experiment

- 1. It should be pointed out that any new technique to acquire information on the properties of a nucleus may realize its potential only at developing of adequate methods of its analysis. This analysis should take into account the peculiarities of the whole complex of the information involved and it should be implemented in algorithms and programs based on the use of the earlier obtained results of other experiments checked by practice, mathematical rules and mathematical statistics.
- 2. Naturally, the algorithms must provide the maximum effective extraction of physical information on the nucleus and its maximum possible reliability. First of all, this condition necessarily requires a maximum possible experimental verification of any even generally accepted statements and hypotheses on the studied object.

The technique of using the intensities of two-step cascades to study the properties of nucleus in the region of high density of its level unresolveable by a spectrometer with the FWHM ($\rho_i^{-1} < FWHM$) line width clearly confirms these two clauses. System (1) of equations relating the cascade intensity in an arbitrary energy region of cascade gammatransitions with the determined parameters ρ and k is strongly correlated. Therefore, the cascade intensity in any point of the measured spectrum depends on the values of ρ and k in the whole region under investigation. It should be added that the experimental spectra of two-step cascades from the point of view of mathematics are a linear sum of unknown

intensities of two-step cascades with primary and secondary gamma-transitions of practically one and the same energy. As a result, any experimental spectra of such cascades may be accurately reproduced by an infinite number of various functional dependences of $\rho = f(E_i)$ and $k = \phi(E_1, E_i)$. The relation of maximal values of these parameters to the minimal ones is limited [15] by a value on the order of $10^1 - 10^2$ due to the non-linearity of the equations. However, it increases greatly and inevitably at the restriction of the energy region of gamma-quanta used, for example in [19], to compare calculation and experiment.

2. The statement on inevitable and fast complication of the structure of excited levels, for example, at the excitation energy increase is generally accepted. But it has not been tested by experiment and does not comply with the theoretical calculations of dynamics of the states strength fragmentation process on its level for nucleus of various complexity with various excitation energy. It follows quite unambiguously from [20] that, for example, the state 2 quasi-particles \otimes 2 phonons is fragmented considerably weaker than the two-quasi-particle and/or two-phonon states. Since the energy of any state of nucleus grows at the increase of the degree of its complexity, one should expect [20] a considerable change of structure of the nucleus under investigation at the increase of excitation energy. The degree, at which the fragmentation rules in a concrete region of the excitation energy of a concrete nucleus exert influence on the desired ρ and k lower than B_n , may be obtained only from an experiment.

Thus, maximum reliable conclusions on the nucleus under investigation, analysis of intensities of two-step (and of larger multiplicity) cascades may only obtained

- a) after determination of the sequence order of quanta in them and, of course,
- b) without attraction of not tested although generally accepted representations on the nucleus properties.

4.2 Algorithm and necessary data to determine ρ and k in ¹²⁴Te

Further analysis has been carried out meeting these two important conditions.

The intensity of two-step cascades to a first approximation is inversely proportional to the level density of the nucleus under investigation. Therefore, it is necessary to determine the $I_{\gamma\gamma}$ absolute values with the maximum accuracy. Actually, this may be done only at the normalization of the measured relative intensities of the strongest cascades with low-lying intermediate levels of a nucleus on their own absolute values. Renormalization of the experiment carried out earlier in Dubna [16] has been performed using intensities i_1 and branching factors $B_r = i_2/\sum i_2$ from the data [4]. The values of sums of intensities of all possible two-step cascades for the ground and first excited states of ¹²⁴Te obtained in this way equal to 7.8(23) and 16.6(25)% decays.

Their values summarized by 0.5 MeV intervals of intermediate and all final levels are shown in Fig. 1 with an example of typical calculated reproduction. Non-linearity of the $I_{\gamma\gamma} = f(E_1)$ function provides for the finalness of the interval of ρ and k values reproducing the experimental data even on condition that the number of unknown parameters exceeds by a factor of 2 the number of intensities measured in the experiment.

However, this interval includes their real values only on condition that the relation of strength functions for gamma-transitions of one and the same multipolarity and energy $k^{sec}/k^{prim} = f(E_{ex}) \neq const$ is determined for arbitrary excitation energy E_{ex} on the basis of independent information. This problem has not been posed so far by experimenters and has not been solved to the necessary degree even in methods [9]. In order to solve it completely, it is necessary to determine from experiment certain functionals of the process of cascade gamma decay, which are unambiguously connected to the excitation energy of a nucleus right up to $E_{ex} \approx B_n$, as well as to the type of multipolarity of gamma-transition and, which are maximum sensitive to variation of the strength function.

Potentially, a problem of such scale may only be solved in an experiment to investigate the intensities of cascades of the given multiplicity for the final levels up to their maximum possible energy. But qualitative representation on the expected effect and the possibility of its account to the calculations in a first approximation may be obtained from comparison of values of the experimental population P of excited levels of the nucleus under investigation and the calculated total (or only cascade) one up to the maximum possible energy of their excitation for various tested functional dependencies of $\rho = f(E_i)$ and $k = \phi(E_1, E_i)$.

The P value may be determined from the evident relation

$$P_{\gamma\gamma} = i_1 i_2 / i_{\gamma\gamma} \tag{2}$$

purely experimentally with minimal error on the conditions that:

- a) the sequence order of quanta in two-step cascades through various intermediate levels is determined independly of the Ritz combination principle with the obligatory use of the maximum likelihood method (effective algorithm is realized in [21]),
- b) their absolute intensities $i_{\gamma\gamma}$ and also the corresponding intensities of primary i_1 and secondary i_2 cascade transitions have been determined.

Systematic error $P_{\gamma\gamma}$ in such a way of determination is almost completely correlated, and the random one is determined only by the degree, in which approximation of spectrum peaks of the single HPGe-detector resolves multiple structures in the region of E_1 and E_2 . The peak density in spectra $I_{\gamma\gamma}$ for various final levels is usually smaller, the background depends weakly on the energy, and the resolution improves additionally when the technique [6] is used, so a set of data for $i_{\gamma\gamma}$ at the equal detector effectiveness usually exceeds a set of data for i. The amount of data on i_{2n} is proportionate to ϵ^n (n > 2). Unfortunately, a small value of the detector efficiency ϵ in [16] prevents from using the technique [9] to obtain the $P_{\gamma\gamma}$ values in this nucleus. Therefore, analysis of the level population has been performed below only on the basis of the data from Table 2 from [4]. Naturally, the Pry data from the decay scheme [4] (defined as a sum of all the gammatransitions depopulating the given level and placed into the decay scheme), contain extra (comparing to [9]), may be considerable, systematic error. This error grows module at an increase of the excitation energy of a level. Besides, it is impossible to estimate really its value on the basis of data from the decay scheme. Most likely, at the analysis of an experiment the obtained data should be regarded as a $P_{\gamma\gamma}$ lower estimate. First of all, the above mentioned facts refer to maximum energies of the ¹²⁴Te excited levels.

Data on the cascade level population summarized on a small region of the excitation energy are the most effective ones [9] for estimation of the $k^{sec}/k^{prim} = f(E_{ex})$ function.

But only at the determination of $P_{\gamma\gamma} - i_1$ from (2). However, for the data from [4] the error increases strongly with an increase of the excitation energy (only the cascade population $P_{\gamma\gamma}$ decreases faster than the i_1 intensity of the corresponding primary gammatransition decreases). Therefore, it is inevitable that extraction of the information on the $k^{sec}/k^{prim} = f(E_{ex})$ function in this case considerably differs from the procedure used in [9].

So only the average value of population of a single level in a small (200 keV) region of the excitation energy has been determined from the data on the summarized intensity of the secondary gamma transitions placed into the decay scheme [4]. The average value of only the intermediate cascade level population $\langle P_{\gamma\gamma} - i_1 \rangle$ from this region is shown in Fig. 4, and of its sum – in Fig. 5. The data from Fig. 4 have been used to determine discrepancy parameters of the energy dependence of radiative strength functions of the primary and secondary gamma-transitions in a similar manner [9]. The data from Fig. 5 allow one to make certain conclusions about the degree of discrepancy between the obtained estimate of strength functions and the experimental values and the factors causing it. Naturally, accuracy of the used estimate is determined directly by the degree of fluctuations of $P_{\gamma\gamma}$ values for neighboring levels of one and the same spin and parity. If they are large, than the error of estimation of the $k^{sec}/k^{prim} = f(E_{ex})$ function may not be small. However, in this case realistic hypotheses are necessary, which can explain strong selectivity of the gamma-decay process higher than $\sim 0.5 B_n$.

Such selectivity seems to be quite improbable: the parameter $\sum (i_{\gamma}E_{\gamma})/B_n=0.49$ for the data from Table 1 [4] at the value $\sum i_{\gamma}=237\%$ of decays. This means that on average only a half-energy of each cascade is observed in peaks of the capture spectrum of thermal neutrons resolved experimentally in 123 Te (and in Table 1 [4]). Simple extrapolation of the dependence of i_{γ} sum on the $\sum i_{\gamma}E_{\gamma}/B_n$ parameter value to its asymptotic value obtained for various i_{γ} registration thresholds gives a possible value $\sum i_{\gamma}\approx 400-450\%$. It follows that no less than 160-210% of decays fall to the part of gamma-quanta with the intensity less than the threshold in [4]. Out of them about 75% of decays fall to the share of the primary ones. There is no reason to exclude a possibility that the rest ($\approx 80-130\%$ of decays of the intensity of weak gamma-quanta fall to the region of highlying ($E_{ex}>0.5B_n$) levels. Therefore, one must not exclude a possibility that the level population obtained using the data [4] is a lower estimate for levels with the energy higher than $E_{ex}\sim 4-5$ MeV.

4.3 Results of determination of ρ and k in ¹²⁴Te

Level density and strength functions reproducing all the mentioned experimental data in the best way are given in Fig. 2 and 3. Approximation of ρ by the model functional dependence [12] (Fig. 3) has been performed similarly to [10]. Naturally, it contains errors related to the necessity to use more or less realistic hypotheses on the values of coefficient of vibration increase of the level density, the correlation function of nucleons in a heated nucleus, the density of single-particle states near the Fermi surface, etc. Therefore, in principle, there is a possibility to increase the accuracy of approximation comparing to the one observed in Fig. 3.

As in other nuclei studied by now, in 124Te an unconditional stepped structures is observed in the region of ≈ 3.5 and $\sim 7-8$ MeV. Taking into account values of the pairing energy Δ of two neutrons and two protons close to 2.5 and 2 MeV, respectively. on the basis of model representations [12], the first step corresponds to breaking of the neutron pair. Perhaps, the second one is caused by the breaking of the second neutron pair or the first proton one. In other words, in the nucleus under consideration no fundamental discrepancies with the shape and parameters of functional dependence $\rho = f(E_i)$ of other nuclei is observed. The width of the observed region and level density in the region of its almost constant value depends strongly on the accuracy of estimation of the $k = \phi(E_1, E_i)$ function parameters, and also on the values of the analysis parameters - the density of neutron resonances and low-lying levels. The dynamics of the $\rho = f(E_i)$ change in the analysis [8], [18] gives grounds to consider the obtained values of ρ to be overestimated at 4-5 MeV, first of all, because of the lack of reliable data for the level population with the excitation energy higher than ~ 5 and underestimated values of the density of discrete levels lower than ~ 3 MeV. Due to a strong anticorrelation of the values of level density and strength functions, most likely, the values k(E1) + k(M1) are underestimated in the region of $\sim 4-6$ MeV of the primary transitions. The same is true for smaller energies of the secondary transitions exciting levels in the same energy region. A considerable excess of the $\sum (P_{\gamma\gamma} - i_1)$ calculated sum observed in Fig. 5 as compared to the experimental values of the same parameter of the cascade gamma decay at the $\sum (P_{\gamma\gamma} - i_1)$ good reproduction may be explained by hypotheses on:

- · a strong selectivity of the process of cascade gamma decay,
- a considerable systematic underestimate of the summarized intensity of gammatransitions in Table 2 [4] depopulating levels or
- a very strong underestimate of strength functions for the secondary and subsequent cascade gamma-transitions and, as a result, by overestimate of values of the obtained level density.

Approximation of the intensity distribution of the primary gamma-transitions for levels in the given region of their energies or sums of the cascade intensities through one and the same level [26] with the subsequent extrapolation to the zero value of intensities gives an independent estimation of the level density.

It cannot give precise estimates of the level number excited by the primary transitions lower than the threshold of their registration in [4] for the following reasons:

- nobody has verified the Porter-Thomas distribution hypothesis for width deviation from the mean value in the region of the smallest widths necessary for such analysis;
- the retio of the level number of various parity at the given excitation energy is unknown and, most likely, will not be obtained as a parameter of the analysis [26];
- considerable deviations of strength functions from the uniform dependence observed
 for the majority of studied nuclei [9] restrict the width of energy region of levels
 optimal for such analysis, for which the width distribution is approximated.

Nevertheless, such analysis of the experimental data [4] (Fig. 3) shows that the nude matter on a considerable missing of levels does not comply with the available experimental data.

5 Conclusion

Model description of intranuclear processes cannot have the accuracy exceeding that of the experiment at the moment of its development. This may be accepted as an undoubted fact. This and the results of the performed analysis imply that the "statistical" approach to the calculation of the process of cascade gamma-decay gives currently unacceptable error for the ¹²⁴Te compound nucleus.

Model of the level density [12] reproduces its energy variation with higher accuracy than any models, which do not take into account the presence and interaction of usual and superfluid component of the nuclear matter, at least lower than B_n .

Data on the dependence of correlation function of two nucleons in a heated nucleus and the coefficients of vibration increase ρ necessary for this model, as shown in [10], may only be obtained from the analysis of additional information. It seems that the only chance to obtain this result at present is to develop fundamentally new models of radiative strength functions. They must in an explicit form take into account two-component nature of the nuclear matter and their parameters may be fitted from the data for k(E1) + k(M1) obtained from the technique [9].

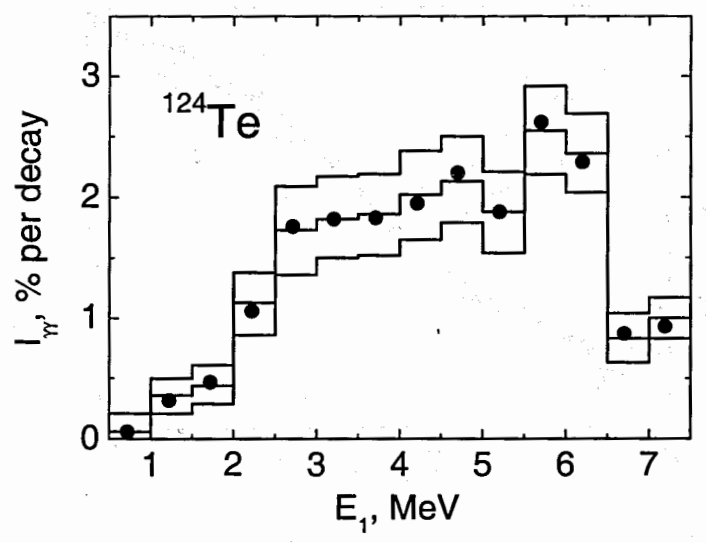


Fig. 1. Histogram – the summarized experimental intensity of two-step cascades in the intervals of 0.5 MeV in the function of the primary gamma transition energy E_1 with statistical errors only [16]. The intensity is renormalized using the data [4]. Points – a typical approximation [9] for the ρ and k data, which are given in Fig. 2 and 3.

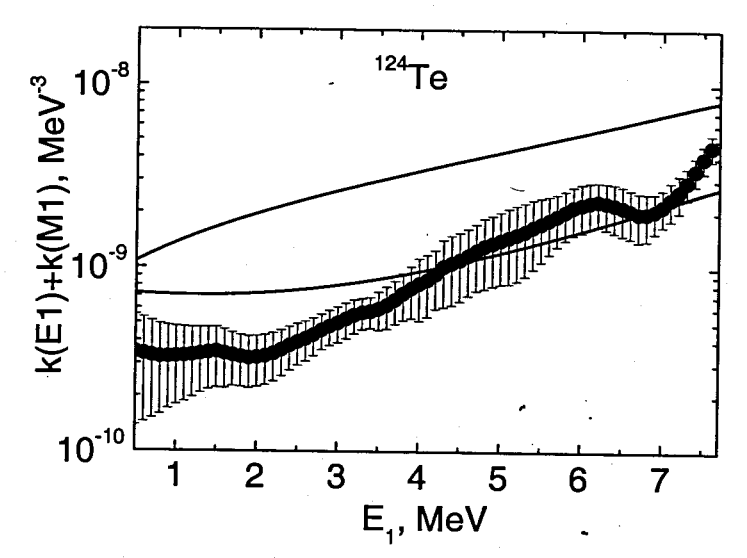


Fig. 2. Solid lines -k(E1)+k(M1) from models [23, 24] (for k(M1)=const). Points with errors – an interval of values of k reproducing $I_{\gamma\gamma}$ (Fig. 1) with practically the same values $\chi^2/f << 1$.

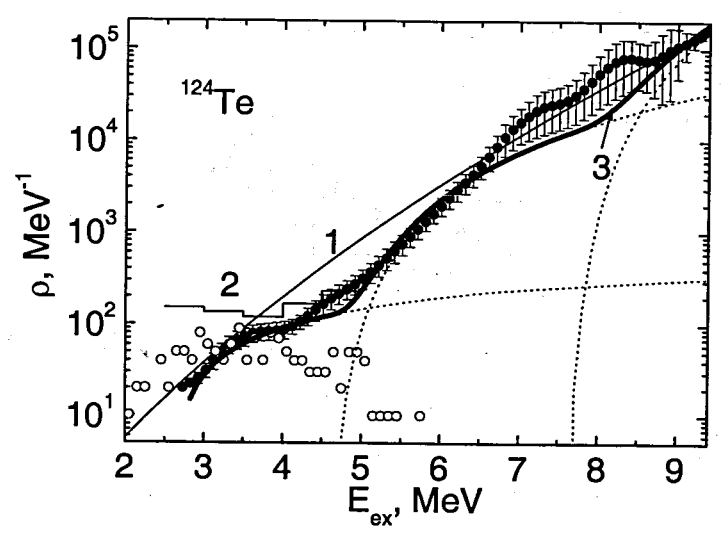


Fig. 3. The same as in Fig. 2 for the level density. Points with errors – the density of intermediate cascade levels [9]. Line 1 – model values [22], line 2 - extrapolation according to the technique [26], line 3 – approximation according to [10]. Dotted lines – the level density with two-, four- and six-quasi-particle structure. Open points – the level density with spins J=0-2 from the decay scheme [4].

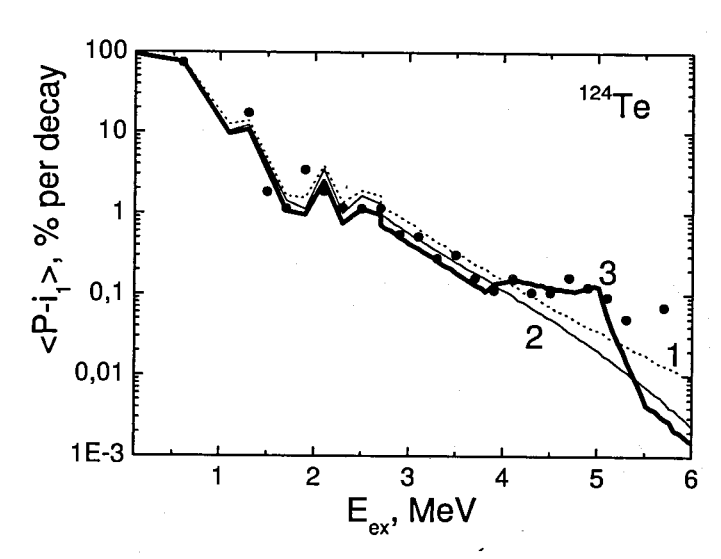


Fig. 4. Points – mean value of the cascade population of ¹²⁴Te individual levels from the scheme [4]. Line 1 – calculation according to the models [23, 22]. Line 3 – calculation of the population with the level density and strength functions from Fig. 2 and 3 taking into account differences of the energy dependence of strength functions of the primary and secondary cascade transitions. Line 2 – the same but without taking into account this dependence.

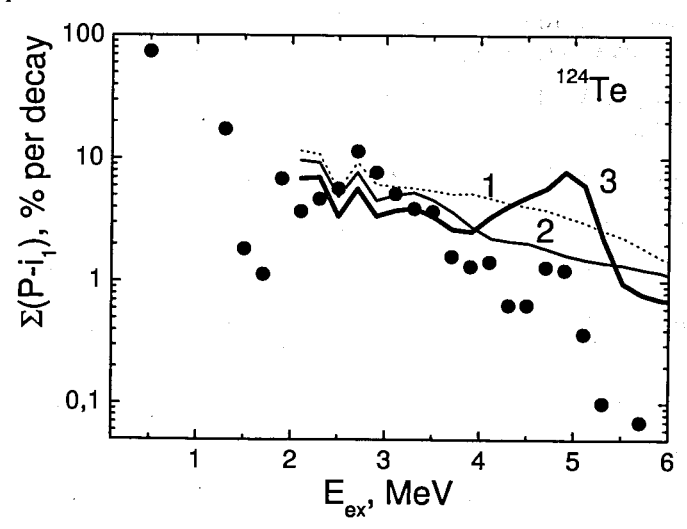


Fig. 5. The same as in Fig. 4 for the cascade population summarized on the excitation energy intervals of 200 keV.

References

- [1] V.G. Soloviev, Theory of atomic Nuclei: Quasiparticles and Phonons, Institute of Physics Publishing, Bristol and Philadelphia, 1992.
- [2] F. Iachello and A. Arima, The Interacting Boson Model, Cambridge University Press, Cambridge, 1987.
- [3] Reference Input Parameter Library RIPL-2. Handbook for calculations of nuclear reaction data. IAEA-TECDOC, 2002, http://www-nds.iaea.or.at/ripl2/ Handbook for Calculation of Nuclear Reactions Data, IAEA, Vienna, TECDOC-1034, 1998.
- [4] T. von Egidy et al., Nucl. Phys. A762 (2005) 167.
- [5] A. Bohr, B.R. Mottelson, Nuclear structure, Vol. 1, W.A. Benjamin, Inc. New York, Amsterdam, (1969).
- [6] A.M. Sukhovoj, V.A. Khitrov, Instrum. Exp. Tech., 27 (1984) 1071.
- [7] S.T. Boneva, E.V. Vasilieva, Yu.P. Popov, A.M. Sukhovoj, V.A. Khitrov, Sov. J. Part. Nucl. 22(2) (1991) 232.
 S.T. Boneva et al., Sov. J. Part. Nucl. 22(6) (1991) 698.
- [8] E.V. Vasilieva, A.M. Sukhovoj, V.A. Khitrov, Phys. At. Nucl. 64(2) (2001) 153, nucl-ex/0110017
- [9] A.M. Sukhovoj, V.A. Khitrov, Phys. Particl. and Nuclei, 36(4) (2005) 359. http://www1.jinr.ru/Pepan/Pepan-index.html (in Russian)
- [10] A.M. Sukhovoj, V.A. Khitrov, JINR preprint E3-2005- 196. http://www1.jinr.ru/Preprints/Preprints-index.html
- [11] A.M. Sukhovoj, V.A. Khitrov, Phys. Particl. and Nuclei, 37(6) (2006) 899.
- [12] V.M. Strutinsky, in Proc. of Int. Conf. Nucl. Phys., Paris (1958) 617.
- [13] S.T. Boneva, V.A. Khitrov, A.M. Sukhovoj, Nucl. Phys. A589 (1995) 293.
- [14] V.A. Khitrov, Li Chol, A.M. Sukhovoj, In: XI International Seminar on Interaction of Neutrons with Nuclei, Dubna, May 2003, E3-2004-9, Dubna, 2004, p. 98.
- [15] V.A. Khitrov, Li Chol, A.M. Sukhovoj, XI International Seminar on Interaction of Neutrons with Nuclei, Dubna, May 2003, E3-2004-9, Dubna, 2004, p. 107. nuclex/0508008
- [16] E.V. Vasilieva et al., Bull. Rus. Acad. Sci. Phys. 58, 1896 (1994).
- [17] http://www-nds.iaea.org/pgaa/egaf.html

- [18] A.M.Sukhovoi, V.A.Khitrov, C.Li, V.A.Plyujko, Bull. Rus. Acad. Sci. Phys. 69, (2005) 727.
- [19] F. Becvar, P.Cejnar, R.E. Crien, J. Kopecky, Phys. Rev. C46 (1992) 1276.
- [20] L.A. Malov, V.G. Solov'ev, Yad. Fiz., 26(4) (1977) 729.
- [21] Yu.P.Popov, A.M.Sukhovoi, V.A.Khitrov, Yu.S.Yazvitsky, Izv.Akad.Nauk SSSR, Ser.Fiz. 48, (1984) 1830.
- [22] W. Dilg, W. Schantl, H. Vonach, M. Uhl, Nucl. Phys. A217 (1973) 269.
- [23] S.G. Kadmenskij, V.P. Markushev, V.I. Furman, Sov. J. Nucl. Phys. 37 (1983) 165.
- [24] P. Axel, Phys. Rev. 126(2), (1962) 671.
- [25] C.F. Porter, R.G. Thomas, Phys. Rev. 104, (1956) 483
- [26] A.M. Sukhovoj, V.A. Khitrov, Physics of Atomic Nuclei 62(1), (1999) 19.

CALCULATION OF THE TOTAL GAMMA-SPECTRA OF THE FAST NEUTRONS CAPTURE IN THE ISOTOPES 117,119Sn FOR THE DIFFERENT PARAMETERS OF CASCADE GAMMA-DECAY

A.M. Sukhovoj, V.A. Khitrov

Frank Laboratory of Neutron Physics, Joint Institute for Nuclear Research, 141980, Dubna, Russia

The gamma-spectra were calculated for the set of different level densities and radiative strength functions. The sufficiently precise reproduction of the experiment is impossible without taking into account the influence of the process of the nucleons Cooper pairs breaking on any nuclei cascade gamma-decay parameters.

1 Introduction

The direct determination of density ρ of excitation levels (number of levels of nucleus in the unit interval of excitation energy) for the larger part of stable and long-life radioactive target nuclei is impossible. This assertion relates also to the radiative strength functions

$$k = \Gamma_{\lambda i} / (E_{\gamma}^3 \times A^{2/3} \times D_{\lambda}) \tag{1}$$

exciting their primary dipole electrical and magnetic gamma-transitions of level of nucleus decaying the excited in the nuclear reaction. Extraction of the parameters of nucleus in question in this situation can be executed by only their fitting to the optimum values, reproducing the experimental spectra and cross section with the minimum standard deviation measured in the nuclear reactions.

This inverse problem of mathematical analysis by its nature is principally ambiguous. Moreover, systems of equations, connecting the number of excited levels and probability of the emission of nuclear products are usually assigned within the framework of some ideas about the mechanism of nuclear reaction and factors determining the dynamics of the studied process.

Thus, for example, the description of the cascade gamma-decay of neutron resonance, is impossible at present without the introduction of some a priori ideas. In particular, within the framework of the ideas about this process following potential possibilities are not taken into consideration:

- the presence of the possible strong dependence of neutron widths Γ_n on the structure of the wave function of resonances (and of the excessive error in determination of their density D_{λ}^{-1} by the neutron time-of-flight method),
- the analogous dependence of the partial radiative widths of primary gamma-transitions $\Gamma_{\lambda i}$ on the structure of the level excited by them, evidently overstepping the limits of the expected Porter-Thomas fluctuations.

Potencial possibility of existence of the enumerated effects and their significant influence on the process of cascade gamma-decay directly follows from the results [1] of model

approximation of the level density, extracted from the reaction $(n, 2\gamma)$ and the comparison [2,3] of the average values of the sums of radiative strength functions with their models [4,5] most often used in practice. Thus, the possible break of sequential Cooper pair [1] with the excitation energy in the region of the neutron-binding energy can change values of few quasi-particle components in the wave function and thus - change [6] values of Γ_n . This possibility directly follows from the results, presented in [1]. Whether this possibility is realizable in principle, to what degree the process of fragmentation of nuclear states mixes up components of different types in the wave functions of the levels in the whole region $E_{ex} \leq B_n$ and at the noticeably higher excitation energies - neither the experiment, nor the theory can answer this at the present.

In particular it is not possible to obtain the realistic estimation of the part of the unobservable levels, which according to the values J^{π} could be excited them as s-resonances. This problem is very essential, since the density of neutron resonances in practice in any experiment to determine this parameter for the excitation lower than B_n is used to standardize its relative values. As a consequence of the above mentioned facts, the measured experimentally in different procedures [2,3,7,8] level densities and the radiative strength functions of primary gamma-transitions can have an unknown systematic error, the value of which directly depends on a systematic error in the conventional values D_{λ} of the spacing between the neutron resonances. And the obtained ideas about these values and properties of nucleus can be erroneous to a greater or lesser extent. However, if we add the fundamental incompatibility of the data about the level density between the results of applying the procedures [7,8] on the one hand, and [2,3] on the other hand, than the need for a maximally possible verification of ρ and k determined from indirect experiments becomes obvious.

Possibilities and the specific character of the verification of the experimentally determined values of ρ and k

The verification of the indicated parameters of nucleus can be partially executed by the calculation of total gamma-spectra for different sets of ρ and k with their subsequent comparison with the experiment. This calculation was carried out by different authors repeatedly [9,10], but, as a rule, without taken into account of:

- the nonconformity of the model assigned ones and real values of ρ or k if to determine
 one of these values purely model presentations about another value are used;
- the specific character of the transfer of errors $\delta \rho$ and δk to an error δS of the calculated spectrum;
- all aspects of the influence of the structure of the excited levels of nucleus on the found parameters ρ and k.

All these problems become apparent to the full during the calculation of the gamma-ray spectra of the radiative capture of thermal neutrons, measured, for example, by Groshev [11], with the use of ρ and k, determined from the gamma-ray intensities in the procedures

[8] or [2,3]. The major part of experimental data on the total gamma-ray spectra of the capture not only of thermal but also fast neutrons was used to verify such data earlier [12].

The measurement [13] of total gamma-spectra in the isotopes 118,120 Sn makes it possible to carry out the same analysis for the spherical nuclei from the region of minimum of neutron strength function for the s-neutrons. And to thus to test obtained and represented into [3] the values ρ and k.

3 The comparison of calculation and experiment

With the comparison it is necessary to consider the specific character of the operation of the transfer of errors $\delta\rho$, $\delta k(E1)$ and $\delta k(M1)$ to an error in the calculated total gamma-spectrum: it is characterized by very low coefficients. (And, obviously, by very large in the opposite case.)

Consequently, calculated spectra, close ones in the quality of reproduction to the data of experiment can be obtained for the substantially being differed values ρ and k. And, all the more, this is correct with the presence experimentally [2] of the established strong dependence of the process of cascade gamma-decay on the nuclear structure, as the minimum, for the excitation energies of $E_{ex} < 0.5 B_n$.

Therefore the comparison of calculation and experiment should be conducted for the maximum collection of the diverse variants of functional dependences ρ and k is without fail on the line scale. It is most expedient also to perform the comparison of total gamma-spectra for the spectrum corresponding to the product of the gamma-quantum intensity on their energy. The condition $\sum I_{\gamma}E_{\gamma}=B_{n}$ ensures the maximally precise normalization intensities of the observed gamma-transitionson in average and the presence of errors of different sign - for different values of gamma-quantum energies.

Reliable experimental data for ρ and k in the nucleus ¹²⁰Sn for the range of the excitation energies of $E_{ex} \approx B_n$ are absent. Therefore is below for calculating the total gamma-spectrum in this nucleus of values ρ and k are converted from the results [3] by the appropriate scaling of these given for the nucleus ¹¹⁸Sn.

The level densities of both parities and spins 0, 1 and 2 for these compound nuclei are given in Fig. 1; the radiative strength functions of primary E1- and M1-transitions with the maximal coefficients [2] of an increase in the radiative strength functions of secondary transitions are given in Fig. 2 respectively. The calculated total gamma-spectra of the capture of fast neutrons in the ^{117,119}Sn are compared with the experiment in Fig. 3 and 4 for few sets of the values of the level density and radiative strength functions. Corresponding calculation data for ^{118,120}Sn are given in Fig. 3,4.

These data are acquired as follows: the level density and radiative strength functions are extrapolated to the excitation energy $E_{ex} = B_n + 100$ keV. And then - they were used for calculating the total gamma-spectra for the spins of the decomposed initial levels of $J^{\pi} = 0^+$, 1^+ and for $J^{\pi} = 0^-$, 1^- , 2^- . The portion of their contribution to the resulting spectrum was determined by the fitting of the function of $S^{exp} = k_j S^{cal}(J^{\pi})$. I.e., with the calculation of total gamma-spectra was considered capture only by s- and p-neutrons, and the portion of the captures of k_j for each of the possible spins of compound- states was the free parameter. Obtained values are given in the table for the minimum χ^2 . Here one

should note, that the minimum χ^2 with the use of standard model [4,5,14] can be achieved only for negative contribution of one of the spin states (in the table it substituted to the zero value). Taking into account great significance χ^2 can be concluded, that procedure [2] determination ρ and k reproduces experimental data on the total gamma-spectra is more accurately, than model presentations of the type [4,5,14]. The existing deviations totally can be connected only with the inevitable errors of experimental data for ρ and k, the obtained from the two-step cascades of capture thermal neutrons into ¹¹⁷Sn. First of all - because of the absence of data according to the radiative strength functions of primary E1-transitions to the levels of these nuclei with the excitation energy less than 2-3 MeV. Or - because of the presence of the strong dependence of the radiative strength functions of primary transitions from the structure of the decayed compound-states not only with the small $(E_{ex} < 0.5B_n)$ excitation energies, but also for $0.5B_n < E_{ex} \le B_n$.

Table. The most probable portion k_J of experimental spectrum, corresponding to the decay of compound-state with the spin of J^{π} with the use of experimental data [2] and model presentations [4] and [14] for the strength functions and the level density.

		¹¹⁸ Sn		¹²⁰ Sn		
ı	J^{π}	[4,14]	[2]	[4,14]	[2]	
	0+	0.16(16)	0.00(30)	0.21(86)	0.18(21)	
	1+	0.18(34)	0.39(33)	0.00(21)	0.29(16)	
	0-	0.21(54)	0.00(30)	0.12(98)	0.28(16)	
	1-	0.21(75)	0.01(30)	0.30(18)	0.07(6)	
	2-	0.16(91)	0.53(83)	0.15(17)	0.04(6)	
	sum	0.92	0.93	0.78	0.86	

The results of the comparison of the spectra, calculated for different functional dependencies of level density and of the strength functions of dipole gamma-transitions with the experiment, quite unambiguously lead to the conclusion, fully coinciding with those obtained earlier:

- "smooth" function $\rho = f(E_{ex})$ reproduces the total gamma-spectrum of the thermal neutron capture noticeably worse, than the stepped functional dependencies obtained in [2,3];
- Is hence automatic (because of the strong correlation ρ and k) follows the impossibility of the precise description of the experimental values of k by model presentations of the type [4,5].

In particular, taking into account the influence of the structure of the excited levels on a change in the form of the energy dependence of radiative strength functions most likely should be carried out up to the neutron binding energy. One must not exclude the possibility that the radiative and neutron strength functions also depend on the structure of neutron resonances at the excitation energies larger, than B_n .

4 Conclusion

The comparison of the total gamma-spectra for different functional dependencies of ρ and k(E1)+k(M1) both on the excitation energy of nucleus and on the energies corresponding to the primary and secondary gamma-transitions for the thermal neutrons capture in 117,119Sn with the experimental data was carried out. The comparison showed that model predictions of the non-interacting Fermi gas level density in these nuclei give worse correspondence, than the level density from the procedures [2,3]. This conclusion corresponded to the one obtained earlier [12].

Large transfer coefficients of the errors δS of total gamma-spectra to the errors $\delta \rho$ and $\delta(k(E1)+k(M1))$ directly follow from the comparison of the data in Figs. 1,2 and 3,4. This circumstance confirms the conclusion [1], that the measurement of such spectra, for example in the procedure [8], requires accuracy on ~ 2 orders larger, than in the procedure [2,3]. And it limits the possibilities of the independent checking of different sets of ρ and k, both of model determined ones and of experimentally obtained ones. The use of total gamma-spectra for their testing necessary requires the comparison of different variants of such data.

And even total reproduction of the experimental total gamma-spectrum by calculation with a certain set of ρ and k is not the proof of the correspondence of these values to the real parameters of nucleus. However, explicit nonconformity is a quite single-valued proof of the presence of larger or smaller systematic deviation for them with the experimental one.

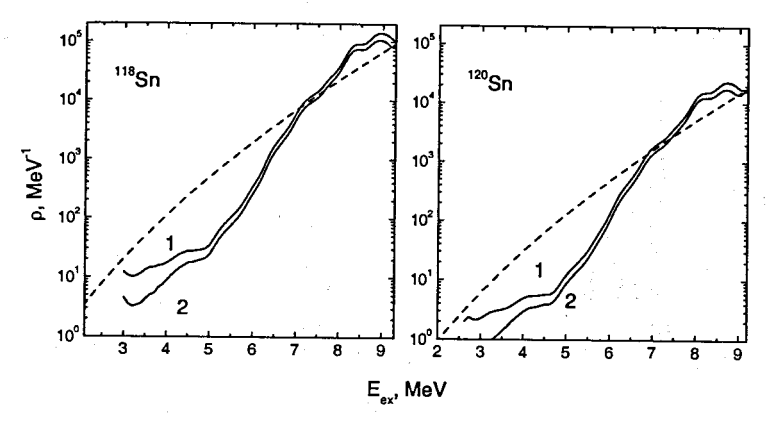


Fig. 1. The level densities of both parities and spins 0, 1 and 2 for compound nuclei 118,120 Sn. Line 1 presented the used in calculations values of the level density with spins $J=(0-2)^+$, line 2 - the same for negative parity only. The dash line represents predictions of the model [14].

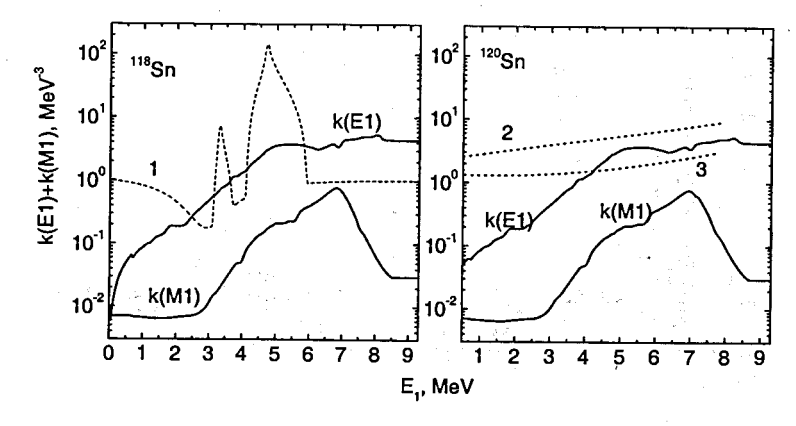


Fig. 2. Solid lines presented the radiative strength functions of primary E1- and M1-transitions (multipleted on 10^9). Line 1- maximum increasing of the radiative strength functions of secondary transitions to the levels with the energy of $E_{ex} = B_n - E_1$. Line 2 and 3 represent predictions of the model [5] and [4] in the sum with k(M1)=const. For both models is used the ratio k(M1)/k(E1) = 0.2 for of $E_1 = 6.5$ MeV.

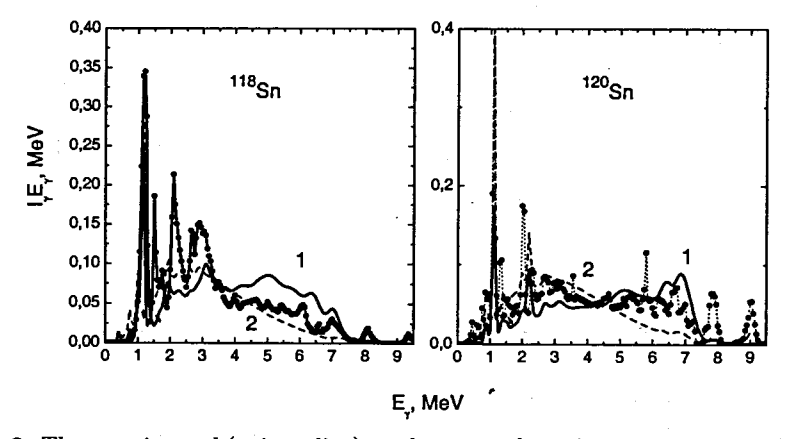


Fig. 3. The experimental (points+line) total spectra of γ -radiation following fast neutron capture for the ^{117,119}Sn targets. Lines 1 represent results of calculation using data of Ref. [2], line 2 - from [4,14], corresponding.

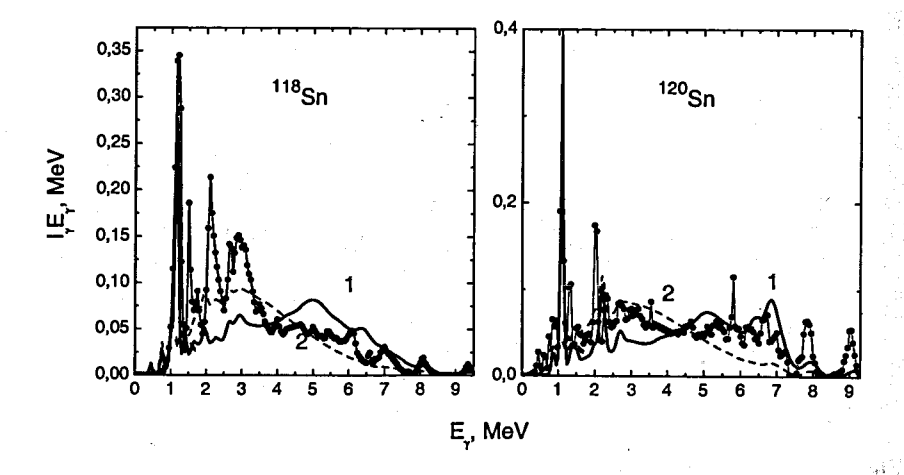


Fig. 4. The same, as on Fig. 3. Lines 1 represent results of calculation using data of Ref. [3], lines 2 - from [5,14], corresponding.

References

- [1] A.M. Sukhovoj, V.A. Khitrov, Physics of Paricl. and Nuclei 37(6) (2006) 899. A.M. Sukhovoj, V.A. Khitrov, JINR preprint E3-2005-196, Dubna, 2005. http://www1.jinr.ru/Preprints/Preprints-index.html
- [2] A.M. Sukhovoj, V.A. Khitrov, Physics of Paricl. and Nuclei, 36(4) (2005) pp. 359-377.
 http://www1.jinr.ru/Pepan/Pepan-index.html (in Russian)
- [3] E.V. Vasilieva, A.M. Sukhovoj, V.A. Khitrov, Phys. At. Nucl. 64(2) (2001) 153, nucl-ex/0110017
- [4] S.G. Kadmenskij, V.P. Markushev, V.I. Furman, Sov. J. Nucl. Phys. 37 (1983) 165.
- [5] P. Axel, Phys. Rev. 1962. 126. No 2. P. 671.
- [6] V.G. Soloviev, Phys. of Elementary Particles and Atomic Nuclei, 3(4) (1972) 770.
- [7] B.V. Zhuravlev, Bull. Rus. Acad. Sci. Phys. 63 (1999) 123.
- [8] G.A. Bartholomew et al., Advances in nuclear physics 7 (1973) 229.
 A. Schiller et al., Nucl. Instrum. Methods Phys. Res. A447 (2000) 498.
- [9] I.A. Lomachenkov, W.I. Furman, JINR, P4-85-466, Dubna, 1985
- [10] O.T. Grudzevich, Phys. At. Nucl. 62 (1999) 192.
- [11] L.V. Groshev et al., Atlac thermal neutron capture gamma-rays spectra, Moscow, 1958.
- [12] A.M. Sukhovoj, V.A. Khitrov and E.P. Grigor'ev, INDC(CCP)-432, Vienna 115 (2002).
 V.A. Khitrov, A.M. Sukhovoj, Pham Dinh Khang, Vuong Huu Tan, Nguyen
 - V.A. Khitrov, A.M. Suknovoj, Pham Dinn Khang, Vuong Huu Tan, Nguyen Xuan Hai, XIII International Seminar on Interaction of Neutrons with Nuclei, Dubna, 22-25 May 2005, E3-2006-7, Dubna, 2006, p. 64, nucl-ex/0508008
- [13] J.Nishyama, M.Igashira, T. Ohsaki, G.N.Kim, W.C.Chung, T.I.Ro, Twelfth International Symposium on Capture Gamma-Ray Spectroscopy and Related Topics, Notre Dame, September 4-9, 2005, World Scientific, Ed. A. Woehr, A. Aprahamian, p. 579.
 - J. Nishyama, T.I. Ro, M. Igashira, W.C. Chung, G. Kim, T. Ohsaki, S. Lee, T. Katabuchi, International Conference on Nuclear Data for Science and Technology 2007, Nice, April 2007, to be published.
- [14] W. Dilg, W. Schantl, H. Vonach, M. Uhl, Nucl. Phys. A217 (1973) 269.

REANALYSIS OF THE PROCESS OF THE CASCADE GAMMA DECAY OF ¹⁹⁸Au COMPOUND STATE

A.M. Sukhovoj, V.A. Khitrov

Joint Institute for Nuclear Research, 141980, Dubna, Russia

B.E. Crawford, S.L. Stephenson

Gettysburg College, 300 N. Washington Street. Gettysburg PA 17325, USA

To further study the "pygmy" resonance phenomena in the photon strength function, we reanalyzed the two-step cascade data for the target nucleus ¹⁹⁷Al using the Dubna group approach. The range of obtained values allows for meaningful conclusions: the level density at low excitation energy shows a step-like behavior; the electric dipole photon strength function has a broad maximum around $E_{\gamma} = 5$ MeV and is not typical of a "pygmy" resonance; the level density below B_n also demonstrates step-like behavior.

1 Introduction

The main task of an experiment in the low energy ($E_{ex} \gtrsim 10$ MeV) physics is to study the influence of structure of excited levels of a nucleus on the parameters measured in the experiment, for example of the process of cascade gamma decay. After that – the extraction of dynamics of intranuclear interactions out of these experimental values and their theoretical interpretation with the development of theoretical models required in practice [1] for the nuclear parameters used in this case. This is necessary, in particular, in order to obtain the maximum realistic evaluation of cross sections of interactions of neutrons with nuclei necessary in practice. This is important especially for actinides where the existing models of level density can not [2] provide for the maximum reliable and accurate evaluation of cross sections with the absolute minimum of accepted hypotheses and assumptions.

In the stated analysis cycle the evident insufficiency of experiments sensitive to the structure of nucleus in the widest region of its excitations still remains the main problem. At present, the co-existence, interaction and defining influence of the nuclear excitations of qualitatively differing types, namely multiquasi-particle and vibration ones, on the structure of nuclei give no rise to doubt. This is the main conclusion of such fundamental models of nucleus as different variants of IBM and QPNM. Unfortunately, the majority of experiments carried out so far give direct and quite reliable information on the structure of nucleus only for too small energies of its excitation. In practice, for example, this region in the even-odd heavy nucleus [3] is still restricted to the interval of excitation energies of the order of 2 MeV. Therefore, there are no direct methods to determine level densities, first of all, at higher excitation energies. The mentioned parameter of a nucleus, like probability of the gamma quantum emission in the whole region lower than the neutron

binding energy or nucleon products of a reaction may only be determined from indirect experiments. Mainly, such analysis uses the spectra of products of a nuclear reaction measured by single detectors. Their amplitude depends both on the number of excited levels and on partial widths of the emission of nuclear reaction products according to the given decay channel of the initial state of an excited nucleus.

The situation is also complicated by the fact that the measured ordinary spectra of one-step reactions are mainly determined by the product of level density of a nucleus on the probability of emission of their products. As a result of strong correlation of these parameters, the transfer of inevitable errors in determination of the spectrum intensity to the unknown values increases abruptly their uncertainties. This circumstance completely excludes a possibility of simultaneous experimental determination, for example of reliable values of level density ρ in a fixed interval of their spins or of radiative strength functions $f = \Gamma_{\lambda i}/(E_{\gamma}^3 \times D_{\lambda})$ of cascade gamma transitions, without attraction of any model notions: first of all, without the hypothesis [4], which is a basic one for the analysis of all the experiments carried out earlier, on the indepedence of cross section of the inverse reaction on the excitation energy of the final nucleus.

Potentially, the task of simultaneous determination of ρ and k could be solved for gamma decay of any excited level λ of an arbitrary nucleus with the mass A with any mean spacing D_{λ} between them at the combining of experimental data of different experiments, for example of the cross sections of radiative neutron capture and spectra of gamma rays occurring simultaneously. However, there are no practical achievements in this direction so far.

A fundamentally new method to solve the problem under consideration was realized for the first time [5] in Dubna. The analysis of intensities of two-step cascades of radiative capture of thermal neutrons in the energy intervals ΔE , fixed according to the method [6], of their intermediate levels $E_i = B_n - E_1$

$$I_{\gamma\gamma}(E_1) = \sum_{\lambda,f} \sum_{i} \frac{\Gamma_{\lambda i}}{\Gamma_{\lambda}} \frac{\Gamma_{if}}{\Gamma_{i}} = \sum_{\lambda,f} \frac{\Gamma_{\lambda i}}{<\Gamma_{\lambda i} > m_{\lambda i}} n_{\lambda i} \frac{\Gamma_{if}}{<\Gamma_{if} > m_{if}}.$$
 (1

made it possible for the first time to determine ρ and k simultaneously and without a model: in the initial variant - on assumption of the independence of partial radiative widths Γ on the excitation energy of the studied nucleus (i.e. using the hypothesis [4]); in the modern one [7] - completely without using it. The indubitable advantage of such experiment is also the circumstence that for any interval of excitation energies ΔE the number $m = \rho \Delta E$ (or n)of levels is fixed by the spin window assigned by an experiment. At the same time systematic errors $\delta \rho$ and δk of the determined parameters are restricted very much by the type of spectra measured in the experiment (in comparison with other methods of similar experiments) and have a quite acceptable value [8] for practically attainable systematic errors δI_{TT} .

Later, similar experiments were carried out in Riga, Řež, Los Alamos, Budapest [9, 10, 11, 12] and started in Dalat. However, the conclusions of different groups on parameters of the cascade gamma-decay process differ fundamentally depending on the method of experimental data processing used by the authors. This difference is of purely technical character and may lead to the appearance of false conclusions about the process

under investigation only if one does not take into account strong correlation in expression (1) of the unknown parameters ρ and k in the analysis. Errors increase particularly in conclusions of the analysis of experiment when anticorrelations of cascade intensities are neglected with the energies of their primary and secondary gamma transitions located in one and the same interval ΔE of each experimental spectrum.

2 Main tasks and problems of model-free determination of ρ and k

Currently, the method [7] is the only source to obtain reliable data on ρ and k for any compound nucleus if only the experimental conditions allow one to limit the energy spread of the excited levels λ to the interval of the order of 1-3 keV and less. However, in contrast to other already existing methods, here a single-valued determination of the unknown parameters is impossible in principle.

For example, for cascade gamma decay at the neutron capture in resonance the information on experimental intensities of two-step cascades, their density and number of known low-lying levels is available. However, it is impossible to obtain unambiguity in determination of ρ and k even using [7] such additional information as the total (or only cascade) population of levels in the low half of neutron binding energy.

A very essential limitation of the region of possible values of level densities and radiative strength functions is provided by non-linearity of equation (1) relative to ρ and k. The non-linearity effect occurs only if its half is extracted [6] out of the experimental spectrum. The half equals to the summarized intensity of two-step cascades, which excite intermediate levels in each given interval of their energy. This very operation during the data processing decreases the interval of values of ρ and k, which accurately reproduce $I_{\gamma\gamma}$ from absolutely non-informative ones [13] to practically accurate values of [8] ρ and k suitable for comparison with the theory. That is why the analysis [7] makes it possible to obtain the maximum realistic notions on the dynamics of the process of cascade gamma decay of any nucleus. However, the existing quite serious discrepancies between the data on ρ and k from the technique [7] and the technique, which is used for a long time, to extract level densities from evaporative spectra point to the necessity of serious comprehensive analysis of both sources of systematic errors in the compared experiments and search of factors, which may influence essentially, in the first place, the determined values of level density.

At present, the problem of studying the influence of structure of wave functions of levels connected by a cascade on its intensity takes on special significance in determination [7] of ρ and k. It is of special importance for heavy odd-odd compound nuclei where, due to the insufficiency of experimental data on gamma ray spectra in the region $E_{\gamma} \sim 0.5 B_n$, we failed to estimate the degree of discrepancy of radiative strength functions of primary and secondary gamma transitions of one and the same energy and multipolarity. It is also true for the nuclei maximally close to the actinide region for preliminary evaluation of the conditions, which may distinctly distort the values of ρ and k obtained with the help of method [7].

The models [1] of radiative strength functions surpass essentially with regard to the extent of working over and account of structure of a nucleus of the level density models. The second ones take into account in an explicit form the existence of two fundamentally different types of nuclear excitations, the first ones still use only excitations of the fermion type [1]. The accumulated data set for each of the nuclei studied in [14] points to the necessity, at least, of phenomenological inclusion of the contribution from excitations (or the corresponding components of wave functions) of vibration type into radiative strength function models.

Taking into account all these factors, the maximum complete data analysis for the compound nucleus ¹⁹⁸Au is of primary interest.

3 Properties of the cascade gamma decay of the ¹⁹⁸Au compound state

Experimental determination of the total gamma ray spectrum of the radiative neutron capture and its interpretation in the framework of the present-day notions made the authors [15] conclude that in this nucleus the gamma decay is "anomalous": at the gamma transition energy of about 5 MeV the so-called "pygmy- resonance" [16] manifests itself in the radiative strength function. This interpretation of the observed increase of the strength function of emission of the corresponding gamma quanta still remains and it became a subject of investigation in [17]. Notions on the "anomality" of gamma decay have been obtained and remain only in the framework of the condition that the level density has been determined by now and is described with the help of a model with a rather high accuracy in the whole region of neutron binding energy by a "smooth" function. From our point of view, no alternative has been considered here.

However, the present-day fully model-free method of simultaneous determination of ρ and k [7] gives another result. Its practical application for more than 20 nuclei from the mass region $(40 \le A \le 200)$ points to the existence in a nucleus of, at the least, two excitation energies, in which abrupt and fundamentally important change of its structure occurs. Approximation [18] of the experimental data for ρ by partial level densities of nquasi-particle excitations shows that this effect with maximum probability may be caused by the breaking of Cooper pairs of nucleons in a heated nucleus with practically any mass. Unfortunately, the lack of data [19, 20] on the spectra of gamma rays of radiative capture of thermal neutrons in ¹⁹⁷Au has prevented from using the method [7] to determine ρ and k in this nucleus. Both level density and radiative strength functions in ¹⁹⁸Au have been determined [14] using only the hypothesis of independence of the radiative strength functions of primary and secondary gamma transitions of one and the same multipolarity and energy on the excitation energy. The use of this assumption must overestimate the ¹⁹⁸Au level density determined experimentally in the region of several MeV around $0.5B_n$ and underestimate the values of k for the appropriate energies of primary gamma transitions. Estimation of the appropriate systematic error may be done on the basis of comparison of the data for ρ from [7, 14] for the nuclei with a different parity of the number of neutrons and protons. Relative smallness of the obtained error indicates that if we take the value into account it will not lead to a fundamental distortion of conclusions of the analysis of the available data.

Nevertheless, it is necessary to perform all possible analysis of the earlier obtained experimental data [14] for this nucleus, in particular, to estimate the degree of possible difference of radiative strength functions for primary and secondary gamma transitions for various final levels of ¹⁹⁸Au, and also to estimate the degree of influence of other parameters of this nucleus on experimental cascade intensities and the form of their dependence on the intermediate level energy.

4 Analysis

It is very characteristic for the nuclei studied in accordance with the methods [7, 14] that the change of sum f(E1) + f(M1) at the change of levels excited by them is of alternating-sign character: a considerable increase of k values in the region of "stepped" structure in the level density of relatively large energies excited by primary transitions of levels is accompanied by some decrease of k for low-lying cascade levels. This effect in an odd-odd nucleus must lead to an overevaluation of calculated cascade intensities at the increase of energy of their final level.

Two-step cascade intensities to the levels of ¹⁹⁸Au with the energy $E_f \leq 450$ keV required for comparison with the experiment [21] have been calculated for the following variants of the level density:

- a) the back-shifted Fermi gas model [22],
- b) combination of the Ignatiuk model [23] higher than 2 MeV with the experimentally determined number of intermediate cascade levels at smaller excitation energies and
- c) the experimental level density from method [14]. In both variants of the method of simultaneous determination of ρ and k the level density of the positive and negative parity is varied independently. However, at the same time the conservation of the average spacing for levels corresponding to s-resonances and the summarized density of "discrete" levels is provided.

Radiative strength functions for E1-transitions are used from results [14] and models [24],[25]. The model presentation for f(M1) for the last two variants is restricted by the case f(M1) = const. The corresponding data is given in Fig. 1.

The summarized level density of both parities for spin window $1 \le J \le 3$ is presented in Fig. 2.

All the variants of the values ρ , f(E1) and f(M1) obtained in accordance with [14] and presented in Fig. 1 and 2 practically precisely reproduce the sum of cascade intensities to levels with the energy less than 514 keV [21] (Fig. 3). The comparison of experimental intensities of two-step cascades to specific low-lying levels of ¹⁹⁸Au for different variants of level densities and radiative strength functions of the gamma transitions is shown in Fig. 4a-c. The signs of random deviations of calculated intensities in different sets of data from [14] anticorrelate with each other for different final cascade levels. The deviations of

average values from the experimental intensities may be partially related to the systematic errors of determination of the sums of cascade intensities for the given final level. Here, there is no reason to exclude a possible dependence of $I_{\gamma\gamma}$ values on J_f^{π} , and the influence of details of the structure of wave functions of E_f levels on the average value of f(E1) and f(M1) for secondary cascade transitions.

5 Discussion of results

In all the nuclei studied by now the final levels, the spin J_f of which differs from the neutron resonance spin J_λ no more than for 2 and has the maximum value at $|J_\lambda - J_f| = 0$, are excited along with the experimentally observed intensity. For the compound state of ¹⁹⁸Au excited at the thermal neutron capture $J_\lambda^\pi = 2^+[26]$, therefore, the excess of cascade intensities calculated according to the data [14] to the final levels $E_f = 347$ and 406 keV with spins $J_f^\pi = 2^-$ [27] over the experimental values may be caused by the presence of unresolved doublets and/or the influence of structure of the enumerated levels on f(E1) and f(M1) of secondary transitions of the cascades. In any case this circumstance may not lead to changes of the obtained conclusions on the process of cascade gamma decay due to the relative smallness of excess of the calculated value in comparison with the value $\sum_f I_{\gamma\gamma}$ observed in the experiment.

If we take into account such possible explanation then the calculation using the data [14] gives a regular excess of intensity over the experiment for cascades on the levels with the energy $261 < E_f < 482$ keV. Due to the lack of other explanations it is possible to accept as the most probable hypothesis that the relation of radiative strength functions of secondary gamma transitions of cascades to the corresponding values for primary ones has the same [7] form as in even-even nuclei and in even-odd ones. In other words, the general dynamics of the process of cascade gamma decay of the neutron resonance is characterized by the regularities, which do not depend on the parity of nucleon number in the odd-odd compound nucleus, as well.

The presence of a local increase of radiative strength function in the region of the "stepped structure" in ρ ($\approx 1.5 < E_{ex} \lesssim 3$ or for primary gamma transitions ($\approx 4 < E_{\gamma} \lesssim 5-5.5$ MeV) reflects, most likely [7], a considerable increase of the influence of vibration components of levels on its value in the region lower than the threshold of appearance of four-quasi-particle excitations. Radiative strength functions of primary gamma transitions decreased at the breaking of subsequent Cooper pairs of nucleons to the levels with four-, six-, etc. quasi-particle components.

In other words, new models of radiative strength functions must in an explicit form take into account the co-existence and interaction of excitations of quasi-particle and phonon types in the whole region under consideration of excitation energy of a nucleus. In the level density models this fact is explicitly taken into account, for example [1], by introducing the vibration enhancement factor of level density of quasi-particle type. Therefore, most likely, no new types of excitation of nucleus (of the "pygmy-resonance" type) should be proposed and included in the k models.

Almost the same value of the calculated cascade intensity in the energy region $E_{ex} \approx$

 $0.5B_n$ of their intermediate levels for all the tested variants of radiative strength functions and level density demonstrates that the conclusions made in [11],[12],[17] by now on the parameters of the process of cascade gamma decay must be in serious error, since they do not take into account a strong correlation of values ρ and k, which are included in I_{∞} .

In the framework of the existing notions it is impossible to reach the conformity of the existing and possible models of ρ and k with the experiment by any parameter variation, if only they do not take into account quite realistically the influence of breaking of the nucleon Cooper pairs on these parameters of the process of cascade gamma decay of the high-excited level.

6 Conclusion

Currently, there are no obstacles in obtaining the experimental data necessary for a rather detailed theoretical description of the properties of nucleus lower than $\approx B_n$. By analogy with the experience of study of two-step cascades at the thermal neutron capture one may assume that reliable data on ρ and k in other experiments may be obtained only at the study of two-step nuclear reactions in coincidences by high-resolution spectrometers.

Erroneous conclusions during the analysis of an experiment of such type may occur only if out-dated model notions on the level density or the probability of emission of nuclear reaction products are used.

The potential models of the level density of a nucleus and radiative strength functions of gamma transitions exciting them must in an explicit form take into account the coexistence and interaction of excitations of quasi-particle and phonon type at least lower than the neutron binding energy. Practical necessity in their development became apparent [2] at the evaluation of contemporary data on cross sections of the interaction of neutrons with fissionable nuclei.

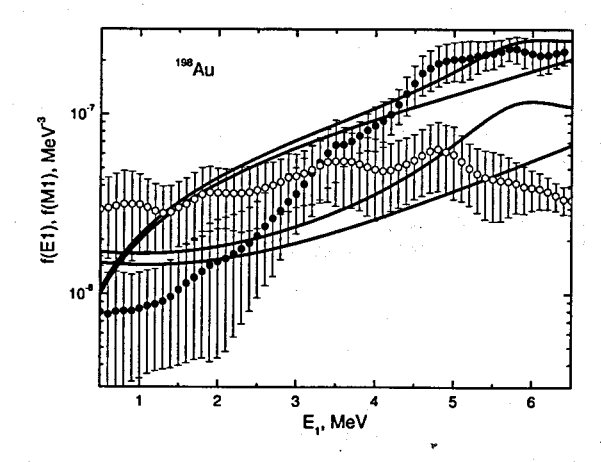


Fig. 1. Solid thick lines - f(E1) from models [24, 25] and their sums with "pygmyresonance" for its parameters from [17]. Open point with errors – region for set of random functions of f(E1), solid points – f(M1), reproducing $I_{\gamma\gamma}$ (Fig. 3) with practically the same values $\chi^2/f << 1$.

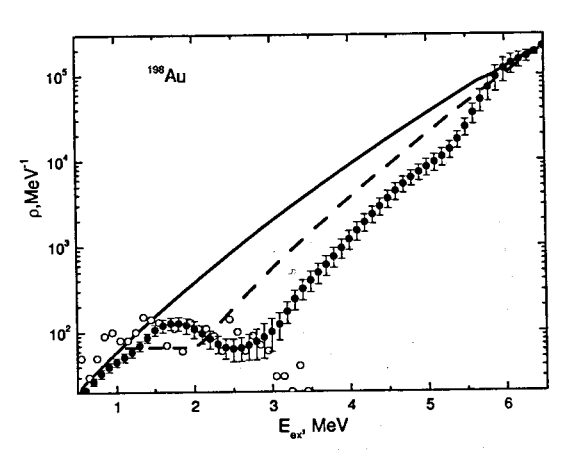


Fig. 2. The same as in Fig. 1 for the level density (solid points with errors). Solid line – model values [22], dotted line – [23] respectively. Open points – the density of intermediate cascade levels [14].

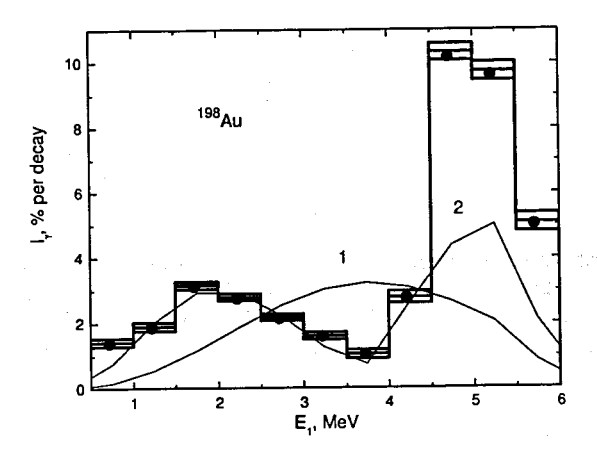


Fig. 3. Hystogram – summarized experimental intensity of two-step cascades in the intervals of 0.5 MeV in the function of energy of the primary gamma transition with statistical errors only [21]. Points – the typical approximation for the data from [14], the examples of which are given in Fig. 1 and 2.

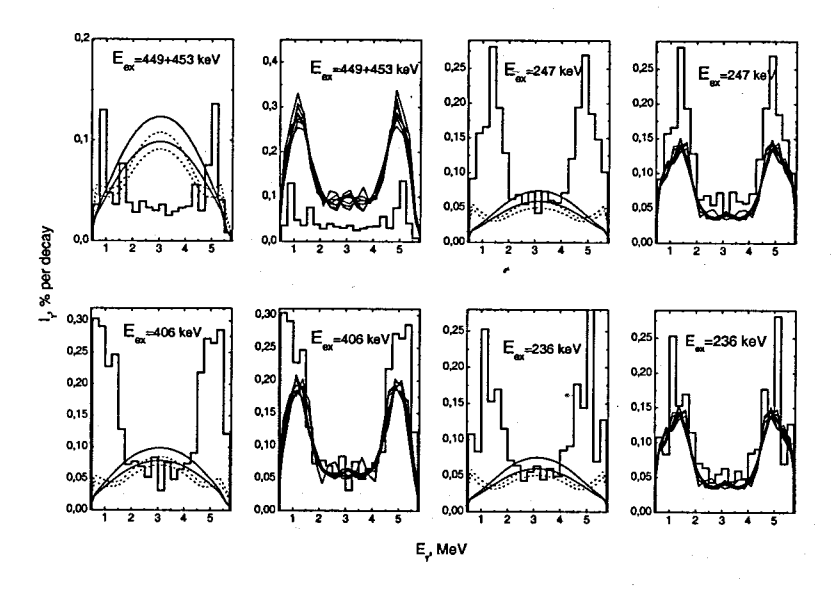


Fig. 4a. Hystogram – experimental intensity of two-step cascades for the levels E_{ex} (summed over the intervals of 250 keV), lines – different variants of the calculation. The first and third columns: combinations of models [22, 24, 25] – thin lines, [23, 24, 25] – dotted line. The second and fourth columns - the intensity is calculated for random sets of ρ and k from [14].

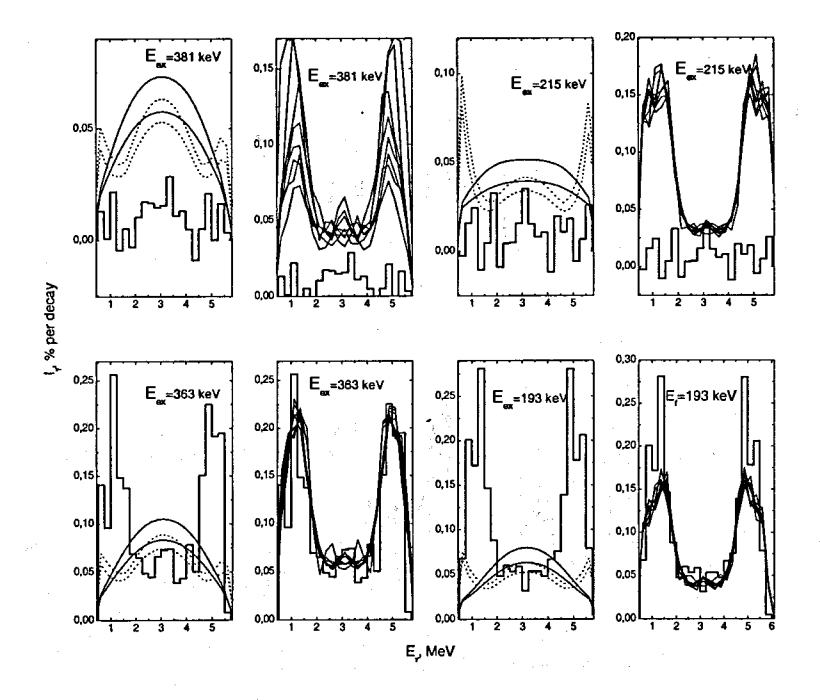


Fig. 4b. The same as in Fig.4a for other final levels.

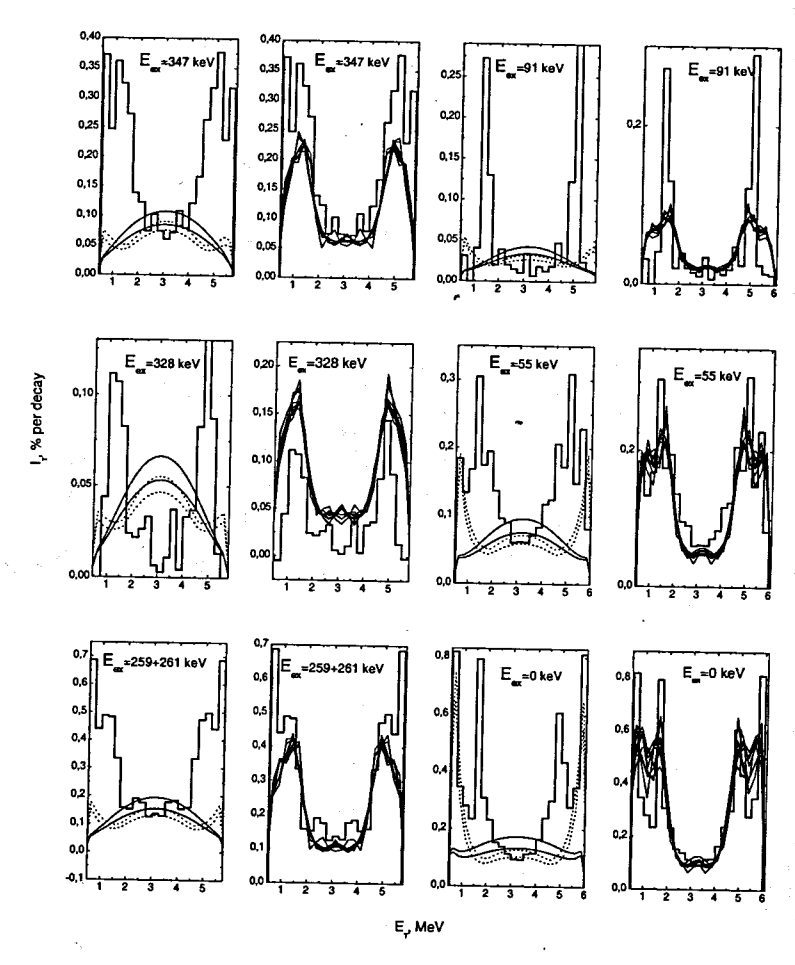


Fig. 4c. The same as in Fig.4a for other final levels.

References

- [1] Reference Input Parameter Library RIPL-2. Handbook for calculations of nuclear reaction data. IAEA-TECDOC, 2002, http://www-nds.iaea.or.at/ripl2/ Handbook for Calculation of Nuclear Reactions Data, IAEA, Vienna, TECDOC-1034, 1998.
- V.M. Maslov, Nucl. Phys. A. 743 (2004) 236.
 V.M. Maslov, Yu.V. Porodzinskij, M. Baba, A. Hasegawa, Nucl. Sci. Eng. 143 (2003)
 1.
- [3] V. Bondarenko et all, Nucl. Phys. A762 (2005) p. 167.
- [4] A. Bohr, B.R. Mottelson, Nuclear structure, Vol. 1, W.A. Benjamin, Inc. New York, Amsterdam, (1969).
- [5] A.M. Sukhovoj, V.A. Khitrov, Instrum. Exp. Tech., 27 (1984) 1071.
 S.T. Boneva et al., Sov. J. Part. Nucl. 22(2) (1991) 232.
- [6] S.T. Boneva, V.A. Khitrov, A.M. Sukhovoj, Nucl. Phys. A589 (1995) 293.
- [7] A.M. Sukhovoj, V.A. Khitrov, Phys. Particl. and Nuclei, 36(4) (2005) 359. http://www1.jinr.ru/Pepan/Pepan-index.html (in Russian)
- [8] Khitrov V.A., Li Chol, Sukhovoj A.M., In: XI International Seminar on Interaction of Neutrons with Nuclei, Dubna, May 2003, E3-2004-9, Dubna, 2004, p. 98.
- [9] Bondarenko V.A. et al., In: Capture gamma-ray spectroscopy, Pacific Grove, CA 1990 /Ed. Hoff R.W., American Institute of Physics, NY, 1990, p.491.
- [10] Gueorguiev G. P., Honzatko J., Khitrov V. A., Panteleev C., Sukhovoj A. M., Nucl. Phys., A740(1-2) (2004) 20.
- [11] A.V. Voinov et al., Phys. Atomic Nuclei 67, (2004)1866
- [12] A. Voinov et al., Phys.Rev.Lett. 93, (2004)142504
- [13] V.A. Khitrov, Li Chol, A.M. Sukhovoj, XI International Seminar on Interaction of Neutrons with Nuclei, Dubna, May 2003, E3-2004-9, Dubna, 2004, p. 92. nuclex/0508008
- [14] E.V. Vasilieva, A.M. Sukhovoj, V.A. Khitrov, Phys. At. Nucl. 64(2) (2001) 153, nucl-ex/0110017
- [15] G.A. Bartholomew, B.B. Kinsey, Canad. J. Phys. 79, (1953) 1025.
- [16]-M.-Igashira et al., Nucl.-Phys.-A457, (1986)-301.
- [17] M. Krtička et al., in: Pros. of XII inter. Symp. of Capture gamma-ray spectroscopy and related topics, ed. by A.Woehr, A.Abrahamian, AIP, 2006, p. 563.
- [18] A.M. Sukhovoj, V.A. Khitrov, JINR preprint E3-2005-196 http://www1.jinr.ru/Preprints/Preprints-index.html

- [19] M.A. Lone, R.A. Leavitt and D.A. Harrison, Nucl. Data Tables, 26(6) (1981) 511.
- [20] http://www-nds.iaea.org/pgaa/egaf.html
- [21] S.T.Boneva et al., Bull.Rus.Acad.Sci.Phys. 59, (1995) 728.
- [22] W. Dilg, W. Schantl, H. Vonach, M. Uhl, Nucl. Phys. A217 (1973) 269.
- [23] A.V. Ignatyuk, In: Proc. of IAEA Consultants Meeting on the use of Nuclear Theory and Neutron Nuclear Data Evaluation (Trieste, 1975) IAEA-190, Vol. 1 (1976) P.211.
- [24] S.G. Kadmenskij, V.P. Markushev, V.I. Furman, Sov. J. Nucl. Phys. 37 (1983) 165.
- [25] P. Axel, Phys. Rev. 1962. 126(2), (1962) 671.
- [26] S.F. Mughabghab, Neutron Cross Sections BNL-325. V. 1. Parts B, edited by Mughabhab S. F., Divideenam M., Holden N.E., N.Y. Academic Press, (1984)
- [27] http://www.nndc.bnl.gov/nndc/ensdf.

DIFFERENTIAL AND ANGLE-INTEGRATED CROSS SECTION MEASUREMENT FOR THE ⁶⁴Zn(n, α) ⁶¹Ni REACTION AT 2.54, 4.00 AND 5.50 MeV *

Yu. M. Gledenov, M. V. Sedysheva

Frank Laboratory of Neutron Physics, JINR, Dubna, 141980, Russia

G. Khuukhenkhuu

Nuclear research Centre, National University of Mongolia, Ulaanbaatar, Mongolia

P. J. Szalanski

University of Lodz, Institute of Physics, Poland

Jiaguo Zhang, Rongtai Cao, Li-an Guo, Jinxiang Chen, Jianyong Wang, Guohui Zhang
Key Laboratory of Heavy Ion Physics, Ministry of Education and School of Physics, Peking
University, Beijing 100871, China

Abstract

The activation method is not feasible for the 64 Zn(n, α) 61 Ni reaction cross section measurement because the residual nucleus 61 Ni is stable. By using a twin-gridded ionization chamber, differential and angle-integrated cross section data of the 64 Zn(n, α) 61 Ni reaction were measured at neutron energies of 2.54, 4.00 and 5.50 MeV. The experiment was performed at the 4.5 MV Van de Graaff accelerator of the Institute of Heavy Ion Physics, Peking University, China. Quasi-monoenergetic neutrons of 2.54 MeV were produced through the T(p,n) 3 He reaction with a solid Ti-T target, and those of 4.00 and 5.50 MeV were produced through the D(d, n) 3 He reaction with a deuterium gas target. A BF $_3$ long counter was used as the neutron flux monitor and the absolute neutron flux was determined by the 238 U(n,f) reaction. Results of present work are compared with other measurements and evaluations.

Introduction

There are large discrepancies among the few existing evaluations and measurements for the 64 Zn(n, α) 61 Ni reaction cross sections [1-5]. The activation method is not feasible for this cross section measurement because the residual nucleus 61 Ni is stable. In our previous work differential and angle-integrated cross sections of the 64 Zn(n, α) 61 Ni reaction were measured at 5.03 and 5.95 MeV by using a twin-gridded ionization chamber [1]. In the present study we extended our measurements to 2.54, 4.00 and 5.50 MeV to get the near threshold and systematic behavior of this reaction.

Project supported by National Key Project for Cooperation Researches on Key Issues Concerning Environment and Resources in China and Russia (Grant No. 2005CB724804), and by National Natural Science Foundation of China (Grant No.10575006).

Experiment

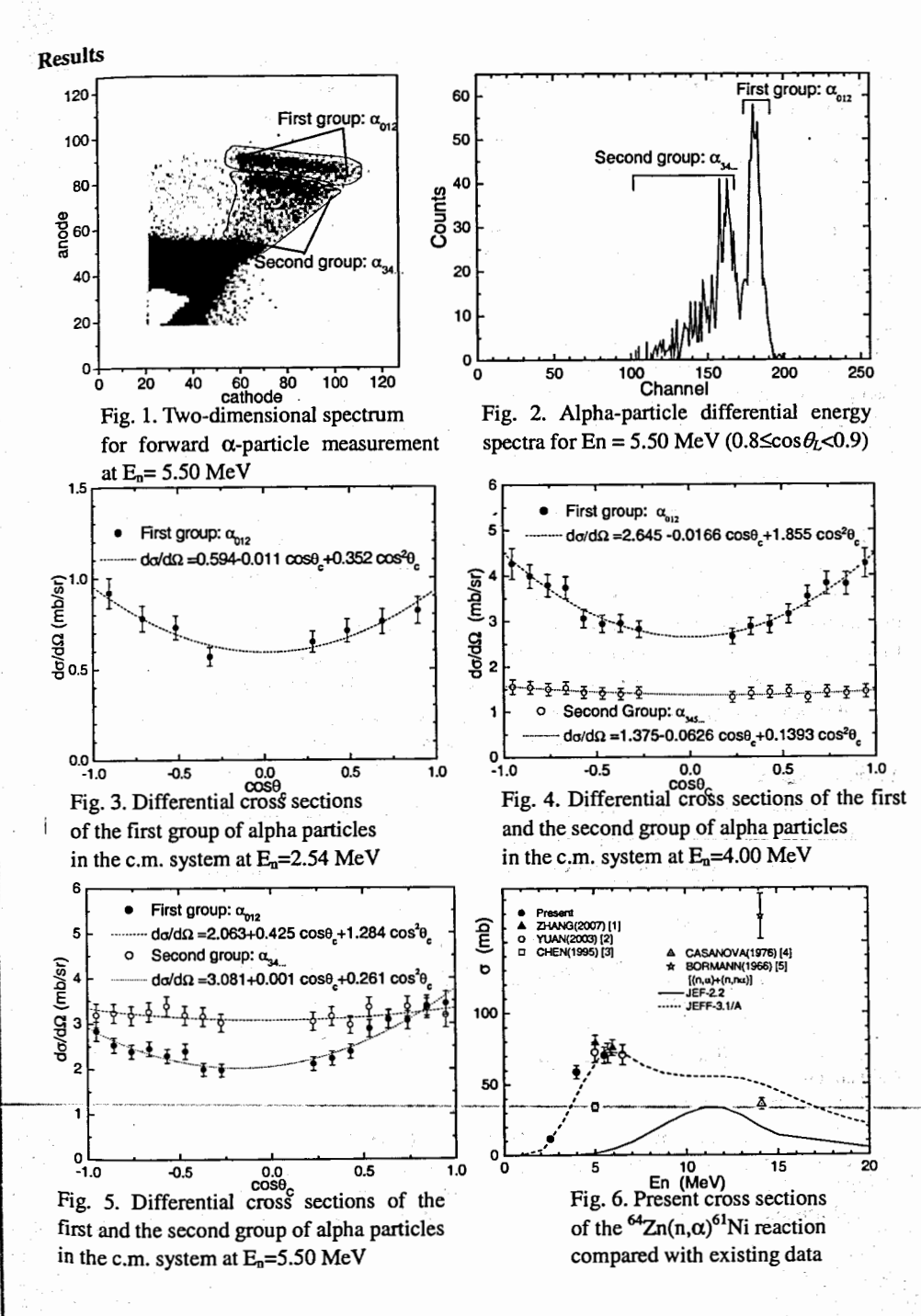
The experiment was performed at the 4.5 MV Van de Graaff accelerator of Peking University, China. A solid Ti-T target and a deuterium gas target were used as neutron source. The thickness of the Ti-T target was $0.80~\text{mg/cm}^2$. Quasi-monoenergetic neutrons were produced through the $T(p,n)^3$ He reaction with the solid target. The energy of the accelerated protons before enter the solid target was 3.35~MeV, and the corresponding neutron energy with energy spread was $2.54\pm0.03~\text{MeV}$. The deuterium gas target was used to produce neutrons through the $D(d,n)^3$ He reaction. The length of the gas cell was 2.0~cm, and the deuterium gas pressure was 2.65-2.80~atm. The cell was separated from the vacuum tube by a molybdenum film (thickness $5~\text{\mu m}$). The energies of the accelerated deuterons before entering the film were 1.77~and~2.84~MeV, and the corresponding neutron energies were $4.00\pm0.21~\text{and}~5.50\pm0.13~\text{MeV}$, respectively.

The setup of the experiment and the twin gridded ionization chamber were the same as in Ref. [1]. The working gas of the ionization chamber was Kr+2.68%CO₂. The pressures of the working gas were 0.90, 1.25 and 1.55 atm for 2.54, 4.00 and 5.50 MeV measurements. The distances from cathode to grid, grid to anode, and anode to shield were 4.4, 2.2, and 1.1 cm, respectively. The grid of the chamber was grounded. The high voltages for the cathode and the anode were -1300, +1000 for 2.54 MeV measurement, and for 4.00 and 5.50 MeV measurement, they were -1500, +1200 V and -1700, +1350 V, respectively.

Two ⁶⁴Zn samples (mass 4.05±0.05 mg and thickness 266.3 μg/cm² each) were attached to the common cathode back-to-back. They were used for simultaneous forward (0 to 90°) and backward (90 to 180°) measurement. The abundance of the ⁶⁴Zn isotope material was 99.4%. Each sample was evaporated on a tantalum backing 4.8 cm in diameter and 50 μm in thickness.

The 64 Zn samples were placed at the first position of the sample changer. Two tantalum films set back-to-back at the second position of the sample changer for background measurement. The absolute neutron flux was determined by a 238 U foil (\oslash 4.50 cm, mass 7.85 \pm 0.10 mg and abundance 99.999%). The 238 U(n_f) cross section was taken from the ENDF/B-VI.8 library. Two compound α sources were used for the adjustment of electronics and energy calibration of the data acquisition system. The 238 U sample and the α sources were placed at the third and the fourth position of the sample changer, respectively. It is suitable to change sample positions using the sample changer without opening the chamber.

A BF₃ long counter was used as neutron flux monitor. The axis of the BF₃ long counter and the center of the gridded ionization chamber were placed at 0° to the beam line. The electrodes of the chamber were perpendicular to the beam line. The distance from the front side of the BF₃ long counter to the neutron target was ~2.9 m. For E_n=2.54 MeV measurement, the distance from the solid Ti-T target to the common cathode of the twin chamber was 23.9 cm. The proton beam current was about 9.0 μ A. Since the ⁶⁴Zn(n, α) Ni reaction cross section is small, the total beam time for E_n=2.54 MeV was about 56.5 h (foreground measurement ~26 h, background ~16 h, neutron flux calibration ~14.5 h). For E_n=4.00 and 5.50 MeV measurements, the distance from the center of the gas cell to the cathode was 18.4 cm. The deuteron beam current was about 4.0 μ A. The total beam time for 4.00 MeV was about 24.5 h (foreground ~13.5 h, background ~4.0 h, flux calibration ~7.0 h) and for 5.50 MeV about 14.5 h (foreground ~6.5 h, background ~3.5 h, flux calibration ~4.5 h).



The cathode-anode two-dimensional spectrum for forward α -particles and differential energy spectrum (0.8 \leq cos θ_L <0.9) at E_n=5.50 MeV are shown in Fig. 1. and Fig. 2.

Two major groups of α -particles can be found from the figures. The first group (with higher energies) corresponds to three energy levels of ⁶¹Ni (ground state, the first and the second excited states of 67 and 283 keV). The second group corresponds to higher excited states of ⁶¹Ni (656 keV, 909 keV, ...).

The measured differential cross sections for the 64 Zn(n, α_{012}) 61 Ni and 64 Zn(n, $\alpha_{34...}$) 61 Ni reaction (correspond to the first and the second group of α -particles) in the center of mass system are plotted in Figs. 3+5. Although the beam time for E_n=2.54 MeV was as long as 56.5 h, there were still too less $\alpha_{34...}$ particles to get the differential cross sections of the 64 Zn(n, $\alpha_{34...}$) 61 Ni reaction at this energy point.

Errors in Figs. 3+5 include the statistics of counts (3.3-5%), the uncertainty of background subtraction (4-6%), and the error of determination of 0° and 90° line (3-5%). There are also scale errors from the uncertainty of the atom number of the 64 Zn sample (1.23%) and 238 U sample (1.27%), the uncertainty of 238 U fission cross section data (2.9%, 2.3% and 3.1% for E_n =2.54, 4.00 and 5.50 MeV), and the uncertainty of fission counts (2.7-3.4%).

One can see that the ratio of the counts of α_{012} to $\alpha_{34...}$ decreases as E_n increases. At E_n =2.54 MeV, almost all the events belong to the first group. At 4.00 MeV there are a few α -events in the second group, but still much less than the first group. However, at 5.50 MeV, the α -events in the second group outnumbers α -events in the first group. The angular distribution for the α -particles in the second group is almost isotropic on the contrary for the first group it is anisotropic. The angular distributions of the α -particles are 90° symmetric at E_n =2.54 and 4.00 MeV, however they are slightly forward peaked at 5.50 MeV.

Angle-integrated cross sections for each group of oparticles are listed in Table 1.

Fig.6 demonstrates the comparison of the present cross sections with existing data.

Acknowledgement

The authors acknowledge thanks to the crew of 4.5 MV Van de Graaff accelerator of Peking University for their kind cooperation.

Table 1. Angle-Integrated Cross Sections for the 64 Zn (n, α) ⁶¹Ni Reaction

E (M-X)	σ (mb)								
E _n (MeV)	First group:	Second group:	Total:						
	64 Zn(<i>n</i> , α_{012}) 61 Ni	64 Zn(n, α_{34}) 61 Ni	64 Zn(n , α) 61 Ni						
2.54 ± 0.03	9.0 ± 0.9	2.6 ± 2.0	11.6 ± 1.1						
4.00 ± 0.21	40.9 ± 3.3	17.8 ± 1.4	58.7 ± 4.7						
5.50 ± 0.13	30.9 ± 2.5	39.6 ± 3.1	70.5 ± 5.6						

References

- 1. G. Zhang, R. Cao, J. Chen, et al., Nucl. Sci. Eng., 156 (2007)115.
- 2. J. Yuan, Z. Chen, G. Tang, et al., Nucl. Sci. Eng., 144 (2003)108.
- 3. Y. Chen, Z. Chen, H. Qi, et al., Chin. J. Nucl. Phys., 17 (1995)167.
- 4. J. L. Casanova and M. L. Sanchez, Anales de Fisica y Quimica 72 (1976)186.
- 5. M. Bormann, U.Seebeck, W. Voights, G. Woelfer, Zeit. fuer Natur., Sect. A, 21 (1966) 988.

Investigations of the Resonance Structure of Neutron Cross-Sections of Mo, Ho, Ta, W at the 50 m flight path of the MMF (INR, Troitsk)

Yu.V.Grigoriev, O.N.Pavlova, B.V.Zhuravlev
Institute of Physics and Power Engineering, Obninsk, Russia
A.A.Alekseev, A.I. Berlev, E.A.Koptelov
Institute for Nuclear Research RAN, Troitsk, Russia
Zh.V.Mezentseva
Joint Institute for Nuclear Research, Dubna, Russia

Abstract The setup REPS was created at the 50 m flight path of the pulsed neutron source RADEKS of the Moscow Meson Factory (MMF INR RAS). It consists of the 8-sectional liquid scintillation detector and the neutron (n, γ)-detector with a total volume of 40 l. The liquid scintillation detector was placed at the 49.3 m flight path and the ³He neutron counter was installed at the 51.5 m from the active zone of the reactor. Time-of-flight spectra were measured for thin metal sample-radiators of Mo, Ho, Ta and W (with diameter of 80 mm) by means of the setup REPS. The setup REPS was shielded by a thick layer of boron and lead in order to reduce background from neutrons and γ-rays scattered in the experimental room. Such a shielding allowed to decrease background by a factor of 4 for tof-spectra obtained at 50 m flight path in comparison with spectra at 30 m flight path. A quite low background and a high energy resolution of spectrometer permitted to resolve some new resonances for W with the energies of 17 eV and 23 eV. Besides, total transmissions, group total and capture cross-sections for Mo, Ho, Ta, W were extracted from measured time-of-flight spectra in the energy region from 1 eV to 10 keV. The similar values were obtained by the GRUCON code on the basis of the estimated data libraries.

Introduction

It is known, that uncertainties in the calculation of the characteristics of power nuclear reactors such as: critical sizes, power density field, reactor life time etc., are caused mainly (about 50 %) by uncertainties in the knowledge of neutron constants of reactor materials. Established admissible errors of neutron constants for all basic reactor materials and fission products are about 1 %. [3]

Required errors for construction materials and fission products must be in the range of 5–10 % for σ_1 , σ_2 , σ_3 , σ_4 and 2–15 % for self-shielding factor with σ_6 =100.

Required accuracy of neutron constants for the majority of reactor materials is not achieved up to now and consequently it is necessary to continue experimental research in this direction.

Measurement procedure

In order to improve the accuracy of neutron cross-sections and their integrated characteristics measurements of time-of-flight spectra were carried out at 50 m flight path of the pulse neutron source RADEX [1] (E_p =209 MeV, I_p = 4 mA, f =50 Hz, τ = 1mkc) by means of the 8-section liquid (n, γ)-detector (L=49.3 m) and the neutron detector with one high-performance ³He counter (L=51.5 m). The pulse neutron source RADEX includes tungsten target with 7cm thickness and water moderator with 7cm thickness. The thin metal disks of Mo, Ho, Ta and W with a diameter of 80 mm were used as radiator-samples.

The analogous measurements were recently performed at 120 m flight path of the pulse neutron source IBR-30 (W = 10 kW, f = 100 Hz, τ = 4 ms) at JINR (Dubna) using the 16-section

liquid (n, γ)-detector PARUS [2] (L=121.65 m) and neutron detector with a small efficiency ε (4.2eV) \cong 0.5%. The neutron detector looked as a battery of 3 10 B counters (L=124 m).

These measurements were applied to compare characteristics of the neutron sources RADEX of the MMF and IBR-30 of JINR. Figure 1 shows a general view of the REPS setup.

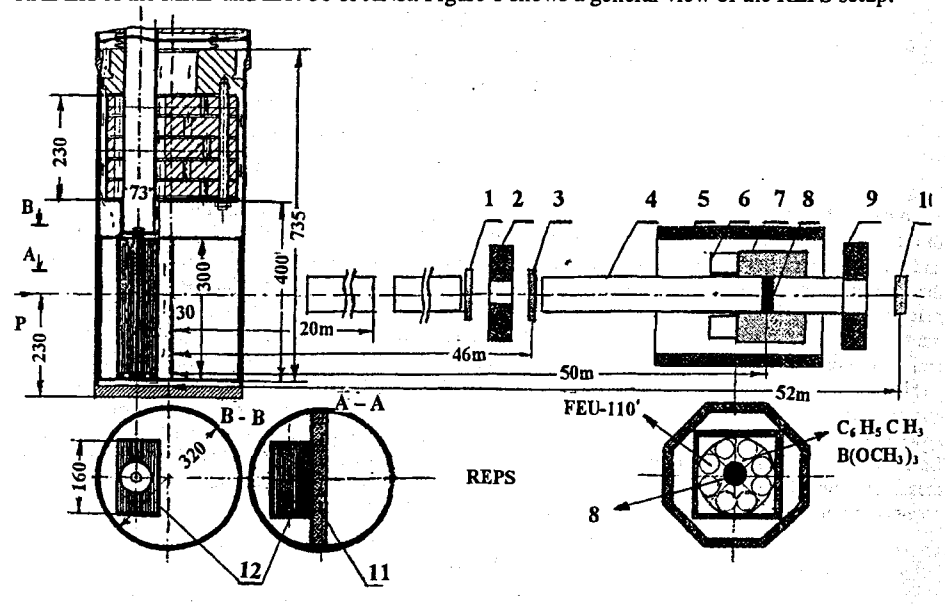


Fig. 1. A general scheme of the REPS setup: 1 – monitor counter, 2, 9 – collimators, 3 – sample-filter, 4 – neutron guide, 5 – boron and lead shielding, 6- FEU – 110 photomultiplier, 7 –multisection liquid scintillation (n,γ) - detector, 8 – radiator-sample, 10 – neutron ³ He detector, 11 – water moderator, 12 – W target.

The REPS setup consists of vacuum neutron guide, neutron collimators, filter-samples and radiator-samples, 8-section liquid (n,γ)-detector with ^{10}B and Pb shielding, neutron detector, spectrometric electronic equipment and measurement module with a PC to accumulate information. Resonance filters from Al, Mn and Cd were positioned in the neutron beam during measurements and served to define the background in the measured spectra and to reduce recycled neutrons with the energy <0.2 eV.

A solution of scintillating additions with a weight of 50 g, 94 % trimethylborate (5.5. l) enriched by ^{10}B and 19.5 l of toluol was used as a scintillating liquid. The detector consists of the cylindrical aluminum tank with a length of 40 cm, a diameter of 40 cm and throughout hole with a diameter of 110 mm. Tank with a volume of 40 l is divided into 8 independent sections, isolated from each other by 2 mm aluminum light-reflecting walls. Each section was viewed by the photomultiplier FEU -110 with a direct contact of the photocathode to a liquid. The efficiency of γ -quanta (662 keV from Cs) registration equals to 30 %, the geometrical efficiency - 96 %, power sanction - about 30 %.

The electronic equipment for the information storage was designed in the CAMAC standard.

The analog signals from each section of the detector were entering into an independent spectrometer channel. The pulses with a width of 30 ns after photomultiplier were magnified by fast current amplifier with a multiplication factor of k=70. The signal amplitudes in each section were calibrated by means of high intensive γ -lines from ⁶⁰Co and ¹³⁷Cs. After linear amplifiers the analog fast signals were coming in parallel on integral discriminators and on linear adder with nine entries. The integral fast discriminator, intercepted signals below 600 keV from background γ -quanta at the capture of neutrons by ¹⁰B nucleus, was connected to the output of the adder. The discrimination level in each channel was corresponded to the energy of γ -quanta equal to 100 keV.

The information selection on the multiplicity spectra from 8 spectrometric channels was made using the multiplicity coder. The formed pulses with a width of 100 ns from integrated gating signal of discriminators were entering into the multiplicity coder (MC). The MC formed a five-digit code, which was coming in the block of digital windows to generate time-of-flight spectra for 8 multiplicities. This information was accumulated in the intermediate memory and saved to disk.

Technique of processing and results of measurements

The analysis of the tof spectra for different multiplicities consisted in the following operations:

- 1. subtraction of background components;
- integral compression of multiplicity spectra in the energy groups in conformity with the constants system BNAB;
- definition of transmission functions and neutron cross-sections with correction for resonance shielding effect by the formulas:

$$T_{t}^{cal}(n,\theta,E) = \frac{\int \Phi(E) * \varepsilon(E) * e^{-\sigma_{t}(E,\theta)^{*n}} * dE}{\int \Phi(E) * \varepsilon(E) * dE}$$
(1)
$$T_{t}^{exp}(n,\theta,E) = \frac{(N_{sample} - F_{sample}) * M}{N_{open/beam} - F_{open/beam}}$$
(2)
$$< \sigma_{t}^{obs} >= -\ln(T_{t}^{exp})$$
(3)

where: n-the thickness of the sample-filter; θ -the temperature of the sample; $\Phi(E)$ -the neutron flux; σ_t -the total cross-section; N_{sample} and $N_{open/beam}$ -the number of counts in the energy groups with and without the sample in the beam; F_{sample} and $F_{open/beam}$ -the background components in the energy groups with and without the sample in the beam; M-the monitor coefficient.

To extrapolate observed cross-sections to the value with a thickness of 0 at/b the self-shielding correction factors in the total cross-sections K_{sh} , calculated for the filter-sample with a thickness of n at/b on the basis of the evaluated data libraries, should be used. The final total cross-sections were determined in the following way:

$$\sigma_{t}^{\exp}(0) = K_{sh} * \sigma_{t}^{obs}(n), K_{sh} = \frac{\sigma_{t}^{cal}(0)}{\sigma_{t}^{cal}(n)} (4)$$

where: $\sigma_i^{\text{exp}}(0)$ and $\sigma_i^{cal}(0)$ -the experimental and calculated group total cross-sections for zero thickness of the filter-sample; $\sigma_i^{obs}(n)$ and $\sigma_i^{cal}(n)$ -the experimental and calculated group total cross-sections for the filter-sample with a thickness n (at/b).

In addition to total cross-sections group radiative capture cross-sections were determined by normalization to the well known standard cross-sections of ²³⁸U under the assumption of the constant registration efficiencies of γ -quanta $\epsilon^U(E) = \epsilon^{Sam}(E)$ from "standard" sample and sample under investigation:

$$<\sigma_{c}>^{i}=<\sigma_{c}>^{u}\frac{M^{u}*S^{u}*n^{u}*N_{c}^{i}*\phi*\varepsilon^{u}}{M^{s}*S^{s}*n^{s}*N_{c}^{u}*\phi*\varepsilon^{z}}=<\sigma_{c}>^{u}\frac{M^{u}*S^{u}*n^{u}*N_{c}^{s}}{M^{s}*S^{s}*n^{s}*N_{c}^{u}}$$
(5)

where: symbol "s" corresponds to a sample under investigation; M^U and M^S – monitor coefficients; S^U and S^S – radiation areas of radiator-samples; n^U and n^S -thicknesses of radiator-samples; n^S and n^S -thicknesses of radiator-samples; n^S and n^S -thicknesses of radiator-samples; n^S and n^S -thicknesses of radiator-samples; n^S -thicknes

Experimental results for Mo, Ho, Ta, W and ²³⁸U and calculated cross-sections using the GRUCON code [4] on the basis of the evaluated data library ENDF/B-6.7 (B-6) [5] are presented in the Table 1 for the energy range from 4.65 eV to 2.15 keV.

Table 1. Experimental data and calculated cross-sections for Mo, Ho, Ta, W and ²³⁸U (barn).

E _g (keV)	Mo ^{exp}	Mo ^{exp}	Ho ^{exp}	Taexp	Taexp	Ta(B-6)	Wexp	U8 (B-6)
	<σ _t >	<σ _c >	<σ _c >	<σ _t >	<σ _c >	<σ _c >	<σ _t >	<σ _t >
2.15-1.0	10.3±0.4	0.9±0.1	3.7±0.3	34.4±3.0	5.3±0.7	7.4	23.1±1.4	1.89
1.0-0.465	11.2±0.5	1.2±0.2	6.7±0.7	40.2±4.0	12.2±1.0	13.0	22.2±1.5	3.31
0.465 - 0.215	10.9±1.3	1.4±0.2	8.2±1.1	48.4±4.0	19.3±2.0	22.8	27.3±1.8	4.56
0.215-0.100	16.2±1.2	4.2±0.4	25.6±3.0	69.6±5.0	49.4±5.0	32.3	32.0±2.0	19.6
100-46.5 eV	18.2±1.3	3.2±1.0	30.3±4.0	63.3±5.0	37.0±4.0	31.0	18.2±1.5	16.4
46.5-21.5 eV	19.8±1.4	27.5±6.0	38.5±5.0	-	166±20	119	48.8±2.5	55.3
21.5-10 eV	18.5 ±1.3	•	124±15	-	134±15	115	80.4±3.5	87.1
10-4.65 eV	16.6±1.2	-	78.6±8.0	•	38.0±4.0	13.7	17.8±1.5	169

Since the IBR-30 reactor was stopped the scintillation (n,γ) -detector and the neutron detector with one ³He counter were transported from JINR (Dubna) to the 50 m flight path of the pulse neutron source RADEX of the Moscow Meson Factory (MMF INR, Troitsk). The purpose was to carry out measurements of time-of-flight spectra at the neutron source of the MMF and to compare some operating characteristics of the spectrometers: the IBR-30 reactor and the RADEKS source of the MMF. The conditions of experiment in Troitsk were chosen similar to the IBR-30: the energy discrimination, parameters of the spectrometer equipment and samples under study to define more precisely neutron fluxes and background components. In order to remove background from recycled thermal neutrons a cadmium sheet with a thickness of 1 mm was placed at the distance of 20 m from the moderator of the neutron source RADEX. To form a neutron beam a collimator with a diameter of 60 mm was installed at the distance of 40 m from the moderator, and a lead collimator with a diameter of 60 mm was positioned before the liquid (n,γ) -detector.

Measurements of the time-of-flight spectra for radiator-samples of Mo, Ho, Ta, W and ²³⁸U were carried out as short series of measuring sessions to sum 8 multiplicities by means of the

 (n,γ) -detector and ³He counter. Figures 2 shows a comparison of measured spectra at the distance of 124 m from the active zone of the reactor IBR-30 and ones on the 51 m flight path of the RADEX source. In Figure 3 time-of-flight spectra for W measured by means of the (n,γ) -detector and the neutron detector at the 51 m flight path of the RADEX source are presented.

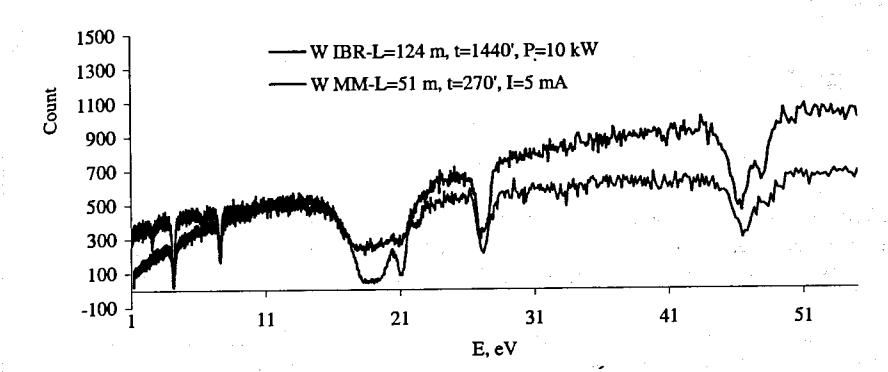


Fig.2. Time-of-flight spectra after transmission of neutrons through W sample-radiator (0.4 mm) measured using the 10 B detector located at the 124 m flight path of the IBR-30 (P=10 kW, f=100 Hz, Δt =4mks, dt_{ch} =2mks) and the 3 He counter installed at the 51 m flight path of the RADEX source of the MMF (I=5 mA, f=50Hz, Δt =1 mks, dt_{ch} =1mks).

These spectra were used to define characteristics of the neutron spectrometer positioned at the 50 m flight path of the MMF. Flux density Φ^{MMF} (n/cm² s eV) for resolved resonances of W was determined from measured time-of-flight spectra (see Figure 2) with known flux density $\Phi^{IBR} = 400/E^{0.9}$ (n/cm² s eV) of the IBR-30 by the formula:

$$\Phi^{MMF} = \frac{S^{MMF} \Phi^{IBR}}{S^{IBR} T_t} \frac{A^{MMF}}{A^{IBR}} (6)$$

where: S^{MMF} , S^{IBR} -areas of radiator-samples used at the RADEX of the MMF and at the IBR-30 (SMMF/SIBR=1.3); T_t - total transmission of Al (70 mm), NaF (10 mm), B₄C (4 mm) resonance filters at the IBR-30; A^{MMF} / A^{IBR} -ratio of integral counts of pulses for a resonance with the energy E_0 (eV) in the energy interval of ΔE_0 (eV).

Also an estimation of the flux density in the location of the neutron ³He detector at the flight path of the MMF was done for these spectra in the energy region of resolved resonances (see Figures 2 and 3) with known neutron registration efficiencies.

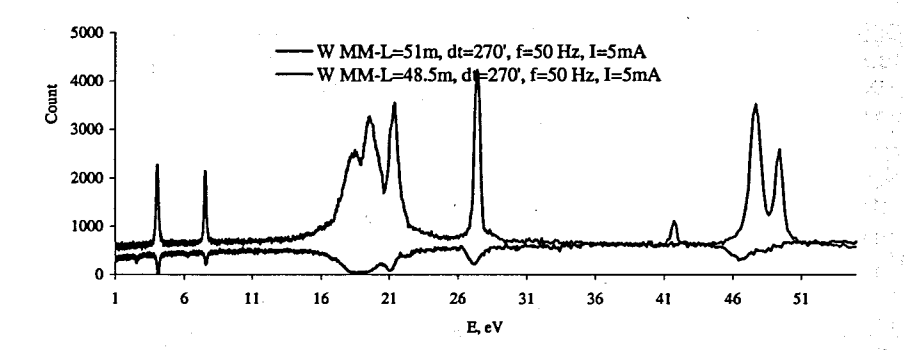


Fig.3. Time-of-flight spectra after transmission of neutrons through W (0.4 mm) radiator-sample measured by the 8 sectional (n,γ) -detector of the REPS setup at the 48,5 m flight path and by the ³He counter at the 51 m flight path (I=5 mA, f=50Hz, Δ t=1 mks, dt_{ch} =1mks)

As one can see from Figure 2 the neutron flux density at the 51 m flight path of the MMF at the energy of 7 eV should be much less, than at the 124 m flight path of the IBR -30 at the above mentioned operating parameters of these spectrometers. In this respect the ratio of the signal to the background of the MMF is several times smaller, than at the IBR-30. For (n,γ) -detector of the MMF setup the time resolution is several times better in comparison with one of the IBR-30. It allows to observe new resonances of W in the low energy range (see Figure 3).

Conclusions.

The new setup REPS is better for some kind of measurements due to its time resolution and the ration of the signal to the background. It was allowed to observe new resonances for W in the low energy region.

In order to continue investigations in this direction we are planning to increase the average current of the proton beam of the MMF and to use more efficient detectors.

References

- Benetskiy B.A., Beketov F.Z., Grachev M.I. et al. Preprint INR RAN INR- 1058/2001, 2001
- Yu.V.Grigoriev, V.Ya. Kitaev, V.V.Sinitsa, H.Faikov-Stanczyk, Hyon Sung Ho. Measurements of the gamma-ray multiplicity spectra of ²³⁵U and ²³⁹Pu with the 16-section liquid scintillation detector, ISINN-6, Dubna, May 13-16, 1998, p.250-259
- Blokhin A.I., Ignatyuk A.V., Kuzminov B.D. et al. // Inter. Conf. on Nuclear Data for Science and Technology (Julich, 1991). – Julich: - FRG, 1991. - P.800
- Sinitsa V.V., Program for calculating the group constants using the library of evaluated neutron data, VANT, ser. Nuclear Constants. 1984, v.5 (59), c.34
- Rose P.F., Dunford C.K., ed. ENDF-102, Data Formats and Procedures for the Evaluated Nuclear Data File, ENDF, report BNL, Upton, New York, 11973, USA, 1988.

STATISTICAL MODEL ANALYSIS FOR (n,α) REACTION CROSS SECTIONS

G.Khuukhenkhuu¹, Yu.M.Gledenov², M.V.Sedysheva², M.Odsuren¹ and J.Badamsambuu³

Nuclear Research Center, National University of Mongolia, Ulaanbaatar, Mongolia.
 Frank Laboratory of Neutron Physics, JINR, Dubna, Russia.
 Flerov Laboratory of Nuclear Reactions, JINR, Dubna, Russia.

Abstract: In the framework of the compound mechanism using the evaporation model and constant nuclear temperature approximation were deduced formulae for fast neutron induced α -particle emission reaction cross section. The semi-classical approach to an inverse reaction cross section and Weizsacker formula for nuclear binding energy were used.

For systematic analysis of known experimental (n,α) cross sections in the energy range of 6 to 16 MeV the statistical model formulae were used. In addition, the theoretical and experimental (n,α) cross sections were compared.

1. Introduction

Investigation of charged particle emission reactions induced by fast neutrons is important for both nuclear reactor technology and the understanding of nuclear reaction mechanisms. In particular, the systematic study of (n,α) reaction cross sections is necessary to estimate radiation damage due to helium production, nuclear heating and transmutations in the structural materials of fission and fusion reactors. In addition, it is often necessary in practice to evaluate the neutron cross sections of the nuclides, for which no experimental data are available. Because of this, in last years we carried out the systematic analysis of known (n,α) and (n,p) cross sections and observed so-called isotopic effect in the wide energy interval of neutrons for the broad mass range of target nuclei [1-3]. In the framework of the statistical model some formulae of the fast neutron induced charged particle emission reaction cross sections were obtained [4]. Also, for systematic analysis of fast neutron induced (n,p) reaction cross sections simple and convenient formulae were deduced [5].

In this paper, using the statistical model certain formulae for the fast neutron induced (n,α) cross section were deduced. For systematic analysis of the fast neutron induced (n,α) reaction cross sections the theoretical formulae were used. The parameters C and K in the statistical model formula for (n,α) cross section were analyzed in the wide energy range of neutrons.

2. Statistical Model Formulae for (n, a) Reaction Cross Section

For fast neutrons using the evaporation and constant nuclear temperature models, semi-classical approach for an inverse reaction cross section and $\Gamma \approx \Gamma_n$ approximation we can obtain the following general formula for the (n,x) reaction cross section [4]:

$$\sigma(n,x) = \sigma_c(n) \frac{2S_x + 1}{2S_n + 1} \frac{M_x}{M_n} e^{\frac{Q_{nx} - V_x}{\Theta}} \left\{ \frac{1 - \frac{W_{nx}}{\Theta} e^{\frac{W_{nx}}{\Theta}} - e^{\frac{W_{nx}}{\Theta}}}{1 - \frac{E_n}{\Theta} e^{\frac{E_n}{\Theta}} - e^{\frac{E_n}{\Theta}}} \right\}$$
(1)

Here: S_x , M_x , V_x , S_n and M_n are the spin, mass, and Coulomb potential for the x-particle and neutron, respectively; Q_{nx} is the reaction energy; $\Theta = kT$ is the thermodynamic temperature; $W_{nx} = E_n + Q_{nx} - V_x$; E_n is the neutron energy. $\sigma_c(n) = \pi (R + \lambda)^2$ is the compound nucleus formation cross section; R is the target nucleus radius and λ is the wavelength of the incident neutrons divided by 2π .

For (n, α) reaction we can get $S_{\alpha}=0$, $S_{n}=1/2$ and $M_{\alpha}\approx 4M_{n}$. So, from (1) we get following formula for (n, α) cross section:

$$\sigma(n,\alpha) = 2\pi (R + \lambda)^2 e^{\frac{Q_{n\alpha} - V_{\alpha}}{\Theta}} \left\{ \frac{1 - \frac{W_{n\alpha}}{\Theta} e^{\frac{W_{n\alpha}}{\Theta}} - e^{\frac{W_{n\alpha}}{\Theta}}}{1 - \frac{E_n}{\Theta} e^{\frac{-E_n}{\Theta}} - e^{\frac{-E_n}{\Theta}}} \right\}$$
(2)

If we use for fast neutrons assumption $(E_n + Q_{ni} - V_i) >> \Theta$ from (2) can be obtained following formula

$$\sigma_{n\alpha}^{com} = 2\pi (R + \lambda)^2 e^{\frac{Q_{n\alpha} - V_{\alpha}}{\Theta}}.$$
 (3)

The termodynamic temperature can be obtained as following [6]: .

$$\Theta = \sqrt{\frac{13.5(E_n + Q_{n\alpha})}{A - 3}} \tag{4}$$

The Coulomb potential of α-particle can be written [7] in the following form:

$$V_{\alpha} = 2.058 \frac{Z - 2}{(A - 3)^{1/3} + 4^{1/3}}$$
 (MeV). (5)

Here: Z and A are the proton and mass numbers of the target nucleus, respectively.

If we use Weizsacker formula for nuclear binding energy can be written following expressions for parent and daughter nuclei:

$$E_1 = \alpha A - \beta A^{2/3} - \gamma \frac{Z^2}{A^{1/3}} - \xi \frac{(A - 2Z)^2}{A}$$
 (6)

and
$$E_2 = \alpha (A-3) - \beta (A-3)^{2/3} - \gamma \frac{[(A-3)-2(Z-2)]^2}{(A-3)}$$
, (7)

Where α =15.7 MeV, β =17.8 MeV, γ =0.71 MeV and ξ =23.7 MeV.

Here odd-even effect parameter was neglected. The (n, α) reaction energy from (6) and (7) is obtained as following

$$Q_{n\alpha} = -3\alpha + \beta (A^{2/3} - (A-3)^{2/3}) + \gamma \left(\frac{Z^2}{A^{1/3}} - \frac{(Z-2)^2}{(A-3)^{1/3}}\right) + \xi \left(\frac{(A-2Z)^2}{A} - \frac{(A-2Z+1)^2}{(A-3)}\right) + \varepsilon_{\alpha}, (8)$$

where ε_{α} is the binding energy of α -particle.

From (3), (4), (5) and (8) we can write following formula for the (n, α) cross section:

$$\sigma_{n\alpha}^{com} = 2\pi (R + \lambda)^2 \exp\left[\frac{1}{\Theta}\left\{-3\alpha + \beta (A^{2/3} - (A - 3)^{2/3}) + \beta \left(\frac{Z^2}{A^{1/3}} - \frac{(Z - 2)^2}{(A - 3)^{1/3}}\right) + \beta \left(\frac{(A - 2Z)^2}{A} - \frac{(A - 2Z + 1)^2}{(A - 3)}\right) + \varepsilon_{\alpha} - V_{\alpha}\right\} (9)$$

If we use designation

$$C = 2\exp\frac{1}{\Theta} \left\{ -3\alpha + \beta \left(A^{2/3} - (A-3)^{2/3} \right) + \gamma \left(\frac{Z^2}{A^{1/3}} - \frac{(Z-2)^2}{(A-3)^{1/3}} \right) + \varepsilon_{\alpha} - V_{\alpha} \right\}$$
 (10)

and
$$K = \frac{2\xi}{\Theta}$$
 (11)

in the case of $A-3 \approx A$ from eq.(9) can be written the (n,α) cross section as following:

$$\sigma_{n\alpha}^{com} = C\pi (R + \lambda)^2 e^{-K\frac{N-Z+0.5}{A}}.$$
 (12)

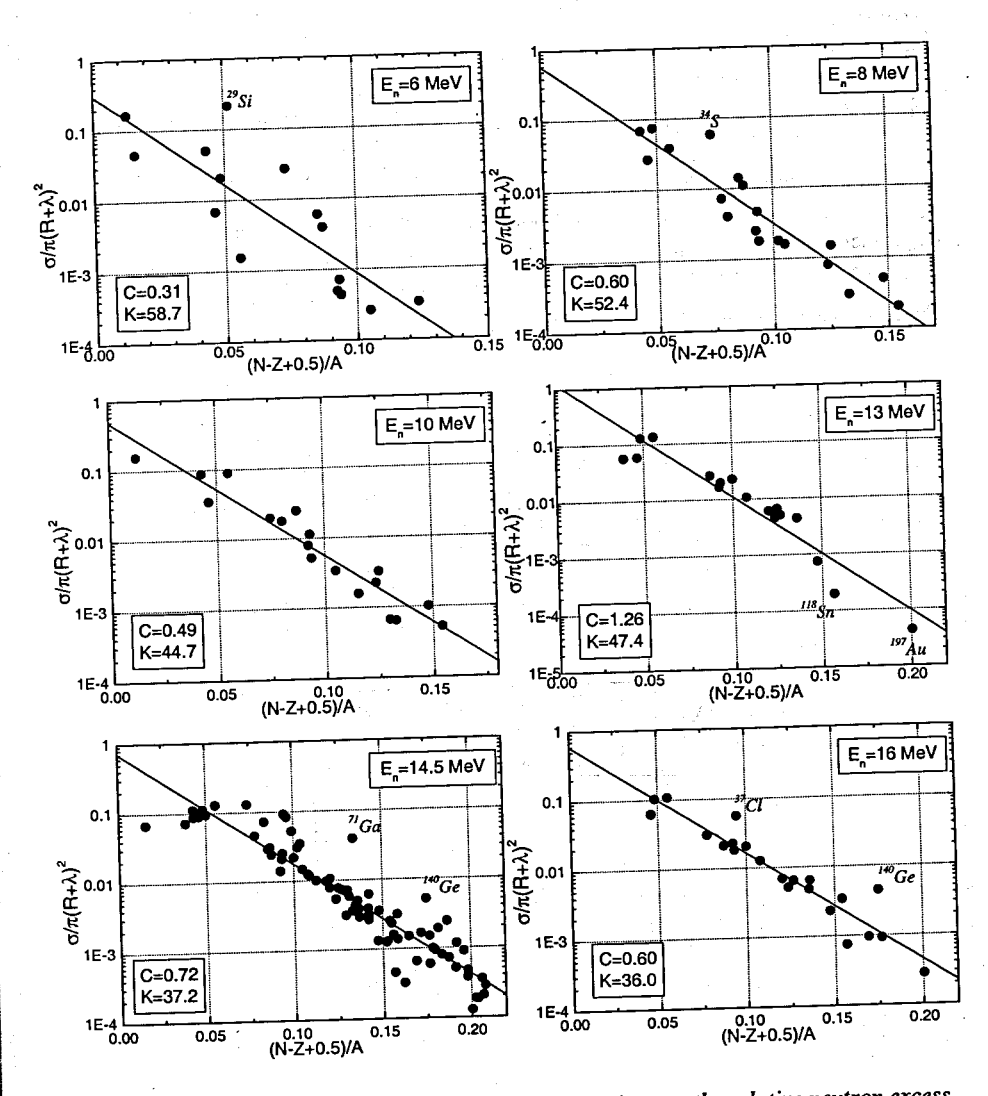


Fig.1. The dependence of reduced (n,α) cross sections on the relative neutron excess parameter (N-Z+0.5)/A for neutron energy of 6, 8, 10, 13, 14.5 and 16 MeV.

3. The Systematic Analysis of (n,α) Cross Sections

The systematic analysis of known (n,α) cross sections for E_n =6, 8, 10, 13, 14.5 and 16 MeV using formula (12) is shown in Fig.1. The values of parameters C and K fitted to experimental data are given in Fig.1, also. It is seen that theoretical line fitted to experimental data is in agreement with known experimental (n,α) cross sections.

The values of the fitted parameters C and K for different neutron energies are given in Table.1. It is seen that the parameter C is almost constant in the energy range of 6 to 16 MeV. At the time the parameter K depends on neutron energy (Fig.2).

The value K=47.4 for $E_n=13$ MeV lies higher than other points. If we except from consideration ¹¹⁸Sn and ¹⁹⁷Au isotopes, for which the experimental (n,α) cross sections are very low, can obtain the values K=38.2 and C=0.59. Then, it is possible to fit by eq.(11) the experimental points for K parameter (solid curve in Fig.2). Also, in Fig.2 are given the values of $Q_{n\alpha}$ and A which are considered and fitted as constants for all isotopes.

Table 1. The parameters C and K for different neutron energies

E _n (MeV)	K	, C
6	58.7	0.31
8	52.4	0.60
10	44.7	0.49
13	47.4 (38.2)	1.26 (0.59)
14.5	37.2	0.72
16	36.0	0.60

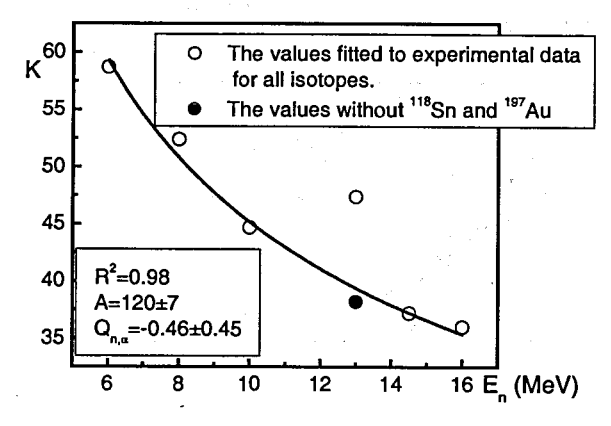


Fig. 2. The energy dependence of parameter K.

4. The Comparison of Theoretical and Experimental (n,α) Cross Sections

The comparisons of the absolute values for theoretical (n, α) cross sections calculated by statistical model with known experimental data at neutron energies $E_n=6$, 8, 10, 13, 14.5 and 16 MeV are shown in Fig.3. It was observed that statistical model formulae give overestimated values for (n, α) cross sections at all energy points of neutrons. Moreover, the theoretical (n, α) cross sections above the average experimental data 4.5 times. These results, perhaps, are caused by the α -clusterization effect (α -particle formation probability) on the surface of nuclei [8]. In future, we should chek this fact and consider the pre-equilibrium and direct mechanisms contributions to the total (n, α) cross sections.

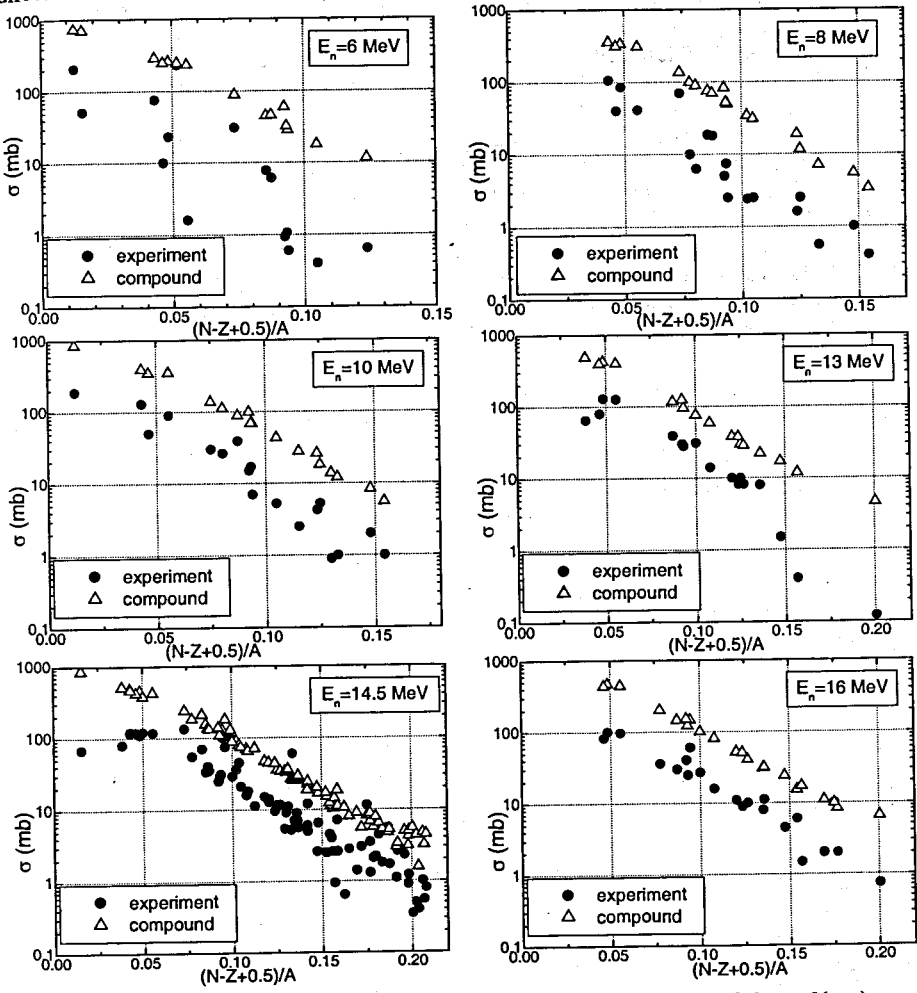


Fig.3. The values calculated by statistical model and experimental data of (n, α) cross sections at neutron energies of 6, 8, 10, 13, 14.5 and 16 MeV.

Acknowledgement

This work was carried out in the framework of the "Nuclear Reactions" project supported in part by Mongolian Science and Technology Foundation.

References

- G. Khuukhenkhuu, Yu. M. Gledenov, M. V. Sedysheva and G. Unenbat. JINR Communications, E3-93-466, 1993, Dubna.
- 2. G. Khuukhenkhuu, Yu. M. Gledenov, M. V. Sedysheva and G. Unenbat. JINR communications, E3-94-316, JINR, 1994, Dubna.
- 3. G. Khuukhenkhuu, G. Unenbat, Yu. M. Gledenov and M. V. Sedysheva. In book: "Porceedings of the International Conference on Nuclear Data for Science and Technology", Trieste, 1997, edited by G.Reffo, A.Ventura and C.Grandi, p.934.
- 4. G. Khuukhenkhuu, G. Unenbat. Scientific Transactions, National University of Mongolia, 7(159), 2000, p.72
- G. Khuukhenkhuu, G. Unenbat, Yu. Gledenov and M. Sedysheva. In book: "Proceedings of International Conference on Nuclear Data for Science and Technology", Tsukuba, Japan, 2001, p.782.
- J. M. Blatt and V. F. Weisskopf. Theoretical Nuclear Physics, John Wiley and Sons, New York, 1952.
- 7. D. G. Gardner and Yu-Wen Yu. Nucl. Phys., v.60, N1, 1964, p.49
- Yu. P. Popov and W. I. Furman. III School on Neutron Physics, JINR, D3-11787, 1978, Dubna, p.390

COMPLETE FILES OF NEUTRON- AND PROTON-INDUCED NUCLEAR DATA UP TO 1 GEV FOR ²⁰⁸Pb, ²⁰⁹Bi, ²³⁵U AND ²³⁸U TARGETS

Martirosyan J.M.¹⁾, Grudzevich O.T.¹⁾, Yavshits S.G.²⁾

1) INPE, Obninsk

2)Khlopin Radium Institute, St. Peterburg

Abstract:

Nuclear data for high projectile energies are needed to design an Accelerator Driven System (target, material activation, heating, shielding etc.). The files of evaluated neutron and proton nuclear data were created in ENDF-6 format for the projectile particle energies from 20 MeV to 1000 MeV. The evaluated data of the files are based mainly on the modern theoretical model calculations with MCFx code. Three mechanism of nuclear reaction were modeled in computing: i) intranuclear cascade; ii) preequilibrium exciton multiparticle emission and iii) statistical decay of excited nuclei. The experimental data available were used to benchmark of the model calculation results. The data on neutron total and reaction cross sections were used to create and to check the set of the optical model parameters in wide energy region. The measured fission cross sections of ²⁰⁸Pb, ²⁰⁹Bi, ²³⁵U and ²³⁸U by protons and neutrons were described without fitting practically.

The files contain total cross sections, fission cross sections, elastic scattering cross sections and angular distributions, proton- and neutron energy-angular distributions. The benchmarking of the data evaluated was performed by the comparison of the results of the transport calculations against the measured neutron leakage spectra from the lead sphere irradiated by protons of 660 MeV.

Theoretical model:

For characteristic calculations of nuclear reaction with intermediate (20 - 200 MaB) and high (200 - 1000 MaB) energy nucleons use a MCFx code [1] in which the mechanism of nuclear reaction includes these stages:

- 1. Optical model.
- 2. Intranuclear cascade.
- 3. Preequilibrium stage of reaction [2].
- 4. Equilibrium nucleus decay (statistical model), including evaporation of particles, gamma-quantum emission, fission etc.

At the first stage for the files creation the optical model parameter (OMP) set for wide region of projectile energies and for the target form ²⁰⁸Pb to ²³⁹Pu was generated. We used ECIS code with relativistic corrections to calculate total, elastic and reaction cross sections. The experimental data available were included into the model calculations testing. So KRI-2006 OMP set was prepared.

$$\begin{array}{lll} V_{\rm R} = (48.65 \mp 15.22 \eta) \cdot (1 - 0.0052 E) + \Delta V_c & 10 < E \leq 80 \; {\rm MeV} \\ = (62.78 \mp 16.16 \eta) \cdot {\rm exp}(-E/100) + \Delta V_c & 80 < E \leq 1000 \; {\rm MeV} \\ r_{\rm R} = 1.26, & a_{\rm R} = 0.626 \\ W_{\rm D} = (8.88 \mp 6.06 \eta) \cdot \left[1 - 1/(1 + {\rm exp}(-(E - 40)/15))\right] & 10 < E \leq 1000 \; {\rm MeV} \\ r_{\rm D} = 1.26, & a_{\rm D} = 0.535 \\ W_{\rm V} = 1 + 10/\left[1 + {\rm exp}(-(E - 51)/10)\right] \mp 4 \eta & 10 < E \leq 80 \; {\rm MeV} \\ = 10.658 + 6.5 \ln(E/180) \mp 4 \eta & 80 < E \leq 1000 \; {\rm MeV} \\ r_{\rm V} = 1.2, & a_{\rm V} = 0.666 \\ V_{SO} = 10.72 \cdot {\rm exp}(-E/160) & 10 < E \leq 1000 \; {\rm MeV} \\ r_{\rm SO} = 1.2, & a_{\rm SO} = 0.5 \end{array}$$

$$\eta = 1 - 2Z / A$$
 and $\Delta V_c = 0.4 \frac{zZ}{A^{1/3}}$

The examples of the comparison of experimental data and results of calculations are presented in fig.1. It can be seen from the figures that generally speaking all experimental data available in the library [3] are described reasonably good simultaneously for wide projectile energy region.

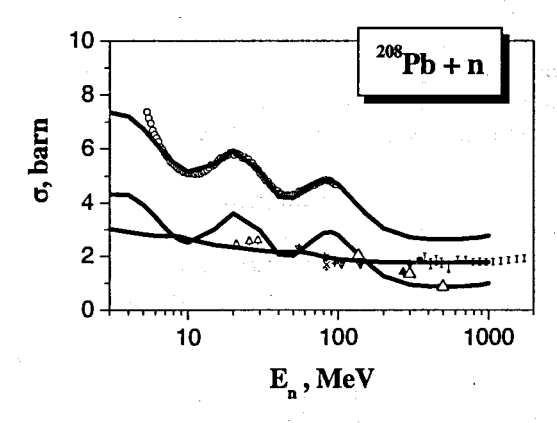


Fig. 1. Total, elastic and reaction cross sections for the interaction of neutrons with ²⁰⁸Pb target. The symbols are the experimental data, the lines are the results of optical model calculations.

We have compiled and analysed experimental data from [3] on proton elastic scattering angular distributions. It should be mentioned the information abun-

dance for ²⁰⁸Pb target for projectile energies from 20 MeV to 1 GeV. Different author's data practically in all cases are in good agreement. Typical descriptions of experimental angular distributions for the intermediate energy are shown in fig. 2. Agreement is good for angles to 30 degrees and bad for higher angles. The discrepancies have no practical importance because the cross sections at these angles are one million times lower then at forward angles, so they are practically negligible.

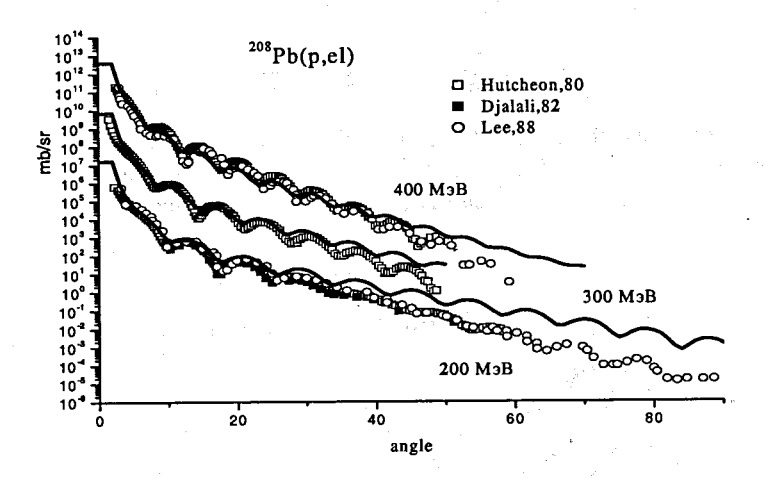


Fig. 2. Angular distributions of the proton elastic scattering on ²⁰⁸Pb for projectile energies 200, 300 and 400 MeV. The symbols are the experimental data, the lines are the results of optical model calculations.

On fig.3-4 descriptions of angular distributions of the proton elastic scattering on ²⁰⁹Bi and ²³⁸U for different projectile energies are shown.

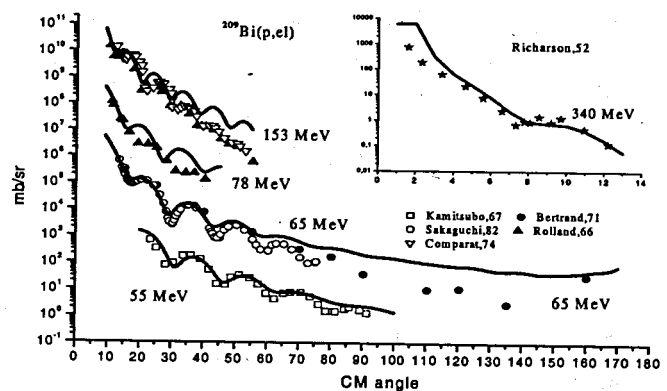


Fig. 3. Angular distributions of the proton elastic scattering on ²⁰⁹Bi for projectile energies 55, 65, 78, 153, 340 MeV. The symbols are the experimental data, the lines are the results of optical model calculations.

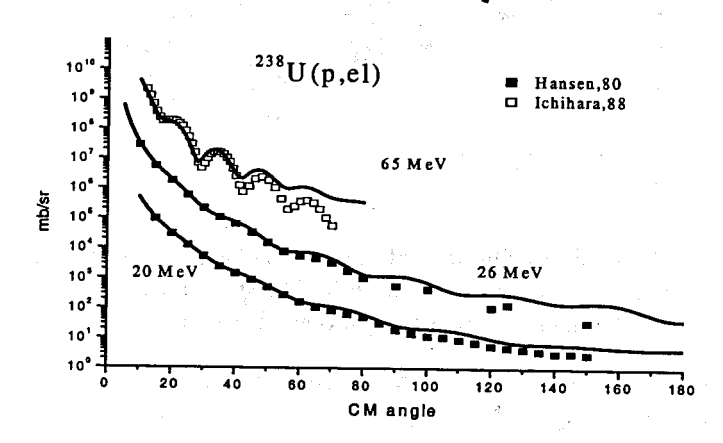


Fig. 4. Angular distributions of the proton elastic scattering on ²³⁸U for projectile energies 20, 26, 65 MeV. The symbols are the experimental data, the lines are the results of optical model calculations.

Fig.5 shows neutron total and reaction cross section for ^{238}U target. Agreement is good.

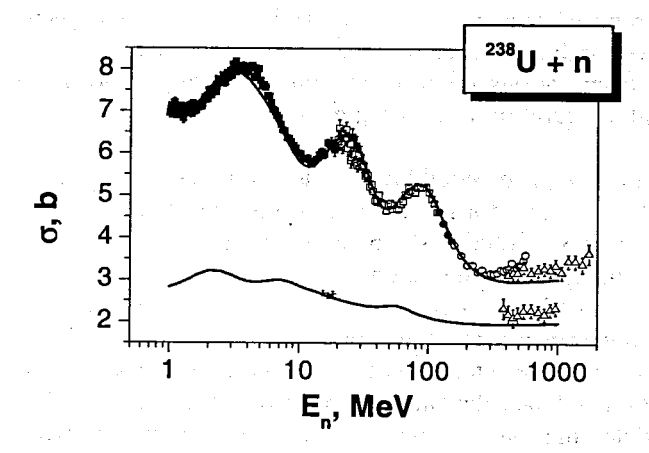


Fig. 5. Cross sections for the interaction of neutrons with ²³⁸U target. The symbols are the experimental data, the line is the results of optical model calculations.

The next fig.6 demonstrates proton reaction cross section for ²³⁸U target.

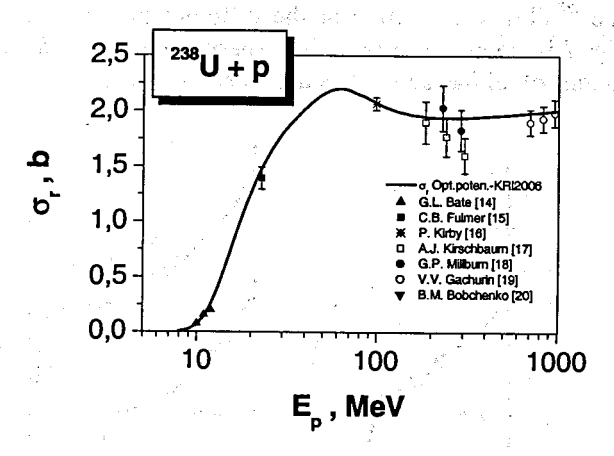


Fig. 6. Cross sections for the interaction of protons with ²³⁸U target. The symbols are the experimental data, the line is the results of optical model calculations.

Results:

In the proposed scheme of calculation (MCP) of the intermediate and high energy nucleon-induced reaction cross-sections at the preequilibrium stage which starts from various initial excitation and configurations, residual nuclei have to transit to equilibrium, emitting nucleons.

MCP stages:

- 1. calculation of all preequilibrium characteristics of all possible nuclei and excitation energies for given initial composite system excitation
- 2. start/stop of ME solution (loop on the time)
- 3. loop on the (p,h) configurations
- 4. a random number is used to select one way of continuation: two particle interaction or neutron/proton emission
- 5. after two particle interaction the system goes to more complicated configuration and the calculation becomes to the step 3.
- 6. if particle emission was realized a random number is used to select the particle energy, the calculations go to the step 2 but with new initial data.

Thus, at sufficient amount of histories the spectra of preequilibrium particles and the populations of the residual nuclei being in the equilibrium state are obtained.

The calculated by MCFx code energy distributions of the secondary neutrons for the ²⁰⁸Pb(p,xn) reaction at the different proton energies are demonstrated in fig. 7 in comparison with the experimental data. No fitting was done. The descriptions of all measured data are more or less good.

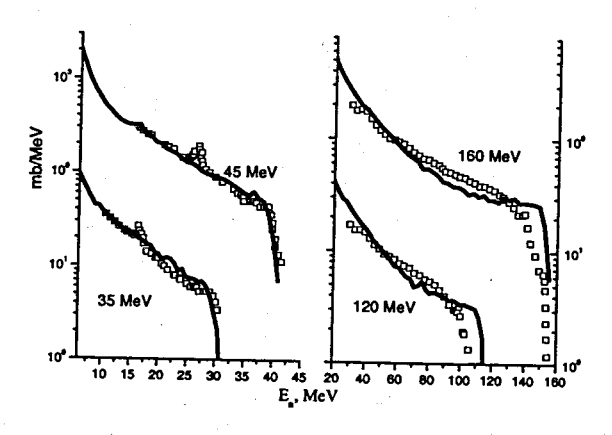


Fig. 7. Comparison of calculated and experimental neutron spectra [4] for ²⁰⁸Pb(p,xn) reaction at 35, 45, 120 and 160 MeV proton energies.

On Fig. 8-10 you can see the calculation results for reactions ²⁰⁹Bi(n,xp), ²⁰⁹Bi(p,xp) and ²³⁸U(n,xp) at various projectile energy after all stages of nuclear reaction (INC, MCP, SM). We can see that the use of proposed model for calculation of spectra give us the results which are in a good agreement with experimental data [5-7].

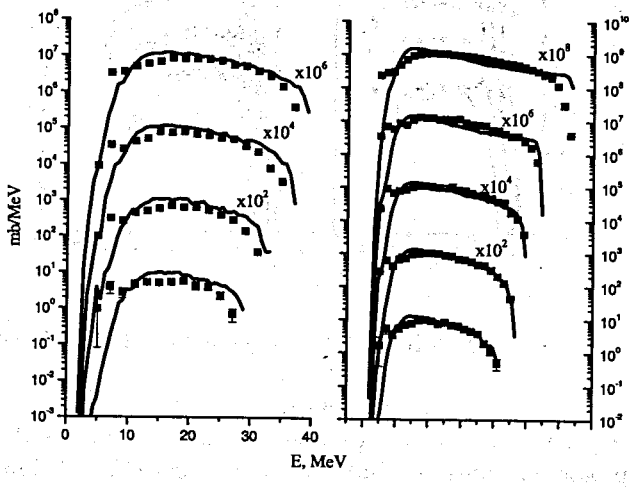


Fig. 8. Spectra of proton for ²⁰⁹Bi(n,xp) reaction (INC+MCP+SM).

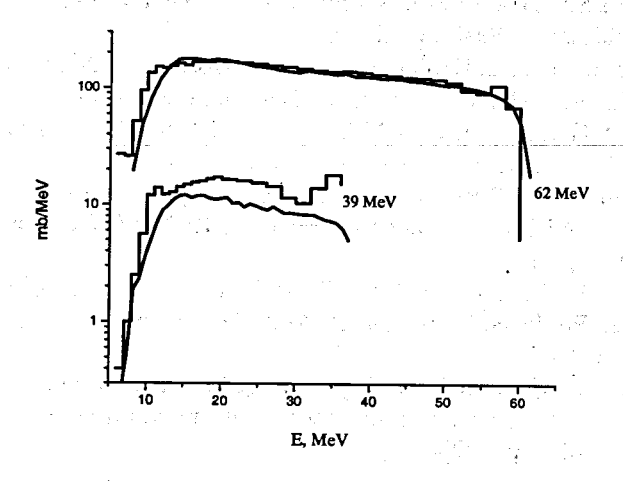


Fig. 9. Spectra of proton for 209Bi(p,xp) reaction (INC+MCP+SM).

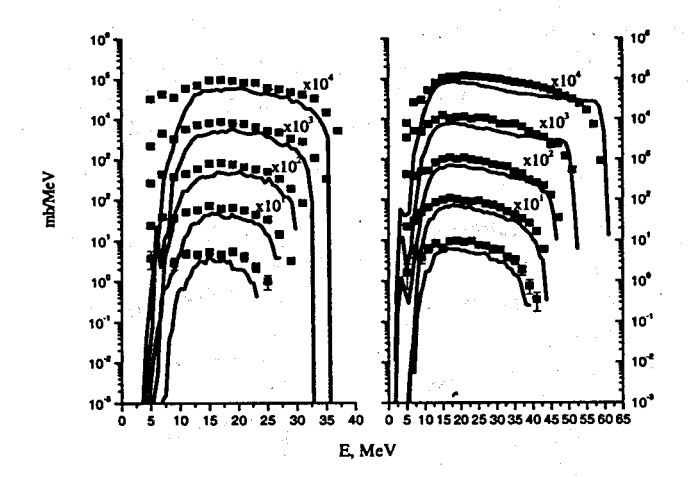


Fig. 10. Spectra of proton for ²³⁸U(n,xp) reaction.(INC+MCP+SM).

Conclusions:

We have generated and tasted complete data files in ENDF-6 format of neutron and proton reactions to 1 GeV for 208Pb, 209Bi, 235U, 238U targets.

References:

- 1. Yavshits S.G., e.a. In Proc. Of Int. Conf. on Nucl. Data for Sci. and Tech., Tsucuba, Japan, 2001. pp.104-107.
- 2. Grudzevich O., e.a. Radiation Protection Dosimetry, 2007 (in press).
- 3. CSISRS File, NNDC, Brookhaven National Laboratory.
- 4. Young P.G. and Chadwick M.B., In Proc. Of Int. Conf. on Nucl. Data for Sci. and Tech., Trieste, Italy, 1997. pp.1440-1442.
- 5. E.Raeymackers, S.Benck etc. Light charged particle emission in fast neutron (25 65 MeV) induced reactions on Bi-209.//Nucl. Phys. 2003. v.A726. p.210.
- 6. Bertrand F. E., .e.a. Tabulated Cross Sections For Hydrogen and Helium Particles Produced by 62 and 29 MeV Protons on 197-Au.//Phys. Rev. 1973. C8. p.1045.
- 7. Raeymackers, S.Benck etc. Light charged particle production in the interaction of fast neutrons (25-65 MeV) with uranium nuclei.//Phys. Rev. 2003. C68. p.24604.

$_{\mbox{\footnotesize p-}}$ and n-induced fission of $^{232}\mbox{Th}$ and $^{238}\mbox{U}$ up to 200 MeV

V.M. Maslov Joint Institute for Nuclear and Energy Research, 220109, Minsk-Sosny, Belarus

Abstract

The excitation energy and nucleon composition dependence of the transition from asymmetric to symmetric scission of fissioning Th(Pa) and U(Np) nuclei is investigated for the 232 Th(n,F) & 238 U(p,F) and 238 U(n,F) & 238 U(p,F) reactions. The simultaneous analysis of the $n+^{232}$ Th and $p+^{232}$ Th data provides a further insight of the role of pre-fission neutron emission in forming the observed symmetric/asymmetric fission yields. The influence of the interplay of fission barriers and entrance channel effects on the fission observables is shown to be different in case of $n(p)+^{232}$ Th and $n(p)+^{238}$ U interactions. In case of $p+^{232}$ Th interaction the fissilities of Pa nuclei are responsible for the higher value of the $\sigma(p,F)$ than $\sigma(n,F)$ cross section at $18 \le E_{n(p)} \le 100$ MeV. In case of $p+^{238}$ U target $p+^{238}$ U ta

Introduction

The excitation energy and nucleon composition dependence of the transition from asymmetric to symmetric scission of fissioning nuclei could be investigated for the 232 Th(n,F) & 232 Th(p,F) and 238 U(n,F) & 238 U(p,F) reactions at projectile energies $E_{n(p)}$ up to 200 MeV. In these specific reactions the Th(Pa) and U(Np) fissioning nuclide properties could be probed. The 232 Th(n,F) and 232 Th(p,F) reaction data represent a mirror-like cases, i.e. for 232 Th(n,F) reaction there are precise cross section data up to E_n =200 MeV, while the data on the 232 Th(p,F) observed fission cross section are scattering quite a lot. At the other hand, while there is virtually no data on the ratio of symmetric-to-asymmetric yields for 232 Th(n,F) reaction, scanty data on the relative yields of symmetric and asymmetric fission for 232 Th(p,F) [1, 2, 3] are available.

The 238 U(n,F) data base is a bit more extensive. For 238 U(n,F) reaction precise cross section data up to $E_n = 200$ MeV are accompanied by the detailed data on the relative yields of symmetric and asymmetric fission [4]. The theoretical analysis based on description of the observed fission cross section and the ratio of lumped symmetric-to-asymmetric yields allows to infer the symmetric and asymmetric fission contributions of U nuclides with $4 \le 239$, fissioning in a competition with successive emission of neutrons [5]. The data on the 238 U(p,F) observed fission cross section are scattering a lot. In 238 U(p,F) and 237 Np(n,F) reactions excited Np nuclei undergo a binary fission in competition with successive emission of pre-fission (p,xnf) or (n,xnf) neutrons. An independent theoretical estimate of the 238 U(p,F) fission cross section, based on the 237 Np(n,F) data description, might be obtained

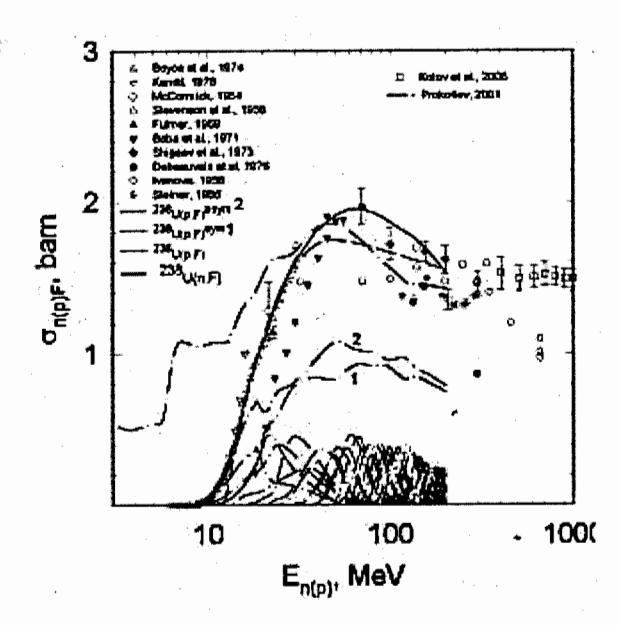


Figure 1: Fission cross sections of $^{238}U(n,F)$ and $^{238}U(p,F)$. Measured data points for $^{238}U(p,F)$ only.

The U and Np nuclides near the beta-stability line demonstrate mostly asymmetric fission, when induced by the neutrons with energies less than (n,nf) reaction threshold [7]. The contribution of the symmetric splits in that excitation energy range is never more than a few percents [8, 9]. It is generally believed that with increase of the excitation energy the influence of the shell effects diminishes and fission observables should be dominated by the macroscopic nuclear properties. However, the pre-fission (pre-saddle) neutron emission decreases the excitation energy of the ensemble of fissioning nuclei, which define the observed fission properties. That peculiarity may quite influence the competition of the symmetric and asymmetric fission modes [10], decreasing the contribution of the symmetric one. The analysis [7] of the TKE-A distributions revealed rather fast increase up to ~ 0.5 at $E_n = 200$ MeV of the symmetric fission contribution $r^{SL} = \sigma_{nF}^{SL}/(\sigma_{nF}^{SL} + \sigma_{nF}^{AS})$ to the observed $r^{238}U(n,F)$ fission yield. At excitation energies higher than (n,nf) reaction threshold the fission observables are composed of partial contributions of the ensemble of uranium fissioning nuclei, which emerge after emission of x pre-fission neutrons (up to $x \sim 20$ at $E_n = 200$ MeV) [6, 11].

The neutron-deficient nuclides, especially those of Th or Pa, emerging in 232 Th(n,xnf) or 232 Th(p,xnf) reactions, might be more susceptible to symmetric fission even at relatively low excitations [12, 13, 14]. Interplay of this trend and the decrease of the intrinsic excitation energy due to pre-fission neutron emission, would define the Th fission observables at high excitations. Symmetric fission contribution $r^{SL} = \frac{\sigma_{nF}^{SL}}{\sigma_{nF}^{SL}} / (\sigma_{nF}^{SL} + \sigma_{nF}^{AS})$ in nucleon-induced fission reactions of 232 Th target nuclides may exhibit rather steep trends with energy.

In case of ²³²Th(n,F) or ²³²Th(p,F) reactions, since Th or Pa nuclei fission probabilities are much lower than those of U or Np nuclei, the influence of preferential (n,xnf) emissive

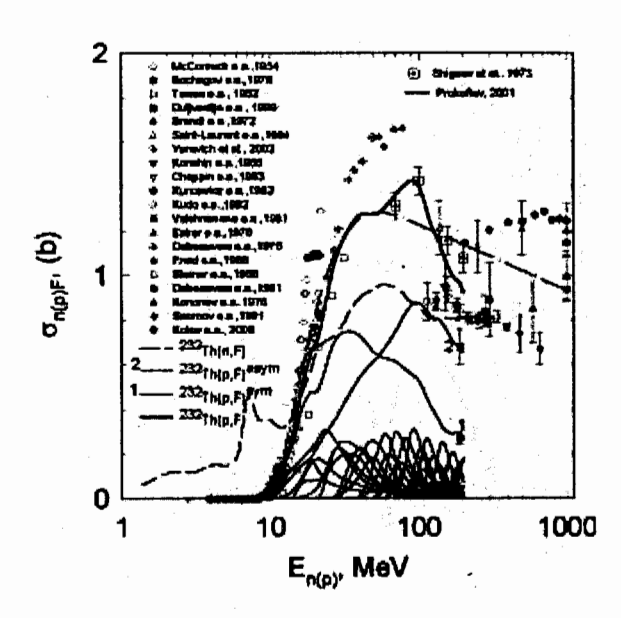


Figure 2: Fission cross sections of 232 Th(p,F) and 232 Th(n,F). Measured data points for 232 Th(p,F) only.

fission contributions to the observed fission cross section is much more pronounced than in case of U or Np targets [5, 15]. The simultaneous analysis of the $n+{}^{232}\mathrm{Th}$ and $p+{}^{232}\mathrm{Th}$ and $n+{}^{238}\mathrm{U}$ and $p+{}^{238}\mathrm{U}$ data sets would be complementary and will provide a further insight on the role of pre-fission neutron emission in forming the observed symmetric/asymmetric fission yields as dependent on the target nuclide fissility. Independent estimate of the ${}^{232}\mathrm{Th}(p,F)$ reaction cross section might be obtained based on the consistent ${}^{232}\mathrm{Th}(p,xn)$ and ${}^{231}\mathrm{Pa}(n,F)$ data description.

2 $p+^{232}Th$ and $n+^{238}U$ interactions

The statistical model calculations of the symmetric/asymmetric fission competition in the emissive fission domain are described elsewhere [5, 9, 15]. Calculated (n,xnf) contributions to the observed fission cross sections are largely defined by the level density parameters a_f and a_n for fissioning (f) and residual (n) nuclides [5], as well as the damping of the rotational modes contributions to the level densities

$$\rho(U, J, \pi) = K_{rot}(U)K_{vib}(U)\rho_{qp}(U, J, \pi). \tag{1}$$

Nuclear level density $\rho(U, J, \pi)$ is represented as the factorized contribution of the quasiparticle and collective states [16]. Quasiparticle level densities $\rho_{qp}(U, J, \pi)$ were calculated with a phenomenological model by Ignatyuk et al. [17], $K_{rot}(U, J)$ and $K_{vib}(U)$ are factors of the rotational and vibrational enhancement. At saddle and ground state deformations factor $K_{rot}(U)$ is defined by the deformation order of symmetry, adopted from the shell correction

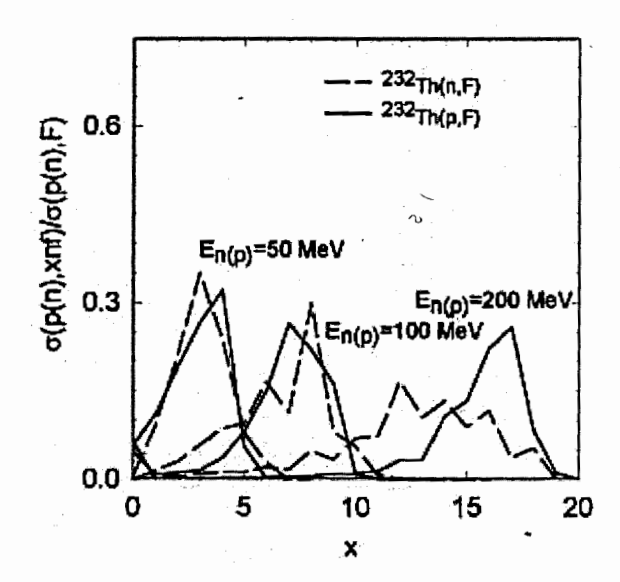


Figure 3: Emissive fission chance distribution of 232 Th(p,F) (solid line) and 232 Th(n,F) (dashed line) reactions, $\tilde{a}_f = \tilde{a}_f(U,A)$.

model calculations [18], except outer saddles for the symmetric scission. For calculation of the fission probabilities of $^{233-x}Th(^{238-x}U)$ and $^{233-x}Pa(^{238-x}Np)$ nuclides we use double-humped fission barrier model, since possible splitting of the outer fission barrier hump is not important in the present context. Damping of the rotational mode contributions to the $\rho(U,J,\pi)$ was anticipated by Hansen and Jensen [19] at rather high excitations $U \geq U_r$. The damping might be different for the axially symmetric and triaxial shapes [20], i.e.

$$K_{rot}^{sym}(U) = (\sigma_{\perp}^2 - 1)F(U) + 1,$$
 (2)

$$K_{rot}^{asym}(U) = K_{rot}^{ax}(U)((2\sqrt{2\pi}\sigma_{\parallel} - 1)F(U) + 1),$$
 (3)

$$F(U) = (1 + \exp(U - U_r)/d_r)^{-1}. (4)$$

Here, σ_{\parallel}^2 and σ_{\perp}^2 are spin distribution parameters (for other details see [5]). The mass asymmetry for the AS-mode at outer saddle doubles the rotational enhancement factors as defined by Eqs. (2, 3). The shell effects in level density are modelled with the shell correction δW dependence of the a-parameter as recommended by Ignatyuk et al. [17]: $a = a(U) = \tilde{a}(1 + \delta W f(\tilde{U})/(\tilde{U}))$.

The deformed optical potential describes the $n+^{232}Th(^{238}U)$ total cross section data up to $E_n=200$ MeV [15, 21]. Prediction of the optical potential for the incident protons based on the optical potential for incident neutrons needs decomposition of the real and imaginary potential terms into isoscalar and isovector components [22]. For $n+^{232}Th(^{238}U)$ interaction we introduced isovector terms, which depend on the symmetry parameter $\eta=(N-Z)/A$,

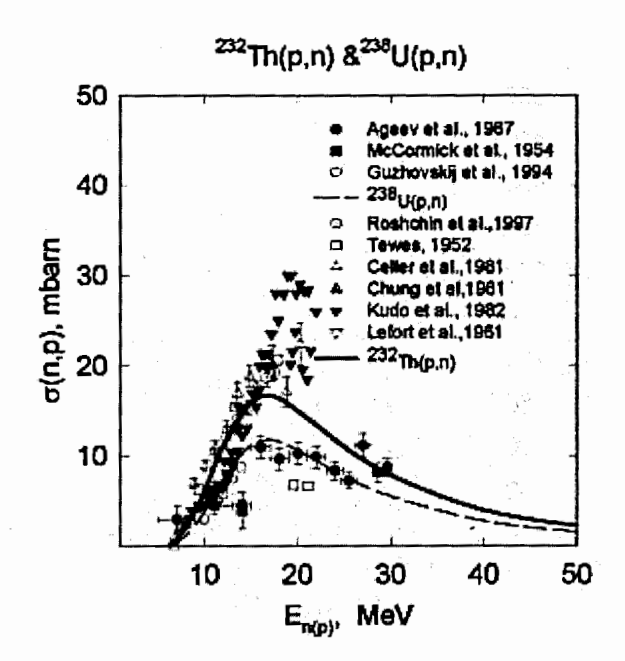


Figure 4: Cross section of ²³⁸U(p,n) and ²³²Th(p,n).

only in a real volume V_R^n and imaginary surface W_D^p potential terms [15]. Values of V_R^p and W_D^p for incident protons could be calculated as $V_R^p = V_R^n + 2\alpha\gamma$ and $W_D^p = W_D^n + 2\beta\gamma$, $\alpha = 16$ and $\beta = 8$ values, obtained by the description of the proton and neutron scattering data for a number of medium weight nuclei [23]. The predicted ²³²Th proton absorption cross section $\sigma_R^p > \sigma_R^n$ at $E_n \gtrsim 50$ MeV is compatible with the experimental data in the same way, as it was shown for the p+²³⁸U interaction [21].

The energy dependence of symmetric fission cross section σ_{nF}^{SL} is defined by the symmetry of the outer saddle of a double humped fission barrier. In summary, for neutron-induced fission of 238 U it was found that rather thin but high outer barrier E^{SL}_{IB} corresponds to the mass symmetric fission, in contrary to the lower mass-asymmetric outer fission barrier E_{IB}^{AS} Actually $(E_{IB}^{SL} - E_{IB}^{AS}) = 3.5$ MeV, independent on the neutron number N, was assumed for U nuclides. In the emissive fission domain the observed fission cross section of ²³⁸U(n,F) and the ratio of symmetric-to-observed fission yields $r^{SL}(E_n)$ are described under assumption that more fissions come from the neutron-deficient U nuclei via (n,xnf) fission chances with high number x of pre-fission neutrons [5, 15]. Light charged particle (LCP) emission is assumed to be negligible. In case of proton-induced fission of ²³⁸U an independent estimate of the observed fission cross section [6], based on the ²³⁷Np(n,F) data description, was obtained (see Fig.1). The lumped contributions of symmetric σ_{nF}^{SL} and asymmetric σ_{nF}^{AS} fission cross sections are shown as well. The measured data on ²³⁸U(p,F) reaction cross sections are scattering [24, 25, 26, 27, 28, 29, 30, 31, 32, 33, 34], at $E_p \gtrsim 30$ MeV the theoretical estimate differs essentially from the phenomenological estimate [35], based on the rough description of the measured data trend for pre-actinide and actinide targets.

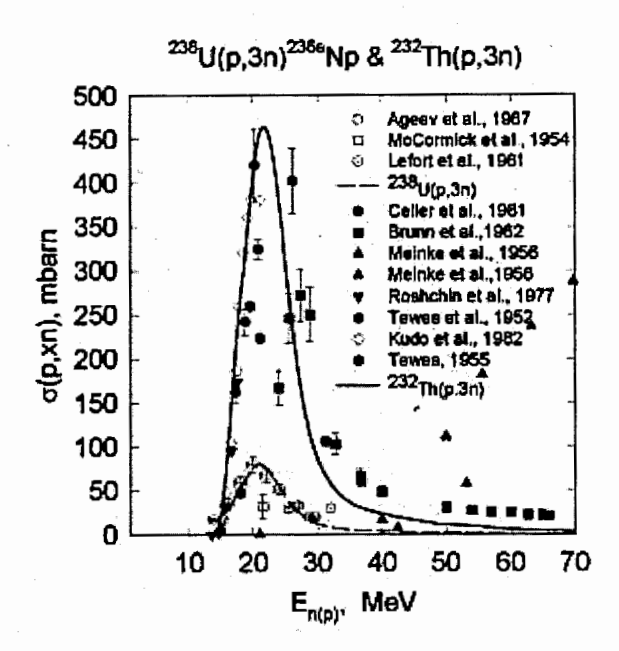


Figure 5: Cross section of $^{238}\text{U}(p,3n)^{236s}\text{Np}$ and $^{232}\text{Th}(p,3n)$.

The ²³²Th target nuclide exhibits the lowest fissility among the actinide nuclides investigated with the neutron-induced fission reactions up to $E_n = 200$ MeV. The observed fission cross section of 232 Th(n,F) reaction is reproduced up to $E_n = 200$ MeV also under assump tion that more fissions come from the neutron-deficient Th nuclei [5, 15]. The data on ²³²Th neutron- and proton-induced fission may provide a complementary information on the evolution of the symmetric/asymmetric fission competition with increase of the projectile energy. The situation with ²³²Th(p,F) data is a mirror-like, as compared with ²³²Th(n,F) data, where precise cross section data are available [36, 37, 38]. The data on the ²³²Th(p,F) observed fission cross section are scattering much more, than in case of ²³⁸U(p,F) reaction cross section (see Fig. 2). The measured data on the symmetric/asymmetric fission yields for $E_p = 20-50$ MeV, [1] and $E_p = 190$ MeV [2, 3] provide an unambiguous evidence for the sharp increase of $r^{SL}(E_p)$ at $E_p \gtrsim 30$ MeV. There is also a strong evidence [13], that fission of $^{233-x}$ Pa and $^{233-x}$ Th nuclei $(x=1\div 20)$ in case of 232 Th(p,F) or 232 Th(n,F) reactions, re spectively, would provoke similar competition of symmetric and asymmetric fission events for the incident proton/neutron energies up to 200 MeV. In case of ²³²Th(p,F) reaction the measured data [24, 27, 31, 32, 34, 41, 42, 43, 44, 45, 46, 47, 48, 49, 50, 51, 52, 53, 54, 55, 56] are scattering a lot and phenomenological data fit [35] much depends on the attributed ex perimental errors. An independent estimate of the ²³²Th(p,F) reaction cross section might be obtained, based on the consistent description of the ²³²Th(p,n), ²³²Th(p,2n), ²³²Th(p,3n) and ²³²Th(p,F) data, while fission probabilities of ^{230–232}Pa nuclides are fixed by the ²³¹Pa(n,F) data description.

In case of nucleon-induced fission of ²³²Th, after the pre-saddle neutron emission the

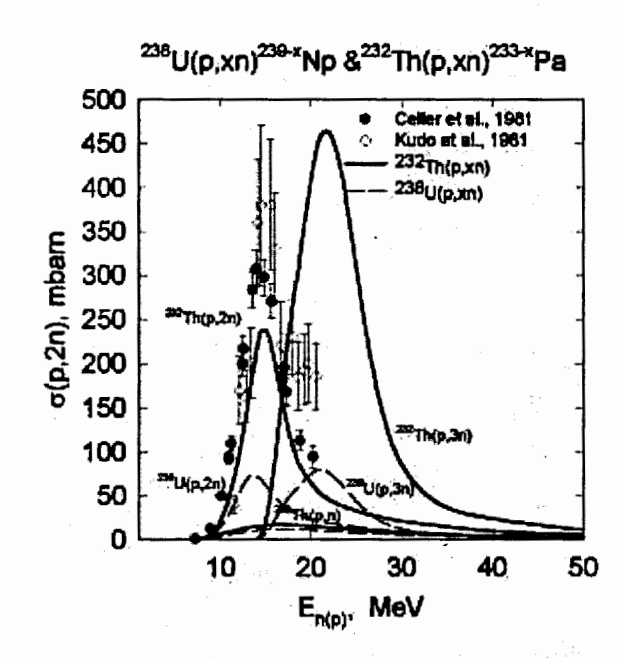


Figure 6: Cross section of $^{238}U(p,xn)$ and $^{232}Th(p,xn)$.

 $^{233-x}$ Th or $^{233-x}$ Pa ($x \sim 1 \div 20$) nuclides contribute to the observed fission cross sections of 232 Th(n,F) or 232 Th(p,F) reactions, respectively. For incident neutron energies $E_n \leq 20$ MeV the 232 Th(n,F) fission chances partitioning could be defined quite unambiguously. Statistical-model calculations [39, 40] consistently reproduce the 232 Th(n,F), 231 Th(n,f), 230 Th(n,f) and 232 Th(n,2n) cross section data and prompt fission neutron spectra of 232 Th(n,F) reaction.

Figure 3 shows the dependence of the distribution of the emissive fission chances 232 Th(n,xnf)/ 232 Th(n,F) and 232 Th(p,xnf)/ 232 Th(p,F) at $E_{n(p)} = 50$, 100 and 200 MeV for $\tilde{a}_f = \tilde{a}_f(U,A)$ [5, 15]. The variation of the level density parameter $\tilde{a}_f(U,A)$ with excitation energy governs the redistribution of the 232 Th(n,xnf) or 232 Th(p,xnf) fission chances contributions. In case of 232 Th(n,F) reaction that peculiarity plays a decisive role, since the fission probabilities of Th nuclides are rather low, consequently, the lower mass (A < 233) Th nuclides may contribute appreciably to the observed 232 Th(n,F) fission cross section. Dashed lines correspond to 232 Th(n,xnf)/ 232 Th(n,F), while solid lines to the 232 Th(p,xnf)/ 232 Th(p,F). At $E_{n(p)} = 50$ MeV the peaks are at $x \sim 3$ -4, at $E_{n(p)} = 100$ MeV the peaks are at $x \sim 6$ -8, at $E_{n(p)} = 200$ MeV the contributions of higher fission chances become overwhelming, peak shifts to $x \sim 17$ for 232 Th(p,F) reaction. In case of 232 Th(n,F) reaction the distributions at $E_n = 200$ MeV becomes rather broad and skewed, while odd-even effects in the $\sigma_{nxnf}/\sigma_{nF}$ ratios are much more pronounced than in $\sigma_{pxnf}/\sigma_{pF}$ in case of 232 Th(p,F) reactions.

Figure 4 shows the comparison of the ²³²Th(p,n) [1, 43, 50, 57, 58, 59] and ²³⁸U(p,n) [27, 60, 61] reaction data descriptions. The ²³²Th(p,n) reaction cross section is only ~50% higher than ²³⁸U(p,n) reaction cross section, as opposed to the predicted trend by Tewes et al. [43]. Figure 5 shows the comparison of the ²³²Th(p,3n) [1, 43, 50, 57, 58, 62, 63,

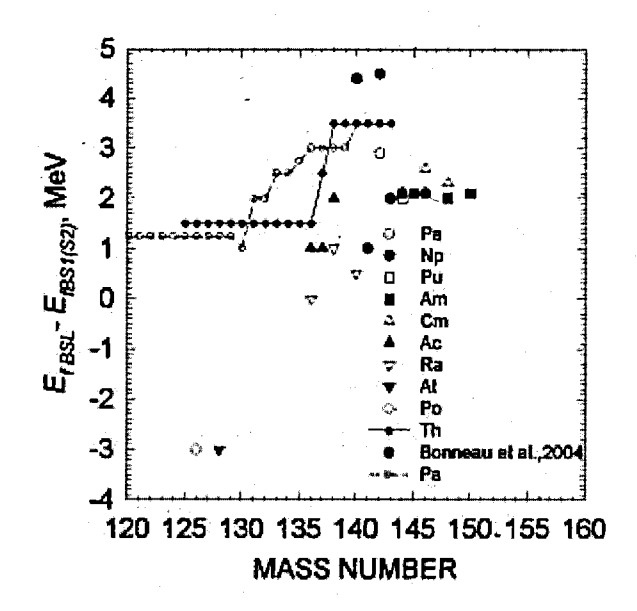


Figure 7: Difference of fission barriers for symmetric and asymmetric splits.

64] and ²³⁸U(p,3n)^{236s}Np [27, 59, 60] reaction data descriptions. A three-fold difference of the calculated cross section values in the peak region is supported by the precise data on ²³⁸U(p,3n)^{236s}Np by Ageev et al. [60] and by most recent data on ²³²Th(p,3n) by Celler et al. [58] (see Fig. 5). In case of ²³²Th(p,2n) there is a two-fold difference of the calculated and measured [50, 58] cross section values in the peak region, while there is no data available in case of ²³⁸U(p,2n) reaction (see Fig. 6).

The ²³²Th(n,F) measured fission cross section data [36] could be reproduced only for the fission chances distribution, corresponding to the preferential contribution of fission of neutron deficient Th nuclides [15]. The ratio of symmetric-to-observed fission yields, for ²³²Th(n,F) cross sections in [15] was obtained based on the assumption that the difference of heights of symmetric and asymmetric saddle points $(E_{fB}^{SL} - E_{fB}^{AS}) = 3.5 \text{ MeV } [5, 15]$ is independent on the neutron number of fissioning nucleus. That estimate is lower, than ~5 MeV lowering of the reflection-asymmetric outer saddle for ²³²Th and ²³⁴Th, obtained within a Hartree-Fock and BCS pairing approach by Bonneau et al. [65]. However, the pronounced isotopic dependence of E_{IB}^{SL} and E_{IB}^{AS} may be the case for Th and Pa nuclides with $A \leq 226$, i.e., the symmetric fission yield may have a tendency to increase for neutrondeficient nuclides [12, 13, 14]. That leads to the increase of the symmetric fission yields in ²³²Th(p,F) and ²³²Th(n,F) reactions due to ²³²Th(p,xnf) and ²³²Th(n,xnf) fission reactions, respectively, at $E_{n(p)} = 50-200$ MeV. Figure 2 shows the sharing of the ²³²Th(n,F) observed fission cross section to SL- and AS-modes when $(E_{fB}^{SL}-E_{fB}^{AS})=1.5$ MeV for Th nuclides with $A\leq 226$, which is achieved by ~ 1 MeV decrease of E_{fB}^{SL} and ~ 1 MeV increase of E_{fB}^{AS} of outer fission barriers, as compared to the barrier values, used in [15]. This is generally consistent with the outer fission barrier estimates by Ohtsuki et al. [66], based on fission

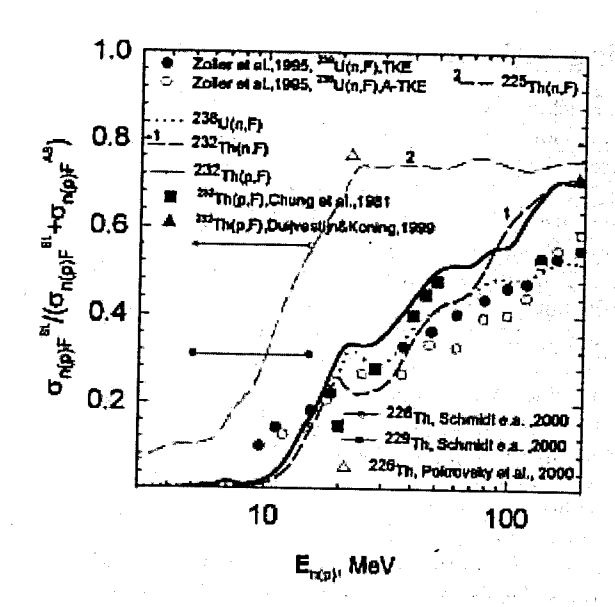


Figure 8: Branching ratio r^{SL} for $^{238}U(n,F)$, $^{232}Th(n,F)$, $^{232}Th(p,F)$.

yield analysis for proton-induced fission of Th, U, Np, Pu and Am nuclei at E_p =8-16 MeV (see Fig. 7). The sharp increase of the 232 Th(n,F) lumped symmetric fission yield at E_n \geq 80 MeV (see Fig. 2) is due to appreciable increase of the 232 Th(n,xnf) contributions of relatively low excited neutron-deficient Th nuclides. The predicted sharing into σ_{nF}^{SL} and σ_{nF}^{AS} is shown for the 230 Th(n,F) reaction.

Figure 2 shows the sharing of the ²³²Th(p,F) observed fission cross section [24, 27, 31, 34, 41, 42, 43, 44, 45, 46, 47, 48, 49, 50, 51, 52, 53, 54, 55, 56] to SL- and AS-modes, which is compatible with the measured estimates of σ_{pF}^{SL} and σ_{pF}^{AS} by Duijvestijn and Koning [2]. The estimate $(E_{IB}^{SL} - E_{IB}^{AS}) = 1$ MeV is used for Pa nuclei with $N \le 135$, fissioning in 232 Th(p,F) reaction. The calculated σ_{pF} cross section at E_p =70-200 MeV is supported by the measured data [31, 42] and [27, 43, 55] at lower energies. Fission probabilities of ²³³Pa, ²³²Pa and ²³¹Pa nuclides are defined by the ²³³Pa(n,F) and ²³¹Pa(n,F) neutron-induced fission cross sections description [67]. Most recent data by Smirnov et al. [56] appear to overshoot the calculated ²³²Th(p,F) cross section. Fig. 2 shows, that the proton-induced fission cross section of ²³²Th is higher than that of neutron-induced at $E_{n(p)} \gtrsim 18$ MeV, while in case of ²³⁸U target nuclide that happens only at $E_{n(p)} \gtrsim 50$ MeV [6] (see Fig. 1). That means in case of p+232Th interaction the fissilities of Pa nuclei are relatively higher than those of respective Th nuclei for the $n+^{232}$ Th interaction, which influences the observed fission cross section at $E_{n(p)} \lesssim 100$ MeV. In case of ²³⁸U at $E_{n(p)} \gtrsim 50$ MeV the decisive factor is the sign of the isovector terms in real volume V_R^n and imaginary surface W_D^n potential terms, while in case of ²³²Th target the entrance channel plays a decisive role at much higher incident energies $E_{n(p)} \gtrsim 100$ MeV. The theoretical estimate of 232 Th(p,F) reaction cross section differs essentially from the phenomenological estimate [35], based on the rough description of the measured data trend.

3 Branching ratio of symmetric-to-observed fission events

The calculated branching ratio of the symmetric-to-observed fission events $r^{SL}(E_p)$ for ²³²Th(p,F) reaction shown on Fig. 8, describes the increasing trend of the data by Croali et al. [68], reported by Chung et al. [1], in the energy range $E_n = 23-57$ MeV. The sharp increase of $r^{SL}(E_p)$ at $E_p = 57-200$ MeV is predicted, though on Fig.3 the decrease of both σ_{rF}^{SL} and σ_{rF}^{AS} is evidenced. The branching ratio of the symmetric to observed fission events $r^{SL}(E_n)$ for ²³²Th(n,F), shown on Fig. 8, is higher than that observed for the ²³⁸U(n,F) reaction [4, 5, 39]. The calculated ratio r^{SL} is much dependent on the (n,xnf) or (p,xnf)fission chances distribution. Because the fissilities of Th nuclides with A < 233 are lower than those of U nuclei with A < 239, the contribution of the first few chances is lower in case of ²³²Th(n,F) reaction. That means the contribution of the fission reactions of neutrondeficient ^{233-x}Th nuclides with low intrinsic excitation energies would be relatively high That might lead to the lowering of r^{SL} for the ²³²Th(n,F) reaction, but this effect could be more than compensated, since for Th nuclei the relative heights of the symmetric and asymmetric outer fission barriers $(E_{fB}^{SL} - E_{fB}^{AS})$, as was already mentioned, might change in favour of symmetric fission contribution [12, 13, 14, 69, 70, 71]. The experimental estimates of the branching ratios r^{SL} for Th nuclides with A < 226 by Itkis et al. [12], Pokrovsky et al. [14] and Schmidt et al. [13] correspond to different excitation energies of composite nuclides. Different contributions of emissive fission reactions to the observed fission fragment yields in ²⁰⁸Pb(¹⁸O,f) reaction [12] and in peripheral relativistic heavy-ion reaction [13] would follow, since the intrinsic excitations of the ensemble of fissioning nuclides also differ. The excitation energies of the fissioning nuclides ²²⁹Th and ²²⁶Th [13], shown on Fig. 8 (~11 MeV), correspond to two-phonon excitation of GDR. The experimental estimate of the symmetric fission contribution to the observed fission fragment yield in ²⁰⁸Pb(¹⁸O,f) reaction [12] is shown for the equivalent incident neutron energy $E_n \sim 20$ MeV. Obviously, the contribution of symmetric fission of Th nuclides with $A \leq 226$ is rather sensitive to the value of fission barrier splitting $(E_{fB}^{SL} - E_{fB}^{AS})$. The estimate of the relative symmetric fission yield [3] for the 232 Th(p,F) reaction amounts to ~ 0.715 , which is quite compatible with the present estimate for the ²³²Th(n,F) reaction. Figure 8 shows also the calculated contribution of symmetric fission events to the observed fission yield for the 225 Th(n,F) reaction up to $E_n \sim 200$ MeV. In case of ²²⁵Th(n,F) the contribution of the neutron-deficient Th nuclei to the fission observables is much higher, it seems to be compatible with the experimental estimates by Pokrovsky et al. [14] and Schmidt et al. [13] (see Fig. 4).

Predicted increase of the symmetric fission yield, which becomes higher than that of the asymmetric fission yield at $E_n \ge 80$ MeV in 232 Th(n,F) reaction, is due to the increased symmetric fission of neutron-deficient Th nuclei.x

4 Conclusion

The influence of the interplay of fission barriers and entrance channel effects on the fission observables is shown to be different in case of $n(p)+^{232}$ Th and $n(p)+^{238}$ U interactions. In case of $p+^{232}$ Th interaction the fissilities of Pa nuclei are responsible for the higher value of the $\sigma(p,F)$ than $\sigma(p,F)$ cross section at $18 \leq E_{n(p)} \leq 100$ MeV. In case of 238 U target $\sigma(p,F) > \sigma(n,F)$ only at $E_{n(p)} \gtrsim 50$ MeV due to the isovector terms in real volume V_{R_n} and imaginary surface W_{D_n} potential terms. In case of 232 Th target the entrance channel (nucleon absorption cross section) plays a decisive role at $E_{n(p)} \gtrsim 100$ MeV.

Independent estimates of the $^{232}{\rm Th(p,F)}$ and $^{238}{\rm U(p,F)}$ fission cross sections are obtained, based on consistent description of available measured data base on $n+^{232}{\rm Th}$ and $p+^{232}{\rm Th}$ and $p+^{238}{\rm U(n,F)}$ interactions, respectively. The description of the observed fission cross sections up to $E_{n(p)}\sim 200$ MeV was achieved under assumption of preferential contribution of fission of neutron-deficient nuclides. The fission chances distribution was obtained by the consistent description of the observed fission cross section and symmetric fission branching ratio for the $^{238}{\rm U(n,F)}$ reaction. The measured data on the branching ratio of symmetric-to-observed fission events for $^{232}{\rm Th(p,F)}$ reaction are reproduced up to $E_p \sim 190$ MeV. The branching ratio description is rather sensitive to the intrinsic energy distribution of Pa nuclei, fissioning in $^{232}{\rm Th(p,F)}$ reaction. Sharp increase of the symmetric fission yield for the $^{232}{\rm Th(p,F)}$ reaction above $E_n \gtrsim 50$ MeV is predicted due to the similar behavior of Th neutron-deficient nuclides.

References

- [1] C. Chung C. and J. Hogan, Phys. Rev. 24 (1981) 180.
- [2] M.C. Duijvestijn, A.J. Koning, J.P. Beijers et al., Phys. Rev. C 59 (1999) 776.
- [3] M.C. Duijvestijn, A.J. Koning and F.-J. Hambsch, Phys. Rev. C 64 (2001) 014607.
- [4] C.M. Zoller et al., Fission fragment properties in the ²³⁸U(n,f) reaction at incident neutron energies from 1 MeV to 500 MeV / IKDA 95/25, Institut für Kernphysik, Darmstadt, 1995.
- [5] V.M. Maslov, Nucl. Phys. A 717 (2003) 3.
- [6] V.M. Maslov, Phys. Lett. B 581 (2004) 56.
- [7] U. Brosa et al., Physics Reports. 197 (1990) 167.
- [8] S. Oberstedt et al., Nucl. Phys. A 644 (1998) 289.
- [9] V.M. Maslov and F.-J.Hambsch, Nucl. Phys. A 705 (2002) 352.
- [10] A. Turkevich and J.B. Niday, Phys. Rev. 84 (1951) 52.
- [11] V.M. Maslov, EuroPhysics Journal. A 21 (2004) 281.
- [12] M.G. Itkis, Yu. Ts. Oganesyan, G.G. Chubaryan et al., Proc. of the Workshop on Nuclear Fission and Fission-Product Spectroscopy, Seissin, France, 1994, edited by H. Faust and G. Fioni (ILL, Grenoble, 1994). p. 77.
- [13] K.-H. Schmidt et al., Nucl. Phys. A 665 (2000) 221.
- [14] I.V. Pokrovsky M.G. Itkis, J.M. Itkis et al., Phys. Rev. C 62 (2000) 014615.
- [15] V. M. Maslov, Nucl. Phys. A 757 (2005) 390.
- [16] A. Bohr and B. Mottelson, Nuclear Structure, vol. 2, (Benjamin, New-York, 1975).
- [17] A.V. Ignatjuk, K.K. Istekov and G.N. Smirenkin, Sov. J. Nucl. Phys., 29 (1979) 450.

- [18] W.M. Howard and P. Möller, Atomic Data and Nuclear Data Tables, 25, 219 (1980).
- [19] G. Hansen and A.S. Jensen, Nucl. Phys. A406 (1983) 236.
- [20] A.R. Junghans, M. de Jong, H.-G. Clerc et al., Nucl. Phys. A629 (1998) 635.
- [21] V.M. Maslov, Yu.V. Porodzinskij, N.A. Tetereva et al., Nucl. Phys. A, 736, 77 (2004).
- [22] J.P. Delaroche, E. Bauge and P. Romain, In: Proc. International Conference on Nuclear Data for Science and Technology, Trieste, Italy, 1997, p. 206.
- [23] P.G. Young , INDC(NDS)-335, p.109, 1994.
- [24] A.A. Kotov, L.A. Vaishnene, V.G. Vovchenko et al., Phys. Rev. C74 (2006) 034605.
- [25] J.R. Boyce, T.D. Hayward, R. Bass et al., Phys. Rev. C 10 (1974) 231.
- [26] A.T. Kandil, J. Inorg. Chemistry 38 (1976) 37.
- [27] McCormick G.H., Cohen B.L., Phys. Rev. 96 (1954) 722.
- [28] P.C. Stevenson, H.G. Hicks, W.E. Nerwick et al., Phys. Rev. 111 (1958) 886.
- [29] C.B. Fulmer, Phys. Rev. 116 (1959) 418.
- [30] S. Baba, H. Umezawa, H. Baba, Nucl. Phys. A 175 (1971) 177.
- [31] O.E. Shigaev, V.S. Bychenkov, M.F. Lomanov et al., V.G. Khlopin Radium Institute, St. Petersburg, Preprint RI-17, 1973.
- [32] M. Debeauvais M., Tripier J., S. Jokic et al., Proc. 9th International Conference on Solid State Nuclear Track Detectors, Neuherberg/Munchen, September 30 – October 6,1976, p. 1179.
- [33] N.S. Ivanova, Zh. Eksp. Theor. Phys. 31 (1956) 413.
- [34] H.M. Steiner, J.A. Jungerman, Phys. Rev. 101 (1956) 807.
- [35] A.V. Prokofiev, Nucl. Instrum. And Methods in Phys. Res. A 463 (2001) 557.
- [36] O.A. Shcherbakov et al., Proc. Int. Conf. Nucl. Data for Sci. and Techn., Tsukuba, Japan, October, 7-12, 2001, p. 230 (2002).
- [37] J.W. Behrens, J.C. Browne and E. Ables, Nucl. Sci. Eng. 81 (1982) 512.
- [38] B.I. Fursov et.al., Sov. Atom. Energ. 71 (1992) 827.
- [39] V.M. Maslov, Nucl. Phys. A 743 (2004) 236 .
- [40] V.M. Maslov et al., Phys. Rev. C 69 (2004) 034607.
- [41] B.A. Bochagov, V.S. Bychenkov, V.D. Dmitriev et al., Sov. J. Nucl. Phys. 28 (1978) 291.

- [42] V.S. Bychenkov, M.F. Lomanov A.I. Obukhov et al., Proc. of the International Conf. 50th Anniversary of Nuclear Fission, Leningrad, USSR, October 16-20, vol. 2, 1989, p. 165, Ed. by L.V. Drapchinskij, V.G. Khlopin Radium Institute, St. Petersburg, Russia, 1992 (in Russian).
- [43] H.A. Tewes and R.A.James, Phys. Rev. 88 (1952) 860.
- [44] R. Bandt, T.F. Carbonara, E. Cieslak et al. Rev. Phys. Appl. 7 (1972) 243.
- [45] F. Saint-Laurent, M. Conjeaud M., R. Dayras et al., Nucl. Phys. A. 422 (1984) 307.
- [46] V.I. Yurevich, V.A. Nikolaev, R.M. Yakovlev et al., Phys. At. Nucl. 65 (2002) 1417.
- [47] V.A. Kon'shin, E.S. Matusevich and V.I. Regushevskij, Sov. J. Nucl. Phys. 2 (1965) 489.
- [48] G.R. Choppin, J.R. Meriwether and J.D. Fox, Phys. Rev. 131 (1963) 2149.
- [49] W. Kurcewicz, J. Szerypo, P. Hornshoj et al., Zetchshrift Fyz. A. 305 (1982) 99.
- [30] H. Kudo, H. Muramatsu, H. Nakahara et al. Phys. Rev. C 25 (1982) 3011.
- [51] L.A. Vaishnene, L.N. Andronenko, G.G. Kovshevny et al., Zetchshrift Fyz. A. 302 (1981) 143.
- [32] R.W. Eaker and G.R. Choppin. J. Inorg. Chem. 38 (1976) 31.
- [3] Freid S.H., Anderson J.L., Choppin G.R., J. Inorg. Chem. 30 (1968) 3155.
- [4] M. Debeauvais M., Tripier J., S. Jokic et al., Phys. Rev. C 23 (1981) 1624.
- [5] V.N. Kononov, E.D. Poletaev P.P. D'jachenko, Sov. J. Nucl. Phys. 27 (1978) 162.
- A.N. Smirnov, I.Yu. Gorshkov, A.V. Prokofiev and V.P. Eismont, Proc. of XXI International Symp. On Nuclear Physics, November 408, 1991, Castle Gaussig, Germany, p. 214, World Scientific Publishing Co., Pvt., Ltd., Singapore, 1992.
- ^{57]} A.Roshchin, S. Yavshits, V. Yakovlev et al., Phys.At. Nucl. 60 (1997) 1941.
- A.Celler, M. Luontama, J. Kantele, J. Zylich, Journ. Phys. Chem. 24 (1981) 930.
- M.Lefort, G.N. Simonoff, X. Tarra, Nucl. Phys, 25 (1961) 216.
- ^[0] V.A. Ageev et al., Yad. Fiz., 1987, 46 (1987) 700.
- B.Ya. Guzhovskij, S.N. Abramovich, A.G. Zvenigorodskij et al., Proc. of the International Conference on Nuclear Data for Science and Technology, September 26 October 1, 2004, Santa Fe, USA, p. 350.
- ² C. Brunn, G.N. Simonoff, Phys. Rev., 23 (1962) 12.
- W.W. Meinke, G.C. Wick, G.T. Seaborg, Journ. Inorg. Chem. 3 (1956) 69.
- A. Tewes, Phys. Rev. 98 (1955) 29.

- [65] L. Bonneau, P. Quentin and D. Samscen, Eur. Phys. J. A 21 (2004) 391.
- [66] T. Ohtsuki, H. Nakahara and Y. Nagame, Phys. Rev. C 48 (1993) 1667.
- [67] V.M. Maslov, M. Baba, A. Hasegawa, et al., Proc. of the International Conference on Nuclear Data for Science and Technology, May 9-13, 1994, Gatlinburg, USA, p. 390.
- [68] I.F. Croall and J.G. Cunninghame, Nucl. Phys. A125, 402 (1969).
- [69] J. Weber et al., Phys. Rev. C 13 (1976) 2413.
- [70] A. Gavron, H.C. Britt, P.D. Goldstone, J.B. Wilhelmy and S.E. Larsson, Phys. Rev. Lett. 38 (1977) 1457.
- [71] H. J. Specht, Nukleonika. 20 (1975) 717.

Total and partial cross-sections of Nb in the energy region from 10 eV to 200 keV

Zh.V. Mezentseva Joint Institute for Nuclear Research, 141980, Dubna, Russia

Yu.V. Grigoriev, V.V. Sinitsa Institute of Physics and Power Engineering, 249020, Obninsk, Russia

H. Faikov-Stanczyk

Lodz University, 90236, Lodz, Poland

Abstract

Neutron total transmissions and self-indication functions for natural Nb have been measured at the 1000 m flight path of the IBR-30 using the neutron detector with a battery of ³He counters. For this purpose metal disks of Nb with different thicknesses and 80 mm diameter have been used. Total group cross-sections, their self-shielding factors and self-shielding factors in scattering cross-sections have been obtained by means of the subgroup parameters in the energy range from 10 eV to 200 keV. The experimental uncertainties are approximately 2-30%.

Also measurements of time-of-flight spectra from 1st to 15th multiplicities have been carried out at 500 m flight path of the IBR-30. After a subtraction of background components and an usage of ²³⁸U like a "standard" radiadite capture cross-sections for natural Nb have been determined.

Analogous values have been calculated by the GRUCON code on the basis of BROND-2, ENDF/B-6.7, JENDL-3.2 and JEF-2.2 evaluated data libraries.

1 Introduction

The multigroup method is used for a calculation of reactor systems. In this case the investigated energy region of neutrons is divided into some energetic intervals [1]. Neutrons with energy range under study are combined into one energetic group.

Interactions of different groups of neutrons with a medium are characterized by a set of group constants. The most important ones are the average group effective cross-sections and of other nuclear values. These values are averaged over a neutron spectrum in the resonance energy region in the approach of constant collision density of neutron with a nucleus and of an isotropic scattering.

The Fermi spectrum smoothed over resonances for all energy groups was chosen as the "standard" spectrum: $\phi_0(E)$ =const. Then an averaging over the "standard" spectrum might be presented as:

$$\langle a \rangle = \frac{\int_{E_1}^{E_2} a(E)\phi_0 dE}{\int_{E_1}^{E_2} \phi_0 dE} = \frac{\int_{E_1}^{E_2} a(E) dE}{\int_{E_1}^{E_2} dE}$$
 (1)

The macroscopic cross-sections of the medium should be averaged and not the microscopic cross-sections of separate elements or isotopes which are part of the medium. In such approach group cross-sections of separate elements are determined as a function of a sum of the total cross-sections of all other elements included in the medium (σ_0) . Then group cross-sections are expressed in terms of σ_0 :

$$\sigma_x(\sigma_0) = \frac{\frac{\langle \sigma_x}{\sigma_t + \sigma_0 \rangle}}{\frac{1}{\langle \sigma_t + \sigma_0 \rangle}} \tag{2}$$

$$\sigma_t(\sigma_0) = \frac{\frac{1}{\langle \sigma_t + \sigma_0 \rangle}}{\frac{1}{\langle \sigma_t + \sigma_0 \rangle^2}} - \sigma_0, \tag{3}$$

where: σ_t – effective total cross-section of investigated isotope depending on the energy; σ_0 – constant, which does not depend on the energy, x = c (capture), s (scattering), f (fission).

The values appearing in the expressions (2) and (3) are expressed in terms of the integrals of the transmission functions $T_t(n, E, \eta)$ and of the self-shielding functions $T_x(n, E, \eta)$:

$$\langle \sigma_x/(\sigma_t + \sigma_0) \rangle = \langle \sigma_x \rangle \int T_x(n)e^{-\sigma n}dn$$
 (4)

$$\frac{1}{\langle \sigma_t + \sigma_0 \rangle} = \int T_t(n)e^{-\sigma n}dn \tag{5}$$

$$\frac{1}{\langle \sigma_t + \sigma_0 \rangle^2} = \int n \times T_t(n) e^{-\sigma n} dn, \tag{6}$$

where transmissions and self-shielding functions can be presented by following formulas:

$$T_t(n) = \frac{1}{\Delta E} \int e^{-\sigma n} dE \tag{7}$$

$$T_x(n) = \frac{\int \sigma_x e^{-\sigma n} dE}{\int \sigma_x dE} \tag{8}$$

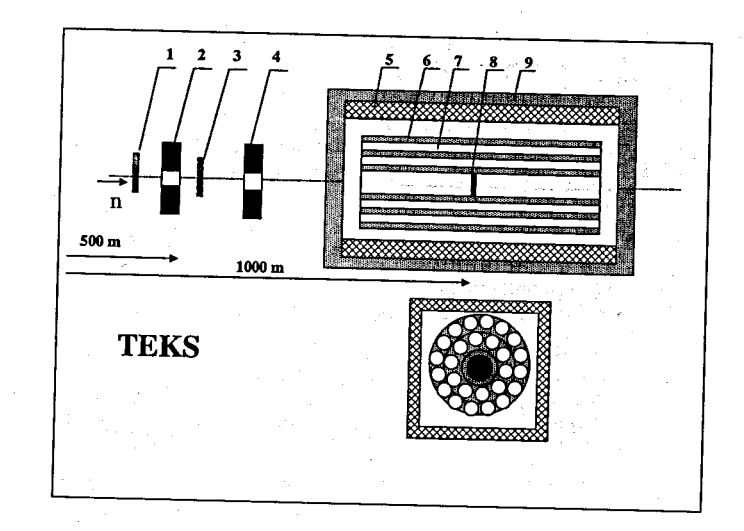


Figure 1: The experimental setup "TEKS" and a system of resonance filters and collimators: 1 – resonance filter, 2, 4 – collimators, 3 – filter-sample, 5 – shielding: paraffin + B_4 C, 6 – neutron counters, 7 – plexiglass, 8 – radiator-sample from Pb (or from investigated material), 9 – cadmium sheet.

The correction factors should be used in the determination of group cross-sections for a medium with intermediate values of σ_0 . These correction factors are called self-shielding factors.

$$f_x(\sigma_0) = \frac{\bar{\sigma}_x(\sigma_0)}{\bar{\sigma}_x(\infty)} = \frac{\langle \sigma_x/\sigma_t + \sigma_0 \rangle}{\frac{1}{\langle \sigma_t + \sigma_0 \rangle}} \times \frac{1}{\langle \sigma_x \rangle}$$
(9)

$$f_t(\sigma_0) = \frac{\bar{\sigma}_t(\sigma_0)}{\bar{\sigma}_t(\infty)} = \left[\frac{\frac{1}{\langle \sigma_t + \sigma_0 \rangle}}{\frac{1}{\langle \sigma_t + \sigma_0 \rangle^2}} - \sigma_0\right] \times \frac{1}{\langle \sigma_t \rangle},\tag{10}$$

2 The experimental setups

Measurements of time-of-flight spectra for the determination of transmission functions and neutron cross-sections have been carried out using the "ROMASHKA" [2] and "TEKS" setups on the flight paths of the IBR-30.

The "TEKS" setup is a neutron detector consisting of a cylindrical battery with 26 3 He counters. Counters are located on two circles into throughout channels of a cylinder made of plexiglass and are combined into 8 sections (3-4 counters in each section). Such geometry allows the corporeal angle of 2π . All surface of the cylindrical detector's frame

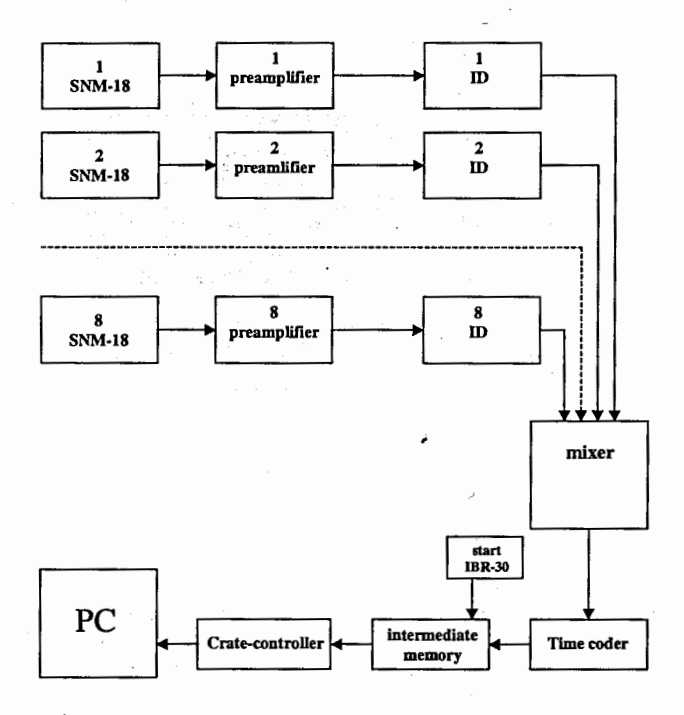


Figure 2: The electronic block-scheme of the "TEKS" setup.

are covered by a cadmium sheet with a thickness of 1 mm in order to reduce background components from thermal neutrons. Owing to the moderator the neutron registration efficiency is approximately 6 % in the broad energy region.

The neutron detector was placed on the 1000 m flight path of the IBR-30 during measurements (see Figure 1). Plates from a mixture of paraffin and boron carbide were installed around the detector setup to remove background components from neutrons scattered in the experimental room. More detailed information about the detector and its characteristics is presented in paper [3].

Total transmissions have been measured when the scatter looks like a disk from metal lead or another material contained carbon (with a thickness of 5 mm and with a diameter of 50 mm) was placed in the center of the detector setup. A thin radiator-sample from an investigated material was fixed into the neutron detector to measure self-shielding functions in scattering cross-sections.

The electronic apparatus of the "TEKS" setup consists of 8 channels (see Figure2). Each section is connected to an independent spectrometric channel including preamplifier, amplifier and discriminator to form standard signals. Then signals from 8 channels are mixed in the standard mixer and enter to the multiplicity coincidence coder, time coder and storage device into a measurement module with a PC. This schematic connection

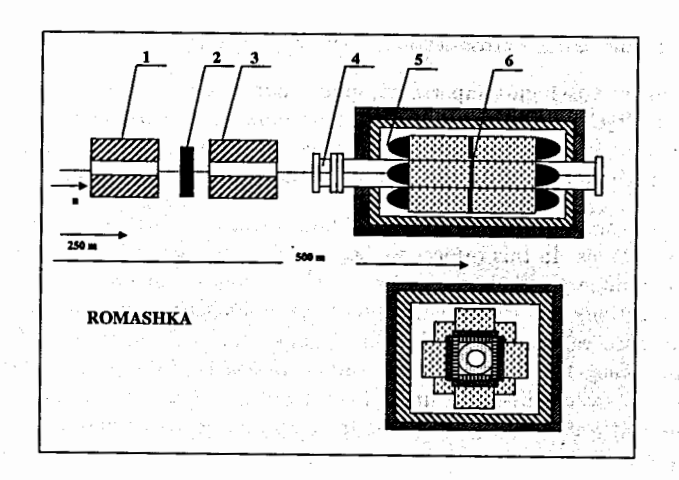


Figure 3: The scheme of the experiment using setup with NaI(Tl) crystals: 1 and 3 – collimators, 2 –filter to remove background recycled neutrons, 4 – vacuum tube, 5 – scintillation detector with NaI(Tl) crystals, 6 – radiator-sample of Nb (or ²³⁸U).

allows two regimes of the information storage: integral from all detector and differential from each section.

To determine scattering cross-sections and self-shielding functions in scattering cross-sections we used thin metal radiator-sample of Nb (with a diameter of 50 mm and with a thickness of 0.0052 at/b) at the 100 % abundance of Nb.

Also in order to obtain radiative capture cross-sections a metal disk of Nb (0.00743 at/b) was used like radiator-sample on the detector setup with NaI(Tl) crystals (see Figure 3. Plates with thicknesses from 0.1 mm to 1.5 mm and with a diameter of 50 mm or 80 mm served as filter-samples to determine the total cross-sections. Powder of U_3O_8 (99.9 % of ²³⁸U) with a weight of 3.86 g (0.000498 at/b) and a metal disk of U238 (0.00121 at/b) with a diameter of 80 mm and with a thickness of 0.25 mm were the "standard" radiator.

The IBR-30 power was monitored using two ³He counters placed at the distance of 70 m from the reactor. To reduce background recycled neutrons a filter from B4C (10 mm thickness) was positioned in the beam. To determine background components in time-of-flight spectra resonance filters from Mn, Co and Al were installed in the beam.

3 Analysis and some experimental results

Application and fabrication of Nb has quickly increased during last years. That is caused by a combination of its properties such as

1. refractoriness,

- 2. relatively low capture cross-section of thermal neutrons.
- 3. ability to produce high-temperature, superconductive and other alloys. For example, alloys of Nb_2O_5 , zirconium carbide and uranium (235) carbide are very important constructional material for solid-phase fuel elements of nuclear reactive engines. Alloys of Nb and Ta or Zr are applied for the design of superconductive solenoids.

Neutron nuclear constants of Nb should be investigated further, especially radiative capture cross-sections. In this respect we have carried out measurements of time-of-flight spectra to determine transmission functions (T_t) , group total cross-sections, radiative capture cross-sections and self-shielding functions in scattering cross-sections (T_s) .

To define these values some background components were subtracted from time-of-flight spectra. Then the compression according to the BNAB constant system [1] was done $(ln\frac{E_1}{E_2})=0.77$, where E_1 -upper limit of the investigated interval, E_2 -lower one). Total transmissions and self-shielding functions in scattering cross-sections were obtained by the following way:

$$T_t(n, E, \theta)^{theor} = \frac{\int_{\Delta E} \varphi(E) \times \epsilon(E) \times exp((-\sigma(E, \theta) \times n) \times dE}{\int_{\Delta E} \varphi(E) \times \epsilon(E) \times dE},$$
(11)

$$T_x(n, E, \theta) = \frac{\int_{\Delta E} \varphi(E) \times \sigma_x(E, \theta)_x \times exp((-\sigma(E, \theta) \times n) \times dE}{\int_{\Delta E} \varphi(E) \times \sigma_x(E, \theta)_x \times dE}$$
(12)

Observed total cross-sections and their errors were defined from total transmissions like:

$$\sigma_t^{ob} = \frac{-lnT_t}{n} \tag{13}$$

$$\frac{\Delta_{T_t}}{T_t} = \sqrt{(\frac{\Delta_{T_s}}{T_s})^2 + (\frac{\Delta_{T_{o/b}}}{T_{o/b}})^2}$$
 (14)

$$\frac{\Delta_{\sigma_t^{exp}}}{\sigma_t} = \sqrt{\frac{1 - \Delta T_t^2}{n \times T_t}},\tag{15}$$

where $\varphi(E)$ – neutron flux, $\epsilon(E)$ – detector efficiency, σ_t – total cross-sections, n – sample thickness, E – neutron energy, θ – temperature of the filter-sample, σ_t^{ob} – observed total cross-section, σ_x – partial cross-section, o/b – opened beam.

Further total transmissions and self-shielding functions were approximated by a sum of exponential functions in conformity with the subsets method developed by M.N. Nikolaev [4]. This method is used to estimate some effects of resonance self-shielding in the energy region of unresolved levels. Then the resonance structure of different cross-sections

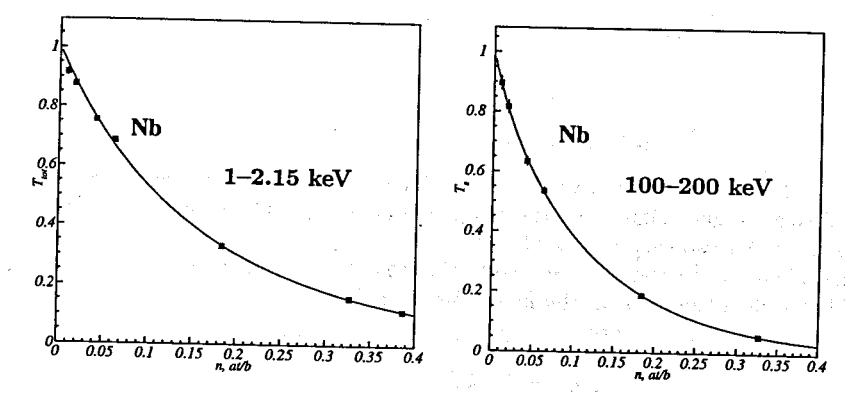


Figure 4: Approximation of total transmissions of Nb: $f(x) = par(1) * e^{-n*par(2)} + (1 - par(1)) * e^{-n*par(3)}$.

into one group is simulated by the step function $\langle \sigma \rangle = \sum_k a_k(\sigma_k)$, and the averaged transmission is simulated by a sum of exponents $\langle e^{-n\sigma} \rangle = \sum_k e^{-n\sigma_k}$.

In such approach whatever averaged into group functional of the cross-section $F(\sigma_k)$ are presented like $\langle F(\sigma) \rangle = \sum_k a_k F(\sigma_k)$. It is necessary to set the subgroup parameters a_k , σ_k to find this functional.

But the question about a physical sense of the subgroup parameters, about a possibility of their prediction using averaged into group transmissions and other integral experiments is kept opened.

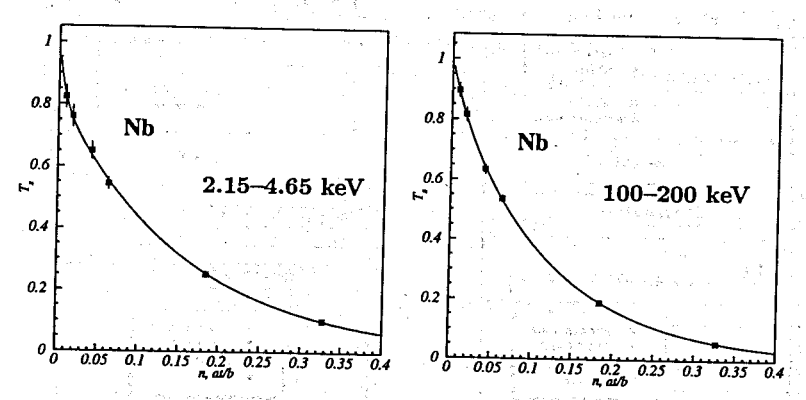


Figure 5: Approximation of self-shielding functions: $f(x) = par(1) * exp^{-n*par(2)} + (1 - par(1)) * exp^{-n*par(3)}$.

Usually, two exponential functions are enough to describe transmissions and self-shielding functions. Figure 4 shows the fitting result of total transmissions.

$$T_t(n) = a_{t1} \times e^{-\sigma_{t1} \times n} + (1 - a_{t1}) \times e^{-\sigma_{t2} \times n}$$
(16)

$$T_{tx}(n) = a_{tx1} \times exp(-\sigma_{tx1} \times n) + a_{tx2} \times exp(-\sigma_{tx2} \times n)$$
(17)

The self-shielding function was fitted similar in a similar way to the fitting of total transmissions. Figure 5 illustrates the fitting result of self-shielding functions in scattering cross-sections for two energy intervals.

The subgroup parameters were used further to determine the real total cross-sections and self-shielding factors in scattering cross-section.

$$\langle \sigma_t \rangle = a_{t1} \times \sigma_{t1} + a_{t2} \times \sigma_{t2} \tag{18}$$

$$\langle \sigma_{tx} \rangle = a_{tx1} \times \sigma_{tx1} + a_{tx2} \times \sigma_{tx2}, \tag{19}$$

where: a_{t1} , a_{tx1} , $a_{t2} = 1 - a_{t1}$, $a_{tx2} = 1 - a_{tx1}$ -portions of subgroup cross-sections, σ_{t1} , σ_{t2} , σ_{t1} , σ_{t2} -cross-sections, x-possible process (c-capture, s-scattering, f-fission).

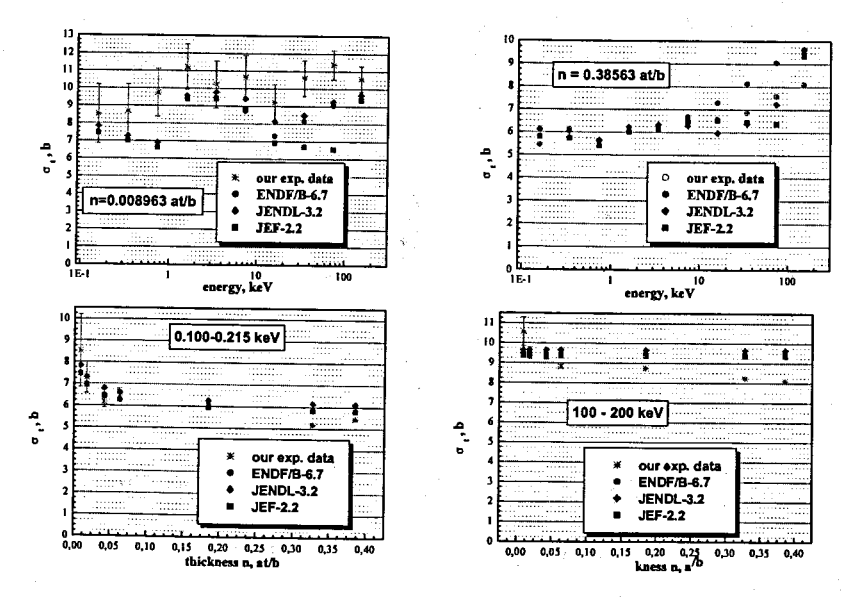


Figure 6: Observed experimental and calculated cross-sections for Nb.

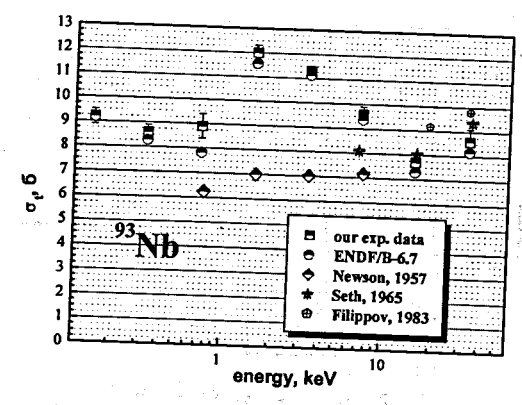


Figure 7: Real experimental total cross-sections for Nb.

Observed total cross-sections obtained from transmissions $(\frac{lnT_t}{n})$ are plotted in Figure 6. The analogous values were calculated using the GRUCON code [5] on the basis of the estimated data libraries JEF-2.2 [6], BROND [7], JENDL-3.2 [8] and ENDF/B-6.7 [9]. The experimental errors of total cross-sections are about 2-6 %. The experimental and calculated data coincide with the exception of the energy range from 10 keV to 100 keV. Especially significant difference are observed between the experimental values and calculated ones of the JEF-2.2 library (which cross-sections are 20 % less than other ones).

As it was already mentioned the total experimental transmissions and self-shielding functions in scattering cross-sections for each energy group were defined using the least-squares method by a sum of two exponents. The subgroup parameters obtained from total transmissions were used to determine group total cross-sections by the formula 18. The real cross-sections of Nb defined using the subgroup parameters are presented in Figure 7.

As it is shown our experimental values agree within the errors limit (10 %) with data of other experimentalists [10, 11] at the energy of 10 keV and higher. The big differences are observed in comparison with data of the paper [11] in the energy range from 1 keV to 10 keV.

The subgroup parameters extracted from the self-shielding functions in scattering cross-sections were used to determine the self-shielding factors in scattering cross-sections. According to the self-shielding factors determination f_t and f_x validated in paper [1] they can be written down as a ratio of areas under the curves of total transmissions and self-shielding functions or by means of the subgroup parameters.

$$f_t(\sigma_0) = \frac{\int_0^\infty T_x e^{-n\sigma_0} dn}{\int_0^\infty T(n) e^{-n\sigma_0} dn}$$
 (20)

$$f_t(\sigma_0) = \left[\frac{\frac{a_{t1}}{\sigma_{t1} + \sigma_0} + \frac{a_{t2}}{\sigma_{t2} + \sigma_0}}{\frac{a_{t1}}{(\sigma_{t1} + \sigma_0)^2} + \frac{a_{t2}}{(\sigma_{t2} + \sigma_0)^2}} - a_0 \right] \times \frac{1}{\langle \sigma_t \rangle}$$
(21)

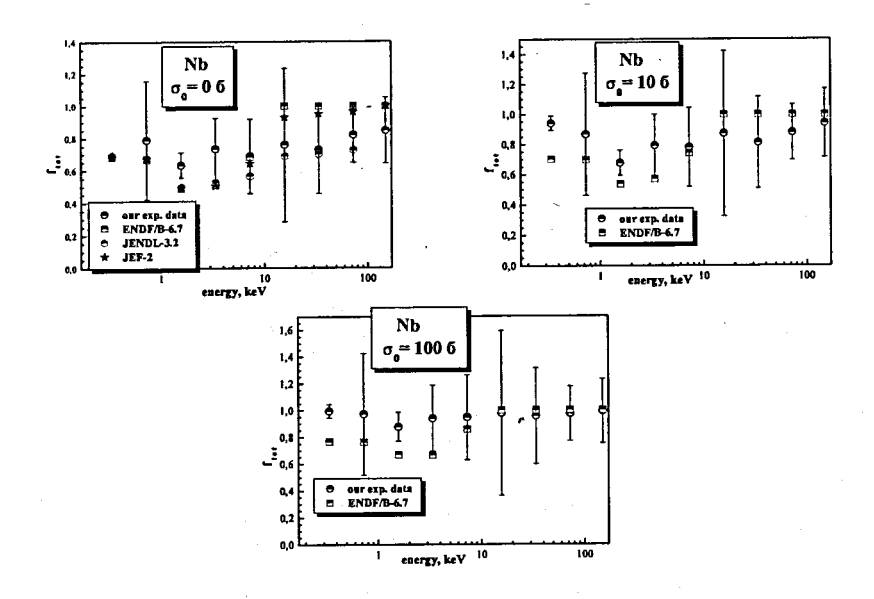


Figure 8: Resonance self-shielding factors in the total cross-sections for Nb.

$$f_x(\sigma_0) = \frac{\frac{a_{tx1}}{\sigma_{tx1} + \sigma_0} + \frac{a_{tx2}}{\sigma_{tx2} + \sigma_0}}{\frac{a_{tx1}}{(\sigma_{t1} + \sigma_0)^2} + \frac{a_{t2}}{(\sigma_{t2} + \sigma_0)^2}},$$
(22)

где: σ_0 —the total cross-sections sum of all other elements included in the medium (counting on one atom of the investigated elements or isotope).

The self-shielding factors in the total cross-sections are shown in Figure 8 for different dilution cross-sections. Also the self-shielding factors in scattering cross-sections are presented in Figure 9.

As it is shown from Figures 8, 9, stronger shielding is observed in total cross-sections and scattering cross-sections in comparison with an estimation for the region of low energy neutrons. Whereas the resonance shielding is weaker in the region of high energy neutrons. The experimental errors of the self-shielding factors are approximately 5-30 %.

In addition to the total cross-sections and self-shielding factors the radiative capture cross-sections were determined using the gamma-quanta detector. These values were defined by a normalization at the well known standard cross-sections of ²³⁸U. Then after the subtraction of background components from time-of-flight spectra and a usage of thin standard radiator-samples under investigation radiative capture cross-sections can be written down by following relation:

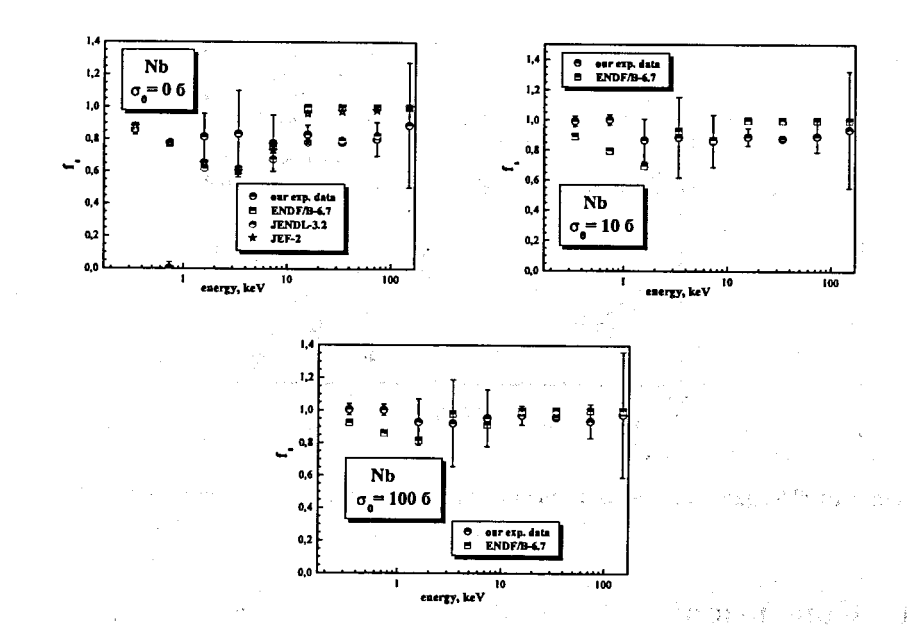


Figure 9: Resonance self-shielding factors in the scattering cross-sections for Nb.

$$<\sigma_c>^{Nb} = <\sigma_c>^U \frac{M^U \times S^U \times n^U \times N_c^{Nb}}{M^{Nb} \times S^{Nb} \times n^{Nb} \times N_c^{U}}$$
(23)

$$\Delta_{\sigma_c^{Nb}} = \sqrt{\frac{N_c^U}{N_c^{Nb}} \left[\Delta_{\sigma_c^U} + \sigma_c^U \left(\Delta_{N_c^U} N_c^U + \frac{\Delta_{N_c^{Nb}}}{N_c^{Nb}} \right) \right]}, \tag{24}$$

where M^U is M^{Nb} —monitor coefficients for ²³⁸U and Nb, S^U is S^{Nb} —areas of radiator-samples, n^U and n^{Nb} —thicknesses of radiator-samples, $\epsilon^U(E)$ and ϵ^{Nb} —registration efficiencies of γ -quanta, N_c —count per channel in the defined group.

Here it was supposed that the registration efficiencies of gamma-quanta are constant. As it is evident from Figure 10 the experimental and calculated data agree within the limit of the systematic errors. At the energy higher than 1 keV (except for the energy group 2.15-4.65 eV, where our experimental value coincides with the paper [12] the experimental data are systematically lower than the other experimental values [13, 14]

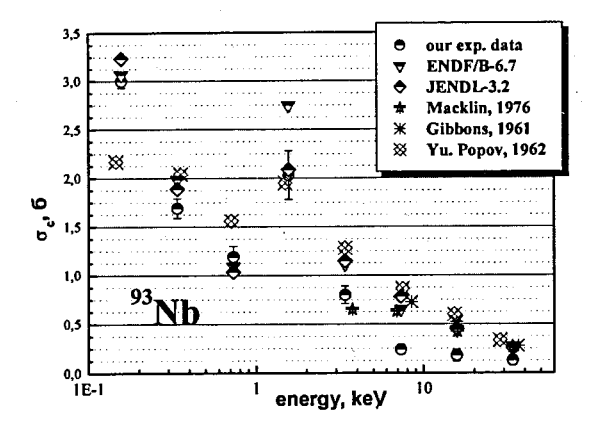


Figure 10: The experimental and calculated group radiative capture cross-sections of Nb.

4 Conclusion

The experiment has shown that stronger resonance shielding are observed in the total and scattering cross-sections for Nb in comparison with the estimated values in the high energy region (more than 10 keV). To understand this phenomenon we are planning to continue our investigation at the better energy resolution and lower background.

References

- [1] Л.П. Абагян, О.А. Базазянц, И.И. Бондаренко, М.Н. Николаев, Групповые константы для расчета ядерных реакторов, Москва, Атомиздат, 1964.
- [2] Г.В. Мурадян, Спектрометрия множественности, Нейтронная физика, т. 8, 1980.
- [3] G.P. Georgiev, Yu.V. Grigoriev et al., A setup for measuring neutron cross-sections and radiation multiplicity from neutron-nucleus interaction, *Preprint JINR P3-88-555*, 1988. // Nucl. Instr. and Meth., v.A313, p. 256, 1992.
- [4] М.Н. Николаев, В.Ф. Хохлов, Система подгрупповых констант, *Бюллетень ИЦЯД*, Атомиздат, вып. 4, с. 420, 1967.
- [5] В.В. Синица, ВАНТ. Серия: Ядерные константы, вып. 5(59), стр. 34, 1984.
- [6] JEF-2, The Evaluated Nuclear Data Library of the OECD Nuclear Agency, Report IAEA-NDS-120.

- [7] A.I. Blokhin, A.V. Ignatyuk, B.A. Kuzminov et al, Proceedings of International Conference for Science and Technology, Julich FRG, p. 800, 1991.
- [8] T. Nakagawa et al., Japanese Evaluated Nuclear Data Library vers ion 3 revision 2: JENDL-3.2, J. Nucl. Sci. Technol., 32, 1259 (1995).
- [9] P.F. Rose, C.K. Dunfort, Data Formats and Procedures for the Evaluated Nuclear Data File (ENDF), Report BNL, Upton, New York, USA, 1988
- [10] K.K Seth, R.H. Tabony, E.G. Bilpuch, H.W. Newson, Neutron Total Cross Sections and Intermidiate Resonancs, *Physical Letters*, v. 16, p. 306, 1965.
- [11] V.V. Filippov, Total Neutron Cross-Sections for some Construction Materials in the Range of Unresolved Resonances, C, Kiev, v. 3, p. 107, 1983.
- [12] Ju.P. Popov, F.L. Shapiro, Energy Dependence of Cross Sections for (N, Gamma) Reactions on a Number of Odd–Z Nuclei, ZET, v. 42(4), p. 988, 1962.
- [13] R.L. Macklin, Neutron Capture Cross Section of Niobium-93 from 2,6 to 700 keV, Nuclear Science and Engineering, v. 59, p. 12, 1976.
- [14] J.H.Gibbons, R.L. Macklin, P.D.Miller, J.H.Neiler, Average Radiative Capture Cross Sections for 7- to 170-keV Neutrons, *Physical Review*, v. 122, p. 182, 1961.

SEARCH OF ¹²Be CLUSTER STATES IN THE CHARGE EXCHANGE REACTION FOR CARBON

Skorkin V.M.

Institute for nuclear research of RAS, Moscow, Russia 117312 Moscow 60-th October Anniversary prospect 7a.

Clustering is a relatively widespread phenomenon. The study of halo systems and clustering in light, neutron-rich nuclei are discussed through illustrative examples taken from the nuclei of 6 He, 6 Li, 8 Be, 10 Be, 12 C [1-3]. The excitation of collective resonance states of light nuclei has received considerable attention recently. In the spectrum of the carbon photo-nuclear reaction can see the high excited $\mathbf{1}^-$ and $\mathbf{3}^ \alpha$ - clustered states of 12 C with isospin T=2 [4].

Cascade model of inelastic interactions of nucleons with light nuclei describes the experimental data for nucleus of 12 C at energy above 50 MeV with an account of 30% α - clusterization [5].

In processes of the clusterization of nuclear substance in light nuclei, the special role belongs to the nucleus of 8 Be. Through this condition state a lot of α - particles, as fragments of all inelastic interaction reactions, are formed [6]. The calculated probabilities of formation of the 8 Be nuclei at the fragmentation of the relativistic nuclei 10 B, 12 C, 16 O equal 20%, 25%, 30% accordingly. This calculation is confirmed experiment. In α -particles spectrum were registered from the metastable states of 8 Be with even moment, positive parity and energy up to 17 MeV [4].

The nuclei of 12 C, 12 B, 12 Be have double analoges states with isospin T=2 (fig.1). Therefore nucleus of 12 Be should be has the high excited α - clustered states.

		12C
		0.0 0+ T=0
	12B	
	0.0 1+	15.1 1+ ———————————————————————————————————
12Be		, , , , , ,
0.0 0+	12.7 0+	27.6 0+ T=2
2.1 2+	14.8 2+	29.7
2.7 2.1 2+	15.5	30.3 T=2
		31.2
4.6		32.3
5.7		33.5
<u>9.1</u>	21.8 3-	36.7 (T=2)
11.2	<u>23.9 1-</u>	38.8

Fig. 1. Double analoges states of the nuclei of ¹²C, ¹²B, ¹²Be,

The nuclei of ¹²Be* can decay through formation of the ⁸Be nuclei and multineutron cluster 4n.

In a recently reported experiment [7] events were observed that exhibit the characteristics of a multineutron cluster liberated in the breakup of 14 Be, most probably in the channel 10 Be+4n. The nucleus 10 Be is strongly bound and the four neutron separation energy for 14 Be is only about 5 MeV with respect to the 14 Be \rightarrow 10 Be + 4n breakup.

The technique is based on the breakup of beams of very neutron-rich nuclei and the subsequent detection of the recoiling proton in a liquid scintillator. The method has been tested in the breakup of intermediate energy ~30–50 MeV/nucleon ¹¹Li, ¹⁴Be, and ¹⁵B beams. Some six events were observed that exhibit the characteristics of a multineutron cluster liberated in the breakup of ¹⁴Be, most probably in the channel ¹⁰Be+ 4n. The lifetime of order 100 ns or longer suggested by this measurement, would indicate that the tetraneutron is particle stable. Alternative experiments such as (⁶He,4n) and (⁸He,4n) are proposed to search for the tetraneutron [8-9].

It is pointed out that from the theoretical perspective the two-body nucleon-nucleon force cannot by itself bind four neutrons, even if it can bind a dineutron [10].

The energy behaviour of the eigen phases, studied in Ref. [11] within the hyperspherical functions method (HSFM), led the authors to the conclusion that the tetraneutron may exist as a resonance in the four-body continuum at an energy of about 1-3 MeV (fig. 2). Nuclear Hamiltonians that provide a good description

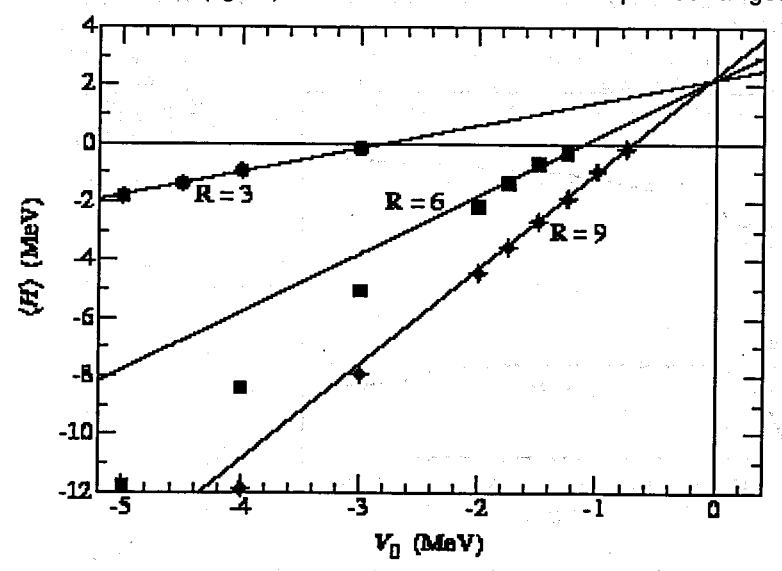


Fig. 2. Energies of 4n in external wells versus the well-depth parameter V_0 .

of nuclei up to A=10 and accurate Green's function Monte Carlo calculations by using the Argonne potential (AV18) and including two- and three-pion exchange *NNN* potentials. A series of model Hamiltonians (the Illinois models) were constructed that reproduce energies for A=3-10 nuclei with errors of 0.6–1.0 MeV.

In this work is presented search of 12 Be clustered states in the charge exchange reaction 13 C(n, 2p) 12 Be $^{\circ}$. The nuclei of 12 C and 12 Be have double analoges lower states and therefore 12 C* and 12 Be* should be has the a similar α - clustered structure high excited clustered states. The α - particle separation energy for 12 Be and 12 C and is 8.93 MeV and 7.37 MeV accordingly. The 12 Be is magic nucleus. The neutron separation energy for 12 Be and 13 Be and is 3.17 MeV and -0.51 MeV accordingly. The neutron separation energy for 8 He and 9 He is and 2.57 MeV and -0.1 MeV accordingly. The proton separation energy for 8 He and 9 Be and 12 Be is $^{\sim}$ 20 MeV with distinction only about 15%. There is a similar α - clustered structure of the 8 He, 8 Be and 12 Be. In the excited states spectrum of 12 Be should be the high excited α - clustered states of 8 He and 8 B with energy up to 30 MeV. In the excited states spectrum of 8 He is states 7 =3 $^{-}$ with energy above 7 MeV.

The reaction 13 C(n, 2p) 12 Be is quasi-elastic knockout 2p out of $1p_{3/2}$ subshell. The cross sections of the 13 C(n, 2p) 12 Be reaction equals 1mb [12] (fig. 3). The 13 C(n, p)X is background reaction.

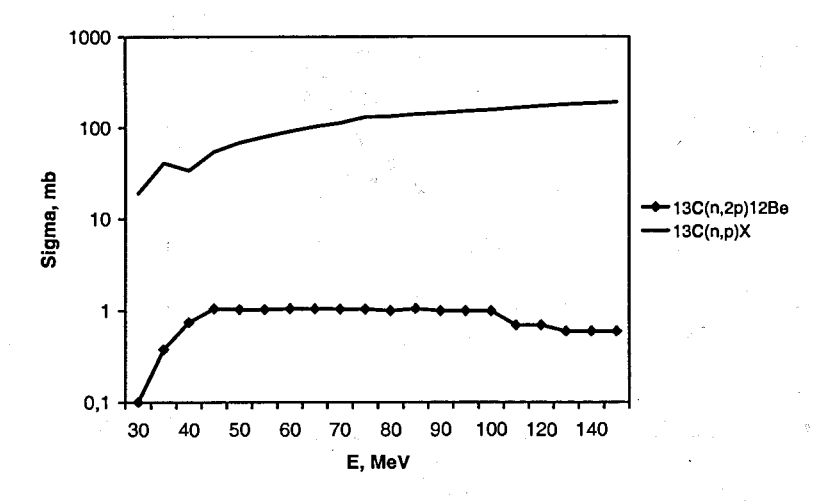


Fig. 3. The cross sections of the ${}^{13}C(n, 2p){}^{12}Be$ and ${}^{13}C(n, p)X$ reactions [12].

The yield energy of the 13 C(n, 2p) 12 Be reaction is ≈ 25 MeV. The four neutron separation energy for 12 Be is ~ 10 MeV. Therefore neutron energy should be above 40 MeV for 12 Be* $\rightarrow ^8$ Be + 4n breakup observation. Excitation energy of 12 Be* should be above 10 MeV at neutron energy about 50 MeV. The cross sections of the 13 C(n, p)X reaction equals 70 mb at energy about 50 MeV.

The 13 C(n, 2p) 12 Be * spectrum at (10-20) $^{\circ}$ has the prominent transition to the analog of excited states. In the 15 $^{\circ}$ spectrum of 13 C(n, 2p) 12 Be * can be observed the

In this work we present registration of 2p from ¹³C(n, 2p)¹²Be* reaction and & decay of the excited clustered states of ¹²Be*. Impulse neutron source (intensity up to 10¹⁵ n/s) used for these studies is based on the proton Linac and the RADEX

Beam Stop. The proton beam (average current up to 100 μ A, energy above 300 MeV and beam pulse repetition rate up to 100 Hz) irradiate tungsten target of the RADEX Beam Stop. The neutron beam is obtained from spallation reaction at 0°, collimated over a 10 m flight path into a scattering chamber. The spectrum of the impulse neutron source has maximum about 50 MeV. The fast neutron flux on target (over 5 cm wide by 5 cm high) is above $10^7 \, n \, \text{cm}^{-2} \, \text{s}^{-1}$. The target used for irradiation are carbon disk (90% 13 C) , 1 g mass.

Scattered charged particles are detected in ΔE -E telescopes with ΔE being measured in Si surface barrier detectors and E in Nal detectors. Three parameters E, ΔE and time-of-flight (TOF) for each telescope are stored event-by-event. TOF and ΔE -E telescopes are used to select events registration of p, 2p and other charge particles. Energy resolution is ~1MeV.

The yield of the 13 C(n, 2p) 12 Be * reaction is about 2 decay/pulse for the proton beam with current up to 50 μ A and beam pulse repetition rate 50 Hz. The nuclei yield of the 12 Be, 12 B and 13 B in the 13 C(n, 2p) 12 Be * , 13 C(n, np) 12 B and 13 C(n, p) 13 B reactions is shown in fig.4.

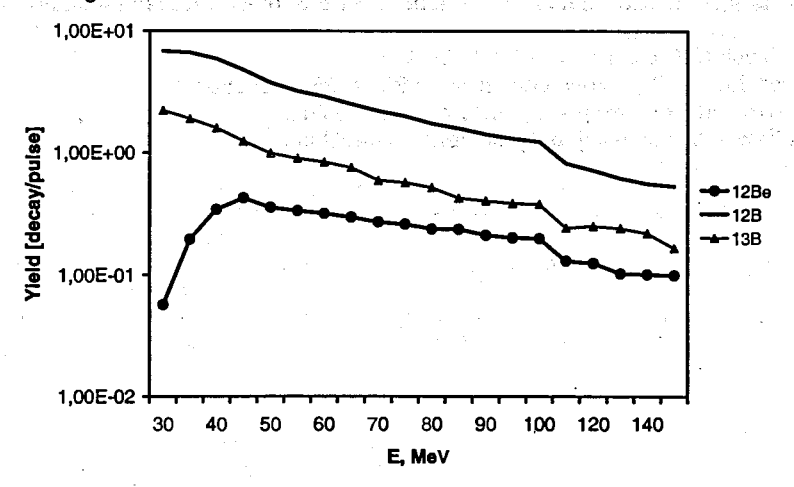


Fig. 4. The yield of ¹²Be, ¹²B and ¹³B.

The ¹²Be, ¹²B and ¹³B have a half-life of 21 ms, 20 ms and 17 ms accordingly. The nucleus of ¹²B decay into 3α - particles (1.5%). This is background for α - particles registration from for ¹²Be* \rightarrow 2 α + 4n breakup.

The yield of multineutron cluster 4n is 0.05 4n/pulse on the assumption 1% probability of the $^{12}\text{Be}^{\star} \to ^{8}\text{Be} + 4n$ reaction. α -particles from $^{12}\text{Be}^{\star}$ decay should be detected between beam pulses. Count rate is $\sim 1\text{s}^{-1}$. α -particles and multineutron cluster are detected in a liquid or plastic scintillator.

REFERENCES

- 1. Orr N.A. // The European Physical Journal A. 2002. V.15, N.1-2, P.109.
- Belaga V.V., Chernov G.M. and Vuminov M.M. // Jr. Phys. At. Nucl. 1997. V.60. P.791.
- 3. Adamovich M.I., Bradnova V.I., Vokal S. et al // Yad. Fiz. 2004. V.67, N.3, P.1.
- 4. Kurgalin S.D., Tshuvil'sky Yu.M. // J. Phys. G. Nucl. Part. Phys. 1999.V.25. P.929. Vestnik VGU. Ser. Fiz. 2001. N.2. P. 25.
- 5. Preprint JINR P2-5991 (1971)
- 6. Lepekhin F.G. // Fiz. El. Chast. At. Yad. 2005. V.36.Vyp. 2. P.436.
- 7. Marques F.M. et al// Phys. Rev. C65. 2002. P. 044006.
- 8. Suzuki Y. et al // Nucl. Phys. A. 2002. V.706. P.123.
- Belovitskii G. E., Zavarzina V.P., Konobeevskii E.S. et al// Preprint FIAN. 2003. N.17.
- 10. Timofeyuk N.K. // J. Phys. 2003. G 29. L.9.
- 11. Pieper S.C. // Phys. Rev. Lett. 2003. V.90. N.25, P.252501-1.
- 12. http://wwwndc.tokai-sc.jaea.go.jp/ftpnd/sae/acl.html.
- 13. http://wwwndc.tokai-sc.jaea.go.jp/ftpnd/sae/acl.html

APPLICATION OF AN ELECTRON LINAC OF THE IREN FACILITY FOR MULTIELEMENTAL PHOTON ACTIVATION ANALYSIS AND PRODUCTION OF RADIONUCLIDES

Baljinnyam N.¹, Belov A.G.², Ganbold G.³, Gangrskii Yu.P.², Gerbish Sh.¹, Maslov O.D.², Shvetsov V.N.¹

¹ – Frank Laboratory of Neutron Physics, JINR Dubna, Russia
² – Flerov Laboratory of Nuclear Reaction, JINR Dubna, Russia
³ – Nuclear Research Center of NUM. Ulan-Bator, Mongolia

Abstract.

The possibility to develop multielemental activation analysis and production of some radionuclides widely used for the nuclear medicine, radiobiology and ecology monitoring at the linear electron accelerator (E_{e^-} =200 MeV) of the facility IREN (FLNP, JINR) are considered.

Based on the experimental data obtained at low energy (E_e -<30 M₃B) electron accelerators as well as the microtron MT-25 (FLNR, JINR) with the power 0.5 kW, are estimated photonuclear reaction yields for some radionuclides for the linear electron accelerator (E_e - = 200 MeV).

Technical parameter of the linac will be as follow as:

the electron beam current 3A in 100 – 250 nanosecond impulse and frequency 50 or 150Hz, that means the electron beam power -1.5 kW in the target. Expected photonuclear reaction yields for some radionuclides are calculated from the experimental data of the microtron MT-25 (FLNR, JINR).

Keywords: linear electron accelerator; photo nuclear reaction; yields of radionuclides; specific activity; bremsstrahlung target; multielemental photon activation analysis.

Introduction

The project of the new Intense Resonance Neutron pulsed source (IREN) for fundamental and applied nuclear physics is being realized in JINR, Dubna [1]. This source is an upgraded variant of the existing IBR-30 pulsed booster and consists of the 200 MeV electron linac. W.I.FURMAN has presented first "Current status of the IREN project" in ISINN-5, 1997, Dubna [2].

At last, this project has been released after 10 years and is expected to be obtain the electron beam in the first part of 2008.

This presentation will try to give some information on the possibility of application of the Bremsstrahlung beam of the LEA - 200 linac of the IREN facility.

Accelerators

The methods of multielemental photon activation analysis (MPAA) and radionuclide production will be developed at the LEA-200 of the IREN facility, FLNP JINR.

Some technical characteristics of the LEA-200 are as follows:

- Maximum Energy of Electrons 100 MeV after the 1st modulator;
- And 200 MeV after the 2nd modulator:

- Peak current
- 3 A;
- Pulse frequency
- -50 or 150 Hz;
- Electron burst width (FWHM) 100 or 250 ns.

A water cooled platinum or tungsten target has been used for the Bremsstrahlung converter. The proposed construction of scheme of the Linac Bremsstrahlung target of the IREN facility, which must be constructed in FLNP JINR, is shown in Fig. 1.

The temperature on the surface of the Pt or W disk of the target must be lower than ~900 °C [3].

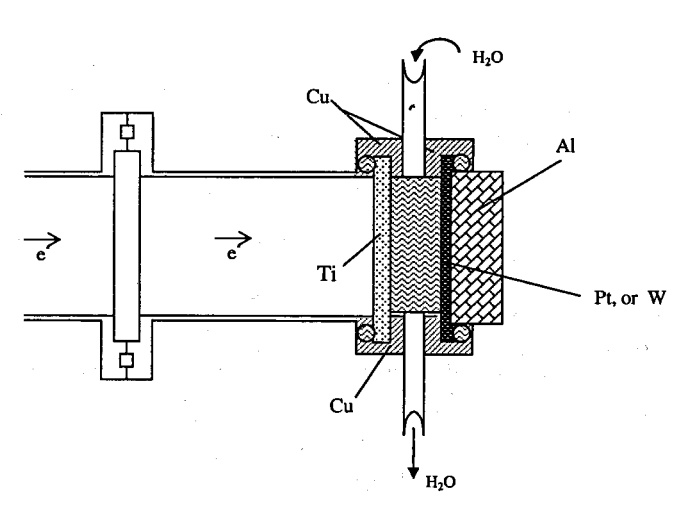


Fig.1. Proposed scheme of a Linac's Bremsstrahlung target of the IREN.

The preliminary methodical investigation was carried out on the cyclic electron accelerator Microtron MT-25 of FLNR, JINR. The Microtron MT-25 was used as the bremsstrahlung source to determine the experimental photonuclear reaction specific activities and yields.

The 0.5 kW power irradiation targets of the Microtron MT-25 were operated with the electron beam -15 μ A current and 23.5 MeV energies. The results of methodical study are given in the present work.

1. POSSIBILITY OF TIN-117m PRODUCTION

At present the requirements for an acceptable radionuclide are still considerably high. The nuclear reactors and cyclotrons are mainly used for the radionuclide production [4,5].

However, they are not able to produce all the required types of radionuclides, therefore, electron accelerators such as Linac and Microtron, that can produce radionuclides using the bremsstrahlung, are suitable complements [6-9].

Properties of the radionuclide ^{117m}Sn are acceptable for clinical and therapeutic use: the short half-life of 13.6 days is necessary to minimize the patient exposure, the gamma emission of 158.4 keV (84 %) photons for imaging, and low energy (127-129, 152 keV). Auger and conversion electrons with abundance (116 %) for delivering a high radiation dose to sites of a bony metastatic disease [4,5].

1.1. EXPERIMENTAL

To estimate the activity and yield of the ^{117m}Sn production, the natural pure tin (0.7677 and 0.1635 g) and enriched ¹¹⁸Sn (98.5 %) isotope (30.4 mg) have been irradiated at the Microtron MT-25 in Dubna, FLNR, JINR by the bremsstrahlung beam of 23.5 MeV with the current of 14.5 µA during several hours at the radial distance of 6 cm from the tungsten (3 mm thick) target. For determination of photonuclear reaction yields of Sn isotopes two experiments have been carried out: the 1st one-the samples are pure Sn granules (0.767 g) and pure gold foil monitors (Au1-1.8mg; Au2 - 2.1 mg; Au3 - 3.2 mg and Au4 - 2.5 mg); the 2nd one - the samples are pure Sn granules (0.1635 g), enriched ¹¹⁸Sn (98.5 %) isotope (30.4 mg), pure gold foil monitors (Au1a - 3.4 mg; Au 2a - 3.9 mg; Au 3a - 4.0 mg; Au 4a -3.6 mg), pure Zr foils (Zr 1-5.9 mg; Zr 2-5.0 mg) and pure Mo foils (Mo 3-6.1 mg; Mo 4 - 5.4 mg).

Activity of the irradiated natural tin, ¹¹⁸Sn enriched samples and monitors were measured by HP Ge detectors of the gamma spectrometer of FLNP, JINR with the energy resolution of 2 keV at gamma lines of 1332 keV for Co - 60. To monitor the flux for bremsstrahlung of electron energies of 23.5 MeV with the current of 14.5 μA, pure metal foils of Au, Zr and Mo have been used. Gamma lines of the radionuclide, which must be detected from samples and monitors have been given in Table 1 and level scheme of the simple energy of ^{117m}Sn has been shown in Fig.2. From the decay scheme one can see that ^{117m}Sn is not a beta emitter; it decays by isomeric transition with the emission of abundance (116 %) of conversion electrons (M4) and the gamma line (M1) of 158.4 keV (84 %). The radionuclide of this class is therapeutically and diagnostically useful in skeletal imaging and for the radiotherapy of bone tumors and other disorders.

From the measured gamma spectrum data the experimental photonuclear reaction activity and yield (see Fig. 3a, 3b.) have been determined for radionuclides ^{117m}Sn and ¹¹¹In. Their experimental values are shown in last columns of Table 1.

Table 1. Nuclear data of TIN Radioisotopes and experimental values of specific activities and yields.

Radi nucli and half-	ide d	Main E ₇ , keV	Inten -sity,	Reaction	Reac- tion E ₇ , MeV	Abun- dance of target, %	Specific Activity, Bq/mg	Yields, Bq/μA mg
117mg	id	158.4	84.0	¹¹⁷ Sn (γ,γ') ¹¹⁸ Sn (γ,n) ¹¹⁹ Sn (γ,2n)	-0.32 -9.65 -16.13	7.57 24.01 8.5	2.0E+4	1.0E+3
117m		158.4	84.0	¹¹⁸ Sn (γ,n)	-9.65	98.5	8.8E+4	6.0E+3
2.83		171.3 245.3	91.0 94.0	¹¹² Sn(γ,p)	-7.73	0.95	1.9E+5 2.0E+5	1.3E+4 1.4E+4

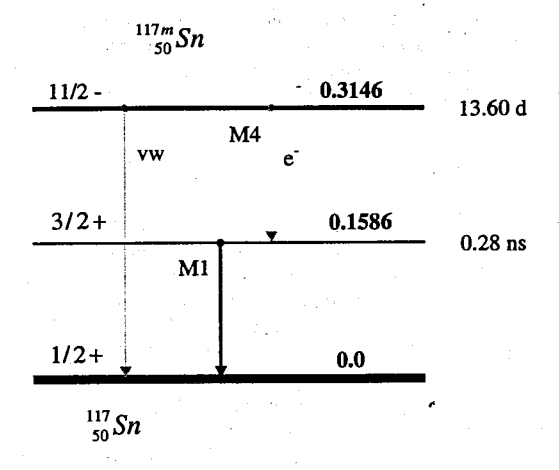


Fig. 2. The simple scheme of energy level of ^{117m}Sn.

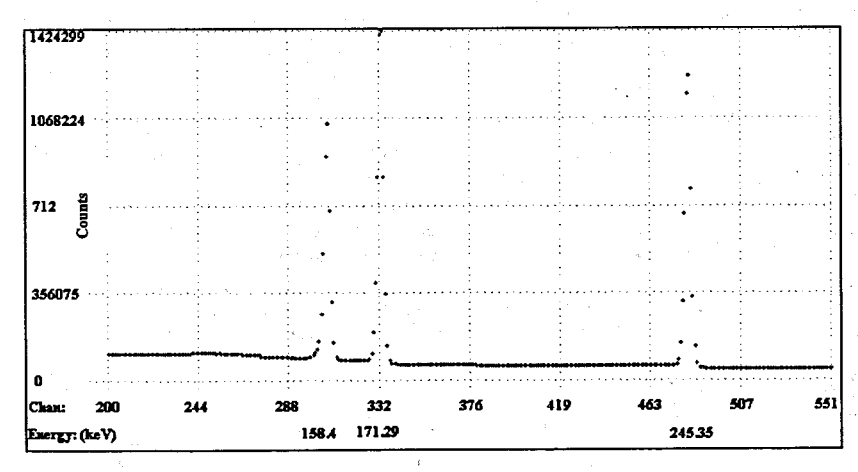


Fig. 3a. A part of radioisotope spectrum of the irradiated natural pure Sn granule (163.5 mg).

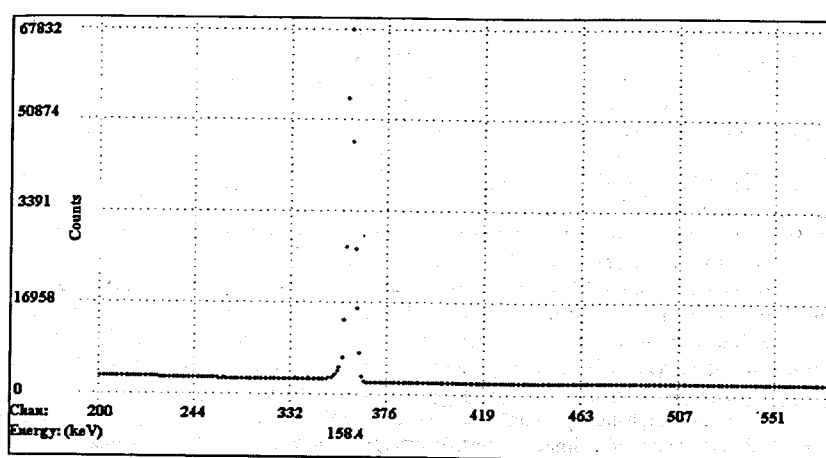


Fig. 3b. A part of radioisotope spectrum of the irradiated enriched ¹¹⁸Sn (98.5%) foil (30.4mg).

2. MULTIELEMENTAL PHOTON ACTIVATION ANALYSIS

In recent years the photon activation analysis has been explained as one of useful analytical tools for the determination of trace amounts of a number of elements in the periodic table [10-15]. The important developments are nondestructive multielemental determinations in complex matrices of current interest such as geological, biological and environmental materials. The sources of high energy photons or bremsstrahlung of the linear electron accelerators have preferably been selected for photon activation analysis and radioisotope production.

The advantages of electron accelerators are their relative cheapness, a possibility of wide-range adjustment of particle energy and intensity, and control within certain limits over the spectral and geometrical parameters of the secondary radiation (bremsstrahlung or photons and photo-neutrons). They are operated at relatively high currents and the energies of the beam are easily varied. Therefore, at present an increasing interest has been shown in the use of these facilities in different areas of nuclear technologies traditionally based on the use of reactors and heavy - particle accelerators. Sensitivities well below 1 µg are obtained for many elements, and the emphasis is put on the determination of the elements such as carbon, nitrogen, oxygen, fluorine, nickel, cadmium and lead having nuclear properties unfavourable for the thermal-neutron activation analysis.

In addition, severe difficulties due to the sample self-shielding are encountered when a mixture to be analyzed contains substantial amounts of elements with large thermal neutron capture cross-sections. In this case the photon activation analysis is found to be very promising [15-17].

A general feature of the photon absorption cross-section for a nucleus is characterized by a peak 5-6 MeV wide at an energy located between the photo-disintegration threshold and about 30 MeV, and in this energy region the main nuclear events are the emission of one neutron or one proton.

A considerable amount of work has been done in the past on the determination of the (γ,n) , (γ,p) and (γ,α) reaction yields for many elements with the bremsstrahlung produced by 20 MeV electrons.

Since the yield is a function of the photon energy, it should be noted that higher sensitivities can be expected from an accelerator giving the bremsstrahlung of higher maximum energies, however, this gives rise to more complex events.

A part from the reactions described above, those with the emission of two or more nucleons become important, thereby causing difficult interference problems in photo-activation analysis. A basic problem in the photo-activation analysis under such conditions is, therefore, the necessity to investigate the production rates or yields of various photonuclear reactions induced simultaneously in a sample to be analyzed, over the energy range of the given bremsstrahlung. It should also be mentioned that the production rates of those reactions depend on a specific target-sample configuration used for activation.

The work described here has been undertaken in order to evaluate the potential for determining trace amounts of many elements by inducing the (y,n), (y,p) and (y,α) reactions with the bremsstrahlung from the electron accelerator for the IREN facility, which is constructed in FLNP, JINR at Dubna, and by detecting the resultant activities by gamma spectrometers with the high purity (HP Ge) germanium detector.

Noble and high-purity metal analysis is still of interest and is developed using the bremsstrahlung beam of a linac to certify reference materials by Ch. Segebade et al. (J. Radioanal.Chem.Vol.49, No.1, 1979, 95-102.)

Some results of the experiments on noble and high-purity metal analysis carried out using the microtron MT-25 are given in Tables 2 and 3. The detection limits determined by L. A. Currie on microtron MT-25 are given in Fig. 4 [18].

Table 2. Results of photonuclear reaction for noble metals

Ele- ments	Reaction	Half-life	Energy, keV	Yields, (Bq/μΑ mg)	Sensiti- vity, µg	
	⁹⁸ Ru (γ, n) ⁹⁷ Ru	2.88 d	215, 324	1.49E+4	0.1	
Ru	¹⁰⁴ Ru (γ, n) ¹⁰³ Ru	39.6 d	496.9, 610	9.92E+4	0.01	Mil.
	⁹⁶ Ru (γ, p) ⁹⁵ Tc	20 h	766, 948, 1074	3.72E+4	1.0	10
Rh	¹⁰³ Rh (y, 2n) ^{101m} Rh	4.3 d	306, 545	5.88E+3	10.0	ηģ.
KII	¹⁰³ Rh (γ, n) ¹⁰² Rh	206 d	475, 628, 1103	3.36E+4	1.0	
F .	¹¹⁰ Pd (γ, n) ¹⁰⁹ Pd	13.5 h	88	3.33E+4	1.0	• 1 <u>.</u> 13.
Pd	106Pd (γ, p)105Rh	35.9 h	306	5.15E+4	1.0	·Na
	¹⁰² Pd (γ, p) ^{101m} Rh	4.3 d	545	4.12E+4	1.0	dit
Δα	¹⁰⁷ Ag (γ, 2n) ¹⁰⁵ Ag	40 d	280, 344	4.98E+3	10.0	uit.
Ag	107 Ag $(\gamma, n)^{106m}$ Ag	8.5 d	450, 616, 716, 1045	3.76E+3	10.0	2.3
	¹⁹¹ Ir (γ, n) ¹⁹⁰ Ir	11 d	187, 371, 407, 518, 605	11.6E+4	0.01	
Ir	¹⁹¹ Ir (γ, n) 190nIr	3.2 h	502	11.6E+4	0.01	
	¹⁹³ Ir (γ, n) ¹⁹² Ir	74.2 d	316, 468	8.96E+4	0.01	
Os	¹⁹² Os (γ, n) ¹⁹¹ Os	15 d	129	7.64E+4	0.01	
	¹⁸⁶ Os (γ, n) ¹⁸⁵ Os	94 d	646	1.46E+4	0.1	oni - CTG
Pt	¹⁹⁶ Pt (γ, n) ^{195m} Pt	4.1 d	98, 129	1.72E+4	0.1	
Pt	¹⁹² Pt (γ, n) ¹⁹¹ Pt	3 d	409, 528	1.37E+3	1.0	đΩ
Au	¹⁹⁷ Au (γ, n) ¹⁹⁶ Au	6.18 d	333, 356	7.89E+4	0.01	18,

Table 3. Results of photonuclear reaction for some high-nurity metals

Ele- ments	Reaction	Half- life	Energy, keV	Yields, (Bq/μA mg)	Sensitivity, ppm
Cu	⁶⁵ Cu (γ, n) ⁶⁴ Cu	12.7 h	1345	3.58E+4	10.0
Zr	⁹⁰ Zr (γ, n) ⁸⁹ Zr	78.4 h	909	6.17E+4	0.1
Мо	¹⁰⁰ Mo (γ, n) ⁹⁹ Mo	66 h	140, 181	5.65E+4	1.0
Sn	¹¹⁸ Sn (γ, n) ^{117m} Sn	13.6 d	158	5.43E+3	10.0
Sii	¹¹² Sn (γ, p) ¹¹¹ In	2.83 _, d	171, 245	5.57E+4	1.0
Ta	¹⁸¹ Ta (γ, n) ^{180m} Ta	8.15 d	93, 103	6.04E+4	0.1

Fig.4. The chemical elements determined using the electron accelerator microtron MT -25 and detection limits.

				4	41 7.1 75		11.0	198 + MG 1
	es es	di par	auth sa	1			He	
			Ç	N 1.0E-7	O 1.0E-6	F 702.00	Ne	
Na	Mg 2.0E-4	A1 2.0E-5	Si 1.0E-3	P	s	Cl 1.0E-6	Ar	
K 2.0E-4	Ca 2.0E-4	- Sc - 8.0E-7	T1 1.0E-4	5.0E-6	Cr 5.0E-6	Mn 4.0E-7	Fe 1.0E-3	Co Ni 1.0E-6 1.0E-6
Cu 1.0E-5	Zn 5.0E-6	Ga 1.0E-5	Ge 1.0E-5	As 5.0E-7	Se: 1.0E-5	Br 5.0E-6	Kr	
Rb 2.0E-6	Sr 2.0E-7	Y 2.0E-7	Zr 6.0E-7	Nb 1.0E-6	Mo 1.0E-6	Te	Ru	Rh Pd 1.0E-4 4.0E-7*
1.0E-4	Cd 5.0E-6	In 1.0E-7	Sn 1.0E-5	Sb 5.0E-7	Te 1.0E-6	I 3.0E-6	Xe	
Cs 5.0E-7	Ba - 5.0E-6	La	Hf	To 5.0E-8	W 1.0E-7	Re 7.0E-7	Os 1.0E-4	lr Pt 1.0E-5 1.0E-7*
Au 2.0E-8	Hg 5.0E-7	T1 7.0E-7	Pb 2.0E-6	Bi 1.0E-6	Po	At	Rn	
Лантан	оиды		2011		1985年1	74.13		
Ce 1.0E-6	Pr 2.01		Sm 5.02-8	Eu 1.0E	Gd	Тъ Dy	Но	Er 1.0E-7, Tm Yb

Note: *- radiochemical method

Th 5.0E-8 1.0E-13*

Elements determined by track method using pho

Discussion and Conclusion

1. Results of these experiments have shown a possibility of the 117mSn radionuclide production using the bremsstrahlung of high energy electron accelerators. In case of irradiation of the natural pure tin, radioisotopes 117mSn and 111 In have been produced, which both are useful for medical purposes.

2. The experimental yield of photonuclear reaction is 6 times higher than when an enriched 118Sn (98.5 %) isotope is used in the target, and from the gamma spectrum in Fig. 3a and 3b one can see the gamma line of 158.4 keV of only one radionuclide ^{117m}Sn. The photonuclear reaction yields of the ¹¹¹In were compared with the data

determined in other works [6-8] and they have sufficient conformity.

3. The isomeric ratio of ^{117m}Sn was estimated from the experimental data of activities of 158.4 (^{117m}Sn); 391.7 (^{113m}Sn) and 1089 (¹²³Sn) keV energy gamma lines. The isomeric ratios were estimated and determined to be 0.15 and 0.44 for the radionuclides ¹¹³Sn, ¹²³Sn, correspondingly.

4. The activities and yields of the ^{117m}Sn and ¹¹¹In radionuclides will be increased at the

bremsstrahlung beam of the 100-200 MeV Linac of the IREN facility, which is

constructed in FLNP, JINR [1, 9].

5. From Tables 2 and 3 it may be concluded:

- that the activities or yields of noble and some high-purity metals will be increased at the bremsstrahlung beam of the 100-200 MeV Linac of the IREN facility;

- noble and some high-purity metals can be analyzed using high energy photons or the bremsstrahlung of LEA-200 for the certification analysis, and the sensitivity will be better than 50 times [18].

- In Table 4. has given some Radionuclides, Gamma-Ray Energies and Intensities, which are used commonly for Routine Mulielemental Instrumental Photon

Activation Analysis (MIPAA) [16,17].

Table 4. Some Radionuclides, Gamma-Ray Energies and Intensities, which are used commonly for Routine Mulielemental Instrumental Photon Activation Analysis [16.17].

Elements	Nuclides	Half life	Energy, (keV) and Intensities, %	Measurement
Na	Na - 22	2.6 y	1274,6 (100)	d
Mg	Na - 24	15 h	1368,5 (100); 2754.1 (100)	b
Cl	C1 - 34	32 m	145.7 (36); 2128.5 (48)	a
K	K - 38	7.6 m	2166.8 (100)	2
	Ca - 47	4.54 d	807.9 (7); 1296.8 (75)	b, c
Ca	K - 43	22.3 h	372 (82); 616 (65)	c
Sc	Sc - 44	3.92 h	1157 (100)	b
	Sc - 46	84 d	889.3 (100); 1120.5 (100)	d
Ti	Sc - 48	43.67 d	893.3 (100); 1037.4 (98); 1311 (100)	ď
Cr	Cr - 51	27.7 d	320.2 (9.8)	d
Mn	Mn - 54	312.2 d	834.8 (100)	d
Fe	Mn - 56	2.58 h	846.6 (99); 1811.2 (30)	a
Co	Co - 58	70.78 d	810.6 (99)	d
Ni /	Ni - 57	36 h	127.3 (15); 1377.5 (85)	ь
Cu	Cu - 64	12.7 h	1345.8 (0.48)	b
Cu				d d
7.	Zn - 65	244 d	1115.5 (50)	b
Zn	Zn - 69	13.9 h	438.9 (100)	
	Cu - 67	61.9 h	93.0 (16); 184.6 (45)	b, c
Ge	Ge - 69	39 h	574.0 (12); 1106.5 (26)	b \ -:-
As	As - 74	17.8 d	595.9 (61); 636 (15)	d
Se	Se - 75	120 đ	135.9 (58); 264.7 (58)	d
Rb	Rb - 84	34.5 d	881.5 (75)	ď
Sr	Sr - 85m	67.7 m	151.3 (11.6), 231.5 (85)	, а
	Sr - 87m	168.6 m	388.4 (83)	b .
Y	Y - 88	108 d	989.0 (93); 1836 (99)	d
Zr	Zr - 89	78.4 h	909 (99)	С
Nb	Nb - 92m	10.15 d	934.5 (95.5)	d
Мо	Mo - 99	66 h	181.1 (6); 739	50 C
	Sn - 117m	13.6 d	158.4 (63)	d
Sn	In - 111	2.83 d	171.29 (91); 245.35 (94)	b, c
	Sb - 122	2.7 d.	564.1 (63); 692.7 (3.27)	c
Sb	Sb - 120	5.76 d	89.8 (77); 197.2 (89); 1171.3 (100)	d
Te	Sb - 124	60.2 d	602.7 (98); 722.8 (10); 1691.0 (50)	d
I	I - 126	13 d		d
			388.5 (35); 666.2 (33)	
Cs	Cs - 132	6.47 d	667.65 (100)	С
Ba	Ba- 133m	38.9 h	275.9 (17)	c
	Ba-135m	28.7 h	268.2 (16)	c
Ce	Ce - 139	137.5 d	165.85 (81)	d
	Ce - 141	32.5 d	145.45 (49)	d ·
Nd	Nd - 147	11.06 d	91.1 (28); 531.0 (13.5)	d
Sm	Sm - 153	46.75 h	103.2 (28)	C
Er	Er - 161	3.24 h	211.1 (12); 826.6 (67)	b
Yb	Yb - 169	31.8 d	130.7 (11); 177.0 (22); 197.8 (40)	đ ·
Tm	Tm - 167	9.25 d	207.8 (42); 531.5 (1.5)	c, d
Hf	Hf - 175	70 d	343.6 (85); 432.8 (14); 307.5 (10)	d
Ta	Ta 180	8.1 h	93.1 (4); 103.4 (0.59)	ь
w	Ta - 183	5 d	107.9 (10); 161.34 (10.4); 246.06 (26)	c, d
	Re - 184	38 d	792 (36); 894.7 (16); 903.2 (36.3)	d
Re	Re - 186	90.64 h	122.61 (0.7); 137.16 (12)	c, d
Au	Au – 196	6.2 d	333.0 (24.4); 355.72 (93.6)	c, d
Hg	Au - 198	2.69 d	411.8 (95.5); 676.9 (0.82)	
	Ti - 202	12.2 d	411.8 (93.3); 676.9 (0.82)	c, d
Tl				d
Pb	Pb - 203	52.1 h	X - rays; 279.2 (81); 401.3 (3.8)	c
Bi	Bi - 206	6.24 d	343.5 (24); 516.1(40); 803 (100)	c, d
Th	Th - 231	25.6 h	X - rays; 102.3 (0.33), 163.2 (0.18)	С.
U	U - 237	6.75 d	X - rays; 207.9 (23); 332,4 (1.3)	c,d

3 h; $t_m = 10-20 \text{ m}$. d) $t_m = 1-2 \text{ d}$; $t_m = 30 \text{ m}$. c) $t_m = 7 \text{ d}$; $t_m = 1 \text{ h}$. d) $t_m = 20-30 \text{ d}$; $t_m = 1-2 \text{ h}$.

References:

- V.L. Aksenov, et. al. Proposal for the construction of the New intense resonance neutron source (IREN). Сообщение ОИЯИ, E3-92-110, Дубна, 1992.
- W.I. Furman. Current status of the IREN project. Proceed. of V International Seminar on Interaction of Neutrons with Nuclei (ISINN-5), May 14-17, 1997, E3-97-213, IINR. Dubna. 1997.
- 2. Yu. G. Teterev, A.G. Belov. Il Atomn. Energiya, V.91, No.3, 2001, pp. 212-216.
- 3. S.C. Srivastava, et al.// Nuclear Medicine and Biology Advances, Ed., by C. Raynaud, vol.2, Pergamon Press, 1983, pp. 1635-1638.
- 4. S.C. Srivastava, et al.//Clinical Cancer Research 61, vol.4, Jan. 1998, pp.61-68.
- A. F. Novogorodov, et al. Simple method of high temperature seperation ¹¹¹In from massive tin target. (in Russian), //Radiokhimiya, No.2, 1987, pp.254-258.
- 6. V. Levin, et. al. // Radiochem. Radioanal. Letters, 1981, vol. 49, No.2, p.111.
- 7. A. Malinin, et. al. // Radiochem. Radioanal. Letters, 1983, vol. 59, No.4, p.213.
- Sh. Gerbish, et. al. Application of the IREN facility for production of radionuclide. (in Russian), Communication of the JINR, P18-2006-116.
- 9. Y. Oka, T. Kato, K. Nomura and T. Saito // Bull. Chem. Soc. Jap. 40 (1967) 575.
- 10. Sh. Gerbish, e. al. //Communication of JINR, P6-91-123, Dubna, 1991.
- 11. Segebade Christian; Weise Hans-Peter; George J Lutz. Photon Activation Analysis..//Berlin; New York: Walter de Gruyter, 1988, pp. 161-310.
- 12. G. J. Lutz. //Anal. Chem., 1969, 41, 424.
- 13. Ch. Engelmann.// Nucl. Instr. Methods, 1971, 93, 197.
- 14. Y. Oka, T. Kato, K. Nomura and T. Saito. // J. Nucl. Sci. Technol., 1967, 4, 345.
- 15. Sh. Gerbish et al. // J. Radioanal. and Nucl. Chem. 1993, vol.168, 2, 503.
- 16. N. Sodnom et al. // Chem. Tverdogo Topliva. (Russian). No.6 (1988). p.29-35
- 17. L. A. Currie. Il Anal. Chem., 1968, V.40. pp. 586-596

CURRENT STATUS AND FUTURE NEEDS OF NUCLEAR ANALYTICAL TECHNIQUES AND THEIR APPLICATIONS: A REVIEW OF IAEA CONSULTANTS' MEETING

M.V. Frontasyeva

Department of Neutron Activation Analysis, Frank Laborarory of Neutron Physics Joint Institute for Nuclear Research, 141980 Dubna, Moscow Region, Russia

A Consultant's meeting was organized in March 19-21, 2007 at IAEA Headquarters, Vienna, Austria, to acquire information on 'trends and new developments in nuclear analytical techniques' to advise the IAEA Secretariat on future needs of assistance to Member State laboratories to stay abreast with international developments. Eight experts from Canada, China, Czech Republic, Germany, Italy, Russian Federation, USA, United Kingdom, and IAEA presented their views briefly summarized in this review. In view of requirements of the international community for mutually recognized analytical data as the basis for decisions in legislation, trade and innovation, developing countries need to expand existing nuclear analytical techniques for compliance with international standards and norms. New developments in technology, improved radioanalytical methods, organizational and managerial requirements (including quality assurance and quality management), supporting sustainability of laboratories, as well as new emerging fields of applications, software and instrumentation need to be adopted and evaluated. Particularly instrumental and radiochemical neutron activation analysis, accelerator based and isotopic techniques for nuclear and non-nuclear applications have the potential to support socio-economic development and self-reliance. Development of human resources in the field of radiochemical and nuclear analytical techniques is a prerequisite for successful implementation of many of the IAEA programmes including medical care, nuclear and conventional safety and environmental monitoring and remediation projects. Training courses, distant learning tools as well as documentary and software provision is a requirement to help ensure a qualified workforce for nuclear applications in IAEA Member States.

INTRODUCTION

For the purpose of this review we define nuclear analytical techniques (NATs) as those that use nuclear reactions, radioactive decay, or nuclear instrumentation to investigate properties of matter. This definition extends from the well-established radiochemistry, neutron activation analysis (NAA), and prompt-gamma activation analysis (PGAA) to advanced methods at the limits of science and technology, and includes the applications of these techniques to the determination of composition and structure of matter for science and technology.

In the past several reviews on trends and applications of NAA have been published [1-5]. Radiochemical methods for various applications and speciation have been reviewed in [6-7]. A review of industrial on-line NAA applications can be found in [8] and application of radiotracers for methodological studies are summarized in [9]. An example of a combined application of various modes of NAA to a material used as RM is given in [10] and a recent article presents the application of PGNAA for very short-lived radioisotope analysis [11].

Many other applications and methodological developments are described in the proceedings of the Modern Trends in Activation Analysis Conferences, e.g MTAA-11 in the *Journal of Radioanalytical and Nuclear Chemistry*, Vol. 271, No. 1-3 (2007).

The broad range of nuclear analytical techniques share a set of advantages over competing methods due to their use of nuclear reactions, radiation properties, or equipment. These advantages include

(i) highly penetrating probe and response radiation; (ii) independence of chemical state and of analytical blank; (iii) non-destructive character; and (iv) sensitivity, and specificity.

NAA in particular is in regular use worldwide to perform elemental analysis of as many as forty elements in a variety of materials important to industrial process development and control, human health, environmental protection, and cultural heritage. We see no decline in the utility of this combination of factors, nor a replacement in all its applications by any other single analytical technique in the next decade. NAA is especially valuable in the case of large samples, complex matrices, solid materials that are difficult to dissolve, and QA/QC. Significant contributions have been made over the past five decades to the characterization of reference materials and assignment of reference values in complex natural materials as well as industrial products. National and international metrology organizations continue to rely on the unique quality parameters of NATs for this purpose. Although NAA is mature, several developing extensions to the method promise greater applicability to the analysis of large ultra pure solids and extremely heterogeneous samples. The broad elemental coverage and high throughput of NAA have made the technique a dominant one in archaeometry.

Several obstacles stand in the way of further use of NATs. Foremost among them is the decline in the number of research reactors in the developed world. This problem may be partly offset by a number of new research reactors in the developing world but also by new developments in DD and DT neutron generator technology. Higher fluence rates, longer life time and reduced size of the tubes make them attractive as a source of neutrons for analytical purposes when combined with appropriate moderator/shielding and counting equipment.

NEED FOR EDUCATION AND TRAINING

In view of declining number of students enrolling in natural sciences in general and in nuclear and radioanalytical chemistry in particular, national support programmes for knowledge conservation and teaching of undergraduate and graduate students must be supported with the highest priority to ensure sufficient staff qualified for maintaining nuclear and radioanalytical laboratories, for radioprotection and for securing the safe operation of existing nuclear installations. The numerous nuclear analytical applications beneficial to human well being can only be developed and further applied if a continuous supply of teachers and trainers will be available in the near future.

NEW DEVELOPMENTS IN ANALYTICAL TECHNIQUES AND APPLICATIONS

Over 200 small and medium charged-particle accelerators are in use in many countries for PIXE and other ion beam analysis techniques. Their applications in materials and life sciences are expanding, especially with microbeam facilities which allow imaging in two or three dimensions (more than 40 operational μ -beam facilities available at this moment).

Charged-particle activation analysis (with or without radiochemistry) can be a complementary technique to NAA for the determination of particular elements in different

matrices (biological, environmental, and certain technologically advanced materials). In the version of TLA (thin layer activation) this technique is effective for wear and corrosion studies on moving mechanical equipments for industrial applications and the assessment of the performances with time of human prostheses as well. There is a remarkable growth in the number and availability of particle accelerators related to the rapid expansion of diagnostic and therapeutic nuclear medicine procedures, notably positron emission tomography (PET), single-photon emission tomography (SPET), (including hybrid systems with CT or MRI), functional diagnosis, molecular imaging, and metabolic radionuclide therapy. For example, more than ten million tests are made with 99m Tc annually in North America alone.

The number of qualified and experienced professional nuclear scientists and engineers, in particular radiochemists and radiopharmacists, has not kept pace with this increase, leading to greater risks in these procedures.

Analytical techniques based on synchrotron radiation are emerging which can provide qualitative and quantitative information on *in-vivo* elemental composition, structure, and molecular imaging. As many as ten of the new large facilities are dedicated to the biomedical sciences.

NON-DESTRUCTIVE ANALYSIS OF ART, ARCHAEOLOGICAL AND ANTHROPOLOGICAL SAMPLES AND THEIR AGE DETERMINATION

Nuclear analytical techniques requiring minimum or no sample preparation at all prior to analysis are an ideal tool for scientific investigation of valuable cultural heritage objects. Due to their deep penetration in solids, neutrons are used for elemental analysis of archaeological artefacts, gem stones and metal objects from museum collections by INAA and PGNAA [12–14].

Neutron resonance capture analysis is a new emerging technique to be applied to archaeological materials successfully [15]. Proton induced X-ray emission (PIXE) and other ion beam techniques are of immense value to study elemental distribution in fragments or large antique objects under vacuum or in air [16–18].

As museum curators dislike to release their valuable objects to analytical laboratories for investigation, a development for portable X-ray fluorescence (XRF) instruments was launched and those instruments are now frequently applied to the analysis of paintings and immovable cultural heritage like frescos and wall paintings [19, 21].

Exact dating of ancient objects excavated from soil and deep sea is of crucial importance for archaeologists and anthropologists. No other competing techniques can reveal the broad range and accuracy of nuclear techniques, such as C-14, TLD/OSL and isotopic ratio determinations for dating. Although conventional C-14 dating using beta spectrometry is a tedious procedure it is still widely used in developing countries. In more advanced laboratories accelerator-mass spectrometry (AMS) has replaced this conventional technique resulting in higher accuracy and sensitivity for a large number of stable and radioactive isotopes [22].

A number of spectacular results in determining the age of human remains have been described in recent articles [23, 24]. Nuclear analytical techniques are indispensable and hitherto non-replaceable by other non-nuclear analytical techniques for the prominent application to cultural heritage. We expect a drastic increase in interest for using NATs in scientific investigations in Member States of the IAEA.

THE ROLE OF TRACE ELEMENTS IN HEALTH AND ENVIRONMENTAL STUDIES

NATs are playing a significant role in the three "new epidemics" (WHO 2000) of cancer, cardiovascular disease, and diabetes. NATs have a unique role to aid in understanding the mechanism of brain-gut interactions related to satiety and obesity, which appear to be related to the new epidemics, and are in other ways an important health issue in rapidly developing countries. It is noted that a few investigations have commenced involving NATs in the determination of the composition of biological tissues in connection with HIV incidence in sub-Saharan Africa.

According with the recommendations of the international and European pharmacopoeia, the quality assurance/control (QA/QC) of labelled compounds and radiopharmaceuticals for human and animal investigations is required to make use of sophisticated and sometimes unusual radiochemical and radioanalytical methods of analysis and NATs,.

The development of rapid methods of analysis and visualization of radioactive specimens would give a substantial improvement to these technologies. The stability with time of the labelled species and the evaluation of the expiration time is of paramount relevance for the performances of labelled species.

Artificially produced radioactive tracers, characterized by short half-life and high specific activity, are finding several applications in the life sciences, in particular in occupational and environmental toxicology, in metallobiochemistry and nanotoxicology as well as in living organisms (cell cultures, plants, animals, and fishes).

REFERENCES

- 1. V.P. Guinn: Past, present and future of neutron activation analysis. J. Radioanal. Nucl. Chem. Vol. 160, No. 1(1992) 9-19
- 2. M. De Bruin: Present and future position of neutron activation analysis. J. Radioanal. Nucl. Chem. Vol. 160, No. 1 (1992) 31-40
- 3. R.E. Jervis: A century of radiochemistry: Its growth and development as a unique scientific discipline. J. Radioanal. Nucl. Chem. Vol. 239, No. 1 (1999) 19-27
- 4. N.M. Spyrou: Neutron activation analysis challenges: Problems and applications in biomedical and other areas. *J. Radioanal. Nucl. Chem.* Vol. 239, No. 1 (1999) 59-70
- P. Bode: A Future for nuclear analytical techniques? Why not? Int. Conf. On Isotopic and Nuclear Analytical Techniques for Health and Environment. June 2003 IAEA Vienna. IAEA-CN-103/163 (2003)
- 6. J.J.M. de Goeij: Radiochemical neutron activation analysis of biological materials: Past, present and future. *J. Radioanal. Nucl. Chem.* Vol. 245, No.1 (200) 5-9
- 7. R. Cornelis: Use of radiochemical methods as a tool for speciation purposes in environmental and biological sciences. *Analyst*, Vol. 117 (1992) 583-588
- 8. C.S. Lim: Recent developments in neutron induced gamma activation for on-line multielemental analysis in industry. *J. Radioanal. Nucl. Chem.* Vol. 262, No. 2 (2004) 525-532

- V. Krivan: Application of radiotracers to methodological studies in trace element analysis. In: Treatise on Analytical Chemistry, Vol. 14, Chapter 6, 339-417, John Wiley & Sons, New York (1986)
- M. Rossbach, M. stoeppler, A.R. Byrne: Prompt and delayed NAA techniques for the characterization of specimen bank materials. Sci. Total Environm. 139/140 (1993) 411-419
- G.L. molnar, Z. Revay, L. Szentmiklosi: New perspectives for very short lived neutron activation analysis. J. Radioanal. Nucl. Chem. Vol. 262, No. 1 (2004) 157-163
- M.D. Glascock: Characterization of archaeological ceramics at MURR by NAA and multivariate statistics. In: H. Neff (ed.) Monographs in World Archeology No.7, Prehistory Press, Madison, WI (1992) 11-26
- C.S. Munita, R.P. Paiva, M.A. Alves, P.M.S. Olivera, E.F. Momose: Contribution of neutron activation analysis to archaeological studies. *J. Trace Microprobe Tech.* 18, No. 3 (2000) 381-387
- Antczak, M.; Antczak, A.; Sajo-Bohus, L., Kasztovszkyb, Zs.: Provenance study of Amerindian ceramic figurines with PGNAA. In: International conference on isotopic and nuclear analytical techniques for health and environment. Conference Proceedings, IAEA Vienna (2004) IAEA-CSP-22/CD
- E. Ioannidou, D. Bougarit, T. Calligaro, J.-C. Dran, M. Dubus, J. Salomon, P. Walter: RBS and NRA with external beams for archaeometric applications. *Nucl. Instr. Meth. B* 161-163 (2000) 730-736
- M. Roumié, S.Y. Waksman, B. Nsouli, P. Reynolds, S. Lemaître: Use of PIXE analysis technique for the study of Beirut amphora production in the Roman period. *Nucl. Instr. Meth. B* 215 (2004) 196-202
- T. Calligaro, J.C. Dran, M. Klein: Application of photo-detection to art and archaeology at the C2RMF. Nucl. Instr. Meth. A 504 (2003) 213-221
- A. Longoni, C. Fiorini, P. Leutenegger, S. Sciuti, G. Fronterotta, L. Strüder, P. Lechner: A portable XRF spectrometer for non-destructive analysis in archaeometry. *Nucl. Instr. Meth. A* 409 (1998) 407-409
- Ž. Šmit, K. Janssens, K. Proost, I. Langus: Confocal μ-XRF depth analysis of paint layers. Nucl. Instr. Meth. B 219-220 (2004) 35-40
- 20. B. Kanngießer, W. Malzer, I. Reiche: A new 3D micro X-ray fluorescence analysis set-up First archaeometric applications. *Nucl. Instr. Meth. B* 211 (2003) 259-264
- 21. W. Kutschera: Progress in isotope analysis at ultra-trace levels by AMS. Int. J. Mass Spectrom. 242 (2005) 145-160
- E.M. Wild, M. Teschler-Nicola, W. Kutschera, P. Steier, E. Trinkaus, W. Wanek: Direct dating of early upper Palaeolithic human remains from Mladeč. *Nature* Vol. 435/19 May 2005, 332-336
- 23. W. Kutschera, W. Muller: "Isotope language" of the Alpine Iceman investigated with AMS and MS. Nucl. Instr. Meth. B 204 (2003) 705-719

BREMSSTRAHLUNG EMISSION FROM A THICK TARGET

N.T. Khai¹, T.D. Thiep¹, T.T. An¹, N.T. Vinh¹, A.G. Belov² and O.D. Maslov²

- 1. Institute of Physics and Electronics, VAST, P.O.Box 429, Boho 10000, Hanoi-VN
- 2. Joint Institute for Nuclear Research, Dubna, Moscow, Russia

Abstract. Bremsstrahlung emission, or radiation loss, is a dominant mechanism for energy dissipation of electron at relativistic energies greater than a few MeV when it is subjected to acceleration in the field of the nucleus or of the electrons. In this work Monte-Carlo calculations for bremsstrahlung spectra have been described for the case of thick tungsten target, where secondary interactions induced by the electrons and photons in the target such as energy loss, absorption, scattering and (e⁺, e⁻) pair-production effects were taken into account.

I. INTRODUCTION

The bremsstrahlung emissions produced from accelerators are intensive and high-energy photon sources. They are widely used in photo-nuclear reaction research and applied nuclear physics. For example, to obtain the dependence of the cross-sections of the photo-nuclear reactions on the photon energy it is necessary to know the bremsstrahlung spectrum as a function of the incident electron energy. As there is not enough experimental data available, improvements in calculation technique based on updating the interaction data of electron and photon are proved to be a good way for bremsstrahlung spectral evaluation for the above mentioned goals of research.

The bremsstrahlung emissions have been calculated by several semi-analytical methods [1-2]. However, due to difficulties in describing analytically the secondary-interaction effects occurred in the target, especially those related to non-zero observation angles, these calculations are limited when a thick target is used, where the affect of secondary interactions can not be ignored.

In this work we would like to use Monte-Carlo calculations based on the experimental data and theory about energy and angular distributions to consider the role of the secondary interaction processes induced by electrons and photons in thick tungsten target. This is necessary in evaluating accurately the production yield and bremsstrahlung

radiation intensity at an incident electron beam. The research is also to resolve the limitations and problems mentioned in the previous research [1-3].

II. CALCULATION TECHNIQUE, RESULTS AND DISCUSSION

In principle, bremsstrahlung can be emitted whenever a charged particle experiences a change in its velocity under the influence of the Coulomb field of a nucleus. Since the rate of energy dissipation due to bremsstrahlung and the cross-section for its production are inversely proportional to the square of the mass of the incident particle [4]:

$$dE_b/dt \sim Z^2 Z_t^2/m^2 \tag{1}$$

$$\sigma_b \sim Z_t^2 (e^2/mc^2)^2$$
 (2)

where m and Z are, respectively, the mass and the charge of the particle, and Z_t is the atomic number of the target. Bremsstrahlung emission is a dominant energy-dissipation mechanism for electron, the lightest charge particle, especially at relativistic energies greater than a few MeV.

The study on angular distribution of bremsstrahlung [4-6] indicated that at very low energies of electrons the radiation intensity is of maximum in a direction perpendicular to the incident beam. However, as the energy is increased, the maximum appears at increasingly forward angles and in the limit of very high electron energies, the emission of bremsstrahlung essentially occurs as a narrow pencil in the forward direction. The average angle of emission is then given by [6]:

$$\theta_{\rm y} \approx m_{\rm e} c^2 / E_{\rm e}$$
 (3)

with Ee being the total energy of the incident electron,

m_ec² is the rest energy of electron.

Simulation for production of the bremsstrahlung and scattered electrons when a relativistic incident-electron beam hitting the thick target has been mentioned in our previous research [3]. Here we are concentrated in considering the role of the secondary processes occurred in the target due to the appearance of these particles to formation of gross bremsstrahlung spectra.

1. Due to the bremsstrahlung emission under the influence of the Coulomb field of the nucleus, the incident electron will be lost an amount of energy that equal to the bremsstrahlung energy emitted (because $M_{nucl} >> m_e$, the recoil energy of the nucleus can

be ignored) and deflected from its moving direction. The remaining energy (T_s) and reflection angle (θ_e) of the electron can be, therefore, determined using laws of conservation of energy and momentum as follows:

$$T_s = T_e - hv \tag{4}$$

$$\gamma_{\rm s} m_{\rm e} v_{\rm s} \cos(\theta_{\rm e}) + h \cos(\theta_{\rm v}) / \lambda = \gamma_{\rm e} m_{\rm e} v_{\rm e} \tag{5}$$

where θ_{γ} is given by formula (3), β and γ are the Lorentz factors of the electron, v_e and v_s are velocities of the incident and scattered electrons.

2. Since the bremsstrahlung production yield is proportional to the strength of the nuclear Coulomb field felt by the electron and the number of its interaction with the nuclei in the target, the intensity of its emission increases with atomic number and thickness of the braking target. However, bremsstrahlung radiation intensity can be considerably reduced by the attenuation effects in the heavy target material. The data on photon cross-sections for a given material in the wide range of energies from 100 KeV to 100 MeV [7] are parameterized as a function of the photon energy:

$$Ln(\sigma_a) = a_o + a_1 Ln(E) + a_2 Ln^2(E) + a_3 Ln^3(E)$$
(6)

$$Ln(\sigma_s) = b_0 + b_1 Ln(E) + b_2 Ln^2(E) + b_3 Ln^3(E)$$
(7)

$$Ln(\sigma_{D}) = c_{D} + c_{1}Ln(E) + c_{2}Ln^{2}(E) + c_{3}Ln^{3}(E)$$
(8)

Where (a_0, a_1, a_2, a_3) , (b_0, b_1, b_2, b_3) and (c_0, c_1, c_2, c_3) are fitting coefficients for the cross-sections of photoelectric absorption, scattering and pair production processes, respectively.

2.1. For the photoelectric effect a quantum can be absorbed if $E_{\gamma} > B_{shell}$ where B_{shell} are the shell energies of electron. The photoelectron is emitted with kinetic energy:

$$T_{\text{photoelect}} = E_{\gamma} - B_{\text{shell}} \tag{9}$$

The polar angle of the photoelectron is determined from the Sauter-Gavrilar distribution for K-shell [8]:

$$\cos\theta_{\text{photoelect}} = \left[(1 - 2\gamma) + \beta \right] / \left[(1 - 2\gamma)\beta + 1 \right] \tag{10}$$

where β and γ are the Lorentz factors of the photoelectron.

2.2 For the Compton-scattering process the energy and angle of the scattered photon are determined as follows: Starting from the quantum-mechanical Klein-Nishina differential cross-section for Compton scattering:

$$d\sigma / d\varepsilon = \pi r_e^2 (m_e c^2 / E_o) Z (1 / \varepsilon + \varepsilon) [1 - \varepsilon \sin^2 \theta_{Compt} / (1 + \varepsilon^2)]$$
(11)

where:

 r_e = classical-electron radius, m_ec^2 = electron mass, E_o = energy of the incident photon, E_1 = energy of the scattered photon and ϵ = E_1 / E_o .

Assuming an elastic collision, the scattering angle θ_{Compt} is given by the Compton formula:

$$E_1 = E_0 \, m_e c^2 / \left[m_e c^2 + E_0 (1 - \cos \theta_{Compt}) \right] \tag{12}$$

The energy of scattered photons is sampled as follows:

The value of ε corresponding to the minimum energy of the photon, i.e. to backward scattering $\theta_{Compt} = 180^{\circ}$ is:

$$\varepsilon_{\rm o} = m_{\rm e}c^2 / (m_{\rm e}c^2 + 2E_{\rm o}) \tag{13}$$

Hence $\varepsilon \in [\varepsilon_0, 1]$. Using the combined composition and rejection Monte-Carlo method described in [9] we set a function depending on ε from the expression of the differential cross-section:

$$\Phi(\varepsilon) = (1/\varepsilon + \varepsilon)[1 - \varepsilon \sin^2\theta_{Compt}/(1 + \varepsilon^2)] = f(\varepsilon)g(\varepsilon)$$
(14)

$$= [\alpha_1 f_1(\varepsilon) + \alpha_2 f_2(\varepsilon)] g(\varepsilon)$$
 (15)

where
$$\alpha_1 = \ln(1/\epsilon_0)$$
; $f_1(\epsilon) = 1/\alpha_1\epsilon$

$$\alpha_2 = (1 - \varepsilon_0^2) / 2$$
; $f_2(\varepsilon) = \varepsilon / \alpha_2$

 f_1 and f_2 are probability density functions defined on the interval $[\epsilon_0, 1]$.

 $g(\epsilon) = [1 - \epsilon \sin^2 \theta_{Compt} / (1 + \epsilon^2)]$ is the rejection function with all the values of $\epsilon \in [\epsilon_0, 1]$ so, $0 < g(\epsilon) \le 1$.

After the successful sampling of ϵ and the polar angles θ_{Compt} of the scattered photon with respect to the direction of the parent photon, the kinetic energy and momentum of the recoil electron are then determined by:

$$T_{\text{recoil-e}} = E_0 - E_1 \tag{16}$$

$$\vec{P}_{\text{recoil-e}} = \vec{P}_{o} - \vec{P}_{1} \tag{17}$$

2.3 For the gamma conversion into an (e⁺, e⁻) pair simulation for total energy carried by one particle of the pair is based on the Bethe-Heiler differential cross-section formula [9]: $d\sigma(Z, \varepsilon) / d\varepsilon = \alpha r_e^2 Z[Z + \xi(Z)] \{ [\varepsilon^2 + (1 - \varepsilon)^2] [\Phi_1(\delta(\varepsilon)) - F(Z) / 2] + (1 - \varepsilon)^2 [\Phi_1(\delta(\varepsilon)) - \Phi_1(\delta(\varepsilon)) - (1 - \varepsilon)^2 [\Phi_1(\delta(\varepsilon)) - (1 - \varepsilon)^2 [\Phi_1(\delta(\varepsilon)) - (1 - \varepsilon)^2] + (1 - \varepsilon)^2 [\Phi_1(\delta(\varepsilon)) - (1 - \varepsilon)^2 [\Phi_1(\delta(\varepsilon)) - (1 - \varepsilon)^2] + (1 - \varepsilon)^2 [\Phi_1(\delta(\varepsilon)) - (1 - \varepsilon)^2 [\Phi_1(\delta(\varepsilon)) - (1 - \varepsilon)^2 [\Phi_1(\delta(\varepsilon)) - (1 - \varepsilon)^2] + (1 - \varepsilon)^2 [\Phi_1(\delta(\varepsilon)) - (1 - \varepsilon)^2 [\Phi_1(\delta(\varepsilon)) - (1 - \varepsilon)^2] + (1 - \varepsilon)^2 [\Phi_1(\delta(\varepsilon)) - (1 - \varepsilon)^2 [\Phi_1(\delta(\varepsilon)$

$$+ \left[2\varepsilon(1-\varepsilon)/3\right]\left[\Phi_2(\delta(\varepsilon)) - F(Z)/2\right]$$
 (18)

where α is the fine-structure constant and r_e the classical-electron radius,

 $\varepsilon = E / E_o$, E_o is the energy of the photon and E is the total energy of one particle in the (e^+, e^-) pair. Therefore, the kinematical limit of ε is:

$$m_e c^2 / E_o \equiv \varepsilon_o \le \varepsilon \le 1 - \varepsilon_o$$
 (19)

In cross-section formula (19) two screen functions $\Phi_1(\delta)$ and $\Phi_2(\delta)$ are introduced:

i. for $\delta \leq 1$

$$\Phi_1(\delta) = 20.867 - 3.242\delta + 0.625\delta^2$$

$$\Phi_2(\delta) = 20.209 - 1.930\delta - 0.086\delta^2$$
(20)

ii. for $\delta > 1$

$$\Phi_1(\delta) = \Phi_2(\delta) = 21.12 - 4.184 \ln(\delta + 0.952) \tag{21}$$

where the screening variable δ is a function of ϵ :

$$\delta(\varepsilon) = 136\varepsilon_0 / \left[Z^{1/3} \varepsilon (1 - \varepsilon) \right]$$
 (22)

The Bethe-Heiler formula is established for plane waves. So, for Coulomb waves a correction, so called a Coulomb-correction function should be introduced in:

$$F(Z) = 8 \ln Z / 3$$
 for $E_o < 50 \text{ MeV}$ (23)

$$F(Z) = 8 \ln Z / 3 + 8 f_c(Z)$$
 for $E_o \ge 50 \text{ MeV}$ (24)

with $f_c(Z) = (\alpha Z)^2 \{1 / [1 + (\alpha Z)^2] + 0.20206 - 0.0369 (\alpha Z)^2 + 0.0083 (\alpha Z)^4 - 0.$

$$-0.00020(\alpha Z)^{6} + \dots \}$$
 (25)

The polar angle of the electron (or positron) is defined with respect to the direction of the parent photon. The energy-angle distribution can be approximated by a density function given by L. Urban [10]:

$$F(u) = [9a^{2}/(9+d)][(ue^{-au} + due^{-3au})$$
 (26)

with
$$a = 5/8$$
, $d = 27$ and $\theta_{\pm} = um_e c^2 / E_{\pm}$ (27)

A sampling of the distribution (27) requires a triplet (q_1, q_2, q_3) of random numbers such that: if $q_1 < 9 / (9 + d)$ then $u = -ln(q_2q_3) / a$, otherwise $u = -ln(q_2q_3) / 3a$ (28)

In all calculations described above the azimuthal angle ψ is generated isotropically.

Fig. 1 shows calculations for the bremsstrahlung spectra produced by 18 MeV-electron beams for cases of the thin-W target (0.03 cm thickness) and the thick one (0.3 cm thickness), where the secondary interactions mentioned above were included in the simulation.

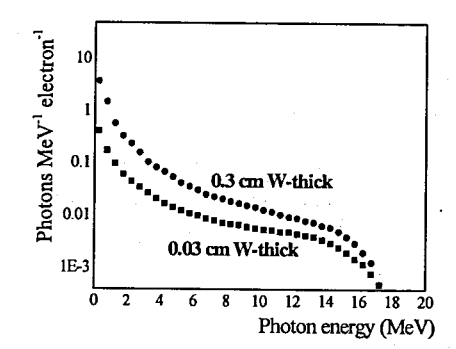


Fig. 1: Bremsstrahlung spectrum produced by 18 MeV electron beam on W-targets.

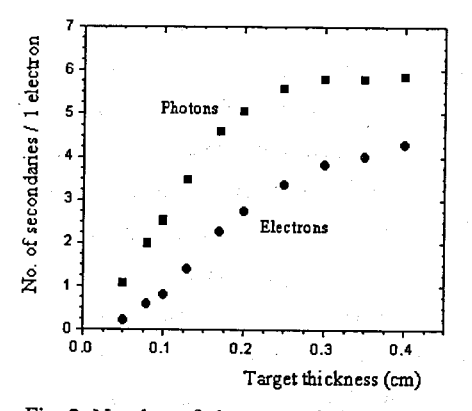


Fig. 2: Number of photons and electrons as a function of W-target thickness for incident

Fig. 2 shows a dependence of emissions of secondary photons and electrons on the target thickness.

In these calculations the numbers of the secondary particles produced, i.e. photons and electrons at the exit of target, were normalized by one incident electron. This is to expose the role of secondary processes occurred in the target to formation of the gross bremsstrahlung spectrum. It can be seen from Figs. 1, 2 that due to the secondary interactions the numbers of electrons and photons exiting the target could be increased, respectively. by up to the factors of approximately 4 and 6 compared with that of incident electrons. This increase of the photons is almost located at very low energies of bremsstrahlung spectrum. The simulation of the spectral characteristics as a function of the target thickness showed that this increase of the photons is mainly due to sequent bremsstrahlung emissions

from the scattered electrons in the target. For a gross bremsstrahlung spectrum these photons can make a broadening in the angular distributions. From the above mentioned results of the dependence of the photon intensity on the target thickness we would like to show two following comments:

- 1. For the nuclear-reaction research with bremsstrahlung the calculations in optimizing both the necessary photon intensity and the possible angular broadening as a function of the thickness should be taken into account.
- 2. From Fig. 1 we can see that enhance of the photon is mainly located at low energies, i.e. at those below the threshold of reactions (γ, p) , (γ, np) , (γ, np) , and (γ, xp) for light nuclei. This suggests about an possibility to use the bremsstrahlung emission from the thick target to produce high-intensity neutron sources by low-threshold (γ, n) reactions, for a typical example ${}^9\text{Be}(\gamma, n){}^8\text{Be}$.

III. CONCLUSION

We have used the Monte-Carlo calculations to study the secondary interactions induced by the bremsstrahlung and the electrons produced by braking accelerated relativistic-electron beams in thick target. Our calculations were performed on the basis of energy and angular distributions of the emitted particles. These distributions are either parameterized from experimental data or from theoretical description. This allowed us to consider contributions of the secondary effects to the production yields of bremsstrahlung and electrons. In this study the role of the secondary-interaction effects was explicitly exposed by considering the emission of photons and electrons as a function of target thickness. For the bremsstrahlung emission from a thick target the simulation showed the increase of the photon intensity and the possible broadening in angular distributions in the region of photo-nuclear reactions due to the secondary-electron emission. Therefore, the optimization calculations for target thickness based on a compromise between two these effects should be taken into account in photo-nuclear reaction research. Moreover, the simulation showed a possibility to produce the high-intensity neutron source by using low-threshold (γ, n) reactions from the bremsstrahlung emission in case of the thick target.

REFERENCES

- 1. D. J. Findlay, Nucl. Inst. And Meth. A276 (1989) 598.
- 2. V.E. Zhuchko and Yu.M. Tsipenyuk, Atomnaya Energiya 39 (1975) 66.
- 3. N. T. Khai and T. D. Thiep, Communications in Physics, Vol. 13, No. 3 (2003)149.
- 4. P. Marmier and E. Sheldon, Physics of Nuclei and Particles, Vol.1, Academic Press, New York and London, 1969.

- 5. W.R. Leo, Techniques for Nuclear and Particle Physics Experiments, Springer-Verlag Berlin Heidelberg 1987, 1994.
- 6. J. A. Wheeler and W. E. Land, Phys. Rev., 1939, 55, 858
- 7. E. Storm and H. Israel, Photon Cross-Sections From 1 KeV to 100 MeV for Elements Z=1 to Z=100, Los Alamos Scientific Laboratory, University of California, Los Alamos, New Mexico 87544.
- 8. M. Gavrila, Phys. Rev. 113 (1959) 514.
- 9. W. Heiler, The Quantum Theory of Radiation, Oxford University Press (1957).
- 10. L. Urban in GEANT3 writeup, section PHYS-211. Cern Program Library (1993).

AIR POLLUTION STUDIES IN OPOLE REGION, POLAND, USING THE MOSS BIOMONITORING TECHNIQUE AND NEUTRON ACTIVATION ANALYSIS

Korzekwa S., Pankratova Yu. S. *, Frontasyeva M.V. *

Institute of Physics, Opole University, Oleska 48, 45-052 Opole, Poland *Frank Laborarory of Neutron Physics, Joint Institute for Nuclear Research 141980 Dubna, Moscow Region, Russia

Biomonitoring of multi-element atmospheric deposition using terrestrial moss is a well established technique in Europe. In October 2006 30 moss samples of *Hylocomium splendens* and *Pleurozium schreberi* were collected over the territory around the city of Opole, capital of the agricultural Opole Region, situated between two industrial regions of Poland: Silesia-Kraków Industrial Region in the east and Legnica-Głogów Copper Basin in the west. A total of 34 elements including heavy metals and rare earths were determined by instrumental neutron activation analysis using epithermal neutrons at the IBR-2 reactor of FLNP JINR.

Introduction

Moss is the most effective type of organism for biomonitoring purposes because of its ability to accumulate and retain pollutants, including trace elements and heavy metals. Mosses have only a rudimentary root system, so the uptake of elements comes mostly from the atmosphere. Nowadays the moss biomonitoring technique is widely used all over the Europe as a method to evaluate atmospheric deposition of metals [1, 2].

The presence of heavy metals in atmospheric deposition within the Polish territory had been previously studied for some specific locations [3-5] including the largest industrial regions the Silesia-Kraków Industrial Region and Legnica-Głogów Copper Basin [6]. In 2006 moss samples were collected over the territory of agricultural Opole Region which lies between these two studied industrial regions and analyzed by multielement instrumental epithermal neutron activation analysis, previously successfully used by one of the authors in similar studies in Russia, Norway, Romania, Northern Serbia and Bosnia, Macedonia [7-12] and several other countries.

The primary task of the present study was to quantitatively characterize the deposition of trace elements including heavy metals over the agricultural Opole Region and to assess the long range atmospheric transport of pollutants from most contaminated neighboring regions of Poland. The results of this study will be submitted to the Coordination Center of the International Cooperative Programme on Effects of Air Pollution on Natural Vegetation and Crops (ICP Vegetation) [13].

Study area

The Opole Region is located in the central part of Silesia, in the south-west part of Poland, with an area of 9,412 square kilometers and population over 1,055,000. It borders in the east with the Silesia-Kraków Industrial Region, with the southern part of the Severomoravský Region of the Czech Republic in the south-west and in the west with the Lower Silesia with Legnica-Głogów Copper Basin. The south of the region is mountainous, but three quarters of the territory are lowlands (about 160 metres above sea level in the centre of region – city of Opole) with the valley of Oder River crossing the region from north-west to south-east.



Forests cover 26.2% of the region (mostly pine forests) and 62% of the region's area is fertile soil used for agriculture.

Sampling

Samples of the two moss species Pleurozium schreberi (more than 85% of all collected samples) and Hylocomium splendens were collected during October 2006 at 30 sites located 5 to 18 km from the center of the town. The sampling was carried out in accordance with the strategy of the European moss survey programme [13]. Samples were collected at least 300 m from main roads, villages and industries, at least 100 m from local roads and houses. The sampling points were situated in forests gaps or clearings, at least 3 m away from the nearest trees to reduce influence from the forest canopy. On each site 5-10 sub-samples were collected within a 50x50 m area to make the moss samples representative. Sampling and sample handling was performed using polyethene gloves and collected material was stored in paper bags. The sampling network is given in Fig. 1.

Analysis

Neutron activation analysis (NAA) was performed in the Frank Laboratory of Neutron Physics, Dubna, Russia. In the laboratory the samples were carefully cleaned from needles, leaves, soil particles and only the green, green-brown shoots representing the last three years growth were analyzed, after being air-dried to constant weight at 30-40°C for 48 hours. The samples were neither washed nor homogenised. Previous surveys based on NAA in moss biomonitoring have shown that samples of about 300 mg are large enough to be used without homogenization [14]. For short-term irradiation samples were pelletized in simple press-forms of about 300 mg and were heat-sealed in polyethene foil. For epithermal neutron activation analysis, simillar pelletized samples of similar weight (about 300 mg) were packed in aluminum cups for long-term irradiation.

The samples were irradiated in the IBR-2 fast pulsed reactor, in channels equipped with a pneumatic system. The neutron flux characteristics are shown in Table 1 [15]. Two kinds of analyse were performed: to determine short-lived radionuclides (Cl, Ca, V, Mn) the samples were irradiated for 3 minutes in the second channel (Ch2) and to determine elements associated with long-lived radionuclides (Na, Sc, Cr, Fe, Co, Ni, Zn, As, Se, Rb, Mo, Sb, Cs, W, Th, U) samples were irradiated for 100 hours in the cadmium-screened Ch1.

Table 1. Flux parameters of irradiation positions.

	Neutron flux density [cm ⁻² s ⁻¹] 10 ¹²						
Irradiation position	Thermal (E=0-0.55 eV)	Resonance (E=0.55-10 ⁵ eV)	Fast (E=10 ⁵ -25 10 ⁶ eV)				
Ch1 (Cd- screened)	0.023	3.3	4.2				
Ch2	1.23	2.9	4.1				

After irradiation gamma-ray spectra were recorded two times for each irradiation using a high-purity Ge detector. The first one after decay periods of 2-3 minutes for 5 minutes, the second one for 20 minutes, 9-10 minutes following the short irradiation. In case of long irradiation, samples were repacked into clean containers and measured after 4-5 days for 45 minutes and 20-23 after days for 3 hours. Table 2 lists selected peak energies for NAA for each analysed element and shows which method of analysis was used to determine that element.

Qualyty control (QC)

The OC of NAA results were ensured by analysis of reference materials: trace and minor elements in lichen IAEA-336 (International Atomic Energy Agency), IAEA-SL-1 (Trace elements in lake sediment) and SRM-1633b (Constituent elements in coal fly ash, US NIST-National Institute of Standards and Technology), SRM-2709 (Trace elements in soil).

Results and descussion

Median values and ranges for the elements studied are presented in Table 2, along with the corresponding data from similar studies in the neighbouring Silesia-Kraków Industrial Region, Legnica-Głogów Copper Basin and Severomoravský Region of the Czech Republic [6]. For comparison with a pristine territory corresponding data for the Northern Norway [14] are shown in the right-hand column. The Norwegian values are from ICP-MS and are based on nitric-acid solutions, possibly leaving out fractions of the elements contained in silicate minerals (soil particles).

The area around Opole is characterized with the highest median for seven elements: As, Cl. Co. Mn. Sc. Th and U. In spite of this for As, Cl and Sr undoubtedly the medians are the highest. In the case of As data from the statistical department shows that emission of that element in Opole Region is the lowest. In Lower Silesia in year 2005 there was over 300 times higher emission [16].

Arsenic and Antimony are mainly associated with coal combustion. Near Opole there is a large conventional power plant "Opole"- the most important source of electricity for the region. Additionally, there are local industrial power plants, heat and water generating plants. In villages around Opole people heat their houses using coal. The most likely source of As and Sb could be fly ash from coal burning. Local abnormalities in distribution of As could be connected with pesticides or wood preservatives using by farmers and forest government (most of sampling sites were situated in forests and some near fields).

Molybdenum is emitted by a metallurgical plant in the town of Ozimek in the east of Opole.

Zinc may arise from cement plant dust or from marble and limestone mines.

Vanadium and Nickel most probably originate from petrochemical emissions because of the chemical industrial enterprises situated in the south-east part of Opole Region. A coke plant situated in the same area as the petrochemisty produces various kinds of coke, cokeoven gas and carbon derivatives: tar, crude benzol and ammonium sulfate.

Calcium Mining in the Opole region is based on marble and limestone, building and road stone, gravel and sand.

Chlorine The reason for the high Cl contamination is not very obviais. Geographical distribution and wind directions suggested that the source of this pollution could be dust from the cement plants, petrochemisty industries or coke plants.

Table 2. Comparison of the results obtained in the present study with neighbouring industrial regions, $\mu g/g$.

Element	(Opole Regio	n	Silesia- Kraków Industrial Region			
	Median	Min.	Max.	Median	Min.	Max.	
Na	198	82	536	-	-	-	
Cl	462	161	1045	183	66	715	
K	8352	5740	17260	-	-	-	
Ca	4870	2785	11660	-	-	-	
Sc	0.23	0.076	1.14	0.18	0.06	0.55	
Ti	140	37	909	-	-	-	
V	2.8	1.1	11.7	3.5	1.5	8.1	
Cr	2.8	1.5	9.1	3.3	1.2	98	
Mn	236	37	882	125	39	410	
Fe	813	240	3086	943	302	4515	
Co	0.5	0.2	1.1	0.2	0.1	0.7	
Ni	2	0.8	4.9	2.3	1.4	7.6	
Zn	64	26	125	118 '	56	877	
As	0.89	0.3	3.12	0.37	0.03	2.85	
Se	0.24	0.07	0.61	0.43	0.13	0.79	
Br	2.43	1	5	1.22	0.08	5.85	
Rb	21	9	37	27	4	50	
Sr	22	12	54	9	0.5	34	
Mo	0.22	0.06	0.53	-	-	-	
Sb	0.36	0.13	0.68	0.39	0.15	3.05	
I	1.4	0.4	5.4	0.9	0.21	1.78	
Cs	0.45	0.12	1.25	0.79	0.16	3.1	
Ba	42	12	97	19	7.2	85	
La	0.88	0.46	4.32	2.1	0.05	14	
Ce	1.9	0.9	9.3	5.6	0.7	43	
Sm	0.14	0.06	0.72	-	-	-	
Tb	0.018	0.009	0.115	0.016	0.005	0.053	
Yb	0.06	0.02	0.41	0.04	0.01	0.32	
Hf	0.18	0.06	1.74	0.12	0.03	1.45	
Ta	0.03	0.01	0.19	0.02	0.01	0.07	
W	0.2	0.14	0.65	0.32	0.01	3.99	
Au	0.002	0.001	0.008	0.003	0.001	0.015	
Th	0.22	0.06	1.3	0.17	0.06	0.59	
U	0.1	0.02	0.51	0.1	0.01	0.24	

Table 2 (continued)

Legnica- Głogów Cont Browkii									
Element		ca- Gło per Ba		Czecl	n Repul	blic		Norway	
	Median	Min.	Max.	Median	Min.	Max.	Median	Min.	Max.
Na	-	-	-	-	-	12.		-	-
Cl	226	123	537	-	-	-		-	: -
K	-		-	-	-		-	_	-
Ca	-			-		-	2820	1680	5490
Sc	0.13	0.03	0.63	-		-	0.052	0.009	0.22
Ti	-	-	-	-	-	-	23.5	12.4	66.4
V	2.5	1.1	8.1	1.52	0.57	5.86	0.92	0.39	5.1
Cr	1.5	0.8	13.1	1.88	0.38	7.66	0.55	0.1	4.2
Mn	222	70	896				256	22	750
Fe	357	147	845	401	176	1850	209	-77	1370
Co	0.3	0.1	1.5				0.202	0.065	0.654
Ni	1.8	0.1	3.5	1.95	0.56	10.2	1.1	0.1	6.6
Zn	45	31	110	35	19.4	149	26.5	7.9	173
As	0.61	0.25	6.04	0.29	0.07	1.4	0.093	0.02	0.505
Se	0.33	0.22	0.77			· . + ·	0.33	0.05	1.3
Br	1.3	0.91	2.85		1	-	4.5	1.4	20.3
Rb	22	2	45	-	-	_::	7.7	1.3	51.5
Sr	7.3	0.7	339	1 1		-	15.8	3.6	43.3
Mo	· <u>-</u>		· · · · · ·	-	-	-	0.135	0.065	0.7
Sb	0.25	0.16	0.79	-	-	-	0.033	0.004	0.24
I	1.11	0.35	2.68	-	-		2.5	0.6	41.7
Cs	0.41	0.16	1.3	-	•	-	0.072	0.016	0.88
Ba	10	5.5	79	-			17.1	5.6	50.5
La	0.5	0.14	1.6	-	-	-	0.189	0.045	2.56
Ce	1.1	0.2	3.7	/ - .		_	0.342	0.095	4.61
Sm	-	-			-		0.33	0.05	1.34
Tb	0.012	0	0.085		-	. 1	0.003	< 0.002	0.03
Yb	0.03	0.01	0.18	· <u>-</u>	_	-	_1V=1,93	34 🚅 3 T	- 4
Hf	0.09	0.01	0.58	. ·	· -	-	No. 2 . 15	* 1 - - 1	-
Ta	0.02	0.01	0.13	<u> </u>	-	-	0.01	<0.01	0.07
W	0.19	0.02	0.62	-	-	5 <u>-</u> 1 -	0.13	0.01	1.23
Au	0.002	0	0.024	_	_		· _ ·	1 <u>2</u> 1	-
Th	0.13	0.08	0.45	•	-	_	0.033	0.004	0.24
U	0.08	0.02	0.99	<u>-</u>	-	-	0.015	0.001	0.138

Conclusin

This is the first attempt to assess the atmospheric deposition of heavy metals and other trace elements within the Opole Region. The study adds this region to the European moss network.

A comparison with the neighboring industrial regions, where similar studies have been conducted in the past [6] shows that the level of toxic elements in moss collected in the agricultural Opole Region are practically the same. Aside from the local industries, the origin of pollutants from the neighboring large industrial areas is obvious. Further detailed moss surveys in Opole Region on larger scales will fill more gaps in the atmospheric deposition map of Europe.

Acknowledgement

The authors express their gratitude to Elena Povtoreyko for help in creating GIS maps and to Ilona Koral for help in moss collecting and research workers from Institute of Physics, Opole University.

References

- European Atlas: Heavy Metals in European mosses: 2000/2001 survey, UNECE ICP Vegetation. Editors: A. Buse, D. Norris, H. Harmens, P. Buker, T. Ashenden and G. Mills. Centre for Ecology & Hydrology, University of Wales Bangor, United Kingdom, March 2003, pp. 45.
- 2. T. Berg, E. Steinnes, Environment Pollution, Vol. 98, 1997, p. 61-71.
- 3. K. Grodzinska, G. Szarek-Lukaszewska, B. Godzik. Survey of heavy metal deposition in Poland using mosses as indicators. Sci. Total Environ., Vol. 229, 1999, p. 41-51.
- 4. K. Grodzinska, G. Szarek-Lukaszewska. Response of mosses to heavy deposition in Poland An overview. *Environ. Pollut., Vol. 114, 2001, p. 443-451.*
- K. Grodzinska, G. Szarek-Lukaszewska, M. Frontasyeva, S.S. Pavlov, S.F. Gundorina. Multielement concentration in mosses in the forest influenced by industrial emissions (Niepolomice Forest, South Poland) at the end of 20th century. *Polish Journal of Environmental Studies*, Vol. 14, No. 2, 2005, p. 171-178.
- K. Grodzinska, M.V. Frontasyeva, G. Szarek-Lukaszewska, M. Klich, A. Kucharska-Fabis, T.M. Ostrovnaya, S.F. Gundorina. Trace element contamination in industrial regions of Poland studied by moss monitoring. *Environmental Monitoring and Assessment*. Vol. 87, No. 3, 2003, p. 255-270.
- 7. E. V. Ermakova, M. V. Frontasyeva, E. Steinnes, Air Pollution Studies in Central Russia (Tula Region) Using the moss biomonitoring technique, INAA and AAS, *Journal of Radioanalytical and Nuclear Chemistry*, Vol. 259, No. 1, 2004, p. 51–58.
- 8. E. V. Ermakova, M. V. Frontasyeva, S. S. Pavlov, E. A. Povtoreyko, E. Steinnes, Ye. N. Cheremisina, Air Pollution Studies in Central Russia (Tver and Yaroslavl Regions) Using the Moss Biomonitoring Technique and Neutron Activation Analysis, *Journal of Atmospheric Chemistry*. Vol. 49. 2004, p. 549-561.
- M. V. Frontasyeva, E. Steinnes, Epithermal Neutron Activation Analysis of Mosses Used to Monitor Heavy Metal Deposition Around an Iron Smelter Complex, The Analyst, Vol. 120, 1995, p. 1437-1440.
- 10. O. A. Culicov, M. V. Frontasyeva, 1 E. Steinnes, O. S. Okina, Zs. Santa, R. Todoran, Atmospheric deposition of heavy metals around the lead and copper-zinc smelters in Baia Mare, Romania, studied by the moss biomonitoring technique, neutron activation

- analysis and flame atomic absorption spectrometry, *Journal of Radioanalytical and Nuclear Chemistry*, Vol. 254, No. 1, 2002, p. 109–115.
- 11. M. V. Frontasyeva, T. Ye. Galinskaya, M. Krmar, M. Matavulj, S. S. Pavlov, D. Radnović, E. Steinnes. Atmospheric Deposition of Heavy Metals in Northern Serbia and Bosnia-Herzegovina Studied by Moss Biomonitoring, Neutron Activation Analysis and GIS Technology, Journal of Radioanalytical and Nuclear Chemistry, Vol. 259, 2004, p. 141–147.
- L. Barandovski, M. Cekova, M. V. Frontasyeva, S. S. Pavlov, T. Stafilov, E. Steinnes, V. Urumov, Air Pollution Studies in Macedonia Using The Moss Biomonitoring Technique, NAA, AAS and GIS Technology, JINR Preprint E18-2006-160, Dubna, 2006.
- 13. http://icpvegetation.ceh.ac.uk.
- 14. E. Steinnes, (2005). Values from pristine regions of Northern Norway in 2005 (unpublished).
- 15. Frontasyeva M.V., Pavlov S.S., Analitical investigation at the IBR-2 Reactor in Dubna: preprint JINR E14-2000-177, 2000.
- 16. Ochrona Środowiska 2006, Informacje i Opracowania Statystyczne, Warszawa 2006.

TEMPORAL VARIATIONS OF ELEMENTAL CONTENT IN ATMOSPHERIC AEROSOL IN BRATISLAVA, SLOVAKIA

J. Meresova¹, M. Florek¹, M. V. Frontasyeva², S. S. Pavlov², K. Holy¹, I. Sykora¹

¹Dept. of Nuclear Physics and Biophysics, Comenius University, Bratislava, SR
²Dept. of Neutron Activation Analysis, Frank Laboratory of Neutron Physics
Joint Insitute for Nuclear Research, 141980 Dubna, Moscow Region, Russia

In the framework of urban air pollution studies the elemental concentrations of atmospheric aerosols collected at urban sites in the capital of the Slovak Republic Bratislava are presented in this paper. Sixteen filter samples were exposed during 7-10 days during different seasons of the year 2004. As a result of two irradiations and four gamma-spectrometric measurements the concentrations of 30 chemical elements (Na, Al, Cl, K, Ca, Sc, Ti, V, Cr, Mn, Fe, Ga, As, Se, Br, Rb, In, Sb, I, Cs, Ba, La, Sm, Dy, Tm, W, Au, Hg, Th, U) were determined using instrumental neutron activation analysis (INAA). Additionally the concentrations of other 5 elements (Cr, Ni, Cu, Zn, Cd, Pb) were measured by atomic absorption spectrometry (AAS). The main goal of this project is to better understand the dynamic processes taking place in the atmosphere and to study the temporal variations of some elements in the airborne particulate matter. For some elements seasonal variations in concentration were observed, for the others the concentrations were relatively stable over the year. The correlations between concentration of elements and some meteorological characteristics are discussed.

1. Introduction

The atmosphere is one of the crucial parts of the environment and its monitoring is essential in the process of evaluating of the actual ecological situation and consequentially deciding on the level of environment protection and intervention required. The air-born particles significantly influence several atmospheric processes, for example like creation of clouds. Therefore it is important to know their chemical composition and physical characteristics to assess the impact on the environment and human health.

There are several epidemiological studies showing positive correlation between different aerosol characteristics and increased human morbidity and mortality [1, 2].

Because of the advantages of instrumental neutron activation analysis (INAA) it was found to be the key analytical method for determining the elemental composition of the solid environmental samples. The main reasons are the small sample quantity needed, multi-elemental analysis, direct non-destructive method, etc [3].

Aerosol particles contain various elements including heavy metals. Some heavy metals are essential biogenic elements (Mn, K, Ca, Na, Cu, Zn) and they play an important role in the nutrition of plants, animals and humans, but if they occur at elevated concentrations, they may produce toxic effects.

The others (Cd, Hg, Pb) are toxic even at very low levels. Heavy metals are released to the environment from a great number of sources like different industrial activities or combustion of fossil fuels. These elements are components of traffic emissions and are emitted into the atmosphere in the form of fine dust and aerosols. Airborne soil particles, volcanic aerosols and forest fires contribute to natural emissions of trace elements [4].

The seasonal variations of pollutants in atmosphere are governed by atmospheric transport processes and circulation. The main features of this behavior are the following [5]: (a) rate of vertical mixing within the troposphere; (b) amount of rainfall.

2. Experimental

Using a sampling device with an air-flow rate of 30 m³·h⁻¹ aerosol particles were collected on the nitro-cellulose membrane filters (PRAGOPOR, pore size 0.8 μ m, collection efficiency ~ 100 %) at the height of 2.85 m above the ground.

The sampling location is situated at the urban site at the Meteorological Station near the Faculty of Mathematics, Physics and Informatics, Comenius University (FMFI UK), Bratislava.

Collection of the aerosol samples was performed during different seasons of the year 2004. The filters were changed every week, and about 3000 m³ of air was pumped through each sample. In September 2004 a new sampling device was installed, and the volume of numped air increased twofold.

The air filter samples were irradiated in the pulsed fast reactor IBR-2, FLNP JINR and the REGATA experimental setup was used for multi-element determination. The irradiation facility is described elsewhere [6].

After sampling the filters were divided into several parts for different examinations. One part was pelletized using simple press-forms and heat-sealed in polyethylene foil bags (~0.4 g) for short-term irradiation.

A special effort had to be taken to avoid contamination of the samples. Since the most interest is on the determination of heavy metals, the press-form is made from plastic. To determine the short-lived isotopes conventional NAA was used.

Samples were irradiated for 10 minutes and immediately measured for 5 min and a second time for 20 min. The time of irradiation depends on the type of sample and the presumed element composition. It can vary from 3 to 20 minutes for short-lived isotopes determination. After the determination of short-lived isotopes, samples repacked into aluminum containers and irradiated in the epithermal cadmium-screened channel for determination of long-lived isotopes. The samples are usually irradiated for 3 days.

Unfortunately the nitrocellulose material is not appropriate for long-term irradiation, thus samples were irradiated only for one hour and measured twice after 4-5 days and 20 days of decay.

The gamma spectra were measured with GeLi detectors with a resolution of 2.5-3 keV for the 1332.5 keV peak of ⁶⁰Co. The data processing was carried out using software developed in FLNP JINR, and element contents were determined on the basis of certified reference materials and flux comparators [6]. For short-term irradiation in Ch2 Au (10 µg) was employed as a comparator.

Certified reference materials were used for quality controls: Lichen IAEA-336 and Cabbage IAEA-359 (International Atomic Energy Agency); SRM-1573a (tomato leaves) and SRM-1633b (coal ash) from the US NIST (National Institute of Standards and Technology). For long irradiations the reference materials were packed together with samples in each transport container. The reference material showing least deviation between measured and certified values of elemental content was chosen.

The major disadvantage of NAA is the inability to determine some elements like Cd, Tl, Pb, Bi. The reasons are a combination of very low activation cross-sections, activation products with very short half-lives, and the emission of radiation not suitable for gamma-spectrometry detection. For this reason the contents of some environmentally important elements like Cr, Ni, Cu, Zn, Cd and Pb were determined using atomic absorption spectrometry at Institute of Geology at Faculty of Natural Sciences at Comenius University with accuracies 5, 17, 1, 2, 25, and 1.4 %, respectively.

3. Results and Discussion

The results of descriptive statistics (min, max, median, average, standard deviation) applied to the experimental data are presented in the Table 1.

Table 1. Concentrations of elements [ng·m⁻³] in atmospheric aerosol

Element	Number of samples	Min	Max	Median	Average	Standard deviation
Na	16	59	308	104	129	72
Al	16	40	912	189	261	223
Cl	16	32	102	49	56	20
K	16	72	290	195	184	- 67
Ca	16	54	312	179	175	91
Sc	7	0.007	0.040	0.032	0.030	0.011
Ti	. 15	3.2	14.1	7.8	7.5	3.6
V	16	0.28	1.62	0.83	0.92	0.43
Cr	9	0.3	8.1	1.1	1.7	2.5
Mn	16	1.9	8.6	~ 4.9	4.9	2.0
Fe	5	85	285	252	204	85
Ni	6	0.39	0.90	0.45	0.51	0.19
Cu	15	4 .	27	8	10	7
Zn	15	20	45	28	30	8 540
Ga	4	0.018	0.024	0.020	0.020	0.003
As	7	0.11	0.71	0.30	0.39	0.21
Se	7	0.13	1.01	0.42	0.45	0.31
Br	16	1.7	8.6	3.5	3.6	1.7
RЬ	3	0.0001	0.0003	0.0001	0.0002	0.0001
Cd	14	0.02	0.40	0.11	0.14	0.10
In	14	0.0004	0.0149	0.0010	0.0036	0.0045
Sb	7	0.5	1.9	1.0	1.1	0.5
I	16	0.28	1.65	0.66	0.78	0.36
Cs	6	0.030	0.072	0.045	. 0.048	0.018
Ba	15	0.7	3.8	2.1	2.1	0.9
La	. 6	0.038	0.166	0.085	0.089	0.049
Sm	7.	0.002	0.016	0.012	0.011	0.005
Dy	14	0.002	0.016	0.010	0.010	0.004
Tm	6	0.025	0.144	0.098	0.090	0.054
W	7	0.05	0.82	0.22	0.27	0.26
Au	7	0.0001	0.0007	0.0002	0.0003	0.0002
Hg	6	0.01	0.56	0.06	0.19	0.24
Pb	15	10	81	22	28	20
Th	5	0.005	0.080	0.042	0.039	0.028
U	16	0.005	0.019	0.012	0.012	0.004

A correlation analysis was performed but as presented in the Table 2 no significant correlation between the elemental concentrations and meteorological parameters was found.

Table 2. Linear correlation coefficients between elemental concentrations and some meteorological parameters

	Pressure	Humidity	· Precipitation	Temperature	Wind
Na	-0.05	-0.13	-0.05	0.43	-0.32
A1	-0.25	-0.32	-0.32	0.65	-0.29
CI	-0.23	-0.29	-0.20	0.70	-0,33
K	0.08	0.48	-0.31	0.09	-0.63
Ca	-0.14	-0.35	-0.20	0.63	-0.41
Ti	0.01	-0.29	-0.20	0.55	-0.42
\mathbf{v}	0.14	0.52	-0.17	-0.12	-0.23
Mn	-0.07	-0.12	-0.40	0.59	-0.44
Cu	-0.14	-0.34	-0.25	0.45	-0.06
Zn	0.25	0.19	-0.33	0.06	-0.58
Br	0.61	0.57	-0.43	-0.39	-0.46
Cd	0.49	0.30	-0.05	-0.35	-0.30
In	0.02	0.04	0.25	0.01	-0.02
In	0.09	0.44	0.11	-0.68	0.01
Ba :	-0.18	-0.31	-0.04	0.60	-0.32
Dy	-0.04	0.02	-0.15	0.33	-0.65
Pb	-0.06	-0.27	0.15	0.30	-0.33
ַ ט	-0.15	-0.13	-0.23	0.59	-0.51

The increased concentrations can be caused by intensive vertical mixing within the troposphere typical for the hot season and hence stronger re-suspension from the Earth's surface. Generally it can be concluded that the air temperature is the main factor influencing temporal variations of elemental content in low-level atmosphere.

The correlations with other meteorological parameters are seldom observed; nevertheless their influence is also important and very complex.

The one-week sampling period is quite long compared with the typical time scale of variations of meteorological parameters so that the correlation might be underestimated. Measurements over more than one year would be needed to truly prove the trend of seasonal variations. For the other elements the concentrations are relatively stable over the year.

Weak correlation between some elements (Al, Cl, Ca, Ti, Mn, Ba, U) and the air temperature was observed. Most of these elements are of terrestrial origin, although they may also be emitted as fly-ash from the combustion of coal, and as dust from other mineral-related activities.

The concentrations of these elements also indicate seasonal variations over the year with elevated values in summer (Fig. 1).

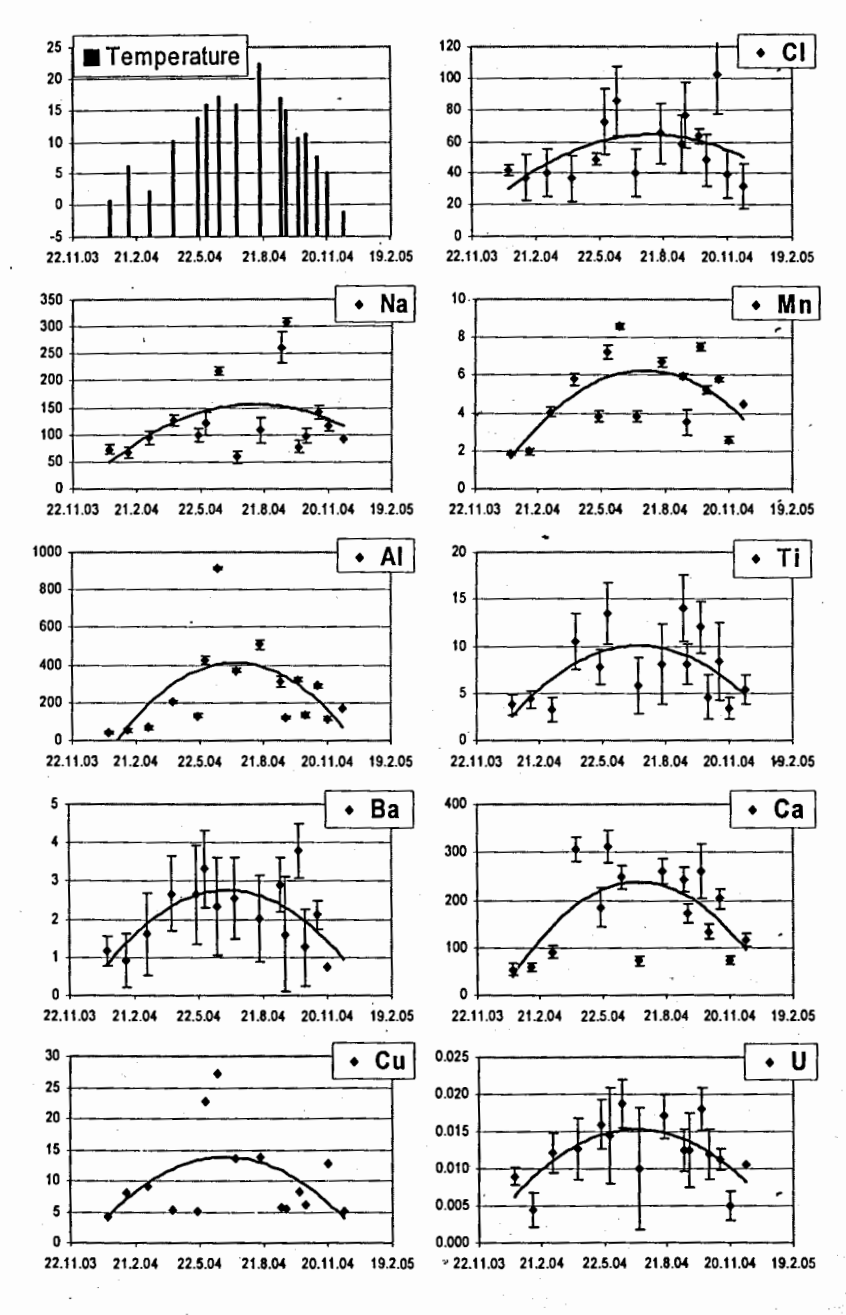


Fig. 1. Air temperature [°C] and temporal variations of concentrations of some elements [ng·m⁻³] in atmospheric aerosol in Bratislava during the year 2004.

4. Conclusion

For the first time an extensive range of elements was determined in air filters in Slovakia. This is also a first study dedicated to seasonal variations of the elemental content in atmospheric aerosol in Bratislava. The temporal variations of some elements, mainly of terrestrial origin were observed. Higher values in summer season may be explained by increased wind activity within the troposphere. Measurements over more than one year would be needed to really prove the trend of seasonal variations.

Atmosphere reflects the industrial activities in the country hence systematic and comprehensive monitoring is important in order to assess the potential environmental hazards connected with air pollution. The data may be useful as reference values for comparison with the future measurements of pollution in Bratislava's atmosphere.

References

- D.W. DOCKERY, et al.: An association between Air Pollution and Mortality in six US Cities. New England Journal of Medicine 329 (1993) 1753.
- [2] C.A. POPE, D.W. DOCKERY, J. and Schwartz: Review of epidemiological evidence of health effects of particulate air pollution. *Inhalation Toxicology 7 (1995) 1*.
- [3] R. DAMS: Pure and Appl. Chem. 64 (1992) 991.
- E. CHMIELEWSKA, H. SPIEGEL: Some Control of an Amplified Heavy Metal Distribution at Immission Sites of Danube Lowland Refineries. *Environment Protection Engineering* 29 (2003) 23-32.
- [5] H.W. FEELY, R. J. LARSEN, C.G. SANDERSON: Factors that Cause Seasonal Variations in Beryllium-7 Concentrations in Surface Air. Journal of Environmental Radioactivity 9 (1989) 223-249.
- [6] M.V. FRONTASYEVA, S.S. PAVLOV: Analytical investigation at the IBR-2 reactor in Dubna. Proceedings of the VII International Seminar on Interaction of Neutrons with Nuclei. Dubna. May 17-20. 2000. E3-2000-192. 219-227. JINR (Also JINR Preprint. E14-2000-177. Dubna. 2000).

POTENTIAL OF THE TAMARINDUS INDICA LEAVES AS BIOMONITORS FOR ATMOSPHERIC CONTAMINATION IN VIETNAM

Trinh T.T. My¹, M.V. Frontasyeva¹, Nguyen Hong Nhung²

¹Frank Laboratory of Neutron Physics, Joint Institute for Nuclear Research, 141980 Dubna, Russia. E-mail: trinh@nf.jinr.ru ²Biology Faculty of University Hochiminh City, Vietnam

Abstract

Higher plants are used as monitors in the heavy metal pollution monitoring in the areas where lichens and mosses are absent. The *Tamarindus Indica (TI)* is a widespread fruit tree, which culturally or wildly grows in tropical and near-tropical areas. Thirty-nine samples of the *TI* leaves collected over Hochiminh City have been used in heavy metal pollution monitoring of the city. Seven samples of the *TI* leaves collected in Cangio, the control region 60 km south-east of the Hochiminh City, at the seaside of the Pacific Ocean, have been used to assess the control level of pollution. A total of 35 elements has been determined by the epithermal neutron activation analysis. Mean elemental concentrations of samples collected in the two regions have shown the relative pollution situations of the two areas and have been used as the base for discussion. The obtained results have been compared with the literary data on other similar deciduous trees.

1. Introduction

Due to rapid urbanization and industrial development in recent years, the pollution has caused serious damage of the environment in Vietnam. Thus, the monitoring of heavy metals and other toxic elements in the urban environment has become an essential part of environmental planning and control programs in Vietnam. Until now in Vietnam air pollution has been studied by a number of monitoring stations for controlling the content of gas exhaust and the atmospheric deposition studies were carried out almost only by using filters ^{1,2}. Biomonitors such as fish, mussels, aquatic biota ³ and bird ⁴ have been used for environment studies. In Vietnam the environment biomonitoring is at the initial stage.

Biomonitors provide a measure of environment pollutant accumulation and expensive technical equipment is not involved in their sample collection. The use of mosses and lichens as biomonitors of atmospheric deposition is a well-established technique ^{5.6}; similarly, the plant needles and plant leaves have been used to monitor the extent of pollution ^{7,8,9}.

Owing to the subtropical and tropical geographical location of Vietnam, lichens and mosses are hardly found there, and so in the present study *Tamarindus Indica* has been used as a biomonitor for studying atmospheric pollution. The *TI* trees have been chosen as a biomonitor due to the following circumstances:

- they can grow widely in the tropical and near-tropical regions (but there is the necessity of the first TI propagation)
- TI fall period is easy to be distinguished and leaf samples can be collected at almost the same exposition time

2. Materials and method

Study area

The 46 leaf samples of TI have been collected from different sites in the Hochiminh City (inner city and suburbs - 39 samples) and in the rural district Cangio (7 samples). Figure 1

Hochiminh City is the largest city, the greatest port, the commercial and industrial center of Vietnam, with a population of approximately 6 million people (2004), producing one-third of the country's industrial output of Vietnam. There is an airport, shipping terminal, many focuses of the country's highways and a condensed system of roadways, waterways over the city. The land area is about two thousand sq. km; the meteorological position is $10^{\circ}47^{\circ}$ N, $106^{\circ}40^{\circ}$ E, and 10 m alt. Alluvial soils are the principal soil type and the rest is the acid sulphate soil. These soils are generally slightly acidic (Hochiminh City groundwater pH: 5.8-6.75) 10 .

Cangio covers the entire estuary of the Saigon-Dongnai river system; its greater part is the mangrove saline soil and the rest is the acid sulphate soil. This is the biosphere reserve region, recognised by the UNESCO. The soil has a high content of nutrients and a pH of 5.8 - 6.5 but in mangrove areas, pH fluctuates widely, between 4.5 and 8.8^{11} .

In the two regions, the climate is generally hot and humid. The relative humidity mainly varies around 80%, which significantly varies between the dry months (December – April: 75 – 80%) and rainy months (May – November: 85 – 89%).

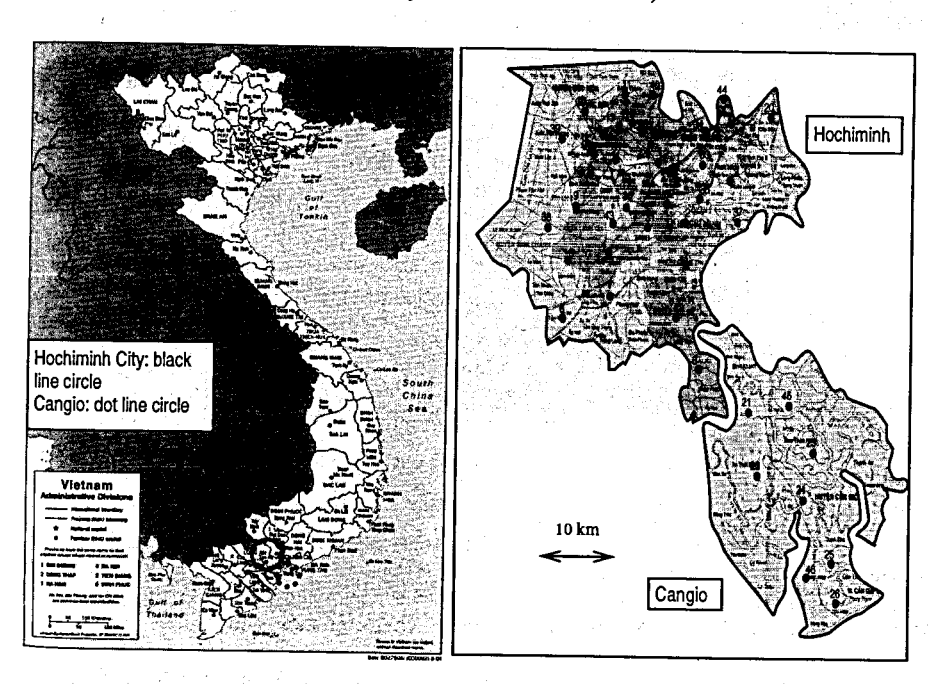


Figure 1. The position of Hochiminh City, Cangio region and the 46 sampling sites

Material

Tamarindus Indica L. (syns. T. Occidentalis Gaertn.; T. officinalis Hook.), of the family Leguminosae; most of its colloquial names are variations on the common English term "tamarind". The tamarind is one of widespread fruit trees, which can culturally or wildly grow in tropical and near tropical areas. The tree tolerates a great diversity of soil types, from deep alluvial soil to rocky land and porous, oolitic limestone. It withstands salt spray and can be

planted fairly close to the seashore. Besides, the *TI* existence somewhere is dependent on its first propagation. The tamarind is mainly propagated from seeds dispersed by animals (ruminants, man, monkeys...); other methods of propagation are cuttings, budding, and grafting¹².

The *Tamarindus Indica* is a deciduous, evergreen tree; it does not lose its leaves at one time, unless some reason damages the tree. The leaf lost because of tree damage and the one at fall period are easily distinguished by observing the tree and its features. The *Tamarindus Indica* leaf is a complex leaf consisting of many small leaves, which are lost gradually in the fall period (Figure 2). Thus, the sample leaves collected in this period are almost at the same exposition time of about seven months.

All the leaf samples were collected from TI trees at the height of 1 to 2.5 meters with a trunk diameter of 8-30 cm except for the trunk diameter of 40-100 cm at site 32. At each sampling site, leaves of at least two to four trees were taken and combined to one collective sample. The sampling was done in July, 2005, and July, 2006, following the instruction of sampling procedure for analysing air pollution effects on forest of the UNECE ICP vegetation project 13 , 14 .

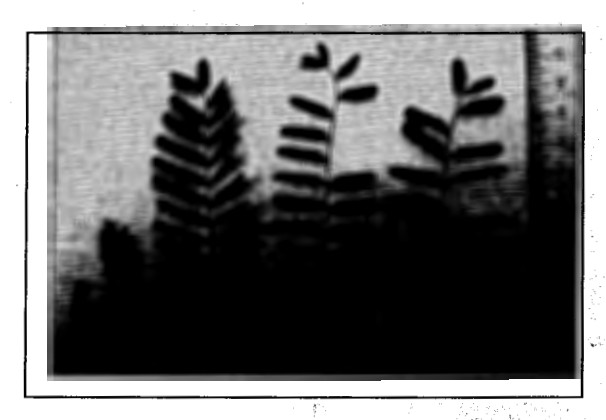


Figure 2. Tamarindus Indica leaves: from young to fall period

Neutron Activation Analysis (NAA)

The leaf samples were dried at 40°C to constant weight of about 0.4g, were heat-sealed in polyethylene foil bags for short-term irradiation and packed in aluminium cups for long-term irradiation in the channel equipped with a pneumatic system in the pulsed fast reactor IBR-2 in Dubna. Neutron flux density characteristics and temperature in the irradiation channels are shown elsewhere ¹⁵.

- To determine the short-lived isotopes, samples were irradiated for 3-5 minutes and measured twice after 3-5 minutes of decay for 5-8 and 20 minutes, respectively, at channel 2 (Ch2).
- Elements yielding long-lived isotopes were determined using Cd-screened channel 1 (Ch1). Samples were irradiated for 4 days, repacked, and then measured twice after 4-5 and 20 days of decay, respectively. The time of measurements was 45 minutes and 2 hours 30 minutes.

- The gamma spectra of the samples were measured with the Ge(Li) detector with the resolution of 2.5 3 KeV for the ⁶⁰Co 1332 KeV line or the HPGe detector with the resolution of 1.9 KeV for the ⁶⁰Co 1332 KeV line.
- Data processing was carried out using the software developed in FLNP JINR.
 Elemental contents were determined on the basis of certified reference materials and comparator fluxes.

Quality control

The QC content of elements yielding short- and long-lived isotopes was ensured by using the certified reference materials: (RM) Lichen 336, soil SL-1 IAEA (International Atomic Energy Agency) and the standard reference materials SRM-1633b (coal fly ash) from the US NIST (National Institute of Standards and Technology). For long irradiation the three reference materials were packed together with 10 – 12 samples in each transport container.

Statistical analysis

Factor analysis is a multivariate statistical technique to reduce the number of variables and to detect the structure in relationships between variables, or to classify variables. The factor analysis has been successfully used in the air pollution studies. It simplifies a large and complex data set of many variables in such a way to create new factors (the number of new factors is smaller than that of original variables) which make it possible to explain the original data set ¹⁶.

The purposes of using factor analysis in our study were to define the common factors (independent pollution sources) and to calculate their factor loadings.

3. Result and discussion

Results

Table 1 has shown mean elemental concentration values of 35 elements determined in the *Tamarindus Indica* leaf samples from 39 sites in Hochiminh City and 7 sites in Cangio district and the ratio of the mean concentrations of two regions (Chow/Compo) for every element. Besides, the ratio of the Hochiminh mean concentration to the minimum one (of all the samples) for every element (Chow/Cmh) is presented in this table. The elements have been found in most of the samples except for mercury (Hg), which has been found in 19 samples (17 in HCM City and 2 in Cangio). Besides, silver (Ag) has been found in 14 samples in the concentration range of 0.01 – 0.5 ppm only in the HCM City samples.

The mentioned data of humidity, soil type and mean pH of the two studied areas have been slightly different hence, it was supposed that these conditions have affected insignificantly to the obtained results.

Table 1. Elemental concentration ($\mu g \cdot g^{-1}$) in leaves of *Tamarindus Indica* and of other deciduous plants

			VIETNA	М	ignation The ext	च 'श		POLAND ²		SRM - 1572	CANADA ²¹
		collected in xp. time:~7 n		CHCM/ Cmin	CHCM/ CCangio	Err.		es collected p. time: ~ 7		exp. time: unknown	exp. time: ~ 5 months
	HCM (mean)	CANG!O (mean)	Min (all sampl.)	Ratio	Ratio		12,33	Mean		Mean	Mean
_Ele.	T. I	* T.1	T.1.			(%)	Willow	Linden	Birch	Citrus	Oak
NA	2100	3800	160	13.1		5				160	87
MG	3700	5400	1000	3.7		15	1640	3000	2750	5800	3200
AL	450	260	120	3.8	1.7	7 -	130.2	498	159.7	92	104

CL 5600 11000 260 21.5 16 18 18200 K 7400 5500 2200 3.4 1.3 15 18200 SC 0.07 0.04 0.01 7.0 1.8 20 0.01 CA 33000 33300 8000 4.1 5 21667 37200 25133 31500 CR 1.5 0.5 0.4 3.0 40 2.8 8.93 3.1 0.8 V 1.2 0.5 0.4 3.0 2.4 30 30 5.8 5 57.2 94.2 253.3 23 Ni 1.5 3 0.5 3.0 30 5.8 7.63 4.7 FE 420 300 100 4.2 1.4 15 200.0 772 282.3 90 CO 0.3 0.5 0.02 15.0 20 0.02 0.02 0.02 0.02 15	145 6600 20000 0.09 96
SC 0.07 0.04 0.01 7.0 1.8 20 0.01 CA 33000 33300 8000 4.1 5 21667 37200 25133 31500 CR 1.5 0.5 0.4 3.0 40 2.8 8.93 3.1 0.8 V 1.2 0.5 0.4 3.0 2.4 30 MN 70 110 12.06 5.8 5 57.2 94.2 253.3 23 Ni 1.5 3 0.5 3.0 30 5.8 7.63 4.7 FE 420 300 100 4.2 1.4 15 200.0 772 282.3 90 CO 0.3 0.5 0.02 15.0 20 772 282.3 90 CO 0.3 0.5 0.02 15.0 20 35	20000 0.09 96
CA 33000 33300 8000 4.1 5 21667 37200 25133 31500 CR 1.5 0.5 0.4 3.0 40 2.8 8.93 3.1 0.8 V 1.2 0.5 0.4 3.0 2.4 30 MN 70 110 12.06 5.8 5 57.2 94.2 253.3 23 Ni 1.5 3 0.5 3.0 30 5.8 7.63 4.7 FE 420 300 100 4.2 1.4 15 200.0 772 282.3 90 CO 0.3 0.5 0.02 15.0 20 0.02	0.09 96
CR 1.5 0.5 0.4 3.0 40 2.8 8.93 3.1 0.8 V 1.2 0.5 0.4 3.0 2.4 30 3.1 0.8	0.09 96
V 1.2 0.5 0.4 3.0 2.4 30	96
MN 70 110 12.06 5.8 5 57.2 94.2 253.3 23 Ni 1.5 3 0.5 3.0 30 5.8 7.63 4.7 FE 420 300 100 4.2 1.4 15 200.0 772 282.3 90 CO 0.3 0.5 0.02 15.0 20 0.02 0.03 0.03 0.03 0.03 0.03 0.03 0.03 0.03 0	96
Ni 1.5 3 0.5 3.0 30 5.8 7.63 4.7 FE 420 300 100 4.2 1.4 15 200.0 772 282.3 90 CO 0.3 0.5 0.02 15.0 20 0.02 0.02 0.02 0.02 0.02 0.02 0.02 0.02 0.02 0.02 0.02 0.02 0.01 4.1 1.5 12 312.3 61.9 574.7 29 0.02 0.02 0.02 0.01 4.0 2.0 35 0.0 0.02 0.03 0.015 0.0 3.0 0.0	
FE 420 300 100 4.2 1.4 15 200.0 772 282.3 90 CO 0.3 0.5 0.02 15.0 20 0.02 0.02 ZN 45 30 11 4.1 1.5 12 312.3 61.9 574.7 29 SE 0.1 0.05 0.015 2.0 35 0.0 35 0.0	
CO 0.3 0.5 0.02 15.0 20 0.02	
ZN 45 30 11 4.1 1.5 12 312.3 61.9 574.7 29 SE 0.1 0.05 0.015 2.0 35	
SE 0.1 0.05 0.015 2.0 35 3.1 3.1 8.2 8.2 8.2 8.2 8.2 8.2 8.2 8.2 8.2 <td></td>	
AS 0.4 0.2 0.1 4.0 2.0 15	
BR 50 110 1.7 29.4 13 6 8.2 SR 90 175 5 18.0 3 74.4 93.5 70.9 RB 12 6 1.5 8.0 2.0 15 4.84 MO 0.1 0.08 0.05 40 0 0.04 SB 0.1 0.03 0.015 6.7 3.3 20 0.04 I 2.5 1.8 0.9 2.8 1.4 15 77.2 92.0 21 BA 21 5 1.7 12.4 4.2 25 20.3 77.2 92.0 21 CS 0.2 0.06 0.015 13.3 3.3 15 0.098 LA 1 1 0.2 5.0 20 0.19 CE 2 2.5 0.3 6.7 18 0.28	
SR 90 175 5 18.0 3 74.4 93.5 70.9 RB 12 6 1.5 8.0 2.0 15 4.84 MO 0.1 0.08 0.05 40 0.00 0.04 SB 0.1 0.03 0.015 6.7 3.3 20 0.04 I 2.5 1.8 0.9 2.8 1.4 15 0.00 BA 21 5 1.7 12.4 4.2 25 20.3 77.2 92.0 21 CS 0.2 0.06 0.015 13.3 3.3 15 0.098 LA 1 1 0.2 5.0 20 0.19 0.19 CE 2 2.5 0.3 6.7 18 0.28 0.28	
RB 12 6 1.5 8.0 2.0 15 4.84 MO 0.1 0.08 0.05 40 0.00 SB 0.1 0.03 0.015 6.7 3.3 20 0.04 I 2.5 1.8 0.9 2.8 1.4 15 0.00 BA 21 5 1.7 12.4 4.2 25 20.3 77.2 92.0 21 CS 0.2 0.06 0.015 13.3 3.3 15 0.098 LA 1 1 0.2 5.0 20 0.19 CE 2 2.5 0.3 6.7 18 0.28	1.04
MO 0.1 0.08 0.05 40 0.03 0.04 SB 0.1 0.03 0.015 6.7 3.3 20 0.04 0.04 I 2.5 1.8 0.9 2.8 1.4 15 0.00 0.04 0.00	7.5
SB 0.1 0.03 0.015 6.7 3.3 20 0.04 I 2.5 1.8 0.9 2.8 1.4 15 0.04 BA 21 5 1.7 12.4 4.2 25 20.3 77.2 92.0 21 CS 0.2 0.06 0.015 13.3 3.3 15 0.098 LA 1 1 0.2 5.0 20 0.19 CE 2 2.5 0.3 6.7 18 0.28	100
I 2.5 1.8 0.9 2.8 1.4 15 —	-
HA 21 5 1.8 0.9 2.8 1.4 15 92.0 21 CS 0.2 0.06 0.015 13.3 3.3 15 0.098 LA 1 1 0.2 5.0 20 0.19 CE 2 2.5 0.3 6.7 18 0.28	
CS 0.2 0.06 0.015 13.3 3.3 15 0.098 LA 1 1 0.2 5.0 20 0.19 CE 2 2.5 0.3 6.7 18 0.28	0.08
LA 1 1 0.2 5.0 20 0.19 CE 2 2.5 0.3 6.7 18 0.28	22
CE 2 2.5 0.3 6.7 18 0.28	1.5
SM 0.1 0.1 0.02 5.0 15 0.025	
	4 1
TB 0.01 0.02 0.004 2.5 25	100
HF 0.02 0.01 0.009 2.2 2.0 30	1000
TA 0.01 0.005 0.002 2.0 40 0.24	4,712
W 0.5 <0.1 0.06 40	
AU 0.01 <0.005 0.0009 40	3 500
Hg 0.1 <0.005 0.002 45	44.14
TH 0.07 0.04 0.01 7.0 1.8 16	407.40
U 0.02 <0.01 0.002 10.0 20	

Except for the elements derived from the marine environment and Ni, concentrations of all other elements characterising metal contamination have been from 1.3 (K) to 4.2 (Ba) times higher in Hochiminh City samples than in those of Cangio. The ratio C_{HCM}/C_{Cangio} has shown the relative difference of elemental pollution levels of the two regions.

In using the concentration minimum C_{min} (of all the samples) of the element as the background concentration value, the ratio C_{HCM}/C_{min} has shown a possible value representing the relative difference of Hochininh City pollution level and a possible background (for the element). A comparison of the two values C_{HCM}/C_{canglo} and C_{HCM}/C_{min} could give a preview about the contaminated situation of Cangio; thus, the Cangio elemental concentration values have been used as a referent data and have not been the background values. Cangio has been contaminated by the impact of its neighbour regions such as Hochiminh City and Vungtau, the oil industry region. Moreover, Cangio covers the ends of the river system; hence, it is polluted by the water discharge flowing into the river system.

The Ni median concentration in the Cangio samples is 2 (3/1.5) times higher than that in the samples of Hochiminh City, for Co this value is 1.7 (0.5/0.3). Nickel is the

characteristic element of oil product and cobalt compounds are naturally present in coal and oil. Shipping routes and oil spills are the obvious sources of the high Ni and Co content in Cangio. From 1992 to 2004, there were 12 oil spills with the volume of more than 100 tons and many smaller ones in the Sai Gon – Dong Nai River system¹⁷. The result corresponded to those of other authors ^{18, 19}.

Table 1 also shows mean concentrations of elements existing in other deciduous leaves, which are as follows:

- The citrus leaves of unknown exposition time (reference material SMR-1572 of NIST,
- The Canada oak leaves²⁰ of five month exposition time,
- The willow, linden and birch leaves collected at one site (their exposition time is about of 6-7 months) in western-south Poland in October of the vegetation season of 2000²¹.

The number of elements determined in TI leaves shows its ability to accumulate a large elemental spectrum. By a rough comparison of the elemental extents of TI leaves to those of other deciduous leaves, the TI leaves show an average ability of elemental accumulation for most of elements.

Factor analysis

The principal component analysis (PCA or another name - factor analysis - FA) was used to identify and apportion sources of contamination, which contribute to an elemental concentration data set of samples (receptor). The fundamental principle of this application is the source/receptor relationship and no assumption is made about the change in relative composition between the source and receptor ²². If large changes in relative composition occur during transport, the source may become unrecognised. The source/receptor model is a good model for metal air contamination studies using mosses or filters.

In this study where plant leaves were used, FA has been used to study sources of 23 elemental pollutants from the 35 detected elements showed in table 1. The plant macro nutrient elements such as K, Ca, Mg were excluded to avoid unwanted changes in relative composition between the source and receptor. Besides, the elements characterising seawater such as Cl, Na, Mg, Ca, Br, Sr have been excluded from FA to decrease the uninteresting variances.

Table 2. Factor loading matrix after the Varimax rotation and explained variances

Element	Factor 1	Factor 2	Factor 3	Factor 4	Factor 5
Percent of variance	26	20	12	12	7
Cumulative percent	26	46	58	70	77
AL	0.93	0.12	0.17	-0.06	0.07
SC	0.95	0.06	-0.02	-0.02	0.18
CR	0.34	-0.15	-0.06	0.30	0.72
v	0.68	0.20	0.04	0.39	-0.01
NI	20562	0.69	(13)	0.01	0.10
FE	0.92	0.02	-0.01	0.06	0.14
CO	-0.15	0.66		0.10	-0.01
ZN	0.03	0.46	0.02	0.13	0.61
SE	-0.02	-0.13	0.61	0.35	-0.20
AS	0.25	-0.04	0.46	0.63	-0.03
RB	-0.08	0.13	0.89	0.02	-0.01

SB	0.37	-0.12	-0.01	0.04	0.60
BA	0.21	-0.08	0.77	0.34	0.21
LA	0.18	0.85	0.31	0.01	-0.10
CE	0.10	0.92	-0.00	-0.14	0.03
SM	0.16	0.89	0.15	-0.09	0.01
ТВ	0.00	0.91	-0.16	-0.03	-0.04
HF	0.78	-0.09 ⁻	0.06	0.21	0.16
TA	0.56	0.10	-0.03	0.56	0.31
w	0.15	-0.00	0.20	0.77	0.29
AU	0.02	-0.13	0.08	0.91	0.06
TH	0.96	0.10	0.12	0.00	0.06
U	0.69	-0.14	-0.01	0.29	0.17

For plant micro nutrient elements, an insignificant change in relative composition between the source and receptor has been supposed. FA has shown a reasonable result for most of them except for nickel (Ni) and cobalt (Co). The loading factors of Ni and Co have been -0.41 and -0.54; it has been supposed to relate to the redistribution of these êlements in plant parts as Ni is required in nitrogen metabolism and Co is required for nitrogen fixation. Nitrogen (N) is a macro, mobile nutrient.

Using FA of five main factors could explain 77% of the total variance. Factor loading after the Varimax rotation and explained variances have been presented in Table 2. The five factors could characterize sources of different elements in the TI leaves as follows.

Factors 1, 2: (26% +20%) are complex factor representing the soil component with a high loading for crustal elements associated with each other (Al, Sc, Fe, Hf, Th, RE...) and V (Zn) suggesting the road dust shaken by traffic. This complex factor has possessed the highest variability 46% of the total variance; the factor apportionment (46%) reflects high construction activities and transportation activities of the Hochiminh City.

Factor 3: (12%) comprises the elements Se, As, Rb, Ba; it could relate to stationary fossil fuel combustion and other industry incinerators.

Factors 4, 5: (12%+7%) represent sources of local industry activities such as Zn, Sb, As, which could relate to the non ferrous metal sector, Cr, Zn to the metal finishing processing sector and Ta, W, Au to other industrial activities.

Acknowledgement

The authors thank the NAA Department staff, Frank Laboratory of Neutron Physics, Dubna for support during the study. This work has been performed within the framework of the JINR Project REGATA.

References

- ¹ Hien, P. D., Binh, N. T., Truong, Y., Ngo, N. T., Sieu, L. N., 2001. Comparative receptor modelling study of TSP, PM₂ and PM₂₋₁₀ in Ho Chi Minh City. Atmospheric Environment, 35, 2669-2678.
- ² Hien P. D., Bac V. T., Lam D. T., Thinh N. T. H. T. 2004. PMF receptor modelling of fine and coarse PM10 in air masses governing monsoon conditions in Hanoi, northern Vietnam. Atmospheric Environment, Vol. 38.
- ³ A. Wagner *et all*. Chemistry and Ecology, Issue1, Feb. 2007. Elemental concentration in air, water, and aquatic biota in two provinces in nothern Vietnam

- ⁴ Minh, T.B., T. Kunisue, N.T.H. Yen, M. Watanabe, S. Tanabe, N.D. Hue and V. Qui, 2002. persistent organochlorine residues and their bioaccumulation profiles in resident and migratory birds from North Vietnam. Environ. Toxicol. Chem., 21: 2108-2118
- ⁵ Ruhling, A. and Steinnes, E., 1998: Atmospheric heavy metal deposition in Europe 1995-1996, NORD 1998:15, pp. 66
- ⁶ Wolterbeek, B., 2002: Biomonitoring of trace element air pollution: Principles, possibilities and perspectives, Environ. Pollut. 120, 11-21.
- Mulgrew, A., Williams, P., 2002: Biomonitoring of air quality using plants, Air hygiene report No. 1-15
- ⁸ Madejon, P. and Maranon, T., 2004: White poplar (Populus alba) as a biomonitor of trace elements in contaminated riparian forests, Environ. Pollut. 132 (2004) 145-155
- ⁹ Daud, M. and Khalid, N., 2006: Potential of Broussonetia papyrifera leaves as biomonitors for atmospheric pollution: use of INAA and AAS techniques, Radiochim. Acta 94, 871-877 (2006)
- ¹⁰UNESCAP, 1995 "Study on coastal zone environment management with emphasis on the Mangrove ecosystem to assist in poverty alleviation. The case study of Cangio Mangrove system", Vietnam Bangkok, Thailand, 51 pp
- ¹¹Tao, Thieu Thi 1998 The socio-economic benefit of eco-aquaculture to women case study from E.A.P. Agricultural Publishing House, 1998: 164-168.
- ¹² Morton, J. 1987, Tamarind, p. 115–121, Fruits of warm climates, Julia F. Morton, Miami, FL
- ¹³UN/ECE-EC, Manual on methods and criteria for harmonised sampling, assessment, monitoring and analysis of the effects of air pollution on forests, PCC-BFH, Hamburg, 1998, pp. 1-30
- ¹⁴ Luyssaert, S. and Raitio, H., Sampling procedure for the foliar analysis of deciduous trees, J. Environ. Monit., 2002, 4, 858-864
- ¹⁵ Frontasyeva, M.V. and Pavlov, S.S. 2000: Analytical investigations at the IBR-2 reactor in Dubna, JINR preprint, E14-2000-177, Dubna.
- ¹⁶ Schaug, J., Ramb/k, J.P., Steinnes, E., 1990: Multivariate analysis of trace element data from moss samples used to monitor atmospheric deposition, Atmos. Environ. 24A, 2625-2631
- ¹⁷E. Wolanski (ed.): The Environment in Asia Pacific Harbours, Chapter 17, 261–291. © 2006 Springer. Printed in the Netherlands
- ¹⁸Trinh, Le and Nguyen Tat Dac. (2001). Main impacts of industrial zones and urbanization on the environment of Can Gio. In: Proceedings on "Building up long term plan for Cangio Biosphere Reserve": 72 pp (in Vietnamese).
- Le Xuan Tuan, Munekage Yukihiro: Environmental Management in Mangrove Areas, Environmental Informatics Archives, Volume 1 (2003), 38-52
- ²⁰ Jervis, R.E., Qureshi, R. Y.: J. Radioanal. Nucl. Chem. Lett. 188(2). 149 (1994)
- ²¹ Krzysztof Piczack, Anna le Sniewicz: Metal concentrations in deciduous tree leaves from urban areas in Poland, Environmental Monitoring and Assessment 86: 273–287 (2003)
- ²² Hopke, Philip K., "A guide to positive matrix factorization", Department of Chemistry Clarkson University, Postdam, NY

EXPERIMENTAL SETUP AND DATA PROCESSING IN STUDYING OF THE REACTION ²³⁵U(n_{th},f) AT THE IBR-2 BEAM¹

A.A. Alexandrov¹, I.A. Alexandrova¹, S.B. Borzakov¹, Yu.N. Voronov¹, S. V. Denisov¹, G.L. Efimov¹, D.V. Kamanin¹, Yu.N. Kopatch¹, E.A. Kuznetsova¹, Yu.E. Lavrova², S.V. Mitrofanov¹, Ts. Panteleev¹, Yu.V. Pyatkov^{2, 1}, V.S. Salamatin¹, I.P.Tsurin¹, A.N. Tyukaykin¹, V.E. Zhuchko¹

¹Joint Institute for Nuclear Research, 141980 Dubna, Russia; ²Moscow Engineering Physics Institute, Moscow, Russia;

Abstract. The MiniFOBOS spectrometer was used for studying the reaction ²³⁵U(n_{th}, f) at the IBR-2 reactor in FLNP of the Joint Institute for Nuclear Research. The experiment was aimed at searching for manifestations of the collinear cluster tripartition (CCT) channel and investigation of fine structures in the fission fragments TKE-M (total kinetic energy vs. mass) distributions. The first experiment aimed at studying of new multibody decay modes in fission of actinides at low excitations was performed at the FOBOS setup at the Flerov Laboratory (FLNR). The effect of CCT was confirmed recently in the experiments of our collaboration in JYFL (Jyväskylä, Finland).

INTRODUCTION

This report is devoted to methodic aspects of the experiment on studying of the reaction 235 U(n_{th} , f) using double-armed time-of-flight spectrometer of fission fragments (FF). The first results obtained are presented in this issue in the separate report.

EXPERIMENTAL SETUP

Our experiment was performed using miniFOBOS spectrometer installed at the channel 6B of the IBR-2 neutron pulsed reactor in FLNP of JINR. Neuron bursts were coming with 5 Hz frequency having 320 µs width. A 20meter long mirror neutron guide was used in order to suppress the background of fast neutrons and gamma-rays at the setup position. In order to increase intensity of the neutron flux the neutron guide was filled with argon at a little bit more than atmospheric pressure. Due to this an increase in flux by approximately factor of two was achieved. The neutron beam was shaped with the collimator fabricated from cadmium. The area of the slot did not exceed 1 cm². We had about 10⁶ n/cm²/sec at the target position.

The scheme of the experimental setup is shown in fig. 1, an overall view of the spectrometer is presented in fig. 2. The miniFOBOS setup devised in FLNR JINR is the double arm time-of-flight-energy spectrometer based on the standard detector modules of the 4D spectrometer FOBOS [1]. One of the main advantages of the FOBOS spectrometer consists in independent measurement of the velocity vector, mass and charge for each fission fragment without any kinematical assumptions about the reaction mechanism. Due to this feature one can study not only binary reactions but multibody decays as well.

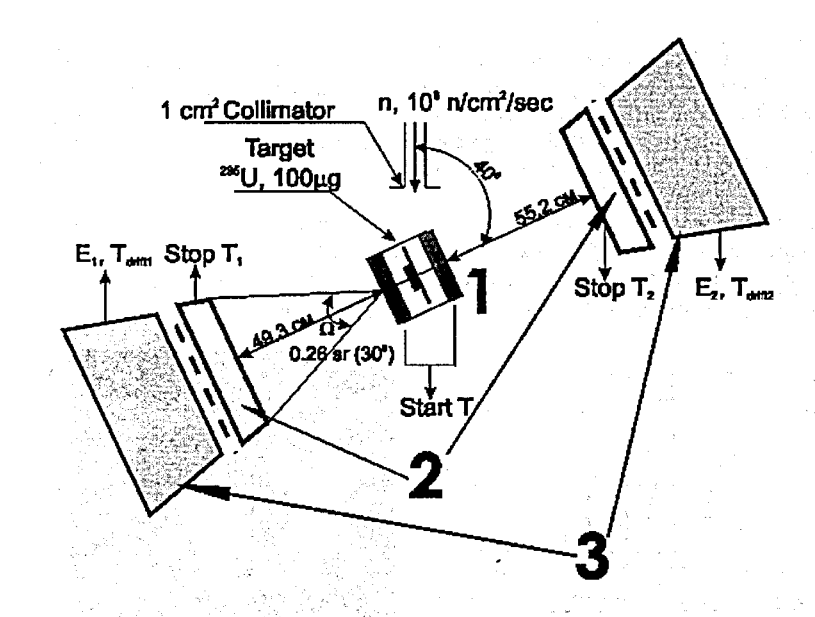


FIGURE I. Scheme of the experimental setup. Here: 1-start avalanche counter; 2-position-sensitive avalanche counters; 3- Bragg ionization chambers.

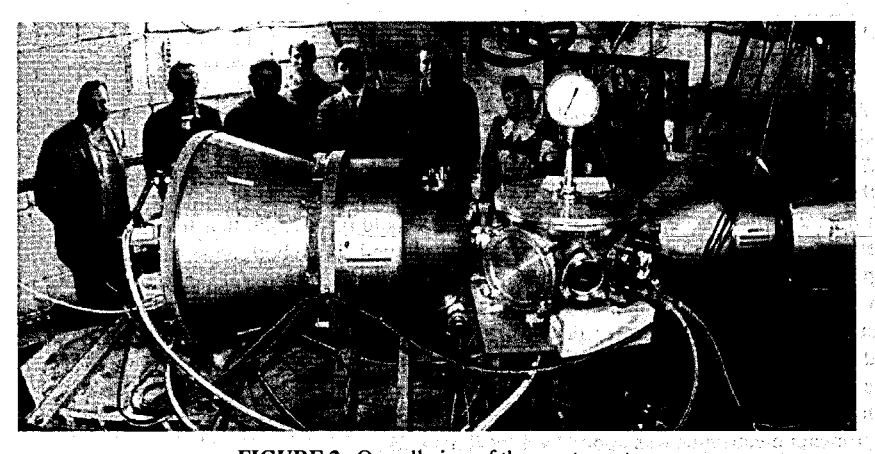


FIGURE 2. Overall view of the spectrometer.

Each detector module used consists of position-sensitive avalanche counter (PSAC) and an axial Bragg ionization chamber (BIC) which registered the full energy-loss distribution (Bragg-curve) of the fragments stopped within the gas-volume. The value of the residual energy is calculated by the real time digital processing method [2]. The system of processing of a BIC signal includes a charge-sensitive preamplifier, a Bragg-curve digitizer and a digital

^{&#}x27;This work is supported in part by the Grant of the Department of Science and Technology of South Africa

processor. Due to the algorithm of its work a constant "step" before the signal is automatically subtracted. It leads to only one parametric calibration "channel vs. residual energy".

The drift time of a track formed after stopping of the fragment in the gas-volume of the BIC is known to be linked with the fragment nuclear charge. Corresponding parameter was measured as a time difference between PSAC signal and the signal from Frisch grid of the BIC.

Specially designed start-detector is a symmetrical double-sided avalanche counter (SAC) with an internal target (fig. 3). Thanks to such design the start-detector delivers proper "start" signal even for multibody events. An active layer of the target was prepared by evaporation of $100 \ \mu g/cm^2$ of 235 U isotope on a $50 \ \mu g/cm^2$ thick Al₂O₃ backing.

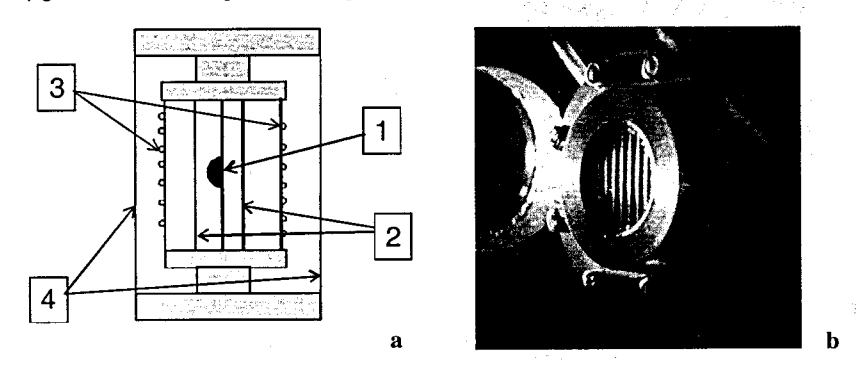


FIGURE 3. Start detector - overall scheme (a) and exterior view at working position (b). Here: active layer of ²³⁵U on Al₂O₃ backing (1); cathode (2); anode (3); entrance windows (4).

A special remote computer-controlled pumping and gas supply system was developed. It consisted of two independent channels which included SAC and both PSACs (pentane filled) from one hand and BICs (filled by the standard mixture of 90% of Ar and 10% of CH₄) from another. The gas pressure in the start-stop detectors and BICs was ~ 600Pa and ~ 11*10³ Pa with the stability 1.5% and 0.8% respectively. It should be stressed that for guaranteeing the necessary stability of the time drift parameter mentioned above both pressure in the BICs and temperature in the experimental hall must be stable. Therefore the temperature of the cave with the experimental setup and the electronics box were supervised by air-conditioners. The vacuum in the reaction chamber does not exceed 5*10⁻² torr due to the leakage through the windows of the detectors. All detectors were operated in a flow-through regime. Sufficient gas exchange rate was chosen experimentally.

Due to essential radiation background in the experimental box the remote control of the spectrometer electronics was applied via local network.

DATA PROCESSING

Thus five parameters have been registered in each spectrometer arm: time-of-flight (TOF) to be time difference between the signals delivered by the SAC and the PSAC, residual energy (Er) of the fission fragment in the BIC, drift time and X, Y coordinates of the point where a fragment hits the PSAC.

The stability of the data was tested by checking of average values and dispersions of the basic parameters such as TOF, drift time and amplitude of the BIC signal for every thousand events. Relative instabilities revealed proved to be the same order of magnitude as the expected experimental resolutions therefore no corrections were made.

The next stage of the data processing is a coordinate calibration of the PSACs. It was performed by comparison of an image in the PSAC of shadow zone from the supporting grid of the window foil of the BIC with known geometrical parameters of the original grid. The spatial resolution of the PSAC amounts to 1.5 mm.

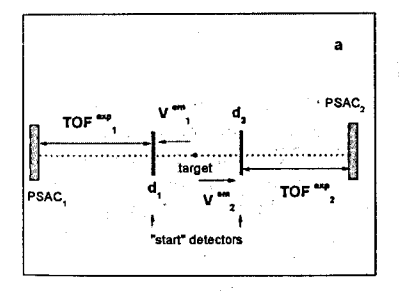
Then a calibration of the time-of-flights was performed. The procedure consists in determination of two calibration parameters of linear time transformation from channels to nanoseconds:

$$TOF^{exp} = T(ch) * dT/dk + T0$$
 (1),

where:

T(ch) is an experimental TOF in channels, TOF^{exp} is a corresponding TOF in nanoseconds, dT/dk, T0 are the calibration parameters.

The slope dT/dk of the calibration line was determined with a help of the precision time-calibrator in each spectrometer arm. As for T0 the idea of our approach was to find such coefficients T0 that both experimental mass (M_{TT}) spectrum and peak positions in the velocity spectrum would be consistent with those known from the literature [3, 4]. In reality the thicknesses of the SAC foils were also the parameters to be précised in the frame of the same procedure. The schemes of the timing channel and the computer code devised are presented in fig. 4.



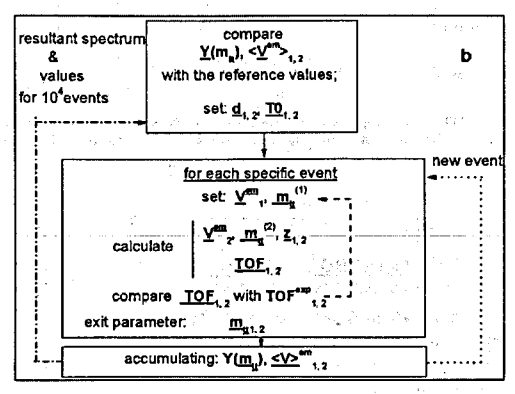


FIGURE 4. An overall scheme of the time calibration. As can be referred from a sketch of the timing channel (a) experimental values of time-of-flights of coincident fragments TOF exp_{1,2} should differ from corresponding "true" or "emission" values due to the energy losses in the foils of start detectors.

But just emission values of the FF velocities and spectrum of the M_{TT} masses known from the literature can be used for fitting unknown parameters what leads to rather complicated procedure (b). See text for detail.

All variables are shown in the scheme (fig. 4b) by the underlined symbols. At the first stage initial values of $\underline{T0}_{1,2}$ and thicknesses of the SAC foils $\underline{d}_{1,2}$ for both spectrometer arms

are set (upper box in fig. 4 b). The procedure (based on the MINUIT minimization code [6] from CERN program library) generates these values in the outer minimization cycle marked by the dash-dot line in fig. 4b.

The inner minimization cycle marked by the dashed line deals with a specific event. Parameters \underline{V}^{em}_1 and $\underline{M}^{(1)}_{TT}$ are varied in the frame of Nelder-Mead algorithm [7] in order to fit current calculating values of \underline{TOF} to \underline{TOF}^{exp} being a function of parameters $\underline{TO}_{1,2}$ defined earlier in the outer cycle. The fragment charges $\underline{Z}_{1,2}$ needed for calculating of energy losses in the start detectors are calculated using unchanged charge density hypothesis. \underline{M}_{TT} and \underline{V}^{em} are the exit parameters of this cycle (see central box in fig. 4b). One calculates these values event by event accumulating spectrum $\underline{Y}(\underline{M}_{TT})$ and mean values $\underline{V}^{em}_{1,2}$ until enough statistics is collected (bottom box and doted line in fig. 4b).

The resulting M_{TT} spectrum and mean velocities are sent into outer cycle (dash-dot line in fig. 4b) for comparison with those known from the literature and so on.

Fig. 3 presents the velocity and mass spectra of the EF from ²³⁵U(n_{th},f) reaction. Our results agree well with the literature data [3, 4].

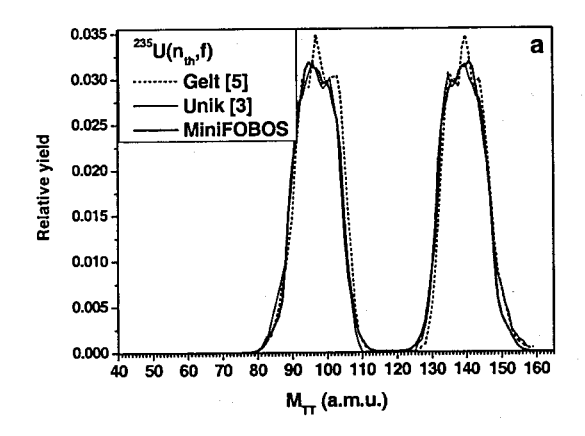
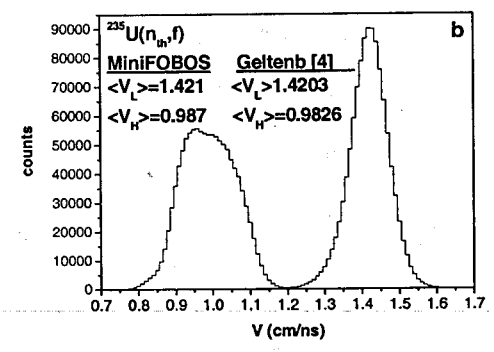


FIGURE 5. Comparison of the FF mass spectrum obtained from the TOF-TOF analysis (a) and velocities spectrum (b) with the corresponding literature data [3-5].



The next stage of the data processing is a calibration of energy (E)-channel. It is not trivial procedure because only less than half of the initial fragment energy is actually measured in the BIC. Big energy losses are mainly due to the thick entrance window of the BIC. It is an evident cost for high aperture of the spectrometer. The idea of E-calibration consists also in fitting of the current spectrum of the M_{TE} quasimasses to the known one. Corresponding approaches both to E-calibration and mass-reconstruction were already discussed in our work [8]. Here the same procedures were exploited. The spectrum of the M_{TE} masses in comparison with the literature data [9] is presented in fig. 6.

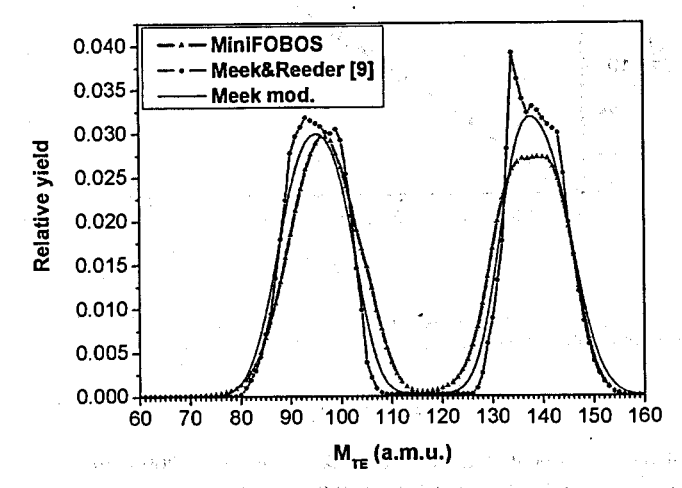


FIGURE 6. Comparison of the FF mass spectrum obtained from the TOF-E analysis with the literature data [9].

For illustration of an influence of the mass resolution onto the shape of the spectrum a convolution of the spectrum from the compilation [9] with the Gaussian (σ =3a.m.u.) is shown in the figure (black line without points). In our data the "tails" streaming to the symmetry partition are partially due to mass resolution and mainly due to scattering of the fragments on the BIC grids.

The next figure 7 demonstrates good agreement between M_{TT} and M_{TE} masses calculated with the procedures mentioned above. Black points in the figure were obtained by subtraction from each mass number mean number of emitted neutrons known from the literature [10]. Thus by definition the ordinate of each point is equal to the mean M_{TE} mass ($< M_{TE}>$) for the M_{TT} value being the abscissa of the point. In order to compare this expected relationship with the experimental one we collected M_{TE} spectrum for each M_{TT} mass and calculated mean value of the spectrum. Only events with approximately equal momenta were selected. This ensures a rejection of the scattered fragments from our consideration and improves M_{TE} mass resolution for the selected events. Corresponding experimental values are shown in fig. 7 by the empty circles.

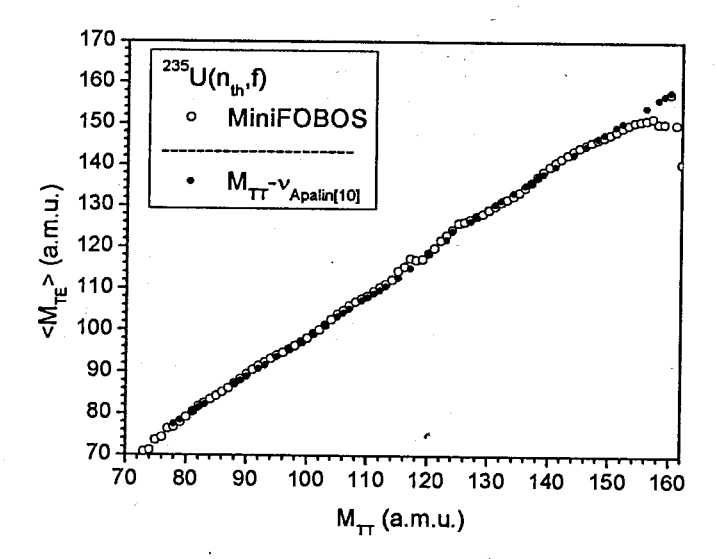


FIGURE 7. Correlation between the mean mass $\langle M_{TE} \rangle$ and expected value $M_{TT} - v$ (M_{TT}), where v (M_{TT}) is the mean number of neutrons emitted by the fragment with mass M_{TT} . See text for details.

CONCLUSIONS

Full time of the experiment is equal to 6 weeks. From them 200 hours (27 %) have been used for the precise adjustments of electronics and experimental setup. No time was spent for calibrations thanks to the approach chosen to the data processing. All in all almost 9*10⁶ fission events were collected. Only small part of them has been rejected by criteria of instability and incompleteness. Thanks to harmonious work of the scientific groups of two laboratories high quality data were obtained and they will be applied for studying rare processes in nuclear fission.

ACKNOWLEDGMENTS

This work has been supported in part by Russian Foundation for Basic Research, grant 05-02-17493 and CRDF, grant MO-011-0.

The authors are grateful to the Directorate of the Flerov Laboratory of Nuclear Reactions and Frank Laboratory of Neutron Physics, namely, Prof. A.V. Belushkin, Prof. S.N. Dmitriev, Prof. M.G. Itkis and Dr. V.N. Shetsov for their substantial support and permanent interest to this study.

REFERENCES

- 1. H.-G. Ortlepp et al., Nucl. Instr. and Meth. A 403 (1998) 65
- 2. H.-G. Ortlepp, A.Romaguera, Nucl. Instr. and Meth. A 276 (1989) 500
- 3. Unik J.P., Gindler J.E., Glendenin L.E., Flynn K.F., Gorski A., Sjoblom R.K., Proc.Symp.Physics and Chemistry of Fission, Vol.2 IAEA, Vienna, 1974, 20
- P.Geltenbort, F. Goennenwein, A. Oed et. al., "Proc. Int. Conf. Nucl. Data for Sci. and Techn.", Santa-Fe, 1985, V2, p1331-1335
- 5. P.Geltenbort, F.Gonnenwein, A.Oed, Radiat.Effects, 93, 57, 1986
- CERN Program Library, MINUIT, http://www.asdoc.web.cern.ch/wwwasdoc/WWW/minuit/minmain/minmain.html
- 7. Nelder-Mead method, http://math.fullerton.edu/mathews/n2003/NelderMeadMod.html
- Yu.V.Pyatkov et al., "New results in studying of the collinear cluster tripartition of the ²⁵²Cf nucleus", Preprint JINR, Dubna, E15-2004-65, April 14, 2004
- 9. Meek M.E., Rider B.F. "Compilation fission product yields" Rpt. NEDO-12154-2,1977
- 10. V.F. Apalin et al, Nucl. Phys. 71 (1965)553

THE THEORY OF THE T-ODD CORRELATIONS IN TERNARY FISSION

Bunakov V.E.¹, Kadmensky S.G.²

¹PNPI, Gatchina 188300, ²Voronezh State University, Voronezh 394006

Abstract: The quantum version of the unified description is presented for the two T-odd effects observed recently in ternary fission induced by polarized neutrons. The effects are explained by the influence of the rotating fissioning system Coriolis interaction on the angular distributions of the light charged particles in the interier and exterier nuclear regions.

The quantum approach is compared with the classical trajectory one.

1.Introduction.

A few words on the hystory of the problem. In our previous papers [1-3] we developed the theory which explained the earlier observed (see e.g. [4]) T-odd correlation of the type:

$$\vec{\sigma}_n[\vec{k}_{LF}\cdot\vec{k}_{\alpha}]$$

in ternary fission induced by polarized neutrons. Here $\vec{\sigma}_n$ is the neutron spin, while \vec{k}_{LF} and \vec{k}_{α} are the momenta of the light fragment and the ternary particle (usually alpha) emitted in ternary fission. This correlation, which was called TRI-correlation, was described by the differential cross-section of the type:

$$\frac{d^2\sigma}{d\Omega_{LF}d\Omega_{\alpha}} = B_0 + D_1 \cdot \vec{\sigma}_n [\vec{k}_{LF} \cdot \vec{k}_{\alpha}] \tag{1}$$

The experimental geometry was chosen in such a way that the directions of the unit vectors $\vec{\sigma}_n$ and \vec{k}_{LF} were parallel to the y and z axes, while the vector \vec{k}_a varied in the (x,y) plane. The effect measured was defined as:

$$D = \frac{\sigma_+ - \sigma_-}{\sigma_+ + \sigma_-} \quad , \tag{2}$$

where σ_{+} and σ_{-} stand for the differential cross-sections with the neutron beam positive and negative helicities. The magnitude of the effect for the ²³³U target was about -3·10⁻³. It is important to point that this magnitude and the sign of the effect were practically independent of the angle θ between the vectors \vec{k}_{LF} and \vec{k}_{α} in a wide range of angles around $\theta \approx 90^{\circ}$.

However, the recent measurements [5] for the 235 U target demonstrated the existence of the new effect, which was called ROT. Contrary to the TRI, this effect does not change with the inversion of either \vec{k}_{LF} or \vec{k}_{α} but changes its sign in the vicinity of $0\approx90^{\circ}$. This effect is rather well reproduced [6] in the classical trajectory calculations of the alpha-particle emission in the rotating Coulomb field of the fission fragments with the angular momentum of about few h, equal to the total spin J of the polarized fissioning nucleus 236 U which appears after the absorption of the polarized neutron by the target nucleus. The inversion of the neutron helicity causes the inversion of the J direction and, therefore to the inversion of the system's rotation direction. This leads to the slight shifts of the alpha-particle angular

distributions with respect to the direction \vec{k}_{LF} of the light fragment emission. The effective angular velocity of the fissioning system's rotation was estimated in [6] as:

$$\vec{\Omega}_{cl} = P(J) \cdot \frac{R}{\Im} \vec{\sigma}_n , \qquad (3)$$

where \mathfrak{I} is the moment of inertia of the fissioning system and P(J) is the compound-nucleus polarization, resulting from the absorption of the neutron with polarization p_n :

$$P(J) = \begin{cases} \frac{2I+3}{3(2I+1)} p_n \equiv \frac{J+1}{3J} p_n & for \quad J = I+1/2\\ -\frac{1}{3} p_n & for \quad J = I-1/2 \end{cases}$$
(4)

The magnitude of the vector \vec{R} (called the angular momentum of the nuclear collective rotation) was related to the values of the total nuclear spin J and its projection K on the nuclear symmetry axis (which coincides in our coordinate choice with the direction of the fragments emission, i.e. with z axis):

$$R = \hbar \sqrt{J(J+1) - K^2} \tag{5}$$

Already here one can see some inconsistency. Indeed, one might expect that after the absorption of the neutron with spin directed along the y-axis, the total spin J (and not R!) is polarized along this axis:

$$P(J) = \frac{\langle J_y \rangle}{I}$$

Since for $K\neq 0$ the directions of \vec{J} and \vec{R} can not coincide, equation (3) seems to be rather questionable. Even in the case of K=0 one might expect the rotation velocity of the system around the y-axis to be:

$$\Omega_{y} = \frac{\langle J_{y} \rangle}{\mathfrak{J}} = \frac{\langle J_{y} \rangle}{J} \cdot \frac{J}{\mathfrak{J}} = P(J) \frac{J}{\mathfrak{J}} , \qquad (6)$$

rather than (3), (5).

The classical trajectory calculations of the alpha-particle angular distributions in ternary fission without the fissioning system's rotation usually reproduce the experimental data fairly well. However the precision of those calculations in the description of the quantum system's rotation with the angular momentum of the order of h and the rotation angle $\delta\theta$ <1 might be questionable.

A more detailed analysis of the experimental data indicates that both TRI and ROT effects contribute simultaneously. However the reason why the TRI-effect dominates for ²³³U target, while the ROT one prevails in the case of ²³⁵U, remains unknown. The experimentally observed lack of correlation between the signs of both effects [5] also can not be explained in the framework of the classical approach.

In the present paper we shall demonstrate that our earlier developed approach [1-3] (see also [7]) allows to give the quantum description of both effects and to show the possible reason of the difference between the effects observed in the two uranium isotopes. We shall also show how the difficulties of the sign correlation and of eq. (3) are resolved in this approach.

2. The products' angular distribution for the ternary fission induced by polarized neutrons with account of the Coriolis interaction

The basic idea of our quantum approach [1-3] was exactly to consider the influence of the fissioning system collective rotation (fixed by the $\vec{\sigma}_n$ direction) on the ternary particles' angular distribution. In the intrinsic coordinate system of the fissioning nucleus this means considering the Coriolis interaction in addition to the nuclear and Coulomb ones. In this case the total Hamiltonian of the ternary particle interaction with the rotating system in classical mechanics would be:

$$H = H_0 - \vec{\Omega} \cdot \vec{l} = H_0 - \frac{\vec{J} \cdot \vec{l}}{\Im} \tag{7}$$

Here \vec{l} is the ternary particle angular momentum, $\vec{\Omega}$ is the angular velocity of the system's rotation, \vec{J} is the system's angular momentum and \Im is its moment of inertia. One can see already from (7) that by the inversion of the neutron beam polarization (i.e. by the inversion of the vector \vec{J} sign) one makes the emission of the ternary particle either easier or more difficult. This might serve the quasi-classical explanation of the TRI-effect.

In quantum mechanics the Coriolis interaction operator is usually [8] written as:

$$\hat{H}_{Cor} = -\frac{\hbar^2}{2S} (\hat{J}_+ \hat{l}_- + \hat{J}_- \hat{l}_+)$$
 (8)

The operators \widehat{J}_{\pm} and \widehat{l}_{\pm} change the projections K or K_{ℓ} of the angular momenta J and ℓ on the deformed nucleus symmetry axis while acting on the function $D^{J}_{MK}(\omega)$ and the spherical function $Y_{\ell,K,\ell}(\Omega_{\alpha})$:

$$\widehat{J}_{\pm}D_{MK}^{J}(\omega) = \sqrt{(J \pm K)(J \mp K + 1)}D_{M(K \pm 1)}^{J}(\omega)$$
(8a)

$$\widehat{l}_{\pm}Y_{lK_{\ell}}(\Omega_{\alpha}) = \sqrt{(l \mp K_{\ell})(l \pm K_{\ell} + 1)}Y_{l(K_{\ell} \pm 1)}(\Omega_{\alpha})$$

Using the technique of [1] in order to take into account the Coriolis interection in the first-order perturbation theory, we obtain for the ternary fission differential cross-section:

$$\frac{d^3\sigma}{d\Omega_{LF}d\Omega_{\alpha}d\varepsilon} = B_0(\Omega_{LF}, \Omega_{\alpha}) + B^{Cor}(\Omega_{LF}, \Omega_{\alpha})$$
(9)

Here the quantity ε is related to the ternary particle energy E_3 by the equation (see [1]): $\varepsilon = \arccos\sqrt{x}$, where $x = E_3 / E_3^{\max}$, while E_3^{\max} is the maximal energy of this particle $E_3^{\max} = Q_c (A_1 + A_2) / A$, $A_{1,2}$ are the fragments' masses, A is the mass of the fissioning nuclei and Q_c is the total kinetic energy of the fission products' relative motion in the c channel.

The first term in (9) describes the angular distributions for the reaction with unpolarized neutrons and is proportional to the modulus squared of the amplitude A_0 of this reaction. The second term is defined by the interference of the A_0 amplitude with the amplitude A^{Cor} of this reaction with account of the Coriolis interaction. It is convenient to choose the coordinate system which corresponds to the experimental geometry – the vectors $\vec{\sigma}_n$ and \vec{k}_{LF} directed

along the y and z axes, while the vector \vec{k}_{α} lies in the (x,y) plane. Then θ is the angle between the vectors \vec{k}_{LF} and \vec{k}_{α} , while $\varphi=0$. With this choice we obtain for (9) the expression:

$$\frac{d^2\sigma}{d\Omega_a d\varepsilon} = \frac{d^2\sigma^0}{d\Omega_a d\varepsilon} + \frac{d^2\sigma^{\text{Cor}}}{d\Omega_a d\varepsilon}$$
(10)

The part of the differential cross-section $d^2\sigma^0/d\Omega_\alpha d\varepsilon$, which is independent of the neutron polarization is given by the expression:

$$\frac{d^{2}\sigma^{0}}{d\Omega_{\alpha}d\varepsilon} = \frac{\pi}{2(2I+1)k_{n}^{2}} \sum_{ss'J_{s}J_{s}cK_{s}} |h_{s'}^{J_{s}}| |h_{s'}^{J_{s'}}| |b_{sK_{s}}^{J_{s}}| b_{s'K_{s}}^{J_{s}} \Gamma_{cK_{s}}(2J_{s}+1) \times$$
(11)

$$\times \sum_{l'} |d_{cl}(\varepsilon)| |d_{cl'}(\varepsilon)| Y_{l0}(\Omega_{\alpha}) Y_{l'0}(\Omega_{\alpha}) \cos(\delta_{sJ_ss'J_s} + \delta_{cl}(\varepsilon) - \delta_{cl'}(\varepsilon)).$$

Here k_n is the neutron wave-vector, I is the target spin, the factor

$$h_s^{J_s} = \frac{\sqrt{\Gamma_{sn}^{J_s}}}{E - E_s^{J_s} + i\Gamma_s^{J_s}/2} = |h_s^{J_s}| \exp\{i\delta_{sJ_s}\}$$
 (12)

is the capture amplitude of the neutron with energy E into the resonance with spin J_s , energy $E_s^{J_s}$, partial neutron width $\Gamma_{sn}^{J_s}$ and total width $\Gamma_s^{J_s}$. The fission width of the neutron resonanance into the channel c is:

$$\Gamma_{sJ_s,cK_s} = |b_{sK_s}^{J_s}|^2 \Gamma_{cK_s}, \tag{13}$$

where Γ_{cK_s} is the transition probability from the pre-scission state with the quantum number K_s into the channel c, while the quantity

$$b_{sK_s}^{J_s} = a_{sK_s}^{J_s} c_{sK_s}^{J_s} \tag{14}$$

contains the probability amplitude $a_{sK_s}^{J_s}$ to find the component with the quantum number K_s in the wave-function of a given neutron resonance and the amplitude $c_{sK_s}^{J_s}$ of the transition from this resonance via the transition state with quantum numbers J_s , K_s to the scission point. Due to the complete K-mixing [9] in neutron resonances the amplitude $a_{sK_s}^{J_s}$ has random sign and the average value $<(a_{sK_s}^{J_s})^2>=(2J_s+1)^{-1}$. The coefficients $d_l(\varepsilon)$ and the phsase shifts $\delta_l(\varepsilon)$ define the ternary particles' angular distribution for the reaction with unpolarized neutrons.

The phase shifts $\delta_{sJ_ss'J_s}$ of the interfering neutron resonances are defined as:

$$\delta_{sJ_ss,J_s} = \delta_{sJ_s} - \delta_{s,J_s}. \tag{15}$$

Introducing the amplitude $A_c^0(\Omega_\alpha, \mathcal{E})$ of the ternary particles' angular and energy distribution in the absence of the Coriolis interaction:

$$A_c^0(\Omega_\alpha, \varepsilon) = \sum_{l} |d_{cl}(\varepsilon)| \exp\{i\delta_{cl}(\varepsilon)\} Y_{l0}(\Omega_\alpha) = |A_c^0(\Omega_\alpha, \varepsilon)| \exp\{i\delta_c^0\}, \quad (16)$$

one can write eq.(11) in the form:

$$\frac{d^{2}\sigma^{0}}{d\Omega_{\alpha}d\varepsilon} = \frac{\pi}{2(2I+1)k_{n}^{2}} \sum_{ss'J_{s}J_{s}cK_{s}} \left| h_{s'}^{J_{s}} \right| h_{s'}^{J_{s}} \left| b_{sK_{s}}^{J_{s}} b_{s'K_{s}}^{J_{s}} \Gamma_{cK_{s}} (2J_{s}+1) \times \cos(\delta_{sJ_{s};J_{s}}) \right| A_{c}^{0}(\Omega_{\alpha},\varepsilon)^{2}.$$
(17)

The amplitude $A_c^{\text{Cor}}(\Omega_\alpha, \mathcal{E})$ of the alpha particles' angular and energy distributions which takes into account the Coriolis interaction can be represented as a sum of the two parts corresponding to the even and odd values of the alphas' angular momenta ℓ :

$$A_{c}^{\text{Cor}}(\Omega_{\alpha}, \varepsilon) = \sum_{l} |d_{cl}^{\text{Cor}}(\varepsilon)| e^{\delta_{cl}^{\text{Cor}}(\varepsilon)} (Y_{l,-1}(\Omega_{\alpha}) - Y_{l,1}(\Omega_{\alpha})) =$$

$$= |A_{c(\text{even})}^{\text{Cor}}(\Omega_{\alpha}, \varepsilon)| \exp\{i\delta_{c(\text{even})}^{\text{Cor}}\} + |A_{c(\text{odd})}^{\text{Cor}}(\Omega_{\alpha}, \varepsilon)| \exp\{i\delta_{c(\text{odd})}^{\text{Cor}}\},$$
(18)

where the coefficients $d_{l'}^{Cor}$ and the phase shifts $\delta_{l'}^{Cor}$ take into account the Coriolis interaction.

It is convenient to choose the coordinate system which corresponds to the experimental geometry – the vectors $\vec{\sigma}_n$ and \vec{k}_{LF} directed along the y and z axes, while the vector \vec{k}_{α} lies in the (x,y) plane. With this coordinate choice one can represent the differences

 $[Y_{l-1}(\Omega_{\alpha}) - Y_{l,l}(\Omega_{\alpha})]$ of the spherical functions in (18) as:

$$\vec{\sigma}_n[\vec{k}_{LF} \cdot \vec{k}_{\alpha}] \{a_0 + a_1(\vec{k}_{LF} \cdot \vec{k}_{\alpha})^2 + ...\}$$
 (19)

for the odd & values, and

$$\vec{\sigma}_n\vec{k}_{LF} \cdot \vec{k}_{\alpha}\{b_1 + b_3(\vec{k}_{LF} \cdot \vec{k}_{\alpha})^2 + \dots\}$$
(20)

for the even ℓ values. Then the amplitude (18) can be written in the form:

$$A_{c}^{Cor}(\Omega_{\alpha}, \varepsilon) = \vec{\sigma}_{n}[k_{LF} \cdot \vec{k}_{\alpha}](\vec{k}_{LF} \cdot \vec{k}_{\alpha}) |F_{c(even)}^{Cor}(\Omega_{\alpha}, \varepsilon)| e^{i\delta_{c(ev)}^{Cor}} + + \vec{\sigma}_{n}[\vec{k}_{LF} \cdot \vec{k}_{\alpha}] |F_{c(odd)}^{Cor}| e^{i\delta_{c(odd)}^{Cor}},$$
(21)

where the functions $F_{c(\text{even})}^{\text{Cor}}(\Omega_{\alpha}, \mathcal{E})$ and $F_{c(\text{odd})}^{\text{Cor}}(\Omega_{\alpha}, \mathcal{E})$ coincide with the amplitudes $A_{c(\text{even})}^{\text{Cor}}(\Omega_{\alpha}, \mathcal{E})$ and $A_{c(\text{odd})}^{\text{Cor}}(\Omega_{\alpha}, \mathcal{E})$ provided one substitutes the differences $\left[Y_{l,-1}(\Omega_{\alpha}) - Y_{l,1}(\Omega_{\alpha})\right]$ of eq.(18) by the expressions in the curly brackets of eqs.(19) and (20).

Now by using the technique of [1] we can obtain:

$$\frac{d^{2}\sigma^{Cor}}{d\Omega_{\alpha}d\varepsilon} = \frac{p_{n}\pi}{2(2I+1)k_{n}^{2}} \sum_{ss'J_{s}J_{s'}cK_{s}} |h_{s}^{J_{s}}| |h_{s}^{J_$$

The ratio $(d_l^{Cor}/d_l)\approx 10^{-3}$ here defines the magnitude of the observed effect caused by the Coriolis interaction (8). The factor $g_{K_tJ_tJ_t}$ coming from the non-diagonal part of the density matrix $\rho_{MM}^{J_tJ_t}$ (see [1]) has the form:

$$g_{K_{s}J_{s}J_{s}} = A(J_{s},J_{s}) \left[\sqrt{(J_{s}+K_{s})(J_{s}-K_{s}+1)} C_{J_{s}1(K_{s}-1)1}^{J_{s}K_{s}} - \sqrt{(J_{s}-K_{s})(J_{s}+K_{s}+1)} C_{J_{s}1(K_{s}+1)-1}^{J_{s}K_{s}} \right],$$
(23)

where

$$A(J_{s},J_{s}) = \delta_{J_{s},J_{s}} \left(\sqrt{\frac{J_{s}}{2(J_{s}+1)}} \delta_{J_{s},J_{s}} - \sqrt{\frac{J_{s}+1}{2J_{s}}} \delta_{J_{s},J_{s}} \right) - \sqrt{\frac{2J_{s}+1}{2J_{s}}} \delta_{J_{s},J_{s}+1} + \sqrt{\frac{2J_{s}+1}{2(J_{s}+1)}} \delta_{J_{s},J_{s}-1},$$
(24)

with $J_2 = I + 1/2$, $J_2 = I - 1/2$.

As pointed earlier (see, e.g. [10]) the conservation of the K quantum number implies that the fissioning system can not be thermalised on its way from the saddle-point to scission. Therefore the superfluid correlations in the neck enhance the formation of alpha-clasters with the orbital momentum $\ell=0$. The admixture of the states with $\ell\neq 0$ is caused by the long-range Coulomb potential of the fragments (pre-fragments) acting on the alpha-particle [11]:

$$V_{Coul} \approx \frac{2(Z-2)e^{2}}{R} + \frac{8(Z-2)e^{2}}{R} \left(\frac{\Delta Z}{Z-2} + \frac{2\Delta A}{A-4}\right) \left(\frac{r}{R}\right) P_{1}(\cos\theta) + \frac{16(Z-2)e^{2}}{R} \left(\frac{r}{R}\right)^{2} P_{2}(\cos\theta) \equiv V_{Coul}^{0} + V_{Coul}^{d} + V_{Coul}^{Q}$$
(25)

Here R is the distance between the fragments' centers, r is the distance between the alphaparticle center and the center of mass of the whole system; Z and A are the charge and mass of the fissioning nucleus. The quantities $\Delta Z=Z_1-Z_2$ and $\Delta A=A_1-A_2$ characterise the charge and mass asymmetry of the fission fragments.

Now the dipole component V_{Coul}^d of this potential dominating in the interior region r<<R adds the cluster states with the orbital momentum $\ell=1$. The quadrupole component V_{Coul}^Q which dominates in the exterior region r≈R adds the states with the orbital momentum $\ell=2$. The first sum in the curly brackets of (22) corresponds to the odd ℓ values and is proportional to $\ell=0$. The first sum is the curly brackets of $\ell=0$ and the same region of the odd $\ell=0$ and $\ell=0$

to $\sin\theta$. Therefore it has a maximum at $\theta=90^{\circ}$ and changes only slightly (from 1 to 0.87) in the range $60^{\circ} \le 0 \le 120^{\circ}$. This sum is responsible for the TRI effect.

The second sum corresponds to the even ℓ values and is proportional to $\cos\theta$. Therefore it changes sign at θ =90 0 . It is responsible for the ROT effect.

Thus, if the Coriolis forces act in the interior region (r<<R), where the dominant dipole term of (25) admixes $\ell=1$ to $\ell=0$, then we have the TRI effect which was described in our earlier publications. If, however, the Coriolis forces act in the exterior region $r\approx R$ then the dominant quadrupole term of the Coulomb potential admixes the even ℓ values to $\ell=0$. This leads to the ROT effect.

As seen from (22) both effects are T-odd. However the TRI effect changes sign with the inversion of each of the three vectors $(\vec{\sigma}_n, \vec{k}_{LF} \text{ and } \vec{k}_{\alpha})$, in agreement with the experimental observations. This, as well as the form of dipole term in (25) shows that the TRI effect is caused by the charge and mass asymmetry of the fission fragments. The ROT effect changes sign only with the inversion of the neutron beam polarization $(\vec{\sigma}_n \rightarrow -\vec{\sigma}_n)$ since it is connected with the quadrupole term V_{Coul}^Q , which is independent of the charge and mass asymmetry. Exactly this is observed in the experiments [5].

In general both correlations should contribute to the observed effect (and, as pointed above, the experimental data do indicate this). However the TRI correlation dominates for the ²³³U target, while the ROT one dominates in the case of ²³⁵U. Both fissioning compound nuclei (²³⁴U and ²³⁶U) are the neighbouring even-even isotopes whose fission modes q and fission channels c practically does not differ. The charge and mass fragments' asymmetries are also practically the same. Even if the K quantum numbers of their transition states are different, our exp. (22) shows that this would only affect the common K-dependent factors in front of both correlations, thus enhancing or hindering both effects simultaneousely. Therefore the question arises – why are the ratios of TRI to ROT contribuions to the B^{Cor} values so different for those two targets?

The only possible source of this difference might be caused by the different energies and other parameters of the interfering neutron resonances contributing to the effects. This would lead to the appearance in eq.(22) of the different phases $\delta_{sI_ss'I_s}$ coming from the interfering resonances. If the phase difference in the arguments of the sines is about zero for the leading even l-values the ROT effect is suppressed and we have the dominant TRI one, and vice versa.

3. The special case of isolated resonance and comparison with the classical approach

Consider now the special case of isolated neutron resonace which is a rather rare phenomenon for the fissioning nuclei where the typical ratio of the total width to the resonance spacing is $(\Gamma/D)\sim0.3$. Then only one term $s,J_s=s',J_s$ contributes to the sums in (17), (22) and those differential cross-sections are:

$$\frac{d^{2}\sigma^{0}}{d\Omega_{\alpha}d\varepsilon} = \frac{\pi}{2(2I+1)k_{n}^{2}} \sum_{cK_{s}} |h_{s}^{J_{s}}|^{2} |b_{sK_{s}}^{J_{s}}|^{2} \Gamma_{cK_{s}} (2J_{s}+1) |A_{c}^{0}|^{2} \qquad (26)$$

$$\frac{d^{2}\sigma^{Cor}}{d\Omega_{\alpha}d\varepsilon} = \frac{p_{n}\pi}{2(2I+1)k_{n}^{2}} \sum_{cK_{s}} |h_{s}^{J_{s}}|^{2} |b_{sK_{s}}^{J_{s}}|^{2} \Gamma_{cK_{s}} (2J_{s}+1)g_{K_{s}J_{s}J_{s}} |A_{c}^{0}| \times \\
\times \{\bar{\sigma}_{n}[\vec{k}_{LF} \cdot \vec{k}_{\alpha}]F_{c(odd)}^{Cor} \sin(\delta_{c}^{0} - \delta_{c(odd)}^{Cor}) + \\
+ \bar{\sigma}_{n}\vec{k}_{LF} \cdot \vec{k}_{\alpha}F_{c(even)}^{Cor} \sin(\delta_{c}^{0} - \delta_{c(even)}^{Cor}) \}$$
Here the phases $\delta_{sJ_{s}s'J_{s}} = 0$ and
$$g_{K_{s}J_{s}J_{s}} = A(J_{s}, J_{s})[\sqrt{(J_{s} + K_{s})(J_{s} - K_{s} + 1)}C_{J_{s}K_{s}}^{J_{s}K_{s}}] = 0$$

 $-\sqrt{(J_{c}-K_{c})(J_{c}+K_{c}+1)}C_{L_{1}(K_{c}+1)-1}^{J_{s}K_{s}}$

It is interesting to compare these results with the classical approach [6] where the angular velocity Ω_{cl} which defines the magnitude of the ROT effect was estimated by the eq.(3) with the polarization of the compound-nucleus spin given by eq.(4):

$$P(J) = \begin{cases} \frac{2I+3}{3(2I+1)} p_n \equiv \frac{J+1}{3J} p_n & for \quad J = I+1/2\\ -\frac{1}{3} p_n & for \quad J = I-1/2 \end{cases}$$
(29)

We shall show now that this expression does not take into account the specific features of the fission channel for the deformed nucleus with the axial symmetry. The wave function Ψ^J_{MK} of this nucleus takes into account the fact that its eigenstates are always doubly-degenerate in the sign of K. Therefore it contains with equal weights the contributions of the functions $D^J_{MK}(\omega)$ and $D^J_{M-K}(\omega)$ depending not only on the total spin J and its projection M on the laboratory z-axis, but also on its projection K on the nuclear symmetry axis. The average values of the system's spin projections on the axes i=(x,y,z) are defined as:

$$\langle J_i(K) \rangle = \sum_{MM'} \rho_{MM'}^J \langle \Psi_{M'K}^J | \hat{J}_i | \Psi_{MK}^J \rangle$$
 (30)

Here ρ_{MM}^J is the density matrix defined in ref. [1]. With our coordinates choice the laboratory z-axis coincides with the direction of the light fragment, while the y-one coincides with the direction of the neutron spin polarization. Now we can choose the Euler's angles ω to be zero, so that the axes of the laboratory and internal systems coincide. Then we can replace the operators \hat{J}_i of the spin projections on the laboratory axes by the projections on the internal axes in (30) and use the expressions similar to (8a). As one should expect, the only non-zero projection with this coordinate choice would be the y-one:

$$\langle J(K) \rangle = \langle J_{y}(K) \rangle = \frac{g_{KJJ}}{2} p_{n} \hbar \tag{31}$$

where g_{KJJ} is defined by eq.(28) and contains the explicit dependence on the K-values. This means that the fissioning system rotates around the y-axis with the angular velocity:

$$\Omega_q(J,K) = \frac{1}{\Im} \langle J(K) \rangle = \frac{\hbar}{2\Im} p_n \cdot g_{KJJ} = \frac{J}{\Im} P_K(J)$$
 (32)

The quantity $P_K(J)$ here means the polarization of the system with the fixed values of J and K:

$$P_K(J) = \frac{\langle J(K) \rangle}{I} = \frac{p_n \cdot g_{KJJ}}{2J}$$
 (33)

Using now (31) and (28), we obtain:

$$\Omega_{q}(J_{s}, K_{s}) = \frac{g_{K_{s}J_{s}J_{s}} \cdot \hbar}{2\Im} p_{n} = \begin{cases} \frac{J_{s}(J_{s}+1) - K^{2}}{J_{s}} \frac{\hbar}{2\Im} \cdot p_{n} & \text{for} \quad J_{s} = I + 1/2 \\ -\frac{J_{s}(J_{s}+1) - K^{2}}{(J_{s}+1)} \frac{\hbar}{2\Im} \cdot p_{n} & \text{for} \quad J_{s} = I - 1/2 \end{cases}$$
(34)

(28)

As mentioned above the coefficients $d_{cl'}^{\text{Cor}}$ take into account the Coriolis interaction.

Therefore our quantum exp. (27) contains the coefficient $\hbar^2/23$ and is proportional to the angular velocity $\Omega_a(J,K)$ in complete analogy with the system's rotation angle in the classical approach [6].

If several transition states with different K-values contribute to fission then it follows from (27) that the effective rotation velocity is:

$$\Omega_{q}^{\text{eff}} = \sum_{K} |b_{sK}^{J}|^{2} \Gamma_{cK} \Omega_{q}(J, K) = \sum_{K} |b_{sK}^{J}|^{2} \Gamma_{cK} \frac{J}{\mathfrak{D}} P_{K}(J)$$
(35)

If all the K-values contribute to fission (i.e. all the coefficients $|b_{sK_s}^{J_s}|^2 = |a_{sK_s}^{J_s}c_{sK_s}^{J_s}|^2$ equal

their average value $(2J_s+1)^{-1}$), then the polarization $P_K(J)$ of eq.(33) is averaged over all the K-values and

$$\frac{1}{(2J+1)} \sum_{K} P_K(J) = P(J) , \qquad (36)$$

where P(J) is defined by (29) used in [6]. It is well known that neutron resonances in deformed nuclei posess no definite value of the K quantum number, as a result of the complete K-mixing caused by the dynamical enhancement of the Coriolis interaction [9]. Therefore for isolated resonances, induced by polarized neutrons their decay into various neutron and gamma channels is governed by the factor (29). However for sufficiently low neutron energies the saddle-point in the fission channel selects only one-two values of K corresponding to the lowest collective excitations. Exactly this specific feature of the fission channel prohibits the use of eqs.(3)-(5).

Notice that the K-dependence of the angular velocity (34) is rather strong. Indeed the value of $\Omega_a(J,K)$ changes by the factor of (2J+1) for K changing from K=0 to K=J. This leads to the additional enhancement of the small K contributions to the TRI and ROT effects. The ratio of the corresponding angular velocities (34) to (3)

$$\frac{\Omega_q}{\Omega_{cl}} = \frac{3}{2} \sqrt{J(J+1) - K^2} \times \begin{cases}
\frac{J}{(J+1)^2} & \text{for } J = I + 1/2 \\
\frac{1}{J} & \text{for } J = J - 1/2
\end{cases}$$
(37)

varies by the numerical factor of 0.5—2 for J=3, 4, while their signs coincide. However the sign of the ROT effect is defined not only by the sign of Ω but also by the function $\sin(\delta_c^0 - \delta_{c(even)}^{Cor})$ in (27)whose sign is defined by the leading even ℓ -values contributing to the effect.

But most important is that the isolated resonance approximation can not explain the difference of the effects in the two neighbouring uranium resonances. As already pointed this difference can be explained only by the neutron resonances' interference in eq. (22).

4. Summary

1. The account of Coriolis interaction in the framework of the quantum ternary fission theory allows to explain both observed T-odd effects.

- 2. Both TRI and ROT contribute always, but their relative contribution varies (confirmed by the preliminary experimental data).
- 3. The changing ratio TRI/ROT arizes ONLY FROM THE RESONANCE INTERFERENCE EFFECTS and can't be explained in classical approach.
- 4. This interference affect the value and the SIGN of both effects (via the signs of $b_{sK_c}^{J_s}$,

 $g_{K_{r}J_{s}J_{s}}$, and of the phases' differences in the sin arguments of (22)). Therefore in general the sign of TRI is not correletaed with the sign of ROT.

- 5. Contribution of different transition states affects the value of both effects simultaneously but does not change the TRI/ROT ratio
- 6. The relative TRI/ROT ratio (as well as their relative sign) should vary for the same target with the variation of the incident neutron energy E_n which considerably changes the phase shifts $\delta_{sJ_ss'J_s} = \delta_{sJ_s} - \delta_{s'J_s}$, of the interfering resonances. (Therefore this energy variation should be larger or of the order of the energy spacing between the neighbouring neutron resonances, i.e. of the order of eV).

This work was supported by INTAS (grant № 03-51-6417) and by RFBR (grant № 06-02-16668).

References

rijk.

- 1. V.Bunakov, S.Kadmensky. Phys.At.Nucl. 66(2003)1846.
- 2. V.Bunakov, S.Kadmensky, L.Rodionova. Izvestija RAN (Fiz.).69 (2005) 625.
- V.Bunakov, S.Kadmensky, L.Rodionova. Izvestija RAN (Fiz.).70 (2006) 1611.
- 4. P.Jessinger et.al. Nucl. Instum. Methods. A440 (2000) 618.
- 5. G.Val'ski, A.Vorobiev, A.Gagarski et al. Izvestija RAN (Fiz.).71 (2007) 368.
- 6. I.Guseva, Yu.Gusev. Izvestija RAN (Fiz.).71 (2007) 382.
- 7. V.Bunakov, S.Kadmensky. Izvestija RAN (Fiz.).71 (2007) 364.
- 8. A.Bohr, B.Mottelson. Nuclear Structure. (Benjamin, NY, 1964) V.2.
- 9. S.Kadmensky, V.Markushev, V.Furman. Yad. Fiz. 35(1982)300. 10. S.Kadmensky. Yad.Fiz. 68 (2005) 2030.
- 11. S.Kadmensky. Yad.Fiz. 67 (2004) 167.

THE ESTIMATION OF SCISSION NEUTRON PARAMETERS FROM N-N ANGULAR CORRELATIONS

I.S. Guseva, A.M. Gagarski, G.A. Petrov, V.E. Sokolov, G.V. Val'ski

Petersburg Nuclear Physics Institute of Russian Academy of Sciences Gatchina, Leningrad District, 188300, Russia

Abstarct

The angular dependences of neutron-neutron coincidences rate in spontaneous fission of ²⁵²Cf from the experiment [1] were compared with the results of calculations based on the Monte-Carlo method for different neutron registration thresholds in the range 425+1600 keV. From this comparison it was concluded that 10-11% of total number of neutrons in ²⁵²Cf(s.f) are emitted isotropically and probably can be attributed as "scission neutrons" arising just at rupture moment. The presented analysis has allowed also to obtain energy distribution of this isotropic component. The similar procedure has been applied also to the description of the neutron - neutron angular correlation of prompt neutrons from ²³⁵U(n_{th},f) reaction.

It is well established that a major part of prompt neutrons evaporates during the fission process from fully accelerated fragments. Such conclusion can be drawn, because instead of isotropic neutron distribution in laboratory system one can observe (see Fig.1 and Fig.2) a significant arising of neutron yields in the direction of light fragment motion, this means 0°, and in the opposite direction [2]. In the first case a part of neutrons emitted from heavy fragment is small and the total spectrum is very close to the neutron spectrum produced by light fragment. On the other hand at 180°

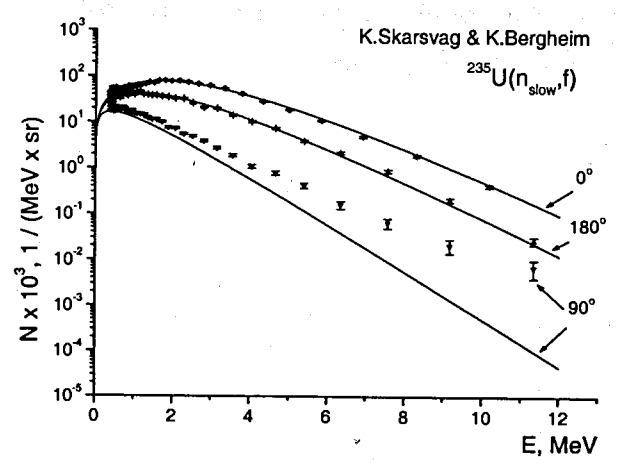


Fig.1 Neutron yields in the lab-system for different angles (0°, 90°, 180°) relative to light fragment motion direction as a function of neutron energy. The solid lines are the results of model calculations with assuming that neutron evaporation goes from fully accelerated fragments.

the contribution of neutrons from light fragment is negligible and the neutron spectrum is shaped by heavy fragment.

The peculiarity of neutron spectra at these angles can be used to determine the temperature parameters of light and heavy fragment, respectively. On the base of these temperature parameters and taking into account final velocities of accelerated fragments one can calculate the neutron yield in any direction of the lab-system.

If we compare (Fig.1) experimentally obtained and calculated neutron spectra in slow-neutron-induced fission of ²³⁵U at the angle of 90° relative to the light fragment motion we can see that the first values exceed the second ones. This leads to a conclusion that a fraction of the total number of fission neutrons can be emitted isotropically in laboratory system of reference.

The same inference may be deduced from a comparison of experimental and calculated angular distributions integrated over all values of neutron energy. The figure 2 also shows the necessity of additional neutron yield at the angle of 90°. It is

assumed that neutrons of isotropic component can appear just after the rupture point (so-called "scission" neutrons).

With the aim to investigate the process of neutron emission the coincidences between prompt neutrons from fission were also measured [3,4]. The orientation of fission axis in such kind of experiments is not fixed and the number of neutron-neutron coincidences for specified angle between neutrons is integrated over its orientation. For this reason the curves of neutron-neutron angular distribution are planer than for neutron-fragment distribution. The ratio between maximal and minimal values in this case is near two, while the count rates of neutron-fragment angular distribution for 0° and 90° relate as 9:1 and as 4:1 for 180° and

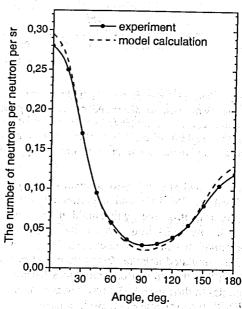


Fig.2. Angular distribution of neutrons integrated over all neutron energy in the reaction $^{235}U(s,f)$ from [2].

Such experiment for investigation of neutron-neutron angular correlations in spontaneous fission of ²⁵²Cf was realized recently in PNPI [1]. The results of angular dependence integrated over all neutron energy values were connected to six different energy thresholds. This allowed us to get some information not only about the contribution of additional component but also concerning its energy distribution.

The values of energy threshold were obtained in process of corresponding time-of-flight spectrum fitting. Every time-of-flight spectrum consists of γ - γ , n-n and γ -n

components. The first two components are in the middle of measured spectrum ("a" and "b" in Fig.3, see also [1]). Especially the scopes of the last one, this means "c", determine the neutron energy threshold.

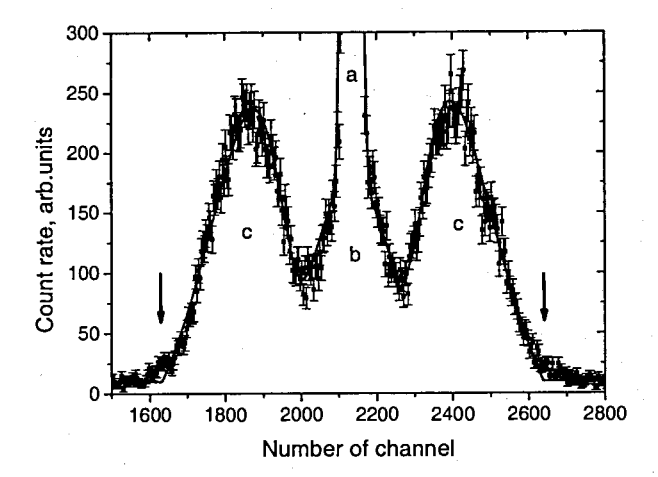


Fig.3. The example of time-of-flight spectrum measured in spontaneous fission of 252 Cf which was used to determine corresponding neutron energy threshold. Position of γ - γ component notates by letter "a", "b"-represents n-n contribution, two letters "c" are placed in that regions where γ -n contributions dominate. The arrows show the scopes of γ -n component in the case of given neutron energy threshold.

We had possibility to compare our experimental result concerned with the energy threshold 750 keV and experimental data obtained by Pringle and Brooks [3] for similar neutron energy threshold, namely 700 keV.

In the Fig.4 you can see the Pringle and Brooks data with their Monte-Carlo calculation simulating neutron-neutron coincidences in spontaneous fission of ²⁵²Cf. The simulated angular distribution was normalized in the range 80°÷180°. It may be seen that the simulation reproduces the form of experimental data reasonably well at angles in the range 100°÷180° but not for smaller angles. This figure demonstrates also PNPI experimental data. Both data were normalized in the range 80°÷100°. Here we can see obvious discrepancy between two experimental data in the range 100°÷180°. The Monte-Carlo simulation of Pringle & Brooks can not describe not only their own data but also PNPI experiment.

To determine the contribution of scission neutron component and its energy spectrum the Monte-Carlo calculations simulating neutron-neutron coincidences in spontaneous fission of ²⁵²Cf were performed in PNPI. The result of this calculation for the energy threshold 750 keV is presented in Fig.4 by solid line. As one can see, our Monte-Carlo simulation and experimental data are in a good agreement.

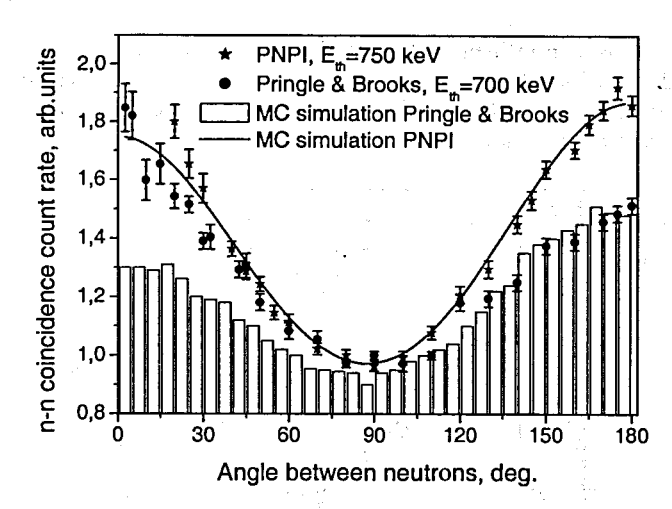


Fig.4. Neutron-neutron angular correlations (experimental data with corresponding MC-calculation) for neutron energy thresholds 700 keV (Pringle&Brooks) and 750 keV (PNPI) obtained in spontaneous fission of ²⁵²Cf.

At the first stage of this calculation it was simulated neutron emission from both fragments with the addition of the necessary contribution of scission neutrons. The averaged total multiplicity of emitted neutrons was taken as $\overline{V} = 3.76$.

The actual number of neutrons evaporated by each fragment was chosen randomly by two-dimensional Gaussian distribution:

$$(\overline{V}_L, \sigma_{uL}^2, \overline{V}_L, \sigma_{uL}^2, \operatorname{cov}(v_L, v_H))$$

with experimentally defined [5] covariance $cov(v_L, v_H) = -0.21$ and known ratio of averaged fragment multiplicities $\overline{V}_L/\overline{V}_H = 1.2$.

The neutron spectrum of each fragment was assumed to be Maxwellian form [6]:

$$N(E) = (\sqrt{E}/T^{3/2}) \cdot \exp(-E/T)$$

with fixed temperature for light and heavy fragment, respectively [7]:

$$T_L = 0.947 \; MeV \; \text{and} \; T_H = 0.850 \; MeV \; .$$

We have performed two versions of calculation. In the first variant the isotropic emission of prompt neutrons in fragment's centre-of-mass system was assumed. On the second way of calculation it was taken into account the presence of maximal neutron emission anisotropy concerned with the angular momentum of each fragment [8].

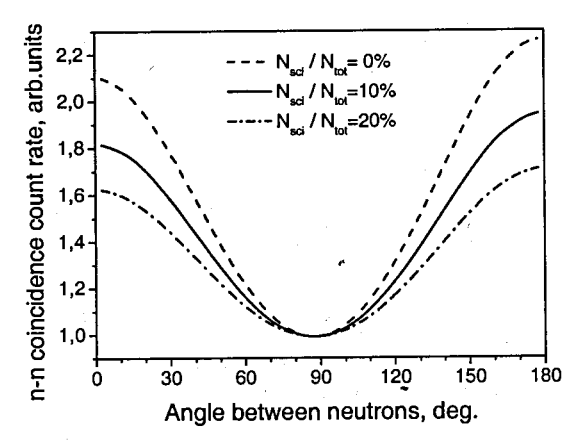
In process of calculation were used final velocities of light and heavy fission fragments with the most probable masses.

The Weisskopf distribution for scission neutron spectrum was assumed:

$$N(E) = (E/T^2) \cdot \exp(-E/T).$$

Thus we had two free parameters (the contribution of scission neutrons and temperature) to fit experimental data of n-n angular distributions measured with six different energy thresholds.

The Fig.5 shows an influence of a contribution of scission neutron component on calculated distribution. As we can see the more this part is supposed the planer calculated curve is. An influence of temperature parameter on calculated curves is more complex (more intricate).



12

Fig. 5. The calculated curves for neutron-neutron angular distributions corresponding to different contributions of scission neutron component.

Nevertheless, in case of suggestion of isotropic neutron emission from fragments all experimentally obtained n-n angular correlations are reasonably well reproduced with one set of parameters, namely: the contribution of scission neutrons is about 10% and temperature is near 0.8 MeV. If we take into account anisotropy of neutron emission in the reference frame of fragment centre-of-mass [8], the result is not changed significantly. In this case we had to increase the contribution of scission neutron component from 10% up to 11%.

Fig.6 demonstrates the set of experimental data of neutron-neutron angular distributions in spontaneous fission of ²⁵²Cf obtained in PNPI for different energy threshold. The solid lines are the results of MC simulations corresponding to these data.

In spite of satisfactory description of experimental data in general, it is necessary to mention systematic excess of experimental count rate at small angles in case of low neutron energy threshold. The region of small angles corresponds to close position of neutron detectors. In this situation the double registration of one neutron simulating spurious coincidence of two different neutrons is more probable. It is possible that such false coincidences were not fully rejected by experimental setup. A second reason for a small discrepancy between experimental and calculated data can be some inaccuracy of the calculation model. Although the correct neutron energy distributions were used, in frame of this simple model we can not include exact correlation between energy values of neutrons evaporated from one fragment, especially for the large neutron multiplicity, but such events happen not very often.

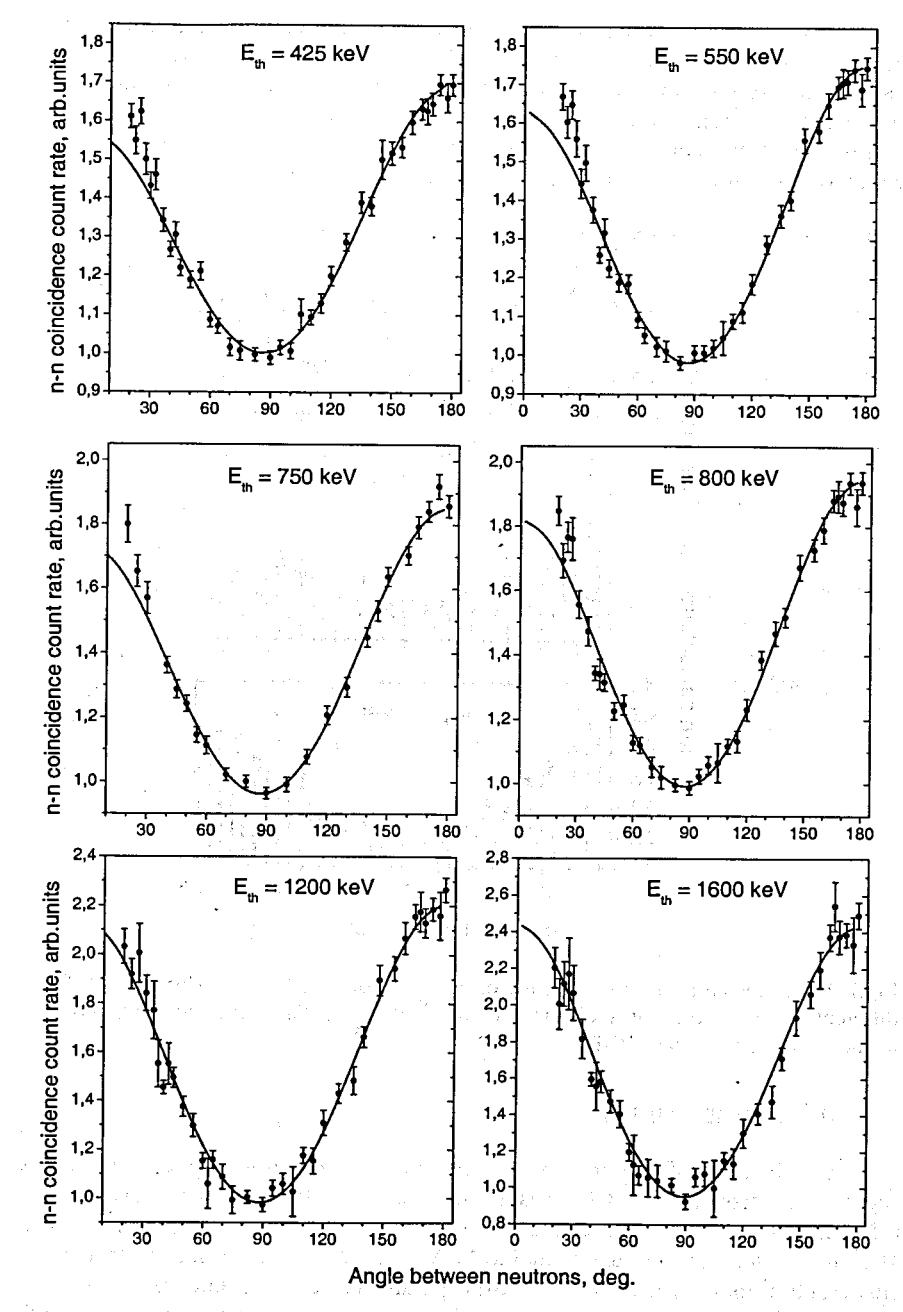


Fig. 6. Experimental data (PNPI) for angular distributions of n-n coincidence count rates concerned with different neutron energy thresholds in spontaneous fission of ²⁵²Cf. The solid lines are the corresponding results of MC simulations.

The same method was also applied to describe neutron-neutron angular correlations in slow-neutron-induced fission of ²³⁵U. The results of calculation for three different neutron energy thresholds are in a good agreement with experimental data [4], if we suppose that the temperature of scission neutrons is about 1 MeV and the contribution of these neutrons equals 15%. These values correspond to Skarsvag's results [2], which were obtained from neutron-fragment angular distributions.

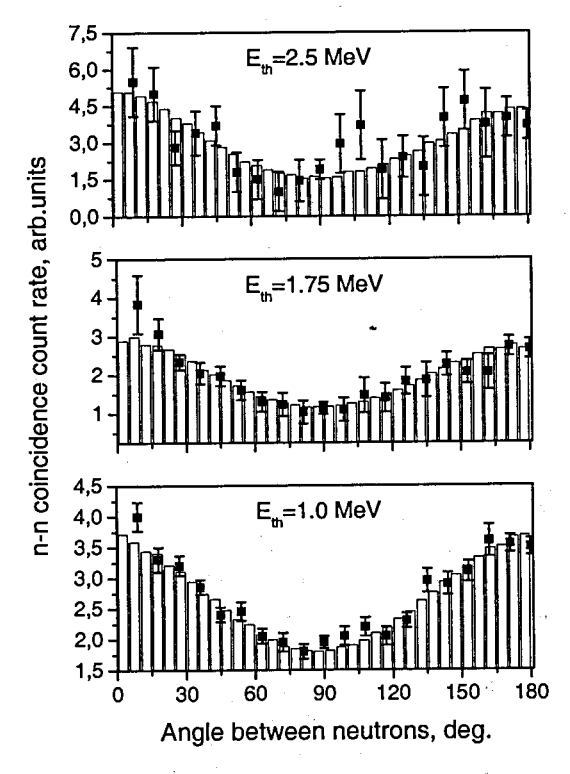


Fig.7. Experimental data for n-n angular distributions obtained by Franklin et al. [4] for three different neutron energy thresholds in reaction 235 U(n_{slow} ,f). The presented histograms are the results of MC simulations (PNPI).

Conclusions and remarks:

The estimation of scission neutron parameters from n-n angular correlations in spontaneous fission of ²⁵²Cf gives us in case of isotropic neutron evaporation in reference frame of fragment centre-of-mass the contribution of scission neutrons near 10% and nuclear temperature about 0.8 MeV with Weisskopf form of distribution. For slow-neutron-induced fission of ²³⁵U these parameters are 15% and 1.0 MeV.

If we take into account the presence of neutron evaporation anisotropy in fragment centre-of-mass-system the results do not change significantly - they increase by 1%. It

is necessary to mention that in our calculations the conception of averaged neutron anisotropy was used [8, 9]. In this conception the suggestion is used that initial angular momentum of each fragment lies in a plane which is perpendicular to a fission axis. Such kind of anisotropy is very useful for neutron-fragment correlation but if we observe coincidences of two neutrons from one fission event it will be more correctly to use anisotropy defined relative to axis directed along fragment spin. Although we believe that such modification could not change appreciably the result of n-n angular correlations, nevertheless the new version of calculation is under development.

This work was supported by INTAS (grant № 03-51-6417).

References

- 1. V.E. Sokolov et al., ISINN-15 (this book), Dubna, Russia.
- 2. K. Skarsvag, K. Bergheim, Nucl. Phys. 45 (1963) 72.
- 3. J.S. Pringle and F.D. Brooks, Phys. Rev. Lett.35 (1975) 1563.
- 4. C.B. Franklyn, C.Hofmeyer and D.W.Mingay, Phys. Lett.78B (1978) 564
- 5. A.S. Vorobyev et. al., ISINN-9, Dubna (2001) p.276.
- 6. K.J. Le Couteur and D.W. Lang, Nucl. Phys. 13, 32 (1959).
- 7. N.V. Kornilov, A.B. Kogalenko and F.-J. Hambsch, Yad. Fiz., 64, №8, 1 (2001).
- 8. V.E. Bunakov, I.S. Guseva, S.G. Kadmensky, G.A. Petrov. "Angular anisotropy of neutrons emission from fission fragments. XIII Intern. Sem. ISINN-13. May 25 28, 2005, Dubna, Russia. Abstracts. p. 18. Proc. ISINN-13. Dubna, 2006. p. 293 300, Izv. RAN, ser. phys., 2006, V.70, №11, pp. 1618-1622.
- 9. A.Gavron, Phys.Rev. 1976. V. C 13. p. 2562.

STUDY OF THE MULTI-CLUSTER DECAYS IN THE NEUTRON INDUCED FISSION OF $^{235}\mathrm{U}^{\dagger}$

D.V. Kamanin¹, Yu.N. Kopach¹, Yu.V. Pyatkov^{2, 1}, A.A. Alexandrov¹, S.B. Borzakov¹, J.E. Lavrova², Ts. Panteleev¹, A.N. Tyukavkin¹

¹Joint Institute for Nuclear Research, Dubna, Russia ²Moscow Engineering Physics Institute, Moscow, Russia

Abstract. First results of the experiment performed on the reaction ²³⁵U (n, f) at the IBR-2 reactor using a two-arm TOF-E (time-of-flight vs. energy) spectrometer miniFOBOS are presented. Different peculiarities in the mass-mass distribution of fission fragments were revealed, which are presumably linked with a new multibody decay channel similar to those observed by us earlier in ²⁵²Cf(sf). We also observe fine structures in total kinetic energy vs. mass distribution of fragments akin to those already found for other fissioning nuclei.

INTRODUCTION

In a series of experiments devoted to the investigation of spontaneous fission of ²⁵²Cf we have found multiple indications of unusual at least ternary decay channel called collinear cluster tripartition (CCT) [1]. For better understanding of the physics of the effect we planned to investigate different fissioning systems at different excitations up to the threshold of the nuclear shells survival. One of the reactions chosen was ²³⁸U + ⁴He (40 MeV). The corresponding experiment was performed recently in Jyväskylä (Finland) [2]. Another one is presented here.

EXPERIMENTAL SETUP

Double arm TOF-E (time-of-flight vs. energy) miniFOBOS [3] spectrometer was installed at the beam of thermal neutrons of the IBR-2 reactor in Frank Laboratory of Neutron Physics of the JINR (Dubna, Russia). A sketch of the experimental setup is shown in fig. 1. For more details we refer you to our report devoted especially to the methodic of the experiment in this issure.

Each of the two spectrometer modules (1, 2) includes a coordinate sensitive avalanche counter and a big ionization chamber. Specially designed gas filled "start" detector (3) with the target of the ²³⁵U isotope inside is placed in the geometrical center of the spectrometer in the collimated neutron beam (4). The detectors allowed us to calculate both pre- and postneutron fragment mass, velocity (momentum) vector, and the range of the fragment in the gas of ionization chamber in each spectrometer arm.

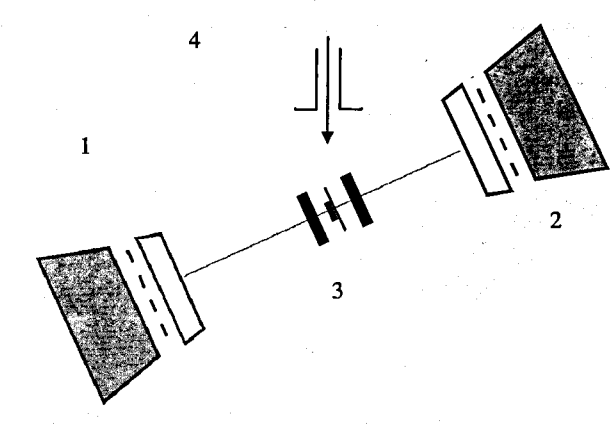


FIGURE 1. Experimental setup used. Each of the detector modules 1, 2 includes both coordinate sensitive avalanche counter and ionization chamber. Detector 3 provides "start" signal. The fissile target located inside of the "start" detector is irradiated by the collimated neutron beam 4.

RESULTS

In our previous experiments when ²⁵²Cf was studied a bright peculiarity in the fragments mass-mass plot was observed with out any selection of the events detected. We mean a specific two-dimensional bump located below the locus of conventional binary fission events [4] (fig. 2a).

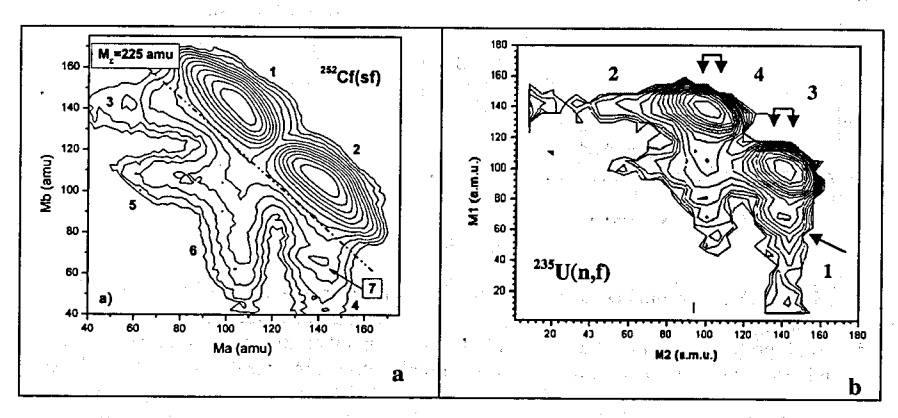


FIGURE 2. Comparison of fragments mass-mass distributions (logarithmic scale) obtained for ²⁵²Cf(sf) (a) and ²³⁵U(n,f) (b). Bumps under discussion are marked at both plots by the arrows 7 and 1 respectively.

As can be referred from fig. 2b, analogous bump is vividly seen there as well. In order to compare quantitatively the parameters of the bumps the mass-mass distribution in fig. 2b was

[†] Work is partially supported by Russian Foundation for Basic Research, grant 05-02-17493, and CRDF, grant MO-011-0.

analysed in the same way as it was done for Cf (sf) data [4]. Namely two-dimensional "tail" 2 was subtracted from "tail" 1 (fig. 2b). The corresponding differential spectrum (the bump actually) is shown in fig. 3a. The projections of two-dimensional bump onto M1 and Ms axis (where Ms=M1+M2) are shown respectively in fig. 3b and fig. 3c, respectively.

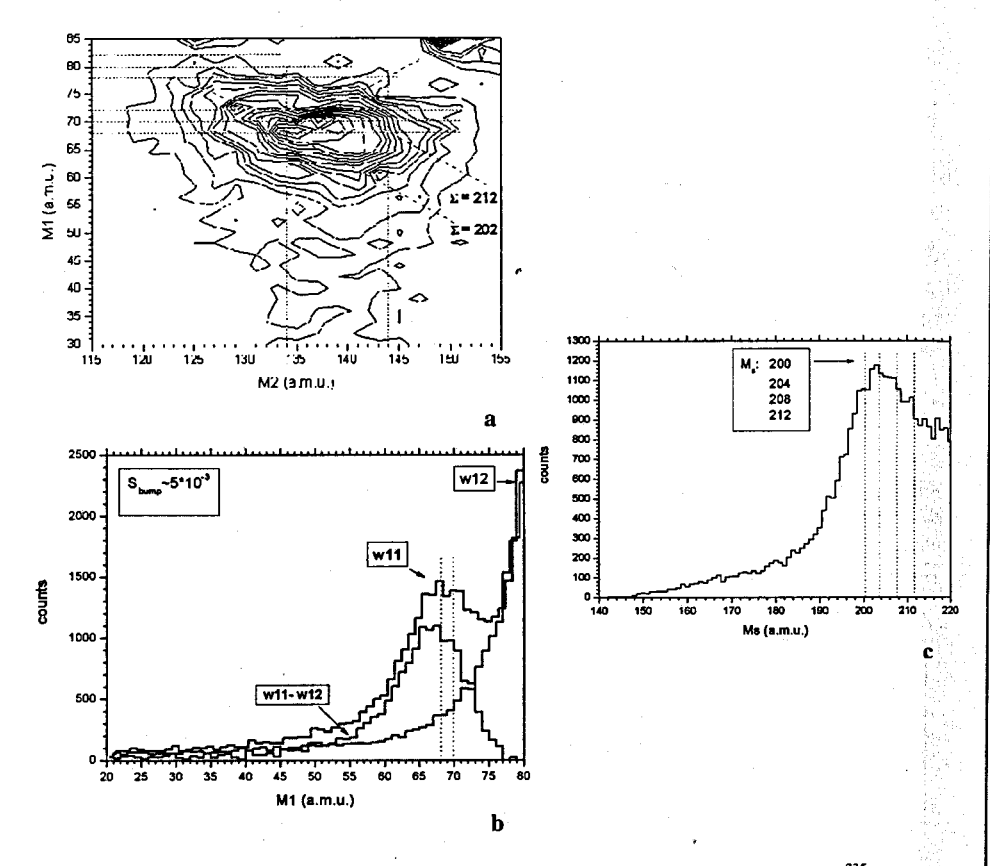


FIGURE 3. Experimental peculiarities of the fragments mass-mass distribution from ²³⁵U(n,t) reaction. Differential two-dimensional distribution (a) obtained by subtraction of "tail" 2 from "tail" 1 in fig. 2b, b-projections onto M1 axis of "tail" 1, "tail" 2 and their difference; c-projection of the w1 region in fig. 2b onto the axis of total mass M, of both detected fragments. See the text for details.

In order to verify whether it is only the light mass peak in the mass-mass distribution which gives rise to the bump lying below it, we compared the sections of equal width, corresponding to the light and heavy mass peaks (shown in fig. 2b by double arrows 3 and 4). Their projections onto M1 axis are presented in fig. 4. The peak is vividly seen only in one of the spectrum.

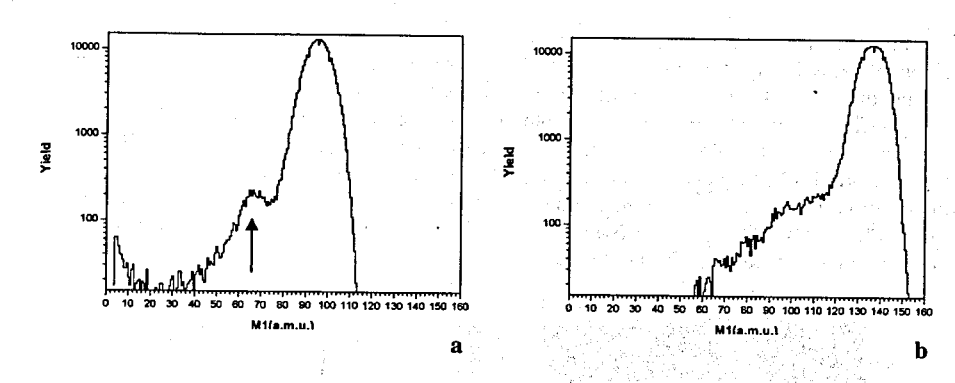


FIGURE 4. Projections onto M1 axis of vertical sections 3 (a) and 4 (b) from mass-mass distribution shown in fig. 2b. Only one of the projections (a) demonstrates a bump (peak) marked by the arrow.

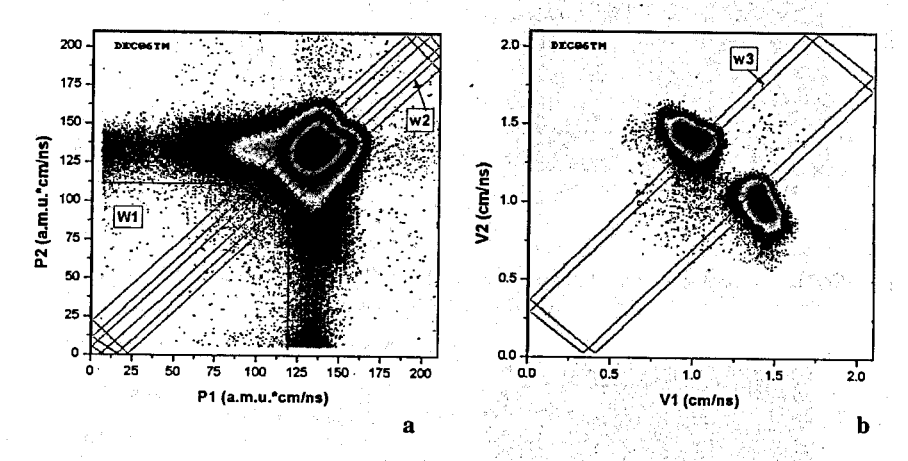


FIGURE 5. FF momentum (a) and velocity distribution (b). The gates for selection of the fission events are shown by contours.

Another manifestation of clustering was obtained by virtue of special processing of the fragment mass-mass distribution. Selection on the FF momentum and velocity was used. Fig.5a shows FF momentum distribution. The tails which stream from the main locus are due to the scattering of the fragments both at the grids of the "stop" avalanche counter and ionization chamber. The FF velocity distribution is shown in fig. 5b.

Using gate W1 we selected events lying exterior both to the tails and the main locus of the conventional binary events. The resulting mass-mass distribution is presented in fig. 6a. It is not uniform but looks like the right angle. As can be referred from the projection of the "angle" onto the M1 axis (fig. 6b) the fragments with the masses in the vicinity of mass 70 a.m.u. prevail.

This tendency becomes more pronounced for the events complying simultaneously to the gates W2&W3 (fig. 5b). Nothing but these events having both approximately equal momentum and velocity of the coincident fragments are shown in fig. 7.

Specific structure in the center of the plot attracts attention. It looks like a right angle with the vertex lying at the plot diagonal in the vicinity of the point (68, 68) a.m.u. (fig. 7b). Using the same kind of gating akin structure (rectangle) was revealed by us earlier in the mass-mass distribution of the fragments from spontaneous fission of the ²⁵²Cf nucleus [5]. Some points in the plot likely lie on the line M1+M2=const (tilted dotted line in fig. 7b). Corresponding "missing mass" in this case is about 65 a.m.u.

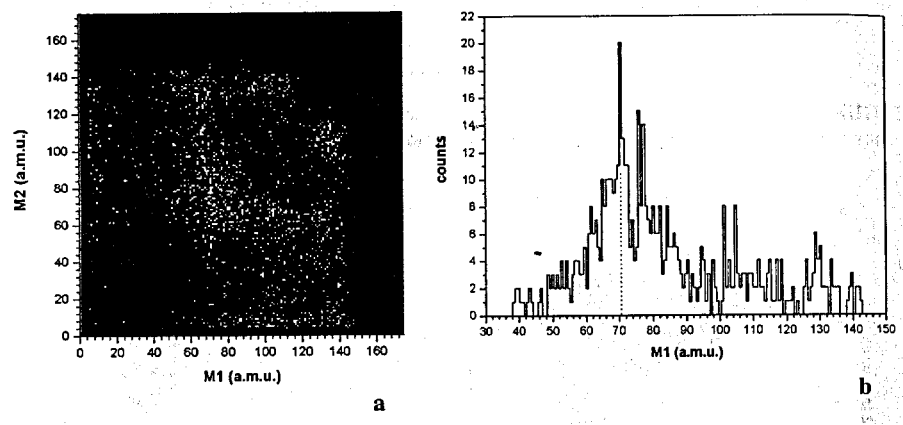


FIGURE 6. Fission events from the box W1 in fig. 5a (a). Projection of the central "right angle" in fig. 6a onto the M1 axis.

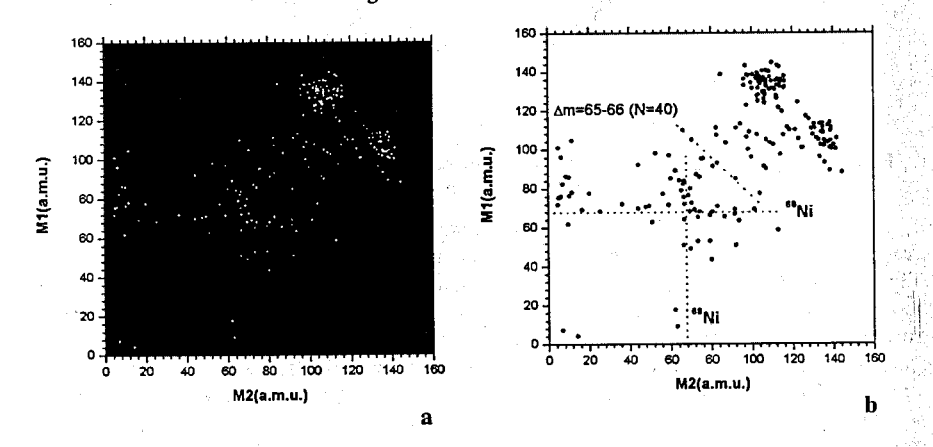


FIGURE 7. Mass-mass plot for the fission events having both approximately equal momentum and velocity of the coincident fragments (a). Specific structure in the form of the right angle is vividly seen in the center of the plot. The vertex of the angle is located in the point (68, 68) presumably linked with the magic ⁶⁸Ni isotope (b). See text for detail.

In our previous works another type of fine structure in total kinetic energy vs. mass (TKE-M) distributions of the FFs was discussed as well [6, 7]. The structure revealed in the FF TKE-M distribution obtained in the frame of the "double velocity" method for the reaction under discussion is shown in fig. 8. It is the result of subtraction of a smooth backing from the initial distribution.

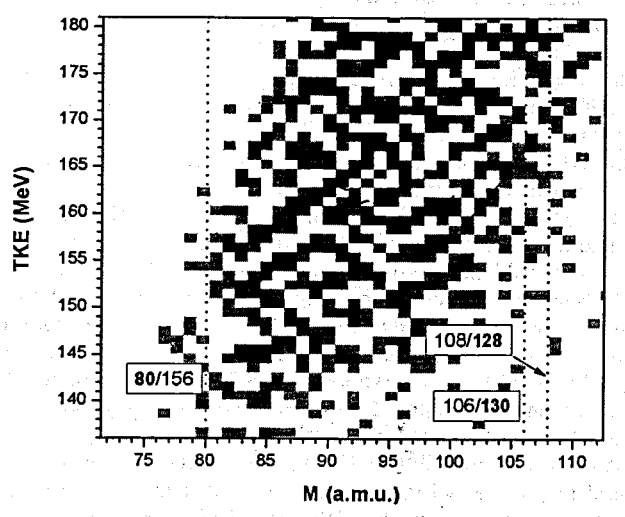


FIGURE 8. Grey-scale map (black corresponds to the highest level of the effect) of the fine structure in the FF TKE-M distribution from the reaction ²³⁵U(n, f). Most pronounced snake-like structures conforming to those observed earlier are marked by the dash curves. See text for details.

DISCUSSION

Detailed physical treating of the effects observed is beyond the scope of this report. Below there are some comments to the plots presented here.

Figures 1-4 are linked with the "bump" in the FF mass-mass distribution. As we have already stressed discussing the effect in ²⁵²Cf(sf) [4], the bump manifests itself only in one arm of the spectrometer while the difference between the arms consists uniquely in the target backing on one side (in arm 1). Basing on the results of this work one can conclude that only light peak of the FF mass distribution gives rise to the effect (fig. 4). It seems to be a strong argument in favor of physical, not methodical nature of the effect. The next point to be stressed is that despite of substantial difference in the masses of the fissioning systems (252 and 236a.m.u.) quantitative parameters of the bumps for ²⁵²Cf(sf) (a) and ²³⁵U(n,f) are close to each other. Really, the projection of the bump onto M1 axis (fig. 3b) peaks at ~ 68-70 a.m.u., the masses which are associated with the magic Ni isotopes [9]. In its turn, projection along the direction of M1+M2=const (graphically along the lines tilted at 45° degrees to the M2 axis) looks like a wide peak ranging approximately from 200 to 212 a.m.u. (fig. 3a, c). In [4] an observation of total mass of two detected fragments in this range was traced back to preformation of a pair of magic nuclei (light and heavy), clusters by definition, in the body of

the fissioning system. Conservation of this range while the mass of the initial system was changed supports such hypothesis.

Figure 5b gives evidence of exceptional role of the proton shell Z=28 and neutron subshell N=40 in the mechanism of a presumable multibody decay decisive for forming both structures (right angle and tilted line) marked in the figure. It is reasonable to suppose that just 68 Ni $_{40}$ stands behind the mass 68 a.m.u. defining the sides of the angle. As for the tilted line it corresponds to the "missing" mass ~ 66 a.m.u. Calculating the most probable charge for N=40 (unchanged charge density hypothesis, or roughly, Z_{ucd} hypothesis) one obtains the value between 25 and 26 (Mn, Fe). Thus, this structure is also demonstrates a preferable yield of the fragments with submagic number of neutrons.

The structures discussed above are linked with at least ternary decay because the total mass of two detected fragments falls far short of the mass of the mother system. For the moment we are far from understanding of mechanism of the decays nevertheless it is clear that shell effects in the fragments (clustering) play a key role in the process. Original way to visualize clustering in conventional binary fission consists in revealing fine structure of the FF TKE-M distributions [6]. Snake-like structures marked in fig. 6 agree well with those obtained earlier [6] within a little (-4 MeV) shift along TKE axis. Presumably, the structures being the tops of the ridges of the increased yields map onto TKE-M (or roughly, system elongation - mass asymmetry) space most preferable trajectories of the fissioning system on the way to scission [8]. The structures seem to be bounded by the lines corresponding to magic fragments (with the masses marked in fig. 6 by the bold numbers) both in the light and heavy mass peaks. From the left side it could be 80Ge (a shift on 2 a.m.u. relative to expected magic 82Ge was already discussed in [10]). From the right side one asymptotic line can be linked with the magic ¹²⁸Sn and the next one with the ¹³⁰Sn instead of double magic ¹³²Sn. Likely it is a compromise value because mass 132 is too far from mass 128 obtained for Z=50 in the frame of the Z_{ued} hypothesis. Thus, the structures testify to the fact that ruptures can occur only in the "neck" between two stable magic clusters.

CONCLUSION

The main conclusion to be drawn from all results presented above is that they confirm in essence the previous results obtained by us earlier for different fissioning systems.

REFERENCES

- 1. Yu. V. Pyatkov et al., Phys. Atom. Nucl. V.66, 1631 (2003).
- Yu. V. Pyatkov et al., Proc. Int. Symposium On Exotic Nuclei, Khanty-Mansiysk, Russia, 17-22 July 2006, p. 144.
- D. V. Kamanin et al., International Symposium on Exotic Nuclei, Peterhof, Russia, 5-12 July 2004. Conference proceedings. Published by World Scientific Publishing Co. Pte. Ltd., 2005, p. 588-591.
- 4. Yu. V. Pyatkov et al., Preprint JINR E15-2005-99, Dubna, 2005
- 5. Yu. V. Pyatkov et al., Preprint JINR E15-2004-65, Dubna, 2004
- 6. Yu. V. Pyatkov et al., Nucl. Instr. Meth. in Phys. Res. A 488 (2002) 381
- W.H.Trzaska et al., Proc. Symp. On Nuclear Clusters, Rauischholtzhausen, Germany, August 5-9, 2002.
 p. 237
- 8. Yu. V. Pyatkov et al., Physics of Atomic Nuclei 67 (2004) 1726
- 9. D. Rochman et al., Nulc. Phys. A 735 (2004) 3
- 10. I. Tsekhanovich et al., Nulc. Phys. A 688 (2001) 633

COLLINEAR MULTICLUSTER DECAYS OF Pu* ISOTOPES

Yu.V. Pyatkov^{1,2} for HENDES and FOBOS collaborations

¹Moscow Engineering Physics Institute, Moscow, Russia ²Joint Institute for Nuclear Research, Dubna, Russia

Abstract. In our previous reports we have presented some results on searching for collinear tripartition of the excited Pu isotopes from the reaction ²³⁸U + ⁴He (40 MeV). Additional arguments in favor of existence of such decay mode are presented. Possible mechanism of the phenomenon observed is discussed as well.

INTRODUCTION

Earlier we have observed unusual decay mode of ²⁵²Cf (sf) which was treated as "collinear cluster tripartition" [1-4]. So far experimental manifestations of this decay channel were obtained in the frame of the "missing mass" method. It means that only two almost collinear fragments were detected in coincidence and they were much smaller in total mass than initial nucleus. Direct detection of all decay partners was the main goal of the experiment under discussion. In order to solve the problem a setup of high granularity should be used. Such kind of spectrometer installed at the JYFL, (Jyväskylä, Finland) was chosen for studying the reaction ²³⁸U+⁴He (40 MeV). The scheme of the experimental setup is shown in fig.1.

EXPERIMENTAL SETUP

The spectrometer includes two arrays 19 PIN-diodes each and two MCP (micro-channel plate)-based start detectors. Each PIN diode provides both energy and timing "stop" signals. Target holder with two targets ($100 \, \mu g/cm^2$ layer of 238 U evaporated on $50 \, \mu g/cm^2$ thick Al_2O_3 backing each) was installed in the center of reaction chamber. The beam (FRC= $14.820 \, MHz$ what gives ~ 67 ns interval between the beam bursts) was focused on the target into a spot of 5 mm in diameter by means of two collimators. Calibration procedures and reconstruction of the fragment mass in the frame of the energy-velocity method are presented in our recent publications [5, 6].

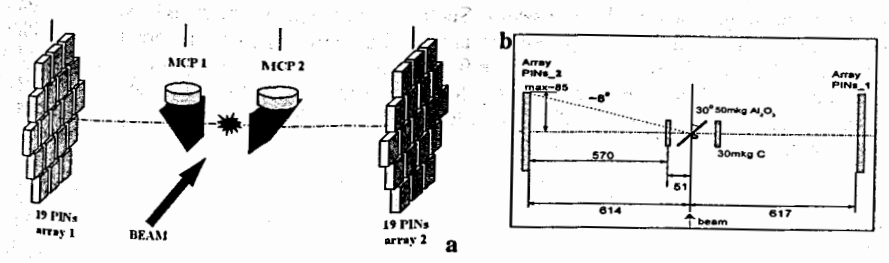


FIGURE 1. Overall scheme of the experimental setup (a) and additional information concerning its parameters (b).

Before coming to the results one essential peculiarity of the setup should be pointed out. It is connected with a position of the "start" detectors namely in 51 mm from the target (fig.1b). In the multibody decay the most faster from the fragments hitting "start" detector gives "start" signal to be common for the corresponding arm. Consequently a velocity of this fragment only will be measured correctly while others fragments detected in the same arm get shifted velocity values. True (emission) velocities can be calculated according formulas in Table 1 where Vexp, Vemis – are, respectively, the experimental and emission velocities.

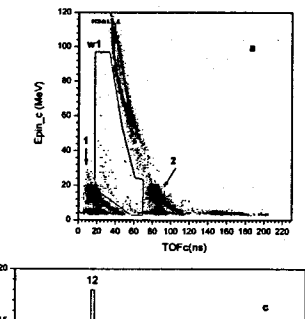
Table 1. Corrections to the fragments velocities

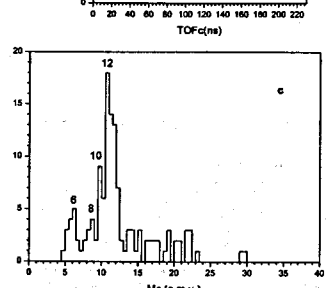
Variant №	Kinematical scheme of the decay mode	Formula for calculation of emission velocity
1	A C C B C C B C C C C C C C C C C C C C	2 fragments formed in the MCP detector fly in the same direction: no corrections, i.e. Vemis= Vexp
2.		2 fragments (fragment C to be faster) were formed in the target: BVemis= 61.6/(56.6/ BVexp + 5.1/Vc)
3		2 fragments were formed in the MCP detector but fly in opposite directions: CVemis= 66.8 / [56.6/CVexp - 5.1(1/ Vb-1/ Va)]

Altogether, about 40 millions binary fission events were collected. Besides binary, ternary and quaternary coincidences were also detected in the experiment. Here we discuss one specific group of events with multiplicity 3.

RESULTS

Preliminary analysis [6] showed that the main part of the triple events detected are due to the random coincidences of the fission fragments (FF) originated from conventional binary fission with both scattered α-particles from the beam and ions of oxygen and aluminum knocked from the target backing by the beam. Such events form pronounced loci in fig. 2a (marked by the arrows). Both loci (1 and 2) are of the same nature but are linked with adjacent bursts. For the sake of convenience the fragments in each ternary event were resorted in order of decreasing of fragment mass namely Ma to be the heaviest one and so on. A long locus in the upper part of fig. 2a should be excluded from the further analysis. It follows from fig. 2b were gating Ms<250 a.m.u. was applied.





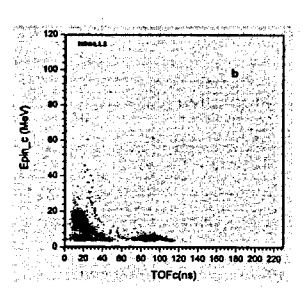
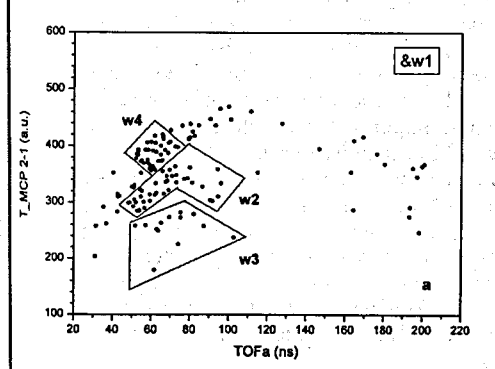


Figure 2. TOF versus energy detected in PIN for the lightest fragment in each ternary event (a). The same under condition that a total mass of all three fragments detected does not exceed 250 a.m.u. (b). Spectrum Y(Mc) for the events included in window w1 (c). Each channel on the mass axis corresponds to 0.5 a.m.u. The numbers above the peaks correspond to their centers.

Thus only the events in the window w1 will be analyzed below. Their projection onto Mc axis is shown in fig. 2c.

For searching for unusual events fig. 3a was used. Here a difference in time when "start" detectors were tripped by the fragments flying apart is plotted on vertical axis. This time is known to be approximately proportional to masse ratio of the FF's from binary fission.

Grouping of the points attracts attention. Corresponding groups are marked in the figure by contours w2-w4. In its turn for instance set of events w2 looks like as some distinct families of points (marked as w5-w8 in fig. 3b) on Ma-Mb plane. Pair of magic fragments which total mass is equal to the mass of compound nucleus (242 a.m.u.) "starts" each family. We have analyzed them event-by-event. Corresponding results are presented below.



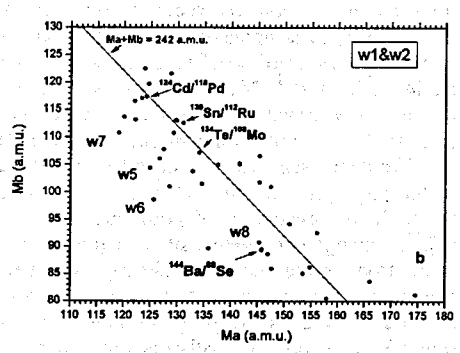


Figure 3. Time-of-flight versus time between "start" signals (a) for the events gated by the window w1 (Figure 2a). Mass-mass distribution for the events selected using condition w1&w2 (b). See text for detail.

Table 2. Information which was taken into account at derivation of the decay scheme for each triple event analyzed (example for an event from the family w5 in fig. 3b).

Point №	parameter		A	В	С	Dcal	Decay scheme
·	PIN number		205	111	208		128 108 6 6 7
4	M (amu)		127.4	107.8	10.8	⁶ He	128 Sn + 108 Mo + 6 He
	V(cm/ns)		0.867	1.22	2		missing
	Efr (MeV)		49.9	83.5	22.6		114 _{Ru}
	Parml(a.u.)	131.6					1
	Parm2 (a.u.)	132.3]				12C from "start" detector
	Ms (amu)	246.1	1				
	Ma+b (amu)	235.2	1				

The following designations are used in the table above. Each column A, B, C, D (in order of decreasing of fragment mass) involves parameters of specific fragment. PIN number – lets one to know which PIN diode was tripped and in which arm. M, V, Efr – are, respectively, FF mass, velocity and true energy deposited in PIN diode (PHD was taken into account). Parm 1,2 – are total momentum of the fragments detected in a corresponding arm. Ms-is a total mass of all fragments detected in this event. Ma+b – total mass of two heaviest fragments. Dcal – is a mass of third fragment calculated using mass conservation law under condition that reference mass of the decaying system to be 242 a.m.u. (a number of prescission neutrons emitted in a specific event is unknown).

For the event under discussion the following arguments were taken into account in order to restore a most reasonable decay scheme could provide the parameters observed in the experiment. For three fragments detected momentum conservation law is met very well. At the same time the total mass Ms is too large even in compare with the maximal possible mass of decaying system (242 a.m.u.). One can surmise that the fragment C could be a Carbon ion knocked from the MCP detector foil. It is known from the Table 2, that fragments A and C fly in the same direction (PIN numbers of both start from the amount "2"). Using Rutherford formula for elastic scattering one obtains that the energy of C-ion scattered at zero angle reference to the velocity vector of fragment A having energy Ea'= Efr_a + Efr_c should be 22.72 MeV, what agrees well with the experimental value 22.6 from Table 2. Experimental values of masses of the fragments A and B are very close to the masses of known magic nuclei ¹²⁸Sn and ¹⁰⁸Mo respectively. It is believed that just these nuclides to be the decay partners. Conservation of nuclear charge and mass requires that the third fragment should exist such as ⁶He by composition. It can be as well ⁴He and two neutrons, 2 ³H and so on.

The decay scenarios restored for the Sn/Ru mode are presented in table 3. The upper line of the table provides the information concerning deformations and nucleon compositions of the shells involved while capital letters in the brackets correspond to the shell minima loci in [7]. Unchanged charge density (Z_{ucd}) hypothesis was used for calculation for instance number of neutrons in the nucleus with magic number of protons (44 Ru Nucd=69.1) and vice versa. The fragment which mass was corrected according the formulas 2 or 3 from Table 1 will be marked by a corresponding number (for instance, 103 Zr 2). Bold symbols in the decay schemes correspond to really detected fragments.

All the cluster families listed in fig. 3b namely

⁴⁸ Cd _{Nucd=75.4} (β2~0.8, "K'") / ₄₆Pd _{Nucd=72} (β2~0.8, "K'"), _{Zucd=52}Te ₈₂ (β2~0, "G") / _{Zucd=42}Mo ₆₆ (β2~0.58, "C"), _{Zucd=56}Ba ₈₈ (β2~0.65, "H") / ₃₈Sr _{Nucd=60} (β2~0.38, "B"") were analyzed in a similar manner. Lacking opportunity to present here the analysis in detail we selected most interesting events in table 4.

Table 3. Summary on Sn/Ru mode (gate w5 in fig. 3b).

	₅₀ Sn ₈₂	(β2~0, "C	i' ", "G") / 44Ru Nucd=69.1 (β2~().55,"C' ")
Point number	Decay scheme	Point number	Decay scheme	Point number	
1	¹²⁹ Sn + ¹¹³ Ru - binary fission ↓ Be from "start" detector	4	128Sn + 168 Mo + 6He ↓ missing · 114Ru 12C from "start" detector	6	129Sn + 103Zr 29 + 4He + 4He missing
2	130 Sn + 112 Ru - binary fission 12 C from "start" detector	5	126 In + 3H + n + 106 Nb + 6Li missing 130 Sn 112 Ru	7	124Cd + 6He + 8Be + 104Zr missing 130Sn 112Ru
3	¹²⁹ Sn + ¹¹³ Ru - binary fission ¹⁹ F from "start" detector				

Table 4. Analysis of some selected events

	all 3 fragments wer	e detected in the events below
Event number	Decay scheme	Comments
13 	Molecule after scission ← 122Cd + ⁶ He + ¹¹³ Ru → 119Pd	There are no shifts in the FF's velocities, thus (see scheme 1 in table 1) ⁶ He was born at the MCP detector due to the decay of the molecule ¹²² Cd + ⁶ He in inelastic scattering on the carbon foil.
14	120Ag + ² H + ⁶ He + ¹¹⁴ Ru ←	There are no shifts in the FF's velocities, thus ⁸ Li was born at the MCP detector. Namely, in the scission point decaying system consisted of two clusterized nuclei of Pd. After scission ¹²⁰ Ag nucleus and the molecule ⁸ Li+ ¹¹⁴ Ru fly apart. The latter decays due to inelastic interaction with the nucleus of the converting foil. The decay products continue to fly in the same direction.
15	¹¹⁹ Pd + ¹¹¹ Tc + ¹² B ³⁾	Scheme 3 from table 1 was used in reconstruction of the decay scheme, thus 12B was born at the MCP detector in a two stage process: 1. ← 119Pd - 123Cd → immediately after scission; 2. ← 12B, 111Tc→ after inelastic scattering of 123Cd on the carbon foil of MCP detector.

Table 4. Analysis of some selected events

	¹⁴⁴ Ba + ³ H + ⁷ Li ³) + ⁸⁸ Se	Also two stage process presumably took place: 1. 144Ba + 98Sr to be clusterized as	
22	⁹⁸ Sr	$^{3}H + ^{7}Li + ^{88}Se$ in the scission point;	
	¹⁴⁷ La	144Ba + 3H form molecule to be equal by composition to 147La, which was really detected.	
		⁷ Li + ⁸⁸ Se form also molecule till the 2-nd stage:	
		2. inelastic scattering of the latter on the carbon	
		foil:	
		← ⁷ Li, ⁸⁸ Se→ (partners fly apart)	
23	¹⁴⁴ Ba + ⁹ Be ³⁾ + ⁸⁹ Se	1. ← ¹⁴⁴ Ba - ⁹⁸ Sr → after scission;	
23		2. ← ⁹ Be, ⁸⁹ Se→ after inelastic scattering of	
	⁹⁸ Sr	⁹⁸ Sr on the carbon foil of the MCP detector	

DISCUSSION

We observe some distinct "families" of events based on two magic clusters each: Sn/Ru, Cd/Pd, Te/Mo, Ba/Sr. Experimental values of masses of the detected clusters prove to be unshifted or in other words agree with calibration obtained at ²⁵²Cf (sf) sours i.e. without beam. At the same time the FF's masses for the conventional binary fission (evidently prompt) are a little bit shifted [6] likely due to influence of the beam on the MCP based detectors. Such difference can be understood if the ternary events analyzed above originate from the decays of isomeric states of Pu isotopes [8], the decays to be delayed by their nature thus appearing predominantly between the bursts.

Analyzing the decay schemes restored one can refer a following general rule. Each initial cluster clusterises during an elongation of the fissioning system (secondary clusterization) forming lighter magic cluster and at least one light particle. The mechanism seems to be close to this standing behind a well known Ikeda rule [9]. A rupture of so prepared multicomponent system can occur along any one of several boundaries of the nuclei involved. Light "remains" of secondary clusterization likely may unit into heavier nucleus (see event 14 from the Table 4).

After scission disintegration of such at least di-nuclear "molecule" can appear to occur via inelastic scattering on the target backing or carbon foil of the "start" detector. It should be stressed that we deal with long lived bounded states bearing in mind a typical time-of-flight (~ 5 ns) between the target and "start" detector where a decay of a molecule is happened (see Table 4).

At the moment it must not be ruled out that the ternary decays observed are of the same nature as known "polar emission" of α -particles and protons [10].

CONCLUSION

Summing up the results presented we came to conclusions presented in the table below.

Table 5. Presumable scenario of the multibody decays observed

Expected configuration of the decaying system	Presumable evolution scenario
¹³⁴ Te	In the reaction ²³⁸ U + ⁴ He (40MeV) a shape- isomer (presumably one of Pu isotopes) is built on a pair of magic nuclei (clusters).
134Te 108Mo 128Sn 6He 10Be 98Sr	Evolving towards the scission point the elongated configuration would lead to possible secondary clusterizations as shown on the picture. This mechanism would generate not only heavy but also lighter magic nuclei such as ⁶ He or ¹⁰ Be.
	Scission leads to the formation of relatively weakly bound but sufficiently long lived "nuclear molecules" (or isomers) build on a magic nucleus and a light cluster.
12°C	Disintegration of such a molecule can happen spontaneously or be triggered, for instance, by inelastic scattering in the target (U or backing) or on the carbon foil of the "start" detector.

Acknowledgments

Work partially supported by Russian Foundation for Basic Research, grant 05-02-17493, CRDF, grant MO-011-0.

REFERENCES

- 1. Yu. V. Pyatkov et al., Proc. Int. Conf. "50Years of Shells", 301 (1999).
- 2. W. Trzaska et al., Proc. Seminar on Fission Pont d'Oye V, Belgium, 102 (2003).
- 3. Yu. V. Pyatkov et al., Preprint JINR E-15-2004-65.
- 4. Yu. V. Pyatkov et al., Preprint JINR E15-2005-99.
- 5. Yu. Pyatkov et al., Proc. Int. Symposium On Exotic Nuclei, Khanty-Mansiysk, Russia, 17-22 July 2006, p.144
- Yu. Pyatkov et al., Proc. 14th Int. Seminar on Interaction of Neutrons with Nuclei: "Neutron Spectroscopy, Nuclear Structure, Related Topics". Dubna, May 24-27, 2006, p. 134
- 7. B.D. Wilkins et al., Phys. Rev. C14, 1832 (1974).
- 8. S.M. Polikanov and G. Sletten, Nucl. Phys. A151, 656 (1970).
- K. Ikeda, Proc. 5th Int. Conf. on Clustering Aspects in Nuclear and Subnuclera Systems, Kyoto, p. 277 (Contributed papers, 1988).
- 10. E. Piasecki, L. Nowicki, IAEA-SM-241/F11, p.193

INVESTIGATIONS OF THE ANGULAR DEPENDENCE OF NEUTRON-NEUTRON COINCIDENCES FROM ²³⁵U FISSION INDUCED BY THERMAL NEUTRONS AND SPONTANEOUS FISSION OF ²⁵²Cf

V.E. Sokolov, G.A. Petrov, A.M. Gagarski, D.O. Krinitsin, D.V. Nikolaev, G.V. Val'sky, V.I. Petrova, T.A. Zavarukhina

Petersburg Nuclear Physics Institute of Russian Academy of Sciences, Gatchina, Leningrad District, 188300, Russia

ABSTRACT

With the aim of the neutron emission mechanism investigation the angular dependence of coincidences between the prompt neutrons from spontaneous fission of ²⁵²Cf have been measured in PNPI (Gatchina, Russia). The same measurements in ²³⁵U fission are performed at present. Thermal neutron beam from the WWR-M reactor is used to induce fission in uranium target enriched to 90% of ²³⁵U.

From the ²⁵²Cf and ²³⁵U measurements at angles of 20° to 180° between the directions of the fission neutrons it was found that the number of coincidences has minimum near 90° and increases by a factor ~ (1.7 - 3) to 20° and 180° in dependence of prompt neutrons energy thresholds. In the ²⁵²Cf theoretical analysis with use of different thresholds for fission neutrons energy the correlation could be adequately described by a simple evaporation model, assuming isotropic neutron emission from the fully accelerated fragments frames in their centre of mass together with about 10% isotropic scission component. The measurements and theoretical analysis for angular correlation of prompt fission neutrons in ²³⁵U fission are in progress.

1. INTRODUCTION

A large fraction of the neutrons emitted promptly in thermal neutron fission can be accounted for in terms of evaporation from the fully accelerated fission fragments. However the origin of the remaining part (10-25%) [1-5] of the neutron emission remains in question. It has been suggested that these neutrons may be emitted at the instant of scission [6,7] or during the acceleration period of the fragments [8,9]. Models of the neutron emission rest mainly on experimental observation of the velocity and angular distributions of the prompt neutrons. The angular distributions being referred to the axis defined by the direction of the light fragment.

The neutron-neutron (n-n) angular correlation experiment does not require the detection of fission fragments. The observations are automatically averaged over all orientations of the fission axis. The correlation is nevertheless sensitive to the characteristics of neutron emission and provides a useful additional method for testing models of emission process.

There are few works [5, 10-11] devoted to the investigations of the (n-n) angular correlation in nuclear fission. But there are some vagueness and questions in obtained results.

We have measured the (n-n) correlation of prompt neutrons from the thermal neutrons fission of ²⁵²Cf for different angles. The aim of the researches is investigation of the neutron emission mechanism. The measurements from thermal neutrons fission of ²³⁵U are in progress now and first preliminary results of the experimental researches are presented.

2. EXPERIMENT

The (n-n) angular correlation researches with ~1 mkg of spontaneously fissile 252 Cf were performed in laboratory room. The measurements in 235 U fission are carried out at the thermal neutron beam $(3\times10^6 \text{ n/cm}^2\text{s})$ of the WWR-M Reactor of PNPI. The 235 U measurements are performed with using a target of ~1 g enriched to 90% of 235 U arranged into Al cylinder container (Ø 6mm × 20 mm). In Fig. 1 the experimental set-up is presented.

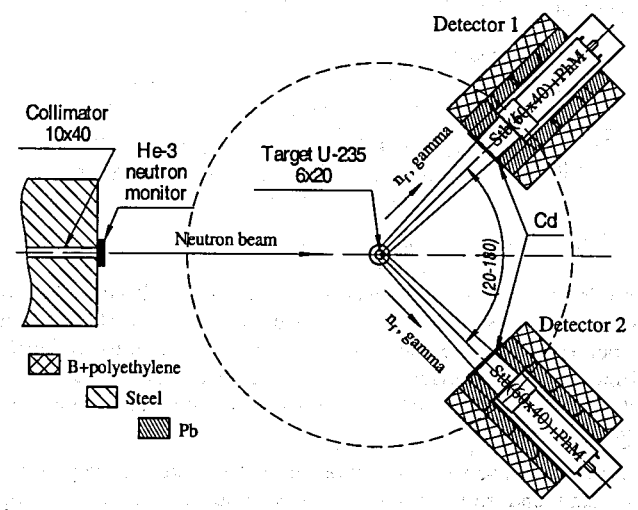


Fig. 1. The experimental set-up for measurement of the angular dependence of coincidences between prompt neutrons in ²³⁵U fission.

Direction of the neutron beam from neutron guiding system is shown. We use two identical plastic photo-multiplier neutron detectors measured the coincidence rate of pairs of fission neutrons emitted at relative angles θ with angular resolution ~ (5-10)°. The range is from 20° (minimal possible) to 180° in (5-10)° intervals. The detectors are into defense consisted of polyethylene and lead. The three different distances (40 cm, 51 cm, and 72 cm) from the target to the two stilbene scintillators (\emptyset 60×40 mm) are used in the measurements.

The main task of the experiment consist in comparison of the prompt neutron-neutron coincidences rate from two detectors for different angles between them.

In this experiment we use technique of time-of-flight measurements, where "start" signals are prompt neutron (or γ -quantum) ones from first detector , and "stops" signals are ones from other detector. In next Fig. 2 simplified scheme of the data acquisition system is presented. Start part consist of Amplifiers (Ampl), Constant Fraction Discriminator (CFD), Counter (Count) and Time - Amplitude Converter . The stop part is analogous, only Time Delay Line (Delay 150 ns) is added to obtain symmetric neutron and gamma coincidences time spectrum. From Time - Amplitude Converter the information comes in Amplitude - Digital Converter , after in CAMAC controller, and at last into Personal Computer for accumulation and analysis.

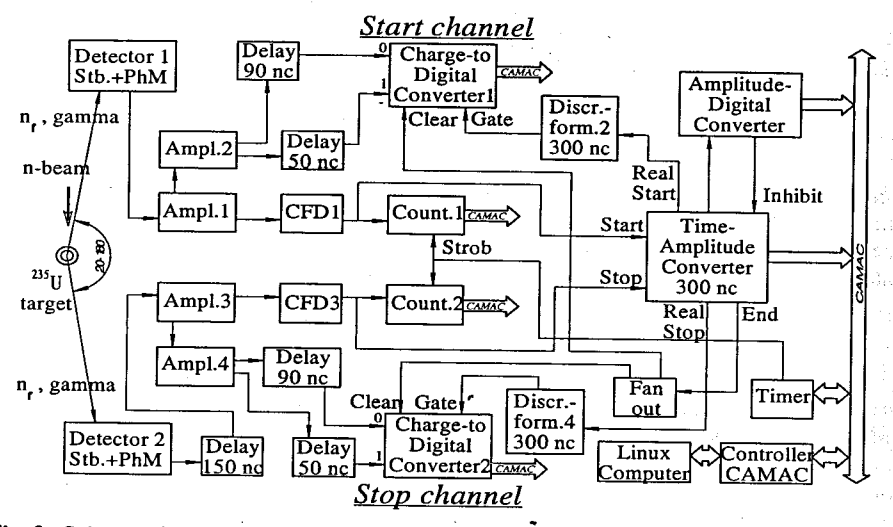


Fig. 2. Scheme of the Data Acquisition System.

In our experiment the gamma-ray events rejection was realized by neutron and gamma pulse shape discrimination. We use the fact that neutron signal duration is more longer then gamma signal one. To realize the discrimination the two Charge-to Digital Converters and two different Time Delay Lines (Delay 50 ns , 90 ns) were used in start and stop channels. The total and slow charge components of start and stop signals were measured in the Data Acquisition System.

In Fig. 3 the results of separation neutron and gamma signals are presented: These are CDC-spectra for start and stop detectors signals. You can see slow charge component dependence from total charge signal and quite good separation is observed.

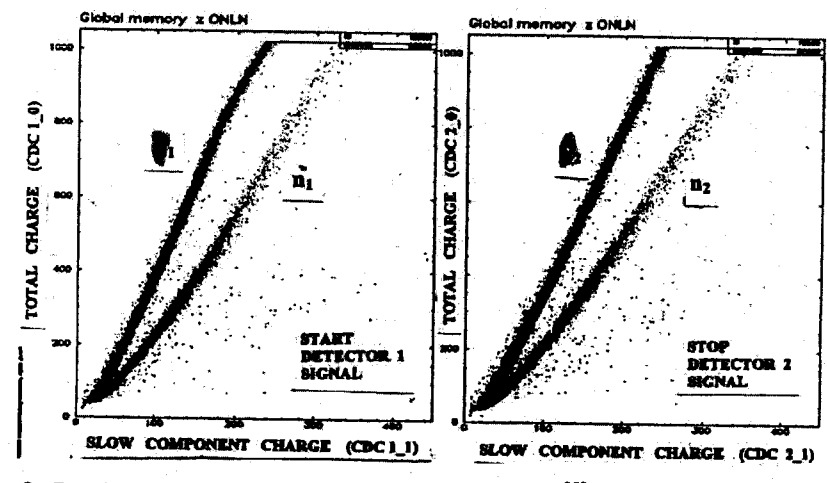


Fig. 3. Results of neutron and gamma signals separation in ²⁵²Cf fission: CDC-spectra for start and stop detectors signals.

Experimental spectrum of coincidences between the γ - and n- signals from the two neutron detectors is shown in next Fig. 4.

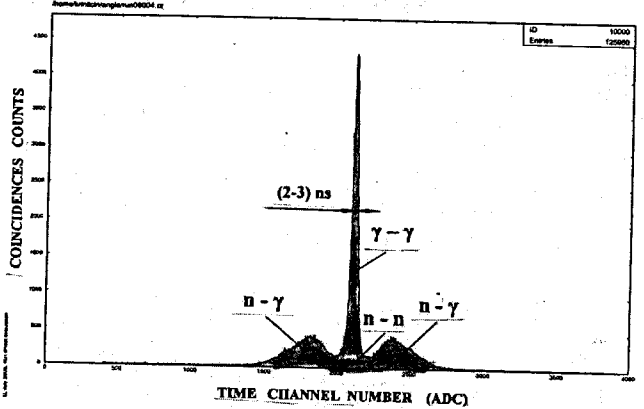


Fig. 4. Experimental spectra of coincidences between the γ - and n-signals from the two neutron detectors in ²⁵²Cf fission.

The $(\gamma-\gamma)$ -quanta coincidences peak is in the centre with time resolution at half-height about (2.5-3) ns. The position is start zero time. Two symmetric humps on the left and right of the peak are connected in first turn with $(n-\gamma)$ coincidences. Main investigated (n-n) coincidences are hided are in the centre under gamma-gamma peak. Background of accidental coincidences is very low in case 252 Cf investigation.

After sorting and analysis of all experimental coincidences spectra we obtain the separated contributions (see Fig. 5) in total time spectrum for:

- neutron-neutron (n-n),
- gamma-gamma quanta (γ-γ),
- -neutron-gamma quantum (n-γ) coincidences.

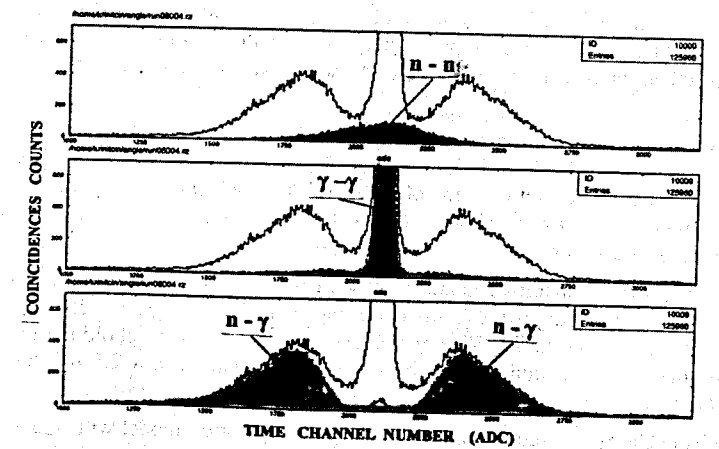


Fig. 5. The separated contributions in total time spectrum for (n-n), $(\gamma-\gamma)$ and $(n-\gamma)$ coincidences in 252 Cf fission.

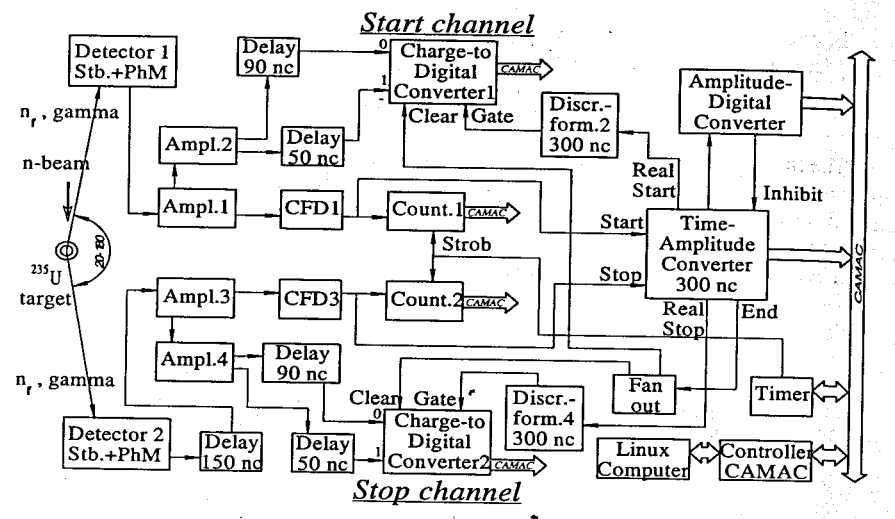


Fig. 2. Scheme of the Data Acquisition System.

In our experiment the gamma-ray events rejection was realized by neutron and gamma pulse shape discrimination. We use the fact that neutron signal duration is more longer then gamma signal one. To realize the discrimination the two Charge-to Digital Converters and two different Time Delay Lines (Delay 50 ns , 90 ns) were used in start and stop channels. The total and slow charge components of start and stop signals were measured in the Data Acquisition System.

In Fig. 3 the results of separation neutron and gamma signals are presented: These are CDC-spectra for start and stop detectors signals. You can see slow charge component dependence from total charge signal and quite good separation is observed.

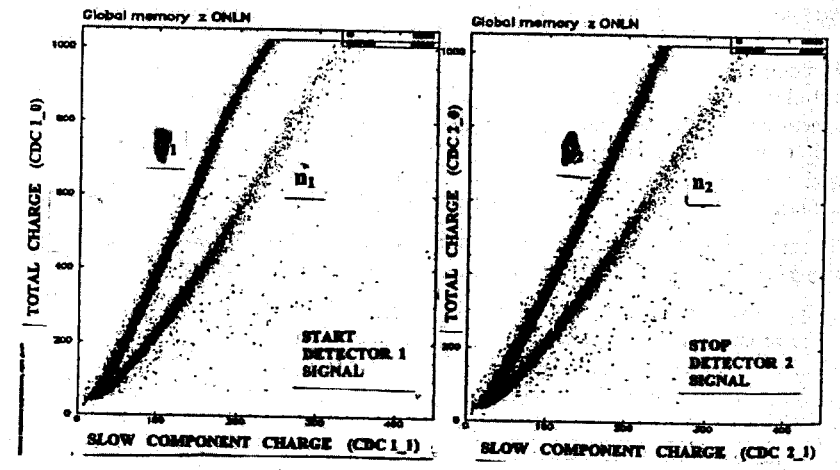


Fig. 3. Results of neutron and gamma signals separation in ²⁵²Cf fission: CDC-spectra for start and stop detectors signals.

Experimental spectrum of coincidences between the γ - and n- signals from the two neutron detectors is shown in next Fig. 4.

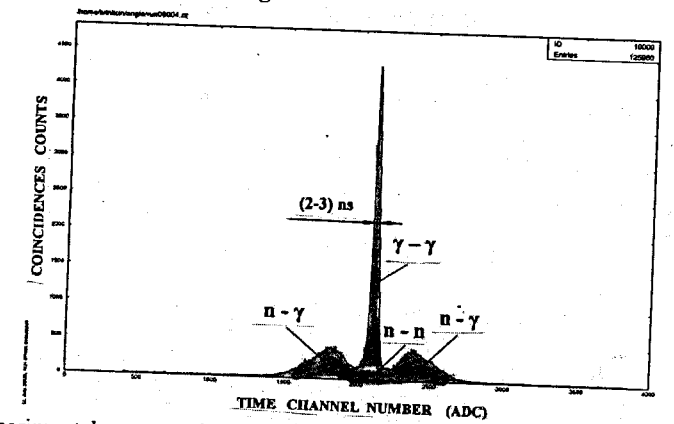


Fig. 4. Experimental spectra of coincidences between the γ - and n-signals from the two neutron detectors in ²⁵²Cf fission.

The $(\gamma-\gamma)$ -quanta coincidences peak is in the centre with time resolution at half-height about (2.5-3) ns. The position is start zero time. Two symmetric humps on the left and right of the peak are connected in first turn with $(n-\gamma)$ coincidences. Main investigated (n-n) coincidences are hided are in the centre under gamma-gamma peak. Background of accidental coincidences is very low in case ²⁵²Cf investigation.

After sorting and analysis of all experimental coincidences spectra we obtain the separated contributions (see Fig. 5) in total time spectrum for:

neutron-neutron (n-n).

- -gamma-gamma quanta (γ-γ),
- -neutron-gamma quantum (n-γ) coincidences.

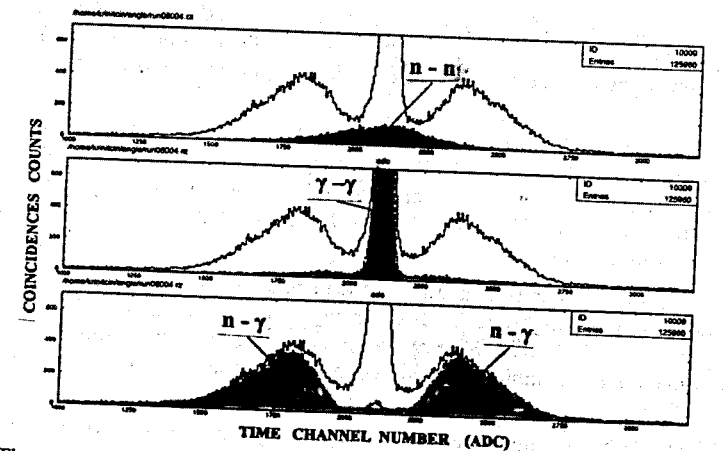


Fig. 5. The separated contributions in total time spectrum for (n-n), $(\gamma-\gamma)$ and $(n-\gamma)$ coincidences in ²⁵²Cf fission.

As result we obtain experimental angular dependences for all separated coincidences.

3. EXRPERIMENTAL RESULTS

In Fig. 6 the experimental angle dependence of (n-n), $(\gamma-\gamma)$ and $(n-\gamma)$ coincidences in 252 Cf fission for fission prompt neutrons having energies more then about 425 keV (minimal experimental threshold) is presented. All coincidences were normalized to count rates in two detectors. Presented errors contain statistical and accidental ones.

From the measurements at angles of 20 degrees to 180 degrees between the directions of the fission neutrons it was found that the number of (n-n) coincidences has minimum near 90° and increases by a factor about 1.7 to 180° and 0°.

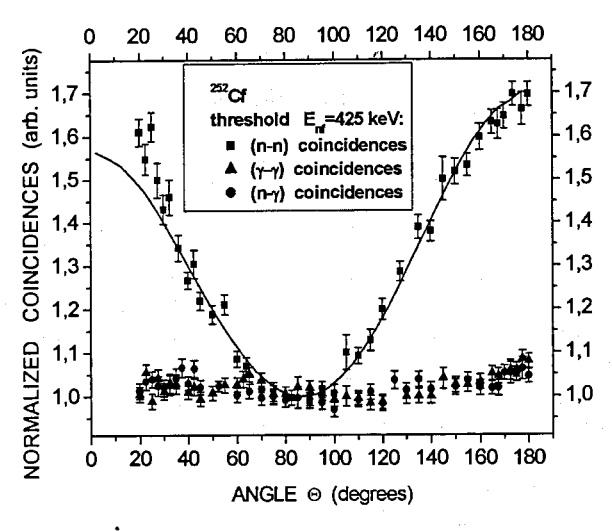


Fig. 6. The experimental angle dependence of (n-n), $(\gamma-\gamma)$ and $(n-\gamma)$ coincidences in ²⁵²Cf fission for prompt fission neutrons having energies more then about 425 keV. The curve is result of theoretical interpretation and analysis of the (n-n) experimental data [12].

For $(n-\gamma)$ and $(\gamma-\gamma)$ coincidences angular dependences some clear dependence is absent in comparison with (n-n) coincidences in limit of errors. But the dependences are similar with (n-n) one. The ratio factor of $(n-\gamma)$, $(\gamma-\gamma)$ coincidences maximum (near 0° and 180°) to minimum (near 90°) is about (1.05 - 1.10) and it is not depended from prompt neutrons energies thresholds.

In Fig. 7 the comparative angular dependences of (n-n) coincidences in ²⁵²Cf are shown for different more high thresholds of prompt neutrons energies: 425 keV, 550 keV, 800 keV, 1200 keV, 1600 keV. With rise of the neutron energy threshold the ratio of (n-n) coincidences maximum to minimum is increasing up to factor about 2.5 for the very high threshold 1600keV.

The Monte Carlo simulation based on a simple evaporation model with some admixture of the other possible mechanisms of neutron emission was used for theoretical description of the experimental data. The (n-n) correlation in ²⁵²Cf fission could be adequately described by

a simple evaporation model, assuming isotropic neutron emission from the fully accelerated fragments frames in their centre of mass together with a $\sim 10~\%$ isotropic scission component (see theoretical curves in Figs. 6, 7). The more detailed theoretical analysis and interpretation of the results you can read in the ISINN-15 Proceedings in article [12] of Irina Guseva.

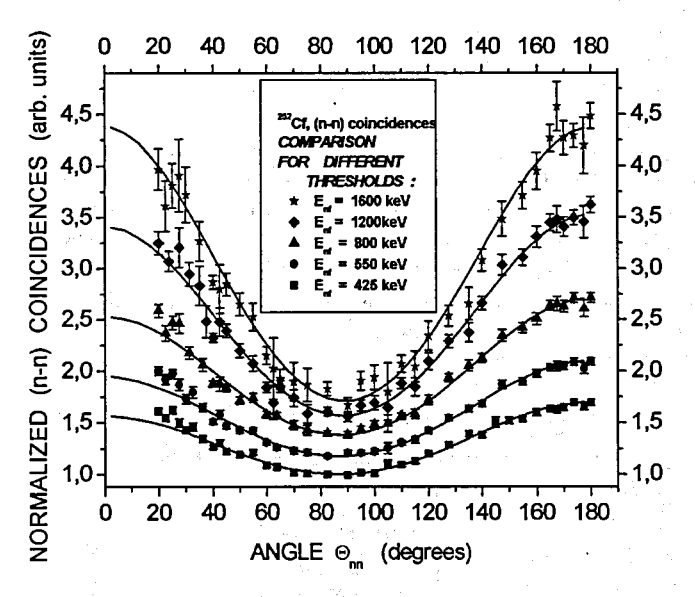


Fig. 7. The comparative experimental angular dependences of (n-n) coincidences in ²⁵²Cf for different thresholds of prompt fission neutrons energies. The curves are result of theoretical interpretation and analysis of the experimental data [12].

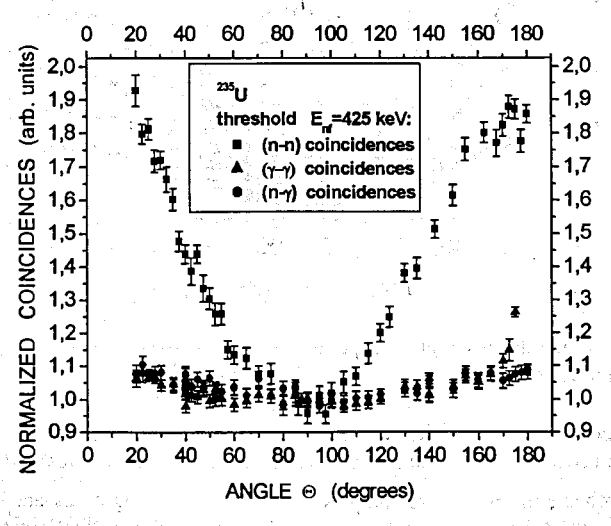


Fig. 8. The angular dependence of (n-n), $(\gamma-\gamma)$ and $(n-\gamma)$ coincidences from ²³⁵U fission.

Now we investigate the angular dependence of the coincidences in ²³⁵U fission induced by thermal neutrons from reactor. For the moment we have first preliminary experimental results. All coincidences were normalized to count rates in neutron beam monitor. Presented errors contain statistical and accidental ones.

In Fig. 8 the angular dependence of (n-n), $(\gamma-\gamma)$ and $(n-\gamma)$ coincidences from ²³⁵U fission for the very low threshold of prompt fission neutrons energy about 425 keV are shown. The ratio factor of maximum (near 0° and 180°) to minimum (near 90°) is about 1.9.

For $(\gamma-\gamma)$ and $(n-\gamma)$ coincidences angular dependences in ²³⁵U fission the clear dependences coincidences are absent in comparison with (n-n) one in limit of errors. But the dependences are similar with (n-n) one. The ratio factor of $(n-\gamma)$ coincidences maximum (near 0° and 180°) to minimum (near 90°) is about (1.05 - 1.10) and it is not depended from prompt neutrons energies thresholds. Only in case of $(\gamma-\gamma)$ coincidences dependence we observe their sharp increasing near 180° degrees connected with annigilation gamma-quanta.

In next Fig. 9 the (n-n) coincidences angular dependences in ²³⁵U are shown for different more high thresholds of prompt neutrons energies: 425 keV, 550 keV, 800 keV, 1200 keV, 1600 keV, 2000 keV.

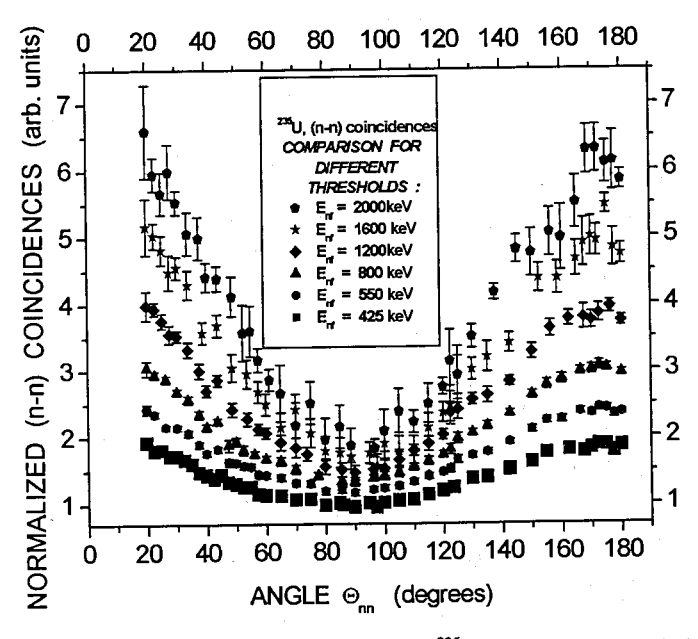


Fig. 9. The (n-n) coincidences angular dependences in ²³⁵U for different thresholds of prompt fission neutrons energies.

For (n-n) coincidences in ²³⁵U with raising of the thresholds it is observed rise of the factor (ratio of maximum to minimum) up to about 3 for maximal threshold 2000 keV.

The researches and theoretical analysis for the ²³⁵U investigations are in progress and possible influence of neutron cross-talks for small angles between the detectors and reactor background are studied for the moment.

4. CONCLUSION

For obtaining of new results in the investigations we plan next steps:

- To study more detailed possible influence of neutron cross-talks for small angles between the detectors and reactor background.
- To finish the measurements in 235 U fission and to perform the theoretical analysis of the experimental data.
- To carry out the same researches in ²³³U fission.
- To perform comparative analysis of the data with results of our researches of angular dependence between prompt neutrons and fission fragments coincidences in ²³⁵U fission obtained at other thermal neutron beam of WWR-M Reactor.

As result we hope to obtain more reliable data for estimations of scission neutrons contribution in prompt neutrons and their description in fission of heavy nuclei.

5. ACKNOWLEDGEMENTS

We would like to thank Yu.S.Pleva for the technical support, O.A. Shcherbakov, and A.S.Vorobiev for the help in performing of the measurements. We are most grateful to all of our colleagues from the WWR-M reactor department for keeping the reactor running in a stable condition during the course of these physical measurements.

This work was supported by RFBR Grant 06-02-16668 and INTAS Grant 03-51-6417.

REFERENCES

- 1. J.S.Fraser, Phys. Rev. 88 (1952) 536.
- 2. H.R.Bowman, S.G.Tompson, J.C.D.Milton, and W.J.Swiateski, Phys.Rev. 126 (1962) 2120.
- 3. S.S.Kapoor, R.Ramanna, and P.N.Rama Rao, Phys.Rev. 131 (1963) 283.
- 4. K.Skarsvag and K.Bergheim, Nucl.Phys. 45 (1963) 72.
- 5. J.S.Pringle and F.D.Brooks, Phys.Rev.Lett. 35 (1975) 1563.
- 6. H.R.Bowman, S.G.Tompson, J.C.D.Milton, and W.J.Swiateski, Phys.Rev. 129 (1963) 2133.
- M.V.Blinov, N.M.Kazarinov, and I.T.Krisyuk, Yad.Fiz. 16 (1973) 1155,
 [Sov.J. Nucl. Phys. 16 (1973) 634].
- 8. K.Skarsvag, Phys.Scripta 7 (1973) 160.
- 9. G.A.Pik-Pichak, Yad.Fiz. 10(1970)321 [Sov.J.Nucl.Phys. 10(1970)185].
- 10. S.DeBenedetti, J.E.Francis, Jr., W.M.Preston, and T.W.Bonner, Phys.Rev. 74 (1948) 1645.
- 11. C.B.Franklyn, C.Hofmeyer, and D.W.Mingay, Phys.Lett. 78B(1978)564.
- 12. I.S.Guseva, XV International Seminar on Interaction of Neutrons with Nuclei. ISINN-15, Dubna, 2008, in publication.

Multilevel Approach in the Evaluation of the Asymmetry Effects on (n,p) reaction for ³⁵Cl and ¹⁴N nuclei

A. I. Oprea, C. Oprea, Yu. M. Gledenov, P. V. Sedyshev, P.J. Szalanski¹
141980 Dubna, FLNP – JINR

¹University of Lodz, Institute of Physics, Poland

Abstract. In our previous work [1] were evaluated the asymmetry effects in (n,p) reaction on ³⁵Cl and ¹⁴N using 2 resonances for ³⁵Cl and 3 resonance for ¹⁴N. In the both cases was used the formalism of the mixing states of the compound nucleus with opposites parities. In the first case of ³⁵Cl were evaluated the asymmetry coefficients in the two-level approximation up to 1 keV. These levels are closed and the next resonance is far from these two so we have a quite good agreement between theoretical and experimental data. Will be of interest to obtain the behavior of asymmetry effects higher then 1 keV and with participation of more resonances. In the second case of ¹⁴N the resonance are far one from other and our evaluation was realized up to 1 MeV where are present more then 10 resonances. In our last evaluation we used only 3 resonance and the asymmetry effects are results of the interference of two positive resonance with more then 100 keV between them. All these indicate that it is necessary to have an evaluation of the asymmetry effects with participation of all resonance in the neutron energy interval.

Introduction. For the evaluation of the asymmetry effects in the (n,p) reaction on ³⁵Cl and ¹⁴N we will used the formalism of the mixing states of the compound nucleus with the same spin and opposite parities. In some of our previous works we realized this task on the two level approximation on ³⁵Cl(n,p)³⁵S [2], [3] up to 1 keV for neutron incident energy and using only 3 resonances for ¹⁴N(n,p)¹⁴C [4], [5] for the neutron incident energy up to 1 MeV. In the both cases is of interest how the presences of other resonances will influence the energetic dependences and the shape of the asymmetry effects. In the works [2, 3, 4, 5] our purpose was to obtain the weak matrix elements starting from the experimental values of the asymmetry effects [6]. Nevertheless the procedure described in [6] will not be useful if we take into account more than 3 resonances because pairs of interfering resonance will introduce a number of some unknown parameters like the neutron ant proton reduced widths. These parameters in principal can be extracted from other reactions and experiments but in the present work we just considered them random parameters having in mind the main our purpose, the behavior of the asymmetry effects.

The evaluated asymmetry effects are the forward – backward, left – right and parity non – conservation. These coefficients are obtained starting from the (n,p) reaction amplitudes defined in [7]. From these amplitudes we obtain the differential cross section (or the angular correlations) and from angular correlations by the relations of definition of asymmetry effects we get the coefficients. The procedure of obtaining the asymmetry coefficients is very well illustrated in the references and we will not insist on in this paper.

Formulas and relations. The target nucleus captures a neutron and after that is forming a compound nucleus. The compound nucleus can be described by a number n of S state and m of P states. Between the states of the compound nucleus there are some states with the same spin and opposites parities and same parities. The states with the same spin and opposites parities by interfering ([7] and references from this) will give us the asymmetry effects and the states with the same spin and parities lead to the interfering effects in the cross

section. In this case the amplitude of (n,p) reaction with the contribution of a number of resonance has the form:

$$f = \sum_{i=1}^{n} f_{Si}^{PC} + \sum_{j=1}^{m} f_{Pj}^{PC} + \sum_{k=1}^{p} f_{(SP)k}^{PNC}$$
(1)

 $f_{S_i}^{PC}$, $f_{P_j}^{PC}$ = the amplitude of the S_i and P_j states both conserving the parity

 $f_{(SP)k}^{PNC}$ = the amplitude of the (n,p) reaction not conserving the parity given by a pair of one S and one P state. This amplitude is proportional with the weak matrix element in the (n,p) reaction W_{SP} , and usually the condition $f_{(SP)k}^{PNC} \ll f_{Si}^{PC}$, f_{Pl}^{PC} is satisfied due to the small value of the weak matrix element W_{SP} . Anyway this condition must be verified for each reaction. In the reactions studied in this work this condition is satisfied. The third term of relation (1)

the reactions studied in this work this condition is satisfied. The third term of relation (1) represents a sum over p pairs of states (resonances) giving parity non conservation effects. The expressions of these amplitudes are given in [7]. The expression (1) is valuable if the following conditions are satisfied [8]. The first condition requests that the resonances are well distinguished and far one from other $(D >> \Gamma)$ and the second condition is kR << 1 where D is the averaged energy interval between resonances, Γ – the width, k – the reduced wave number, R – radius of target nucleus. These conditions are fulfilled in the 35 Cl(n,p) 35 S higher than 100 keV for neutron incident energy, but not fulfilled in the all neutron energy interval up to 1 MeV for 14 N(n,p) 14 C reaction. With this introduction we can now write the expressions of the cross section and asymmetry effects.

1. The cross section in the (n,p) reaction. Starting from the amplitude of (n,p) reaction and respecting the condition mentioned above the cross section is:

$$\sigma_{np} = \int_{(\Omega)} \frac{d\sigma}{d\Omega} d\Omega = \int_{(\Omega)} \left(\sum_{i=1}^{n} \left| f_{Si}^{PC} \right|^{2} + \sum_{j=1}^{m} \left| f_{Pj}^{PC} \right|^{2} + \sum_{i \neq j} 2 \operatorname{Re} f_{Si}^{PC} f_{Sj}^{PC*} + \sum_{i \neq j} 2 \operatorname{Re} f_{Pi}^{PC} f_{Pj}^{PC*} \right) d\Omega =$$

$$= \sum_{i=1}^{n} \sigma_{S}^{i} + \sum_{j=1}^{m} \sigma_{P}^{j} + \int_{(\Omega)} \left(\sum_{i \neq j} 2 \operatorname{Re} f_{Si}^{PC} f_{Sj}^{PC*} \right) d\Omega + \int_{(\Omega)} \left(\sum_{i \neq j} 2 \operatorname{Re} f_{Pi}^{PC} f_{Pj}^{PC*} \right) d\Omega =$$

$$= \sum_{i=1}^{n} \sigma_{S}^{i} + \sum_{j=1}^{m} \sigma_{P}^{j} + \sum_{i \neq j} \sigma_{SiSj} + \sum_{i \neq j} \sigma_{PiPj}$$
(2)

In relation (2) were neglected terms corresponding to the amplitude non conserving the parity due to their small values and also the terms corresponding to the interference between S and P waves because their integration on full solid angle is zero. The third and fourth terms of relation (2) represent the interference between resonances with the same spin and parities. The existence of such kind of interference can be observed in the cross section. Using the definition of (n,p) amplitudes from [7] the interfering terms between two S resonances (S_i-S_j) and two P resonaces (P_i-P_j) have the form:

$$\sigma_{sisj} = \pm \eta_{sisj} \, 2g_{sisj} \pi \lambda^{2} \frac{\left(E - E_{si}\right)\left(E - E_{sj}\right) + \frac{\Gamma_{si}\Gamma_{sj}}{4}}{\left[\left(E - E_{si}\right)^{2} + \frac{\Gamma_{si}^{2}}{4}\right]\left(E - E_{sj}\right)^{2} + \frac{\Gamma_{sj}^{2}}{4}}\right] \sqrt{\Gamma_{si}^{n} \Gamma_{sj}^{n} \Gamma_{si}^{p} \Gamma_{sj}^{p}}}$$
(3)

The contributions of the S or P resonance to the cross section of Breit – Wigner type are:

$$\sigma_{s}^{i} = g_{s}^{i} \pi \lambda^{2} \frac{\Gamma_{si}^{n} \Gamma_{si}^{p}}{(E - E_{si})^{2} + \frac{\Gamma_{si}^{2}}{4}}, \sigma_{p}^{i} = g_{p}^{i} \pi \lambda^{2} \frac{\Gamma_{pi}^{n} \Gamma_{pi}^{p}}{(E - E_{pi})^{2} + \frac{\Gamma_{pi}^{2}}{4}}$$
(4)

$$\sigma_{P_{i}P_{j}} = \pm \eta_{P_{i}P_{j}} 2g_{P_{i}P_{j}} \pi \lambda^{2} \frac{\left(E - E_{P_{i}}\right)\left(E - E_{P_{i}}\right) + \frac{\Gamma_{P_{i}}\Gamma_{P_{j}}}{4}}{\left[\left(E - E_{P_{i}}\right)^{2} + \frac{\Gamma_{P_{i}}^{2}}{4}\right]\left(E - E_{P_{j}}\right)^{2} + \frac{\Gamma_{P_{i}}^{2}}{4}}\right]} \sqrt{\Gamma_{P_{i}}^{n} \Gamma_{P_{j}}^{p} \Gamma_{P_{i}}^{p} \Gamma_{P_{j}}^{p} h_{P_{i}P_{j}}(X, Y)}$$
(5)

The η parameters are coming from the phases but for simplicity we will consider them equal to one. The expressions (4) and (5) will increase or decrease the cross section and depends on η parameters. The effects of terms (4) and (5) can be observed experimentally. The function h(X,Y) depends of neutron and proton reduced widths X, Y. The X, Y, parameters are unknown and in our calculation they are taken randomly. They can be obtained from other experiments or from theoretical evaluation.

2. The forward - backward coefficient. The relation of definition of the forward - backward effect is:

$$\alpha_{FB} = \frac{W(\theta = 0) - W(\theta = \pi)}{W(\theta = 0) + W(\theta = \pi)} \tag{6}$$

where $W(\Omega)$ = the angular correlation depending on solid angle. The angular correlation is proportional with the differential cross section. From (6) and taking into account a number of resonances and the definitions of (n,p) amplitudes [7] we obtain:

$$\alpha_{FB} = \frac{2\operatorname{Re} \sum_{i \neq j} f_{Si}^{PC} f_{Pj}^{PC}}{\sum_{i=1}^{n} \left| f_{Si}^{PC} \right|^{2} + \sum_{j=1}^{m} \left| f_{Pj}^{PC} \right|^{2} + \sum_{i \neq j} 2\operatorname{Re} f_{Si}^{PC} f_{Sj}^{PC^{*}} + \sum_{i \neq j} 2\operatorname{Re} f_{Pi}^{PC} f_{Pj}^{PC^{*}}} \bigg|_{\theta=0}$$
(7)

The forward – backward effect is a result of interference between S and P waves corresponding to pairs of S and P resonances. This effect is not involving the weak nuclear interaction and can be evidenced using unpolarized neutron beam. The presence of a number of resonance influences the value and the shape of the effect due to the interference of the compound nucleus states with the same spin and parities. These assumptions are valuable also for the other effects studied in this work.

3. The left – right coefficient. In the (n,p) reaction with polarized transversal neutrons reveals the left – right asymmetry effect. This effect is a result also of interference between S and P waves conserving the parities [7]. The left – right effect is defined as:

$$\alpha_{LR} = \frac{W\left(\theta = \frac{\pi}{2}, \phi = \frac{3\pi}{2}\right) - W\left(\theta = \frac{\pi}{2}, \phi = \frac{\pi}{2}\right)}{W\left(\theta = \frac{\pi}{2}, \phi = \frac{3\pi}{2}\right) + W\left(\theta = \frac{\pi}{2}, \phi = \frac{\pi}{2}\right)}$$
(8)

Following the same procedure of calculation results:

$$\alpha_{LR} = \frac{2\operatorname{Im}\sum_{i \neq j} f_{Si}^{PC} f_{Pj}^{PC}}{\sum_{i=1}^{n} \left| f_{Si}^{PC} \right|^{2} + \sum_{j=1}^{m} \left| f_{Pj}^{PC} \right|^{2} + \sum_{i \neq j} 2\operatorname{Re} f_{Si}^{PC} f_{Sj}^{PC*} + \sum_{i \neq j} 2\operatorname{Re} f_{Pi}^{PC} f_{Pj}^{PC*}} \bigg|_{\theta = \frac{\pi}{2}, \phi = \frac{\pi}{2}}$$
(9)

4. The parity non conservation coefficient. This effect is a result of interference between the (n,p) amplitudes conserving the parity and (n,p) amplitudes non conserving the parity due to the weak interaction between nucleons in the compound nucleus. Also this effect appears when the neutron beam is polarized. The definition of the effect is:

$$\alpha_{PNC} = \frac{W(\theta = \frac{\pi}{2}, \phi = 0) - W(\theta = \frac{\pi}{2}, \phi = \pi)}{W(\theta = \frac{\pi}{2}, \phi = 0) + W(\theta = \frac{\pi}{2}, \phi = \pi)}$$

$$(10)$$

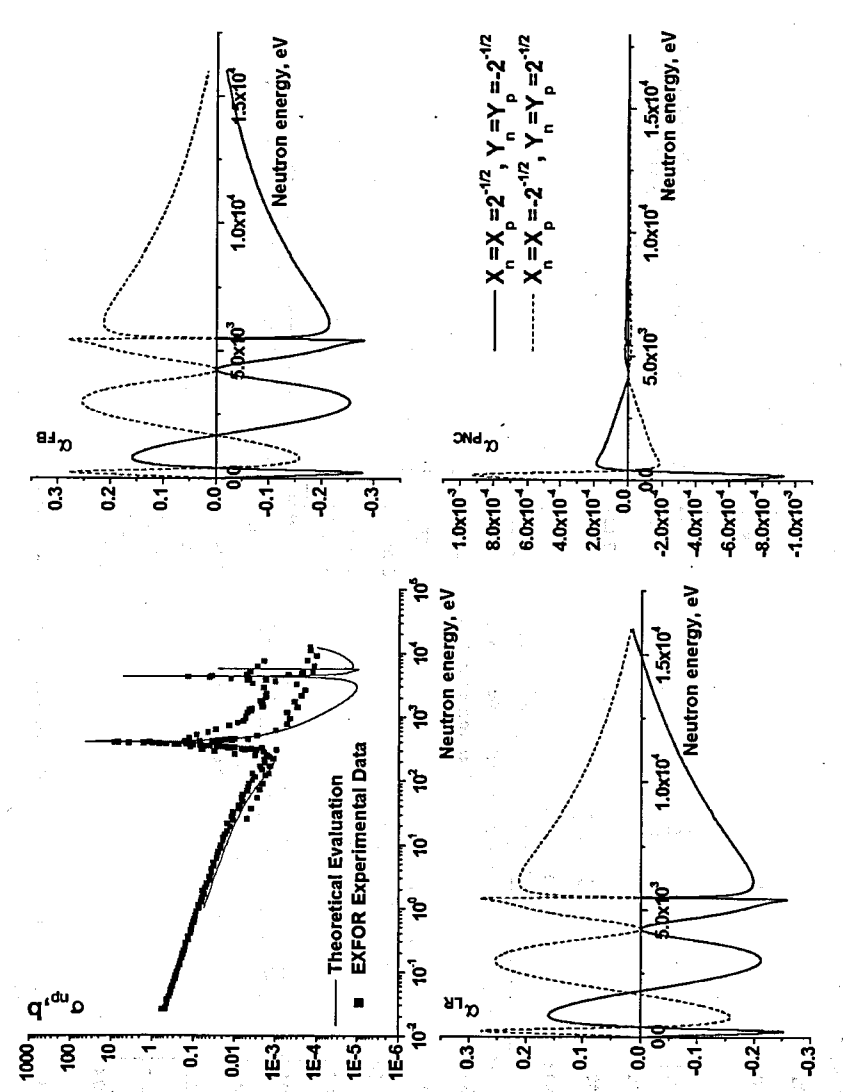
$$\alpha_{PNC} = \frac{2\operatorname{Re} \sum_{i \neq j} f_{Si}^{PC} f_{SiPj}^{PNC^*} + 2\operatorname{Re} \sum_{i \neq j} f_{Pj}^{PC} f_{PjSi}^{PNC^*}}{\sum_{i=1}^{n} \left| f_{Si}^{PC} \right|^2 + \sum_{j=1}^{m} \left| f_{Pj}^{PC} \right|^2 + \sum_{i \neq j} 2\operatorname{Re} f_{Si}^{PC} f_{Sj}^{PC^*} + \sum_{i \neq j} 2\operatorname{Re} f_{Pi}^{PC} f_{Pj}^{PC^*} \Big|_{\theta = \frac{\pi}{2}, \phi = 0}}$$
(11)

Discussions and results. For the evaluation of the asymmetry effects and the cross section in the ³⁵Cl(n,p)³⁵S and ¹⁴N(n,p)¹⁴C reaction were realized special computer programs. These programs use symbolic formulas [3], [4], [7] for the terms responding for the asymmetry effects in the two level approximations for pairs of interfering resonance and expressions for (n,p) cross section including processes of interference in the cross section between states with the same spin and parities. One of the main purpose of the experimental and theoretical evaluation of the asymmetry effects is to obtain the matrix element of the weak interaction in nuclear processes. In the two level approximation the extraction of the weak matrix element from experimental values of the asymmetry effects was realized by us for ³⁵Cl(n,p)³⁵S reaction [2], [3]. In principal this procedure can be applied easy in the case of ¹⁴N(n,p)¹⁴C reaction if we should have experimental values of the asymmetry coefficients (forward - backward, left - right and parity non - conservation). Until now there are not yet data for all asymmetry effects in ¹⁴N(n,p) ¹⁴C reaction. If we take into account a number of resonance more than three and exist two ore more pairs giving asymmetry effects by interference then the extraction of the weak matrix element become more complicated. Each pair of interfering resonance introduces the unknown parameters X, Y (the reduced neutron and proton widths - in number of four for each pair of resonance). Also the weak matrix for each pair of resonance can be different. In this case it is necessary to obtain the necessary data from other experiments or theoretical evaluations or if we have only data of mentioned three asymmetry effects it is possible to obtain some averaged values on X, Y parameters and weak matrix element. For the neutron resonance parameters we used data from [9], [10].

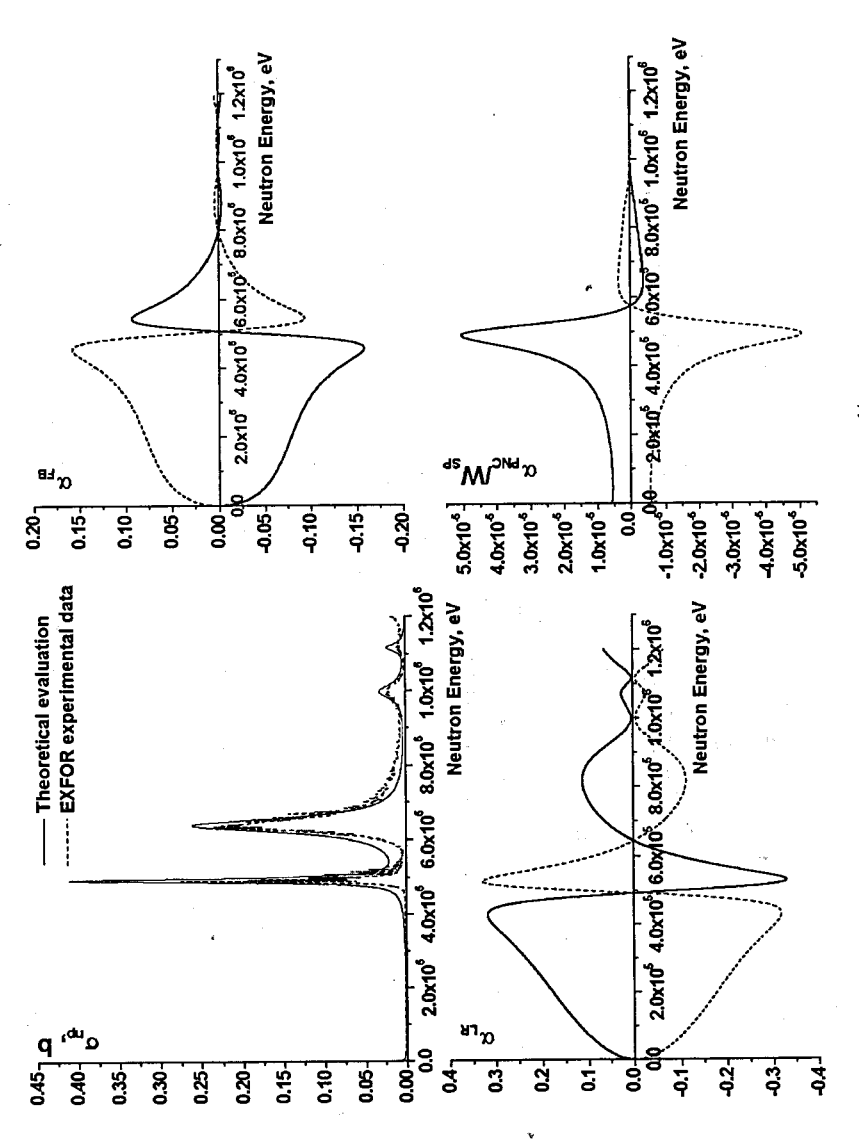
1. The ³⁵Cl(n,p)³⁵S reaction. For this reaction the main condition of the formalism of mixing states with the same spin and opposite parities of the compound nucleus are satisfied. calculations were resonances: $\{E_{c_1} = -180 \,\text{eV}, J_{c_1}^{\pi} = 2^+\}, \{E_{p_1} = 398 \,\text{eV}, J_{p_1}^{\pi} = 2^-\}, \{E_{p_2} = 4249 \,\text{eV}, J_{p_2}^{\pi} = 1^-\},$ $\{E_{P3} = 5496 \,\mathrm{eV}, J_{P3}^{\pi} = 1^{-}\}, \{E_{S2} = 14802 \,\mathrm{eV}, J_{S2}^{\pi} = 2^{+}\}.$ In the cross section exist interference between the states P_2 - P_3 and S_1 - S_2 . These interference will influence the cross section and the shape and magnitude of the asymmetry effects. Our evaluation of the cross section confirm the experimental value from [9] in the thermal point $\sigma_{nn}^{exp}(0.0253eV) = 0.489$ b. As is seen from figure 1, until the first P resonance the theoretical evaluation and experimental are in a very good agreement. Also after the first P resonance it can be considered a good agreement between theoretical evaluation and existent experimental data. Differences we have between resonances were the value of the cross section is very small and in future it is necessary to understand this difference. One of possible explanation may be a combination between the influence of the resonances not taken into account and the possible influence of other open channels in the region were the cross section has a very small value. The asymmetry effects are given in the studied case by the interference between by the pairs of states S_1 - P_1 and S_2 - P_1 and these pairs give their contribution to the total effects. If neglect the interference between states with the same spin and parities in the cross section it is expected that the shape of the effects of a pair of states is like in the two level approximation (see [2], [3]). Since now the only experimental data for the asymmetry effects are given in [2], [3], [11]. For the forwardbackward effect we have $\alpha_{FR}(3.1eV) = (5.3 \pm 7.6) \cdot 10^{-3} \alpha_{FR}(195eV) = (1.68 \pm 0.5) \cdot 10^{-1} \alpha_{FR}(398eV) = (7.4 \pm 3.6) \cdot 10^{-3}$ Our evaluation confirms the experimental values. As is seen in the figure 1 the presence of other resonances has no such an important influence until the first P resonance. Our theoretical evaluation shows that after this resonance the presence of other states becomes significant. For the left - right and parity non conservation effects exists only the value in the thermal point (neutron energy equal to 0.0253 eV). These values are: $\alpha_{LR} = -(2.4 \pm 0.43) \cdot 10^{-4}$ and $\alpha_{PNC} = -(1.51 \pm 0.34) \cdot 10^{-4}$. The theoretical evaluation is in a very good agreement with the experimental data for both effects. Like in the forward backward effects the presence of the other states has a small influence until the first P resonance and this fact indicates that the two level approximation is correct for the energy neutron range up 05-1 keV. For the neutron energy higher than 1 keV the theoretical evaluation shows a very complicated energy dependence and shape of the asymmetry effects. Future experimental data and an attentive analysis of neutron resonances parameters will infirm or confirm the predicted dependences.

2. The ¹⁴N(n,p)¹⁴C reaction. In this reaction initially were taken into account more than 10 resonances but after a detail analysis of the neutron resonance parameters were selected the following states of the compound nucleus ¹⁵N: { $E_{P1} = 492.6 \,\mathrm{keV}, J_{P1}^{\pi} = (1/2)^{-}$ }, $\{E_{S1} = 639 \text{ keV}, J_{S1}^{\pi} = (1/2)^{+}\}, \{E_{S2} = 837 \text{ keV}, J_{S2}^{\pi} = (1/2)^{+}\}, \{E_{S3} = 997 \text{ eV}, J_{S1}^{\pi} = (3/2)^{+}\},$ $\{E_{sa} = 1116 \,\mathrm{eV}, J_{sa}^{\pi} = (3/2)^{+}\}$. With these states asymmetry effects are given by the following pairs of states, P_1 - S_1 and P_1 - S_2 . The incident neutron energy is taken up to 1 MeV. Interferences in the cross section with this set of states are given only by the pair S_2 - S_3 . With this set of resonances the experimental data on the cross section agreed satisfactory the theoretical evaluation from 100 keV to 1 MeV. A serious disagreement we have in the thermal point were the theoretical evaluation is more than five time higher than the experimental accepted values $(\sigma_{np}^{exp}(0.0253eV) = 1.8b)[9]$. Analyzing the set of resonance parameters it was concluded that the S_2 state gives a big contribution in the thermal point. The parameters for this state are obtained for the isobaric analogue resonance of ¹⁵C with isotopic spin T=3/2 [10]. Other authors [12], [13] don't use this resonance. If this resonance will be eliminated from estimation then the agreement between theoretical cross section and experimental data become very good. Then in the thermal point the theoretical estimation is 1.78 b. Eliminating the S₂ state we get practically the two level approximation where the effects are results of interference between one pair of states with no interference effects in the cross section. Between resonances as it was observed for ³⁵Cl, the theoretical evaluation and experimental differ. Other resonances in this case will decrease the magnitude of asymmetry effects. Experimental values on asymmetry effects are only the left - right effects in the thermal point $\alpha_{IR} = (0.66 \pm 0.18) \cdot 10^{-4}$ [11] which is in very good agreement with our evaluation and the preliminary zero value of parity non conservation effect. The parity non conservation effect is very small and result it is expected because the energy interval between resonances is of order of hundred keV and not hundred of ev like in the reaction on ³⁵Cl. The evaluation of the cross section and asymmetry effects are illustrated in figure 2.

The work was realized by financial support of the project of Romanian Plenipotentiary Representative to JINR Dubna, №359/21 from 01.06.2007 and grant № 05-02-16260 from Russian Foundation for Basic Researches (RFBR).



301



element is unknown. For the the {X,Y} parameters have an opposite sign like for the continuous line. effects in the ¹⁴N(n,p)¹⁴C reaction. The

References.

[1] A. I. Oprea, C. Oprea, Yu. M. Gledenov, P. V. Sedyshev, Proceeding on ISINN 14, E3-2007-23, ISBN 5-9530-0139-8, 24-27 May 2007, Dubna

[2] Gledenov Yu.M., Machrafi R., Oprea A.I., Salatski V.I., Sedyshev P.V., Szalanski P.I., Vesna V.A., Okunev I.S.— A search for P-odd and P-even correlations in the $^{35}Cl(n,p)^{35}S$ reaction. Nucl. Phys., 1999, v. A 654, p.943c.

[3] Весна В. А., Гледенов Ю. М., Окунев И. С., Опря А., Салацкий В. И., Седышев П. В., Шаланьски П. – Измерение коэффициента асимметрии вперед-назад в реакции ³⁵Cl(n,p)³⁵S на резонансных нейтронах. Сообщение ОИЯИ, РЗ-2002-175, Дубна, 2002.

[4] A. I. Oprea, C. Oprea, Yu. M. Gledenov, P. V. Sedyshev, P. J. Szalanski, Proceedings on the Thirteenth International Seminar on Interaction of Neutron with Nuclei (ISINN-13), 25-28 May 2005, Dubna, ISBN 5-9530-0102-9, E3-2006-7

[5] A. I. Oprea, C. Oprea, Yu. M. Gledenov, P. V. Sedyshev, XIV – th Proceedings of International Seminar of Interactions of Neutrons with Nuclei, 24-27 May 2006, E3-2007-23, ISBN5-9530-0139-8, p. 170

[6] С. В. Зенкин, Н. А. Титов., Препринт П-0367, ИЯИ АН СССР (М., 1984).

[7] G. Rigol. Preprint Dubna P4-85-70, Угловые корреляции в реакции (n,p)

[8] V. V. Flambaum, G. F. Gribakin, Progr. Part. Nucl. Phys., Vol. 35, p. 423 - 503, 1995

[9] Mughabghab S.F., Divadeenam M., Holden N.E. - Neutron Cross Sections. NY, Academic Press, 1981, v.1.

[10] S. Mughabghab, Atlas of Neutron Resonances, Resonance Parameters and Thermal Cross Sections. Z=1-100, Elsevier, March 2006

[11] А. Антонов, В. А. Весна, Ю. М. Гледенов и др., ЯФ, 48, 305, (1988).

[12] C. H. Johnson, H. H. Barschall, Phys. Rev., vol. 80, № 5, p. 818, 1 December 1950

[13] C. H. Johnson, B. Petree, R. K. Adair, Phys. Rev., vol. 84, № 46, p. 775 November 15, 1951

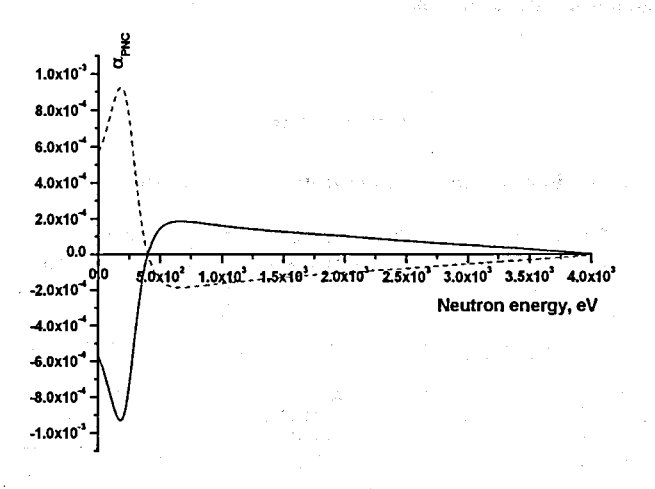


Fig. 3. The parity non conservation coefficient for $^{36}\text{Cl}(n,p)^{36}\text{S}$ reaction. For all pairs of resonances we have taken $\{X_n = X_p = \pm \frac{1}{\sqrt{2}}, Y_n = Y_p = \mp \frac{1}{\sqrt{2}}, W_{SP} = 0.06 \text{ eV}\}$ for the continuous and dash lines respectively

SEARCH FOR PT-NONINVARIANT EFFECT IN NEUTRON INDUCED GAMMA-TRANSITIONS

V.G.Nikolenko¹, I.S.Okunev², S.S.Parzhitski¹, Yu.P.Popov¹ A.V.Sinyakov³, Yu.M.Tchuvil'sky³

¹Joint Institute for Nuclear Research, 141980, Dubna, Russia

²St.-Petersburg Institute of Nuclear Physics RAS, 188350, Gatchina, Russia

³Skobeltsyn Institute of Nuclear Physics, Moscow State University, 119992, Moscow, Russia

Abstract. Long and, unfortunately, unfinished way of well know lanthanum experiment, which was considered as optimal tool of search for PT-noninvariance in nuclear processes, from the idea to an actual measurement make it reasonable to analyze other possibilities provided by neutron induced nuclear reactions. A number of schemes based on spin-angular correlations of initial neutrons and γ -quanta produced in neutron capture process which look promising are proposed. One of the principal advantages of the scheme in comparison with using radioactive sources of γ -quanta ones is the fact that high-energy γ -quanta produced by neutron capture make the problem of simulating of the effect by final state interaction of photons with atomic electrons inessential.

MOTIVATION

Nonconservation of discrete fundamental symmetries in physics.

If the CPT-theorem is valid there are four terms in Grand Lagrangian which are distinguished by their discrete fundamental symmetry properties. They are presented in the table 1.

Table 1. Symmetric and symmetry breaking terms of Grand Lagrangian.

С	P	T	Comment 1	Comment 2
+	+	+	Invariant	
_	_	+	P-odd, T-invariant (P)	
_	+	_	P-even, T-noninvariant (T)	CP-noninvariant
+	ı	_	P-odd, T-noninvariant (PT)	terms

P-, T-, and PT-noninvariant amplitudes shape the complete set of discrete fundamental symmetry breaking terms of Grand Lagrangian. The first one is leading symmetry breaking term. It is relatively well studied in a lot of parity violation measurements.

Up to now a CP-violation effect is observed in the decays of K- [1] and B-mesons [2] only. In the Standard Model (SM) the amplitude of the discussed effects are very small and turn out to be visible due to unique enhancement takes place in the mentioned decays. These amplitudes are described by Cabibbo-Kobayashi-Maskawa matrix:

$$\begin{pmatrix} d' \\ s' \\ b' \end{pmatrix} = \begin{pmatrix} c_1 & s_1 c_3 & s_1 s_3 \\ -s_1 c_2 & c_1 c_2 c_3 - s_2 s_3 e^{i\delta} & c_1 c_2 s_3 + s_2 c_3 e^{i\delta} \\ -s_1 s_2 & c_1 s_2 c_3 + c_2 s_3 e^{i\delta} & c_1 s_2 s_3 - c_2 c_3 e^{i\delta} \end{pmatrix} \begin{pmatrix} d \\ s \\ b \end{pmatrix},$$

where $C_i = \cos \theta_i$, $S_i = \sin \theta_i$, θ_i are mixing angles, and δ is the phase shift determining the value of the discussed break up term. The extremely small measured values of the effects result in some problems in explanation of the absence of antimatter in the Universe. For this reason it is assumed that a major contributor to these effects is something beyond the SM and related to a new physics. Some models predict rather large effects. Therefore search for CP-nonconserving amplitudes which are essentially larger than the ones predicted by the SM in other processes makes sense.

It should be noted that the phase shift δ is not related to the systems consisting of quarks of the first generation (u and d) only. That is why nuclear systems are interesting objects of the discussed investigations.

Upper limits of permanent electric dipole moments (PEDM) of elementary particles and atoms are the most informative data concerning the PT-noninvariant effect in light-quark systems up to now. In the framework of SM only second order diagrams presented in fig.1 contribute in PEDM value.

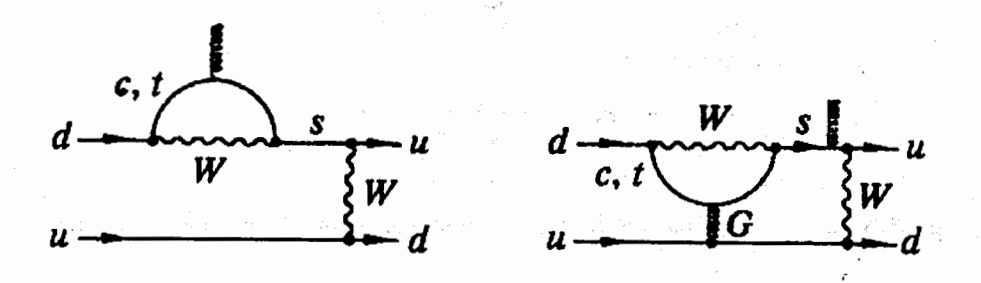


Figure 1. PEDM-producing diagrams of SM. W and G denotes W-boson and gluon respectively.

Recent upper limits of PEDM of elementary particles and atoms are presented in the table 2.

Table 2. PEDM values of microobjects.

	Experiment (10 ⁻¹³ e · cm)	Standard Model (10 ⁻¹³ e · cm)	New physics (10 ⁻¹³ e · cm)
е	1.6 ·10 ⁻¹⁴	≤10 ⁻²⁵	≤1 ·10 ⁻¹⁴
p	1.0 ·10-9	~10 ⁻¹⁸	≤6 ·10 ⁻¹³
n	2.9 ·10 ⁻¹³	~10 ⁻¹⁸	≤3 ·10 ^{·13}
¹⁹⁹ Hg	2.1 · 10-15	~10 ⁻²⁰	≤2 ·10 ⁻¹⁵

It can be concluded from this table that some measurements of PEDM directly impact on construction of the new theoretical approaches. Thus an analysis of alternative schemes promising for setting upper limits on CP-violating effects and, in particular, on PT-noninvariant amplitudes in nuclei seems to be promising.

Nuclear processes as tests on PT-violation.

It is important to note that the list of amplitudes involved in PT-nonconserving nuclear processes does not limited by that contributing PEDM. So search for the effects here is anyway interesting independently on their compatibility with PEDM approach. If, nevertheless, one intends to compete and believes that PT-violation effect display itself only in $N \to N + \pi$ vertex (see the diagram in the fig. 2) then

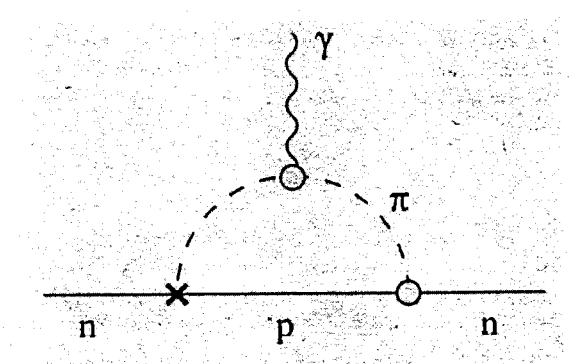


Figure 2. Diagram producing PEDM of neutron. The cross denotes PT-nonconserving vertex.

neutron PEDM measurements set the following constrains on the PT-nonconservation constants of the diagram in the fig. 2:

$$g_{pt}^{\Delta T} \le \begin{cases} 0.7 \cdot 10^{-11} \, \Delta T = 0 \\ 0.5 \cdot 10^{-10} \, \Delta T = 1 \\ 0.7 \cdot 10^{-11} \, \Delta T = 2 \end{cases},$$

where ΔT is the isospin change. So to compete with these measurements one should achieve a similar precision if only for isovector constant. Fortunately nucleus is an amplifier of isovector effects.

Let us list principal features of the PT-nonconservation studies in nuclear processes.

- 1. Resonance nuclear reactions are of a great advantage because their cross sections are usually larger and one can expect various effects of enhancement in them. As a last resort low-energy particle-nucleus collisions in which the contribution of one or two partial waves are dominant in the cross section may be put in to use.
- 2. Simultaneous measurements of effects P- and PT-nonconservation are desirable because the ratio of values PT- to P-violating effects weakly depends on the structure of a particular nucleus [3,4]. For the discussed purposes one can consider P-odd NN-amplitude to be known good enough. It should be noted that in nuclei ρ -meson diagrams contribute a dominating part to the latter effects while the former ones are determined in the most part by π -meson vertex (fig. 2), that is why nuclear medium amplifies PT-nonconservation effects more strongly. The ratio of matrix elements of the discussed effects is defined in [3,4] by the expression

$$-i \frac{\langle J_{c}(p) | V_{pt} | J_{c}(-p) \rangle}{\langle J_{c}(p) | V_{p} | J_{c}(-p) \rangle} \prod_{c} K \frac{g_{pt(\pi NN)}^{\Delta T=1}}{g_{p(\rho NN)}^{\Delta T=0}}.$$
(3)

This expression contains nuclear matrix elements of parity violation and PT-nonconservation potentials V_p and V_{pt} with the states of opposite parity p in their left- and right-hand sides, $g_{p(\rho NN)}^{\Delta T=0}$ and $g_{pt(\pi NN)}^{\Delta T=1}$ are constants making dominant contribution to the respective

effects, κ is a factor on nuclear enhancement which is estimated in [5] and turns out to be equal on average to 3.2 in various nuclei. The value of the P-violation constant is $g_{p(\rho NN)}^{\Delta T=0}$

- -11.4·10⁻⁷. Thus for actual competition of the "nuclear" studies of PT-nonconservation with PEDM ones one should achieve the ratio of amplitudes containing in formula (3) of about 2·10⁻⁴.
- 3. Other factors of enhancement of both effects in nucleus are of one and the same nature. If an object of study of P- or PT-nonconservation is a transition between two nuclear states then the correlation coefficient $a_{p(p)}$ characterizing the value of an effect may be schematically written in the form:

$$a_{p(pt)} = F_{\{J\}}^{p(pt)} \frac{2 < J_c(p) |V_{p(pt)}| J_c(-p) >}{\Delta E} \sqrt{\frac{\Gamma^{irreg}}{\Gamma^{reg}}}$$

(4)

where $\sqrt{\Gamma^{reg}}$ and $\sqrt{\Gamma^{irreg}}$ are the transition amplitudes related to the investigated level of a nucleus and its partner of opposite parity, ΔE – the energy distance between these levels, $F_{\{J\}}^{p(pt)}$ – the product of the elements of the Racah algebra (see bellow). The expression (4) demonstrates advantageous conditions of the experiment: a small value of ΔE and a large value of the ratio of the decay widths. Another important condition is a large value of cross section of the investigated resonance providing a high counting rate and thus a good statistics. The greater P-odd effect, the tighter constraints on PT-nonconservation constants may be attained. The examples of objects promising for search for the latter effect should display strong P-violation properties or these properties should be expected.

4. Search for PT-noninvariant effects in γ -transitions is preferable because otherwise, for strong and Coulomb interacting particles, false effect producing by a final state interaction is too large and the T-invariant P-odd amplitude together with the final (or initial) state interaction will simulate the effect under discussion.

In fact nuclear radioactive processes and neutron reactions induced by thermal, resonance and, perhaps, few keV-energy neutrons are promising for the discussed purposes and no other. Indeed, cross section of the process induced by photons are too small, and the emission of γ -quanta is unlikely for resonance proton reactions – (p,α) -reaction is typical process in this case.

In the present talk we concentrate on the discussion of PT-nonconservation effects in γ -transitions induced by reactions of neutrons with nuclei.

CURRENT STATUS OF SEARCH FOR PT-NONINVARIANT CORRELATIONS IN γ-TRANSITIONS

In spite of the declared goal let us discuss all known experimental data concerning the discussed topic.

1. Measurements of PT-noninvariant five-vector correlation $((\vec{k}_{\gamma_1} \cdot [\vec{J} \times \vec{k}_{\gamma_2}])(\vec{k}_{\gamma_2} \cdot \vec{J}))$

where \vec{J} – vector of orientation of a sample (produced by cryogenic means) using 501 keV line of radioactive source ^{180m}Hf and the subsequent 332 keV line as an analyzer (see fig. 3) [6] result in the upper limit of the effect ~10⁻² approximately equal to the measured value of the P-odd effect of the value 1.6·10⁻² in this transfer.

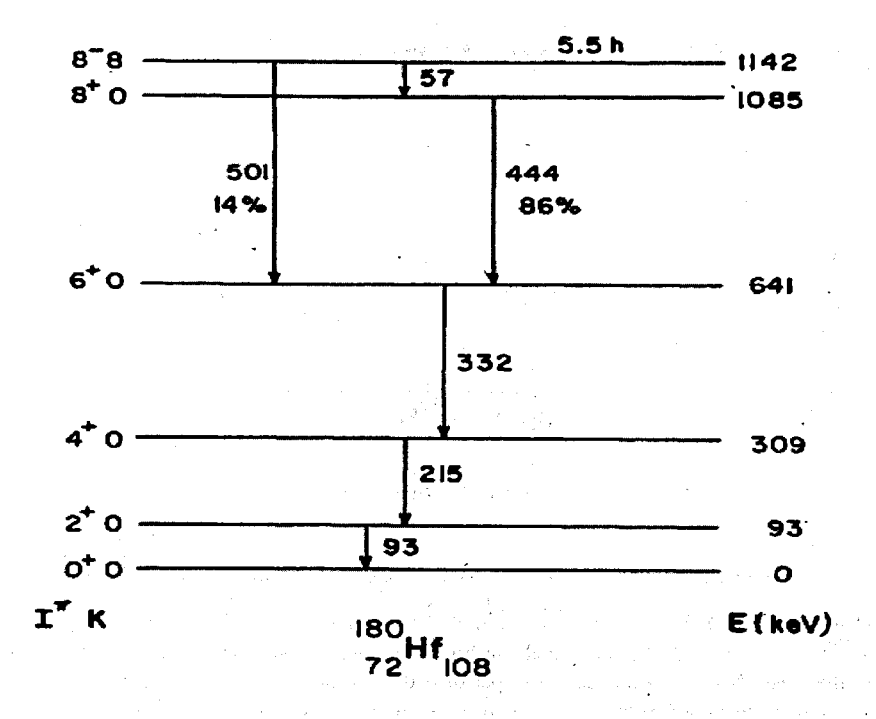


Figure 3. 180mHf decay scheme.

2. Study of the $(\vec{k}_{\gamma} \cdot [\vec{\mathcal{E}} \times \vec{J}])(\vec{J} \cdot \vec{\mathcal{E}})$ ($\vec{\mathcal{E}}$ – linear polarization of γ -quantum) correlation of gamma-radiation of ^{119m}Sn (see scheme on fig. 4) based on Moessbauer approach [7] provided the ratio of the upper limit of PT-noninvariant amplitude to measured P-odd one $\sim 4.0 \cdot 10^{-2}$. This example is a good demonstration of advantages of linear polarization of γ -quantum measurements (it was proposed by Z.Szymanski [8] and realized first time in the discussed work) compare to coincidence scheme with the second transfer as an analyzer – a current integrator but not a counter detecting system is in use, thus counting rate turns out to be essentially larger. A problem (probably – theoretical) is that experimental value of P-odd effect $(0.9\pm0.1)10^{-3}$ [9] looks anomalously great in the absence of parity mixing dublet.

CAST COMMENT OF THE PROPERTY O

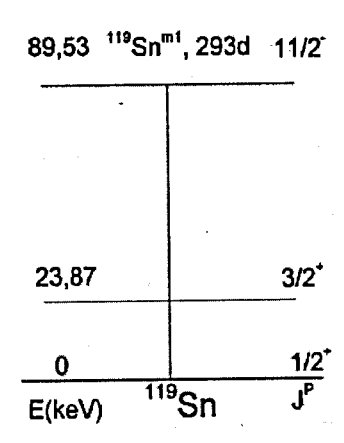


Figure 4. 119m1 Sn decay scheme.

The researches of PT-noninvariance in neutron reactions were concentrated last two decades basically on the case of $(\vec{\sigma}_n[\vec{k}_n \times \vec{J}])$ $(\vec{\sigma}_n$ is the neutron spin) correlation in the n + ¹³⁹La collision [10]. Mentioned above final state interaction problem turns out to be arduous in that case. No one experiment was performed up to now. The above mentioned correlation was measured in collisions of fast neutrons with polarized ¹⁶⁵Ho target [11]. Accuracy is not so high and the results are loosely interpretable because of contribution to the effect of a large number of amplitudes. Some other schemes of such a type are proposed [12–15].

So the problem of PT-invariance break up in nuclear processes remains to be topical.

CLASSIFICATION OF (n, y)-EXPERIMENTS

Advantages of experiments basing on observation of γ -transitions induced by neutron beams in comparison with produced by radioactive sources ones are the following:

- 1. Low and resonance energy neutron reactions are useful tools of producing of oriented sources themselves.
- 2. High-energy γ -quanta are typical for these experiments therefore final state interaction of such γ -quanta with atomic electrons is inessential.
- 3. There is a broad assortment of nuclear states manifesting relatively strong P-violation which can be excited by neutron beams.

Several approaches look reasonable for use in the discussed neutron experiments. These approaches vary in, first, measurement setup in which circular polarization sensitive detector of γ -quanta may be built-in, or linear polarization sensitive detector of γ -quanta may be embedded, or only spin-insensitive detectors may be in use. Second, method of orientation of an initial sample may be varied. So, it may be polarized beam. The alignment may be produced by preceding ejectile, or measured by subsequent particle emission, beam-produced alignment in neutron p-resonances also looks promising, at last in some cases target polarized

by cryogenic means may be used. Both thermal and resonance neutron sources are applicable for the discussed purposes.

Thermal neutron experiments

Scheme with a circular polarimeter

Polarized thermal neutron beam is required for this experiment. The scheme is based on $(\vec{\sigma}_n[\vec{k}_1 \times \vec{c}_\gamma])$ correlation in $(n,p\gamma)$ -, $(n,\alpha\gamma)$ -, and $(n,\gamma\gamma)$ -reactions, where \vec{c}_γ is circular polarization of the second γ -quantum. First transition of the discussed correlation is an object in which PT-noninvariant amplitude is searched for, and the second one is an analyzer. Taking into account mentioned above problem of final state interaction we limit ourselves by consideration of $\gamma\gamma$ -cascades only. Distribution of the products takes the form:

$$W_{LJF}(\theta_{\gamma_{1}},\theta_{\gamma_{2}},\phi_{\gamma_{1}},\phi_{\gamma_{2}}) = \sum \rho_{j}^{m}(I) \, \varepsilon_{j_{n}}^{m_{n}} * (L_{\gamma_{1}} p_{\gamma_{1}}, L'_{\gamma_{1}} p'_{\gamma_{1}})$$

$$\varepsilon_{j_{\gamma_{2}}}^{m_{\gamma_{2}}} * (L_{\gamma_{2}} p_{\gamma_{2}}, L'_{\gamma_{2}} p'_{\gamma_{2}}) \, \varepsilon_{j'}^{m'_{\gamma}} (F) \, \widehat{I}^{2} \widehat{J}^{2} (j_{\gamma_{1}} m_{\gamma_{1}} j_{\gamma_{2}} m_{\gamma_{2}} | j m)$$

$$\begin{cases} J & L_{\gamma_{1}} & I \\ J & L'_{\gamma_{1}} & I \\ j_{\gamma_{2}} & j_{\gamma_{1}} & j \end{cases} \begin{cases} F & L_{\gamma_{2}} & J \\ F & L'_{\gamma_{2}} & J \\ 0 & j_{\gamma_{2}} & j_{\gamma_{2}} \end{cases} \widehat{j}_{\gamma_{1}} \widehat{j}_{\gamma_{2}}^{2} \langle J | L'_{\gamma_{1}} p'_{\gamma_{1}} | I \rangle * \langle J | L_{\gamma_{1}} p_{\gamma_{1}} | I \rangle$$

$$\langle F | L'_{\gamma_{2}} p'_{\gamma_{2}} | J \rangle * \langle F | L_{\gamma_{2}} p_{\gamma_{2}} | J \rangle.$$
(5)

Here $\hat{b} = \sqrt{2b+1}$; 3×3 table is 9j-syumbol; $\rho_J^m(I)$ is the orientation tensor of a state; $\mathcal{E}_{j_\nu}^{m_{i\nu}}(lp,l'p')$ - efficiency tensor of a detector of irradiated particle; I denotes initial compound nucleus state, J - intermediate one, and F is a final state; $L_{\gamma_i}p_{\gamma_i}, L'_{\gamma_i}p'_{\gamma_i}$ - multipolarities of the transitions; $\langle I'|lp|I\rangle$ - amplitude of a transfer. The elements of the Racah algebra containing in (5) shape the factor denoted in (4) as $F_{\{J\}}^{p(pt)}$. The sum is over all indexes contained in (5) besides I, J, F. The residual nucleus is not registered therefore its efficiency tensor $\mathcal{E}_{j'}^{m'}(F)$ should be written as:

$$\varepsilon_{j'}^{m'}(F) = \hat{F}\delta_{j'0}\delta_{m'0}.$$

(6)

Let us consider longitudinally polarized neutron beam and direct z-axis along the beam direction. If S-resonance absorption is dominating, polarization tensor (rank j = 1) produced by the polarized neutron beam takes the form:

$$\rho_{j=1}^{0}(I) = (1/\sqrt{32}\pi) \hat{j}\hat{I}_{0} p_{z} \begin{cases} I & s & I_{0} \\ I & s & I_{0} \\ 0 & j & j \end{cases} \langle I \mid j \mid I_{0} \rangle \langle I \mid j \mid I_{0} \rangle^{*}.$$

(7)

Here s= 1/2 is the neutron spin, p_z - the degree of neutron polarization. The scalar part of the density matrix may be expressed similarly to (7) by substitution j = 1 for j = 0 and p_z for $1 - p_z$.

The form of the efficiency tensor of a detector of γ -radiation insensitive to linear polarization is the following:

$$\varepsilon_{j_{\tau}}^{m_{\tau}}(lp,l'p') = (1/16\pi)Q(j_{\tau})(-1)^{l'-1}\widehat{l}\widehat{l}'(l1l'-1|j_{\tau}0)[S(0)+S(3))+(-1)^{l}(S(0)-S(3))]$$

$$(\sqrt{4\pi}/\widehat{j}_{\tau})Y_{j_{\tau}m_{\tau}}^{*}(\theta\varphi),$$
(8

where $f = (p-p')/2 - j_{\gamma}$; $Q(j_{\gamma})$ - parameter, characterizing a geometry of the detector; θ and φ are the angles describing rotation from detector coordinate system to laboratory one; S(r) is a Stokes parameter of the detector: S(0) is determined by total (including both geometric and physical characteristics) efficiency of registration of unpolarized γ -radiation, and S(3) - by total efficiency of detection of its circular polarization including, in addition to the characteristics similar to that of S(0), polarization resolution capability.

The angular-dependent part of the expression (5) combined with the formula (7) can be written as:

$$S(3) \sum_{m=-1,1} (1m1 - m | 10) (\sqrt{4\pi} / \hat{1}) Y_1^m (\vec{p}_{\gamma}) (\sqrt{4\pi} / \hat{1}) Y_1^{-m} (\vec{k}_1) = \\ S(3) (111 - 1 | 10) 2 \text{Im} \{ (\sqrt{4\pi} / \hat{1}) Y_1^m (\vec{p}_{\gamma}) (\sqrt{4\pi} / \hat{1}) Y_1^{-m} (\vec{k}_1) \} =$$

$$(1/\sqrt{2})$$
S(3)sin(θ_{γ})sin(θ_{1})sin(ϕ),

(9)

thus directions of the detector axes are bound to be orthogonal to the direction of neutron polarization and to each other for the maximum efficiency. The effect is proportional to the difference between the counting rate of coincidents for positive and negative value p_z . In fact

19.

to get rid of systematic inaccuracy of measurement setup one needs in two detector of the first γ -quantum + two detector of the second γ -quantum setup. High-precision goniometry is necessary anyway.

The choice of a target depends first of all upon P-violation effect in a chosen γ -spectrum. Recently such effects in neutron reactions with 35 Cl, 56 Fe, 113 Cd, 117 Sn, 133 Cs, and 139 La targets are known (see collected data in [16] and references there). In the last two examples integral γ -spectrum is investigated. Other measurements were performed using a certain γ -line. Both approaches were used in the study of 35 Cl nucleus. Evidently either "single line" or "integral" approach may be used for search for PT-noninvariance. The first method allows one to use a line in which the effect of P-violation is relatively large, the second one provide a counting rate of coincidents being essentially higher. In should be noted that in the second case the coincidence scheme discriminates a significant part of γ -background.

The weak point of the single line approach is a strong limitation of counting rate of a detector performing the amplitude analysis of the signal. This limitation is less than 105 counts/s. The single line approach may in principal be realized using for example transition 7.28 MeV ($1^+ \rightarrow 2^+$) in ¹¹⁷Sn nucleus in which a very large P-nonconservation effect $-6.7 \cdot 10^{-3}$ (unfortunately unresolved with the effect in 7.27 MeV $(1^+ \rightarrow 0^+)$ line which is useless for the discussed purposes) is observed [16]. However line intensity is as small as (0.18±0.05)% of the total intensity of the γ - spectrum. Because of that counting rate of γ -quanta under study does not exceed 10^2 counts/s. Even a large solid angle of the second detector $\Omega_2 = 10^{-1}$ provides the coincidents counting rate of about 10¹ counts/s. Taking into account a small value of polarization resolution capability of the circular polarimeter which does not exceed 3% and the fact that the upper limit of the effect under study is linearly dependent on the efficiency of such a type one can conclude that the exposition time necessary to achieve even the value of the upper limit of the PT-nonconservation effect approximately equal to the measured value of P-violation one turns out to be very long. The example of ¹³⁵La looks more promising. Two lines of thermal neutron beam induced γ-spectrum of ¹⁴⁰La compound nucleus: 4.843 MeV and 5.098 MeV possess the intensities more than 9 % each. P-violation effect is not measured for any line of ¹³⁹La spectrum individually. At the same time the value of integral effect of Pviolation here is large enough being (1.6±0.3) 10⁻⁴ [17], therefore one can expect individual effect several times greater. If, fortunately, it is true for one of the discussed lines then the upper limit of the ratio of PT-noninvariant and P-violating effects $\xi \sim 10^{-0.5}$ may be achieved. An array of 10 presented targets placed on a powerful neutron beam could decrease this value by half an order.

The example of 139 La looks also promising for measuring of PT-noninvariant $\gamma\gamma$ -correlations in the (semi-)integral approach. Two just mentioned lines possess the overall branching ratio of about 19 % i.e. almost one half of total intensity of the hard part of the γ -spectrum. Thus the scheme including the following elements with high time resolution: a) a detector with a filter of the soft part of the spectrum in the first channel, b) a detector sensitive mainly to this soft part in the second channel, c) a coincidence scheme of signal fronts of these channels allows one to perform mostly the measurements of aggregate PT-noninvariant effect of two $\gamma\gamma$ -cascades beginning by the discussed lines. Therefore an attenuation of the integral effect in comparison with one line effect would be relatively small in the discussed case. The value of the P-violation effect in the proposed scheme is expected to be few times grater than presented above measured value of integral one. At the same time the amplitude analysis of a signal in not required in the discussed case therefore one can use "fast" γ -detectors. Due to that limit of the counting rate is put by coincidence scheme resolution time

or neutron beam intensity and may be brought to 10^5 counts/s. Thus the value of the discussed ratio $\xi \sim 10^{-2}$ may probably be achieved in a cumbersome experiment at a power thermal neutron source.

Advantages of the scheme are:

- 1. High-intensity thermal neutron beams are explored.
- 2. Polarized beam is a convenient and effective method of producing of a polarized sample.
- 3. No polarized target is required.

Disadvantages of the approach are:

- 1. Necessity in use of the coincident scheme and therefore counter but not current integrator method of registration.
- 2. Low efficiency of circular polarimeter.
- 3. Difficulties of the experiment, connected with P-even circular polarization of γ -quanta produced by a polarized sample. This polarization is perpendicular to measured one only approximately.

Scheme with a linear polarimeter

The scheme based on the measurement of the linear polarization is free of the second drawback, as it is the case in the presented above experiments with radioactive sources. This approach exploits the same correlation $(\vec{k}_{\gamma_2}[\vec{\mathcal{E}}\times\vec{k}_1])(\vec{k}_1\vec{\mathcal{E}})$ and thermal neutron beam is used here to produce a source of radiation only. Alignment turns out to be measured due to registration of a direction of a particle \vec{k}_1 , preceding γ -quantum in a cascade. A subsequent particle can also be used for the same purpose. As in the previously discussed scheme measurement of coincidents is necessary. If analogously to the previous case a cascade of two γ -quanta is considered in which the first one provides orientation of the sample, the angular distribution of it has the form (5) with m=0, $\rho_I^0(I)=\widehat{I}^{-1}$. Efficiency tensor of the first γ -quantum is expressed by the formula (8) in which the angles θ and φ are the angles determining direction of the first detector axes in the laboratory system. Isotropy of the initial state allows one to define the axes by the expressions $\theta_1=0$ and $\varphi_1=0$.

In a realistic case in which symmetry axis of the linear polarization sensitive (and, of course, circular polarization insensitive) detector of the second γ -quantum z is directed on to the target (m=0) the related efficiency tensor of the detector can be expressed as:

$$\begin{split} & \mathcal{E}_{j_{\gamma_{2}}}^{m=0}(lp,l'p') = & (1/16\pi) ll' \{2(-1)^{l'\cdot 1} \left(l1l'-1 \middle| j_{\gamma_{2}} 0\right) S(0) P_{j_{\gamma_{2}}}(\cos\theta_{2}) + \\ & p' \sqrt{\frac{(j_{\gamma_{2}}-2)!}{(j_{\gamma_{2}}+2)!}} \left(l1l'1 \middle| j_{\gamma_{2}} 2\right) P_{j_{\gamma_{2}}}^{(2)}(\cos\theta_{2}) \left[S(1)(1+(-1)^{f})-iS(2)(1-(1)^{f})\right] J, \end{split}$$
 (10)

where $P_{j_{r_2}}(\cos\theta)$ is Legendre polynomial, $P_{j_{r_2}}^{(2)}(\cos\theta_2)$ – ajoint Legendre polynomial of the second order, θ_2 is the angle between symmetry axes of the first and the second detectors. Obviously there is no dependence on φ_2 due to invariance of the set up about the direction of the first γ -quantum emission. The Stokes parameters S(1) and S(2) determine

linear polarization sensitivity of the discussed detector and are the functions of the angle ψ_2 which is defined as the angle, determining the direction of linear polarization sensitivity of the second detector: $S(1)=A\cos 2\psi_2$, $S(2)=A\sin 2\psi_2$. Thus the case S(1)=1, S(2)=0 is related to the plane of linear polarization passing through x-axis, the case S(1)=0, S(2)=1 is related to the plane passing through the bisector of x and y. It is the $\sin 2\psi_2$ -dependent term that is produced by PT-noninvariant amplitudes. Other terms of (10) involved in angular distribution (5): scalar one ($j_{\gamma_2}=0$), ψ_2 -independent, and $\cos 2\psi_2$ -dependent are sources of a strong background in the search for them. The optimal conditions for search for this correlation are obviously the following: $k_{\gamma_1} \perp k_{\gamma_2}$, and $\psi_2 = \pm \pi/4$. The experimental setup is schematically illustrated by fig. 5. Obviously in reality four-detector scheme is necessary to get rid of systematic inaccuracy of measurement setup. High-precision goniometry of the setup is necessary again.

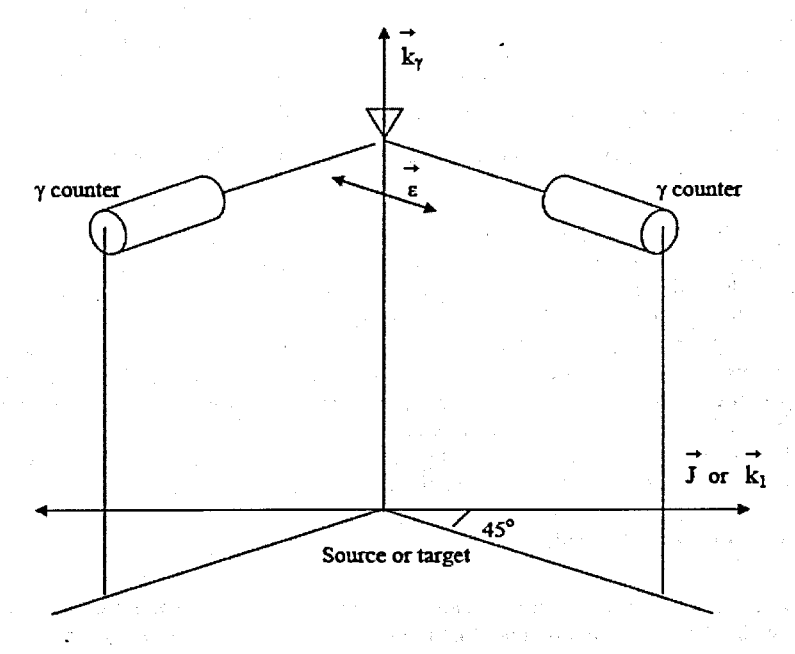


Figure 5. Registration scheme of $((\vec{k}_{\gamma_2}[\vec{\varepsilon} \times \vec{k}_1])(\vec{k}_1\vec{\varepsilon}))$ and $((\vec{k}_{\gamma_2}[\vec{\varepsilon} \times \vec{J}])(\vec{J}\vec{\varepsilon}))$ PT-noninvariant correlations.

What about promising examples of targets they are the same as in the previous case. The value of polarization resolution capability of the linear polarimeter is significantly (by about one order of magnitude) higher than the circular one. On the other hand effective solid

315

angle of it Ω_2 is the product of the solid angles of the scatterer and the detector $\Omega_2 = \Omega_s \ \Omega_d$ and thus it is no more than 10^{-2} . However measured upper limit of an effect depends on a square root of this value, therefore the scheme with a linear polarimeter may decrease the value of the limit by half an order. Therefore the value of the ratio $\xi \sim 10^{-2.5}$ may probably be achieved.

Advantages of this scheme in comparison with the previous one are:

- I. Higher value of efficiency of linear polarization measurements and less violent working conditions lower counting rate of the second detector.
- 2. Possibility to study PT-noninvariant amplitude either in the secondary γ -transfer of the cascade as it is just presented or in the primary γ -transfer i.e. use of the correlation $(\vec{k}_{\gamma_1} \cdot [\vec{\varepsilon} \times \vec{k}_2])(\vec{k}_2 \cdot \vec{\varepsilon})$ in which linear polarization of the first γ -quantum of a cascade is measured and the second one serves as an analyzer. Usually P-violation effect is grater in this case. On the other hand efficiency of a linear polarimeter working with high-energy primary γ -quanta is smaller.

Disadvantages of the scheme are:

- 1. Necessity in use of the coincident scheme and in the work under severe background conditions remains.
- 2. A linear polarimeter possesses small effective solid angle. Perhaps there exist examples in which detection of linear polarization may be advantageously replaced by detection of two γ -quanta in analogy with the work [6], thus three-shoulder coincident scheme (correlation $(\vec{k}_{r_0}[\vec{k}_{r_0} \times \vec{k}_{r_0}])(\vec{k}_{r_0}\vec{k}_{r_0})$) should be used in the proposed approach.

The sole way to get rid of a coincidence scheme in the thermal neutron experiments is to measure the correlation $(\vec{k}_{\gamma_2}[\vec{\mathcal{E}}\times\vec{J}])(\vec{J}\vec{\mathcal{E}})$, where \vec{J} is the vector of orientation of nuclear spin, thus one should create an aligned target. Cryogenic methods allow one to do it relatively easy for rear-earth isotopes and nuclei of elements constituting ferromagnetic composites. Unfortunately there is no example in which P-violation effect is measured in such nuclei excluding the effect in ⁵⁷Fe compound nucleus which is equal to $(6.4\pm0.5)\cdot10^{-5}$ (see [18]) i. e. it is relatively small. Additional troubles appear due to the strong background creating in this particular case by construction materials of the refrigerator. For other isotopes the temperatures about few mK are required to achieve a reasonable value of nuclear alignment. In addition one meets stringent requirements on frozen capability of a refrigerator and axial symmetry of a setup as a whole. Thus technical problems turn out to be crucial in the approach. That is why this scheme is beyond the scope in the current paper.

Resonance neutron experiments

In contrast to thermal neutron capture in which S-wave is strongly dominating and therefore such a beam does not produce an alignment (tensor of the rank j=2), this tensor is nonzero in neutron P-resonances with the total angular momentum $I \ge 1$. Thus one can get rid of coincident scheme by another way namely studying the correlation $(\vec{k}_{\gamma_2}[\vec{\mathcal{E}} \times \vec{k}_n])(\vec{k}_n \vec{\mathcal{E}})$ of γ -radiation of a P-resonance involving the vector of bombarding neutron linear momentum \vec{k}_n (see fig. 5). Formalism of this correlation involves the expression

$$\begin{split} W_{LF}(\theta_{\gamma_{2}},\phi_{\gamma_{2}}) &= \sum \rho_{j}^{0}(I) \, \mathcal{E}_{j_{\gamma_{2}}}^{m=0} * (L_{\gamma_{2}} p_{\gamma_{2}}, L'_{\gamma_{2}} p'_{\gamma_{2}}) \, \mathcal{E}_{j'}^{m'*}(F) \, \hat{j}_{\gamma_{2}} \, \hat{I}^{2} \\ \begin{cases} F & L_{\gamma_{2}} & I \\ F & L'_{\gamma_{2}} & I \\ 0 & j_{\gamma_{2}} & j_{\gamma_{2}} \end{cases} \Big\langle F \big| L'_{\gamma_{2}} p'_{\gamma_{2}} \big| J \Big\rangle * \Big\langle F \big| L_{\gamma_{2}} p_{\gamma_{2}} \big| J \Big\rangle, \\ (11) \end{split}$$

where the efficiency tensor of the polarimeter $\mathcal{E}_{j_2}^{m=0}*(L_{\gamma_2}p_{\gamma_2},L'_{\gamma_2}p'_{\gamma_2})$ is determined by formula (10). Orientation tensor of a system after a capture of unpolarized particle with the spin s $\rho_k^0(I)$ takes the form:

$$\rho_{k}^{0}(I) = (1/4\pi) \sum_{ll'j} (-1)^{l'} \hat{l} \hat{l}' \hat{I}_{0} \hat{s}^{-1} \hat{k}^{3} \hat{I}^{2} \hat{j} \hat{j}' (l0l'0 \mid k0) \begin{cases} I & j & I_{0} \\ I & j' & I_{0} \\ k & k & 0 \end{cases}$$

$$\begin{cases} l & s & j \\ l' & s & j' \\ k & 0 & k \end{cases} \langle I_{0} \mid j' \mid I \rangle^{*} \langle I_{0} \mid j \mid I \rangle,$$
(12)

It is important to keep in mind that typical values of the last multiplier in the expression (4) are significantly smaller for (n,γ) -reaction than in neutron transmission processes if one and the same target is used. For this reason it would be expected that for low-lying P-resonance states of nuclei ⁸¹Br, ¹¹¹Cd, ¹¹⁷Sn, and ¹³⁹La, displaying very strong P-odd asymmetry $(10^{-2.5} \div 10^{-1.5})$ in neutron transmission experiments [19] (see also up-to-date review [20]), respective values of the asymmetry are would be less by almost one order of magnitude if a convenient γ -line would be chosen. For the integral approach these values are expected to be still less by about one-half order. The one line approach is in fact useless because of very intensive γ -flux on a detector at a pulse time. Moreover the current integrator detecting system is the sole reasonable for application. If however such a system is used just mentioned examples look promising for the discussed investigations in spite of moderate value of the P-violation effect. Indeed, assuming that the experiment with ¹¹¹Cd target is carried out at a powerful resonance neutron source such as SNS and polarimetry system possess the effective solid angle $\Omega_2 = 10^{-2}$ and polarization resolution capability $10^{-0.5}$ one may conclude that the value of the ratio $\xi \sim 10^{-3.5}$ may probably be achieved.

In neutron resonance spectra of nuclei there is a multitude of P-resonances of relatively high energy manifesting strong P-violation properties [20]. Many of them are suitable for the studies of PT-noninvariant effect in the proposed scheme and, probably, some of them could turn out to be more promising than the just discussed example. However the experimental

conditions (target thickness, pulse time and frequency, etc.) adopted peculiarly for any resonance are necessary for realization of the potentialities of the approach. This problem merits special investigation.

Nevertheless it is reasonably safe to suggest that the discussed scheme turns out to be promising to become compatible with PEDM measurements in providing constraints on isovector PT-noninvariant amplitudes.

It is interesting to note that using transversely polarized P-resonance neutrons (or polarized target with the orientation tensor of the rank j=3 placed into a thermal unpolarized neutron beam) one can investigate P-even T-noninvariant effect by measuring linear polarization in the seven-vector correlation $(\vec{k}_{\gamma_2}[\vec{J}\times\vec{\mathcal{E}}])(\vec{J}\vec{\mathcal{E}})(\vec{J}\vec{k}_{\gamma_2})$ in one-step γ -transition process. Recently this correlation has already found use in search for the just mentioned effect in a convenient for this purpose γ -transition in ¹⁷¹Yb nucleus spectrum induced by radioactive decay [21]. Naturally in search for this effect in neutron experiments the list of useful targets is not limited by those possessing the strong P-violation effect also. The choice of a target is determined by suitability of it for experimental operating.

CONCLUSION

- 1. Study of neutron-induced γ -transitions is promising tool for search for PT-noninvariant effects.
- 2. Both thermal and resonance neutron sources are applicable for these purposes.
- 3. Some versions of such experiments are capable to reduce upper limit of the effect achieved recently in nuclear experiments by about two orders of magnitude and approximate it to the level of accuracy attained in PEDM measurements for isovector PT-noninvariant amplitude.

ACKNOWLEGEMENTS

Authors express their gratitude to prof. G.E.Mitcell and prof. V.G.Tsinoev for fruitful discussions.

Work supported by RFBR, grant No. 04-02-17409.

REFERENCES

- 1. J.H.Christensen, J.W.Cronin, V.L.Fitch, R.Turlay. Phys. Rev. Lett. 1964. V. 13. P. 138.
- 2. B.Aubert et al. 2004. hep-ex/0407057.
- 3. P.Herczeg. Hyperfine Interact. 1992. V. 75. P. 127.
- 4. P.Herczeg. In: Tests of Time Reversal Ivariance. Ed. by N.R.Robertson, C.R.Gould, and J.D.Bowman. (World Scientific, Singapoure,
- 1987) P. 24.
- 5. I.S.Towner, A.C.Heyes. Phys. Rev. 1994. V. C 49. P. 2391.
- T.Murdoch et al. Phys. Lett. 1974. V. B 52. P. 325.
- 7. V.G.Tsinoev et al. Phys. At. Nucl. 1998. V. 61. P. 1357.
- 8. Z. Szymanski, Nucl. Phys. 1968. V. A113. P. 385.
- 9. A.V.Baluev et al. ZETP Lett. 1986. V. 43. P. 656.
- 10. Y.Masuda In: Time Reversal Invariance and Prity Violation in Neutron Reactions. Eds. C.R.Gould, J.D.Bowman, and Yu.P.Popov. (World Scientific, Singapore, 1993) P.126.

- 11. J.P.Soderstrom et al. Phys. Rev. 1988, V. C38, P. 2424.
- 12. L.Stodolsky. Phys. Lett. 1986. V. B 172. P. 5.
- 13. V.R. Skoy. Phys. Rev. 1996. V. D 53. P. 4070.
- I.S.Okunev, Yu M.Tchuvil'sky. In: Proceedings of ISINN 10, Dubna, JINR, 2003. P.
- 15. V.G.Nikolenko et al. Part. Nucl. Lett. 2007 V. 4. P. 42.
- 16. L.M.Smotritsky, V.N.Dobrynin. Preprint PNPI-2041, Gatchina, 1995.
- 17. V.A. Vesna et al. JETP Lett. 1982. V. 36. P. 169.
- 18. A.I.Egorov et al. Preprint LNPI-1067, Leningrad, 1985.
- 19. V.P.Alfimenkov et al. Nucl. Phys. 1983. V. A 398. P. 93.
- 20. G.E.Mitchell, J.D.Bowman, S.I.Penttila, E.I.Sharapov. Phys. Rep. 2001. V. 354. P. 157.
- 21. V.G.Tsinoev et al. Phys. Rev. 2007. V. C 76. P. 045503.

FACTOR ANALYSIS OF NEUTRON DATA

Cristiana Oprea, Alexandru Ioan Oprea

Frank Laboratory for Neutron Physics, JINR, Dubna 141980, RF

Abstract The interpretation of neutron spectra patterns is subjective and difficult by instrumental means and sometimes the analytical methods have proved unsatisfactory to reduce uncertainty in nuclear data. In the present report, we investigated how to detect underlying nuclear characteristics of different neutron spectra by means of common statistical methods and Factor Analysis. We applied basic and multivariate statistical analysis methods with the use of co-occurrence and run-length matrices to analyze the spectra patterns. Factor Analysis was used to determine whether a large number of independent variables actually measured one or more underlying common variables.

Keywords: nuclear neutron data, basic statistics, uncertainty, Factor Analysis

Introduction

The physics of the reactors and their fuel cycles is rather well understood. Their optimization, in order to meet more effectively the requirements, and their evolution, need the research and development in all fields, in particular for innovative fuel development and processing, and also in the reactor physics field. In the last area, the role of neutron data is quite important taking into account their requirements for the development and applications of nuclear science and technology. Most neutron data are large available in the databases of world neutron data centres, but their up-to-dating in terms of improvements, accuracy and validation is still a major concern.

In order to make a comprehensive assessment, the tools of sensitivity and uncertainty analysis are needed. These tools have been widely developed in the past, in particular for the assessment in the 1970s and 1980s of the performance of fast reactors.

In the following sections we performed, in a breakdown by applications, a preliminary study on the impact of neutron data uncertainties on the neutron reactions of the reactor, using the all neutron reactor spectrum by the hypothesis of partial energy correlations.

Finally, an approach to define a set of optimized integral experiments in order to reduce uncertainties on the reference systems has been proposed.

Neutron nuclear data requested in fast fission reactor technology

The common needs in fission reactors are concerned with the improvement of specific neutron cross-sections for fast reactor design calculations and modeling. Furthermore, the specific requests include the neutron data for specific reactor working and safety aspects such as reactor shielding and safety analysis, radiation damage and neutron flux monitoring, reactor coolant activation and reactor materials.

The neutron data are organized in a matrix form as follows. The columns contain the elements or isotopes and the rows comprise the various types of neutron nuclear reaction data requested, including also the accuracies (usually $\pm 1\sigma$). It is supposed that these matrices should serve as input data for basic and multivariate statistical analysis, either for measurements or for evaluations.

The specific needs in fast reactor design and control calculations suppose the extending of knowledge of the neutron absorption and inelastic scattering properties of reactor materials acting on the reactor neutron spectra.

The reactor shielding calculations include nuclear neutron data of neutron emission, γ-production, elastic and inelastic scattering data for different shielding materials and the interpretation of experimental shielding benchmark results.

The estimation of radiation damage of pressure vessels supposes specific tasks related to improvement of the accuracy of neutron activation reactions used for flux monitoring purposes inside reactors.

A number of requests are concerned with improving of standard reference data needed to convert relative cross section measurements to absolute values.

A small fraction of the overall nuclear neutron data requirements includes asks for safeguards and biomedical purposes.

Measurement uncertainties

Commonly there are two categories of uncertainties:

- 1. Random uncertainty which is different for each measurement of the same quantity. In repeated measurements it get a different value each time. Often it is assumed to be statistically independent, but usually it is not.
- 2. Systematic uncertainty that is the same for each measurement within a group. It is the component of measurements that remains unchanged. It can be caused by error in calibration or zeroing.

In neutron cross-section experiments, sources of uncertainties include:

- i) Random uncertainties from counting statistics for primary process and monitoring process and given by background of the measurement. Usually it is easy to assess them.
- ii) Systematic uncertainties connected with integrated beam intensity, target impurities, target thickness, detector efficiency, count rate corrections, measurement geometry, corrections for contributions from other processes, etc. Such types of experimental errors require being carefully analyzed/estimated.

The best estimation of uncertainties in the measurement data is based on a thorough understanding of probabilistic nature of the fluctuations in the data. In neutron physics, we are fortunate to have control over the measurements. Then we need to calibrate and study the measuring devices. Observing the measurements to characterize random fluctuations, we calculate the shape of the probability density function and the standard deviation/variance of fluctuations. Then we identify and try to explain the presence of outliers. Later we calculate the correlation matrices and perform the multivariate statistical analysis (in particular, Factor Analysis).

The application of factor analysis in nuclear neutron physics

Our aim is to present a short overview of factor analysis and probabilistic modeling, to cover basic Factor Analysis methodology relevant to nuclear neutron physics, especially cross section evaluation and to point the way to how to do it. Furthermore, we wish to demonstrate that Factor Analysis is a reasonable approach to applying for measurement uncertainty.

Factor Analysis approach is concerned with the few main factors central to understanding quantifying the degree of uncertainty. It can simultaneously manage over large neutron data basis, compensate for random error and invalidity, and disentangle complex interrelationships into their major and distinct regularities.

The most often employed techniques of Factor Analysis is the R-mode Factor Analysis which is applied to a matrix of correlation coefficients among all the variables. Specifically, such correlation matrix present the following features:

- 1. The Pearson's coefficients of correlation express the degree of linear relationship between the row and the column variables of the matrix;
- 2. To interpret the coefficient, it is necessary to square it and then multiply by 100 and this will give the percent variation in common for the data on two nuclear variables;
- 3. The Pearson's coefficient of correlation between two variables is the cosine of the angle between the variables as vectors plotted on the coordinate axes;
- 4. When the correlation matrix is to be factored, the principal diagonal contains communality estimates which measure the variation of a variable in common with all the others.

Correlations in the fission cross-section are best represented by the covariance matrix, whose diagonal and off-diagonal elements represent the standard deviations and the correlations, respectively.

After factorization, the factors (columns) represent the significant meaningful independent/uncorrelated patterns of relationship among the variables. Their loadings measure the features of the probability distribution that are in general not known for nuclear models. The rotated factors delineate the distinct clusters of relationships, if such exist. The factor score matrix contains the scores of the patterns which can be ascertained for the variables

The proposed approach

Uncertainty assessment using R-mode factor analysis

To make a nuclear neutron data evaluation we should to determine the set of independent neutron reaction channels and the grid of neutron energies.

The sensitivity coefficients of an integral parameter R to variations of a nuclear neutron data σ is defined as

$$S_{R} = (S_{x,i}) = \begin{pmatrix} S_{\Gamma} \\ \vdots \\ S_{J} \\ \vdots \\ S_{N} |_{x,i} \end{pmatrix}$$

$$(1)$$

where $S_{j,x,i} = \frac{\partial R}{\partial \sigma_{j,x,i}} \cdot \frac{\sigma_{j,x,i}}{R}$ (2) and i, x and j are the indices for the isotope, cross-section type

and the energy group, respectively.

The variance matrix is

$$V = (V_{x,i}) = \begin{pmatrix} V_{11}, V_{12}, \dots, V_{1N}, \\ V_{21}, \dots, V_{jj}, \\ \dots, V_{NN} \end{pmatrix}_{x,i}$$

$$(3)$$

Then the uncertainty on the integral parameter can be wrote as:

$$\Delta R_0^2 = S_R^T V S_R \tag{4}$$

Further a formal approach was adopted in order to establish the target accuracy requirements regarding cross-section data uncertainty reduction. It consists in solving the minimization

problem of uncertainty data requirements v_l for parameters l not correlated among themselves):

$$\sum_{l} \frac{\lambda_{l}}{v_{l}^{2}} = \min_{r} l = 1, \dots L, \tag{5}$$

where L is the total number of parameters that fulfils the condition

$$\sum_{i} S_{ni}^{2} v_{i}^{2} < (R_{n}^{T})^{2}, \dots, n = 1, \dots, N$$
 (6)

where N is the total number of integral parameters, S_{nl} are the sensitivity coefficients for the integral parameter R_n , R_n^T are the target accuracies on the N integral parameters, λ_l are the significance parameters related to each σ_l and account for the difficulty of improving that parameter (for example, reducing uncertainties with an appropriate experiment).

The sensitivity coefficients

The sensitivity coefficients of neutron source are

$$S_{j}^{i} = P_{i} \cdot \frac{\partial n_{F}^{i}}{\partial \sigma_{i}} \cdot \frac{\sigma_{j}}{n_{F}^{i}} = \frac{P_{i}}{n_{F}^{i}} \int_{t_{i}}^{t_{F}} n^{*} \sigma_{j} n dt$$
 (7)

where effects due to the neutron production cross-section (e.g., by spontaneous fissions) P_i cross-section variations are supposed to be negligible.

Factor analysis application to some neutron data

From uncertainties and variances for U and transuranics nuclear data using integral experiment analysis, one can distinguish among four classes of isotopes:

- 1. Major isotopes as ²³⁵U, ²³⁸U and ²³⁹Pu;
- 2. Other U and Pu isotopes as ²³⁴U, ²³⁶U, ²³⁸Pu, ²⁴⁰Pu, ²⁴¹Pu and ²⁴²Pu;

- 3. Minor actinides up to ²⁴⁵Cm as ²³⁷Np, ²⁴¹Am, ²⁴²Am, ²⁴³Am, ²⁴²Cm, ²⁴⁴Cm and ²⁴⁵Cm;
- 4. Higher mass minor actinides; and 5 energy regions (Figure 1):
- i) The region above the threshold of fertile isotope fission cross-sections;
- ii) The region of the continuum down to the upper unresolved resonance energy limit;
- iii). The unresolved resonance energy region;
- iv). The resolved resonance region;
- v). The thermal range

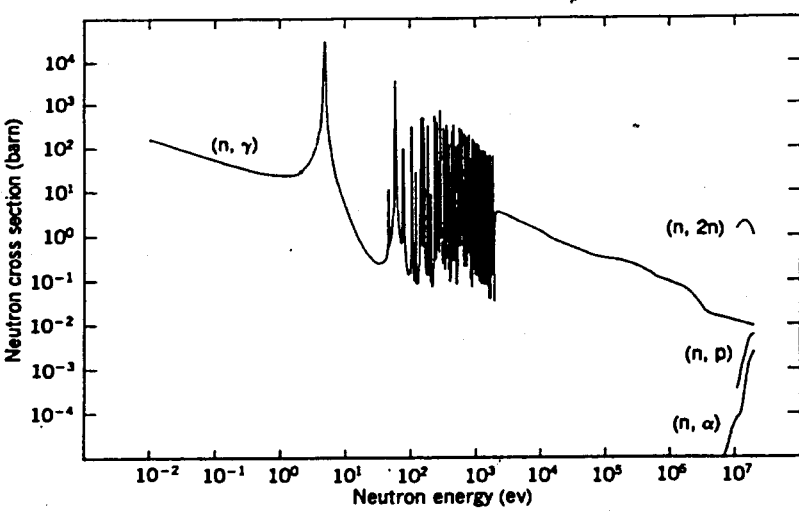


Figure 1. Energy distribution of neutron flux at the reactor.

No correlation among different reactions or different isotopes has been considered at this stage. The uncertainty values are consistent with the five distinct regions of energy (Figure 1). In the resonance region, the uncertainties are for broad energy-average cross-sections, and do not apply to individual resonances.

A few relevant factors were underlined (F1, F2 and F3):

F1. For some major isotope reactions the factor values of R-mode factor analysis of neutron data are fairly close to specifically evaluated data. This factor includes 239 Pu σ_f , 238 U σ_c , 235 U σ_f , etc.

- F2. In this factor the evaluated data uncertainties are very low and not consistent with the performance of neutron data in integral experiment analysis.
- F3. The evaluated data are similarly with the estimated variances (partial energy correlation).

Conclusion

In this paper we developed a Factor analysis approach to predict important nuclear cross-sections and quantify uncertainties in those predictions. Furthermore, increased sensitivity of neutron scattering results obtained with this approach has contributed to better assessments of past neutron experiments.

This study shows that the combination of Factor Analysis and nuclear neutron physics gives an improved model for neutron experiment evaluations and uncertainty degree quantification. Also it has quite appropriate statistical characteristics.

References

- [1] Aliberti, G., G. Palmiotti, M. Salvatores, C.G. Stenberg. 2004. Transmutation dedicated systems: an assessment of nuclear data uncertainty impact. Nucl. Sci. Eng. 146:13.
- [2] Bohr, N., and J.A. Wheeler. 1939. The Mechanism of Nuclear Fission. Phys. Rev. 56:426.
- Cecchini, G., U. Farinelli, A. Gandini, M. Salvatores. 1964. Analysis of integral data for few group parameter evaluation of fast reactors. A/CONF 28/P/267, Geneva, Switzerland.
- [3] Gandini, A. 1988. Uncertainty analysis and experimental data transposition methods in uncertainty analysis. In: Ronen, Y.(Ed.), CRC Press, Boca Raton.
- [4] Palmiotti, G., M. Salvatores. 1988. Proposal for nuclear data covariance matrix. JEFDOC1063 Rev.1.
- [4] Palmiotti, G., M. Salvatores, R.N. Hill. 1994. Sensitivity, uncertainty, assessment, and target accuracies related to radiotoxicity evaluation. Nucl. Sci. Eng. 117:239.
- [5] Shcherbkov, O., A. Donets, A. Evdomikov, A. Fomichev, T. Fukahori, A. Hasegawa, et al. 2002. Neutron induced Fission of ²³³U, ²³⁸U, ²³²Th, ²³⁹Pu, ²³⁷Np, ^{nat}Pb, and ²⁰⁹Bi Relative to ²³⁵U in the Energy Range 1-200 MeV. J. Nucl. Sci. Technol. 1(2):230.
- [6] Smith, D.L. 1991. Probability, Statistics, and Data Uncertainties in Nuclear Science and Technology. OECD/NEA Monograph Series, Am. Nucl. Soc., La Grange Park, Illinois.
- [7] Smith, D.L. 2005. Covariance matrices for nuclear cross-sections derived from nuclear model calculations. Report ANL/NDM-159, Argonne National Laboratory.
- [8] Staples, P., and K. Morley. 1998. Neutron-Induced Fission Cross-Section Ratios for ²³⁹Pu, ²⁴⁰Pu, ²⁴²Pu and ²⁴⁴Pu Relative to ²³⁵U from 0.5 to 400 MeV. Nucl. Sci. Eng. 129(2):149.
- [9] Szondy, E.J. 1982. Application of factor analysis to neutron spectrum unfolding. Report BME-TR-RES-2/82, Budapest.

Experiment for the measurement of the neutron-electron scattering length in liquid Pb at the TS-3000K thermostat from IBR-2 reactor

C. Oprea, A.I. Oprea, G.S. Samosvat, V.G. Nikolenko, V.V. Savostin, V.M. Morozov, Zh.A. Kozlov

FLNP-JINR, 141980 Dubna, Russian Federation

Abstract. At the DIN-2PI channel from the IBR-2 reactor an experiment for the measurement of the neutron-electron scattering length on molten Pb using the thermostat TS-3000 K was realized.

Introduction. At the channel DIN-2PI from IBR-2 reactor t the TS-3000K device (very high temperature thermostat) an experiment for evaluation of the neutron-electron scattering length obtained from the structure factor S(q) for liquid metals is proposed. The first proposed experiment is on liquid Pb (low melting point) and in case of good results other experiments on liquid metals with higher melting points will be proposed.

The literature data on neutron-electron scattering length lead to discrepancy in theoretical interpretations of the results obtained. It is connected with difficulties of the precise measurement of the neutron-electron scattering length, this one being very small and negative $(\sim 10^{-3} \text{ fm})$ [1].

The measurements effectuated at the end of 2006 and of the working time of the IBR-2 reactor had a methodical character. First, these measurements demonstrated that the TS 3000K device is in working state and ready for experiments. We mention also that during 2006 were also effectuated other measurements on some metals (Ta and V) up to 2300 K (Kelvin degrees) [2] and some tests without any samples when the temperature on the TS 3000K was increased up to 2700 K. The TS3000K device was designed and projected to National Institute for Physics an Nuclear Engineering (http://www.nipne.ro), Bucharest, Romania.

Very shortly we presents the goal and the research area of TS 3000K device.

Goal

- to heat and to maintain with high precision the temperature of a large sample (ϕ = 80x80 mm²) in order to perform inelastic and quasi-elastic slow neutron scattering and neutron diffraction experiments in vacuum in condensed matter field, over a very large temperature range (up to 3000 K).

Research area

- Investigation of oxygen disorder, thermal parameters, lattice vibrations and elastic constants of the nuclear fuel oxides as: UO₂, THO₂, PuO₂, at temperatures up to 3000 K;
- Structure and dynamics of the liquid metals and alloys both in the high purity state and with impurities;
 - Investigation of the material for fusion reactors at temperatures up to 3000 K;
- Investigation of the fast ion conductors lattice dynamics (super-ionic) using neutron scattering techniques;
 - Large and small angles neutron scattering experiments of disordered materials;
 - High temperature mass spectrometric measurements
 - High purity materials

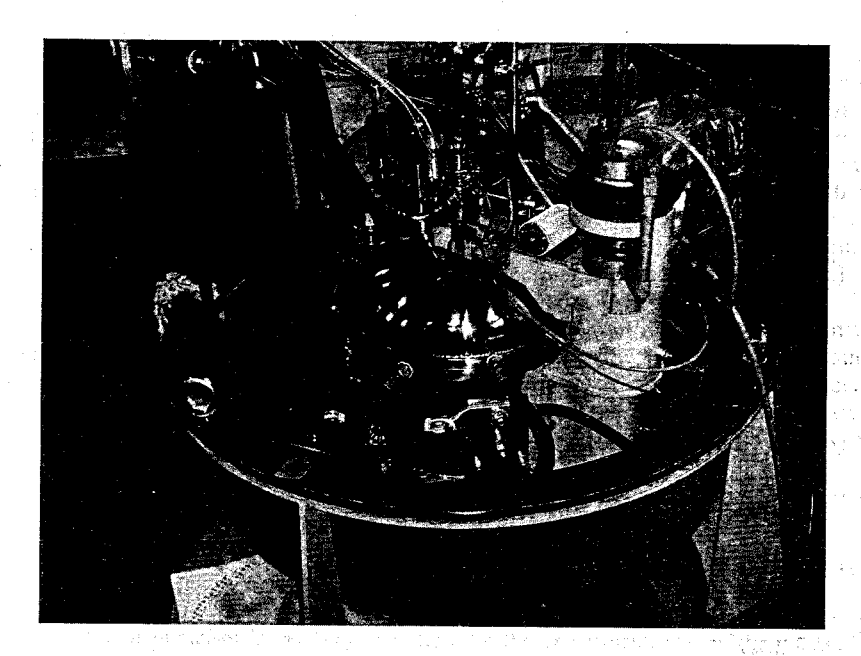


Fig.1. TS-3000K installation

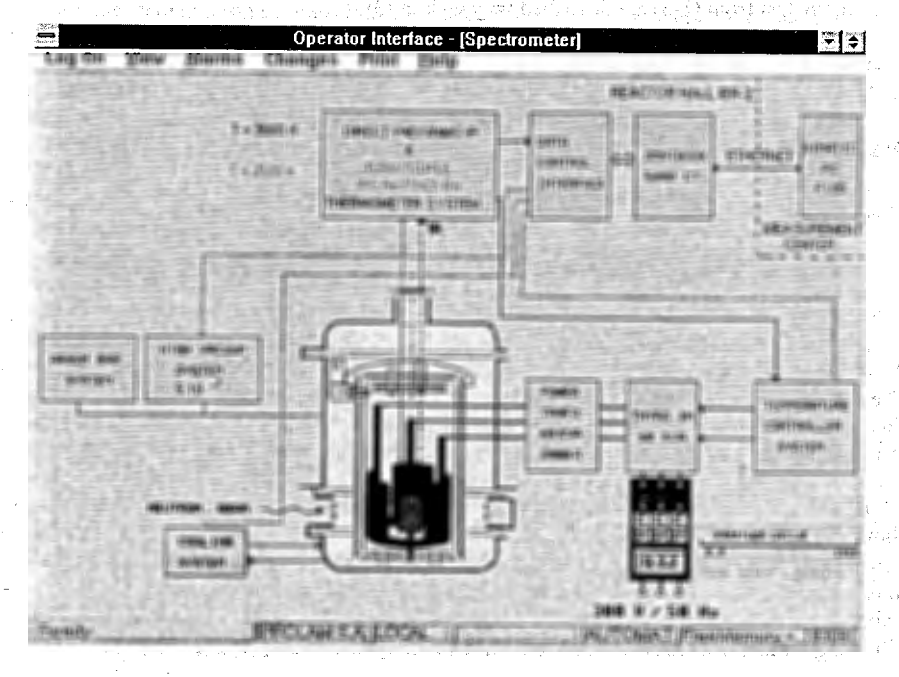


Fig. 2. TS-3000K General view

A brief theoretical overview. The question of the measurement of the neutron – electron scattering length was started in the '40 years of the last century and is connected with the supposition that the neutron has an internal electromagnetic structure. From Yukawa's theory the neutron is not an elementary particle. The neutron is a structure of a proton surrounded by a cloud of negative pion allowing the strong interaction of the neutron. From this description the neutron must have a non zero electrical dipole moment. This moment is very small but in principal can be evidenced by the interaction of the neutron with any electrical charged particle and in our case with electrons of the atomic shells of the nucleus (see [3] and the references from that).

The authors from [4] proposed a new method for the extraction of the neutron – electron scattering length from the structure factor S(q) obtained from the interaction of the neutron with noble gases. They have proposed an empirical model for the experimental stricture factor which take into account the diffraction effects on the structure of the local orders. The structure factor has the following form [3]:

$$S^{\exp}(q) = 1 + Bf(q) + [\gamma + Bf(q)][S(q) - 1], \tag{1}$$

$$S(q) - 1 = \frac{nC(q)}{1 - nC(q)} \tag{2}$$

$$C(q) = A_1 e^{-A_2 q} Sin \left(\frac{2\pi q}{A_3} + A_4 \right)$$

$$Y^{\exp}(q) = \frac{S^{\exp}(q_1)}{S^{\exp}(q_2)} \tag{3}$$

The parameters from (1-3) are described very well in [3].

An improvement of the method proposed in [3] is realized by using in our case a model for liquid Pb described in [4].

$$S^{\exp}(q) = 1 + Bf(q) + [\gamma + Bf(q)][S(q) - 1], \tag{1}$$

$$S(q) - 1 = \frac{nC(q)}{1 - nC(q)}$$
 (2)

$$nC(q) = -24\eta(q\sigma)^{-6} \left\{ \alpha(q\sigma)^{3} \left(\sin(q\sigma) - q\sigma \cos(q\sigma) + \beta(q\sigma)^{2} \left[2q\sigma \sin(q\sigma) - ((q\sigma)^{2} - 2)\cos(q\sigma) - 2 \right] \right\} + \gamma \left[(4q^{3}\sigma^{3} - 24q\sigma)\sin(q\sigma) - (q^{4}\sigma^{4} - 12q^{2}\sigma^{2} + 24)\cos(q\sigma) + 24 \right] \right\}$$
(4)

$$\gamma = \frac{\eta \alpha}{2}, \alpha = \frac{(1+2\eta)^2}{(1-\eta)^4}, \eta = \frac{\pi n \sigma^3}{6}, \beta = \frac{-6\eta \left(1+\frac{\eta}{2}\right)^2}{(1-\eta)^4}$$
 (5)

 σ - radius of the atom and parameters of the fit are σ , b_{ne} , K

The proposed function describes well the experimental data but not describes the attenuation. To describe well the attenuation before the function nC(q) we have introduced an attenuation term of the form a exp(-bq).

Results and discussion. The evaluation effectuated in [1] using the both models showed that if we want to obtain the neutron – electron interaction length with a precision of with a precision of 10^{-2} it is necessary to measure $S^{exp}(q)$ with a precision of 10^{-4} . Also we must take into account that in the case of liquid Pb (metal) the diffraction effects will be 2 order of magnitude higher than in the case of noble gases. The authors from [4] proposed the following value for neutron – electron interaction length, $b_{ne} = -1.35 \times 10^{-3} \, fm$. This value is

in contradiction with that proposed in [3] where the author suggests a value of $b_{ne} < -1.4 \times 10^{-3}$ fm which is in agreement with the Yukawa's theory of the nuclear forces.

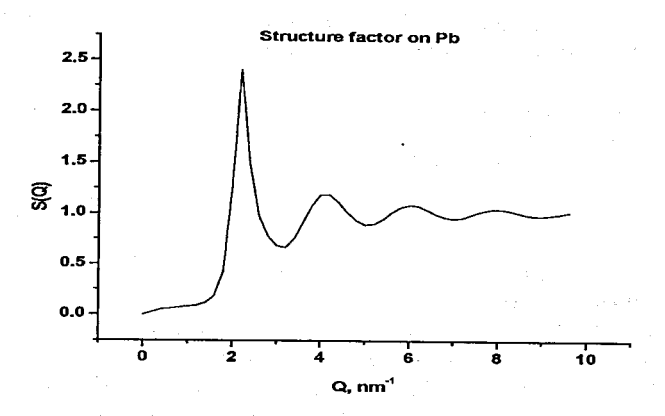


Fig. 4. Preliminary measurements-Liquid Pb with TS3000K device

In the figure 4 we have the experimental structure factor of the liquid Pb. Unfortunately until now. One of the main causes is the very short time for the experiment. Due to the liquid Pb the diffraction effects were amplified. In the future it is necessary to effectuate measurements at the more intensive neutron sources. In the Pb atom the electron shells are not closed and the magnetic moment of the neutron will interact with the spin of the un paired electron. Also the magnetic moment of the neutron can interact with the electric field of the nucleus (Schwinger interaction). All these interaction must be evaluated as well as possible for a successful evaluation of the neutron – electron interaction length.

The work was supported by the grants of the Romanian Plenipotentiary Representative to JINR in the 2005 and 2006, the National Institute for Physics and Nuclear Engineering from Bucharest – Romania, the Laboratory of Neutron Physics of JINR Dubna and IPPE Obninsk from Russian Federation.

References.

- [1]. A.I. Oprea, C. Oprea, G.S. Samosvat, V.G. Nikolenko, Zh.A. Kozlov, 2007. Proposal for the investigation of the neutron-electron scattering length in liquid Pb by the TS-3000K thermostat at IBR-2 reactor. Proceedings of ISINN-14, May 24-27, 2006, Dubna
- [2] V. A. Semenov, G. A. Kozlov, L. Craciun, G. Mateescu, V. M. Morozov, A. I. Oprea, C. Oprea, I. Padureanu, A. V. Puchkov, Preprint № 3098, FEI Obninsk, 2007
- [3] Yu. A. Alexandrov, Preprint JINR Dubna, E3-2006-142, 2006
- [4] Structure factor and n-e scattering, L.V. Mitsyna, V.G. Nikolenko, S.S. Parzhitski, A.B. Popov, G.S. Samosvat, Preprint Dubna E3-2003-183
- [5] The Structure Factor for Liquid Lead, U. Dahlborg, M. Davidovic, K.E.Larson, Phys. Chem. Liq., 1977, vol.6, p.149-166

"ZERO" EXPERIMENT AND FINAL RESULT OF THE MEASUREMENTS OF THE P-ODD ASYMMETRY IN THE 6 Li(n, α) 3 H REACTION.

Vesna V. A.¹, Gledenov Yu. M.², Nesvizhevsky V. V.³, Petukhov A. K.³, Sedyshev P. V.², Soldner T.³, Shulgina E. V.¹, Zimmer O.^{3,4}

¹Petersburg Nuclear Physics Institute of RAS, Gatchina, Russia. ²Frank Laboratory of Neutron Physics, JINR, Dubna, Russia. ³Institut Laue-Langevin, Grenoble, France. ⁴TU München, Garching, Germany

The "zero" experiment for the P-odd asymmetry in the reaction $^6\text{Li}(n,\alpha)^3\text{H}$ has been carried out at the PF1B instrument of the ILL reactor. An obtained result is $\alpha_0 = -(0.0 \pm 0.5) \ 10^{-8}$. Earlier, the P-odd asymmetry coefficient of triton emission in main experiments has been measured to be equal to $\alpha_i = -(8.6 \pm 2.0) \cdot 10^{-8}$. Comparison of these two results shows that the effect of the P-odd asymmetry in the main experiment is really due to the studied reaction.

INTRODUCTION

Present experiment has been performed within a framework of program on determination of the weak meson-nucleon coupling constants, especially a pion constant f_{π} (in the literature f_{π} is also frequently called h_{π} or h^{l}_{π}), which is dominated by neutral currents in the nucleon-nucleon (NN) weak interaction.

Our current understanding of nuclear parity violation is far from complete [see, e. g. Refs. 1-3]. Still there is the question how to describe NN parity violation starting from the Standard Model. The difficulty is twofold: these experiments require high precision to discern the small parity violation signal, and in theory, the nonperturbative character of the quark-gluon dynamics makes a "first-principle" formulation of parity violation NN interactions as yet impossible. From the other hand, the study of PV phenomena is valuable for many reasons [see, e. g. Ref. 4]. First of them, it is only way to study the neutral weak interactions between quarks at low energy.

The most complete theoretical description of NN parity violation is an approach of Desplanques, Donoghue and Holstein (DDH) [2, 5]. According this model, at low energy the electroweak NN interaction is described in terms of the exchange of the lightest mesons π , ρ , ω . Weak NN-potential is parameterized by a set of weak meson-nucleon coupling constants: f_{π} , h_{ρ}^{0} , h_{ρ}^{1} , h_{ρ}^{2} , h_{ρ}^{1} , h_{ω}^{0} , h_{ω}^{1} , where subscript denotes the meson-mediator, and superscript is the amount of the isospin transfer (Δ T). All the physics of W and Z gauge bosons exchange between the quarks is hidden inside of these constants. The f_{π} constant is important because it is completely determined by electroweak neutral currents. DDH provided theoretical "reasonable ranges" and "best values" for the meson-nucleon coupling constants using SU(6) symmetry, constraints from non-leptonic hyperon decay data, and the quark model to estimate the experimentally unconstrained terms. There are other works devoted to estimations of the coupling constants [6 – 9]. Some of them give the couplings significantly differ from the DDH "best values". The experimental results from nuclear and hadronic PV measurements have been analyzed using the DDH framework, leading to constraints on combinations of the

that typically enter PV observables [1, 3, 10, 11]. The results are in general agreement with the DDH reasonable ranges, though the ranges themselves are quite broad, and the constraints from different experiments are not entirely consistent with each other. A particular quandary involves f_{π} The constants, which are dominated by charged currents, are in consistent with the DDH "best values". From other side, the neutral current f_{π} constant varies within a broad range from 0 up to $\sim 9 \cdot 10^{-7}$ for different experiments (the DDH "best value" $f_{\pi} = 4.6 \cdot 10^{-7}$). The strongest restrictions on the f_{π} value were obtained from the ¹⁸F experiments: $-1.0 \cdot 10^{-7} \le f_{\pi} \le 1.1 \cdot 10^{-7}$.

A meson-exchange model may be not a best representation of the NN interaction at the quark level. During last years the weak NN interaction effects have been analyzed actively in the framework of the effective field theory [3, 12, 13]. This approach is more general and systematic compared to the one-meson-exchange model. Nevertheless, the results of DDH still remain as the benchmark for the PV meson-nucleon couplings. Despite strong activity in this field, the progress in our understanding of weak NN interaction is still low. The reasons of it are both experimental and theoretical. The experimental problems are due to small size of P-odd effects for NN interaction and few-nucleon systems, the theoretical difficulties arise in trying to express the observables in terms of weak coupling constants, especially for the precise data from many-body systems. A conceptually simple observable sensitive to f_{π} is the P-odd asymmetry of emitted γ -quanta from the np \rightarrow d γ reaction with thermal polarized neutrons. Now, this experiment is in progress at LANSCE [14]. However, the expected effect is only $2 \cdot 10^{-8}$ in the best case, and reaction cross section is rather small \sim 0.2 b. According estimations, statistics accumulation takes not less than 1 year of beam time at the LANSCE instrument.

In our opinion, a very promising alternative approach is the reactions of slow polarized neutrons with light nuclei (A=6-10), in particularly, the $^6\text{Li}(n,\alpha)^3\text{H}$ and $^{10}\text{B}(n,\alpha)^7\text{Li}$ reactions. Light nuclei, including $^{6,7}\text{Li}$ and $^{10,11}\text{B}$, are well described in cluster and multycluster schemes [15, 16]. Then the task of calculation of the P-odd effects can be solved, using methods, applied for the few-nucleon systems. In Ref. [17] within the framework of such approach the P-odd correlation of the triton emission in the $^6\text{Li}(n,\alpha)^3\text{H}$ reaction with the thermal polarized neutrons was calculated, and expression in terms of weak meson constants has been received:

$$\alpha_{PNC}^{t} = -0.45 f_{\pi} + 0.06 h_{\alpha}^{0}. \tag{1}$$

Estimations show, that the possible contribution of neutral currents to the values (1) is about 30-70 %. Expected value of the P-odd correlations is about one order of magnitude more than those for the $n(p,\gamma)d$ reaction, and large cross sections with thermal neutrons (940 b) gives the possibility to get the P-odd asymmetry with an accuracy of ~10⁻⁸ for reasonable beam time.

EXPERIMENTAL SETUP AND TECHNIQUE. MAIN RUNS RESULT

We performed three series of experiments on the measurements of the P-odd correlation of the triton emission in the ${}^6\text{Li}(n,\alpha)^3\text{H}$ reaction, one at the Petersburg Nuclear Physics Institute (PNPI, Gatchina, Russia) at a vertical neutron beam of a PWR reactor [18] and two [19, 20, 21] at the PF1B instrument [22] of the reactor of the Institute Laue-Langevin (ILL, Grenoble, France). A multisection ionization chamber was used as a charged particle

detector [23]. The targets utilized practically whole neutron beam and convert it to the secondary particle emission. The current method of event detection was applied [24, 25]. The current in the detector circuit was converted to the voltage and accumulated by the capacitor of the integrator. The measured effect was determined as a subtraction of integrator voltages at different neutron polarization directions. The longitudinally polarized neutron beam was used in main runs. In order to remove the apparatus instabilities the neutron polarization was changed every 1-2 s. The detector was designed as a two-channel system. The signs of investigated P-odd effect in the detector channels was opposite at synchronous measurements. At subtraction of synchronously measured values of effect for each channel the compensation of the reactor power fluctuations was occurred. In order to remove an influence of the electromagnetic signals induced by other working facilities the direction of the guiding neutron spin magnetic field at the detector was changed periodically. The contribution of the induced signals was canceled at subtraction of effects at different guiding field directions.

About an ionization chamber and experimental technique one can find in Ref. [23]; a modernized data acquisition system is described in [19, 26]. The result of three main runs is [20, 21]

$$\alpha_{PNC}^{I} = -(8.6 \pm 2.0) \cdot 10^{-8}$$
.

We emphasise that the three stages of signal evaluation all work with differences:

- between variable parts of the signals (absolute effect of the P-odd asymmetry) for opposite neutron spin polarisations; these differences are calculated for every pair of measurements for both detectors.
- between the absolute effects for the two detectors (using compensation coefficient [18-21, 23, 26]). Since the P-odd asymmetries in the detectors have opposite signs, the effect is doubled. These differences are calculated for each direction of the guiding magnetic field.
- 3. between the effects for each direction of the guiding magnetic field. P-odd effects are added in this case, because they have opposite signs.

At each of the 3 stages of calculation described above we subtract values measured for two opposite conditions. Effects of equal sign and equal size thus cancel, and the asymmetry persists. A combination of the procedure for the compensation of the reactor power fluctuation, a periodic change of the guiding field direction and certain sequence of data acquisition and treatment allowed one to compensate all possible false apparatus effects.

Taking the third difference, for instance, any influence of the guiding magnetic field on the currents in the chamber, or changes in neutron absorption as a function of the field direction would cancel unless the effect is due to P-odd effects from impurity nuclei. This conclusion is valid as well for electromagnetically-induced false effects. Such influences were checked many times using electronic test signals as described in refs. [18-21]. For instance, a small effect was caused by switching the radio-frequency of the adiabatic spin-flipper on and off. After normalisation with the constant signal components and the coefficient of amplification the measured asymmetry contained a false shift of -(0.4±1.5)×10⁻⁹ [27]. This is considerably smaller than the experimental uncertainty. The identical treatment of the results for two detectors and for the two directions of guiding magnetic field thus allows us to avoid completely any influence of parasitic electromagnetic effects. The Earth's magnetic field and stationary magnetic fields from other experimental installations are not shielded. These magnetic fields could increase a contribution to the P-odd asymmetry of the left-right asymmetry, which has the same sign for opposite directions of the guiding magnetic field [28]. If the number of series for the opposite field directions is equal and the results of these

measurements are subtracted from each other, as described above, the contribution of this effect is suppressed.

The left-right asymmetry for the correlation $\vec{\sigma}_n \cdot [\vec{p}_n \times \vec{p}_t]$ cannot be compensated because of it also changes its sign with changing direction of the guiding neutron spin magnetic field at the detector. In the considered reaction this coefficient is $\vec{\sigma}_{LR} = (1.06 \pm 0.04) \cdot 10^4$ [29]. In order to reduce the effect of left-right asymmetry we align these three vectors within accuracy $\epsilon \sim 10^{-2}$, that can be readily achieved. Then, as it can be easily seen, the contribution of the left-right asymmetry decreases in proportion to ϵ^2 , falling below a value of 10^{-8} . The control experiments for the contribution of the left-right asymmetry are described in Refs. [18 - 21].

P-ODD EFFECTS CAUSED BY IMPURITY NUCLEI

Parity violating effects due to contaminant nuclei in the target cannot be compensated. A source of such background on the signal is the reaction of neutrons with the construction materials of the experimental installation, from which charged particles, γ -quanta and electrons from β -decay of radioactive nuclei are emitted. These false effects cannot be reliably estimated and cannot be tested in measurements with unpolarised neutrons.

A potential source of false effects is the asymmetry in the β -decay of nuclei with small lifetimes; in this case a non-zero nuclear polarisation after capture of a polarised neutron can persist until β -decay. The most abundant (~10%) impurity in the target material is ⁷Li, which produces ⁸Li ($T_{1/2} = 0.84$ s) by neutron capture. In [30] the β asymmetry of a pure ⁷Li sample was measured as $\alpha = -0.08 \pm 0.01$. In our present setup, with an average energy of ~ 13 MeV the β -particle passes through nearly the entire sensitive volume of the ionisation chambers. The absorption is low and the energy is released in forward and in backward chambers. The P-odd effect due to β -particles from ⁷Li in the targets was estimated to be below 3×10^{-9} . The small value is due to the small neutron cross section of ⁷Li compared to that of ⁶Li; due to small fraction of ⁷Li in the target; and due to the small absorption of β -particles in the chamber.

The ionisation chambers are assembled using materials containing fluorine F. The halftime of 20 F is $T_{1/2} = 11.16$ s; and the end-point energy of the β -particles is 5.4 MeV. One cannot exclude a P-odd effect with β -particles either. It is hardly possible to estimate the contribution of this reaction to the P-odd effect, given our poor understanding of the mass of 20 F and the flux of neutrons scattered through the construction materials of the chamber. It is also true that the degree of nuclear polarisation after capture is uncertain. Therefore this and similar effects were investigated by the zero experiment described below.

In the reaction 35 Cl(n,p) 35 S a P-odd proton emission asymmetry was found with a large coefficient of $a = -(1.5 \pm 0.3) \times 10^{-4}$ [31]. The proton path in aluminium is 1.5 mg/cm². Thus, these protons can not traverse the aluminium foils surrounding the targets (their thickness of 14 µm corresponds to 3.78 mg/cm²). Therefore protons from possible Cl impurities in the targets can not contribute to the P-odd effect. Even if the Cl admixture in the aluminium foils were as high as unrealistic 1%, the calculated ratio of chamber current due to protons to current due to tritons from 6 Li would be as low as $\sim 5.7 \times 10^{-10}$.

Calculations showed that an additional P-odd asymmetry due to γ -quanta from all known cases is lower than 10^{-10} . The P-odd asymmetry for β -decay of various nuclei with long half-life in the construction materials (for instance, β -decay of aluminium) is not

significant either, because those nuclei decay within a few minutes, and the interaction of the nuclear magnetic moment with the atomic environment immediately destroys nuclear orientation produced by polarised neutron capture.

As it is difficult to provide a complete estimate of all contributions to the P-odd effect from impurity nuclei, we performed a control experiment.

"ZERO EXPERIMENT"

Studies of tiny asymmetries usually include a control measurement ("zero experiment") with a polarised neutron beam, in which the products of the reaction are not detected.

Total absorption of the tritons and α particles is provided by additional 20 μ m thick aluminium foil covering of the targets. All results in this section are given normalised to the constant component of the detector signal in the main experiment and to the solid angle and neutron polarisation, in order to make them directly comparable with the asymmetry in the main experiment. The result obtained at PNPI in Gatchina was $a_0 = (2.0\pm1.7)\times10^{-8}$ [18]. The zero-test carried out at the PF1B neutron beam at the ILL was performed with a neutron polarisation of more than 94% and yielded [27]:

$$a_{0-\text{test}} = (0.0 \pm 0.5) \times 10^{-8}$$
 (12)

Note that this measurement also tests for influences of electronics and noise from the flipper. In addition, we also carried out an asymmetry measurement with the neutron beam switched off which is sensitive to these latter effects, only. The result is [20, 21]:

$$a_{\text{noise}} = -(0.6 \pm 0.5) \times 10^{-8}$$
 (13)

Hence, all these false effects are at least 10 times smaller than the observed asymmetry.

FINAL RESULTS

Table 2 shows the results of the three measurements of the P-odd asymmetry coefficient in the reaction $^6\text{Li}(n,\alpha)^3\text{H}$ obtained by the authors. The results in tables 1 and 2 are corrected for the neutron polarisation P and for the effective solid angle of triton detection Ω .

Table 2.

Tubio 2.					
	$P\Omega$	$\alpha_{_{P-odd}}$	α_{0-test}	α_{noise}	
PNPI, vertical channel	0.66	-(5.4±6.0)·10 ⁻⁸	(2.0±1.7)·10 ⁻⁸		[18]
ILL, PB1B beam	0.66	-(8.1±3.9)·10 ⁻⁸		(0.6±0.4)·10 ⁻⁸	[19]
ILL, PF1B beam	0.70	-(9.3±2.5)·10 ⁻⁸	(0.0±0.5)·10 ⁻⁸	-(0.6±0.5)·10 ⁻⁸	[20, 21]
Average		-(8.6±2.0)·10 ⁻⁸	(0.2±0.5)·10 ⁻⁸	(0.1±0.3)·10 ⁻⁸	

We measured the parity-violating (P-odd) triton emission asymmetry coefficient a_{P-odd} in the $^6\text{Li}(n,\alpha)^3\text{H}$ reaction with polarised cold neutrons. Taking into account an additional test for a false asymmetry due to eventual target impurities ("zero test") we obtain the final value for this experiment:

$$a_{\text{P-odd}} = (-8.8 \pm 2.1) \times 10^{-8}$$

We analyse this result within the nuclear cluster model. Using the formula (3) for the relation of the P-odd effect with the effective weak couplings and supposing that the charged weak current constant is given by the DDH best value $h_{\rho}^0 = -11.4 \times 10^{-7}$, the neutral weak constant f_{τ} and its uncertainty would be given by:

$$f_{\pi} \approx (0.4 \pm 0.4) \times 10^{-7}$$
.

Keeping in mind that the weak constant has to be positive, we obtain the following constrain for the neutral weak constant at 90% confidence level:

$$0 \le f_{\pi} \le 1.1 \times 10^{-7}$$
.

This result agrees with the most precise value obtained in the measurement of circular polarization of γ -quanta in the reaction with ¹⁸F [32]:

$$f_{\star} = (0.3^{+1.0}_{-0.3}) \times 10^{-7}$$

However, it contradicts to the "best value" 4.6×10⁻⁷ for the weak constant in the DDH model. This work is supported by the Russian Foundation for Basic Research, Grant No. 07-02-00138-a.

References.

- 1. E. G. Adelberger and W. C. Haxton. Annu. Rev. Nucl. Part. Sci. 35 (1985) 501.
- 2. B. Desplanques. Phys. Rep. 297 (1998) 1.
- 3. M. J. Ramsey-Musolf and S. A. Page. Annu. Rev. Nucl. Part. Sci. 56 (2006) 1.
- 4. W. M. Snow. J. Res. Natl. Inst. Stand. Tech. 110 (2005) 189.
- 5. B. Desplanques, J. Donoghue, and B. Holstein. Ann. Phys. 124 (1980) 449.
- 6. V. M. Dubovik, S. V. Zenkin. Ann. Phys. 172 (1986) 100.
- 7. N. Kaiser and U.-G. Meissner. Nucl. Phys. A510 (1990) 759.
- 8. E. M. Henley, W.-Y. Hwang, and L. Kisslinger. Phys. Lett. B 367 (1996) 21.
- 9. G. A. Lobov. Phys. At. Nucl. 65 (2001) 561.
- 10. W. C. Haxton, C.-P. Liu, M. J. Ramsey-Musolf. Phys. Rev. Lett. 86 (2001) 5247
- 11. W. C. Haxton, C.-P. Liu, M. J. Ramsey-Musolf. Phys. Rev. C 65 (2002) 045502
- S.-L. Zhu, C. M. Maekawa, B. R. Holstein, M. J. Ramsey-Musolf, U. van Kolck. Nucl. Phys. A748 (2005) 435.
- 13. C.-P. Liu. Phys. Rev. C 75 (2007) 065501.
- S. A. Page et. al. (NPDG collaboration). J. Res. Natl. Inst. Stand. Tech. 110 (2005) 195.

- 15. V.I. Kukulin, V. M Krasnopol'ski, V. T. Voronchev, P. B. Sazonov. Nucl. Phys. A 417 (1984) 128.
- 16. Toshitaka Kajino, Takehiro Matsuse, Akito Arima. Nucl. Phys. A 413 (1984) 323.
- 17. N. N. Nesterov, I. S. Okunev. JETP Letters 48 (1988) 573.
- 18. V. A. Vesna, Yu. M. Gledenov, I. S. Okunev, Yu. P. Popov, E. V. Shul'gina. Phys. At. Nucl. (Yad. Fiz.) 59 (1996) 23.
- 19. Yu. M. Gledenov, V. A. Vesna, V. V. Nesvizhevsky, A. K. Petukhov, P. V. Sedyshev, T. Soldner, E. V. Shul'gina, O. Zimmer. ISINN-11. (Dubna: JINR, 2004) E3-2004-9, 26.
- 20. A. Vesna, Yu. M. Gledenov, V. V. Nesvizhevsky, A. K. Petukhov, P. V. Sedyshev, T. Soldner, E. V. Shul'gina, O. Zimmer. JETP Letters 82 (2005) 519.
- 21. A. Vesna, Yu. M. Gledenov, V. V. Nesvizhevsky, A. K. Petukhov, P. V. Sedyshev, T. Soldner, E. V. Shul'gina, O. Zimmer. ISINN-14. E3-2007-23 (Dubna 2007) 243.
- 22. H. Abele, D. Dubbers, H. Häse et al. Nucl. Instr. and Meth. A 562 (2006) 407.
- 23. Yu. M. Gledenov, I. S. Okunev, S. S. Parzhitskii, E. V. Shul'gina, V. A. Vesna. NIM A350 (1994) 517.
- 24. V. M. Lobashev. Phys. Atom. Nucl. 5 (1965) 957.
- 25. V. M. Lobashev, V. A. Nazarenko et. al. Phys. Lett. B 25 (1967) 104.
- 26. V. A. Vesna, Yu. M. Gledenov, V. V. Nesvizhevsky, A. K. Petukhov, P. V. Sedyshev, T. Soldner, E. V. Shulgina. Bulletin of the Russian Academy of Sciences: Physics. 67 (2003) 125.
- 27. V. A. Vesna, Yu. M. Gledenov, V. V. Nesvizhevsky, A. K. Petukhov, P. V. Sedyshev, T. Soldner, E. V. Shulgina. PNPI Preprint-2697 (Gatchina 2006), (in Russian).
- 28. V.A. Vesna, Yu.M. Gledenov et al., Phys. Atom. Nucl. 59(1) (1996) 19.
- 29. N.V. Borovikova et al., JETP Letters. 30 (1979) 495.
- 30. Y. G. Abov et al., Nucl. Phys. 34 (1962) 505.
- 31. A. Antonov, V.A. Vesna et al., Phys. Atom. Nucl. 48 (1988) 305.
- 32. S. A. Page, H. C. Evans et al., Phys. Rev. C35 (1987) 1119.
- 33. Igashov S.Yu., Sinyakov A.V., Tchuvil'sky Yu.M. ISINN-11. (Dubna: JINR, 2004) E3-2004-9, 34.

Научное издание

NEUTRON SPECTROSCOPY, NUCLEAR STRUCTURE, RELATED TOPICS

XV International Seminar on Interaction of Neutrons with Nuclei Proceedings of the Seminar

НЕЙТРОННАЯ СПЕКТРОСКОПИЯ, СТРУКТУРА ЯДРА И СВЯЗАННЫЕ ВОПРОСЫ

XV Международный семинар по взаимодействию нейтронов с ядрами Труды семинара

Ответственный за подготовку сборника к печати А. М. Суховой.

Сборник отпечатан методом прямого репродуцирования с оригиналов, предоставленных оргкомитетом.

E3-2008-26

Получено 18.02.2008. Подписано в печать 18.03.2008. Формат 60×90/16. Бумага офсетная. Печать офсетная. Усл. печ. л. 21,37. Уч.-изд. л. 38,04. Тираж 180 экз. Заказ № 56086.

Издательский отдел Объединенного института ядерных исследований 141980, г. Дубна, Московская обл., ул. Жолио-Кюри, б. E-mail: publish@jinr.ru www.jinr.ru/publish/